Schlumberger

Fundamentals of Borehole Seismic Technology

Schlumberger

Fundamentals of Borehole Seismic Technology

Editors

Alejandro Martinez Pereira

Michael Jones

Schlumberger
225 Schlumberger Drive
Sugar Land, Texas 77478

www.slb.com

Technical Editor: Joyce M. Evans
Production Layout: Daigrafiks
Produced by Schlumberger Oilfield Marketing Communications

09-FE-00

ISBN-13: 978-097885307-5

ISBN-10: 097885307-5

Contents

Foreword

Borehole seismic data provides the critical depth and velocity parameters needed to link surface seismic data with downhole log and well data.

Borehole seismic tools have evolved from single-component sensors to modern seismic array tools. These modern tools, when combined with the latest technology in seismic source quality, navigational positioning, and computational abilities, can deliver in real time high-resolution borehole seismic images that extend beyond the wellbore or into the interwell volume to r duce risk in drilling and development decisions. This book provides a review of the latest tools, tech nologies, and applications of borehole seismic technology. A discussion of survey des gn and modeling is also provided.

Fundamentals of Borehole Seismic Technology is the second of a series of Sch umberger reference books produced for current and future oilfield technical professionals.

Catherine MacGregor
President, Wireline
Clamart, France
May 2010

Acknowledgments

This book project originated under the sponsorship of Wireline Marketing Communications Manager Martin Isaacs and Wireline Geophysics Domain Champion Michel Verliac. Alejandro Martinez Pereira and Michael Jones shared the enormous task as editors as well as contributing authors. Alejandro Martinez Pereira provided overall project coordination and, together with Michael Jones, designed chapter content and integrated text and graphics from contributing authors. Their dedication and long-standing support and that of their colleagues and management are greatly appreciated.

Thanks are extended to all chapter coauthors: Steve Horne, Michael Jones, Joël Le Calvez, Scott Leaney, Gwenola Michaud, Alejandro Martinez Pereira, Lisa Stewart, John Tulett and J Craig Woerpel. Special thanks are also extended to contributors, who provided specialized ontent that was incorporated into the text, and to the technical reviewers that collectiv ly improved the final product. They are gratefully acknowledged in the list below.

In the final stages of the project, Wireline Geophysics Domain Champi n Henry Menkiti selflessly provided critical support that facilitated completion of the project. His assistance is g eatly appreciated.

Above all, we thank the Schlumberger OMC editorial staff: Te hnical Editor Elsa Kapitan-White and Editorial Advisor Gretchen Gillis; their continual guidance, experience, and suggestions enhanced communication and effected improvements in the fina manuscript. They conducted the final editorial review and helped to polish the completed m nuscript for final production.

Chapter 1

- Reviewers: Gretchen Gillis and John Tulett

Chapter 2

- Stewart Thomas Taylor: Drill-Bit Seismi * survey
- Reviewers: Joël Le Calvez, John Tule t and Les Nutt

Chapter 3

- Olimpiu Adrian Catoi: High-temperature analog tool data
- Emmanuel Coste: Appl cations of the Omega Lok tool
- Cengiz Esmersoy: Seismi acquisition while drilling (seismicVISION* system)
- Ahmed Shabbir Non mpulsive sources, controllers, and navigation
- Reviewer: Peter MacLeod

Chapter 4

Revi wers: Ed Knight, Henry Menkiti, and Ric Smith

Ch pter 5

- Reviewers: Philip Armstrong and Alejandro Martinez Pereira

Chapter 6

- Allan Campbell: Near-salt and subsalt imaging
- Marcia Couëslan: Time-lapse seismic data

- Hugues Djikpesse: Interferometry
- Nobuyasu Hirabayashi: Migration
- Reviewers: Philip Armstrong and Igor Borodin

Chapter 7

- Cengiz Esmersoy: Seismic while drilling
- Andy Hawthorn: Seismic while drilling
- Hari Kurniawan: Geosteering
- Stewart Thomas Taylor: Drillbit seismic surveys
- Reviewers: Philip Armstrong, Scott Dingwall, Roger Griffiths, and Henry Menkiti

Chapter 8

- Reviewers: Shawn Maxwell and William Underhill

Chapter 9

- Reviewers: Philip Armstrong and Mark Puckett

We are grateful to the publishing companies and organizations that gave permission to reproduce figures from their publications:

American Association of Petroleum Geologists (*AAPG Bulletin*)
American Geophysical Union (*Journal of Geophysical Research*)
European Association of Geoscientists & Engineers (EAGE) (*First Break*)
Schlumberger (*Oilfield Review, The Technical Review*)
Seismological Society of America (*Bulletin of the Seismological Society of America*)
Society of Exploration Geophysicists (SEG) (*Geophysics, The Leading Edge*)
Society of Petroleum Engineers (SPE) (*Journal of Petroleum Technology*)
Society of Petrophysicists and Well Log Analysts (SPWLA)
US Geological Survey

1 Borehole Seismic Technology

Alejandro Martinez Pereira

1.1 Introduction

Geophysics is a branch of geology that studies the physics of the Earth, especially its electrical, gravitational, and magnetic fields, and the propagation of elastic (i.e., seismic) waves within it. A major part of the search for oil and gas is the search for suitable geological features in which hydrocarbons may be trapped. Such features may be 1 to 100 km^2 in extent and may occur at subsurface depths of 1 to 10 km.

Seismic surveys are acquired by the generation of seismic waves and the recording of the waves (i.e., reflection waves) interacting from subsurface geologic horizons. These surveys allow scientists to map the subsurface distribution of different types of rocks and the fluids they contain.

Seismic surveys can be divided into two main categories—surface seismic surveys and borehole seismic surveys. The principle is the same for both except that, in surface seismic, the source and receivers are positioned on the surface or close to it; whereas, in borehole seism c, sources are typically located at surface and the re ivers are located in the well. Other configurations ar possib e. In fact, drillbit noise is used as a borehole seismic source with receivers placed at surface. The s ismic source can be anything that generates a seismic w ve— ypically, dynamite and vibrators are used onshore, nd airguns are used offshore—although ther are ot er sources that achieve specific source characteris ics

Figure 1-1 illustrates how the wave train recorded by the receivers can be urned into an image of the subsurface structures through processing. Data from Wells A, B, and C were acquired using the borehole seismic technique; the remain er of the data was acquired as a surface seismic s rvey.

To nder tand reservoirs requires the integration of spatiall exten ive surface seismic surveys with verti- c lly sampled logs and other well data. Borehole seismic surveys uniquely forge this link by quickly providing high-resolution, calibrated answers for drilling and development decisions.

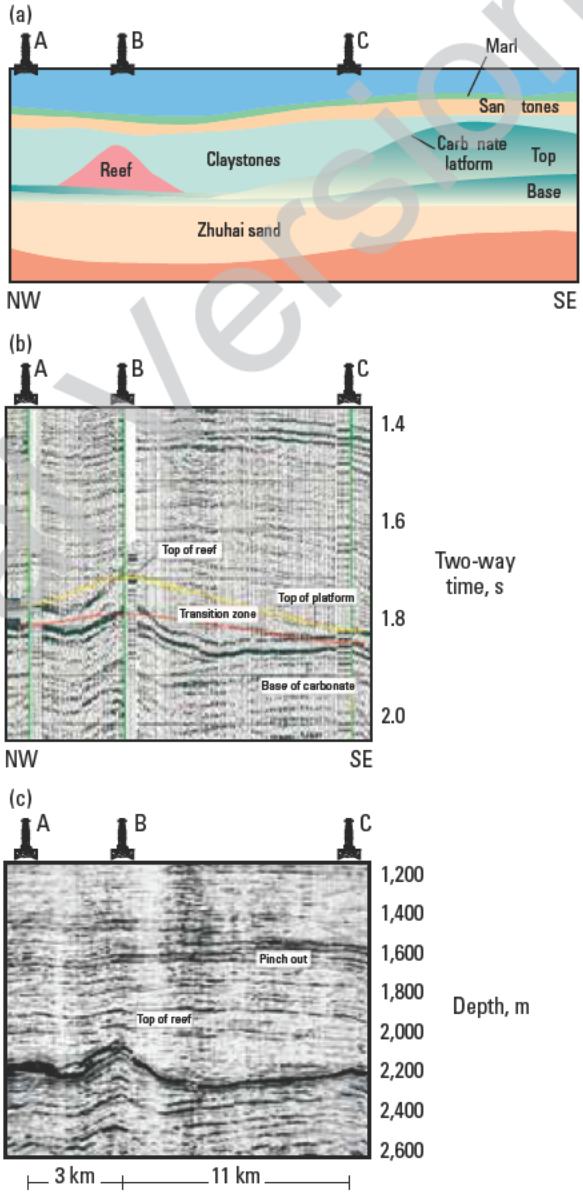

Figure 1-1. Seismic interpretation of the subsurface. A schematic geologic cross section (a) shows approximate locations of wells and formation boundaries. A seismic section (b) shows actual well locations and formations in the time domain; borehole seismic data is shown in the well profiles. The seismic section was converted to the depth domain (c) by using borehole seismic information acquired in Wells A, B, and C. Schematic in (a) was modified to align horizontal scale with seismic. (From Schlumberger, 1992; this graphic is copyright Schlumberger, Ltd. Used with permission.)

1.2 Overview of borehole seismic technology

The value of any oilfield technology can be expressed in terms of its ability to reduce risk. Borehole seismic surveys deliver considerable value to exploration and production (E&P). First, they provide vital depth and velocity parameters to surface seismic surveys, matching seismically imaged layers to precise borehole depths. Second, they provide high-resolution images that extend hundreds of meters around the wellbore and into the interwell volume.

In addition to providing structural and stratigraphic information, borehole seismic technology can also help to monitor fluid movement and predict lithology and rock or reservoir properties when calibrated with logs, core, production data, or other information. Geological interpretations made from only surface seismic data are limited: the exact velocity, frequency changes, amplitude losses, and phase shifts that occur in the seismic wavefield as it travels through the Earth cannot be determined because only the upgoing waves are recorded.

Seismic surveys are acquired for various purposes (Table 1-1), and although surveys vary depending on the objectives, the basic principle is the same. Typically, a seismic source positioned on surface is triggered to produce a wave that propagates into the Earth as direct waves from the surface source and as downgoing multiples, and it returns back toward the surface as primary reflections and upgoing multiples. The borehole seismic record is recorded by the geophones placed in the borehole. The record contains information about the reflection and transmission properties of the Earth, and its coverage depends on the geometry of the survey and the structure near the well. Figure 1-2 shows schematically the typical surface layout of a seismic survey and a sketch of the downhole seismic acquisition equipment. A summary of some of the survey types is found in Chapter 2 with detailed explanation of each type in the chapters that follow.

1.3 Schlumberger involvement in borehole seismic technology

Schlumberger launched the wireline-logging industry in 1927. Borehole seismic acquisition, later introduced in the 1970s, was a natural extension of the original technique.

The first borehole seismic method was a basic well-tie technique designed to bring time-based surface seismic sections into the depth domain. From this humble beginning, geophysicists have since developed a wide variety of sophisticated calibration techniques. Drillers now update the drillbit location relative to seismic sections using time-depth information acquired by borehole seismic tools deployed while drilling. Geophysicists use log and borehole seismic data to predict seismic response and to plan more informative surface seismic surveys.

Table 1-1. Classification of Borehole Seismic Applications

Surface Seismic Helper	Stand Alone Product	Other
Checkshot or sonic calibration	Salt-proximity survey	Inversion
Zero-offset VSP†	Offset VSP for imaging	Seismic while drilling
Q analysis	Converted-wave imaging from offset VSP	Modeling
Multiple identification	Walkaway VSP for imaging	Time lapse and fluid monitoring
AVO‡ walkaway	Prediction ahead of the bit	Permanent sensors
Anisotropy (TI)§	Shear anisotropy for fractures	Logging-while-drilling VSP
Phase analysis	Crosswell tomography	Hydraulic fracture mapping
Matched filter	Dip determination from VSP	
VSP-guided processing for surface seismic		
VSP traveltimes to migrate seismic		

† Vertical seismic profile.
‡ Amplitude variation with offset.
§ Transverse isotropy.

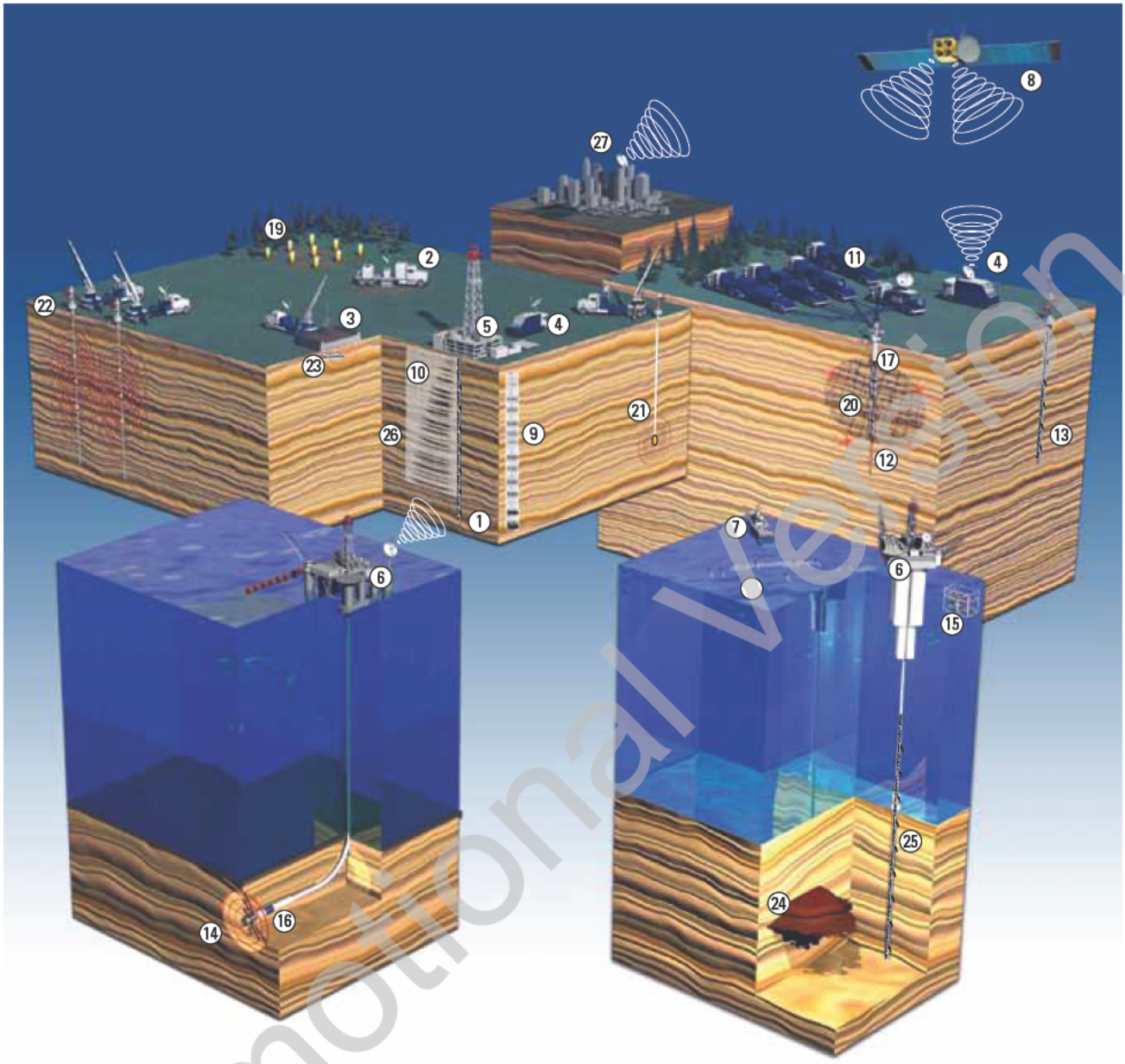

1. VSI* tool
2. Vibrator
3. Airgun
4. Wirelin truck
5. Land rig
6. Offs ore rig
7. Vessel
8. Satellite
9. Corridor stack
10. Offset image
11. F acturing crew
12. Hydraulic fracture monitoring
13. StimMap* stimulation diagnostics
14. Drill-Bit Seismic* VSP
15. Marine airgun
16. seismicVISION* service with drillbit source
17. Microseismic reservoir monitoring
18. Marine seismic acquisition
19. Dynamite shots
20. Permanent monitoring system
21. Downhole source
22. Crosswell survey
23. Buried airgun
24. 3D VSP volume
25. Geomechanics application: overpressure
26. Look-ahead capabilities
27. Processing center

* Mark of Schlumberger

Downhole seismic tools have evolved from single-component sensor technology to modern seismic array tools. For Schlumberger, the foundation for high-quality seismic data from the borehole lies with the VSI* Versatile Seismic Imager tool. This wireline tool consists of up to 40 multicomponent sensor modules with superior data-quality capabilities and high operational efficiency.

Recent developments in seismic sources, especially source controllers such as the TRISOR* acoustic source control element of the TRILOGY* onboard data management system, provide more predictable and consistent source performance, rendering superior signal quality. The TRISOR source controller has been perfected during 10 years of development by WesternGeco and is now regarded as a superior seismic source controller in the marine environment.

Advances in navigation have made it possible to accurately control the position of seismic sources both in onshore and offshore environments. With the highly advanced SWINGS* seismic navigation and positioning system, it is now possible to achieve a static positioning accuracy better than ±1 m. Complicated survey geometries, such as walkaways, deviated-well vertical seismic profiles (VSPs), 3D VSPs, and simultaneous acquisition of surface and borehole seismic data are now routinely used in seismic exploration, as described in later chapters.

The advent of computers allows geophysicists to deliver high-quality VSP results quickly. When required, data from large surveys can be compressed to reduce data-transmission times from wellsite to computing center to allow near-real-time data processing.

The combination of the VSI acquisition tool, TRISOR in-sea source controller, SWINGS navigation and positioning system, and onsite processing capability forms part of the suite of services known as the Q-Borehole* integrated borehole seismic system, which leverages the latest technology for downhole and surface hardware, advanced processing software, and people to deliver the most optimized and best-in-class borehole seismic solutions. Equipped with these improved tools, geophysicists now acquire high-quality borehole seismic data more cost-effectively than before. Specially trained borehole seismic personnel are available to perform sophisticated processing, such as inversion, on the rig. These tools have been deployed in many regions and environments worldwide.

1.4 Quality, Health, Safety, and Environment (QHSE) management in borehole seismic operations

Borehole seismic service provides critical geophysical information to the oil industry with regard to hydrocarbon reservoirs. The operation involves the use of complex and potentially dangerous surface and downhole equipment.

Schlumberger has devised standards for its wireline borehole seismic operations that are conducted to mitigate the risks to a state "as low as reasonably practical" (ALARP) while ensuring that the highest quality product is delivered. These standards define the requirements and minimum acceptable criteria for conducting borehole seismic service operations worldwide. The standards are used in conjunction with extensive borehole seismic service procedures, guidelines, and checklists that adhere to international standards and the seismic industry's best practices.

In terms of quality, a clearly defined line of responsibilities ensures correct and prompt delivery of services from line management, the seismic specialists, and support personnel. Seismic operations assessments are an integral part of the QHSE management system, allow the identification of potential problems of borehole seismic service operations, assessment of their impact and corrective actions to be taken before any incident occurs that could jeopardize the HSE of personnel or affect the quality of the data product. These assessments involve periodic review of various aspects concerning people (i.e., training), seismic equipment (i.e., type, age, quantity, safety compliance, maintenance), and processes (i.e., job planning, log quality control).

All personnel involved with borehole seismic service operations receive formal training and are certified competent on the equipment and systems that they are operating.

Seismic equipment and its accessories are operated, maintained, and tested regularly in accordance with the manufacturers' specifications. Documentation records of testing and re-certification of equipment are maintained and inspected regularly.

Schlumberger ensures minimum environmental impact through its borehole seismic service operations, with consideration given to the safe transportation of seismic equipment and pressurized systems and to mitigation plans for oil spills and disturbance of local fauna.

1.5 Overview of *Fundamentals of Borehole Seismic Technology*

This book is the second in a series of reference books about wireline logging technologies for current and future oilfield technical professionals. A general knowledge of the oil field and of geophysics is assumed. References are supplied so that readers can find additional detailed information elsewhere.

Chapters 2 and 3 introduce geophysical principles, field technology, and operational techniques. Chapters 4 through 8 illustrate seismic methods and applications. Chapter 9 is a discussion of survey design and modeling.

1.6 References

Schlumberger: "Reservoir Appraisal in the South China Sea," *Oilfield Review* (April 1992) 4, No. 2, 4–7.

Geophysical Principles of Borehole Seismic Data

Lisa Stewart, Michael Jones, Alejandro Martinez Pereira, and John Tulett

Borehole seismic surveys are among the most versatile of all downhole measurement techniques used in the oil field. The various types of waves generated and survey geometries achieved combine to deliver information about reservoir depth, extent, and heterogeneity as well as about hydrocarbon content, rock mechanical properties, pore pressure, enhanced-oil-recovery progress, elastic anisotropy, natural-fracture orientation and density, and induced-fracture geometry. Borehole seismic surveys, or VSPs, reduce the uncertainty of reservoir properties near the borehole. With their measurement scale between those of well logs and surface seismic surveys, VSPs extend near-wellbore observations, explore interwell volumes, and link time-based surface seismic images with depth-based logs.

2.1 Introduction to seismic methods

Seismic imaging has become the single most important formation evaluation technique used to find and delineate reservoirs. The advent of three-dimensional (3D) seismic data and seismic interpretation workstations introduced substantial improvements in reservoir imaging such that thin, 10-m beds buried 3 km (or deeper) can be imaged. As a result, seismic data has become an indispensable source of information for exploration and field delineation. Seismic interpretation is one of the first steps in exploration. The identified targets can be mapped and characterized with seismic attributes. When confirmed by exploration wells, reservoirs of commercial interest are drilled and the field is developed on the basis of the information obtained from surface seismic data.

Borehole seismic acquisition—the deployment of receivers and sources in a borehole—opens the door to a wide variety of new survey geometries that can address specific questions about the seismic image or about the properties of the rock represented in the image. Figure 2-1 shows schematics of the most common geometries used in borehole seismic acquisition. Borehole seismic data provides the bridge between the directly measured data of well logs and the remote-sensing data acquired by the surface seismic method.

The term borehole seismic data covers all the applications of seismic techniques in which either the source or the geophone, or both, are deployed below the surface of the Earth. The conventional VSP, with an array of geophones along the borehole and the source on the surface, is the most familiar example, but the variety of possible arrangements, borehole orientations, and objectives is much wider than this. This change in viewpoint opens up a wealth of new possibilities that are not available from data collected at the surface.

The seismic method measures traveltimes, amplitudes, and direction (polarization) of elastic waves propagating through the subsurface. Unfortunately, initial surface-acquired seismic maps are scaled in time units, whereas reservoir evaluation and well-construction procedures require reliable subsurface structure and property maps in depth units. In its traditional and most basic role, borehole seismic data establishes an absolute link between seismic data in time and well logs in depth. Surface seismic data processing parameters and algorithm selection can be calibrated using borehole seismic measurements, and the reliability of the resulting image and attribute maps can be better assessed quantitatively.

Borehole techniques offer improved image resolution compared with that of surface seismic data. The fine details are recovered because borehole seismic sensors are deployed below unconsolidated, absorbing layers and close to the zones of interest. This brings resolution to the potentially costly and challenging imaging and interpretation problems in deep water and around salt structures as well as to common resolution and wavelet phase problems.

Stand-alone imaging surveys are not confined to the exploration stage of the reservoir but are used increasingly during reservoir development. Offset, walkaway, and 3D VSP surveys (in which sources are stepped away from the borehole receivers) provide high-resolution seismic imaging around wellbores and offer an efficient means to acquire or calibrate time-lapse surveys.

Borehole techniques routinely record high-quality shear-wave data. Shear-wave images are of even higher definition than conventional compressional images and

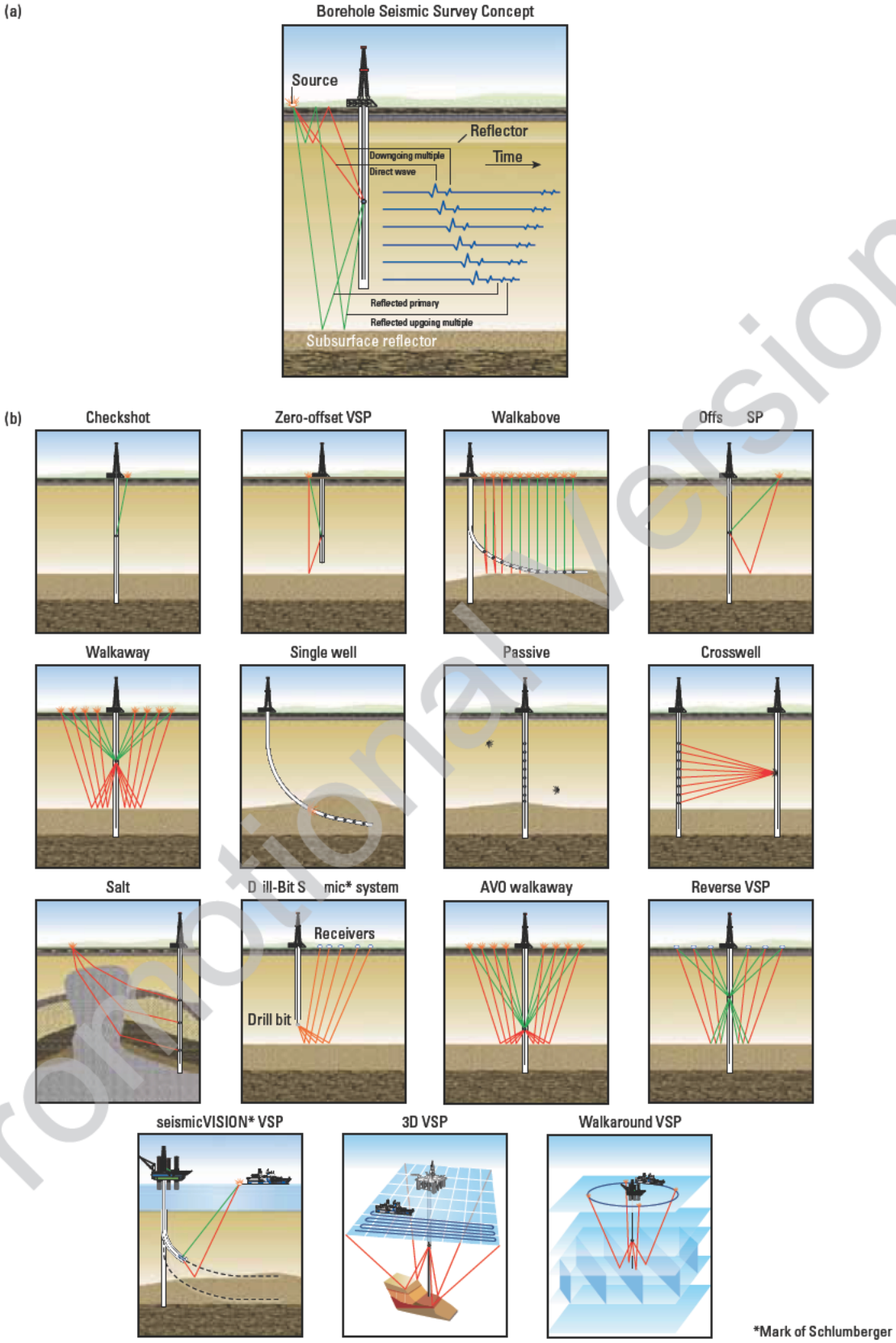

Figure 2-1. Representation of a VSP survey (a). Borehole seismic surveys can have a variety of geometries (b). (Adapted from Hope *et al.*, 1998; this graphic is copyright Schlumberger, Ltd. Used with permission.)

are critical for calibration of multicomponent surface seismic data. Many reservoirs that are below the necessary thickness to be directly imaged by compressional waves, or that lack the compressional impedance contrast to be visible, can be illuminated by the direct or converted shear waves. The relationship between compressional and shear responses for a reservoir is the key to any direct interpretation of reservoir fluids and to the distinction between fluids and lithology.

Reservoir evaluation can be enhanced by exploiting the seismic amplitudes. One of the key applications is to discriminate between reservoir fluids and lithologies. Ultimately, the goal is to invert the borehole seismic data for reservoir properties such as porosity, permeability, gas content, or oil/water contacts.

Borehole seismic techniques can be applied while the well is being drilled. Seismic-while-drilling techniques deploy sensors within drillpipe or behind the drill bit or even use the drill bit itself as the seismic source to allow data acquisition during the drilling process. Of all the well log measurements, only borehole seismic measurements have look-ahead and look-around capabilities—structure and formation attributes far below and around the drill bit can be mapped as drilling progresses. The goal of all seismic-while-drilling methods is to optimize the drilling process by reducing risk and uncertainty. Exploration risk can be reduced by providing time-to-depth conversion in real time and by optimally positioning the wellbore trajectory relative to the surface seismic data. These surveys help steer the drill bit to prevent missing target locations. Drilling risk can be managed by the real-time prediction of hazardous drilling conditions, such as excess pore pressure, or by predetermination of optimal casing depths.

During the well completion stage, passive seismic monitoring methods can be employed. Continuous listening for acoustic emissions when a well is hydraulically fractured shows in real time where the fractures are propagating. Vital decisions could be made on-the-spot during fracture treatments. Future well placement and completion strategies benefit from these surveys as well.

In addition to continuous reservoir pressure, temperature, and flow measurements, permanent downhole seismic installations are increasingly being used during reservoir production. The prime application employed is to monitor reservoir properties and fluids to identify bypassed reservoir compartments. A fully instrumented reservoir will allow the recording of time-lapse surveys to image fluid movement around the well and to calibrate time-lapse surface seismic data with known changes around the well. These surveys use permanently deployed sensors in the same locations to image any genuine change in seismic signal over a period of time. Careful completion planning plays an important role in order to install this equipment and to operate without interfering with actual well operations, which is often an obstacle to greater use of this borehole seismic technique.

2.2 Surface seismic versus borehole seismic data

Borehole seismic techniques address one of the major constraints of conventional surface seismic measurements: the requirement for sources and receivers to be positioned on the surface or close to it. This imposes three important limitations on the data

- Time and depth cannot be directly related. Because the transducers are restricted to the surface, any traveltime measurement for a reflection event requires knowledge of the velocity along the raypath to determine the depth. It is possible to estimate the velocity from a variable-offset dataset, but only at the expense of making numerous assumptions about the homogeneity of the velocity field and the isotropy (or anisotropy) of the intervening medium.
- Only the upgoing body waves can be recorded. The wavefield propagating in the Earth in response to an input signal is composed of various elements, some traveling upward, some downward. The inability to record both components of the wavefield means:
  - The shape of the propagating wavelet must be estimated by statistical methods.
  - Propagation effects as the seismic pulse propagates through the Earth (attenuation and dispersion) cannot be measured.
  - Processing imperfectly removes multiple reflections from the seismic record.
  - The wavelet phase is generally unknown after processing.
- Resolution is limited in time and offset. Vertical resolution is limited by the loss of high frequencies as the seismic energy travels from the reflector back to the surface. Horizontal resolution is limited by the size of the Fresnel zone at the target depth.

When the seismic receivers or sources are deployed as a subsurface array along the wellbore, most of the restrictions listed above are effectively eliminated. Figure 2-2 illustrates schematically the difference in source-receiver geometry between surface seismic and common VSP surveys.

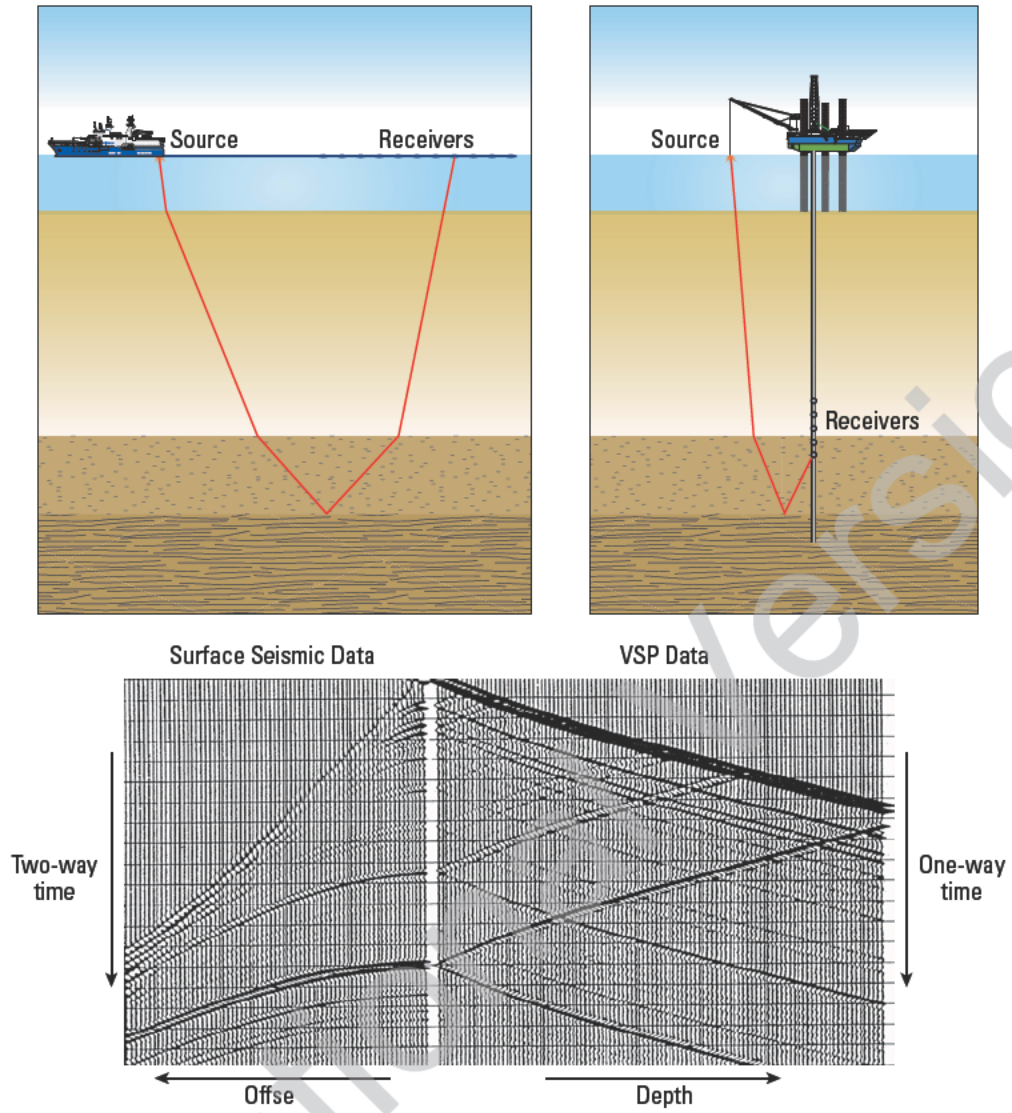

Figure 2-2. Comparison of surface and borehole seismic survey geometries (top). (From Arroyo *et al.*, 2003; this graphic is copyright Schlumberger, Ltd. Used w th permi sion.) Comparison of surface seismic data and VSP data (bottom) shows differences in time, depth and offs t pa ameters.

Traveltime from a s rface source to a receiver array in a borehole can be mea ured directly, thus providing a reliable time depth elation. At each receiver sensor depth in the well, both the upgoing and the downgoing wa fields are recorded. Because of the acquisition geomet y, energy belonging to the two propagation di e tions may be separated easily. The downgoing wavefield is the measured far-field signature as a function of geophone depth. It contains all the multiples generated between the source and receiver and, therefore, can be used to recover any desired wavelet phase and to collapse the multiples.

Receiver sensors placed downhole can record seismic data at higher frequencies. The greatest loss of high frequencies in the seismic wavelet occurs in the shallowest part of the Earth. Because the signal has to traverse this part of the Earth only once for a VSP dataset, instead of twice as in the case of surface

seismic acquisition, the frequency content is higher, thus enhancing the vertical resolution. In addition, with the geophone located closer to the target zone, horizontal resolution is further improved.

Surface geophone or hydrophone signals are contaminated by ambient noise such as wind, human activities, and sea swell. For the wellbore receivers in a VSP dataset, the environment is quiet, the sensors are coupled more strongly to the formation or well casing, and near-surface and elevation statics do not degrade the downhole data.

2.3 Wave types

The main type of waves generated and recorded in borehole seismic surveys are body waves emitted by point sources or frequency-sweep sources; they consist of compressional, or primary (P), waves and shear, or secondary (S), waves. These waves propagate from man-made sources near the surface to borehole receivers at depth. (For more information on sources and downhole hardware, see Chapter 3.) In the case of VSPs acquired with airguns, typically only P-waves are generated; but depending on the receiver geometry and formation properties, both P- and converted S-waves may be recorded (Fig. 2-3). In land VSPs with vibroseis or other sources coupled directly to the Earth, both P- and S-waves are generated and may be recorded.

The signals recorded by borehole receivers depend on the incoming wave type, the survey geometry, and the type of receiver. Most modern downhole h rdware for recording VSPs, such as the device used by Schlumberger, consist of clamped, calibrat d m lticomponent or three-component (3C) geophones o acceleerometers, both of which are able to record all components of P- and S-wave motion, includ ng ver ical shear (SV) and horizontal shear (SH) waves

The downhole sensors may be conveyed by wireline and clamped into open ho e cased hole, or drillpipe; or they also may be conv yed by drillpipe or deployed while drilling (Fig. 2-4)

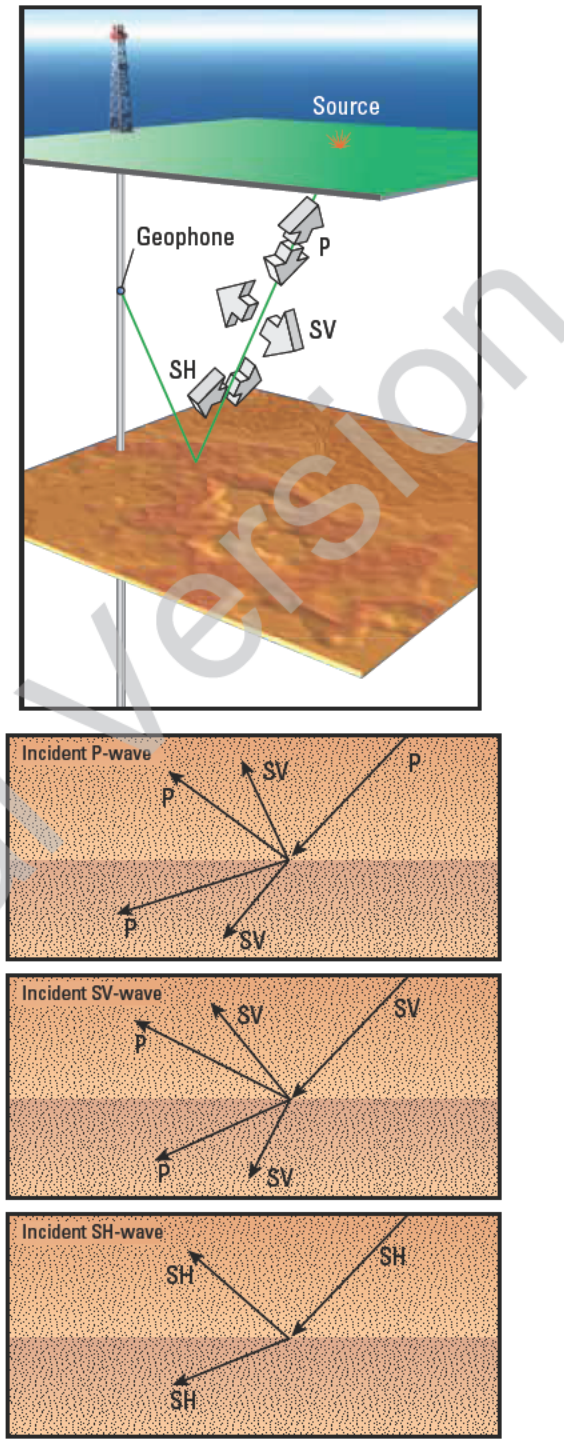

Figure 2-3. Three-dimensional wave propagation in offset profiling. P-waves and vertical shear (SV) waves are polarized in the plane containing the well and source. Horizontal shear (SH) waves are polarized perpendicular to this plane. When either a P- or SV-wave strikes a reflector at an oblique angle, four new waves result: an upgoing and a downgoing P-wave and an upgoing and a downgoing SV-wave. The new waves leave the interface at all amplitudes and angles. An incident SH-wave creates only SH-waves, upgoing and downgoing.

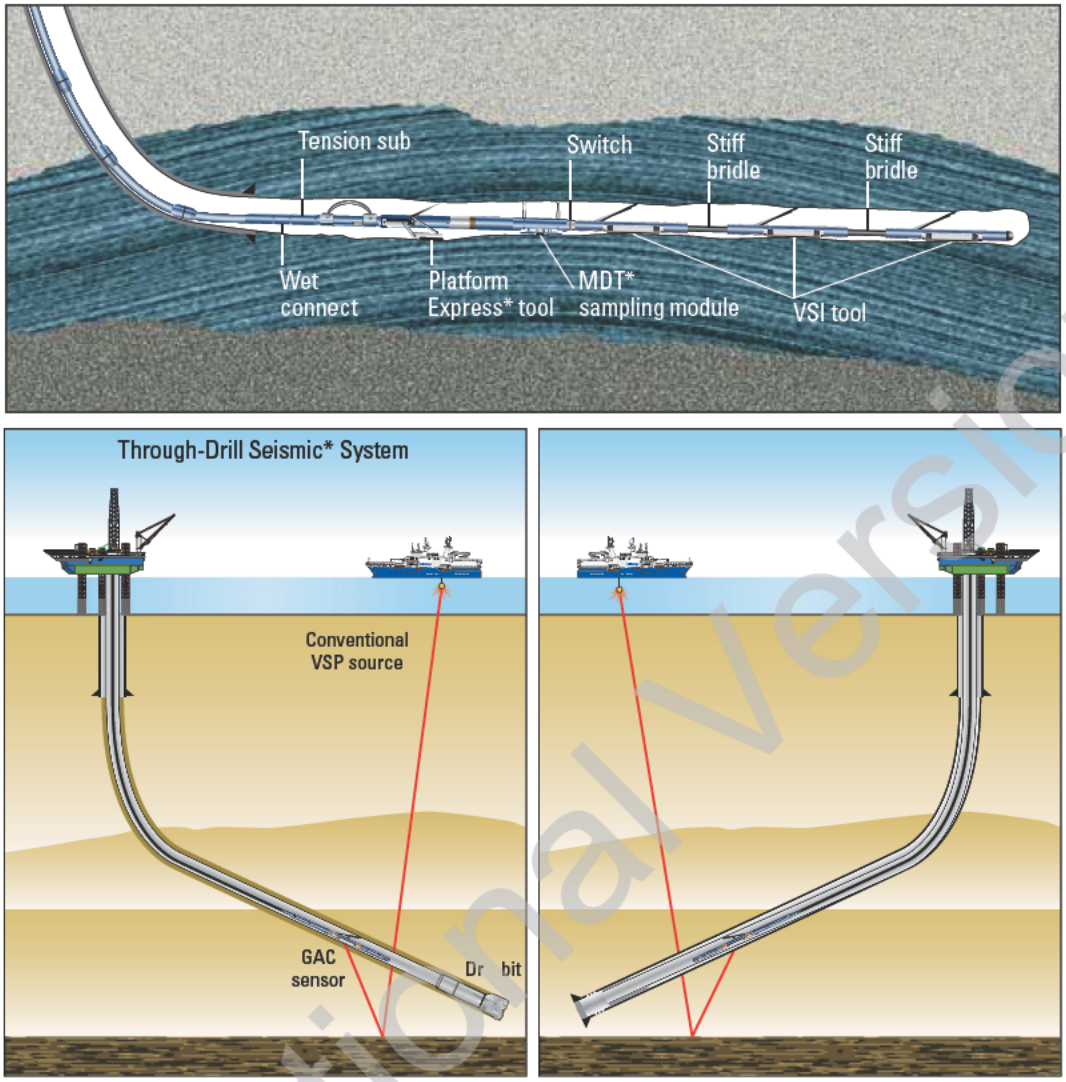

Figure 2-4. Pipe-conveyed borehole seismic a quisi (top). The Through-Drill Seismic system deploys the VSI tool through drillpipe (bottom le t). Throu h-tubing deployment is also possible (bottom right).

An advantage tha boreh le seismic surveys have over their surface eismic counterparts is the ability to record the irect signal in a low-noise environment. The direct sign l tra els downward to the receivers; theref re, i is known as a downgoing signal. Waves that eflect at deep r interfaces and then travel up to a borehole receiver are recorded as upgoing signals (Fig. 2-5). Upgoing signals therefore contain reflection information and are used to create seismic images of subsurface reflectors. Both upgoing and downgoing signals can contain multiples (multiply reflected energy) that can interfere with the real signal. Signals without multiples are called primary arrivals. The downgoing signals can be used to distinguish multiples from primary arrivals and thus allow more reliable processing of the surface seismic upgoing wavefield.

In addition to P- and S-waves that propagate from a near-surface source to the receiver, there are tube waves, a type of noise that arises when source-generated surface waves transfer energy to the borehole fluid. The resulting guided wave travels down and up the borehole, forcing the borehole wall to flex radially (Fig. 2-6). Geophones clamped to the borehole wall may record tube-wave energy on the vertical and horizontal components. Tube

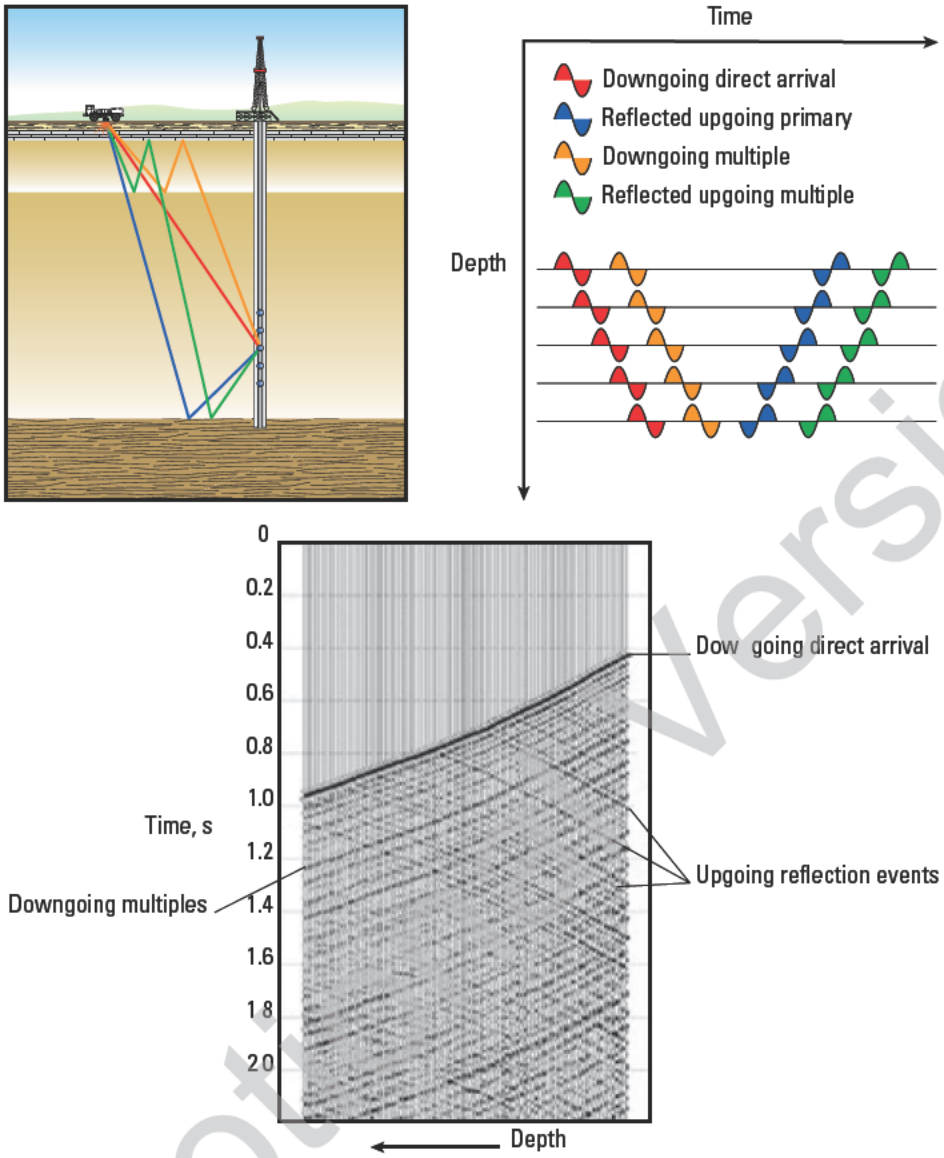

Figure 2-5. Schematic representati ns o differe t seismic arrivals within a seismic dataset.

waves are sensitive to changes in borehole dimension, which can cause tube waves to reflect. Tube waves can also reflect at the bottom of the hole. Tube waves can be minimized with proper source-to-wellbore geometry. Any tube w ves emaining on the data are considered noise and are emoved through processing.

The majority of VSPs use compressional and shear wav s from man-made sources to image reflectors, but energy from other sources can be recorded and processed to yield information about the subsurface. For example, the drill bit can act as a downhole source to generate vibrations that are detected by sensors deployed at surface or on marine cables. These recordings require specialized processing but can produce important results in time for decisions to be taken while drilling.

Hydraulically induced fractures emit energy in much the same way as natural earthquakes, and these microseisms can be recorded by sensors in neighboring boreholes. (These events excite P- and S-waves, but with strike-slip radiation patterns, which are different from those of implosive and explosive sources.) Similarly, production or injection of fluids for enhanced recovery or waste disposal may induce stress redistribution that, in turn, can cause detectable microseismicity. Borehole sensors can also be used to record natural seismicity.

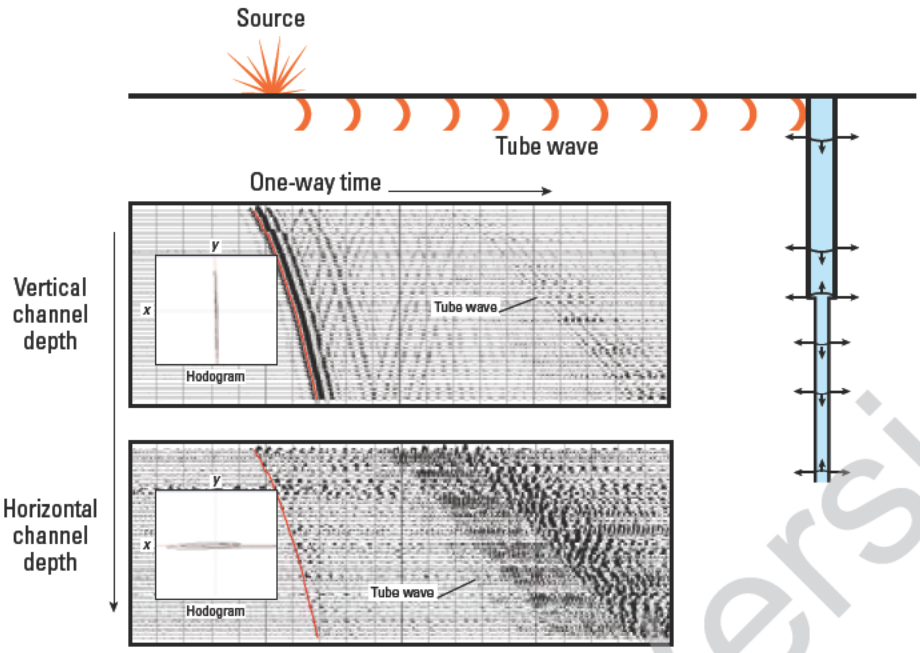

Figure 2-6. Tube waves. Tube waves are generated when surface waves from the source com in contact with the borehole fluid and become a guided wave traveling up and down the borehole. As the tu wave travels vertically in the borehole, it pushes the wall horizontally. When the geophones are properly clamped to the b r hole wall, most of the tube-wave energy will be seen in the horizontal channels. Some of the tube wave energy will be reflected back to the surface at places where the borehole dimension changes and when the ene gy reaches the bottom of the hole.

2.4 Survey types

Borehole seismic surveys are usually categorized by survey geometry, which is determined by source offse borehole trajectory, and receiver array depth. The survey geometry governs the dip range of rock interfaces a d the subsurface volume that can be imaged.

2.4.1 Checkshot and zero-offset VSP

Checkshot and zero-offset VSP re the most common types of borehole seismic surveys. The energy source is placed close to the wellhe d, typically 40 to 100 m away. The geophones usually are l cated at depths that are evenly spaced in the well, from TD upward (Fig. 2-7). Spacing between the g ophones is governed by the slowest velocity and highest frequency anticipated within the depth nterval of the VSP. The spacing is derived f om th requirement to sample the spatial wavelength t lea t twice per full wave oscillation. Typical depth inc ments would be 15 to 20 m. The regular spacing would normally extend up the hole to a point above the shallowest reflector of interest, and then a few, more widely separated levels (checkshots) would be planned from there to surface for velocity control.

In the simple case of a vertical well with horizontal geological interfaces, the reflection points for all the interfaces into all the geophones will occur in a narrow column adjacent to the well. However, the seismic wavelet is influenced by the bulk volume of rock, approximately 60 m in radius, not the few centimeters that affect a sonic logging tool.

The traveltimes can then be used to correct sonic logs for dispersion and hole conditions, such as washouts, so that a synthetic seismogram can be built that is based on the slowness measured at seismic frequencies rather than at sonic frequencies. Rocks typically display a slower velocity for low frequencies than for high frequencies. The impact of this phenomenon is discussed in Chapter 4.

The downgoing wavefield from the VSP shows how the wavelet changes as it propagates and how multiples contaminate it. The upgoing wavefield, in turn, shows the reflection response of the subsurface in depth and time. After processing, the upgoing wavefield can yield a true zero-phase response—one of the "Holy Grails" of the seismic method. That response can be extended below TD, unlike in a synthetic seismogram, which is truncated at the zone of interest. The response beyond TD can be used for prediction ahead of the bit to predict distance to a drilling hazard or to the target reflector.

The standard output from a zero-offset VSP is the corridor stack, a summation of the VSP response immediately following the first arrivals into a single seismic trace that is repeated several times for clarity and comparison with surface seismic images.

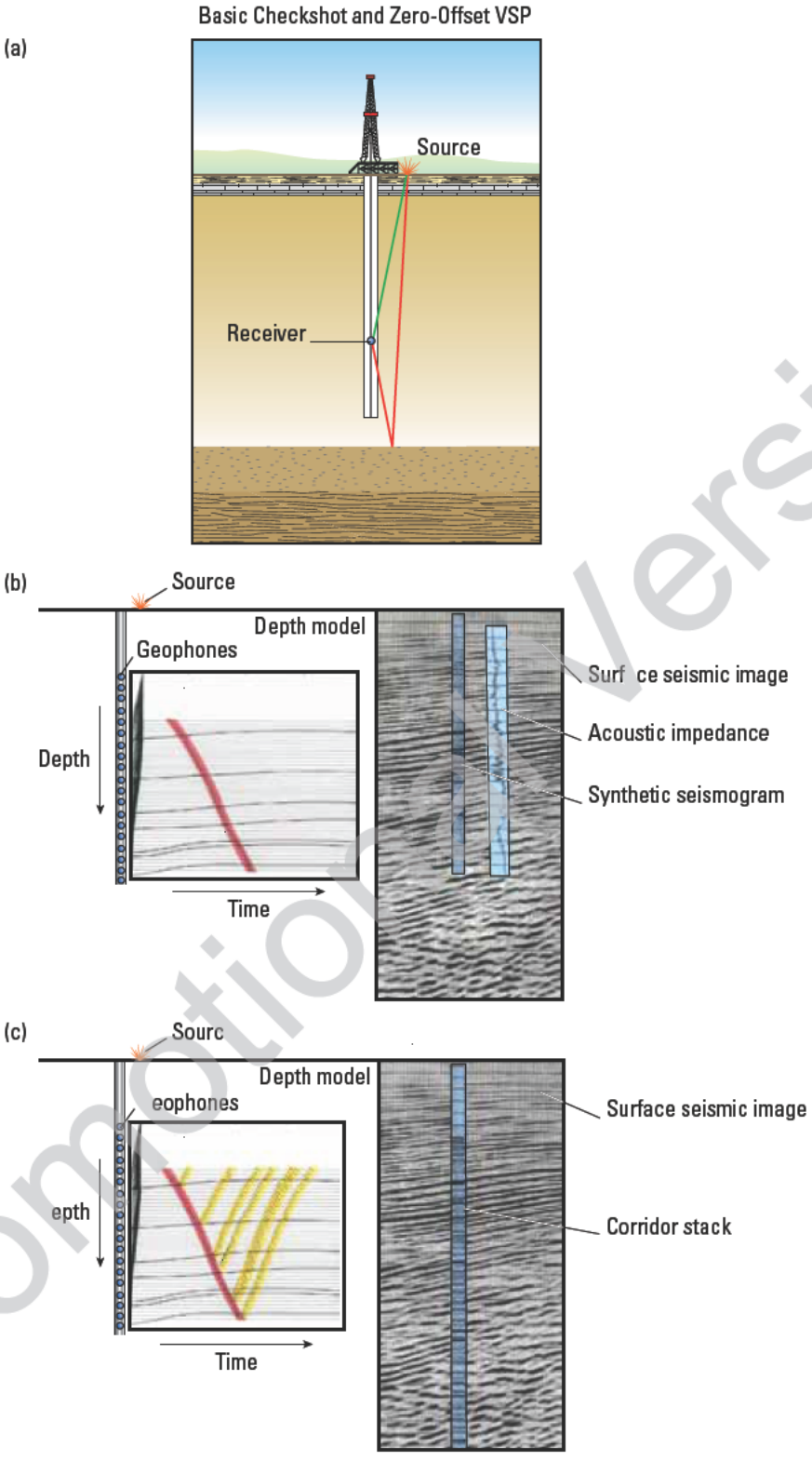

Figure 2-7. Configuration for a basic checkshot and zero-offset VSP survey featuring a borehole seismic receiver array and a near-borehole seismic source (a). First time arrivals in the checkshot (b) are colored red. Checkshot information is used as input to calibrate the acoustic impedance log (light blue) and the synthetic seismogram (blue), which are shown superimposed on the surface seismic image (b). In view (c), the downgoing first arrivals are shaded red, and the reflections are yellow. The final product of zero-offset VSP is the corridor stack (blue), which is shown inserted into a surface seismic section at the well location for comparison.

2.4.2 Deviated wells: Vertical-incidence checkshot and walkabove VSP

Another type of checkshot and zero-offset VSP is also known as a walkabove or vertical-incidence checkshot or vertical-incidence VSP. It is designed to ensure that the source is always directly above receivers deployed in a deviated or horizontal wellbore. This survey acquires an image of the region below the borehole (Fig. 2-8). In addition to formation velocities and an image for correlation with surface seismic data, the benefits of a walkabove VSP include good lateral coverage and fault and dip identification beneath the well.

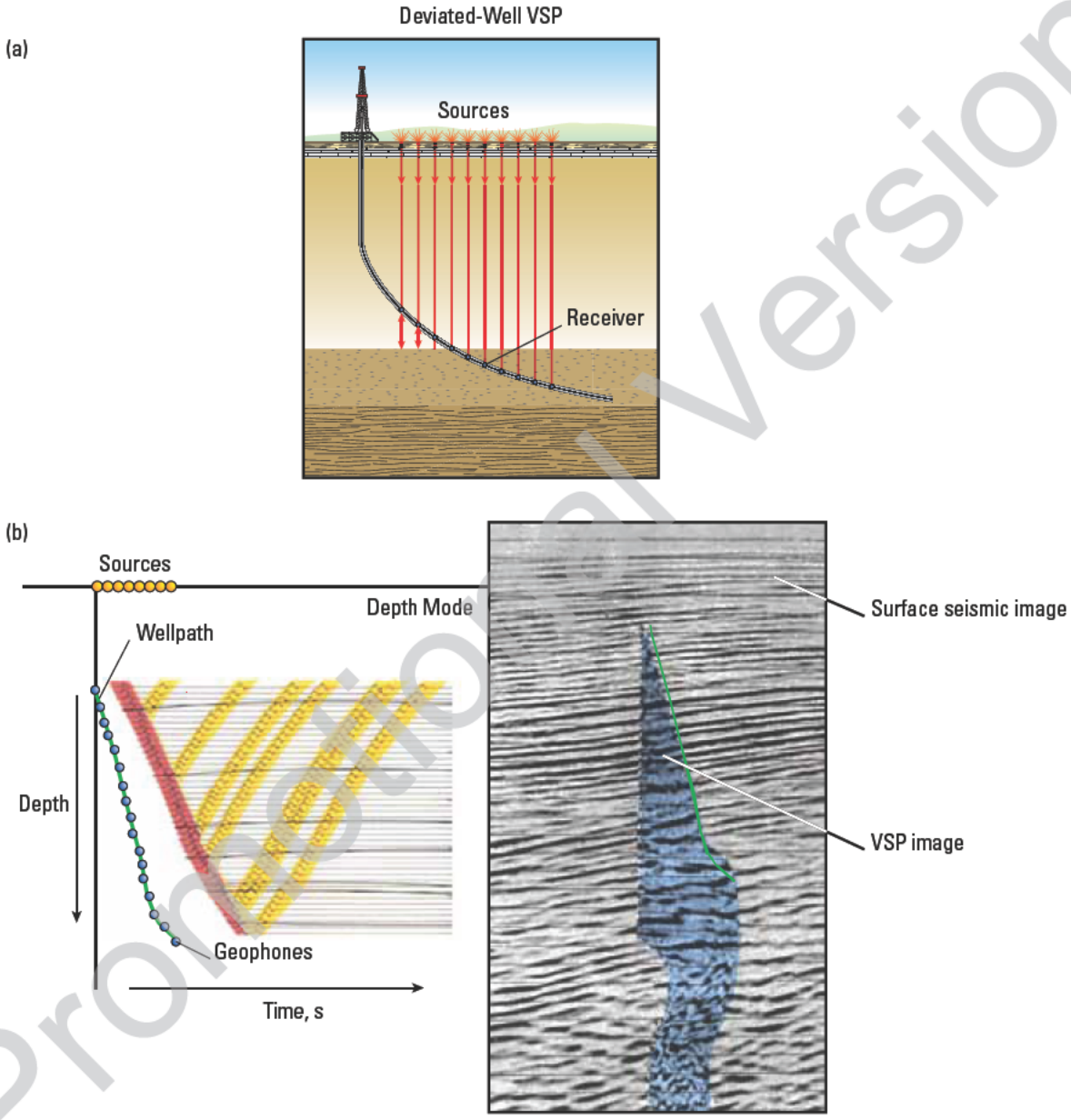

Figure 8. Configuration for a vertical-incidence checkshot or walkabove VSP survey featuring a seismic receiver array in a deviated borehole and seismic source locations above each receiver (a). In the checkshot data (b), the downgoing first arrivals are shaded red, and the reflections are yellow. The image obtained from the VSP data (blue) is superimposed on a seismic section that includes the well location (green). (Graphic in (a) from Arroyo *et al.*, 2003; this graphic is copyright Schlumberger, Ltd. Used with permission.)

2.4.3 Offset VSP, walkaway VSP, and walkaround VSP

Offset VSPs are acquired with the source offset from vertical incidence. In this geometry, the source is placed at one offset, and receiver arrays are deployed at a wide range of depths in the borehole (Fig. 2-9). The offset increases the volume of subsurface imaged and maps reflectors at a distance from the borehole that is related to the offset and the velocity structure. The additional image volume enhances the usefulness of the image for correlation with surface seismic images and also for identification of faulting and dip laterally away from the borehole. In addition, the offset causes conversion of P-waves to S-waves, thus introducing the possibility of

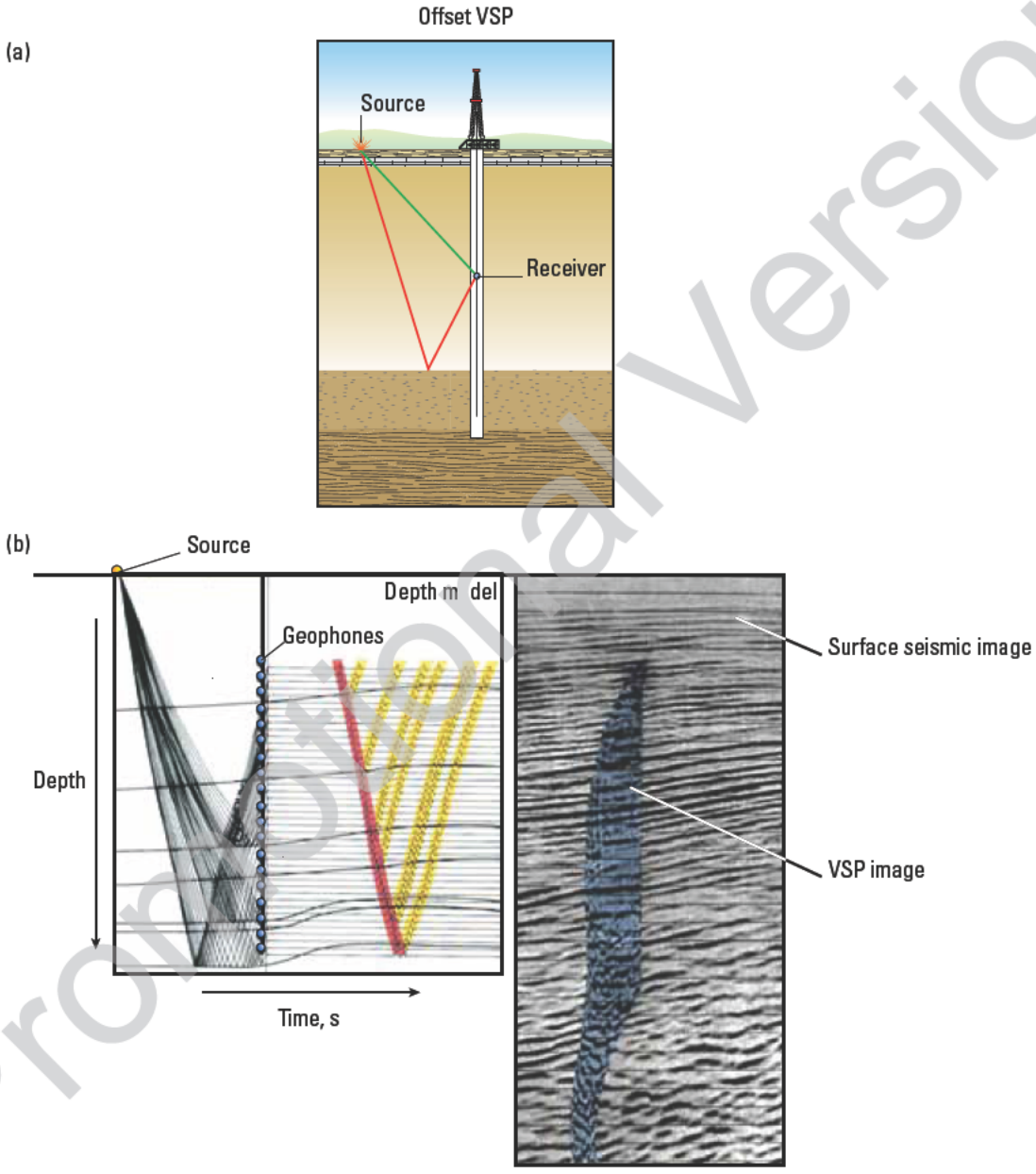

Figure 2-9. Configuration for an offset VSP survey featuring a seismic receiver array in a vertical borehole and a seismic source at a significant offset (a). In the checkshot data display (b), the downgoing first arrivals are shaded red, and the reflections are yellow. The image obtained from the VSP data (blue) is superimposed on a seismic section through the well location. (Drawing in (a) from Arroyo *et al.*, 2003; this graphic is copyright Schlumberger, Ltd. Used with permission.)

shear-wave, AVO, and anisotropy analysis. The degree to which P-waves convert to S-waves depends on offset and interface rock properties. Shear waves can also be generated directly at the seismic source (i.e., shear-wave vibroseis), instead of relying on P-to-S wave conversion. Acquisition, processing, and applications of offset VSPs are described in Chapter 5, and their special application to imaging salt bodies is explained in Chapter 6.

Walkaway VSPs are similar to offset VSPs in that the source is offset from vertical incidence, but the acquisition geometry is somewhat reversed such that the borehole receiver array remains at one depth in the borehole while the source "walks away" or is deployed at a range of offsets (Fig. 2-10). The range of offsets acquired in a walkaway VSP is particularly useful for studying shear-wave, AVO, and anisotropy effects, especially when the

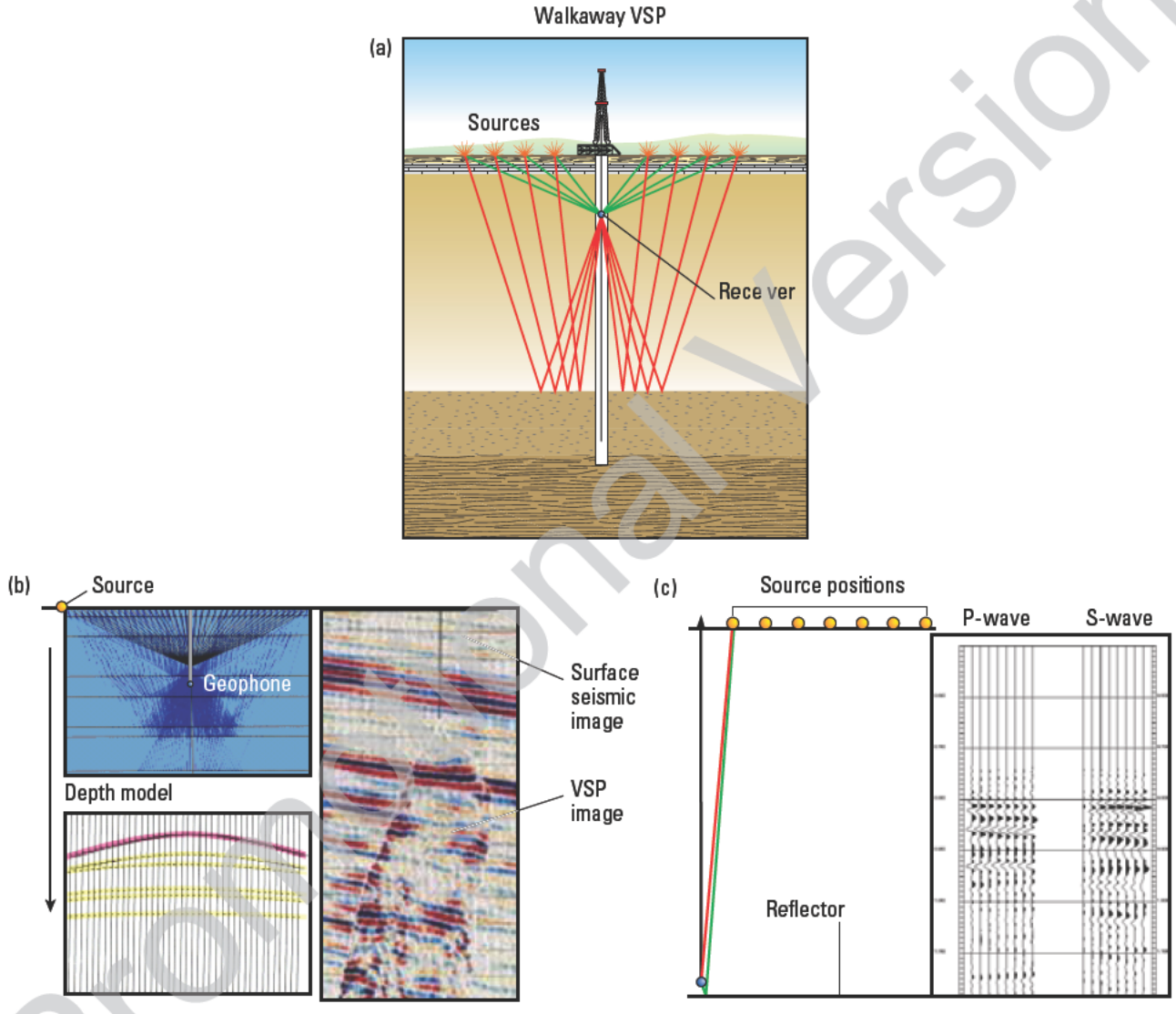

igure 2- 0. Configuration for a walkaway VSP survey featuring a seismic receiver array in a vertical borehole and seismic source l catio s at an array of offsets (a). In the model, downgoing first arrivals are shaded red, and the reflections are shaded yellow (b). The walkaway VSP image is shown superimposed on a seismic section through the well location. An extension of the walkaway acquis tion technique, in which seismic receivers are placed immediately above the geologic feature under study, may be used to map the AVO of seismic features (c). (Drawing in (a) from Arroyo *et al.*, 2003; this graphic is copyright Schlumberger, Ltd. Used with permission.)

receiver array is near a reflector of interest. Because they illuminate a large volume of subsurface, offset and walkaway VSPs are useful steps in the design of later surface seismic surveys. Chapters 5 through 8 include discussion of acquisition, processing, and the application of walkaway VSPs.

Several borehole seismic technologies are available for understanding fracture systems, both natural and hydraulically induced. Walkaround and multiazimuthal VSPs are designed to characterize the direction and magnitude of anisotropy that arises from aligned natural fractures. In walkaround surveys, offset source locations span a large circular arc to probe the formation from a wide range of azimuths (Fig. 2-11). In multiazimuthal VSPs, the source is moved radially outward from the wellbore along lines of various directions. Ideally, walkaround and multiazimuthal VSPs can be combined to generate a spiderweb geometry in which a wide range of offsets and azimuths are analyzed. These survey geometries are treated in Chapter 6.

2.4.4 Three-dimensional VSP

The surveys described previously are all designed to provide information and images in one or two dimensions. However, to adequately illuminate 3D structures requires 3D acquisition and processing. In the same way that surface seismic surveys have progressed from 1D and 2D to 3D, so have VSPs.

Three-dimensional VSPs can be acquired on land or at sea, the latter being more common. Acquisition of 3D marine VSPs is similar to that of 3D marine surface seismic surveys, and the survey geometries can follow parallel lines or concentric circles around the borehole (Fig. 2-12). Three-dimensional VSPs de iver high-resolution subsurface imaging for exploration nd development applications and require detailed p ejob modeling and planning. In addition to produ ing images at higher resolution than that of surface seismic methods, 3D VSPs can fill in areas that cannot b imaged by surface seismic surveys because of interfering surface infrastructure or difficult subsurface conditions, such as shallow gas or salt bodies. Acq isition nd processing of 3D VSPs are covered in Chapter 6.

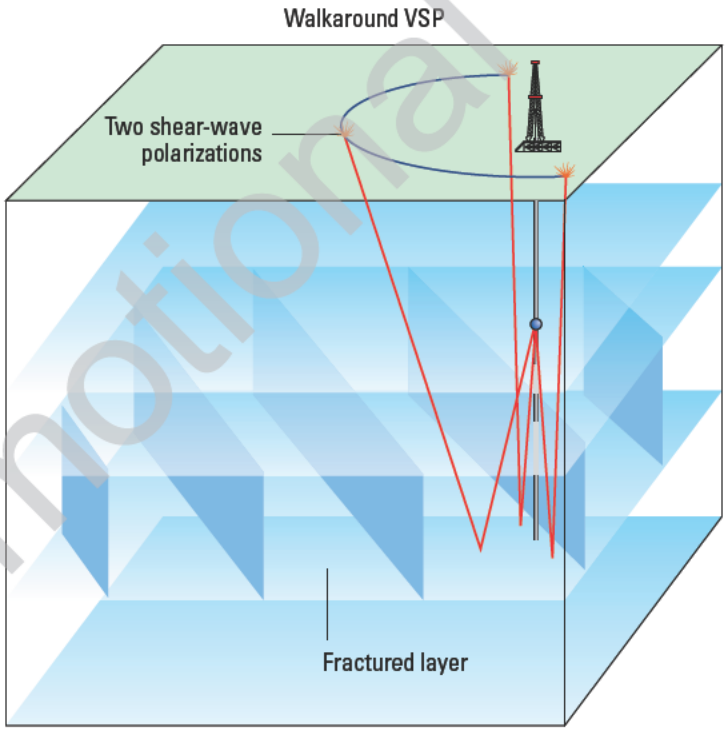

Figure 2-11. Walkaround VSP survey geometry used to study azimuthal variations of seismic attributes. Ideally a spiderweb pattern will provide full anisotropy and AVO effects on seismic images. (Adapted from Christie *et al.*, 1995; this graphic is copyright Schlumberger, Ltd. Used with permission.)

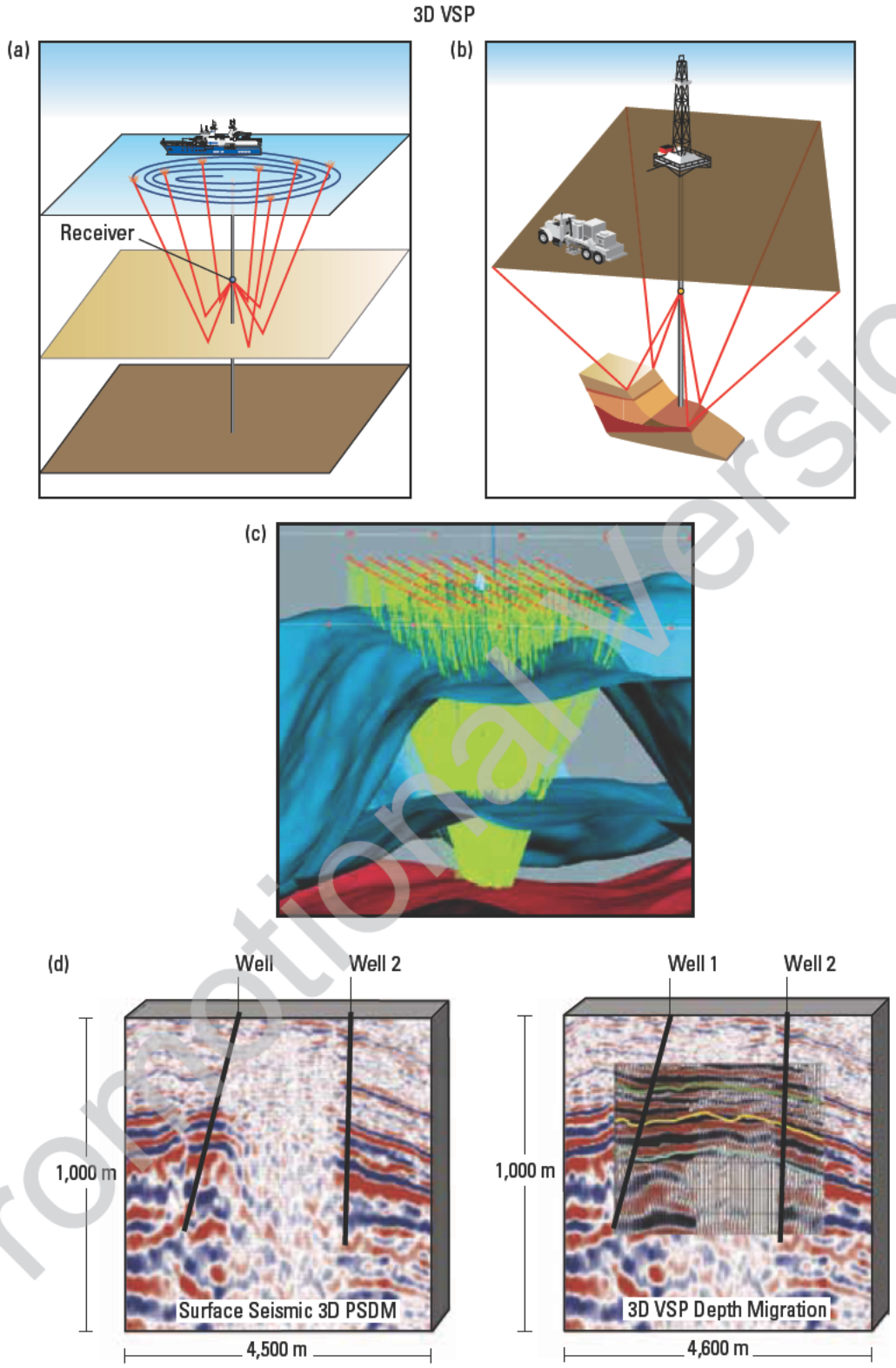

Figure 2-12. Configuration for a 3D VSP survey with an array of seismic receivers in a vertical borehole and surface source points at locations determined by the survey objectives. A spiral or concentric circles are commonly used source-point geometries for marine surveys (a). Surface in-lines or a swath are source-point geometries used for onshore surveys (b). Modeling (c) indicates complex raypaths are needed to achieve imaging of the subsurface. An image obtained from a 3D VSP dataset is superimposed on a seismic section (PSDM = prestack depth migration) through the well location to complete the picture (d). (These graphics are copyright Schlumberger, Ltd. Used with permission: (a) Arroyo *et al.*, 2003; (b) Christie *et al.*, 1995; (c) Blackburn *et al.*, 2007; (d) Hope *et al.*, 1998.)

2.4.5 Salt-proximity survey

Where hydrocarbon reservoirs are trapped against the sides of salt domes, the need to know the shape of the salt flank and its distance from the well becomes very important. The size of the reservoir is dependent on the point at which the reservoir rock truncates against the dome. Surface seismic methods have difficulty imaging the bed terminations when the sedimentary layers dip steeply up against the salt flank, which itself has a strongly conflicting dip and is overturned. Figure 2-13 shows the geometry of a salt-proximity VSP survey.

A basic approach of the salt-proximity method uses traveltime tomography that exploits only the first-arrival time of the seismic pulse. Salt is assumed homogeneous, and its velocity is generally considered known. For a given source-receiver pair, the traveltime is the sum of the time spent in the salt and that spent in the sediment after emerging from the salt. From this, a set of aplanatic curves can be built and a curve can be constructed to connect their tangents to image the salt flank shape.

Modern processing techniques can take this further. By using 3C geophones, a better-constrained solution can be achieved. The 3D shape of the flank can be derived, not just a 2D projection. This is discus ed with more detail in Chapter 6.

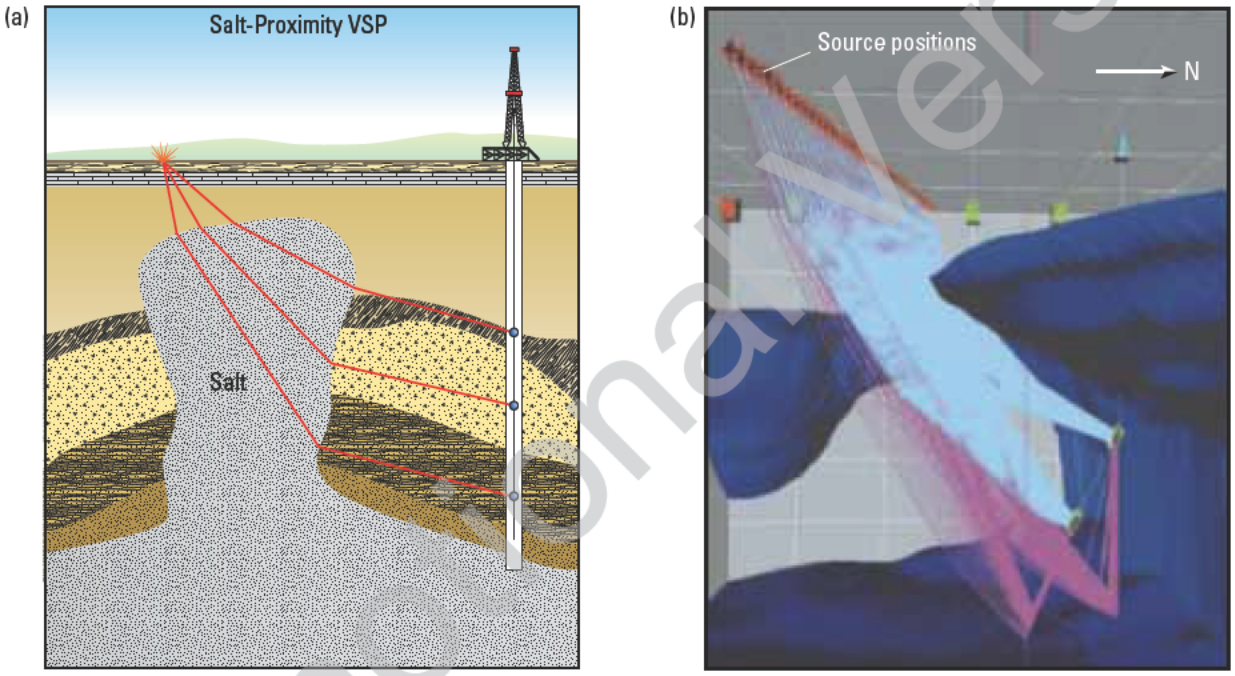

Figure 2-13. Configuration for alt-proximity survey featuring a seismic receiver array in a vertical borehole and a seismic source at a fixed offset (a). Ray- ce modeling ensures that this type of survey provides an accurate salt-face image (b). (Graphic in (a) from Christi *et al.*, 1995; (b) from Arroyo *et al.*, 2003; these graphics are copyright Schlumberger, Ltd. Used with permission.)

2.4.6 Crosswell VSP and reverse VSP

Propagating seismic signals between wells creates yet another type of borehole seismic profile known as the crosswell seismic survey. In these surveys, downhole seismic sources, such as downhole vibrators or buried airguns, are deployed at selected depths in one borehole, and they shoot to a receiver array in another borehole (Fig. 2-14). Because the direction from source to receiver is subparallel to layer boundaries, most raypaths propagate without reflecting. Recorded data are processed to extract information about the velocities in the interwell region. Because crosswell data do not contain much information about reflectors, layer boundaries in the initial velocity model used to process the crosswell data typically come from sonic logs or other VSPs.

Crosswell seismic surveys render high-resolution images used in many development and production problems, especially in mature and complex reservoir environments. Some examples of reservoir features that can be studied with crosswell methods include reservoir compartmentalization, bypassed producing zones, thin beds, and subseismic faults.

A limitation of the crosswell method is the maximum allowable distance between boreholes—typically 300 to 600 m—which varies with rock type, attenuation, source strength, and frequency content. Crosswell seismic surveys are briefly discussed in Chapter 6.

Reverse VSP offers yet another geometric configuration seldom used in the oil industry (Fig. 2-15). The concept here is to use multiple source locations along the borehole and to record the seismic energy with geophones at the surface. This alternative would significantly reduce the survey time and cost. Having the source deeper in the well allows obtaining higher frequency data and reaching deeper targets. Limitations of the method most often are related to the reliability of the downhole seismic source and the integrity of the borehole.

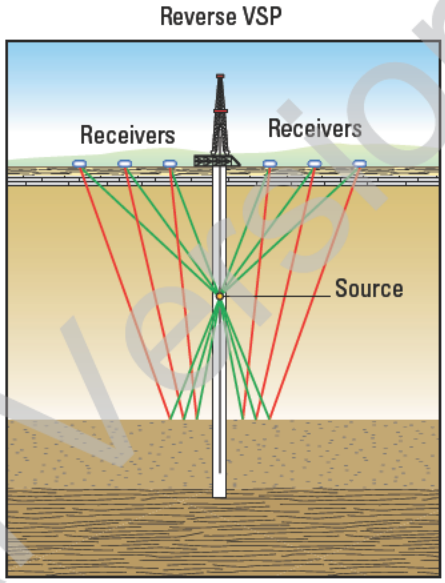

Figure 2-15. Configuration for a reverse VSP survey featuring a seismic receiver array at surface and seismic source locations in a borehole. Source can be downhole airguns, vibrator, or the drill bit.

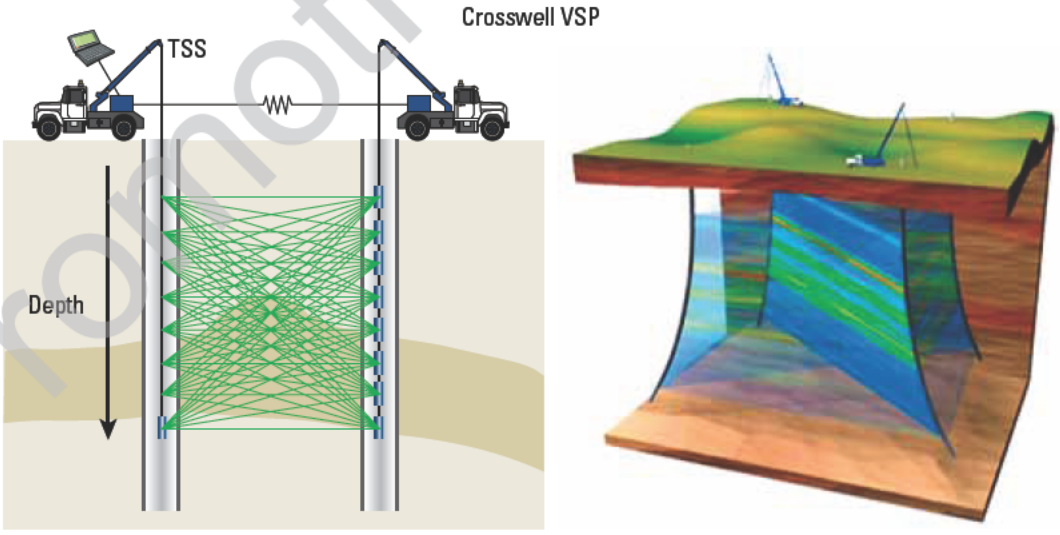

Figure 2-14. Schematic and 3D rendering of a crosswell VSP survey configuration. The transmitting seismic source (TSS) is located downhole in the left well; the receivers comprise a downhole seismic array in the right well. A crosswell VSP is particularly useful when run in time-lapse fashion. A complete survey is typically accomplished by moving the source and receivers to complete the full extent of the image in the interval of interest.

Drill-Bit Seismic* VSP with drillbit source is a type of reverse VSP and it is explained later in this chapter. The single-well seismic option illustrated in Fig. 2-1, which is yet another borehole seismic geometry, could also be classified as a reverse VSP. This technique has very specific applications that are not discussed in this book.

2.4.7 Borehole seismic while drilling

VSPs have long been used to tie time-based surface seismic images to depth-based well logs. In many exploration areas, the nearest wells may be too distant, so VSPs are not available for calibration before drilling begins on a new well. Without accurate time-depth correlation, depth estimates derived from surface seismic images can carry high uncertainties, thus adding risk and the cost of contingency planning to drilling programs. One way to develop a time-depth correlation is to perform an intermediate VSP; i.e., to suspend drilling and run a wireline VSP. These surveys provide reliable time-depth conversions but add cost and inefficiency to the drilling operation and may be too late to forecast drilling trouble. Figure 2-16 shows alternatives to conventional wireline-conveyed VSP acquisition systems and extends the options to while-drilling techniques such as measurement-while-drilling (MWD) and logging-while-drilling (LWD) techniques, an area in which Schlumberger has a great deal of expertise.

2.4.7.1 Drill-Bit Seismic survey

To help reduce uncertainty in time-depth correlation without having to stop the drilling process, g ophysi cists devised a real-time VSP that is acquired using the drill bit as the seismic-energy source. Drill-Bit Seismic surveys use the energy generated by r ller-cone bits to create velocity profiles and images head of the bit. Unlike typical VSP sources, drillbit noi e cannot be controlled or synchronized To determine traveltimes, uphole accelerometer me surements of axial vibrations of the drillstring are correlated with surface receiver data (Fig. 2-17). The method has limitations, such as bit type dril tring attenuation, well deviation, formation conso idation, and weight on bit. Despite

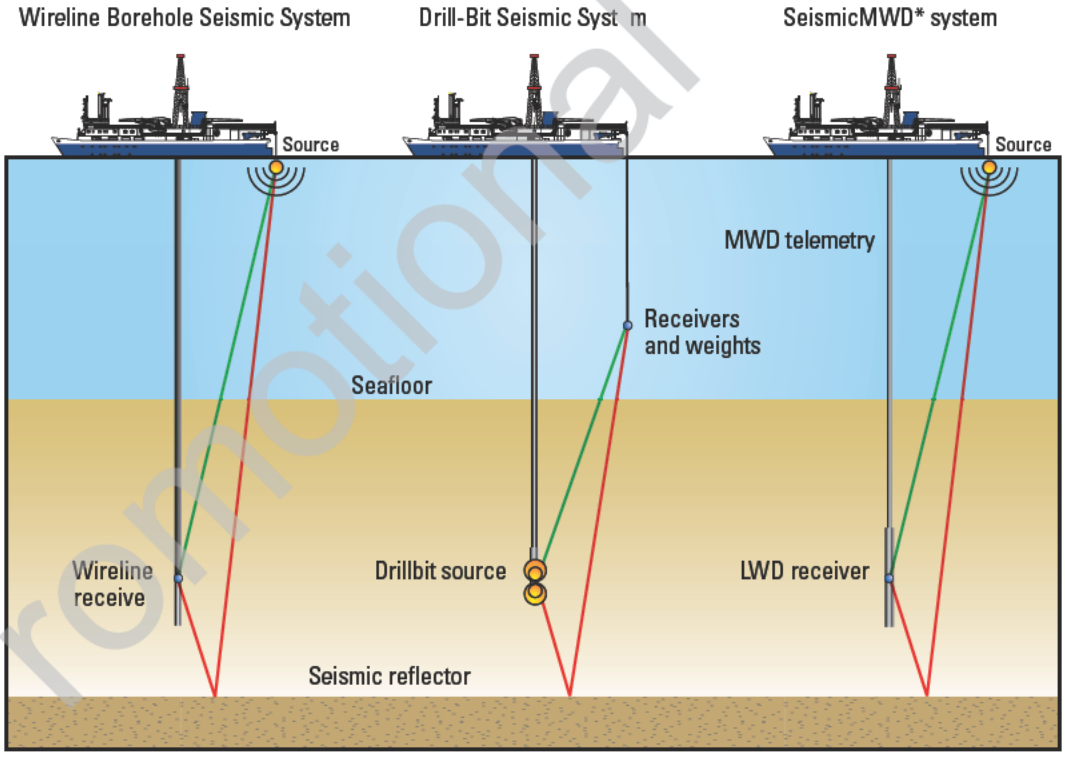

Figure 2-16. Options for wellbore seismic information while drilling. A wireline borehole seismic measurement (left) may be made only between drilling runs. The receivers are lowered and a surface source provides the signal. With the advent of Drill-Bit Seismic VSP with drillbit source, noise from drilling acts as a source and the receivers are on the surface (middle). The SeismicMWD* system provides time-depth/velocity information during the drilling process using a surface source and downhole receiver (right), but measurements can be obtained while drilling only as each stand of drillpipe is added or removed. Next-generation seismicVISION* seismic-while-drilling service improves on this capability to deliver time-depth/velocity information through real-time continuous data transmission without disrupting drilling operations. (From Bratton *et al.*, 2001; this graphic is copyright Schlumberger, Ltd. Used with permission.)

these limitations, the Drill-Bit Seismic method has allowed companies to optimize the drilling process, especially when drilling toward overpressured zones or other seismically detectable hazards. Aspects of drill-noise VSPs are described in Chapter 7.

2.4.7.2 seismicVISION seismic-while-drilling service

Another real-time, while-drilling borehole seismic survey can be acquired with a survey geometry inverted relative to the drill-noise VSP—the seismicVISION seismic-while-drilling service. This technology uses a conventional

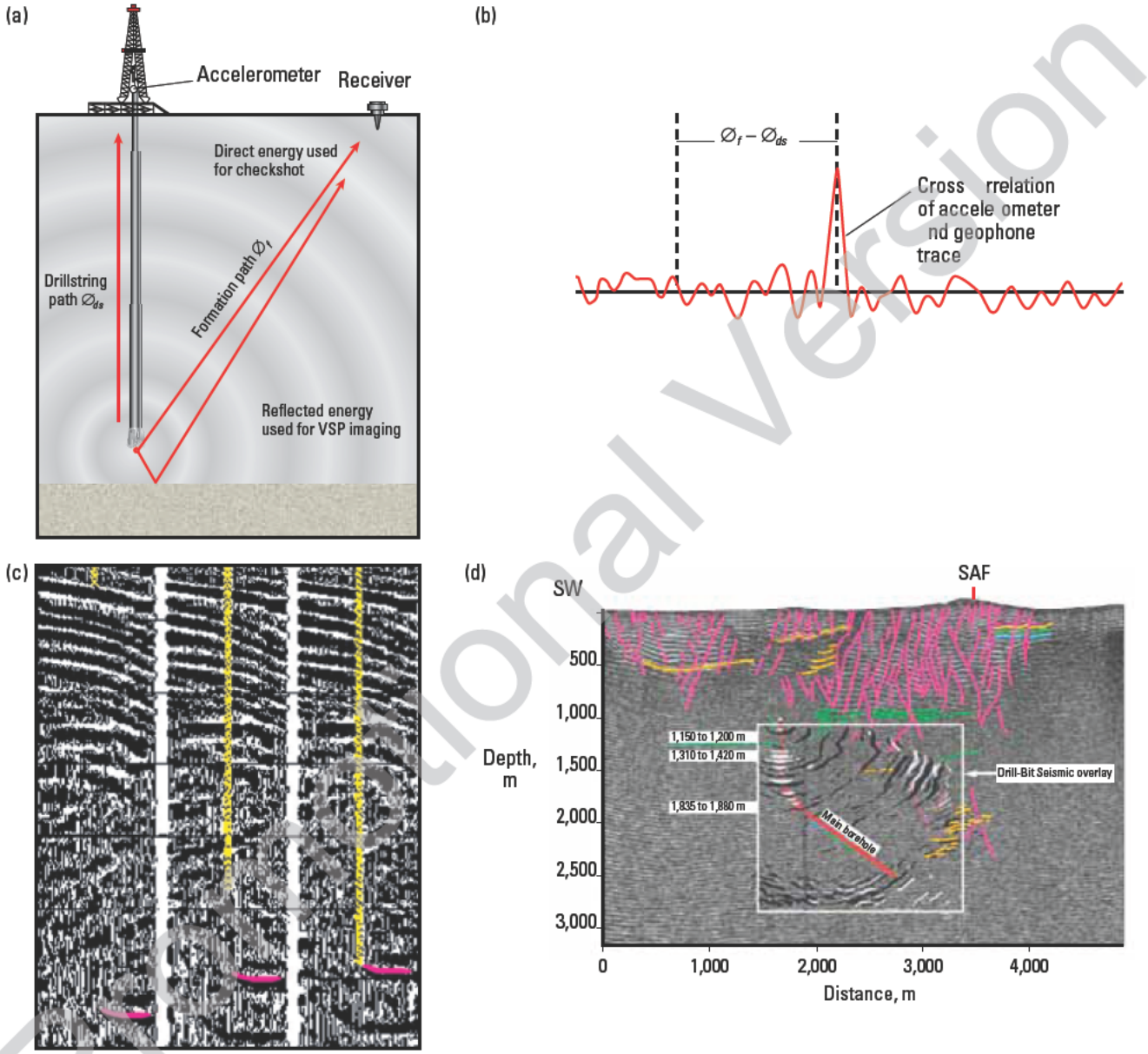

Figure 2-17. Configuration for a drillbit VSP survey with a seismic receiver array on the surface (a). This survey type uses the energy from the drill bit to create velocity profiles and images ahead of the bit. Real-time drillbit VSP image (c) indicates the relocation of the seismic target (pink). (Graphics a, b, and c from Borland *et al.*, 1997; these graphics are copyright Schlumberger, Ltd. Used with permission.) Example of Drill-Bit Seismic data shows high-resolution imaging in highly fractured environment (d). SAF = San Andreas fault. (From Coates *et al.*, 2006; originally adapted from Catchings *et al.*, 2002. Used with permission.)

seismic source at the surface, an LWD tool containing seismic sensors on the drillstring, and an MWD telemetry system to transmit information to the surface (Fig. 2-18). Because drilling generates noise that could jeopardize seismic data quality, source activation and signal measurement must take place during quiet periods when drilling has paused for other reasons, such as during drillpipe connections. A limitation of this method is that the seismic LWD receivers, as part of the drillstring, are not clamped to the borehole wall. However, formation-receiver coupling generally improves with well deviation. Also, current telemetry systems have limited data transmission rates to send waveforms uphole. Therefore, checkshot data is usually acquired and processed in real time, whereas full VSP data is retrieved from memory when the drillstring is back at surface. LWD seismic surveys are included in the discussion of real-time surveys in Chapter 7

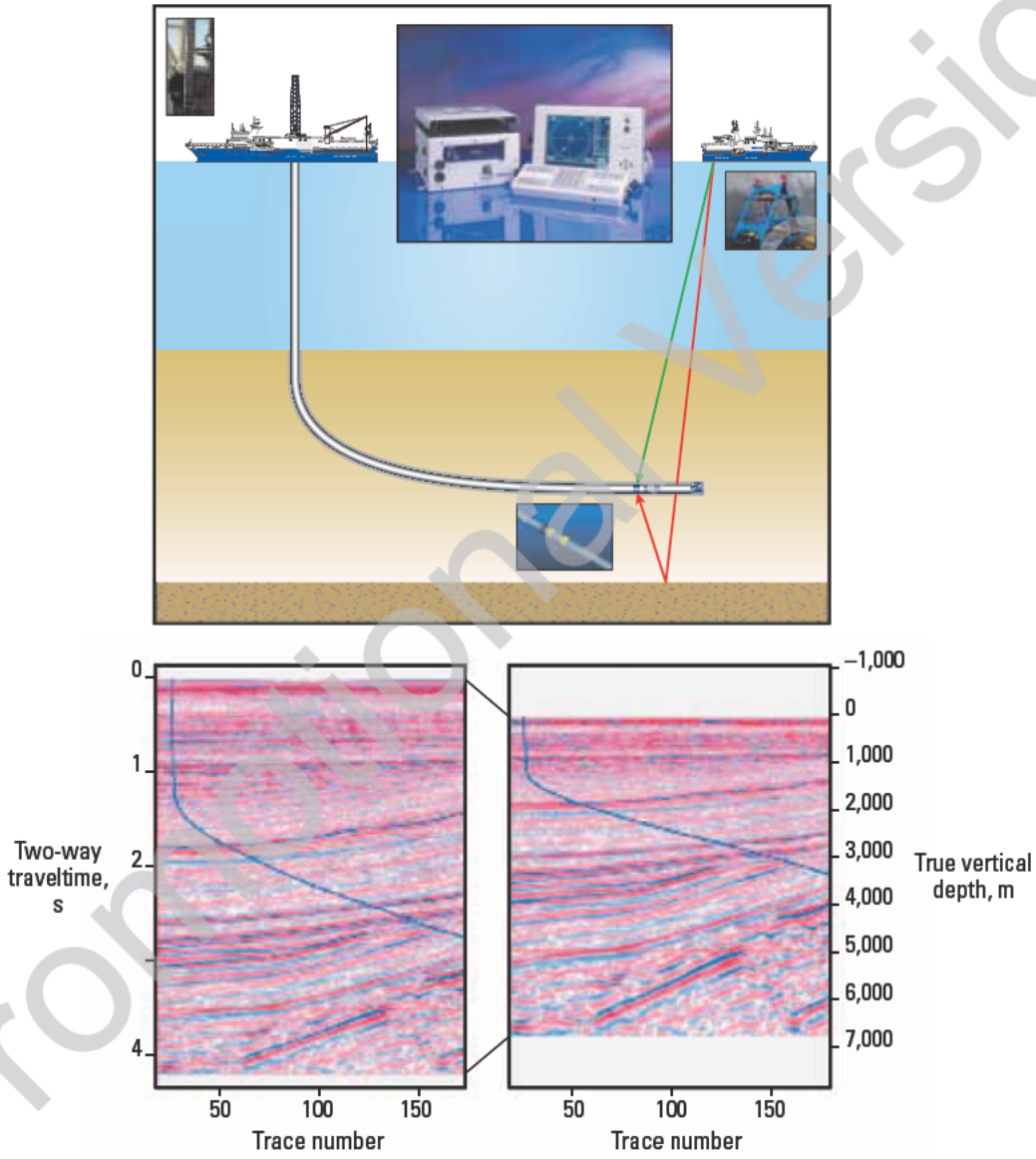

Figure 2-18. Schematic of a seismic-while-drilling survey (top) acquiring data during quiet periods of the drilling process. Seismic receivers are located on a drill collar, and traditional seismic sources are deployed at the surface. The position of the bit is known (bottom) from measured depth, inclination, and azimuth along the wellpath (blue). Checkshot measurements transmitted to surface while drilling locate the bit on the seismic section in terms of depth. (Top graphic is modified from Breton *et al.*, 2002; bottom is from Bratton *et al.*, 2001. These graphics are copyright Schlumberger, Ltd. Used with permission.)

2.4.8 Borehole microseismic survey

Passive seismic monitoring characterizes fractures by recording microseismic signals generated when fluid is produced from, or injected into, a naturally fractured reservoir. (Note that the fluid injection under discussion here is for pressure support, not for hydraulic fracturing.) When fluid injection and production modify the stress state to cause shear-slipping events, the resulting acoustic emissions can often be recorded in nearby monitoring wells by arrays of multicomponent borehole receivers (Fig. 2-19). Modern technology extends this type of monitoring into the flowing well, thus eliminating the need for a monitoring well. Specialized processing adapted from earthquake studies localizes the microseismic events, which can be plotted in space and time to identify the fractures that are responding to the change in stress state. To determine event location relative to the receivers requires an accurate P- and S-wave velocity model. Because the timing of microseismic events cannot be predicted, acquisition systems for passive seismic monitoring must be different from standard VSP acquisition systems. Recording systems need to be active for long periods of time while waiting to be triggered by acoustic emissions. In some cases, permanent installations of receiver arrays record for extended periods of time, usually months or years. Microseismic monitoring is discussed in Chapter 8.

Hydraulic-induced fractures can also be monitored using borehole seismic methods. While the fracture is being created by pumping fracturing fluid into the treatment well, a multicomponent receiver array in a monitor well records the microseismic activity generated by propagation of the fracture (Fig. 2-20). Hydraulic-induced microseismic events are located in space in the same way as are injection- and production-induced events, which require an accurate P- and S-wave velocity model. Mapping the extent of the fracture with time, time reveals the progress of stimulation treatments, and this allows comparison between actual and planned fractures. Real-time information about fracture extent and orientation promises to help stimulation engineers optimize treatments by allowing them to modify pumping rates and volumes when observed fractures differ from plan. A drawback of the method is that nearly all applications have required deployment of the receiver array in a monitoring well because it is believed that the treatment well will be too noisy. The cost of drilling a monitoring well could be saved if the technology could be applied in treatment wells. Hydraulic fracture monitoring is discussed with other fracture-characterization methods in Chapter 8.

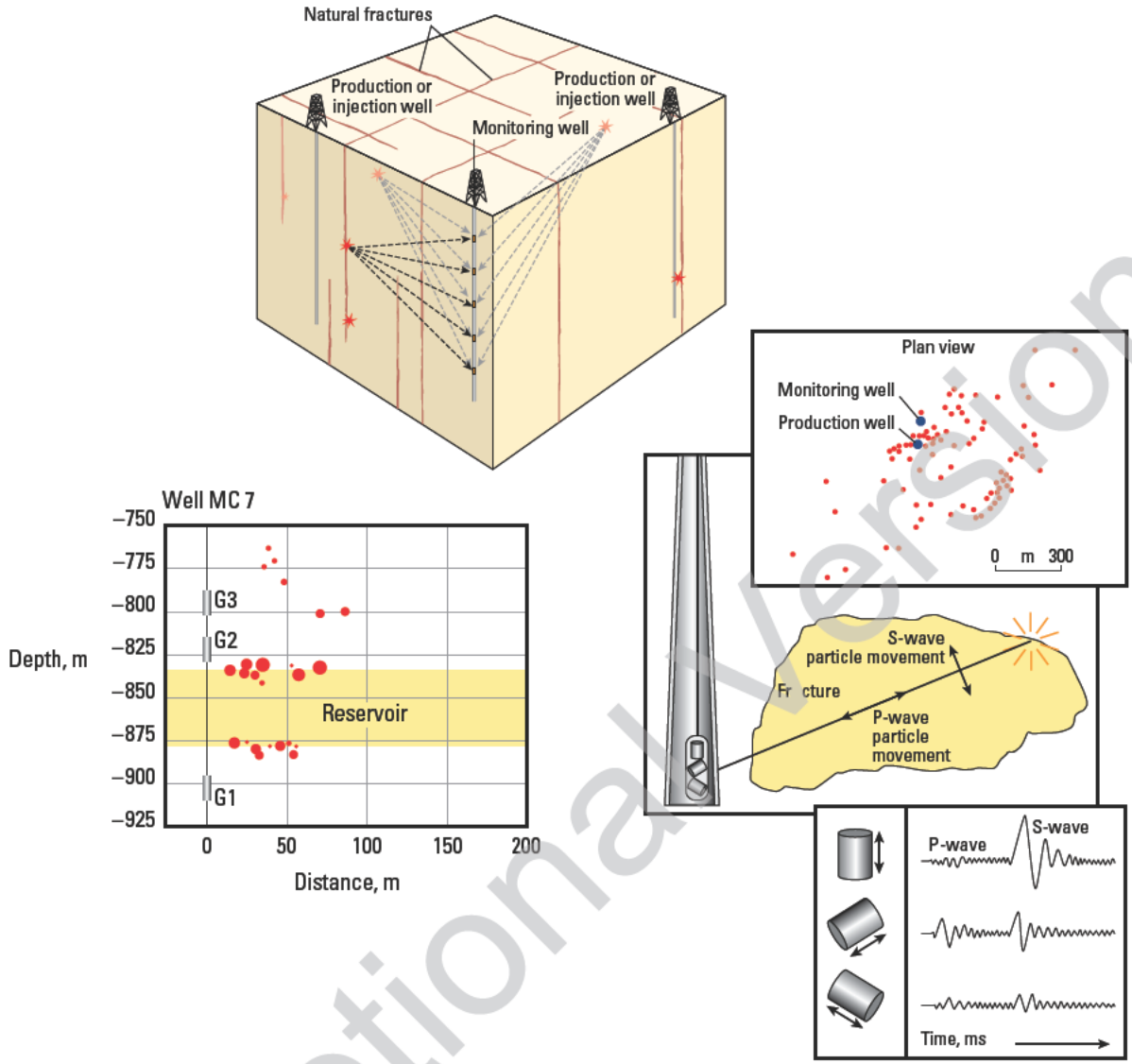

Figure 2-19. Setup to track acoustic em ssions i duced by fluid production, injection, or natural seismicity (top). Production from rock or injection into ro k in the subsurface changes net stress in fractures and faults to induce small shear events that emit acousti sign ls (ed stars). These emissions can be recorded in nearby monitoring wells that contain sensitive mul compo ent seismic recording equipment (bottom). Special localization processing creates a record of events in space and time. These acoustic emissions are located in 3D space and help to identify fracture and fault rections (From Bratton *et al.*, 2006; Albright *et al.*, 1994; these graphics are copyright Schlumberger, Ltd. U d with permission.)

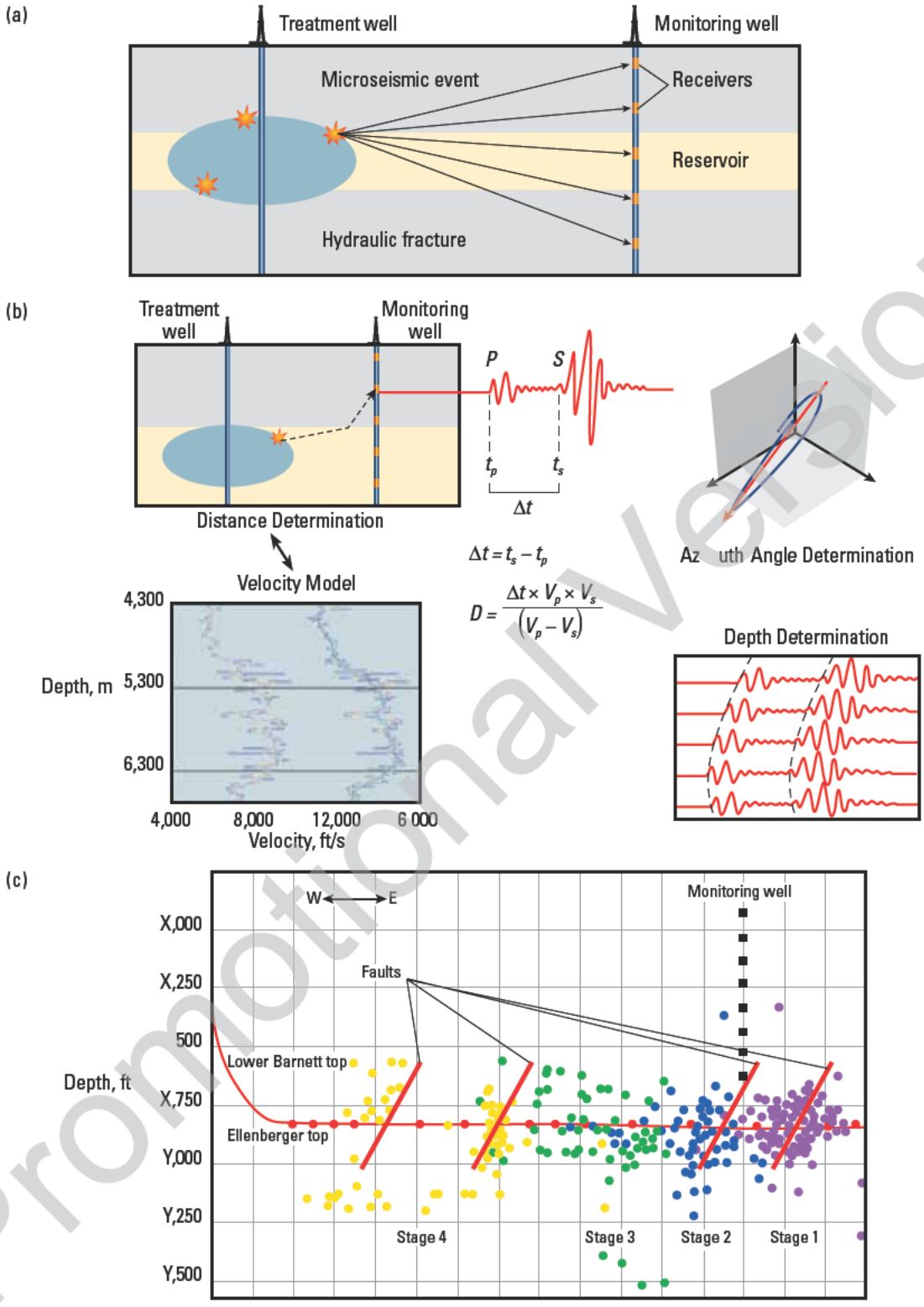

Figure 2-20. Schematic of microseismic method used to record acoustic emissions caused by rock shearing during hydraulic fracturing (a). To locate acoustic emissions, the distance (D) to the event is determined by measuring the time difference (Δt) between the arrival times of the P-waves and S-waves (i.e., t_P and t_S, respectively) and depends on the velocity model (b). The velocity model is usually described by the P- and S-wave velocities (V_P and V_S, respectively) of each layer in the model. The azimuth to the event is determined by examining particle motion of the P-wave using a hodogram (top right). Hydraulic fracture stimulation diagnostics interpretation (c) indicates that microseismic activity is concentrated around some fault planes and is influenced by the presence of faults near stages 1, 2, and 4. Microseismic events are represented as colored dots. (Courtesy of Chesapeake Operating, Inc.) (From Bennett *et al.*, 2005; this graphic is copyright Schlumberger, Ltd. Used with permission.)

2.5 Time-lapse seismic surveys

Many of the borehole seismic surveys mentioned in this chapter can be acquired at different stages in the life of a reservoir. Offset VSPs, walkaways, 3D VSPs, and crosswell surveys acquired in time-lapse fashion can reveal changes in the position of fluid contacts, changes in fluid content, and other variations, such as changes in pore pressure, stress, and temperature. Repeat surveys may be acquired with traditional hardware or with permanently installed receiver arrays. As with time-lapse surface seismic surveys, care must be taken to repeat acquisition conditions and processing as closely as possible so that differences between baseline and monitoring surveys may be interpreted as changes in reservoir properties. More discussion on time-lapse or 4D VSPs can be found in Chapter 6.

Time-lapse seismic surveys share common goals with those acquired using electromagnetic methods. Potential combination of seismic and electromagnetic techniques is currently a matter of extensive research efforts in the oil industry. The effective combination of these types of surveys provides information not only on how reservoir fluids can move, but also on what type of fluid is contained in the formation.

2.6 Seismic data applications

The VSP method has evolved from its humble beginnings as a time-depth tie for surface seismic data to encompass a wide range of solutions for exploration and production problems. Among other things, VSPs provide high-resolution images, detect fracture networks, illuminate fluid contacts, and reduce drilling uncertainty ahead of the drill bit. However, although VSPs offer valuable stand-alone information about rock and fluid properties in the vicinity of the borehole, they will derive their greatest future value when applied in combination with other measurements.

Borehole seismic surveys yield a great amount of information that can be delivered in several products. These deliverables may be grouped into five main categories:

- Reservoir definition—Here the main information provides traveltimes and formation velocities as well as parameters to improve surface seismic data (e.g., phase rotation, multiple pattern analysis, Q factor).
- Reservoir imaging—Borehole seismic data images the wellbore as well as zones ahead of the drill bit and around the wellbore. Depending on the survey geometry, this imaging process will extend from the 1D imaging case (the corridor stack) to 2D imaging laterally away from the wellbore, to 3D imaging that encompasses large volumes of rock around the borehole.
- Reservoir evaluation—Identification of reservoir properties can be obtained using seismic attributes.
- Drilling solutions—Borehole seismic surveys allow calibration in real time of the time-depth conversion to locate the drill bit on the seismic section and to position it with respect to potential drilling hazards such as high-pressure layers.
- Reservoir monitoring—This category includes all surveys that are obtained through passive seismic or in time-lapse fashion. These surveys are typically designed to dynamically monitor a property in the reservoir.

Table 2-1 establishes a link between seismic applications and the survey geometries typically used to achieve them.

Table 2-1. Borehole Seismic Applications and Techniques

	Checkshot	Zero-Offset VSP	Walkabove VSP	Offset VSP	Walkaway VSP	3D VSP	Walkaround VSP	Single-Well VSP	Crosswell and Reverse VSP	Passive Monitoring
Reservoir Definition										
Formation traveltime and velocity	●	●	●			●			●	
P_p surface/borehole correlation and log calibration	●	●	●							
P_s surface/borehole correlation and log calibration		●	●	●						
Improving surface seismic data										
Phase matching	●	●	●							
Multiple pattern analysis		●	●		●	●				
Demultiple method selection		●								
Frequency absorption versus depth		●	●	●	●	●				
Q_p, Q_s		●	●	●	●	●				
P-wave velocity model	●	●	●	●		●				
S-wave velocity model					●	●				
Anisotropic P- and S-wave velocity model					●	●				
Survey evaluation and design		●	●	●	●	●				
Reservoir Imaging										
1D corridor stack or synthetic seismogram	●	●								
2D P_p and P_s high-resolution structural and stratigraphic imaging		●	●	●	●				●	●
3D P_p and P_s high-resolution structural and stratigraphic imaging						●				
Salt-flank, subsalt, or intrasalt imaging (AVA)†		●		●	●	●				
Reservoir Evaluation										
AVO calibration					●	●				
Lithology prediction and fluid (porosity, contact, front)		●			●	●				
Fracture orientation and density				●	●		●	●		●
Log-property extension			●	●	●	●				
Drilling Solutions										
Well placement and steering‡	●	●	●		●					
Prediction ahead of the bit and away from the well										
Imaging		●	●	●	●					
Distance to target or pore pressure prediction		●								
Casing point selection		●			●					
Input to geomechanical models (V_p, V_s)	●	●		●	●	●			●	
Reservoir Monitoring										
Hydraulic fracture monitoring (geometry, caprock integrity)								●	●	●
Acoustic emission monitoring (natural or induced seismicity, injection, depletion, or flooding monitoring)										●
Time-lapse (4D seismic)		●	●	●	●	●		●	●	●

P_p = downgoing P-wave reflected as upgoing P-wave.
P_S = downgoing P-wave reflected as upgoing S-wave.
Q_p = P-wave qual ty factor.
Q_s = S-wave quality factor.
V_p = P-wave velocity.
V_s = S-wave velocity.
† Salt-proximity method uses traveltime tomography; AVA = amplitude variation with angl e.
‡ Remote telemetry option is available when using the Drill-Bit Seismic system or the s micVISION em while g.

2.7 References

Albright, J., Cassell, B., Dangerfield, J., Deflandre, J-P., Johnstad, S., and Withers, R.: "Seismic Surveillance for Monitoring Reservoir Changes," *Oilfield Review* (January 1994) 6, No. 1, 4–14.

Arroyo, J.L., Breton, P., Dijkerman, H., Dingwall, S., Guerra, R., Hope, R., Hornby, B., *et al*.: "Superior Seismic Data from the Borehole," *Oilfield Review* (Spring 2003) 15, No. 1, 2–23.

Bennett, L., Le Calvez, J., Sarver, D.R., Tanner, K., Birk, W.S., Waters, G., Drew, J., *et al*.: "The Source for Hydraulic Fracture Characterization," *Oilfield Review* (Winter 2005) 17, No. 4, 42–57.

Blackburn, J., Daniels, J., Dingwall, S., Hampden-Smith, G., Leaney, S., Le Calvez, J., *et al*.: "Borehole Seismic Surveys: Beyond the Vertical Profile," *Oilfield Review* (Autumn 2007) 19, No. 3, 20–35.

Borland, W., Codazzi, D., Hsu, K., Rasmus, J., Einchcomb, C., Hashem, M., Hewett, V., Jackson, M., Meehan, R., and Tweedy, M.: "Real-Time Answers to Well Drilling and Design Questions," *Oilfield Review* (Summer 1997) 9, No. 2, 2–15.

Bratton, T., Canh, D.V., Que, N.V., Duc, N.V., Gillespie, P., Hunt, D., Li, B., *et al*.: "The Nature of Naturally Fractured Reservoirs," *Oilfield Review* (Summer 2006) 18, No. 2, 4–23.

Bratton, T., Edwards, S., Fuller, J., Murphy, L., Goraya, S., Harrold, T., Holt, J., *et al*.: "Avoiding Drilling Problems," *Oilfield Review* (Summer 2001) 13, No. 2, 32–51.

Breton, P., Crepin, S., Perrin, J-C., Esmersoy, C., Hawthorn, A., Meehan, R., Underhill, W., *et al*.: "Well-Positioned Seismic Measurements," *Oilfield Review* (Spring 2002) 14, No. 1, 32–45.

Catchings, R.D., Rymer, M.J., Goldman, M.R., Hole, J.A., Huggins, R., and Lippus, C.: "High-Resolution Seismic Velocities and Shallow Structures of the San Andreas Fault Zone at Middle Mountain, Parkfield, California," *Bulletin of the Seismological Society of America* (August 2002) 92, No. 6, 2493–2503.

Christie, P., Dodds, K., Ireson, D., Johnston, L., Ruthe ford, J., Schaffner, J., and Smith, N.: "Boreho e Seismic Data Sharpen the Reservoir Image," *Oilfield R view* (Winter 1995) 7, No. 4, 18–31.

Coates, R., Haldorsen, J.B.U., Mill r, D., Malin, P., Shalev, E., Taylor, S.T., Stolte, C., and V liac, M "Oilfield Technologies for Earthquake Science," *Oilf eld Review* (Summer 2006) 18, No. 2, 24–33

Hope, R., Ireson D., L aney, S., Meyer, J., Tittle, W., and Willis, M.: "Seism c Integration to Reduce Risk," *Oilfield Review* (Autumn 1998) 10, No. 3, 2–15.

Me han, R., Miller, D., Haldorsen, J., Kamata, M., and Underhill, B.: "Rekindling Interest in Seismic While Dri ling," *Oilfield Review* (January 1993) 5, No. 1, 4–13.

Field Technology

Michael Jones, John Tulett, and Alejandro Martinez Pereira

3.1 Introduction

Recording the seismic wavefield within the confines of a 12-cm tube that may be deeper than 5 km downhole, in a fluid that may be hotter than boiling water, at high pressure, and in corrosive environments poses unique and challenging problems in instrumentation. Sophisticated tools evolved quite rapidly from the early 1980s to the present, and modern tools not only overcome the physical environmental problems but measure body waves in the Earth with very high fidelity.

Seismic recording tools now exist that are tailored for specific environments and job types. Schlumberger offers the VSI tool and slim hostile seismic tools as wireline-conveyed VSP tools. Some other sensor types and conveyance methods used in specialized applications are also briefly discussed here.

Controlled seismic sources are of an importance equal to that of the seismic recording tools. Full synchronization between the source signals and the acquired seismic waveforms is a requirement for extracting meaningful seismic parameters thereafter. The increasing complexity of surveys demands more predictable and stable seismic sources. Seismic sources most commonly used in offshore and onshore environments are discussed here together with the control and navigation systems associated with their operation

3.2 Seismic sources

Seismic sources are devices, such as an airgun, explosive charge, or vibrator, that provide energy for acquisition of seismic data. A source generates acoustic or elastic vibrations that travel into the Earth, pass through strata with different seismic responses and filtering effects, and return to the surface to be recorded as seismic data.

3.2.1 Airguns, controllers, and navigation

There are several manufacturers of marine airguns, each using different variations of the same basic principle. Figure 3-1 shows the Sercel G. GUN airgun with a schematic representation of its functionality.

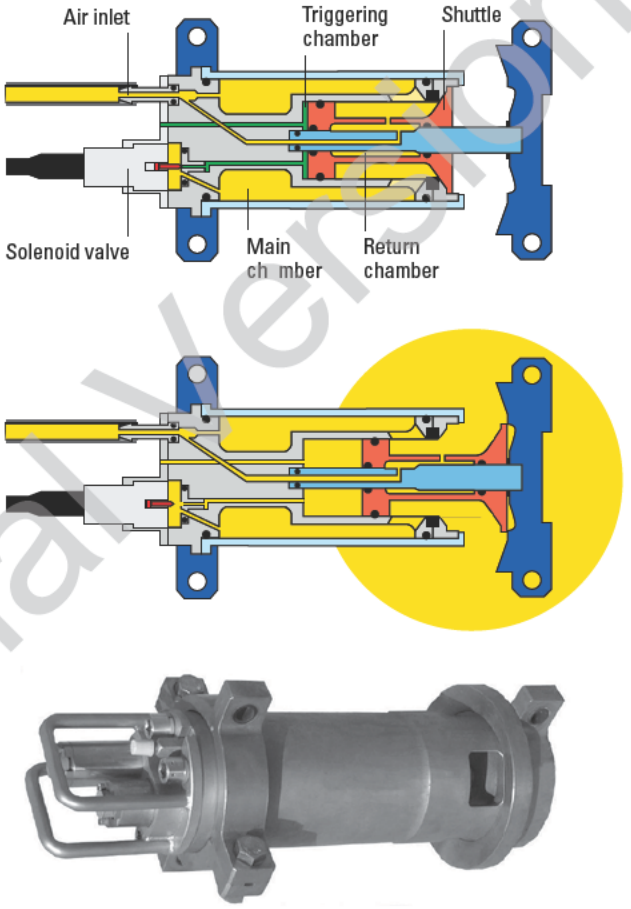

Figure 3-1. The Sercel G. GUN 150 marine airgun. Its operating principle is shown above: Initially, the main chamber is full of compressed air. When the *fire* pulse is sent to the solenoid valve, it allows the compressed air to fill the triggering chamber, which pushes the shuttle outward to release the air into the surrounding water. The incoming air in the return chamber pushes the shuttle to its original position, the solenoid valve closes, and the gun is ready to repeat the cycle. (From Sercel, 2009; used with permission.)

To operate an airgun, high-pressure air is injected into the return chamber through the shuttle or firing piston and into the main (firing) chamber. When the gun is fully armed, it may be fired by activating the solenoid valve. This allows air from the firing chamber to reach the triggering chamber, which causes the shuttle to unseal. The lightweight shuttle then moves very fast, and at the point at which the exhaust is uncovered, the air in the firing chamber is explosively released into the surrounding fluid.

When the high-pressure air (typically 2,000 psi) from the firing chamber is released into the surrounding water at a much lower pressure (slightly greater than 1 atm), it forms a bubble that expands rapidly. (The seismic industry uses both bar and psi units to measure air pressure, but generally only bar pressure units are used for measuring source signature strength. The underwater acoustics industry uses the SI pressure unit system. Airgun chamber volumes are quoted in cubic inches, which is the unit commonly used in the seismic industry. Liters are seldom referred to when quoting airgun chamber volumes. See "Units" for conversion values.) Eventually, the air in the bubble reaches a pressure equal to that of the surrounding fluid, but inertia causes the bubble to continue to expand, i.e., to overshoot. Finally, expansion stops at a point when the pressure in the bubble is less than that of the surrounding fluid, and a contraction stage sets in. These oscillations continue for several cycles before being completely damped. Figure 3-2 shows the pressure pulse from an airgun as a function of time. The repeated signature is the effect of the bubble oscillation.

The bubble series shown in Fig. 3-2 appears to have a period of about 80 ms. This introduces a series of spikes and notches into the amplitude spectrum of the pulse at frequencies of 0, 12.5, 25, 37.5 Hz, and so on, as shown in Fig. 3-3. These spikes and notches are undesirable features of the pulse shape because they are within the useful signal bandwidth. Bubble effects are minimized to a certain extent by clustering of airguns. With a gun cluster that uses two or more airguns spaced at a critical intergun distance, the amplitude of the main burst is emphasized whereas coalescing of the air bubbles helps attenuate the subsequent bubble oscillations.

3.2.1.1 Towing

Airgun sources normally are deployed a few meters below the water surface. The water/air interface acts as a very efficient acoustic reflector, which reverses the polarity of the reflected pulse. This gives rise to a ghost pulse of similar amplitude to the primary but of opposite polarity as shown schematically in Fig. 3-4. When the

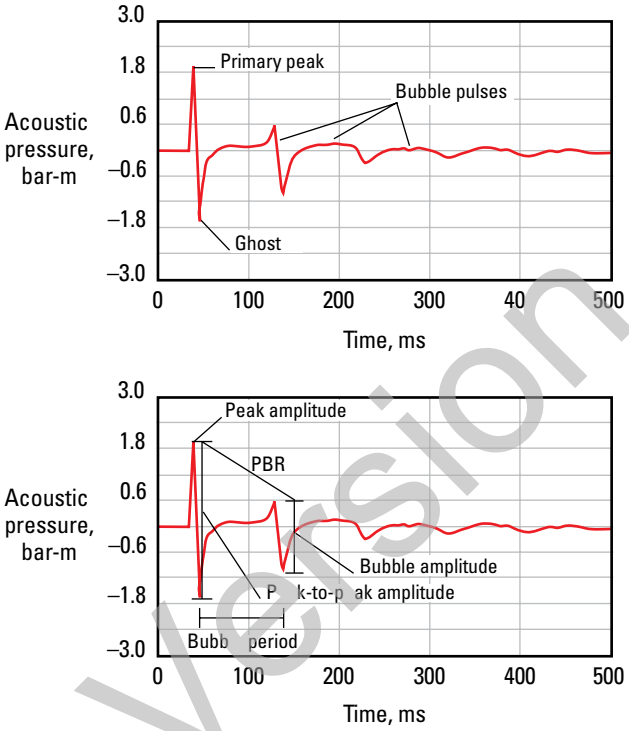

Figure 3-2. Typical hydrophone signature of an airgun seismic pulse. Attributes of the hydrophone signature are shown. PBR = primary-to-bubble ratio.

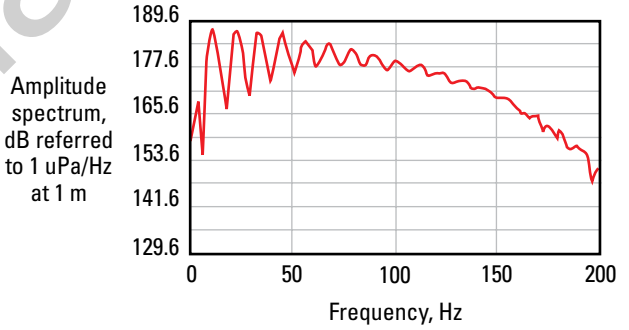

Figure 3-3. Hydrophone spectrum of an airgun seismic pulse as shown in Fig. 3-2.

gun depth (D) is 4 m, the time for the primary pulse to travel from the airgun to surface and back to the airgun (t_{ghost}) can be approximated by

$$t_{ghost} = 2\left(\frac{D}{V_{water}}\right) = 2\left(\frac{4\text{ m}}{1{,}524\text{ m/s}}\right) = 5.25\text{ ms}, \qquad (3\text{-}1)$$

where the value of V_{water} is 1,524 m/s, which is a typical velocity of sound in water (velocity of sound in water is a function of water temperature and salinity). Because this ghost pulse will negatively interfere with the pri-

mary pulse, it introduces a series of notches (n) into the spectrum of the signature (F_{notch}), in this case at a frequency

$$F_{notch} = \frac{n}{t_{ghost}} = \frac{n}{0.00525} = n(190\ \text{Hz}) \quad (n = 0,1,2,3,\ldots). \tag{3-2}$$

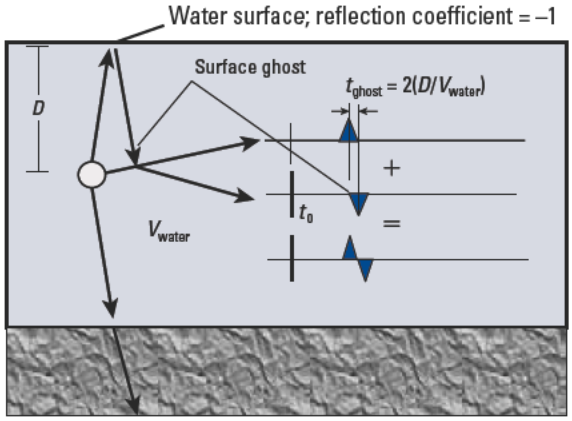

Figure 3-4. Schematic representation of the surface ghost.

3.2.1.2 Airguns onshore

Although airguns are most often associated with seismic acquisition in the marine environment, they are also used as an energy source for onshore borehole seismic surveys. The usual technique is to dig a pit at the desired source location, line it with a geotextile, and fill it with water. The airgun is then deployed in the center of the pit using a crane. It is important to maintain the dimensions of the pit and the fluid level to ensure a good signature, even though the pit tends to cave in.

Airguns deployed in water-filled pits often render limited bandwidth data. One way to overcome this is to deploy the airgun below the slow-velocity layer. Figure 3-5 shows data acquired with the gun in a pit and data acquired with the airgun deployed in a 30-m-deep hole. From the spectra (Fig. 3-5), the data from the latter deployment shows much higher frequencies in the direct arrivals at similar depths.

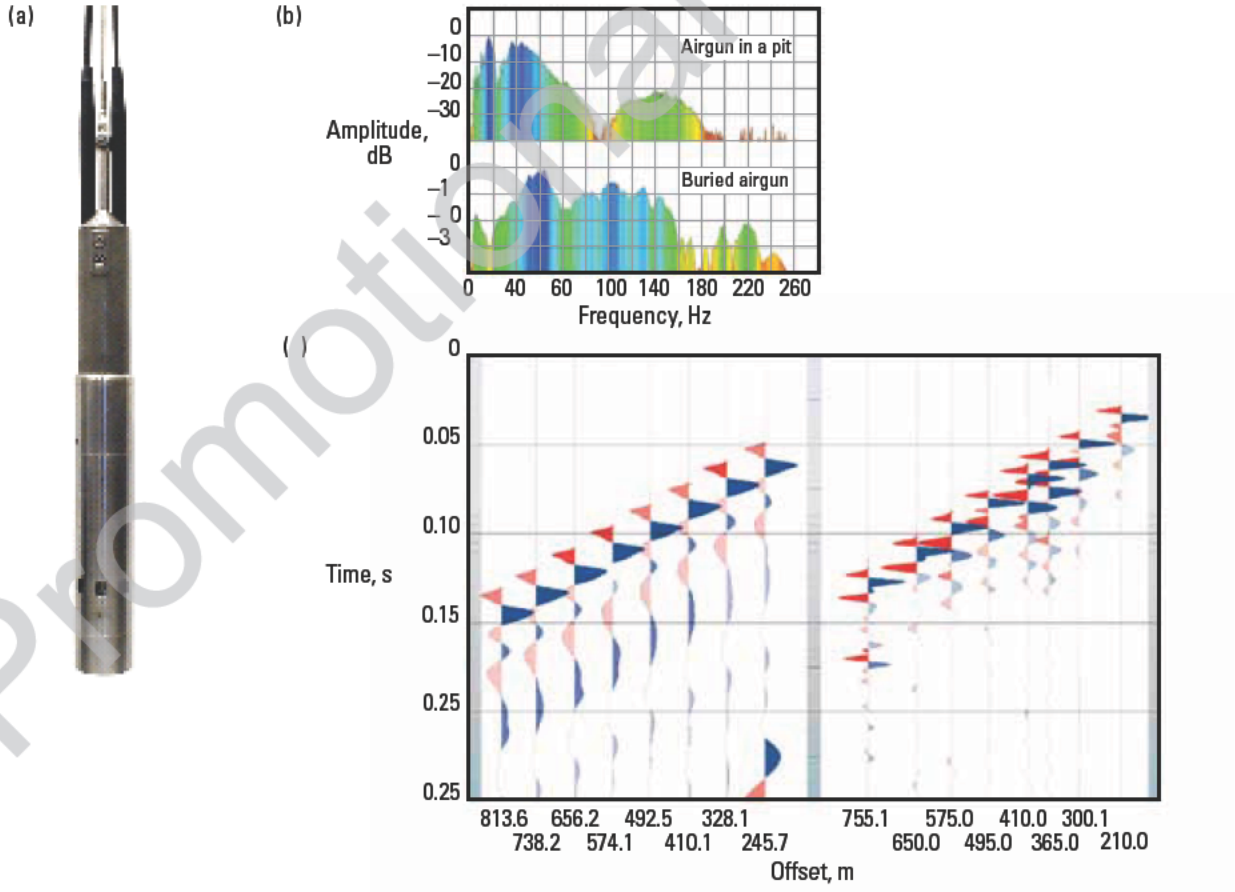

Figure 3-5. Airgun data comparison. (a) Buried airgun is shown in a hole. (From Bolt Technology Corporation; used with permission.) (b) Amplitude spectrum comparison is from an airgun in a surface pit and an airgun in a 30-m hole. (c) Downhole seismic traces acquired with a pit airgun (left) are compared with those from an airgun in a 30-m hole (right).

The buried airgun is ideal for zero- and fixed-offset survey geometries, particularly in difficult or wet terrain where access by vibrator vehicles is restricted. The airgun is positioned below the weathered zone to preserve high-frequency content. A key operational feature of the buried airgun source provided by Schlumberger is a slim housing, which minimizes hole size, drilling, and deployment and retrieval effort. The buried airgun technique has a lesser footprint; therefore, it requires less presurvey land clearance and postsurvey cleanup compared to that of airguns deployed in a mudpit. The buried airgun technique is limited to the source strength of a single gun, and retrieval from the wellbore may be difficult sometimes.

3.2.1.3 Source characterization

Characterization of airgun arrays for borehole seismic surveys is of extreme importance. Table 3-1 presents a summary of the source signatures of different airgun arrays studied and their suitability for different borehole seismic survey types.

Schlumberger has quantitatively studied various parameters in airgun array deployment, including effects of gun dropouts on amplitude and spectral output; optimal deployment depths, operating pressure, and airgun chamber size to achieve required source spectral output; calibration of source output to control signal peak amplitude; and reduction of spurious noise. Complete results can be found in Schlumberger (2002); three common VSP airgun sources are presented herein.

Table 3-1. Seismic Survey Type Matc ed with Optimal Source

Borehole Seismic Survey Type	Rec m ende S ismic S urce
Checkshot	Single gun
Checkshot in deep well	Two- or three-gun cluster
Vertical seismic profile (V P)	Two- or three-gun cluster
VSP in deep well	Six- or eight-gun array
VSP for deep sub alt imag ng	Dual six- or eight-gun arrays

Three- un cluster

Thi source has been used for VSP and seismic-while-drilling surveys worldwide (Fig. 3-6). Figure 3-7 shows results for the three 150-in^3 G. GUN airgun systems. The three-gun system has a total cluster volume of 450 in^3. A 250-in^3 airgun system with a total three-cluster volume of 750 in^3 is also available. The figure clearly shows how bubbling is minimized every time a gun is added to the simultaneous firing sequence. When all guns in the cluster are fired simultaneously, the main pressure spike is emphasized, whereas coalescing of the bubbles helps minimize the bubble effects. Figure 3-8 shows the far-field source signature, in time and frequency, acquired from a three-gun cluster at various depths.

F u e 3-6. Three-gun cluster. This triple airgun configuration, shown in a qualification test, has the gun controller below.

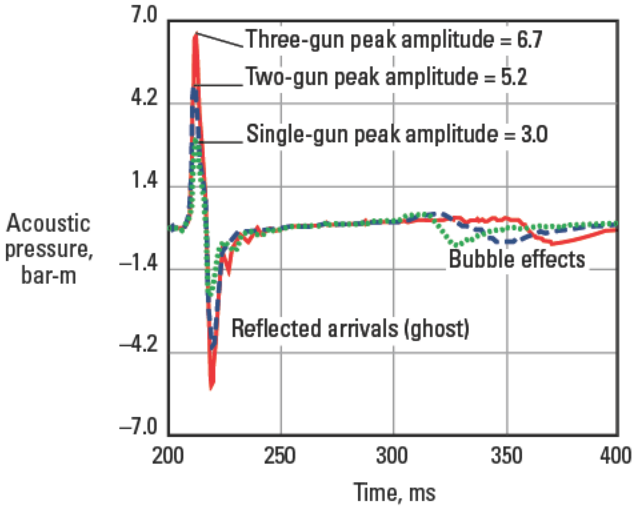

Figure 3-7. Comparison of the peak amplitudes taken from far-field measurements. Data examples are for the G. GUN three-gun cluster, two-gun cluster, and a single gun. Note that the bubble period, peak amplitude, peak-to-peak amplitude, and PBR increase as more guns are used in the cluster, which all improve seismic data quality.

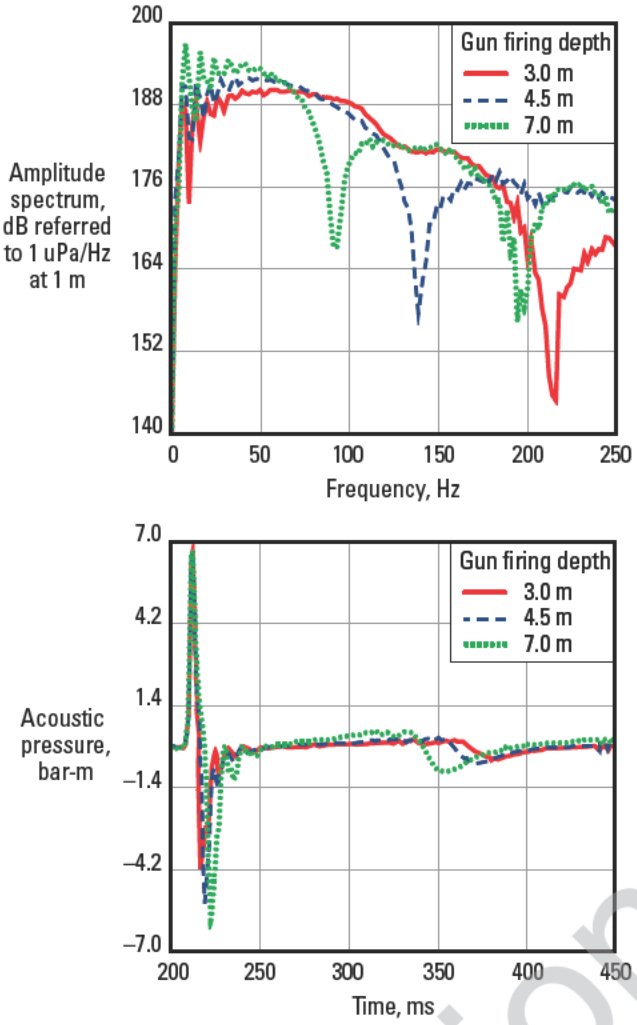

Figure 3-8. Source characterization: Far-field signa re da a example for a three-gun cluster deployed at depths 3 m, 4. m, and 7 m.

Figure 3-9. High-perform nce ITAGA source with an eight-airgun configuration. (Pi ture f om Gulf of Mexico operation.)

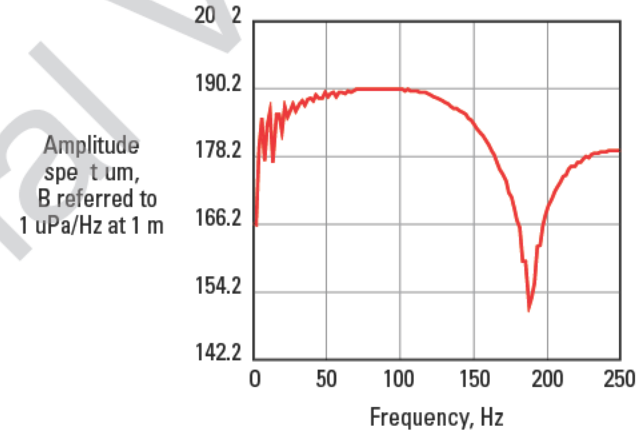

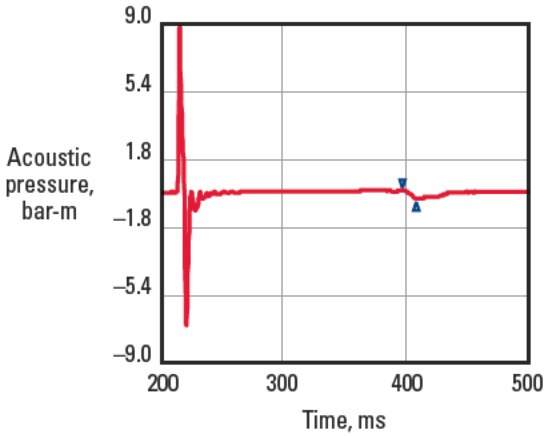

Figure 3-10. Performance of ITAGA eight-gun array deployed at 3-m depth. Note the onset of the bubble at 400 ms.

High-performance ITAGA eight- irgun array

Widely used in North Amer ca, the ITAGA™ source combines wide bandwidth high amplitude, and efficiency (Fig. 3-9). It has been us d in dual configuration for Gulf of Mexico expl ration wells in water depths of 2,800 m and well depths of 9 m. The configuration comprises four 150-in^3 airguns plus four 40-in^3 guns for a total a ray vo ume of 760 in^3. Performance results are shown n Fig 3-10.

High-performance Magnum six-gun array

The high-amplitude Magnum* seismic airgun source array is used in the North Sea and North America. In six-gun mode, as shown in Fig. 3-11, it has achieved 4 to 65 Hz of usable bandwidth in deep subsalt wells in the Gulf of

Mexico. The array is composed of three 150-in^3 and three 250-in^3 airguns for a total volume of 1,200 in^3. The performance of this gun array is presented in Fig. 3-12.

Figure 3-11. High-performance Magnum six-gun array. (Picture from North Sea operations.)

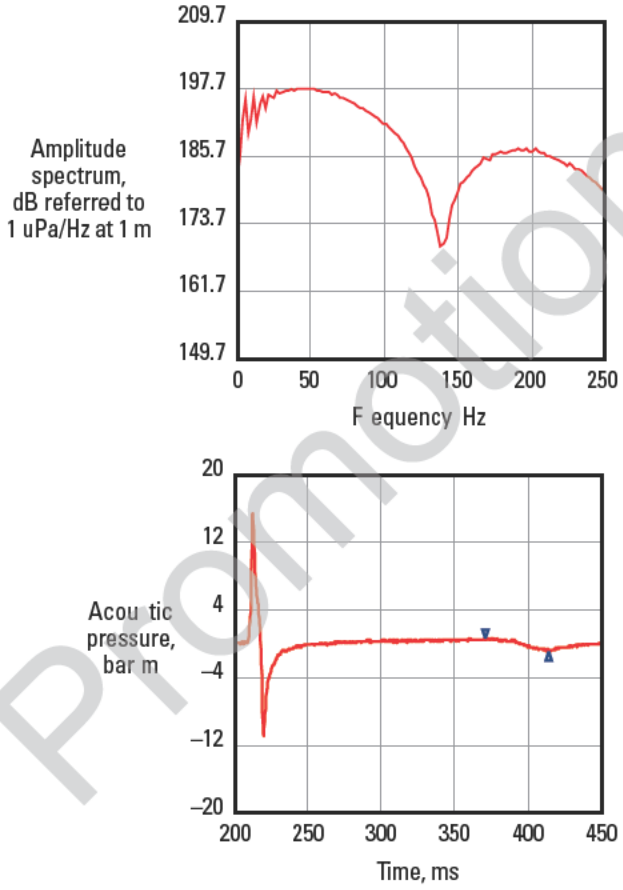

Figure 3-12. Performance of the Magnum six-gun array deployed at 5-m depth. Arrowheads indicate the period of the bubble.

3.2.1.4 Generic gun controllers

Airgun control systems, either manual or automatic, are used to fire several airguns simultaneously and to record hydrophone signatures (e.g., the Macha TGS-8, a product of Macha International, Inc., has eight gun channels). These systems provide airgun control for both zero-offset (rig side) and offset, or walkaway, operations. Offset operations use a control system at both the rig and the remote locations. The two units communicate by eans of a high-speed-data radio link.

The hydrophone information is recorded during acquisition to provide an absolute time reference for d wnhole waveforms and for deghosting dat in subsequent processing stages.

3.2.1.5 TRISOR controller

With petroleum exploration occurring in deeper wells and in more compl x subsurface formations, and with steadily higher expe tations of VSP operations, there is a need for seismic sources that can deliver more predictable, more consistent, superior signal quality. The TRISOR acoustics ource controller offers a new level of saf ty, data quality, and efficiency (Fig. 3-13). This new system for borehole seismic operations provides stable, noi e-fre digital signatures with advanced quality and contr l features.

For a source controller to function correctly—to ensure all guns in the cluster or array fire at exactly the same time—the quality of the shot sensor signal from each of the guns needs to be clean and consistent every time the guns are fired. The TRISOR controller does not use a conventional umbilical as is used in other source controllers to carry the analog signals from the shot sensors. These umbilicals are usually longer than 100 m, and the hydrophone data can be corrupted by external radio signals, electrical leakage, and crosstalk or electrical interference when the umbilical is run across the deck of a rig or boat. When using a conventional source controller, interpretation of the correct zero-time on the shot sensor signals can often be difficult because of noise, and the result is poor source synchronization.

The TRISOR controller uses very short pigtail leads from the guns to the in-sea controller to minimize noise. The in-sea controller handles the control of each gun. An Ethernet connection between the in-sea controller and the surface panel provides digital communication synchronized with the downhole acquisition system. Overall accuracy of the airgun, controller, and recording system is ±0.5 ms or better, typically ±0.1 ms.

The TRISOR controller constantly monitors and controls the data quality from the in-sea sensors. This data is continuously displayed for the end user through a

quality control panel. This means that the chance of a survey continuing while something is wrong with the equipment is significantly reduced. Figure 3-14 shows the difference between near-field signatures of an airgun source controlled by a conventional gun controller and by a TRISOR controller.

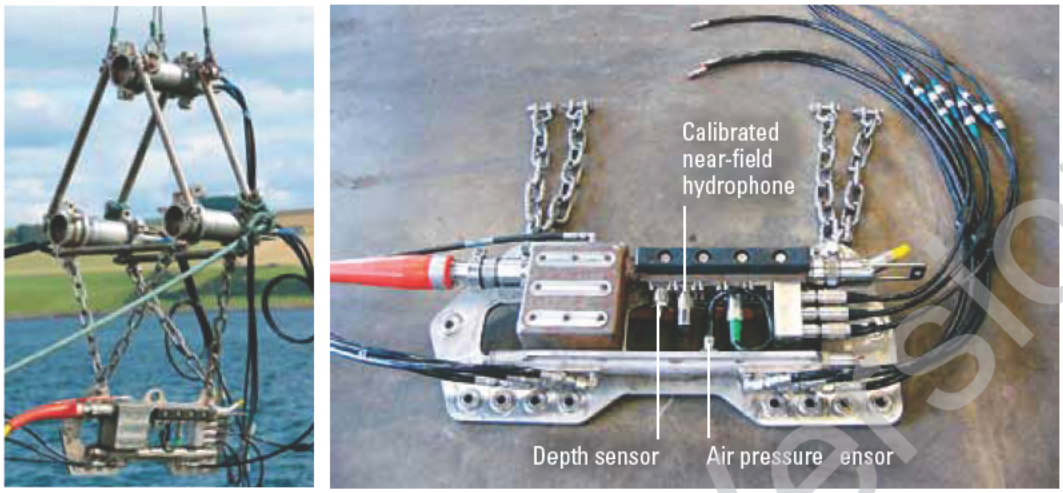

Figure 3-13. TRISOR source controller installed in a three-gun cluster (left). Closeup view of the TRISOR system with its external sensors noted (right).

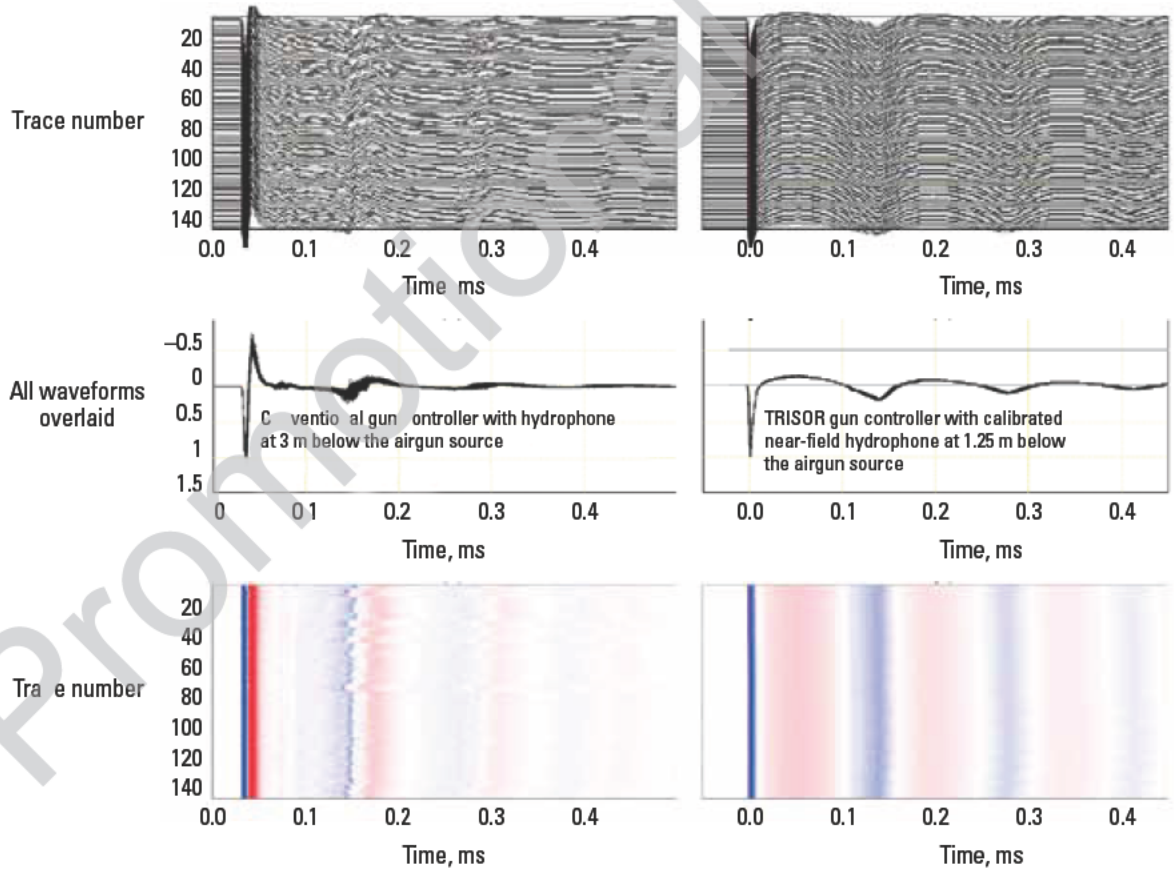

Figure 3-14. Airgun signature controlled by manual tuning system (left) and by the TRISOR system (right).

3.2.1.6 SWINGS navigation system

Typical navigation systems rely on global positioning system (GPS) technology. A discussion of GPS is not provided here; the reader can refer to abundant reference material available elsewhere on this topic. Navigation requirements for offshore VSP acquisition must include the following capabilities.

- Monitor the position of the vessel carrying the source in real time.
- Provide a real-time display of vessel position to steer the boat over the desired shotpoint locations.
- Generate a firing pulse to the gun system when the boat position comes within a prespecified proximity to the shotpoint location.
- Record the exact location and time at which the gun fired.
- Interface with the recording system to write this information to the data record.

SWINGS seismic navigation and positioning system represents the latest technology in navigation systems and is designed to be integrated with the Q-Borehole integrated borehole seismic acquisition and processing system. The SWINGS system includes vessel movement monitoring, navigation system, and radio link between vessel and rig. Figure 3-15 is a photograph of the main module for such a system. The system requires a minimum of four satellites to be above the horizon in a suitable geometry; with this requirement met, the overall system's accuracy is 1 m, which is updated 5 times per second.

When the source comes within a specified distance of the selected shotpoint, the navigation system sends a *fire* pulse to the gun controller, which triggers the acquisition system. At the same time, the system records the exact time and position at which the airgun source was fired by the TRISOR controller and also writes this information to the data recorded by the recording system. Figure 3-16 illustrates the functionalities of the SWINGS navigation system.

3.2.2 Nonimpulsive sources, controllers, and navigation

For borehole seismic acquisition on land, the preferred source is vibroseis because it is safe, repeatable, controllable, and moveable. In the late 1950s and into the 1960s, vibroseis was developed to provide a surface source (no drilling) with high-production capabilities (mobile), low-impact characteristics (no shot holes or blowouts), and source-design flexibility and repeatability in terms of frequency and amplitude.

Vibrators come in a variety of shapes and sizes. Truck-mounted vibrators are particularly useful for VSP work because they can be driven directly to the jobsite. Figure 3-17 shows the new-generation Q-Borehole vibrator truck from Schlumberger.

Schlumberger maintains a set of stringent operating procedures to ensure vibrator safety, both while in transit to and from the wellsite and during operation of a seismic survey.

The philosophy behind vibroseis is that, whereas impulsive sources, such as airguns or dynamite, put out

Figure 3-15. SWINGS portable navigation and positioning system.

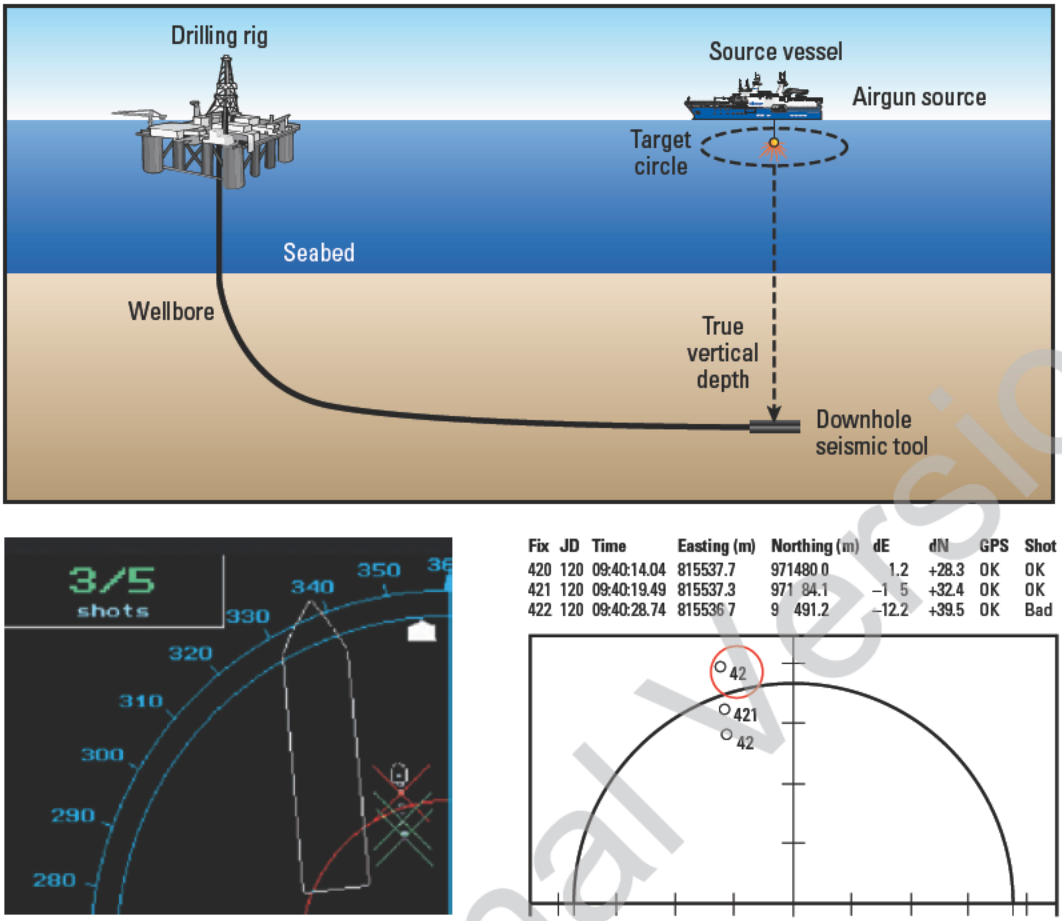

Figure 3-16. Illustration of the SWINGS navigation and positioni g system installed on source vessel for a vertical-incidence VSP operation (top). Real-time SWINGS display (ottom left) shows shot positions relative to circle of tolerance. Source vessel is represented by the rrow and the a gun is shown in the box at the right-rear end of the vessel. Red line indicates target circle, and blue arcs in cate bearings. Red cross indicates shot fired outside of the target circle. Green crosses correspond to s ots fired with he target circle. The red circle in the post-acquisition QC plot (bottom right) shows that one shot was ired ou ide of the target circle.

Figure 3-17. The Schlumberger latest generation of truck-mounted vibrator, with 60,000 lbf peak force.

all the energy of the shot in a few milliseconds and generate energy at all frequencies concurrently, a vibratory source spreads its pulse over a longer time and injects only one frequency at a time. Although the power (i.e., the rate of energy delivery) of both source types is drastically different, the resulting energy (power × time) may be the same (Fig. 3-18). In the case of explosive energy, its frequency and amplitude depend on the type of explosive and the positioning, which cannot be changed easily, whereas frequency and amplitude of vibroseis energy can be customized more easily.

If the pulse, or sweep, shape is known, then in the reflection record, the response from any reflector will have the same shape as the injected pulse. It is necessary only to identify every timepoint in the reflection record at which this happens and to replace the drawn-out pulse with a spike. This identification is performed by crosscorrelating the recorded data trace with the known input sweep signal so that each event on the trace will be replaced by the autocorrelation of the input sweep. The vibrator start time—equivalent to the time break in impulsive sources—is the autocorrelation function of the sweep. This is always a symmetrical sinc pulse; the origin of a vibroseis record is at the center of symmetry of the zero-time pulse. Figure 3-19 illustrates the autocorrelation process used in vibratory seismic acquisition.

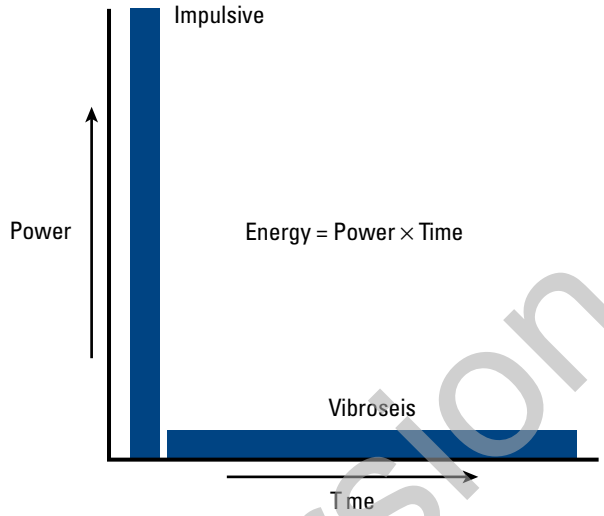

Figure 3-18. Schematic illustration of power spectra for impulsive and vibroseis seismic sources. Although the energy of both sources may be the same, the rate of delivery of power is very different.

Two important parameters in a sweep are the sweep bandwidth and the central frequency, which determine the definition and the resolution of the seismic wavelet, respectively; see the relative size of the central peak for definition and width of the central lobe in Fig. 3-20. An

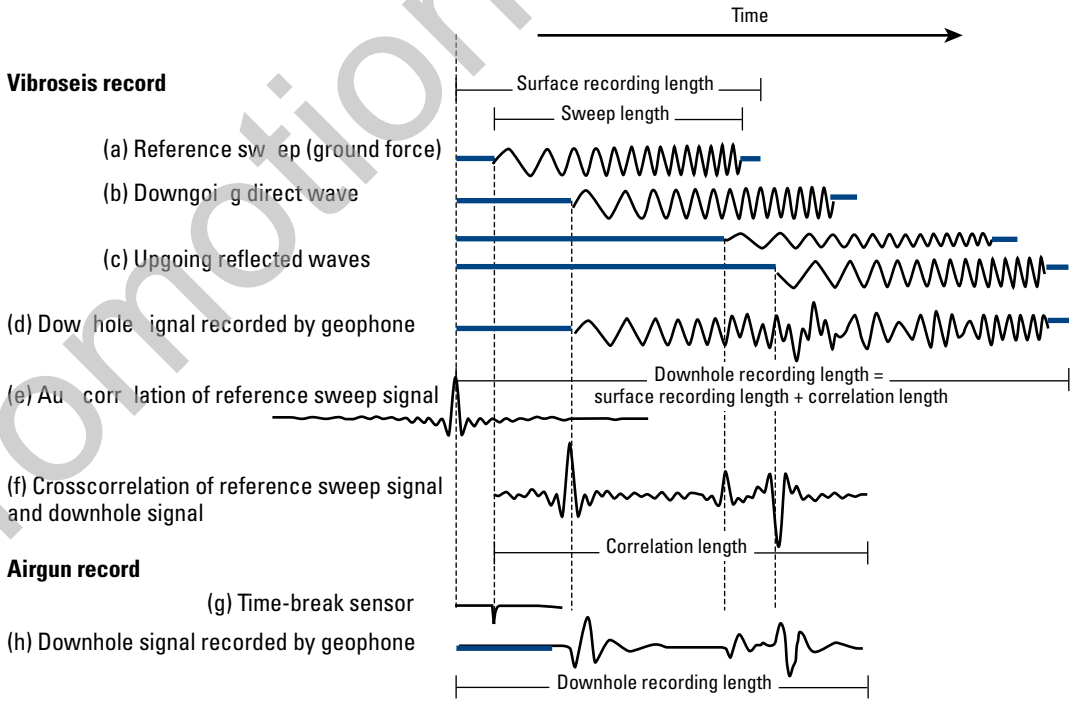

Figure 3-19. Vibroseis record versus airgun record.

important point is that definition increases with sweep bandwidth. As shown in Fig. 3-20a, as the bandwidth increases (i.e., as 25–35 Hz increases to 10–50 Hz), so does definition. Note that in this case, the central frequency remains constant (i.e., 30 Hz). Equally important is the fact that resolution increases with an increase of central frequency. Figure 3-20b illustrates a sweep with a constant bandwidth of 1 octave (constant definition) as it is moved upward through the frequency range so that the central frequency increases (i.e., from 22.5 Hz to 60 Hz).

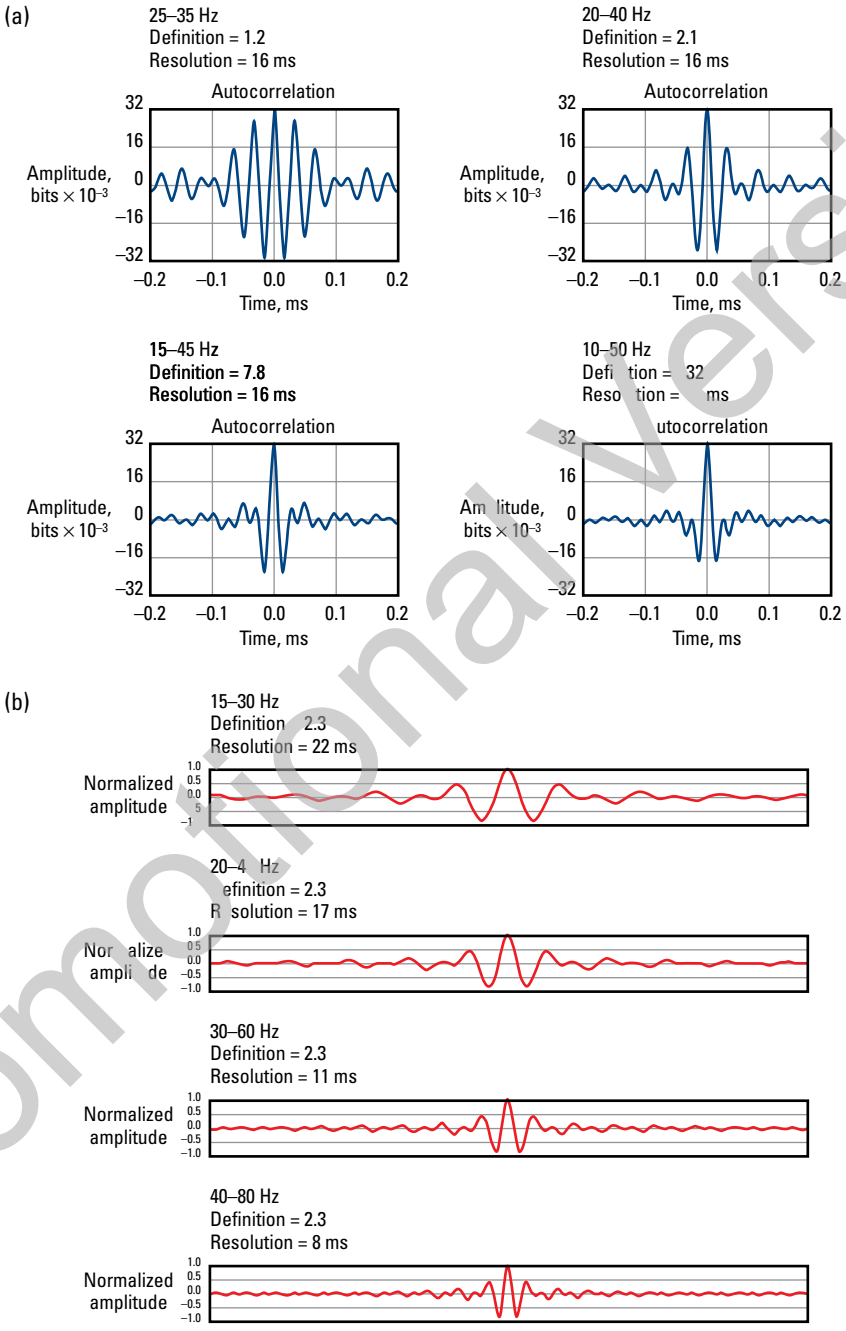

Figure 3-20. Definition and resolution of sweep signals. (a) Definition increases with bandwidth (examples of constant central frequency shown). (b) Resolution increases (value in milliseconds decreases) with increase of central frequency (examples of constant bandwidth for a single octave shown).

3.2.2.1 Source interaction

A group of vibrators is generally used to provide seismic energy at depths of interest. When multiple vibrators are placed in-line with a separation between baseplates of at least 10 m, tests have shown that the "quiet" vibrator picks up energy from the "active" vibrator at a level of –50 dB below the active vibrator's local accelerometer signals; this is an insignificant level of interaction. However, if vibrators are closely positioned side-by-side, and only spherical spreading is assumed, the increase in energy is about +40 dB. Note that phase variation related to the different control systems and to the propagation delay between vibrators would lead to additional degradation of signal control.

3.2.2.2 Sweep types

The signal input into the Earth is an applied force, usually sweeping upwards from a low frequency to a high frequency, for example, from 8 to 96 Hz. The sweep is often a simple linear function of time and lasts about 8 to 12 s. More complex spectral characteristics and sweep durations are possible and may be specified in particular projects (Fig. 3-21). Low- and high-frequency output is normally limited by hydraulic and mech nical performance of the vibrator. Low-frequency r cording is typically reduced even further by the perform nce of the geophone sensors, whereas high-frequency recording is limited by the highest frequency that is reasonably expected to be transmitted thr ugh the Earth in

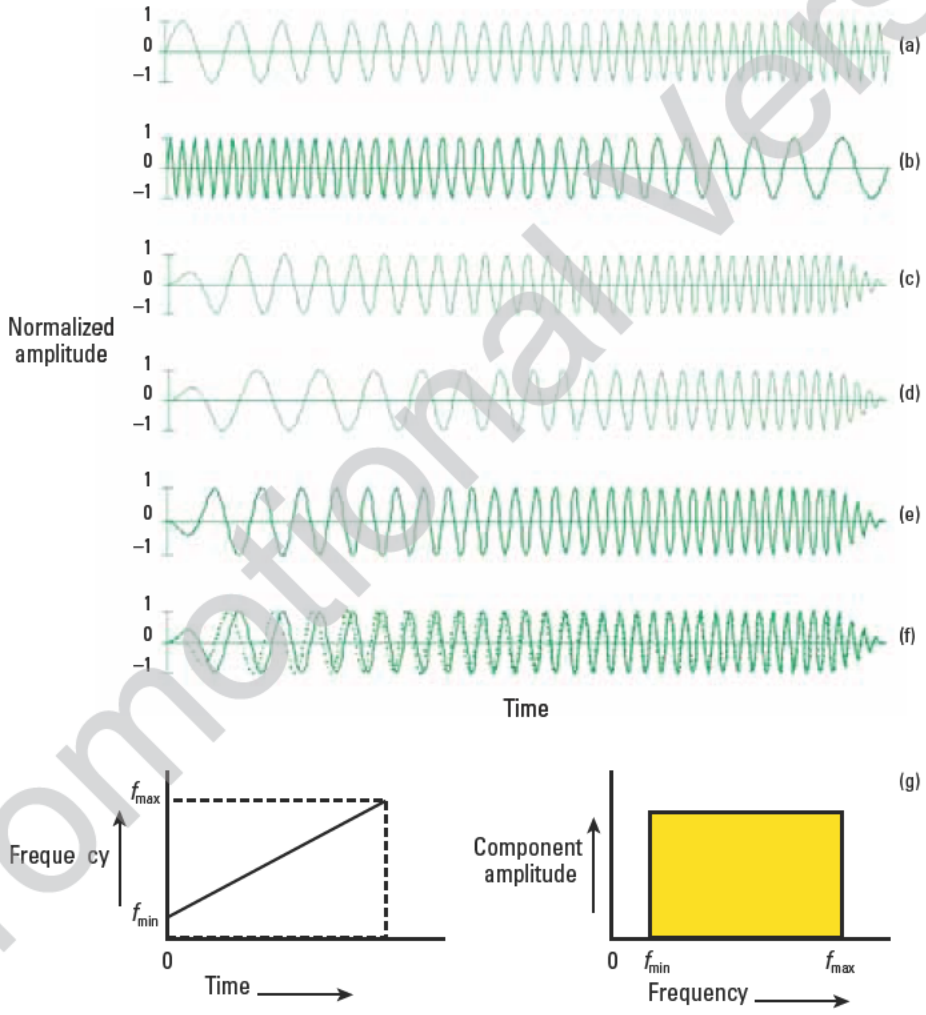

Figure 3-21. Different types of sweeps: (a) linear upsweep, (b) linear downsweep, (c) tapered linear upsweep, (d) tapered nonlinear upsweep, (e) phase-inverted, tapered linear upsweep, and (f) tapered linear upsweep with different phase characteristics. (g) Linear upsweep characteristics are shown in the frequency domain.

this location—the Earth acts as a high-bandpass filter. Sweeps are typically tapered at both ends to ease the hydraulic functionality of the vibrator.

Linear and nonlinear sweeps

Standard vibroseis signals are used for the vast majority of applications. According to sweep (a) in Fig. 3-21, the frequency varies at a constant rate in linear sweeps; this maintains the same level of amplitude throughout the shaking time. Both the imparted and autocorrelated signals have a flat amplitude spectrum. Linear sweeps find their limitation when the noise level at depth of interest critically approaches the signal level. Increasing the bandwidth while keeping the same sweep length would render adverse effects, such as a worse signal-to-noise ratio (SNR), whereas longer sweeps would improve SNR at the expense of operation inefficiency (Fig. 3-22).

Ideally, an efficient sweep would maintain constant SNR bandwidth over the entire spectrum (Fig. 3-23). That is the concept behind the nonlinear sweep. In a nonlinear sweep, vibrators sweep slowly through the frequencies that needed to be strengthened and more rapidly through those where sufficient strength has be n achieved. Figure 3-23 compares nonlinear sweeps with a linear one.

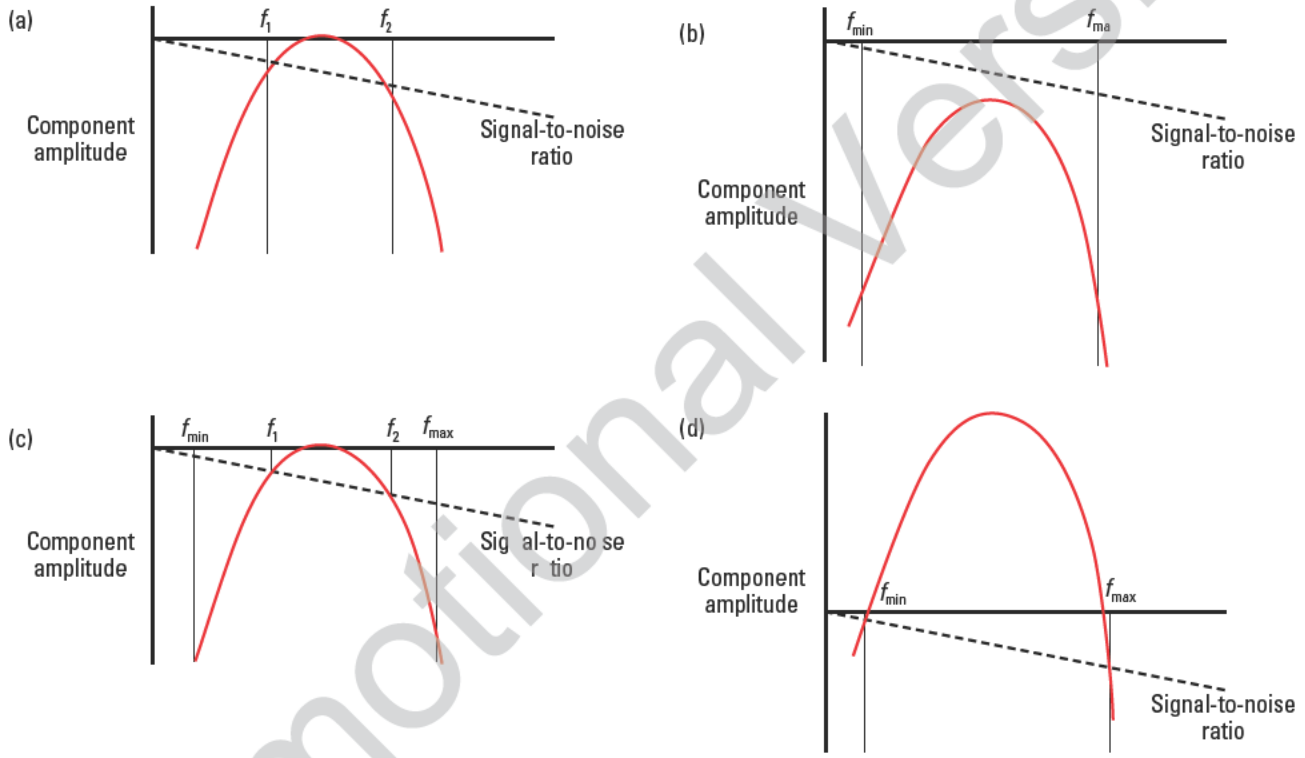

Figure 3-22. Effects of swe p freque cy and sweeping length on output signal-to-noise bandwidth: (a) original sweep bandwidth and length (b) inc eased bandwidth but same sweep length causes the signal spectrum to fall below the noise because les time is spent at each frequency, (c) increased bandwidth but twice the sweep length brings the original bandwidt back to ts original level, and (d) desired signal-to-noise bandwidth achieved by sweeping much more than tw ce as ng a the original.

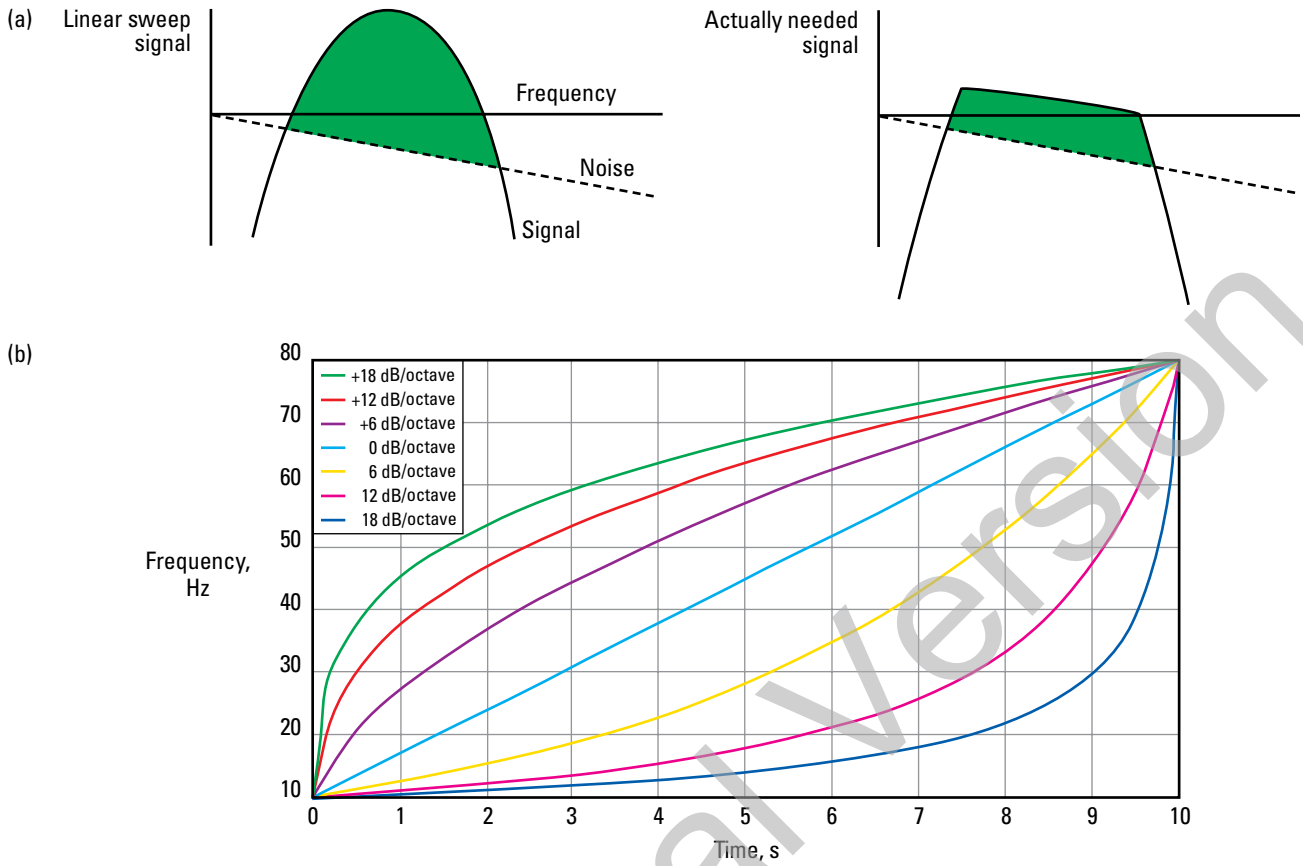

Figure 3-23. (a) Linear sweep compared to an ideal, more efficient sweep. ( ) Comparison of a linear sweep (0 dB per octave) with nonlinear sweeps (positive and negative B per ctave).

High-productivity sweeping techniques

Rig time is costly for operating compani Coll cting data in a drilling well costs rig time and increases risk of failure because the reservoir is exposed to wellb re fluids and the openhole well section may becom unsta le.

HFVS™ High Fidelity Vibr tory Seismic (developed by Mobil Corporation) a d the echnique of Cascaded Sweeps™ radically al er th time frame in which land borehole seismic data is acquired. In the HFVS technique, particularly v luab e in multioffset surveys, all source position are swept simultaneously with identical sweep parameters ex ept that a unique phase rotation is applied to one location (Fig. 3-24). The cascade sweeping technique, on the other hand, is created by linking together sweeps of a conventional sweep cycle series. The concatenated components, or segments, that make up cascaded sweeps are identical except that a unique phase rotation is applied to each segment (Fig. 3-25).

The HFVS technique enables the seismic crew to acquire multiple source positions simultaneously on a single descent into the well, which otherwise are acquired sequentially in conventional borehole seismic operations. Cascade sweeping technique reduces operating time dramatically by eliminating downtime between sweeps.

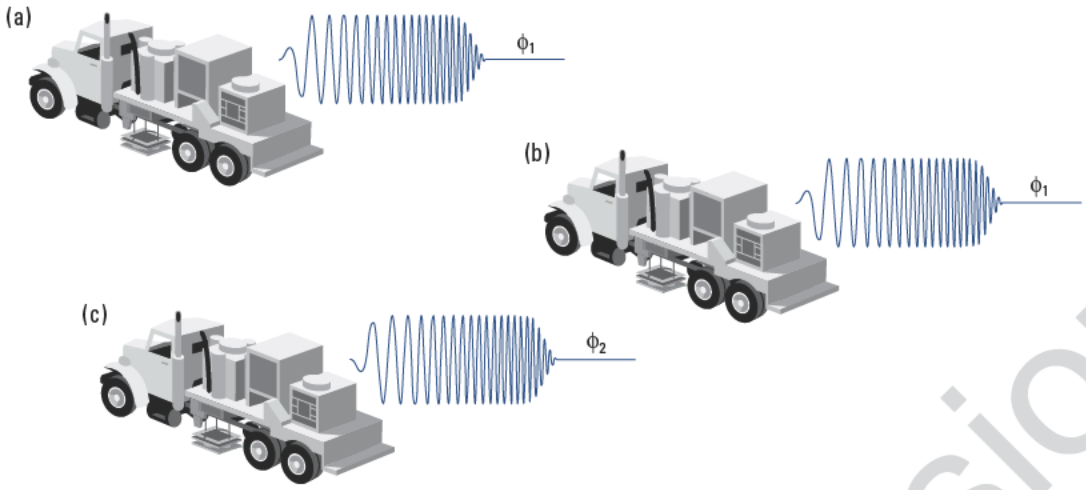

Figure 3-24. Idealization of HFVS acquisition. Note that lower truck (c) shakes with the same sweep, but phase (ϕ) is rotated.

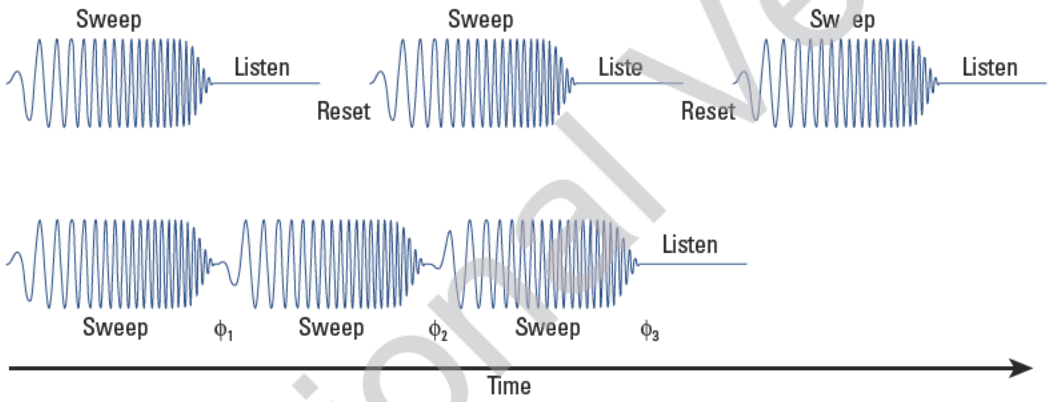

Figure 3-25. Schematic representation of the a cade sweeping technique.

The HFVS and cascade tec niques use inversion, not crosscorrelation, to ext ct th sei mic signal from the recorded sweep. Each trace recorded downhole is inverted using the ground f rce recorded in each vibrator; this extracts each downhole trace for each source position recorded. Occas onally, because of this inversion technique the h gher frequency harmonics can be included. This is how bandwidth broader than the sweep an sometimes be obtained. Figure 3-26 shows seismic data gathered with conventional and HFVS sweeping techniques.

S ip sweeps is yet another technique that has been used for many years in the surface seismic industry to increase productivity by enabling data recording from a series of overlapping sweeps from different groups of vibrators. This technique, as illustrated in Fig. 3-27, requires continuous downhole recording and subsequent shot separation and sorting in data processing. Data degradation caused by harmonic contamination (which was a major constraint in the past) is eliminated with this technique by using SHARP* Slip-sweep Harmonic Removal Procedure, which is a patented WesternGeco technology.

The concept of MD Sweep* design methodology (MD - maximum displacement) that provides the most energetic low frequencies possible from the vibrator (proprietary of WesternGeco) has also been long discussed in the surface seismic industry. Only since very recent advances in vibrator technology (Fig. 3-17) became available has this type of sweep become

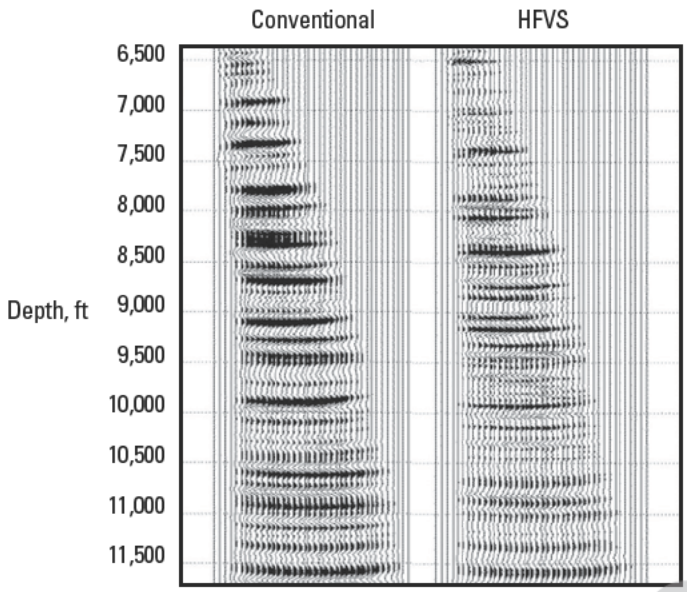

Figure 3-26. Example of depth-migrated images for one of the far-offset VSPs at a field tes acqu red with the conventional vibroseis method and with the HFVS method. The lateral image span i 2,000 (From Moldoveanu *et al.*, 2000; used with permission.)

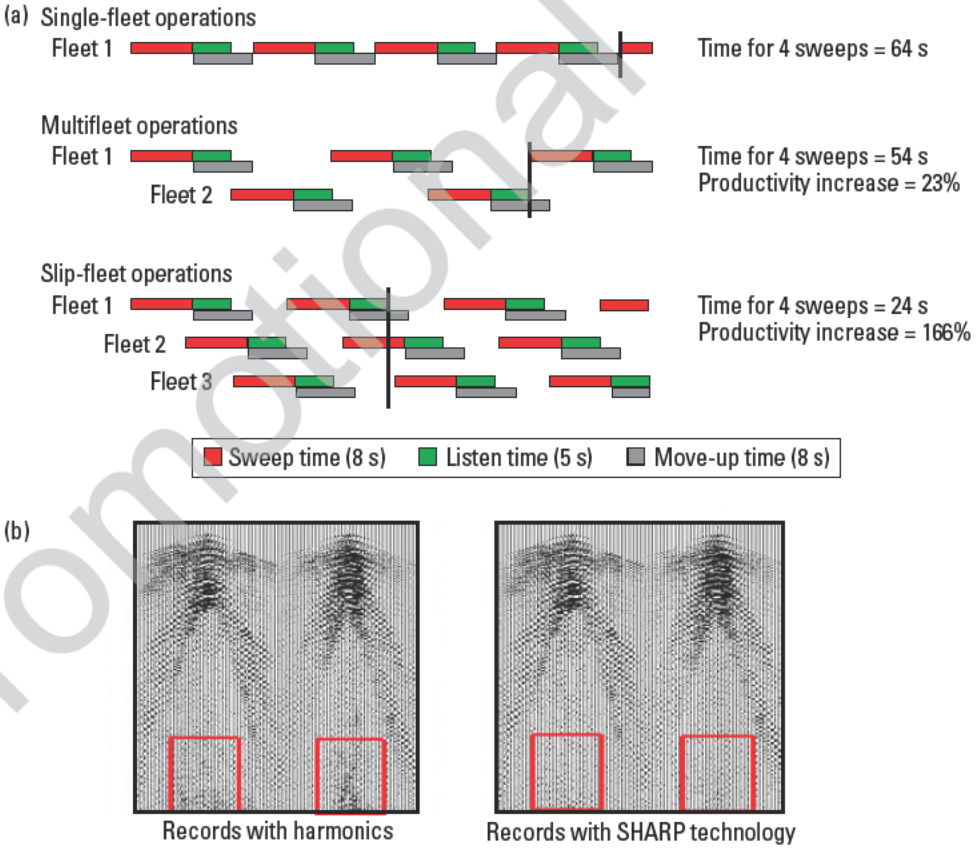

Figure 3-27. (a) Comparison of sweep techniques. Slip-sweep operations increase vibroseis productivity. (b) Vibroseis records with harmonics are shown on the left; records with SHARP technology (right) have attenuated harmonic noise from adjacent vibrators.

reality. The MD Sweep technique outputs the required ground-force power spectral density without spending more time than is necessary to generate the critical low frequencies (Fig. 3-28).

A borehole seismic survey using any high-productivity technique is a highly specialized service. It requires a minimum of two, ideally four, vibrators, which may require tuning equipment beyond the vibrator's normal specifications. Operations require a great deal of "bookkeeping" to ensure that the downhole data and vibrator information are synchronized. From the geophysical point of view, if the ground is not representative of the far-field signatures, the deconvolution applied in data processing is not correct, and a harmonic ghost may contaminate the data, typically at late arrivals.

3.2.2.3 Vibrator description

A vibrator source consists of a baseplate, which is pressed down on the ground by the weight of the truck. A dual-acting piston inside a large mass is mounted above the baseplate with a hydraulic system to drive this mass up or down relative to the baseplate (shown schematically in Fig. 3-29). The force on the mass and on the baseplate is constantly controlled by a feedback system to maintain the output force in-phase with the reference signal generated by the electronic signal generator (schematically shown in Fig. 3-30).

The conventional vibrator unit generates vertical force at the Earth's surface. For most recording geometries, this would be regarded as a compressional-wave source because, for points beneath the vibrator, the particle motion of the propagating wavefield is longitudinal. At large angles to the vertical, the source is also generating strong, vertical shear (SV) waves and much weaker compressional waves.

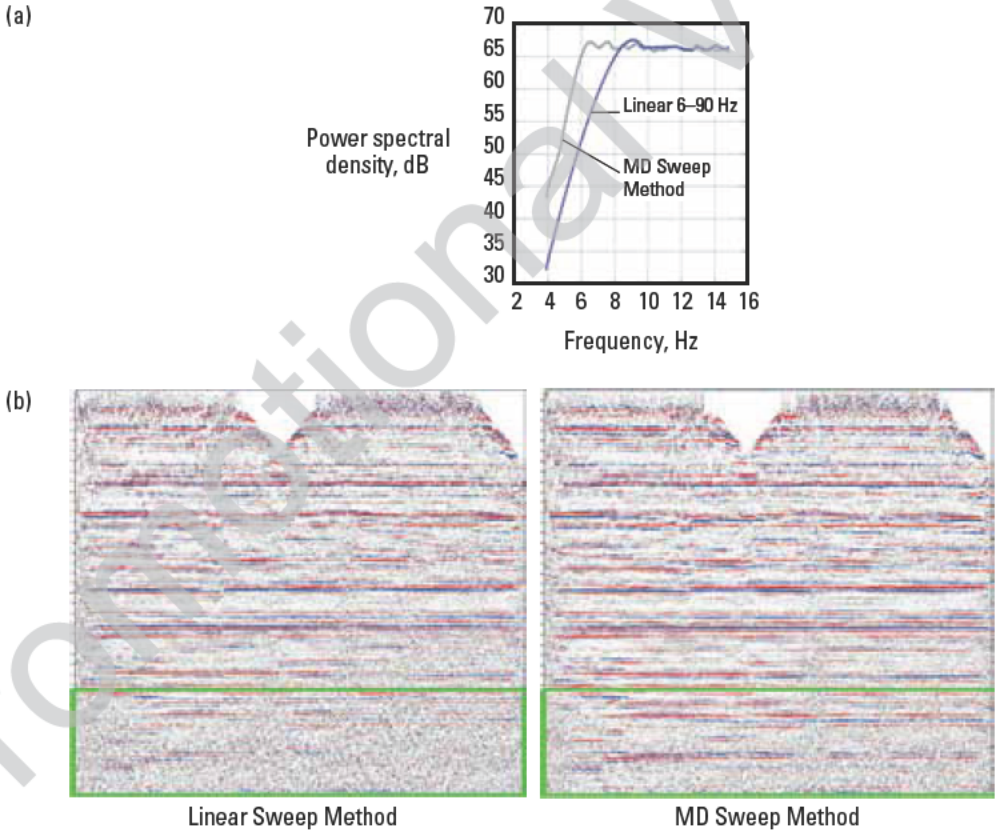

Figure 3-28. Comparison of MD Sweep methodology with conventional linear sweep method. The power spectral density comparison (a) and the results of both methods shown in surface seismic sections (b) were acquired on the same line using the same parameters.

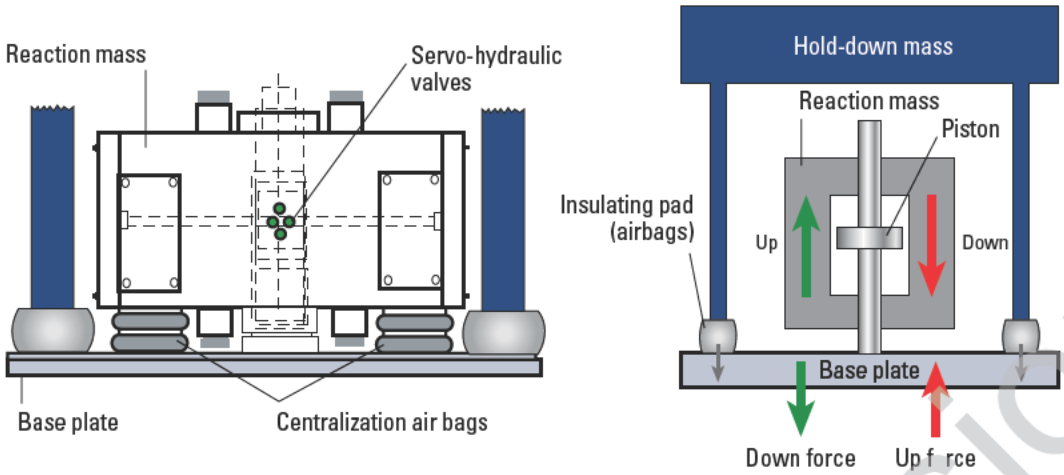

Figure 3-29. Vibrator schematic (left) and functionality (right). The reaction mass is accelerated upward and downward relative to the base plate to produce a fluctuating force signal in the Earth.

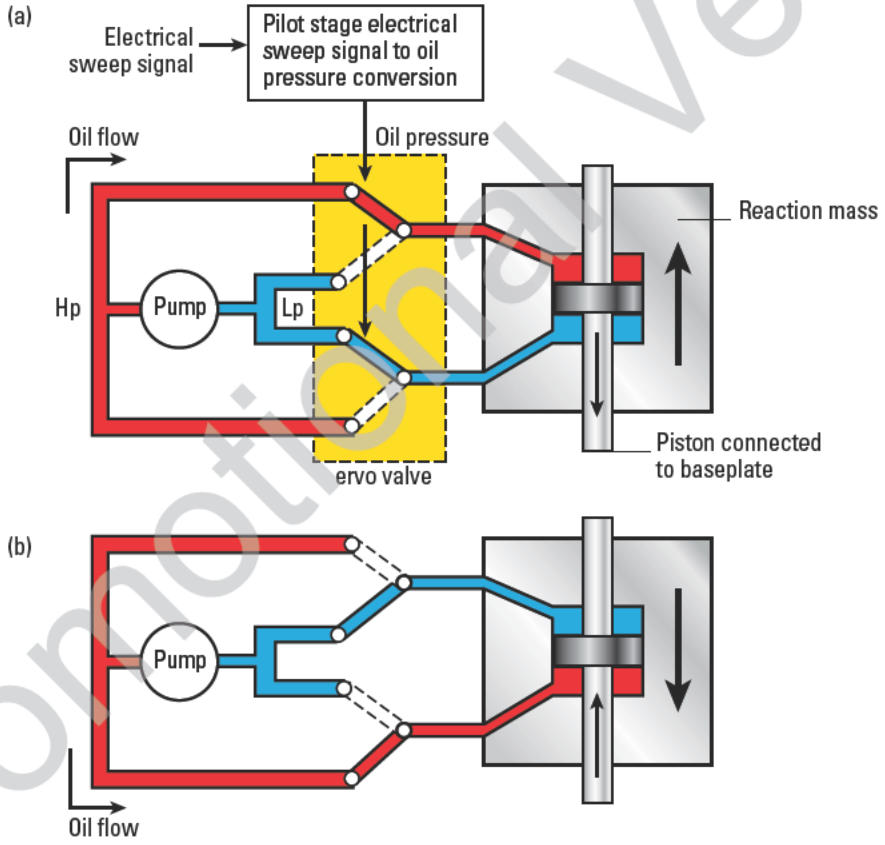

Figur 3-30. Schematic of vibrator hydraulic actuator with reaction mass: (a) reaction mass moving up (piston conn cted to baseplate moving down), (b) representation of reverse cycle. Hp = high pressure; Lp = low pressure.

A variation of the basic vibrator system—the special shear-wave actuator—is used to generate seismic shear waves at the surface. By rotating the reaction mass through 90 degrees and placing a shear-wave attachment at the base plate, as shown in Fig. 3-31, a horizontal, or shearing, force can be imparted to the surface. Shear-wave vibrators are specialized equipment available through a limited number of vendors.

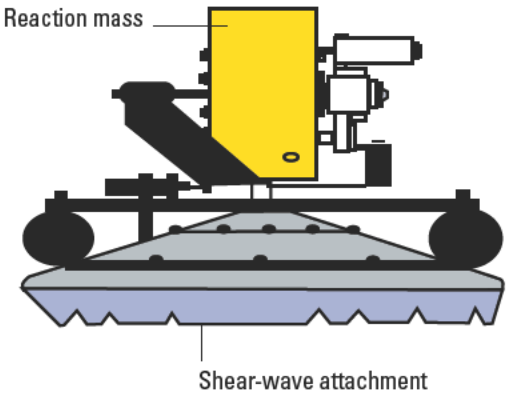

Figure 3-31. Special equipment: shear vibrator baseplate attachment.

3.2.2.4 Vibroseis controllers

The Advance III Vib Pro™ servo-hydraulic system (Fig. 3-32) typically consists of one encoder unit and multiple decoder units. Each Vib Pro unit can be configured as either an encoder or decoder. The encoder is typically connected to a seismic recording system, and the decoders are each installed in a servo hydraulic vibrator. Additional GPS functionalities provide source positioning and remote triggering of downhole equipment recording, which are particularly important when acquiring walkaway and 3D VSP surveys. Detailed information on vibroseis controllers is available directly from the manufacturers.

Figure 3-32. Pelton Vib Pro encoder. (ION Geophysical Corporation, 2008.)

3.2.3 Other sources

Dynamite is a cost-effective and compact commodity that produces a high-energy pulse with very desirable spectral characteristics. To preserve high-frequency content in surface seismic acquisition, dynamite is usually deployed in shot holes drilled below the weathering layer to a depth of 10 to 20 m.

Dynamite is lightweight and portable, thus making it ideal for moving-source geometries such as walkaway lines in difficult or wet terrain. However, the handling and loading procedures for explosives are very stringent to minimize environmental impact, security risk, and health risk. Safe detonation distances from structures and pipelines, dependent on charge size and depth, are computed based on a knowledge base built from extensive worldwide experience.

The requirement for VSP work is usually to generate a large number of shots at the same point on the Earth's surface while the recording tool is moved up the wellbore. Both the amplitude and frequency content of these shots should be as similar as possible; therefore, the explosive should be detonated in nearly identical conditions for each shot. Two methods are commonly used to achieve this. One is to predrill an array of shot holes and fire them sequentially as the tool moves. This has two drawbacks: it requires a large number of holes for a deep well, and there is the risk that the signature from different holes may be different. If a survey requires 100 shots, this might be a 30 m × 30 m grid with 3 m between shot holes, over which near-surface ground conditions may significantly vary. Additionally, each shot will have a slightly different static correction associated with it owing to depth, fill material, and position, which will degrade the repeatability of the source.

A second, and preferred, approach is to drill a large-diameter hole at the desired location, case it, cement the casing in place, and then fill this with water. Charges can then be lowered into the hole and detonated. This has the advantage of maintaining a consistent environment in which to explode the dynamite. Operationally, care must be taken to maintain the water level in the borehole and to maintain a consistent depth at which the charges are exploded. Small charges and a large hole diameter will help to extend the life of this velocity barrel.

3.2.4 Safety recommendations and environment

Borehole seismic jobs entail the use of explosives, heavy tools, high-pressure air or hydraulics, and remotely operated equipment. Failure to follow established seismic procedures presents high risk of a catastrophic incident.

Quality, health, safety, and environmental (QHSE) considerations are fundamental to the design of borehole operational procedures. Schlumberger makes full use of the advanced technology and proven procedures developed and applied worldwide by WesternGeco for surface seismic operations, particularly as they relate to source deployment; to determination of safe operating distances from rigs, vessels, structures, and pipelines; and to minimization of environmental impact.

It is critical for all personnel involved in seismic operations to follow stringent QHSE guidelines and recommendations to conduct operations as safely and efficiently as possible. Substitution of equipment and materials in seismic operations should not be made by using inferior products that may not be intrinsically safe. Responsible operators use both equipment and procedures that adhere to highly demanding international test standards and seismic industry best practices. Schlumberger performs continual monitoring and revision of these standards during auditing processes as part of its Quality Management System (QMS).

3.3 Wireline seismic tools

The design of acquisition hardware for VSP is in continuous evolution. Materials and manufacturing processes improve, electronic components become smaller and more integrated, and data quality and precision requirements become more stringent. At the same time, market shifts dictate changes in the direction of the tool design as a function of demand.

3.3.1 VSI Versatile Seismic Imager

For Schlumberger, the foundation for high-quality seismic data from the borehole lies with the VSI Versatile Seismic Imager tool. The VSI tool is the product of the market pressures and design improvements that resulted in the progression of old-generation seismic tools into the modular design concept of the modern VSI tool, which can be used both in cased and openhole environments. Comparison between different Schlumberger seismic tools is shown in Fig. 3-33. Note that the tool diameter is substantially less than in previous seismic tools, which improves the serviceable mark by as much as 25.5 mm, and in particular, provides access up to a 70-mm hole with a fully featured seismic tool. The outside diameter (OD) of a standard VSI tool is 85.7 mm; in slim configuration, the OD is 63.5 mm.

The VSI tool is designed to service both the simple borehole seismic applications and the large-scale, complex applications with the same hardware. This is largely because of its modular design that accommodates 1 to 40 shuttles (the tool section carrying seismic sensors), which allows a distribution of sondes through a large survey area. Conventional seven-conductor logging cable—heptacable—allows changes in spacing between the shuttles and easy maintenance. An alternative intershuttle connection is possible with solid spacers. Such tool can be deployed on drillpipe in poor borehole conditions or in horizontal wells.

Figure 3-34 shows the modular design concept, and Fig. 3-35 shows a photograph of a shuttle and a sketch of its overall layout. The expandability of the number of

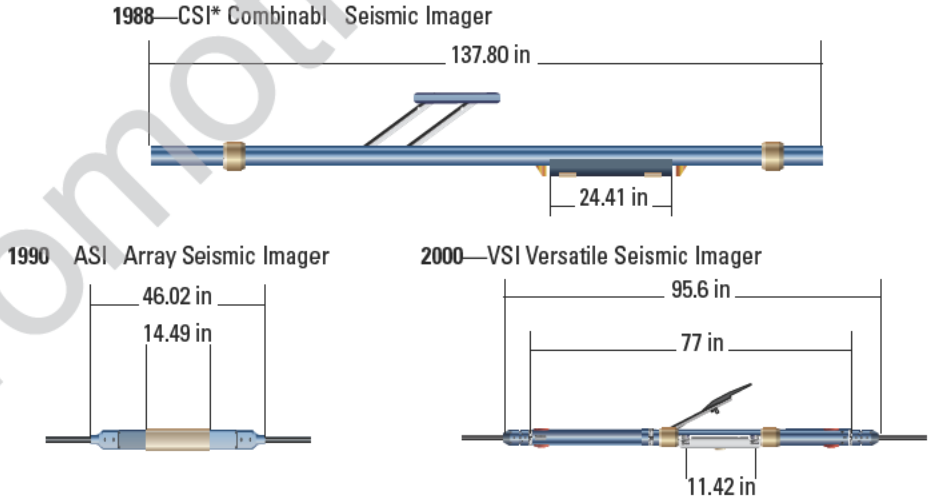

Figure 3-33. Historical evolution of Schlumberger seismic tools. The modern VSI tool combines features of its predecessors: size and bridle interconnection between shuttles from the ASI* array seismic imager, and decoupled sensor package and caliper-actuated anchoring system from the CSI* combinable seismic imager.

shuttles is one of the most exciting features of this tool. Large arrays create possibilities for

- full-aperture-imaging surveys
- large-depth-range anisotropy surveys
- full AVO calibration surveys
- passive-monitoring surveys
- simultaneous acquisitions with surface seismic.

As with the previous-generation tools, the 3C geophone package is decoupled from the sonde body, and a shaker is incorporated to evaluate the geophone coupling response. The sensor elements are wide-bandwidth

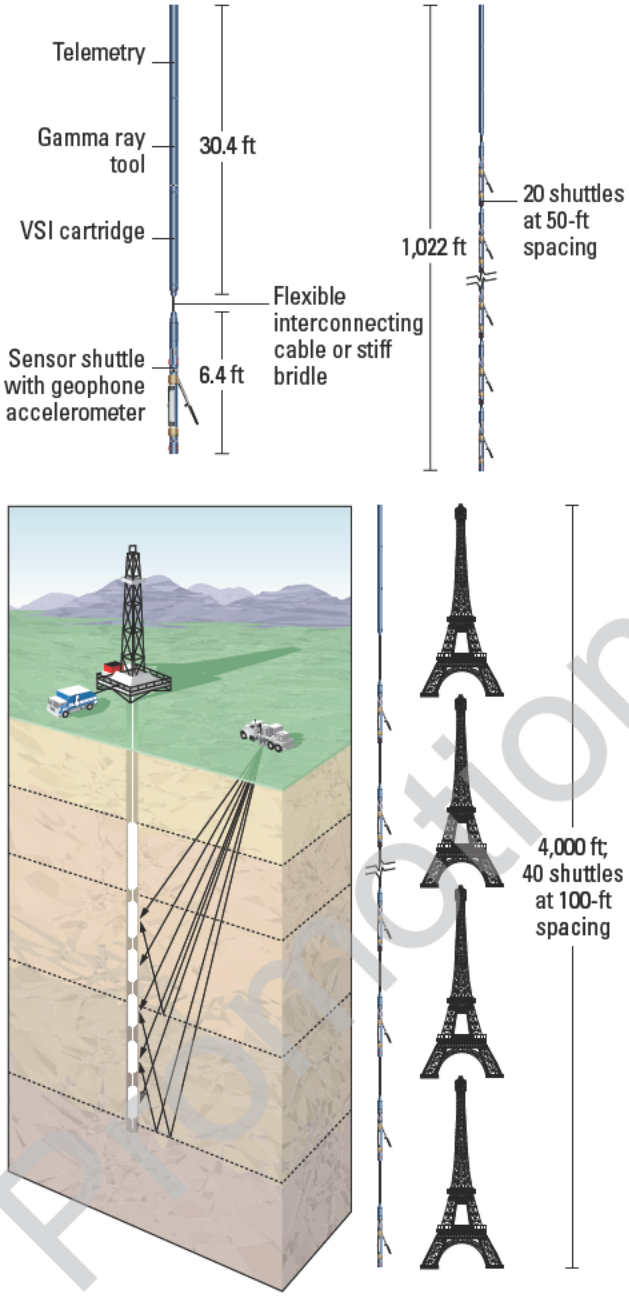

Figure 3-34. The VSI tool. Elements of a VSI tool (top) add flexibility for field deployment as a basic toolstring (bottom left) or as a very large VSI array for 3D VSP surveys (bottom right). (From Hope *et al.*, 1998; this graphic is copyright Schlumberger, Ltd. Used with permission.)

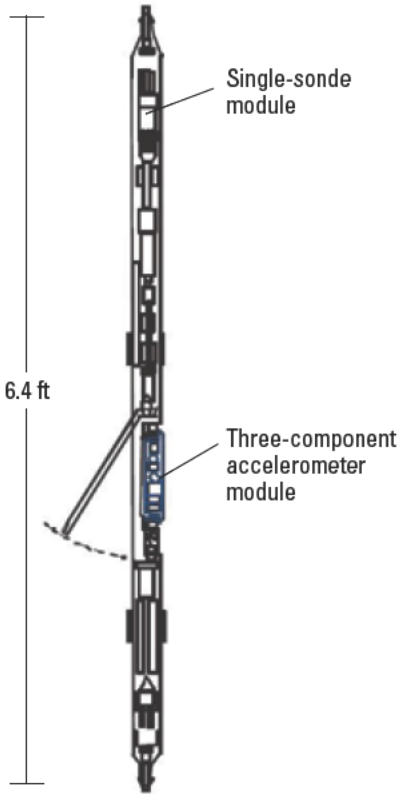

Figure 3-35. VSI modular shuttle.

geophone accelerometers—GACs. Figure 3-36 shows how the sensor is decoupled from the main tool body and shows the three-point contact in the sensor package, which provides the most stable contact in boreholes. An in situ shaker test is shown in Fig. 3-37 to illustrate the importance of this feature on a borehole seismic tool.

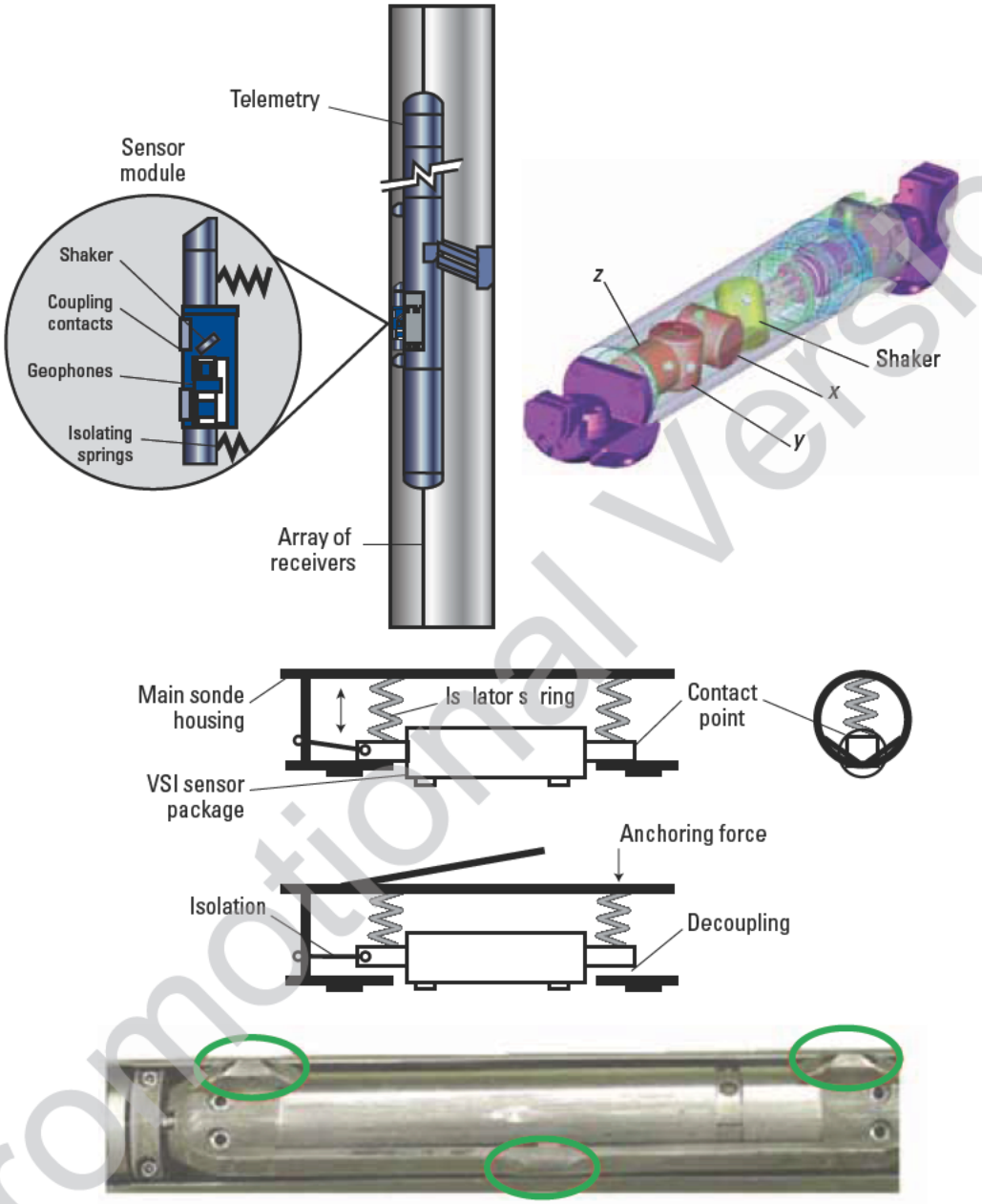

Figure 3-36. VSI tool with sensor module. The sensor module contains a GAC 3C geophone system, preamplifiers, and a shaker. The middle illustration depicts how sensor decoupling is achieved in the tool. A photograph (bottom) of the VSI sensor housing shows the three-point contact (green ovals) achieved in the borehole for superior data quality.

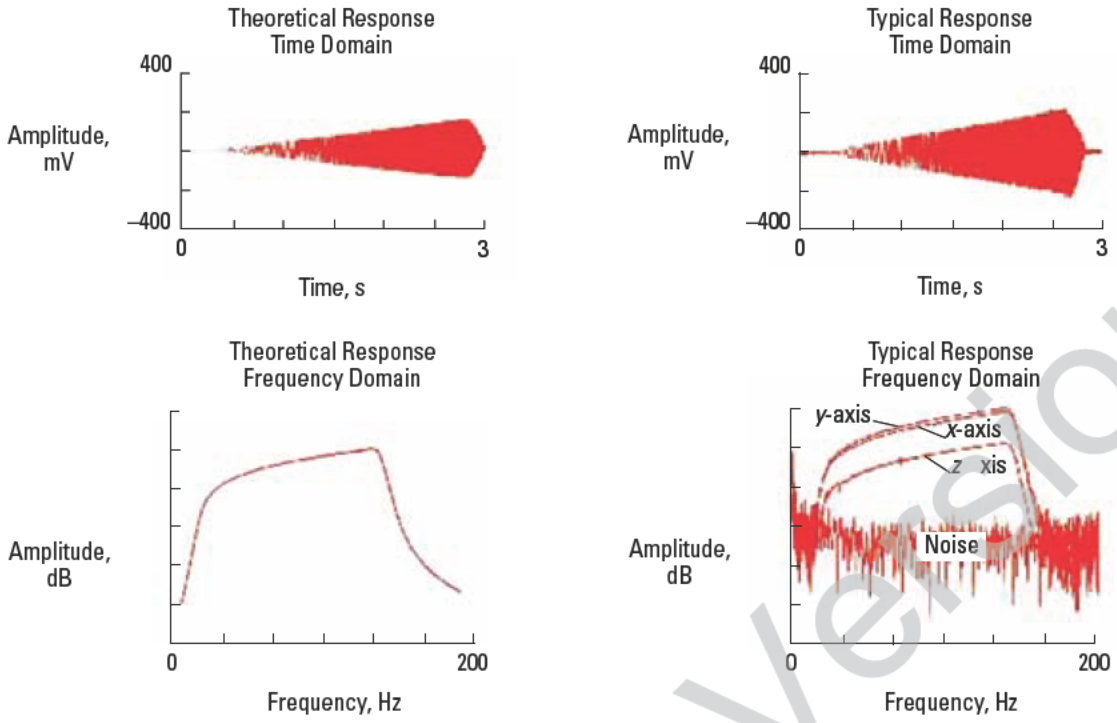

Figure 3-37. Results of a VSI tool in situ shaker test. The theoretical response ses a perfectly coupled geophone model; the typical response is a real response from a well-coupled g ophone. If there are resonances in the coupling system within the excited bandwidth, they are visibl as peaks on the amplitude spectrum and as departures from the linear response in the me domai This example shows good coupling between geophone and borehole.

3.3.1.1 Equipment and specifications

As shown in Fig. 3-34, the downhole equipment includes a VSI power cartridge, which controls the power supply for the cartridges and shuttles. The controller ar- tridge includes the tool controller and th shuttle motor power supply. The shuttles are e uipped with three orthogonal geophone accelerometer detectors installed in a small sensor package that is acousti- cally isolated from the main sonde body. A single arm provides the anchori g forc for the shuttle. The coupling between th forma ion and the sensor pack- age is achieved by springs. The VSI tool provides high- speed transm ssion f high-quality multicomponent information from the downhole tool to the surface acquisition system. Shuttle interconnect spacing, using either cables or stiff bridles, can be customized to a maximum length of 50 m.

The VSI tool can be directly combined with a gamma ray (GR) sensor or casing collar locator (CCL) for depth control purposes and combined with other special equip- ment such as the tractor or gyro. In terms of surface equipment, the VSI tool communicates to acquisition computers by means of a modular interface. External trigger boards are also available to receive an external trigger signal coming from the shooting system to signal the VSI tool downhole to start recording. This capabil- ity is especially useful in large walkaway surveys, 3D VSP surveys, and simultaneous acquisition of borehole and surface seismic data. The VSI tool also features GPS-controlled surface acquisition boards, which can be used for synchronization of simultaneous recording sys- tems, for example, those of various VSI tools and surface seismic equipment.

Table 3-2 shows the specifications of the VSI tool. The tool has an 85.7-mm OD in standard configuration, with standoff and acoustic isolation springs to give the best acoustics performance. The VSI tool can be slimmed down to 63.5 mm by removing standoffs and isolation springs, which may limit its acoustics performance. The tool has been used successfully in borehole diameters ranging from 76 to 560 mm. It is light and withstands most logging environments; it has an upper operating limit of 175 degC and 20,000 psi. A VSI tool that can operate at 25,000 psi is also available.

Table 3-2. VSI Tool Specifications

Max. number of shuttles	20; 40 in newest series
Max. temperature	350 degF [175 degC]
Max. pressure	20,000 psi [1,360 bar], standard; 25,000 psi [1,700 bar] for high-pressure version
Tool OD	3⅜ in [85.7 mm] standard; 2½ in [63.5 mm] for slimhole version
Anchoring hole size	3½–22 in [88.9–558.8 mm]
Intershuttle spacing	8–100 ft, 150 ft in special applications
Sampling rate	1, 2, and 4 ms, 0.5 ms in special applications
Combinablilty	Gamma ray and casing collar locator, standard; all other wireline tools by special switch
Cartridge length	20.9 ft [6.37 m]
Cartridge OD	2½ in [63.5 mm] 2.6 in [66 mm] for 25,000 psi [1,700 bar] high-pressure versio s
Shuttle makeup length	6.4 ft [1.96 m]
Cartridge weight	190.8 lbm [86.5 kg]
Shuttle weight	70.6 lbm [32 kg]
Sensor package	Three omnitilt geophone acceler meters; one shaker
Sensitivity	> 0.5 V/G ± 5%
Natural frequency	20-Hz flat bandwidth in ac elera io 2–200 Hz
Dynamic range	> 105 dB (at 36-dB gain)
Distortion	< 0.15%
Digitization	24-bit ADC
Length	11.4 in [290 mm]
Weight	6.4 lbm [2 kg]
Coupling force	63 9 lbf 11.0 lbf [284.4 N ± 49.0 N]
Coupling force-to-sensor weight ratio	10:
VSI sonde mechanical strength	
Standard compressive	5,0 0 lbf [22,241.1 N] standard; 10,000 lbf [44,482.2 N] w th TLC* tough logging conditions stiffener
Standard tensile	18,000 lbf [80,068 N]
VSI cartridge mechanica strength	
Standard compress e	10,000 lbf [44,482.2 N]
Standard tens e	43,000 lbf [191,273.6 N]
Well deviati	No limitation
Stiff brid spacin	49.61 ft [15.12 m]
Sti f bridle OD	2½ in [63.5 mm]
Stiff brid e mechanical strength	
Standard compressive	8,000 lbf [5,585.8 N]
Standard tensile	40,000 lbf [177,928.9 N]

3.3.1.2 Seismic sensors

Most geophones traditionally used in the seismic industry respond to low natural frequencies and can be used only within very limited tilt angles; hence, the upper limit of frequency response (spurious frequency) is reduced.

Schlumberger uses the proprietary GAC sensor, which has been designed to address the limitations of conventional geophones. The GAC is a moving-coil accelerometer, featuring a light, moving coil suspended in a strong magnetic flux field. The mechanical structure is similar to a geophone. The GAC has a flat frequency response from 3 Hz to 200 Hz, with any angle of tilt, and superior sensitivity up to 800 Hz. In contrast, the natural frequency range of geophones used in most tools for borehole seismic acquisition has limited, lower frequency response (Fig. 3-38). In the VSI tool, the use of GACs results in small, light sensor packages that deliver unsurpassed coupling and vector fidelity. In addition, the industry-unique decoupled sensor package that houses the three-axis geophone is designed to keep all tool resonance outside the useful frequency of the seismic signal.

High-bandwidth capability in the tool gives us the potential for more accurate break-time picks. The detection of low-frequency events is important for seismic inversion and enhanced deep imaging.

The detected signal at the GAC is passed through the analog-to-digital conversion and decimation filters located in each shuttle; then it is transmitted to the cartridge. The sampling interval can be 0.5, 1, 2, or 4 ms. Communication within the tool and with uphole equipment is activated as soon as the tool is powered up and runs continuously. The data are temporarily stored in memory, and the software running in the surface acquisition system instructs as to which portion of data is to be sent uphole via digital telemetry. Precise synchro i-zation is achieved by knowing the downhole s mpling events in relation to the telemetry frame

3.3.2 Slim hostile-environment tools

The maximum ratings of the standard VSI tool are 175 degC and 20,000 psi. It is normal however, to find borehole temperatures ex eeding 200 degC in some parts of the world. Schlumberger has available slim tools (42.9 and 85.7 mm OD) that can withstand temperatures up to 260 degC Thes tool have been used extensively throughout the world to successfully acquire checkshots and VSPs in envi onments with temperatures exceeding 230 degC. The analog nature of this type of tool, however, dictates that the acquired data is prone to noise. Nevertheless, simple filtering techniques can help improve the data quality as shown in Fig. 3-39.

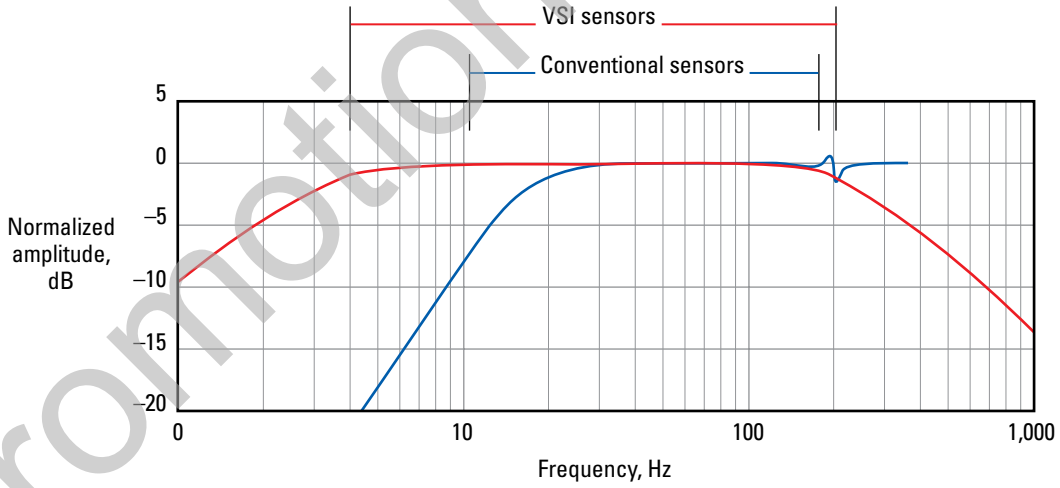

igure 3- 8. Respo se of a VSI tool GAC sensor (red), flat from 3 to 200 Hz. The ability to record frequencies b low he 10-Hz lower limit and above the 100-Hz upper limit of traditional borehole geophones (blue) allows the SI tool to record wide-bandwidth data for high-resolution images. (From Arroyo *et al.*, 2003; this graphic is copy ight Schlumberger, Ltd. Used with permission.)

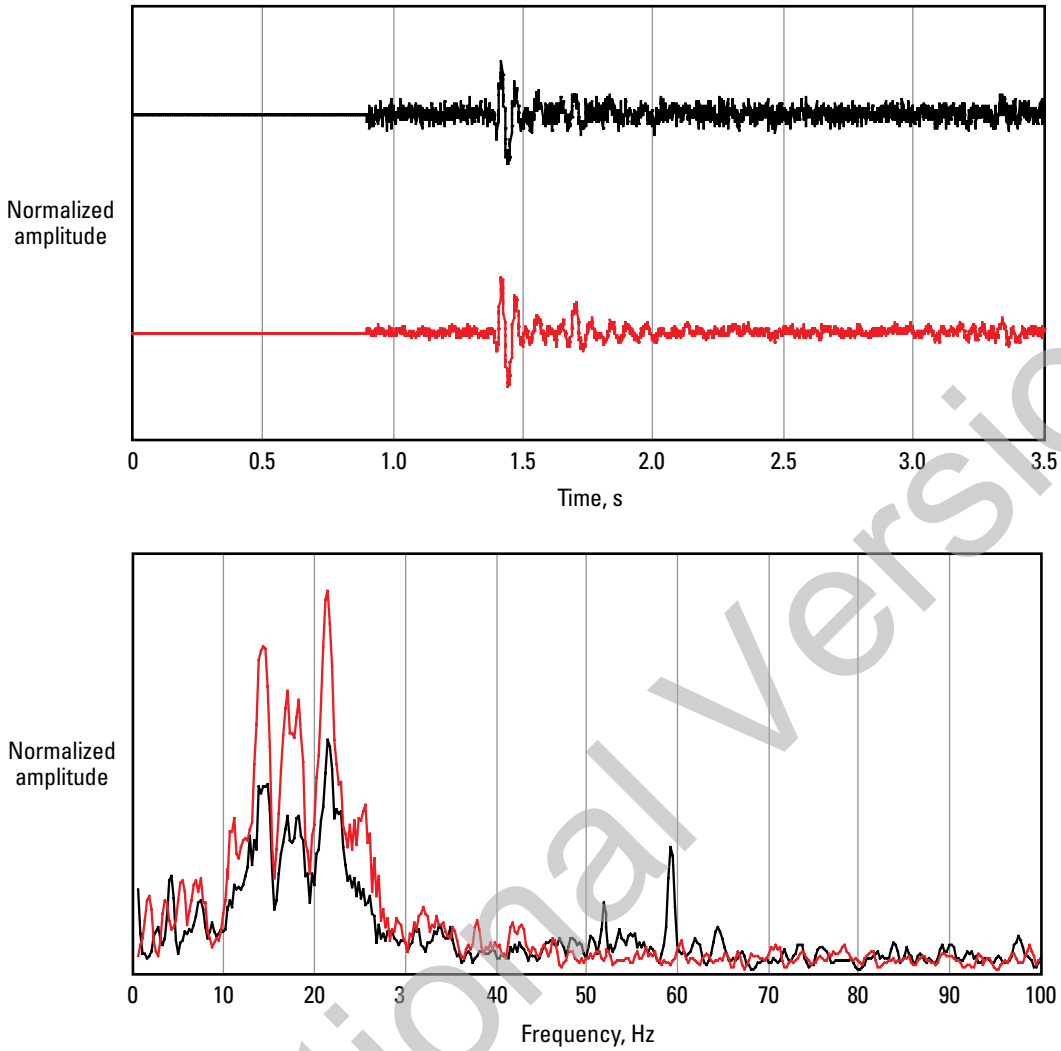

Figure 3-39. Data example from a high-temper ture a alog tool. Black line indicates data acquired without noise-reduction filter. Red line indicates data acqu ed at same depth with noise-reduction filter. Note effective suppression of 60-Hz electrical noise and 50-Hz mechanical noise (machinery), whereas the spectral shape remains unchanged. Data obtained in outh Lo siana with a slim hostile environment seismic tool in a well 15,000 ft deep with bottomhole temperatu es ex eeding 395 degF.

3.4 Acquisition software

Real-time qual y control of the seismic data acquired at the wellsite remains one of the most important factors in a VSP job. The acquisition specialist has to recognize problems with he data during the job to be able to take imm diate corrective actions. It would be too late if the problem were to be discovered after the job. In a VSP survey, the change in source signature during a survey can have a detrimental effect on VSP processing, and this can happen even when the surface hardware or downhole tools are apparently working fine. Without real-time log quality control, subtle changes could go unnoticed.

Key QC checks are

- source signature, both surface hydrophone source signature and downhole tool source signature (similar checks are available for sweep QC when using vibrators)
- consistent timing at both ends (i.e., time breaks), surface and downhole waveforms
- noise control, both environmental and tool noise (Fig. 3-40).

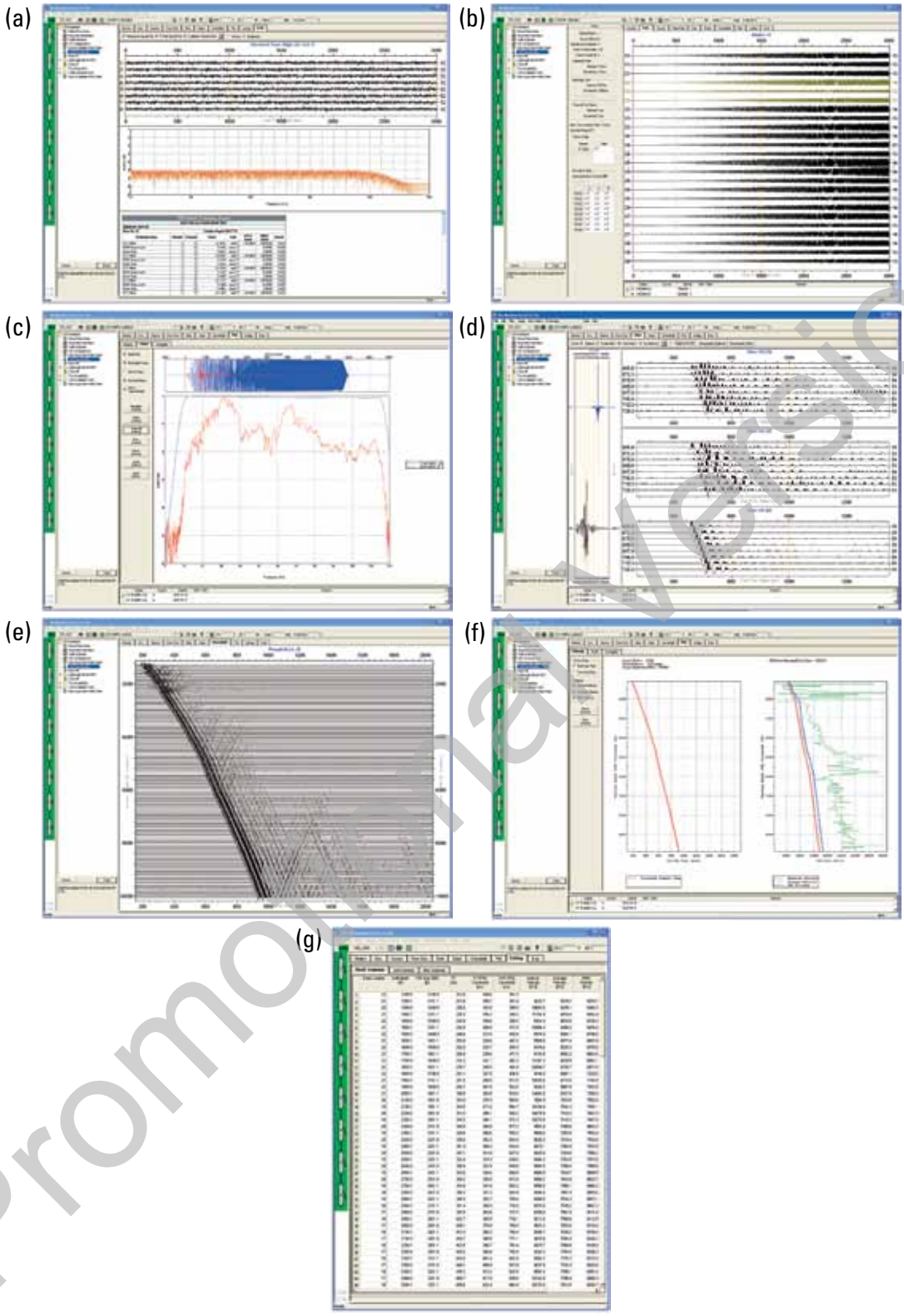

Figure 3-40. Interactive acquisition QC and data visualization panels that are used to monitor data quality and VSI tool performance: (a) tool evaluation QC, (b) shaker test indicates good coupling to formation (note: second shuttle, from top to bottom, shows less that perfect coupling), (c) shot QC compared with actual downhole recording, (d) multicomponent downhole data visualization, (e) wavefield QC, (f) time-arrival curves and preliminary formation velocities, and (g) observer notes.

3.4.1 Seismic source tests

Ensuring that the source characteristics remain constant throughout the seismic operation is fundamental for borehole seismic data quality. In the case of airguns, the following parameters should be monitored: gun-cluster tuning error, which shows whether the guns are tuned properly and whether one gun has dropped out; airgun pressure, which should be consistent throughout the job (variation range of 5%–10%); and airgun cluster depth, which directly affects the data quality by affecting the ghost reflection and the bubble period. When the TRISOR system gun controller is used, detailed, real-time QC is available at the wellsite, which includes plots of the gun sensor waveforms, tuning errors, gun pressure, and gun depth as shown in Fig. 3-41.

In the case of vibrators, two main checks are performed to ensure data quality: vibrator radio similarity test and vibrator force output test. The main function of the radio similarity test is to verify that the vibrator is putting into the ground the correct timing, start/stop frequency, and sweep length. Sweep waveforms should be clear and recorded in their full length without saturation or noise. Similarity checks should show zero-phase Klauder wavelets in crosscorrelated vibrator surface signals (e.g., radio reference versus true reference). The correlation waveform should be a clean sinc function with flat spectral amplitudes and a zero-phase spectrum across the swept frequency range (Fig. 3 42).

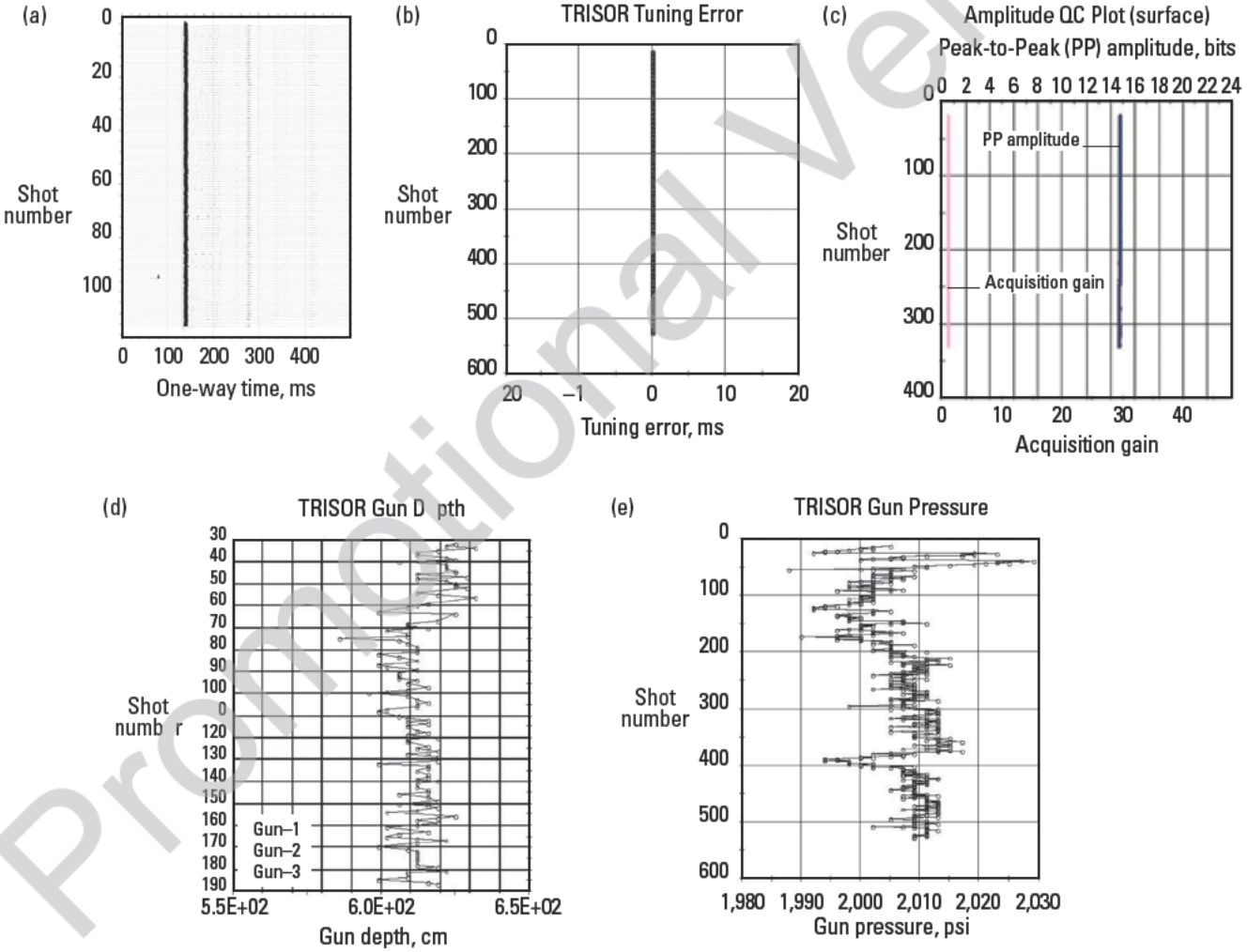

Figure 3-41. Seismic-source QC data. When a conventional hydrophone is used, the signature of the surface sensor (a) is monitored. If the TRISOR system is used, other QC information can be displayed, such as tuning error (b), amplitude and acquisition gain of surface sensors (c), both of which are ideally kept constant during the survey, gun depth QC (d), and gun pressure (e), which should not vary drastically to maintain a constant source signature.

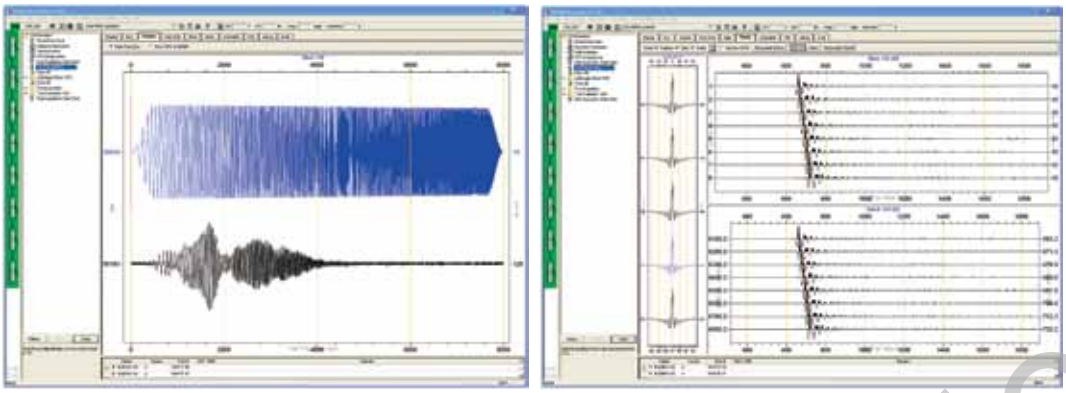

Figure 3-42. Vibroseis QC data: on the left, typical linear sweep (blue) and auxiliary surface-channel display (ground f rce, curve in black); on the right, consistent clear-sinc sweep function across all shots acquired for a stack.

3.4.2 Downhole tool tests

Thorough checks can be carried out on the complete downhole tool using electronics built into the VSI tool, and the results are part of the end-user final report. Table 3-3 presents the downhole checks for the VSI tool, which consist of a series of interna electronic tests performed for each shuttle and each axis.

The main factor ffecting the fidelity of the response of the recorded downhole signal is the nature of the coupling between the geophones and the formation,

Table 3-3. VSI Tool Diagnostic Checks

Test Description	Item Evaluated	Value or Tolerance
Electrical noise low test		
	DC offset	0 ± 100 mV
	rms noise le l	< 0.5 uV
	N se pea	< 2 uV
Electrical noise high test		
	D offset	0 ± 100 mV
	rms noise level	< 0.5 uV
	Noise peak	< 2 uV
Electrical distortion test	Total harmonic distortion	< –90 dB
System dynamic range test	System dynamic range	> 103 dB
Amplifier gain tests (done r the gains = 2, 4, 8, 16, 32)		
	Gain accuracy	0 ± 0.5 dB
	Gain step accuracy	0 ± 0.5 dB
Crosstal test (d ne separately for the axes *x*, *y*, and *z* to compare each with the re a ning two channels)	Crosstalk of the channel being tested compared with the other two channels	< –90 dB for each channel
Impulse response test		
	Amplitude (0.3 Hz)	–5 dB to 0 dB
	Amplitude (400 Hz)	–5 dB to 0 dB
	Impulse amplitude	Value mentioned – no tolerance
	Phase difference at 0.3 Hz from X1	Value mentioned – no tolerance

which may involve casing and cement integrity. The tool allows the quality of this coupling to be evaluated while it is in the anchored configuration, immediately before or after acquiring a seismic record. In the case of poor coupling, the tool can be moved a few centimeters to improve coupling.

A known mechanical signal is input to the sensor module by a shaker, and the response of the 3C geophone is then recorded and analyzed. The input signal is a linear upsweep from 0 to 150 Hz. Some illustrative shaker responses are shown in Fig. 3-43. The ideal response for a well-coupled geophone is a sweep in which amplitude increases linearly with frequency. If poor coupling exists, the recorded shaker-induced time domain trace will show anomalously high amplitudes as the sweep passes through resonant frequencies, and the amplitude spectrum will show spikes at these frequencies. This test can be used to decide whether the trace recorded at a particular level is the best that could be obtained or if it would be worth trying to re-anchor or move the tool to realize a better tool plant.

In the VSI tool, the sensor package is decoupled from the main tool body; the advantage of this feature can be seen in the tool response to tube waves. Tube waves propagate from the source to the wellhead as ground roll and then travel down the interface between the wall of the wellbore and the fluid in the hole. Tube waves travel slowly and are usually inadequately sampled and of varying amplitude from receiver to receiver. They can only contaminate a vertical-component geophone record if there are resonances in the coupling system within the seismic bandwidth (Wuenschel, 1988). To illustrate this point, a record obtained with the CSI* Combinable Seismic Imager (a Schlumberger previous-generation tool) is used. This tool offered the option to mechanically decouple the sensor from the tool body. A seismic trace recorded in a well with the geophone module retracted into the tool (Fig. 3-44) shows a strong tube wave contaminating the data at later times. The sonde is clamped in the well, and the geophone module can be considered part of the sonde body for this trace. If the module is extended against the borehole wall, which is the normal operating configuration, the resulting trace shows no tube wave energy because there are no resonances in the coupling system for the extended-module configuration.

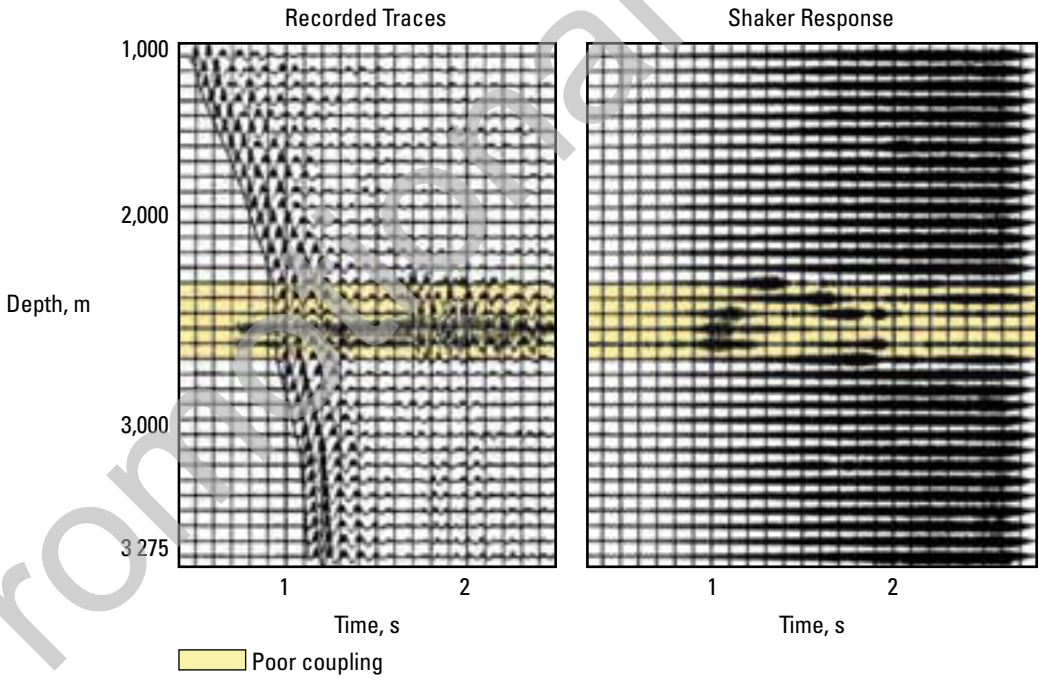

Figure 3-43. Real-time wellsite assessment of VSI shuttle anchoring quality. For each tool level, the shuttles are anchored to the borehole. Quality of the shuttle-to-borehole coupling is tested by activation of a shaker within each shuttle. If the shuttle is not anchored adequately (yellow shading), response to the shaker (right) is irregular, and recorded traces (left) contain noise. Here, data are displayed with equidistant trace spacing, although these data were recorded with variable receiver spacing. (From Arroyo *et al.*, 2003; this graphic is copyright Schlumberger, Ltd. Used with permission.)

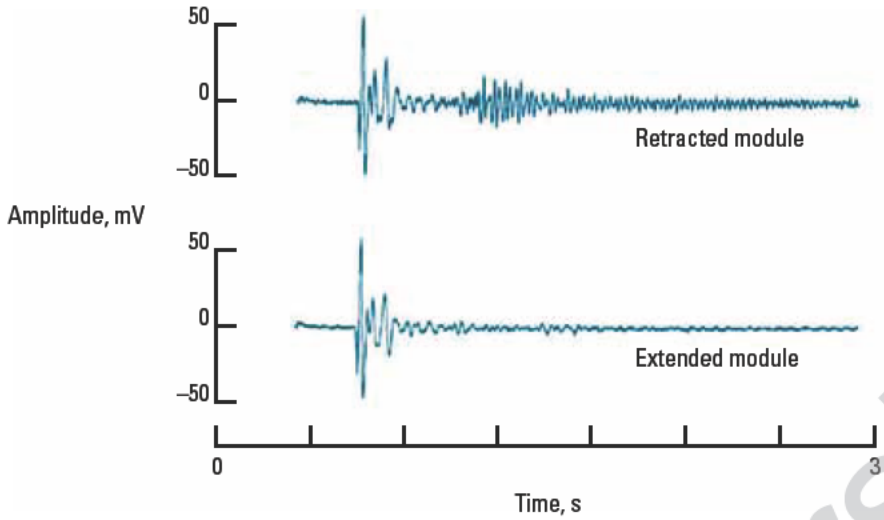

Figure 3-44. Amplitude versus time data for the CSI tool sensor module, with normal operation shown in e lower trace (extended module). The CSI tool is designed to have low sensitivity to noise and tube waves becau he se sor module is decoupled from the tool body. This concept was successfully implemented in latest-generatio tool such as the VSI tool. Acoustically isolated from the tool's body, the decoupled sensor module of the VSI too acqu re high quality triaxial data unaffected by the coupling and modal resonance that causes distortion in one-piece too s. Sch mberger is the only seismic acquisition provider using the decoupled-sensor technology.

3.4.3 Data display, output, and delivery

The VSI acquisition software allows basic data processing and display of seismic traces for QC purposes Figure 3-45 shows the sequence of the front-end data handling for both data acquisition display and outp t. The data shown in the "Raw shot tab" is the actual raw data received from the tool; no manipulation s made to the data. This is used to evaluate acquisitio parameters, such as acquisition gains, and hardw e pe formance, such as the coupling condition.

When impulsive sources are used, th raw shot data is divided by acquisition gains and followed by the sensor transform applied to the downhole hannels. The sensor transform changes the G C response (acceleration) to the conventional geophone response (velocity). Break-time detection is applied to downhole channels by correlating against the pil t sweep signal. The software automatically detects whether it should use *z*-axis data only or who e 3C waveforms for the time picking.

For Vibro eis data, acquisition gains are applied both o surfa e and downhole channels, but sensor transform is no applied to downhole channels. Break-time detection s applied to downhole channels by autocorrelation against the transmitted sweep signal.

The shot data after sensor transform and time picking is shown in the "Shot tab." The same data, but with one axis selected, is also shown in the upper panel of the "Stack tab." This is intended for the side-by-side evaluation of the last shot and last stack.

Tra es are then selected for the mean/median stacking eith r manually or automatically. By default, the softw re selects traces (yes/no to stacking) based on the coherency of the multiple traces. For instance, for five shots at a station level, the similarity of those five traces is calculated. The similarity calculation is based on the coherency factor; 1.0 indicates a perfect match, and 0.0 corresponds to absolute incoherency.

The traces selected for stacking are then used for mean/median stacking. Time picking of the stack data completes this workflow. The stack data is displayed on the lower pane of the "Stack tab" and is also accumulated into the "Wavefield tab" in depth-sorted order.

Several types of data are created during acquisition:

- pure hardware digital data after analog-to-digital conversion
- raw shot data, which is acquisition-gain compensated and has sensor transform applied to it
- mean/median raw stack data using the raw shot data.
- wavefield data, which is data with basic editing and processing applied to it (i.e., bad-trace removal, band-pass filtered).

Data can be streamed continuously in real time and sent to a remote host, which allows fast processing for decision making and, in general, reduces the turnaround of the end product to the user.

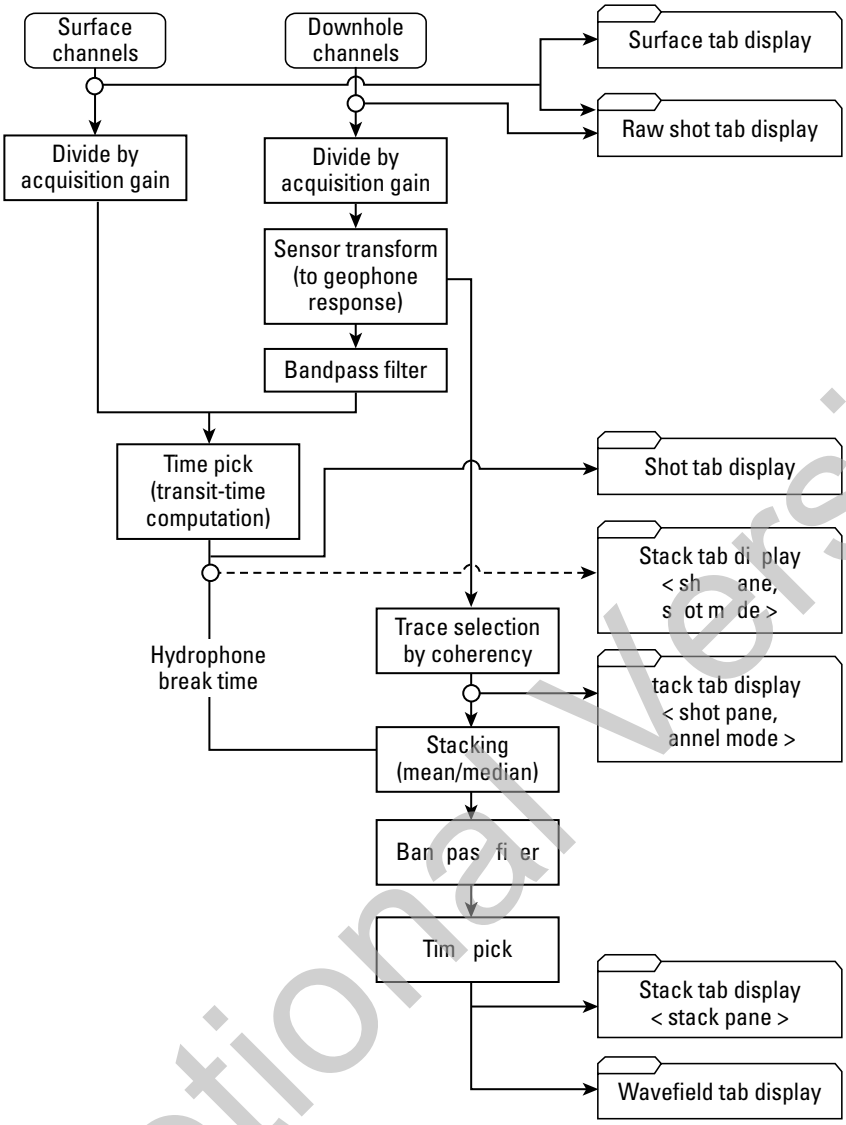

Figure 3-45. Acquisition data processin chain when impulsive sources are used.

3.4.4 Data processi g at the wellsite

It is valuable to hav at f eld level a seismic processing tool that allows editing and stacking of raw shot data and the capabi ity to analyze, filter, and deconvolve data hrough the different processing steps to the inal imaging of the subsurface by corridor stacks. Schlumberger offers software that allows seismic pro essing at two levels:

- A basic mode assumes that the user is a field specialist (i.e., has fair geophysical knowledge), where a fixed, predefined VSP chain is set at startup. This mode has several constraints whereby users cannot change the processing chain, and variation of the parameters is also limited only to the crucial ones. Those features are intended to avoid unnecessary complexity and human error. An example of a standard processing chain is illustrated in Fig. 3-46. The example shows the same seismic dataset processed in two ways, in the specialized processing center and in the field.
- The advanced mode is for field processing personnel or geophysicists. In the advanced mode, users can build any processing chain by adding or removing processing, and by connecting or reconnecting data flow in the process chain.

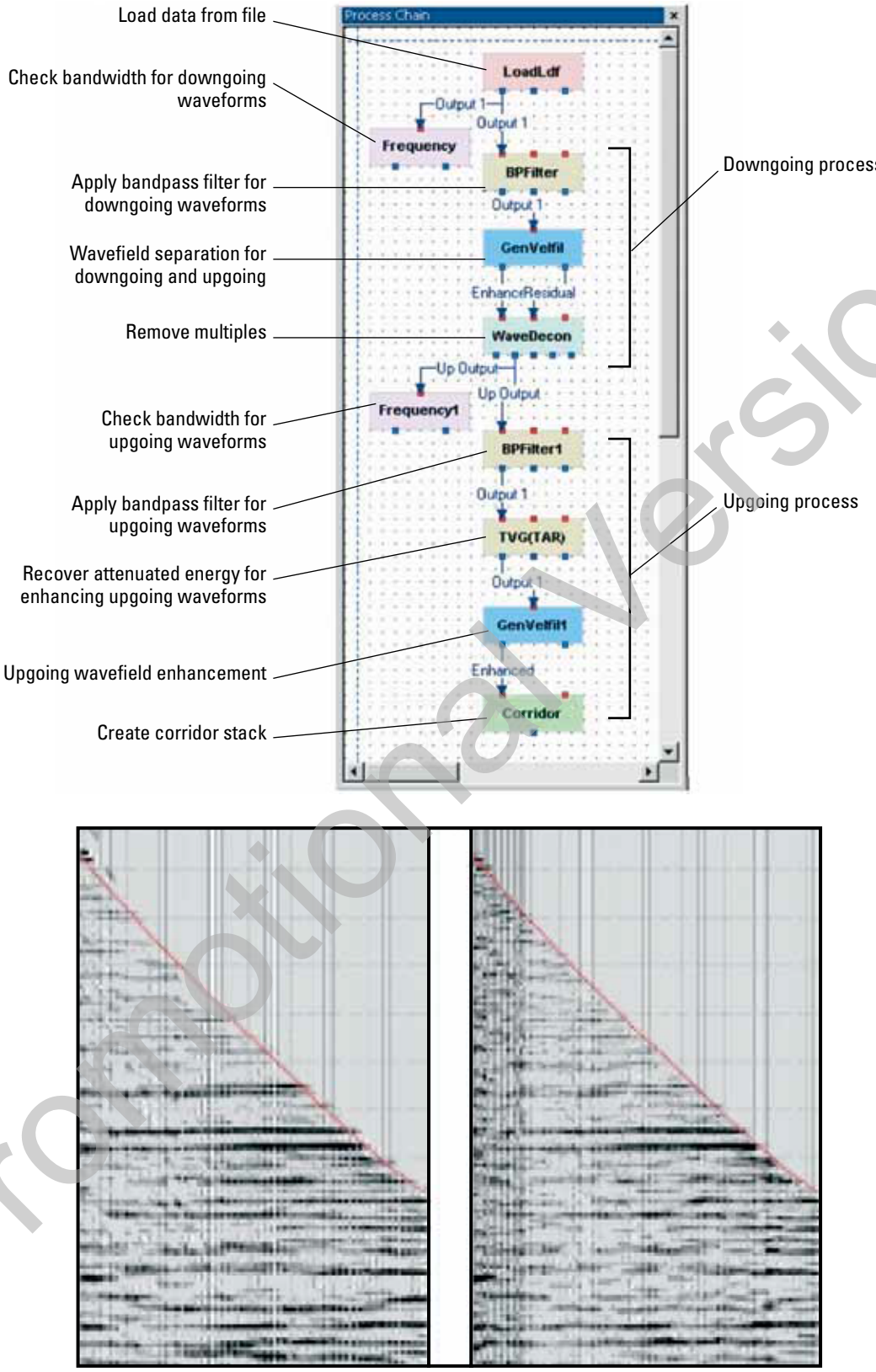

Figure 3-46. Standard processing chain at field level (top). Field-processed data (bottom right) compares favorably with the final product from the processing center (bottom left).

3.5 Seismic acquisition while drilling

The seismicVISION* seismic-while-drilling service is a new logging-while-drilling (LWD) system from Schlumberger, designed to optimize drilling, reduce costs, and improve safety. It is important to point out that this is not the technology commonly known in the industry as "seismic while drilling" that relies on passively listening to the drillbit noise at the surface. The seismicVISION service is the LWD implementation of conventional wireline VSP technology with a surface seismic source and downhole receivers. Achieving this has been an industry desire for a long time, but the technical roadblocks that prevented its realization have only recently been overcome.

The system offers measurements that can significantly reduce drilling uncertainty in environments where risk and well costs are high. Key applications of the seismicVISION service include placing the bit on the seismic map, updating a velocity model for seismic processing, predicting pore pressure, updating target depth, and optimizing the landing of the well in a reservoir.

The seismicVISION service consists of a surface-source control system and a downhole tool placed in the bottomhole assembly (BHA). The seismic source is fired during stand connections. The surface system is locked into the satellite GPS atomic clocks to fire the seismic source at precisely the desired times (Fig. 3-47). The source firing sequence is completed within the typical connection times of most drilling operations, i.e., within 2 to 3 minutes. Therefore, shooting does not require extra stops or rig time under normal conditions.

The downhole tool is 4.26 m long and weighs approximately 680–1,134 kg, depending on the diameter. The tool is available in 17.15-cm, 20.96-cm, and 22.86-cm OD sizes, and it is designed to work at 63- and 126-L/s flow rates and downhole pressures up to 25,000 psi. The sensor package consists of three orthogonally mounted geophones and two omnidirectional hydrophones (Fig. 3-48). The z-component points uphole along the tool axis and the (x, y, z) components form a right-handed coordinate system. The geophones, located in the outer housing of the tool, are specially designed and mounted to manage the large G-forces applied to them while drilling and are well protected from drilling abrasion, wear, high flow rates, and pressures (Fig. 3-49). The geophones couple to the formation by the weight of the collar. This is best achieved for deviation angles of 5° or larger, resulting in high-quality waveforms.

The hydrophones are located under protective shields on the exterior of the collar and do not require coupling to the borehole wall to acquire good data. Instead, the hydrophones respond to pressure changes in the drilling fluids that occur as the seismic waves pass through the

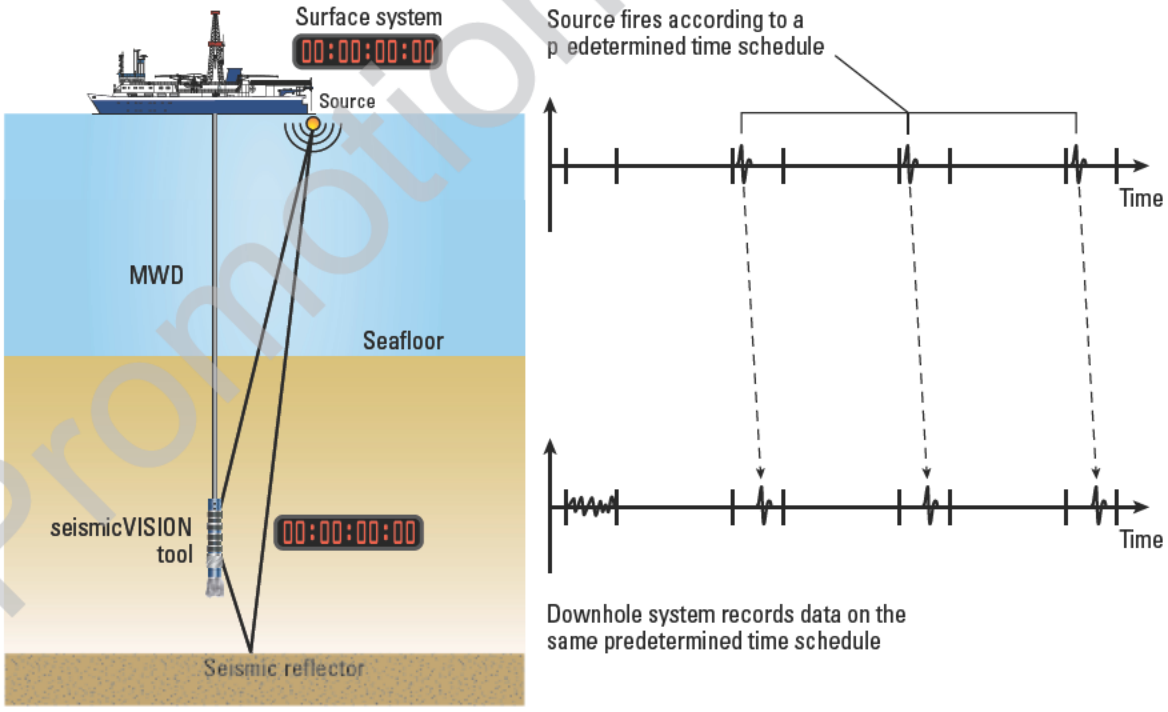

Figure 3-47. Acquisition-timing diagram for seismicVISION service. Surface clock is locked to GPS; the rugged downhole clock is synchronized with high precision to surface clock prior to running in hole.

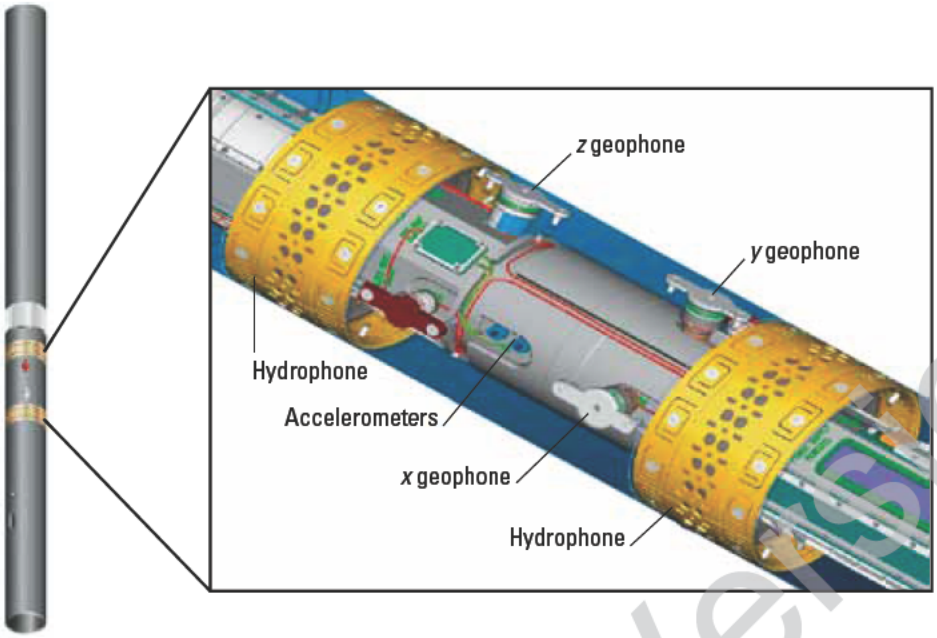

Figure 3-48. Schematic representation of the seismicVISION tool sensor section.

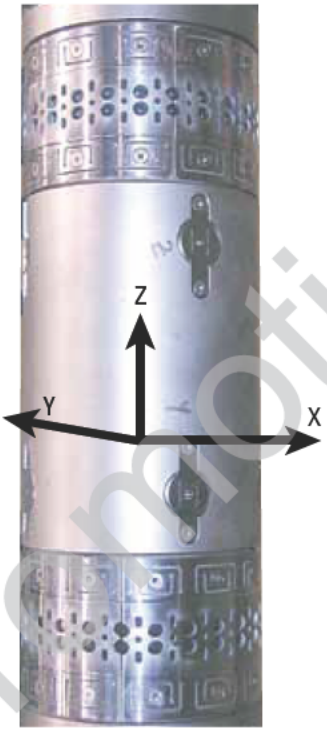

Figure 3-49. Sensor section of the seismicVISION tool with 3C geophone orientation.

section of the well containing the tool, they compress and expand the borehole. This, in turn, causes a transient pressure change in the drilling fluid that is picked up by the hydrophones. At the same time, the geophones record the motion of the tool as it moves together with the borehole as the wave goes by. This combination sensor package allows the tool to be operational in all hole sizes and angles, including vertical. Data have been acquired through multiple strings of casing all the way up to, and in some cases even beyond, the mudline.

The surface-downhole time synchronization is provided by an ultra-high-precision clock in the tool that is synchronized to the satellite GPS system prior to going downhole. The GPS clock is also used to fire the seismic source with the surface computer system at precisely the desired times. By this method, the tool and the surface system maintain the same reference time, and shooting and recording take place at predetermined intervals, provided that certain tool logic conditions are met. For example, the tool is preprogrammed to listen for a source firing at every 15 seconds, starting on the minute, if drilling has stopped. And the surface source is fired exactly at these times (if desired) when there is no drilling.

The seismic energy is produced from a conventional seismic source such as a tuned airgun array that can be used for rig-based or offset surveys on a boat. A proprietary technique enables source activation and data acquisition during drilling pauses when the downhole environment is quiet. Suitable times to acquire data, without impacting the normal drilling operation, are during pipe connections, whether drilling ahead or tripping in or out of the hole. The tool detects when the

pumps are on, or when the pipe is being moved, and then waits until the environment is quiet before beginning acquisition. Each of the surface shots received is acquired, and good shots are selected for stacking by a patented technique that includes the repeatability or coherence of the received energy. If the stack quality exceeds a preprogrammed level, then the tool executes a fully automated time-picking algorithm and calculates a real-time checkshot value together with a quality indicator for that checkshot. The stacked waveform, the real-time checkshot times, and the quality indicators are sent to surface using mud pulse telemetry.

Unprocessed or raw shot waveforms are written directly to downhole tool memory. The tool is normally set to record 3 seconds of multichannel waveform data to memory at each level. Stored waveform data are dumped from the tool at the surface after each bitrun, thus enabling further processing and QC. The tool has approximately 100 Mb of memory available for recording waveforms; that provides about 7 hours of continuous recording time if all four channels (components) are recorded. Bitruns typically last longer than this; therefore, seismicVISION service uses several proprietary techniques to prevent the tool from recording drilling noise and yet capture all useful data.

After a connection is made, as the mud pumps are turned on to resume drilling, the stacked waveform, time picks, and a number of QC indicators are received at the surface by the mud pulse telemetry system. The real-time waveforms are first used to QC the tool time picks and then are sent to the processing center for further VSP processing, such as look-ahead imaging. The time-depth data are used to display the well position on the seismic map at the wellsite or in the office.

The seismicVISION concept works without the limitations of previous real-time seismic techniques. It has been proved in a wide range of environments, including all well geometries, wells deeper than 7,500 m vertical, openhole and cased hole environments, hard and soft formations, moored and dynamically positioned rigs, unlimited water depth, and zero-offset and vertical-incidence VSPs. The seismicVISION service is combinable with all Schlumberger LWD tools.

Finally, seismicVISION service is not an across-the-board replacement for the wireline borehole seismic. The tool is slick and, unlike a wireline seismic tool, does not actively couple the geophones to the formation or decouple them from the tool itself. Consequently, geophone data may not be of equivalent quality to wireline data and lacks some frequency characteristics. The seismicVISION tool has only one four-component (4C) sensor and cannot be run as a multishuttle array; in this way, it is unlike the wireline tool whereby multiple sensor positions can be shot at the same time. Therefore, walkaway, or 3D-type, high-end reservoir characterization applications are likely to be very time-consuming and expensive with this technology. Best-value applications are real-time rig-source, or walk-above checkshot, and look-ahead for well placement together with trip-in or trip-out shooting for highly deviated wells to better plan the next bitrun.

3.6 Surface recording equipment for real-time VSP acquisition

Figure 3-50 shows a schematic of the Drill Bit Seismic system. It requires no special downhole equipment; however, at present, it works best only with roller cone bits. A multicomponent accelerometer is mounted on the rig's top swivel and is connected to the recording system via the accelerometer cable. An array of either hydrophones, geophones, or a combination of the two is deployed beside the rig, generally at distances of about 1,000 m. An extension cable connects the array to the acquisition box located on the rig floor. The acquisition boxes digitize the receiver signals and send them to the front-end processor.

The front-end processor detects when drilling is occurring (as opposed to when the rig is circulating drilling fluid, for example) and performs correlation and stacking operations continually as drilling proceeds. Field processing is available once a sufficient amount of data has been acquired.

3.7 Permanent monitoring

Permanent downhole recording systems represent a breakthrough in borehole seismic tool technology and open up much wider opportunities for borehole seismic instrumentation and reservoir monitoring within the oil and gas industry.

Deployed during the well completion stage, the sensors are permanently coupled to the casing and can record data continuously. Because these seismic sensors have a fixed orientation, they provide ideal conditions to perform repeated VSP (4D seismic). They can also be used for reservoir monitoring to record the microseismic events generated by the reservoir fractures.

One of the challenges of the permanent borehole seismic technology is the flow noise generated by the oil production, which dramatically affects the measurement. The passive seismic system overcomes this difficulty by deploying the Ω-Lok (Omega Lok) tool, shown in Fig. 3-51.

The Ω-Lok tool is a mechanical C-spring that hosts the seismic sensors. It is held in a compressed state during the run-in-hole operation. Once the tubing is in place, the mechanism can be released by elevating the

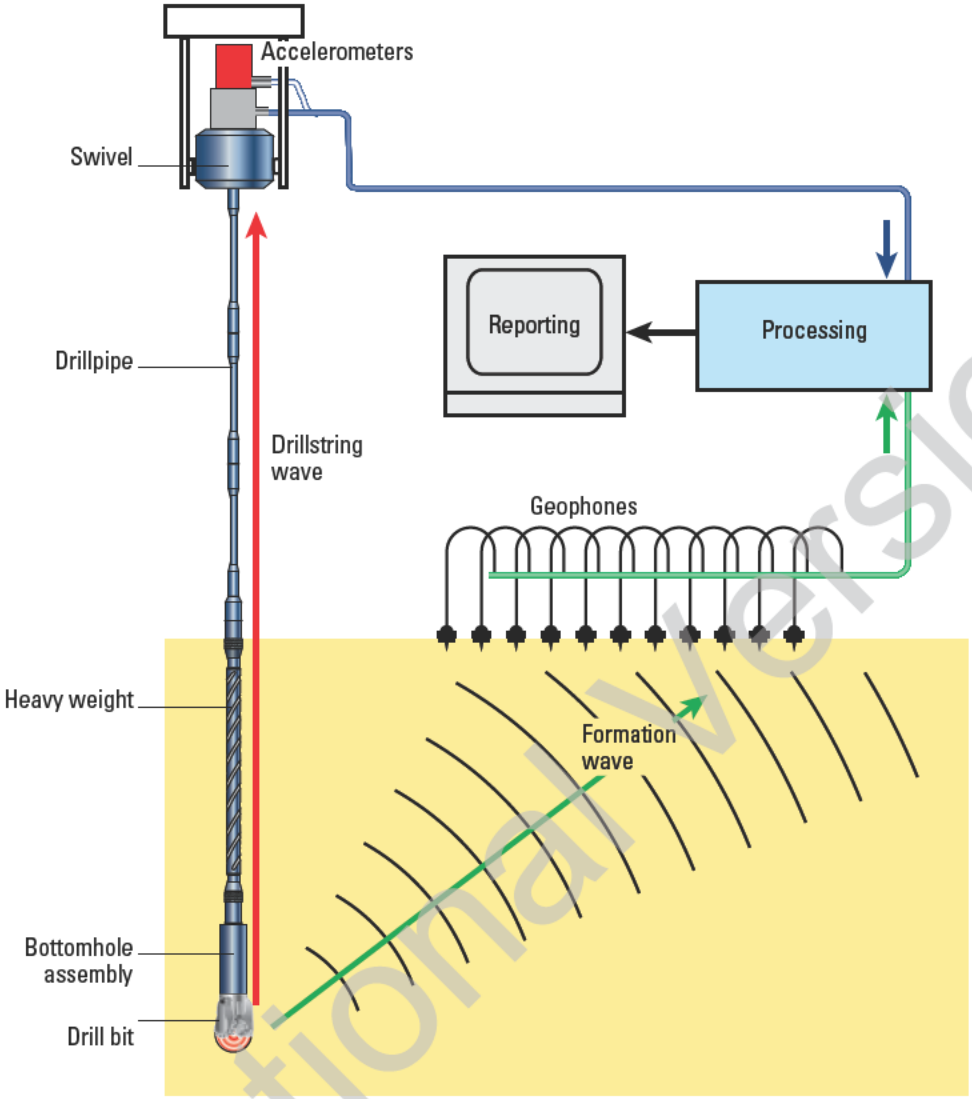

Figure 3-50. Schematic representation o Drill- it Seismic components.

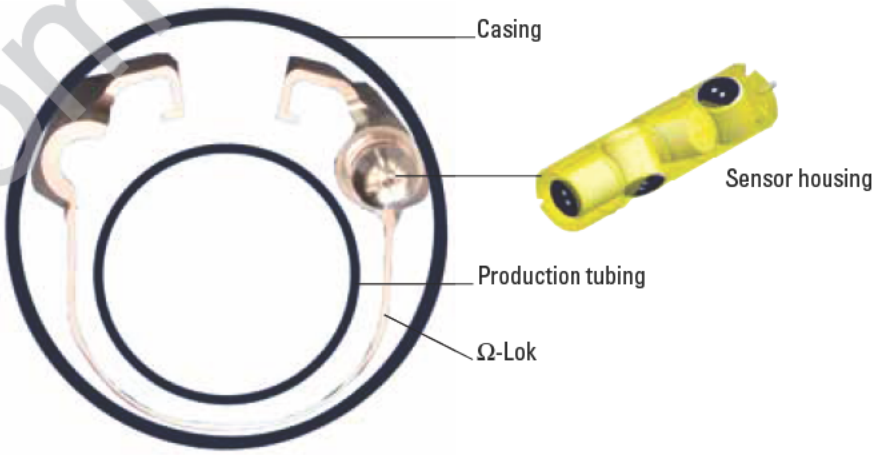

Figure 3-51. Schematic cross section of the Ω-Lok tool while in use.

pressure in either the tubing or the annulus or via a hydraulic line. Once released, the Ω-Lok apparatus clamps itself to the inside of the casing to effectively couple the seismic sensors permanently to the casing, and hence, to the formation. In addition, the Ω-Lok apparatus is completely decoupled from the tubing, and hence, also from the production noise.

With the seismic sensors acoustically decoupled from the flow noise and firmly coupled to the formation, the noise floor is dramatically reduced, thus allowing the detection of much smaller and more distant seismic or microseismic signals.

The deployment system of the Ω-Lok spring is located on a mandrel (Fig. 3-52), which is assembled on the tubing string as a regular joint.

The system is fully expandable by varying the number of levels and their positioning along the production string. Each level of the system uses a patented four-axis tetrahedral sensor configuration. This allows real-time QC of the data and provides a level of redundancy that cannot be achieved using the traditional three orthogonally mounted sensors. The system has been designed so that it is capable of deploying geophones, microelectromechanical (MEM) accelerometers, fiber-optic sensors, or other types of sensors such as pressure and temperature sensors. The system is rated to 150 degC and 10,000 psi.

Permanent monitoring systems finally enable continuous acquisition of high-quality active and passive seismic data in flowing wells for the entire well life.

Figure 3-52. The Ω-Lok decoupling tool.

3.8 Simultaneous surface and borehole seismic acquisition

Combined surface and downhole seismic data acquisition is undertaken by deploying a 3C, multilevel downhole seismic tool in the well while surface seismic is being acquired. The configuration is similar to a walkaway VSP survey in which the multilevel tool is stationary and the source is moved away from the well. The borehole acquisition system is then remotely triggered by the surface seismic recorder and fully synchronized by GPS.

In offshore seismic surveys, the TRILOGY onboard data management system provides three functionalities required in these surveys:

- The TRILINK module transmits all necessary signals between source and acquisition accessels to the downhole recording system to acquire seismic data simultaneously.
- The TRINAV* integrated navigation/positioning system module provides all navigation commands related to positioning of seismic sources and surface recording.
- The TRIACQ* acquisition recording system module enables real-time QC of navigation and acquisition parameters.

Figure 3-53 shows schematically the setup needed to acquire seismic data simultaneously on surface and in the borehole. The downhole tool is positioned to seismically illuminate the target horizons in and around the well. The lateral extent of this illumination depends upon the maximum allowable source offset, which generally is determined through seismic ray-trace modeling. The 2D or 3D surface seismic acquisition geometry can be adapted to shoot combined surveys.

Downhole acquisition not only provides a higher resolution image, as compared with the 3D seismic image, but also provides supplementary data to evaluate the source characteristics. In addition, the downgoing multiples that originated at different horizons can be recorded before getting reflected back at target horizons.

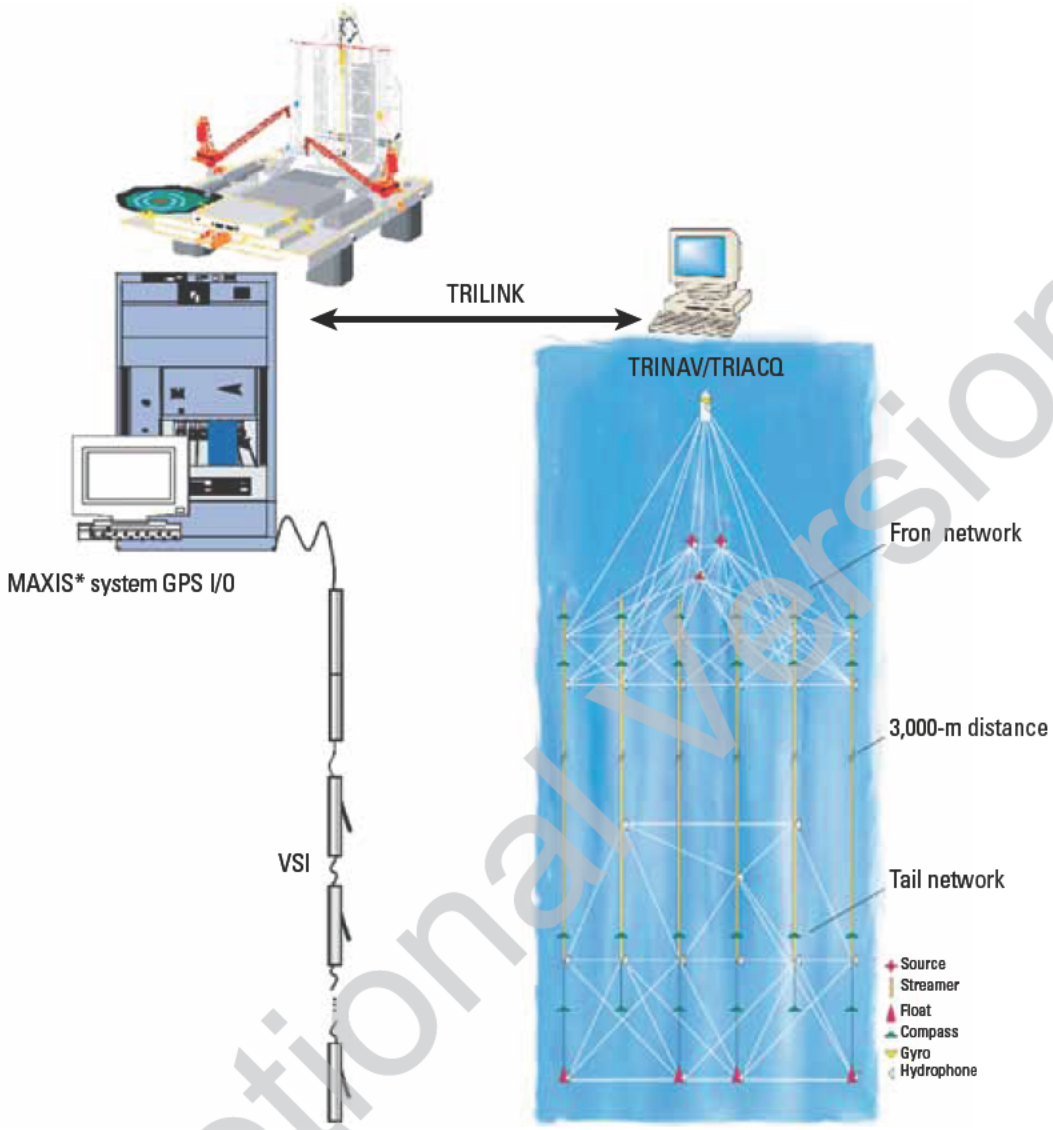

Figure 3-53. Schematic illustration of si ultaneo s acquisition of seismic data at surface and in the borehole. The TRILINK, TRINAV, and TRIACQ modules are par of the TRILOGY onboard data management system (from WesternGeco). The TRINAV module is the navigatio sys m, the TRIACQ module controls acquisition of surface seismic data, and the TRILINK module provides voice and a communication between rig and vessel acquisition systems. The MAXIS* Multitask Acquisition and Imaging S stem i remotely controlled by the TRINAV and TRIACQ modules. The TRINAV module and the TRISOR element send sour e position and signature, respectively, to the MAXIS recording system after each shot.

Combined surface and downhole seismic acquisition offers optim l data to study the seismic signal propagation effects; to estimate the quality factor Q, vertical velocities, and anisotropy parameters; to characterize he source signature in changing surface conditions; and to evaluate the static variations at different source positions.

The seismic data recorded in this combined configuration is not only economically viable, as the same source will be used in both the surface and the downhole acquisition, but is also helpful in validating the surface seismic interpretation.

Careful planning for these surveys is a must. Positioning of the communications equipment is critical to this type of survey because the shooting vessel generates the acquisition trigger for each shot. Any shadowed areas will result in missed shots or, at least, in missed navigation information. Extensive testing should be conducted to minimize the shadowed areas. Preparation to handle a large amount of data should be considered not

only in terms of storage capacity but for consistency of the data (i.e., coordinate systems, seismic data format). The turnaround time for the gunboat between sail lines is used to move the tool between the required station depths to fulfill the survey needs as well as to back up the acquired seismic data.

3.9 The Q-Borehole system

The Q-Borehole integrated borehole seismic system optimizes all aspects of borehole seismic services that have been discussed in this chapter. This includes services during wireline operations and seismic operations while drilling. It combines all aspects, beginning with job planning, continuing through data acquisition, data transmission, processing, and final interpretation.

The ultimate goal of the Q-Borehole system, part of the family of Q* single-sensor seismic acquisition and processing methodology developed by Schlumberger, is to deliver high-quality, high-resolution, multicomponent seismic data with accurate signal preservation, intelligent noise removal, and optimum sampling in all surface and downhole applications.

Superior seismic imaging is achieved through 3D presurvey planning and raypath modeling; improved downhole sensor coupling, isolation, and excellent vector fidelity (as found in the VSI tool); accurate source positioning (SWINGS system); calibrated source with fully characterized signatures (TRISOR source controller); and real-time quality control. Figure 3-54 illustrates th s as the Q methodology.

3.10 References

Arroyo, J.L., Breton, P., Dijkerman, H., Dingwall, S., Guerra, R., Hope, R., Hornby, B., *et al.*: "Superior Seismic Data from the Borehole," *Oilfield Review* (Spring 2003) 15, No. 1, 2–23.

Bolt Technology Corporation: "PDF_DHS_Borehole," http://www.bolt-technology.com/images/PDF_DHS_Borehole.pdf (accessed December 12, 2009).

Hope, R., Ireson, D., Leaney, S., Meyer, J., Tittl W., and Willis, M.: "Seismic Integration to Reduce Risk," *Oilfield Review* (Autumn 1998) 10, No. 3, 2–15.

ION Geophysical Corporation: "121043G-DATASHEET_Vib_Pro," (July, 2008), http://www.iong o.com/content/includes/docManager/121043G_DATASHEET_Vib_Pro.pdf (accessed August 18, 2009).

Moldoveanu, N., Puckett, M., Campbell, A., and Meyer, J.: "High Fidelity Vibratory Seismic Applications for VSP," *Expanded Abs ract* 70th SEG Annual International Meeting and Exposition, Calgary, Alberta, Canada (August 6–11 2000), 1759–1762.

S hlumberger: "Offshore Borehole Seismic Sources: Optimum Performance for any Type of Survey," (September 2002), SMP-4101, http://www.slb.com/resources/other_resources/brochures/seismic/offshore_borehole_seismic_source_brochure.aspx (accessed Ap il 30, 2010).

Sercel: "Marine Sources," http://www.sercel.com/Products/sources/ggun.bak-07-30-09.php; ftp://ftp.sercel.com/pdf/brochures/Marinesources.pdf (accessed August 18, 2009).

Wuenschel, P.: "Removal of the Detector-Ground Coupling Effect in the Vertical Seismic Profiling Environment," *Geophysics* (1988) 53, No. 3, 359–364.

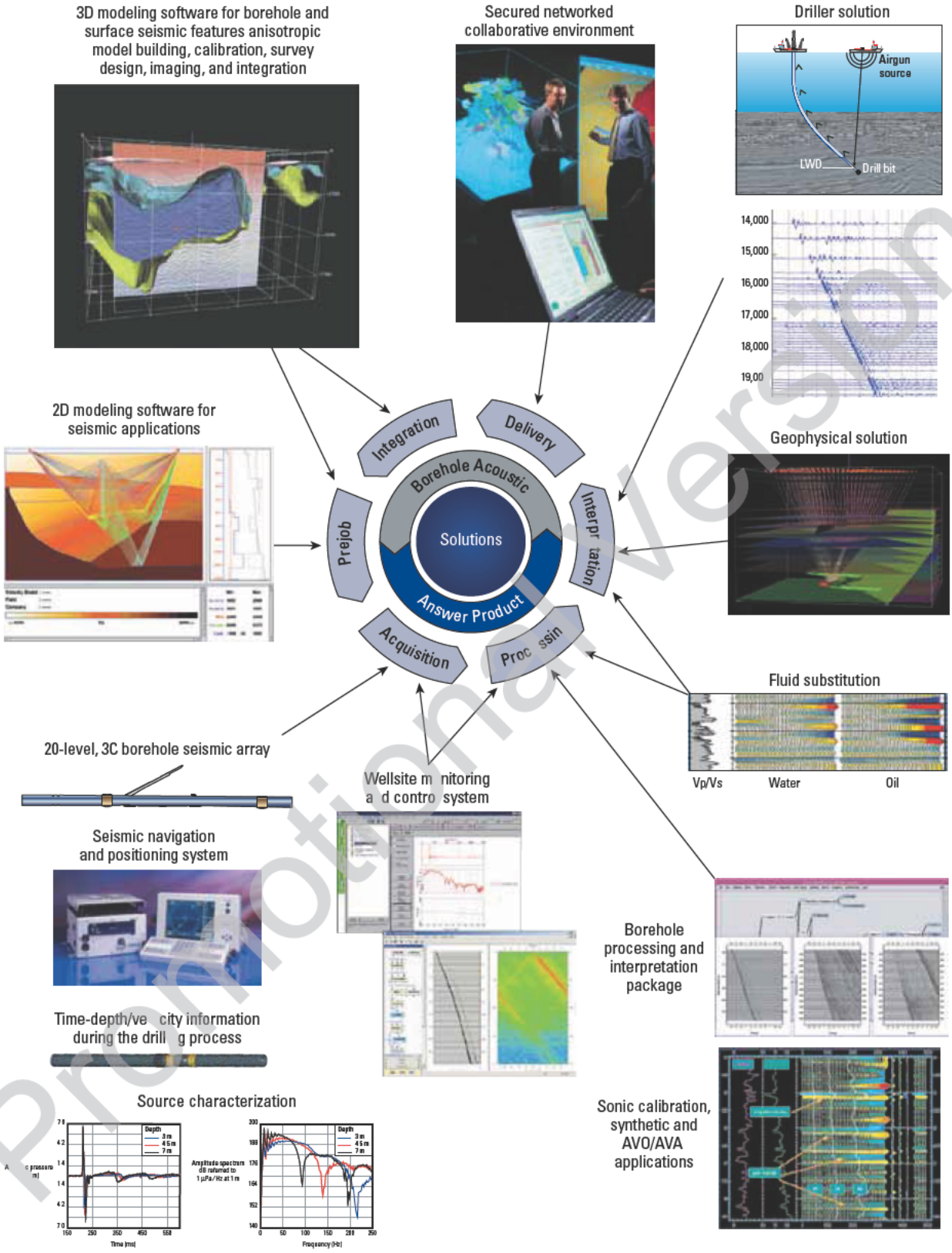

Figure 3-54. Q* methodology creates synergy by fully integrating services, hardware, and software that produce seismic solutions.

Well Tie—Checkshot and Zero-Offset VSP

Michael Jones and Alejandro Martinez Pereira

4.1 Introduction

Soon after the initial publications about borehole seismology (post 1910), checkshot surveys were used to determine the site-specific velocity from the surface to a geophone deployed at a known depth in a well. During a checkshot survey, a geophone attached to a wireline is used to record the traveltime from the surface to a known depth. Based on the analysis of borehole geophysical log depths, this simple concept was used to determine the two-way seismic traveltime of a reflection event from a stratigraphic unit at the level of the geophone.

Acquisition geometry of an incremental zero-offset VSP survey is similar to that of a checkshot survey—the surface source remains stationary, and the geophone is moved to different levels within the well. Figure 2-7 shows the typical acquisition geometry for the basic zero-offset VSP in which the source is located at or close to the well. After the source is activated and a cording is made at one level, the seismic tool is moved to the next level and the procedure is repeated. As shown in Fig. 4-1, the primary difference between the checksho survey and the VSP survey is that VSP rec rdings are more finely sampled in time and depth for incr ased accuracy in wavefield evaluation.

4.2 Time-depth curve and velocity profile

The most fundamen l observation that can be made from a borehole seismic survey is the time at which a direct arrival reac es the downhole seismic receiver. If a seismic receiver is positioned at the depth of a known geol gical interface in the well, then the traveltime, from a seismic pulse emitted at surface to that interface, can e measured directly. Traveltimes are then used to

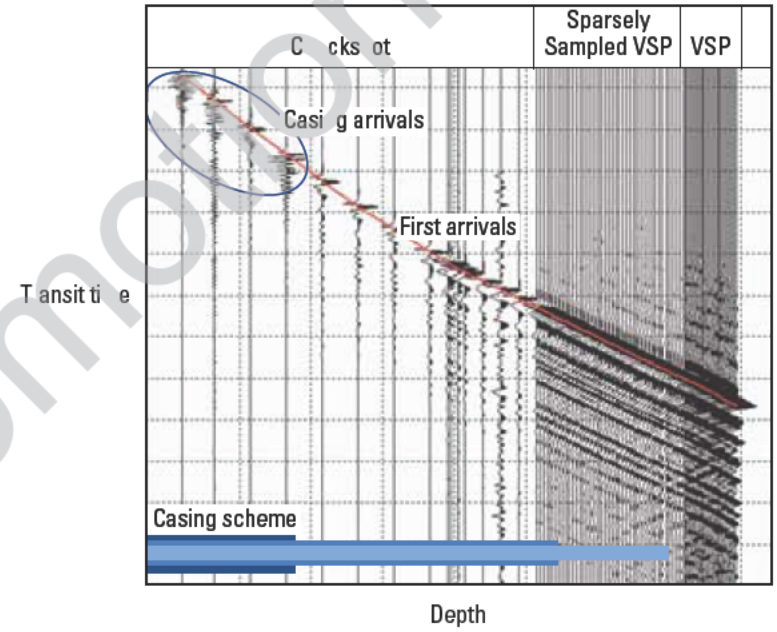

Figure 4-1. Seismic display showing difference in recorded information obtained by a checkshot survey and a VSP survey; generally data are recorded every 150 m and 15 m, respectively. An intermediate step is illustrated as sparsely sampled VSP in which depth increments are of 30 m approximately. Note the different detail of seismic information obtained at the different scales. Casing scheme is added to help explain the noisy traces as a result of casing arrivals. (From Campbell *et al.*, 2005.)

determine velocity, which is calculated using the time difference at which the seismic pulse arrives at the geophones and the distance between receiver points. In the case of impulsive sources, this requires picking the time of the first energy arrival at the geophone. For vibrator data, in which the embedded wavelet after crosscorrelation is assumed to be zero phase, it is necessary to pick the peak of that wavelet as the first arrival.

The use of seismic cross sections of the subsurface is based on the principle that geological events at depth, as interpreted from well logs or cores, can be correlated with reflection events in time on surface seismic data. The property that ties depth and time data together is the velocity of sound in the rock. This rock property can be measured quite accurately by sonic logging tools deployed in the wellbore or less accurately from the surface seismic traveltimes as a function of source-receiver offset.

Figure 4-2 shows the direct arrivals of a few traces from a VSP dataset generated with an airgun source. The data are sampled at 1 ms, and the traveltime picks are shown on the traces and displayed numerically. It is assumed that traveltimes are picked accurately because data follows adequately the sampling theorem both in frequency and space (Nyquist, 1928).

From this figure we can estimate that the energy arrival can be picked consistently within 0.2 ms. The implications that this might have on the velocity estimate for intervals between geophone stations are clear. If the downhole geophones are 15 m apart and the background

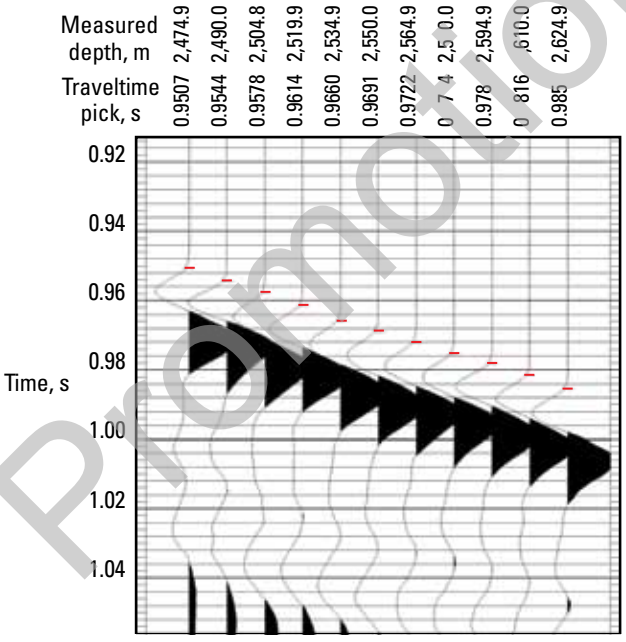

Figure 4-2. Example of direct-arrival picking in a VSP dataset. Red lines indicate the user's best estimate.

velocity is 4,000 m/s, then the arrival time difference between geophones (t_{2-1}) will be

$$t_{2-1} = \frac{15}{4{,}000} = 3.75 \text{ ms.} \qquad (4\text{-}1)$$

With a picking accuracy of ± 0.2 ms (for both surface sensor and downhole sensor), the interval traveltime will have an accuracy of ±0.4 ms, and therefore, the calculated velocity will be

$$V = \frac{15}{0.0037 \pm 0.0002} = 4{,}000 \pm 225 \text{ m/s} \qquad (4\text{-}2)$$

Although this may seem like a large error (± %), this is just caused by the proximity of the two receivers. For the velocity calculated over a depth interval of 45 m, the equivalent error is less than 2%, and f over 90 m, it is less than 1%.

A similar argument applies to the accuracy of depth measurement n a well The depth of the tool in a well is normally taken fro the wireline depth measurement recorded by the l gging truck. This depth is compensated for the anticipated cable stretch based on the weight of the tool and cable, and the depth scale is tied to the depth scale of the openhole logs by recording a gamma ray log with the VSP tool. However, this is still only as good as the depth accuracy of the original wireline logs u ed or depth correlation. If the vertical increment between geophone positions is small, even small inaccuracies in depth can affect the estimated traveltime between geophone stations. The relative accuracy of velocity estimates improves as the receiver spacing increases. This explains why interval velocity plots from direct arrival times can show significant scatter if the spacing between receivers is small.

4.3 Sonic log correction and formation velocity

Sonic logs are calibrated using checkshot or VSP traveltimes to adjust the sonic integrated traveltime to the measured seismic time. The corrected sonic log data is used to compute formation or interval velocities and also to convert depth to seismic time. It is also used to derive the formation acoustic impedance, which is used to generate synthetic seismograms (explained in Section 4.4). Interval velocities are used to constrain the velocity model used in the migration of offset data, 3D VSP data, and surface seismic data.

Consider Fig. 4-3, which shows a sonic log in depth and, in the ideal case, some direct-arrival traveltimes for vertical-incidence sound waves from a VSP survey. Consider the two geological events at depths z_1 and z_2;

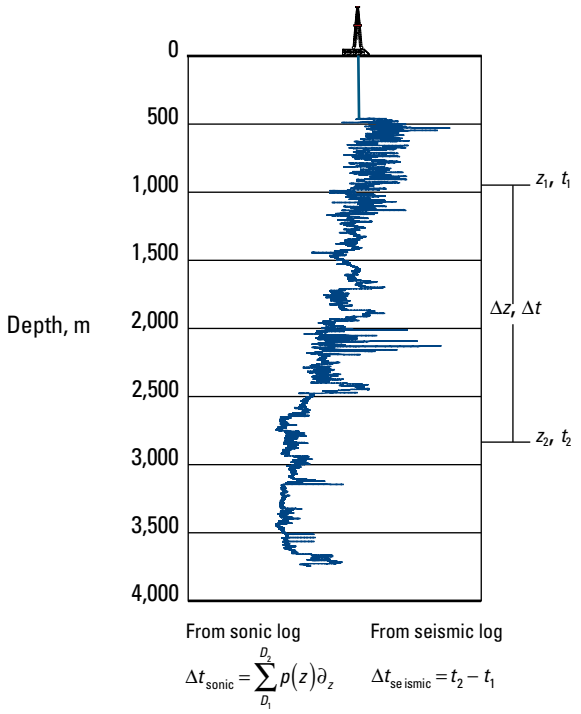

Figure 4-3. Calculation of drift in the sonic log uses the slowness value *p*.

there are two ways to predict the time interval between them that would be expected in a surface seismic experiment. The first way, using only the log data, would be to integrate the slowness values from the sonic log over the depth range from z_1 to z_2. The second way is to find the time difference between the direct-arrival traveltimes at the two depths. In general, these methods do not yield the same result, and they may differ by a time shift that is greater than the fundamental period of the seismic wavelet.

The discrepancy arises for a number of reasons, practical and fundamental ones, as listed in Table 4-1. The second of these dispersion relates to velocity variation with frequency that causes a fundamental difference between the velocities of seismic waves and those measured by sonic logging tools. The main cause for dispersion is attenuation (anelasticity), with additional dispersion resulting from layering and fluid effect. These effects cause sound waves to travel faster at high frequency than at low frequency. Stewart *et al.* (1984) proposed the following equation to estimate the variation of velocity as a function of frequency:

$$c(f_2) = c(f_1)\left[1 + \frac{1}{\pi Q}\ln\left(\frac{f_2}{f_1}\right)\right] \quad (4\text{-}3)$$

where $c(f)$ is the phase velocity at a frequency f.

The element Q is the quality factor that describes the anelastic energy loss per cycle of the propagating waveform. If a sonic log is recorded at 15 kHz and the borehole seismic traveltime is measured at a frequency of 30 Hz with a value of 100 for Q, the bracketed term on the right-hand side of Eq. 4-3 is 1.02, which predicts that sonic velocities are 2% faster than those of seismic data. If we assume Q to be 50, a value found in poorly consolidated rock, the right-hand term becomes 1.04, which suggests that sonic velocities are now 4% faster.

As an example, consider two events separated in depth by 1,000 m, and the velocity of sound in the rock is 2,500 m/s. The two-way traveltime between the events will be 0.8 s. If the difference between sonic and seismic velocities is 4%, the two-way traveltime difference will be 32 ms. This value is close to 33 ms or one period of a signal at a frequency of 30 Hz, which is a common central frequency for seismic data. Therefore, in a surface seismic section, these two events may be displaced by a whole cycle in time as a result of dispersion. From the depth viewpoint, a 30-ms difference in two-way time might result in an error of 37.5 m in a depth estimate.

Another possible error in the time-depth relationship is the incorrect assumption that the time from the corrected sonic log will automatically tie the absolute time

Table 4-1. Causes of Sonic and Seismic Traveltime Differences

Effect	Cause
Sonic times too long	Noise, cycle skipping, hole conditions such as rugosity, borehole enlargement Formation alteration
Sonic times too short	Noise, cycle skipping, velocity inversion due to gas, high dips Dispersion
Checkshot times too long	Time-picking precision Different raypath
Checkshot times too short	Different raypath Anisotropy, high-dip formations relative to borehole, lateral formation changes

on the surface seismic section. The time scale derived for the corrected sonic positions corresponds to vertically corrected seismic arrival time at that depth, possibly with a static shift to change the datum from ground level to a specified datum. It represents the actual time required for the pulse to travel down through that thickness of Earth. Surface seismic data, on the other hand, has undergone a different process that involves an estimate of the thicknesses and velocities of the near-surface layer(s) followed by their replacement with a layer having a velocity closer to that of consolidated rock.

To derive an absolute time tie between the two, the refraction static model used at the well location must be known for the surface seismic data as well as the replacement velocity used to derive its static corrections.

Figure 4-4 shows a traveltime plot with a borehole-compensated sonic log in blue that is plotted as a function of depth. Note that the sonic log only starts at approximately 500 m; therefore, the start time at the top of the log is arbitrary. Here the traveltime curve above that point has been filled in from the VSP times. The other two curves shown on the traveltime plot represent estimates of the traveltime of sound waves from the surface to any depth in the well. The dark blue curve represents the traveltime actually measured from the arrival times of the seismic pulse in the borehole, and the magenta curve represents the traveltime obtained by integrating the slowness values from the sonic log. Even at this scale, an increasing divergence between the curves with increasing depth is observed.

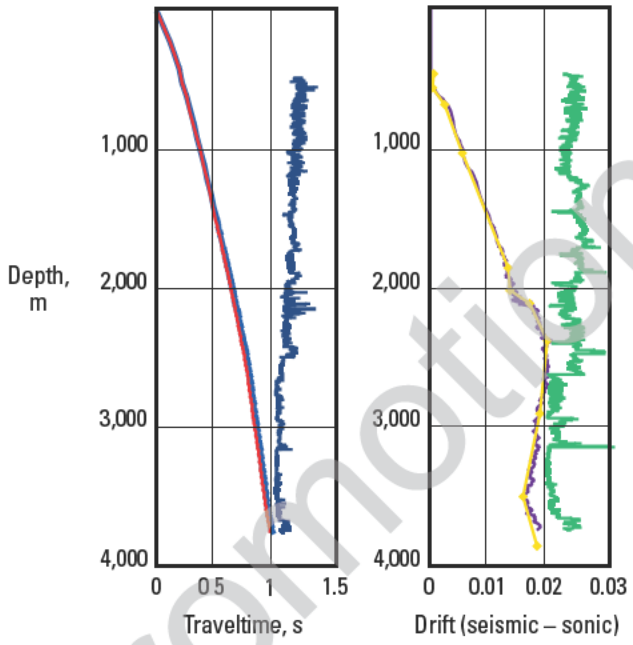

Figure 4-4. Illustration of sonic drift. Sonic log in depth (left) shows traveltime curves as obtained from VSP measurement (blue) and integrated slowness from sonic logs. Note that the curves almost overlay, but a time shift is evident from 1,500 ft. The actual difference between estimates of traveltime using VSP and sonic data (purple) is shown on the right. The yellow curve superimposed on the drift is what is actually used in models for simplicity. The gamma ray log is shown in green.

The difference between these two sets of traveltime data—the drift—is shown as a function of depth by the purple curve in the plot on the right. Between 500 and 2,500 m, the drift is 20 ms, which represents an interval mistie of 40 ms between synthetic data and seismic data. This difference is associated with dispersion, which is controlled by Q. It might be expected that Q would vary with large-scale lithologic variations; therefore, a curve made of straight-line segments has been fitted over the drift curve, which is shown in yellow. The gradient of this curve defines a correction to apply to the slowness values in the sonic log to make the final drift less than 1 ms everywhere. The gamma ray log is shown in green on Fig. 4-4; changes in the slope of the drift curve occur at changes in the gamma ray log because they are lithologically driven.

An idealized example of drift calculation is shown in Fig. 4-5. Several strategies may be adopted to correct the sonic values from the measured drift values. The procedures shown in Fig. 4-6 are standard techniques to make the corrections.

The correction for negative drift is an empirical approach based on observed differences in the measured drift between sonic data acquired with a conventional sonic tool and data acquired with a long-spaced sonic tool. The longer the source-detector spacing in the sonic tool, the deeper the measurement will be. Altered zones are much more likely to affect the conventional sonic tool, thus increasing the amount by which the sonic tool is reading "slow." The "Delta-t_{min}" correction is designed to correct these zones more than the faster, deeper-reading zones. Zones with slowness values less than the Δt_{min} value will not be affected by the correction.

Once the sonic log has been corrected, there is a consistent time-depth relationship between the seismic data and the log data for vertical raypaths. It is now possible to interpret exactly what the seismic response to a given geological boundary is and to track that away from the well. It is possible to derive time-depth lookup tables, velocity models, root-mean-square and average velocity curves, and impedance logs.

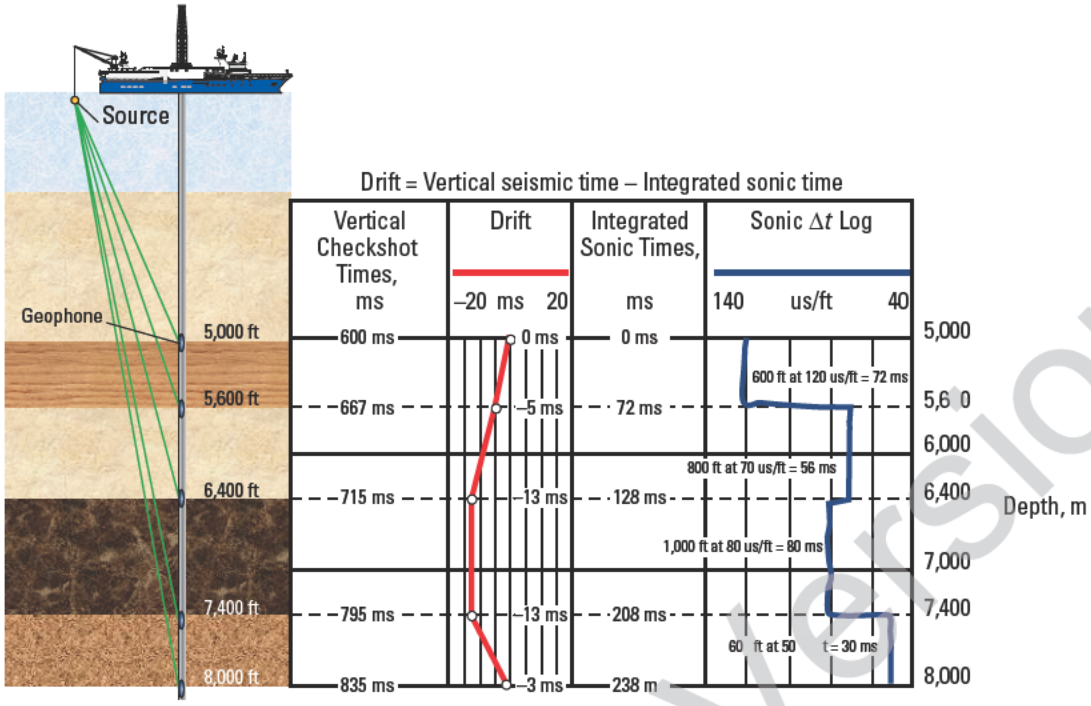

Figure 4-5. Example of drift calculation. Note that drift values come from the simple equation sta when adding 600 ms to all integrated sonic times, which corresponds to filling the traveltim curve with the VSP times.

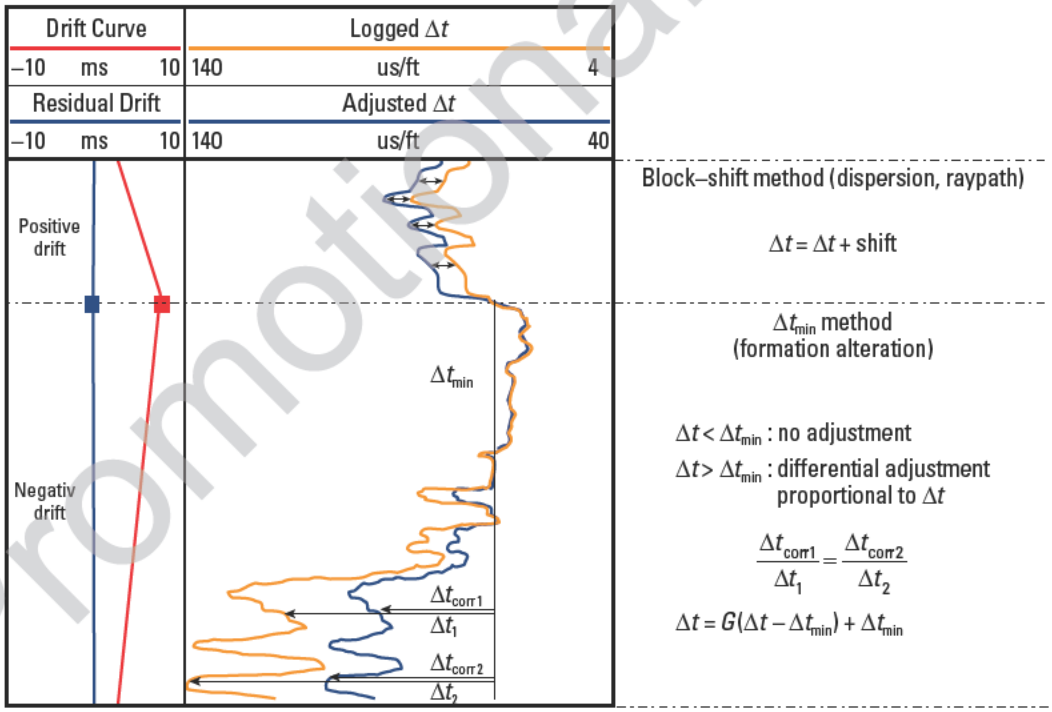

Figure 4-6. Procedures to correct the sonic values from the measured drift values. *G* represents the proportionality factor to be applied to each sample. The parameter Δt_{min} is a threshold slowness below which the log is not considered corrupted. The assumption is that the slowest log values are the ones likely to need the most correction.

4.4 Synthetic seismograms

Having obtained traveltimes, the next step is to make a synthetic seismogram at the same time scale as a measured seismic response. The procedure is fairly straightforward:

1. Start from the drift-corrected sonic.
2. Convert corrected sonic and density (ρ) logs to time.
3. Calculate the acoustic impedance (Z) log:

$$Z = \rho V. \tag{4-4}$$

4. Calculate the reflection coefficient (R) between each pair of successive acoustic impedance values:

$$R = \frac{Z_2 - Z_1}{Z_2 + Z_1}. \tag{4-5}$$

5. Convolve the resulting reflection coefficient series with a desired wavelet.

More sophisticated synthetics are possible. Multiples from a free surface can be included, or all possible multiples can be included. Transmission losses can be included at each interface to reduce the amplitude available for reflection at the next interface. Lateral offset can be introduced to generate pseudoshot gathers, and anisotropy and dispersion can be included. Nevertheless, almost every synthetic seismogram generated is the simple, multiple-free, one-dimensional form.

When a synthetic seismogram is calculated in is way, it may be expected that all time intervals b tween events within the depth range of the log will be the same on the synthetic as they are on the seismic reflection data, whether it is surface seismic dat or VSP data. The scheme detailed here for drift correction of the sonic works in almost every case. This is no eworthy because all the corrections are based on measu ed traveltimes with no reference to the refle tion data

4.5 Basic VSP pro essing

VSP processin is eas est for the simplest geometry: a vertical well wi h flat trata and a seismic source positioned nea the surface location of the well. However, most of this discussion is also applicable to more complex geometries in which raypaths are not vertical or normal to the reflectors. For challenges specific to these compl x geometries, refer to subsequent chapters.

This section focuses on VSP information content that is made available by data processing rather than on the specific details of the applied processes.

The objective of the acquisition stage is to measure traveltimes and amplitudes of the seismic waves at the borehole to recover the Earth's response to a point source at or near the surface. Because it is generally neither possible nor desirable to deploy a continuous array of geophones over the whole depth extent of the well, the response is approximated by a discrete spatial array, which is sampled finely enough to meet the requirements of sampling theorem (Nyquist, 1928). A second approximation is the assumption that the Earth's response to identical shots is identical. This a lows us to sample only part of the borehole for each f a s ries of shots and to assume that the esult is the ame as that which would have been sampled by recording all receiver locations for the same sh t.

Figure 4-7 shows the synthe ic w v field for a simple case. Three downgoing ev nts are shown (one direct arrival and two multiples) with the raypaths that generate them. Model and traces are plotted at the same depth scales. No she r-wa e conversion is shown. The downgoing direct arriv ls oc ur at later times as the receiver depth increases, nd for the zero-offset case, the slope of the direct-arrival curve gives the velocity of the medium at that depth. That is, the seismogram displays distance vers s time, and the gradient of the arrival times (x/t) is the sound velocity in the x direction.

The second event type shown in Fig. 4-7 is a downgoing multiple. Multiples are waves reverberating between p irs of interfaces. The raypath generating this class of event is shown in the upper figure. The delay introduced between the arrival time of the direct arrival and that of the multiple is independent of the geophone depth. For the zero-offset case, the multiple will always be parallel to the direct arrival; its slope is governed only by the velocity with which it traverses the geophone array at any depth.

In the VSP geometry, multiples can be identified easily because they appear in a certain pattern. For the downgoing multiple shown in Fig. 4-7, the multiple can only exist as a downgoing event for receivers positioned below the shallower of the two generating interfaces. As the synthetic shows, for all receiver depths above the top generating interface, the multiple does not exist. Real data seldom show large-amplitude multiples truncating at intermediate depths, which implies that most large-amplitude multiples are related to a shallow interface either at the surface, or possibly at the base of weathering (for land data), or at the seabed and sea surface for marine data.

It is important to remember that all pairs of interfaces will generate multiples in the final wavefield, and the number of possible multiples increases rapidly with

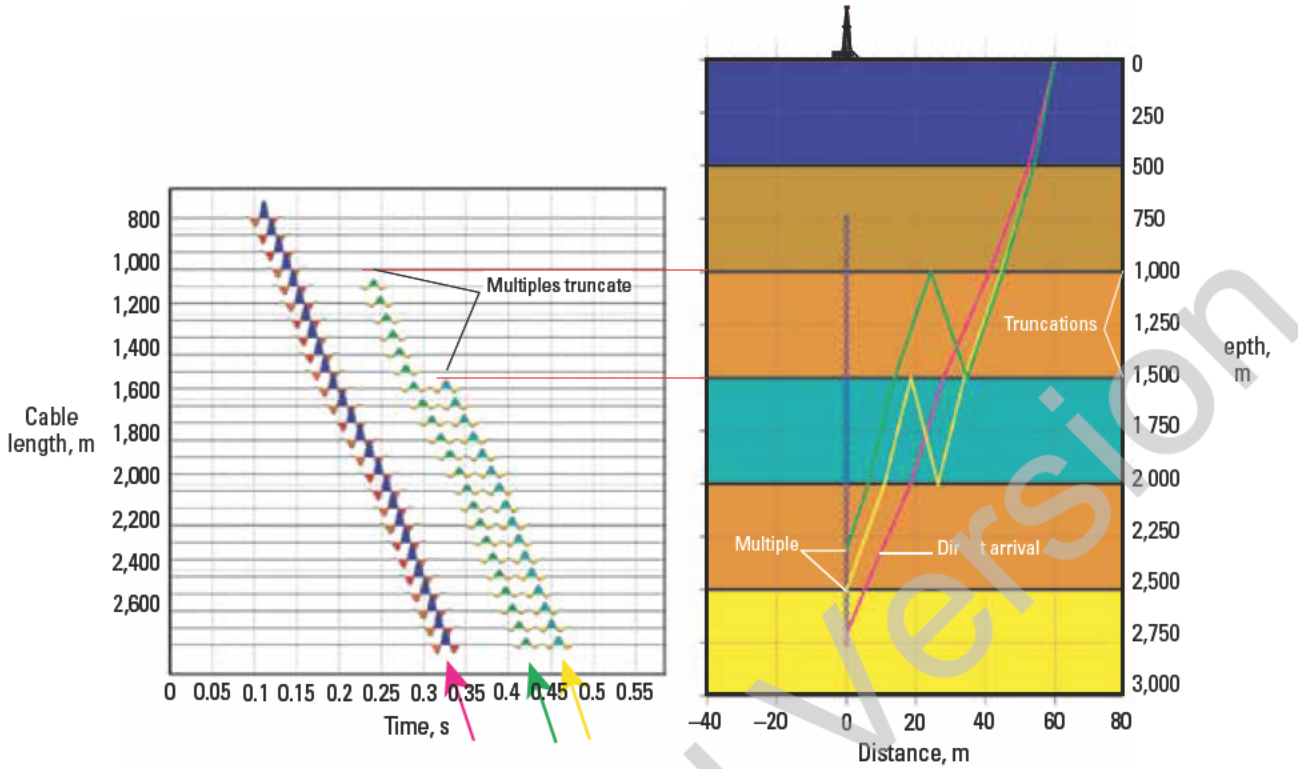

Figure 4-7. Simplified model and synthetic VSP showing downgoing direct arrival (magenta) and two general multiples (green and yellow). In reality, all pairs of interfaces will generate downgoing multiples. In the synthetic wavefield, transit time corresponds to direct and multiple arrivals. Colored arrows indicate the waves corresponding to the same colored raypaths in the model.

the number of interfaces. The period of each pair of multiples will generally be random, but the rule that the downgoing multiple will only exist below the shallower of the two interfaces between which it is generated will always hold. If the depth and time of the top interface and the period of the multiple are known, then the depth and time of the lower interface of the multiple-generating layer can always be found.

The direct arrival normally represents the earliest time that energy from the source can reach each of the geophones in the borehole. After exiting the geophone, the wavefront continues to propagate in the Earth. Therefore, the only "primary" event in the downgoing wavefield is the direct arrival (or a converted downgoing shear wave). All other downward-propagating energy passing the geophone array must have been delayed by multiple bounces on its way between source and receiver.

Figure 4-8 shows the corresponding case for upgoing wavefields. Here, reflections from two of the interfaces are shown with both interfaces intersecting the array of receivers. As the receivers become shallower, both distance and time from the reflector increase to cause the event to have the opposite slope (or moveout) to the downgoing wavefield. Like the downgoing wavefields for the zero-offset case, the slope of the event gives the velocity of the medium. Each event truncates at the direct-arrival curve (shown in blue). Clearly, a reflection can be recorded only when the receiver is above it. This point deserves some elaboration. The point at which the upgoing event coincides with, or intersects, the direct-arrival curve is the point in time and depth at which the reflection actually takes place. Primary reflections are the only upgoing events that intersect the direct-arrival curve—all upgoing multiple events truncate before they reach the direct-arrival curve. It is this property of simultaneously representing the data in time and depth that leads to many of the interpretive benefits of VSP.

Multiples generated as the wavefield progresses downward to the reflector become part of the signature for the reflection event. Thus, the multiple shown in Fig. 4-7 is manifested in the reflection response of Fig. 4-8 as the events indicated. Because these events are part of the downgoing signature after they have

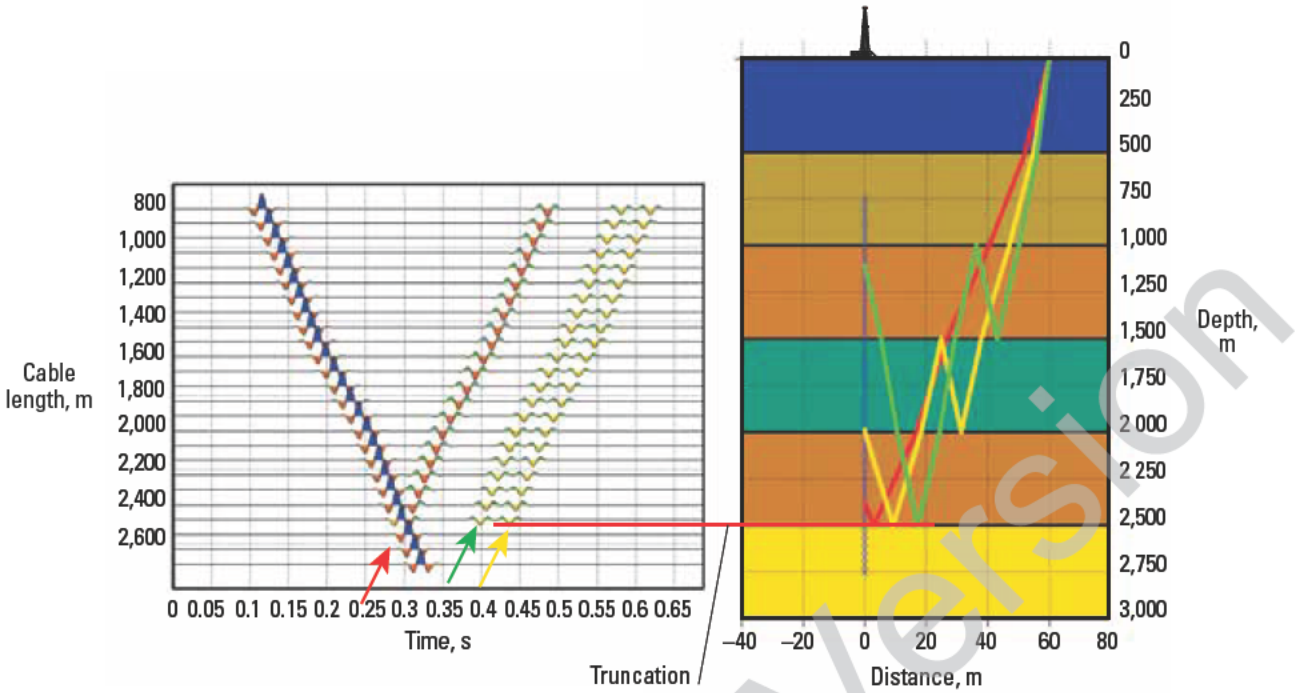

Figure 4-8. Model and synthetic VSP showing that multiples in the upgoing wave appear wh never the reflector is below the multiple generator but the geophone is above the primary reflecto (at 2,500 m here).

been created, they are visible only for those receivers that "see" the reflection event, and they appear to truncate at the reflection interface. This provides another rule for discriminating between primary and multiple events—only primary reflection events intersect the direct-arrival event.

The key benefit of the VSP geometry in xpl ration is its ability to record both upgoing and owngoing wavefields, which allows direct observation of the changes in the wavefield as it propagates into the Earth. The VSP records the exact far-field signa ure at a well-sampled array of depth points in the Earth All changes in the pulse shape can be mea ured, both simple-amplitude and phase-shifting ef ects. Multiples can be directly observed and identified particularly where they are generated within the depth range of the geophone array.

Real recorded dat includes the superposition of upgoing and downgoing wavefields, not the separate and dis inct ones diagrammed in Figs. 4-7 and 4-8. (This applies equally to all the other wave types in the data, in luding shear waves and tube waves.) Figure 4-9 shows the combined wavefields discussed in Figs. 4-7 and 4-8 with the addition of the primary reflection events from th two shallower interfaces in the model. For clarity, only the one multiple is included.

Given the data of Fig. 4-9, the remaining question is: How effectively can the distinct upgoing and downgoing components be separated? They can be separated very effectively, provided that the data have been adequately sampled during acquisition. The geometry of the experiment results in the two wavefields having moveout of opposite sign, thus allowing various forms of velocity filter to be applied to separate the wavefields.

Figure 4-10 shows a real zero-offset dataset. Even in the raw data, the upgoing and downgoing events can be clearly seen. A flow diagram of a processing chain is shown in Fig. 3-43. Our intention is to discuss some processing steps to reveal the information contained within a VSP dataset. VSPs offer more than what could be obtained by correcting a sonic log and generating a synthetic seismogram.

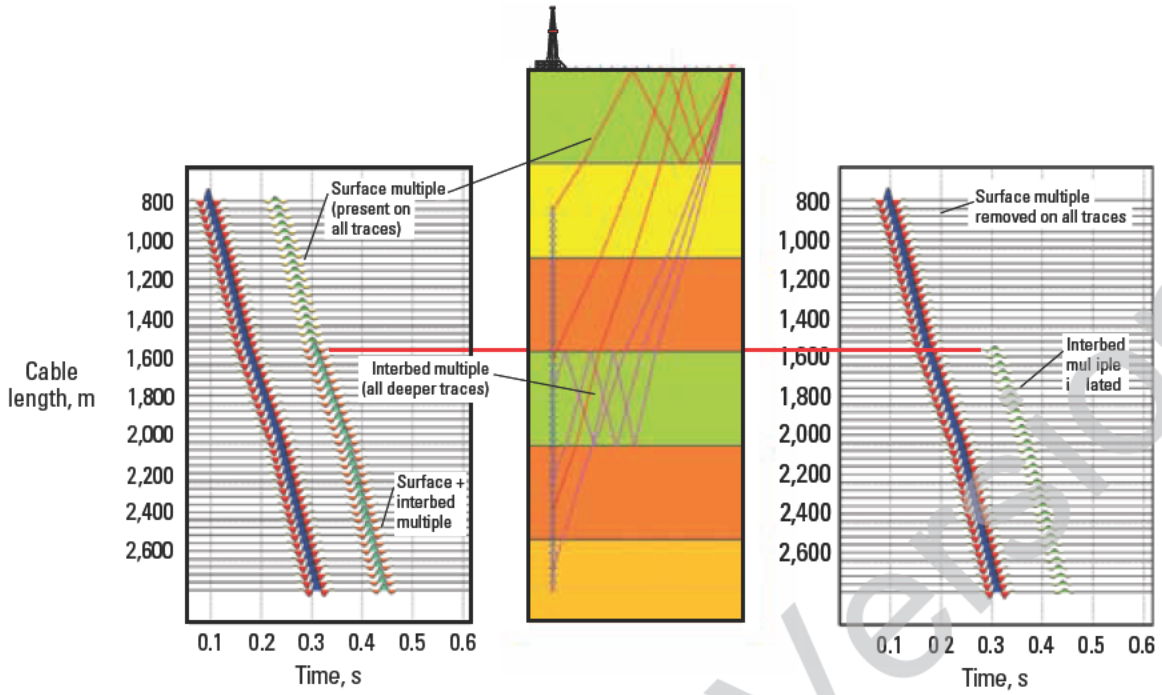

Figure 4-9. This model and synthetic data combines the events of Figs. 4-7 and 4-8 and incl des the primary reflections for the two shallower interfaces.

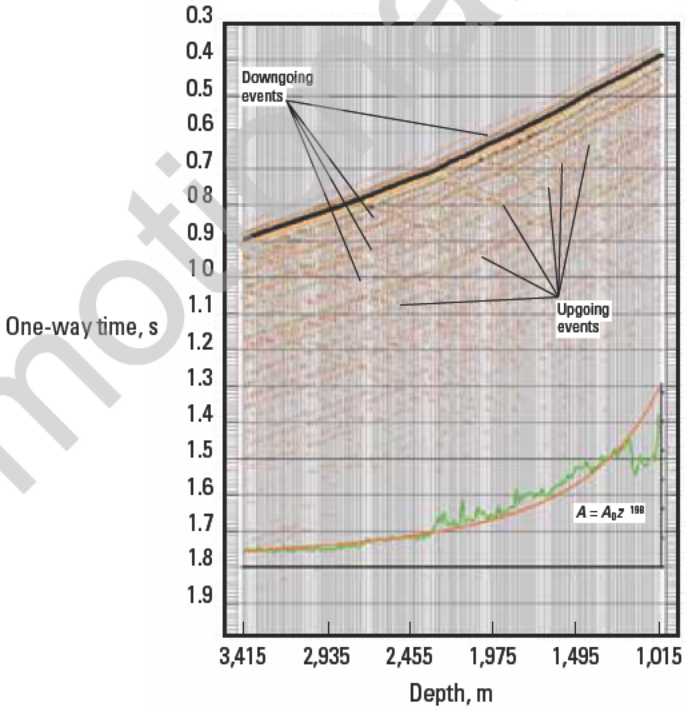

Figure 4-10. Raw vertical-component VSP data plotted trace-normalized. At the bottom is the trend line of the direct-arrival amplitude, as a function of depth, together with the "best-fit" power-law expression for the orange line. Equation symbols are as follows: A is amplitude, A_0 is initial amplitude, and z is depth.

4.5.1 Amplitude recovery

Amplitude is an important property of seismic data. As soon as the interpretive interest moves from major structural concerns to lithology, porosity determination, pore fluids, or stratigraphy, the need for strict amplitude control is paramount. The potential exists to extract extremely accurate amplitude information from VSP data and to correct for the various propagation effects accurately. Alternatively, the various effects can be measured and distinguished between to enhance the quality and value of surface seismic data. At every step, the direct arrival helps calibrate the applied process. The downgoing wavefield provides the means to analyze propagation effects on amplitude and phase, whereas the upgoing wavefield contains the amplitude information to interpret stratigraphic variations.

The objective is to arrive at a version of the reflection dataset in which amplitude variation is directly related to some change in the geology or pore fluids, not to artifacts resulting from the acquisition geometry. Section 4.5.6 explains how the role of downgoing normalization, inherent in trace-by-trace deconvolution, compensates for amplitude losses at the receiver level in the upgoing wavefield and that residual gain corrections are needed only for the look-ahead section.

4.5.2 Acoustic impedance and geophone sensitivity

The first distortion that can be removed in processing is the amplitude change of the propagating body wav as it travels through material of differing cous c impedance. When a wave passes through a dense rock, slower particle-motion velocity will result from wave of a given energy than when the medium is less dense. The energy in a wave (E) is given by

$$E = A^2 Z, \tag{4-6}$$

where A is amplitude and Z is acoustic impedance or

$$A \propto \frac{1}{\sqrt{Z}}. \tag{4-7}$$

Generally, there will be a trend of increasi g acous tic impedance with depth that will reduce me sured amplitudes with depth. To compensate for this, he trace from each geophone can be scaled by the square root of the impedance; the impedance as a function of depth is derived from the wireline logs. Failure to pply this correction may result in

- attributing the apparen amplitude decay to one of the other decay processes discussed next, which will then be corrected using the wrong relationship
- interpreting he amplitude changes as reflectivity chang s (or A O) in the final product. This is of particular concern for offset VSPs, where the amplitude variation with depth will be mapped or migrated to la eral amplitude variation.

is effect is demonstrated in Fig. 4-11. Here the VSP data amplitudes of the direct arrivals are compared with the acoustic impedance as a function of depth. The VSP amplitudes have been corrected for Q (see Sections 4.5.3 and 4.8), and a geometrical spreading correction (see Section 4.5.4) with depth has been applied. The remaining amplitude variation correlates well with the inverse square root of the acoustic impedance, as predicted by Eqs. 4-6 and 4-7.

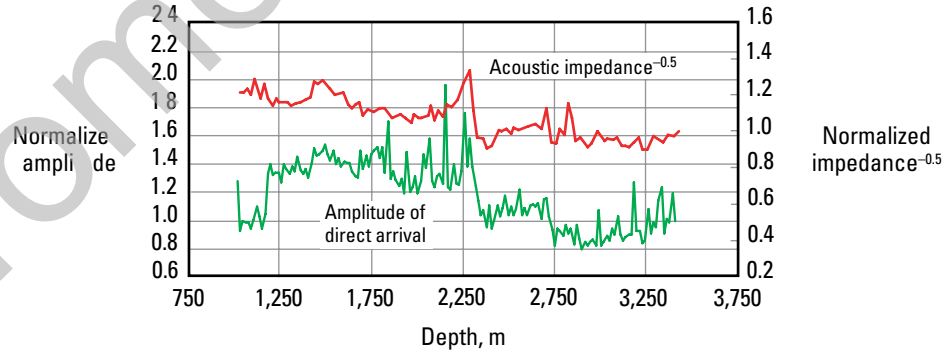

Figure 4-11. Direct-arrival amplitude compared with logged acoustic impedance. Both curves have been normalized by their deepest values. The acoustic impedance log, sampled at a 15-cm [6-in] depth of investigation, has been smoothed and resampled before presentation.

4.5.3 *Q* recovery

High frequencies decay faster than low frequencies because rocks are not completely elastic. Some of the energy is lost in heating the rock. If the proportion of energy lost per oscillation is constant, the higher frequencies will lose energy faster than the lower frequencies. This inelasticity results in dispersion—the phenomenon in which lower frequencies propagate more slowly than higher frequencies. VSPs provide a convenient tool to measure this. Dispersion, similar to the acoustic impedance effect described, causes amplitude reduction with increasing distance from the source. Dispersion correction should be done separately. How to measure Q is discussed in Section 4.8.

4.5.4 Spherical divergence

The largest amplitude decay mechanism is geometrical spreading. For simplicity, geophysicists might consider that it is the only decay mechanism. Figure 4-10 shows the amplitude of the direct arrival as it varies with depth, and the best-fit power-law decay is an exponent of 1.98.

Amplitude decreases with distance because the constant energy in the wavefront spreads over the surface of an ever-expanding sphere. Because it is amplitudes that are being measured, a decay exponent caused by geometrical spreading alone should be close to unity. Other decay processes, described in the previous sections, contribute significantly to the estimate of the decay exponent.

In the ideal case of spherical spreading, the energy decay will be

$$E_2 = E_1\left(\frac{r_1}{r_2}\right)^2. \tag{4-8}$$

Similarly, the amplitude decay could be expressed as

$$A_2 = A_1\frac{r_1}{r_2}, \tag{4-9}$$

or

$$A \propto \frac{1}{r}, \tag{4-10}$$

where r_1 and r_2 are two arbitrary distances from the source, and A_1 and A_2 are the wave amplitudes measured at those distances. A constant velocity is assumed and r in Eq. 4-10 is replaced with t, the traveltime.

The geometrical spreading correction is normally applied as a function of time, so the direct arrival amplitude for the data of Fig. 4-10 is plotted as a function of time in Fig. 4-12, with the best-fit power-law decay also as a function of time. The exponent in the time domain is now –2.8 as a result of the velocity gradient. As depth increases, velocity increases, and hence, the interval transit time between similar depth intervals decreases. If the velocity gradient b is linear,

$$V = V_0 + bz; \tag{4-11}$$

therefore, the traveltime will be

$$t = \int \frac{dz}{V_0 + bz}, \tag{4-12}$$

which integrates to

$$t = b\log_n\left(1 + \frac{bz}{V_0}\right). \tag{4-13}$$

Therefore, the assumption that amplitude decay as a result of geometrical spreading can be corrected by applying a correction in the form of t^n is a simplification, at best.

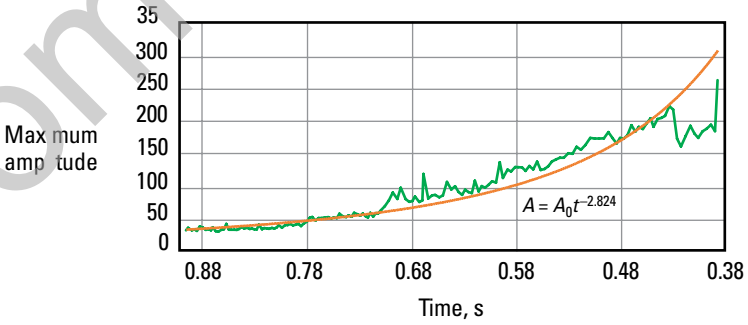

Figure 4-12. Amplitude decay as a function of time for the same data as in Fig. 4-10. Again, a power-law fit has been superimposed. Note the changed exponent, which is a function of the velocity gradient (see text).

Figure 4-13 shows this effect. A simple $1/r$ amplitude-decay-with-depth relationship is shown as a function of time. Also shown is the best-fit inverse power-law representation with an exponent of –1.37. The actual value of this exponent relative to the depth exponent of –1 will vary with the depth range analyzed and with the functional form of the velocity gradient. More realistic corrections are possible (see Ursin, 1990; Grech *et al*., 1998).

One deduction from this discussion is that upgoing and downgoing events at the same time on different geophone traces require different gain corrections. The direct arrival passes through the velocity structure once in a given time. In the same time, a reflection from a shallower event twice traverses a shallower part of the velocity structure, probably a lower velocity, thus experiencing a different spreading exponent in time. Generally, the only correct way to compensate amplitude loss is through ray-trace-based corrections.

Often, all three of the effects—acoustic impedance, Q, and spherical divergence—are treated together as if they were simply spherical divergence. The impedance effect should be a constant scalar versus time for any trace, and the Q-effect should be exponential; therefore, to treat them as part of an inverse power law will result in inaccurate relative amplitudes, particularly at later times in the data.

One final effect is the transmission loss as the seismic pulse passes through each interface in a layered medium. The amount of energy lost at interfaces with small impedance contrasts is rather small, but the combined effect of many small-impedance interfaces can have a significant effect on the seismic pulse. An in-depth discussion of this is beyond the scope of this book, and the reader is referred to O'Doherty and Anstey (1971) and Ziolkowski and Fokkema (1986).

4.5.5 Wavefield separation

Wavefield separation is the general term for the process of dividing the recorded wavefield into components. The recorded data consists of upgoing shear and compressional waves, downgoing shear and compressional waves, and noise (possibly with the addition of diffractions), tube waves, or out-of-plane events. For a zero offset VSP in a vertical well or for cases in which all raypaths cross all interfaces at normal incidence, shear waves will not be present because conversion from compressional to shear only occurs for transmission at non-normal incidence.

The upgoing, downgoing compressional, and shear components are distinguished by their moveouts or time gradients with depth. Consequently, most types of dip filtering produce reasonable results, although the most commonly used method for VSPs is spatial median filtering. This approach is preferred because VSP data contain various components that would be expected to truncate abruptly. For instance, the multiples in the downgoing wavefield truncate as the geophone moves above the generating interfaces, and one of the properties of the median filter is that it passes step-functions unchanged but removes spikes and outliers from the data. A filter of length n treats any anomaly of length less than $n/2$ as a noise event to be rejected.

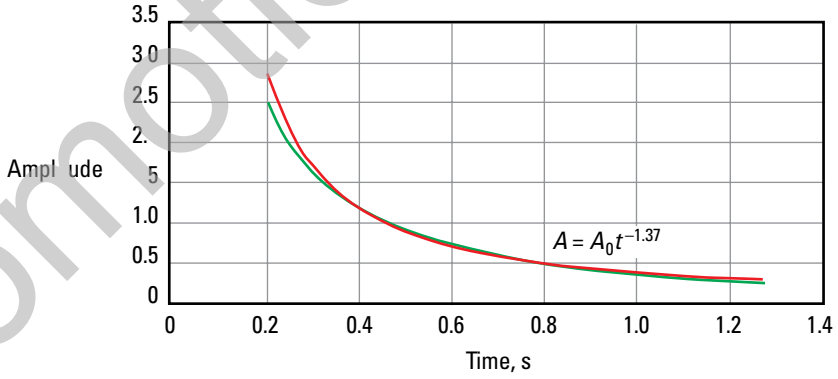

Figure 4-13. Geometrical spreading as a function of time for synthetic data with a linear velocity gradient. The effect of the gradient on the value of the exponent will vary with well depth and gradient value because only the inverse power law is approximating the decay.

The median filter is applied across an array of samples from successive traces at a specified moveout. Provided that the filter is long enough, any event crossing the array of samples appears as noise to the filter and is rejected. Thus, the filter extracts a wavefield having a specific moveout.

Figure 4-14 shows the dataset of Fig. 4-10 after gain recovery. Amplitudes are well balanced and many different events can be seen through the data. The result of applying a median filter to extract the downgoing P-waves is shown in Fig. 4-15. The filter is applied parallel to the direct arrivals, which can include changes in

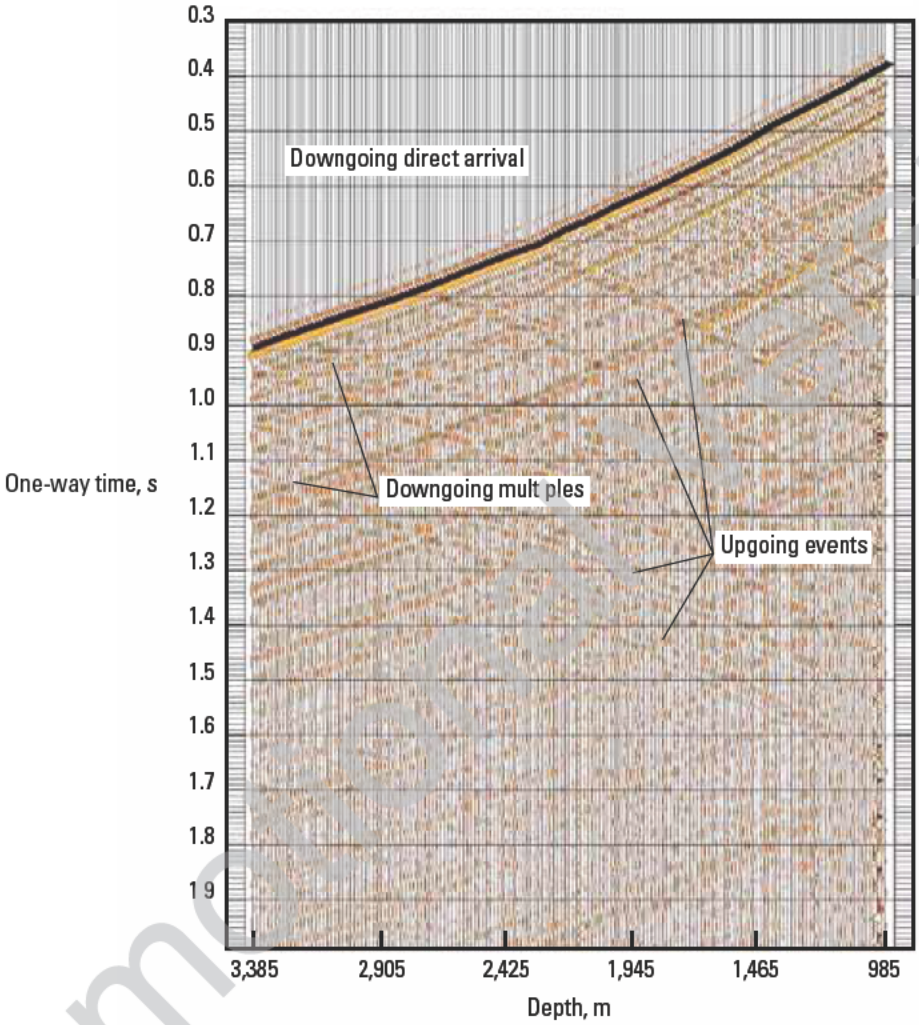

Figure 4-14. Amplitude-corrected VSP. Upgoing events can be seen across the entire dataset on geophone traces from a complete range of depths. For a zero-offset VSP, all reflections come from immediately beside the well; therefore, the only variable that should affect the reflections recorded at different-depth geophones is the propagation through an increasing thickness of rock.

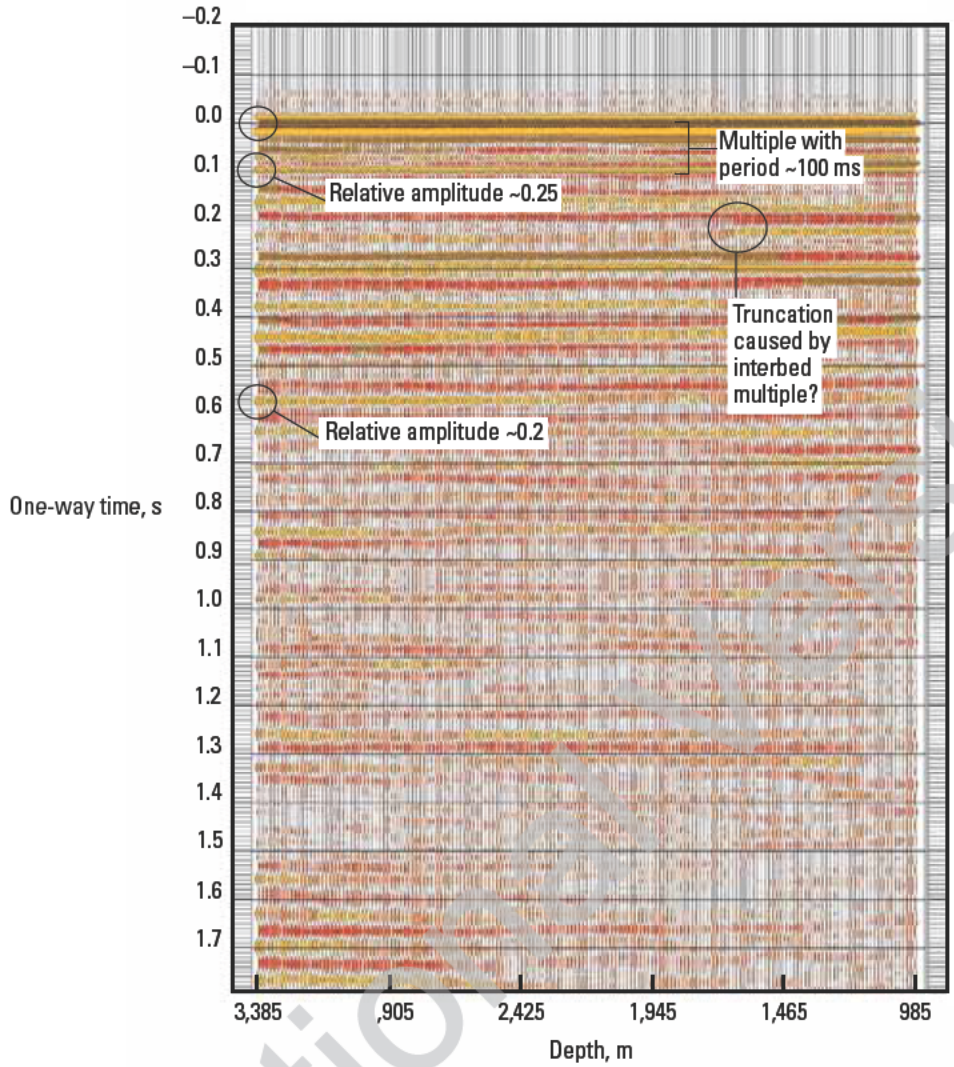

Figure 4-15. The downgoing wavefield extracted using a spatial median filter. All events that lie parallel to the direct arrivals are retained, and all other a reje ted The amplitudes are plotted with a larger-than-normal gain to highlight the indicated events.

slope. The result is subtra ted, sample-by-sample, from the total wavefield to ave th upgoing waves and noise behind (Fig. 4-16).

A second application of the median filter to this "residual" dataset, a igned parallel to the upgoing event (i.e., at the opposite dip to the downgoing direct arrivals), enhances the upgoing events at the expense of the noise. Figure 4-17 shows the wavefield aligned in two-way time. For a zero-offset VSP, this can be accomplished by applying a static shift to each trace whose value is equal to the arrival time of the direct arrival. In this alignment, the reflection events become horizontal.

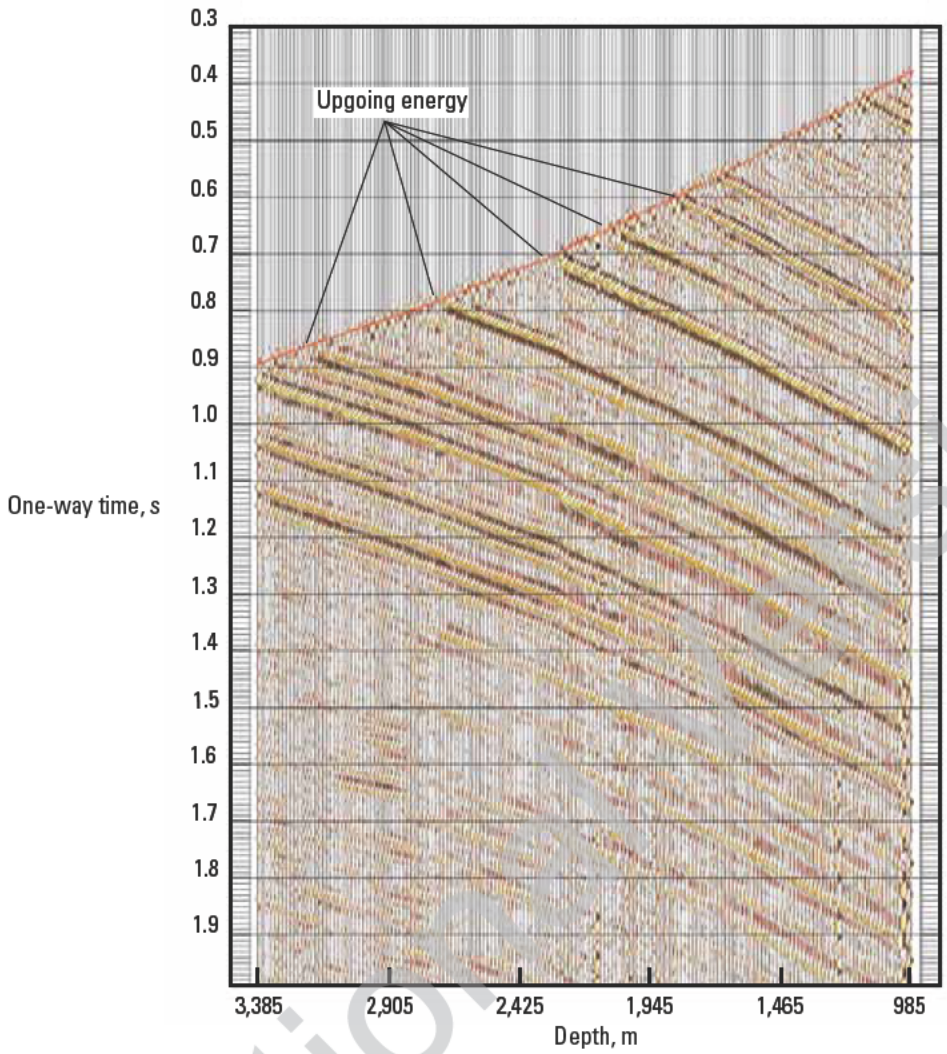

Figure 4-16. Upgoing wavefield—the result of s btracti g the downgoing wavefield from the original wavefield. With the exception of the downgoing compressio al waves, this wavefield, for the zero-offset VSP case, contains everything—upgoing compressional wav s, mul iples, and noise.

For those familiar with looking at surface seismic records, displays such as Fig 4-17 may appear "mixed," "smeared," or "synthe ic" because the trace-to-trace consistency is o high The consistency is not so unreasonable in consideration that all the reflections come from a restricted lateral area around or beside the well. The same section of subsurface is being sampled for each geophone for any given event, the source is

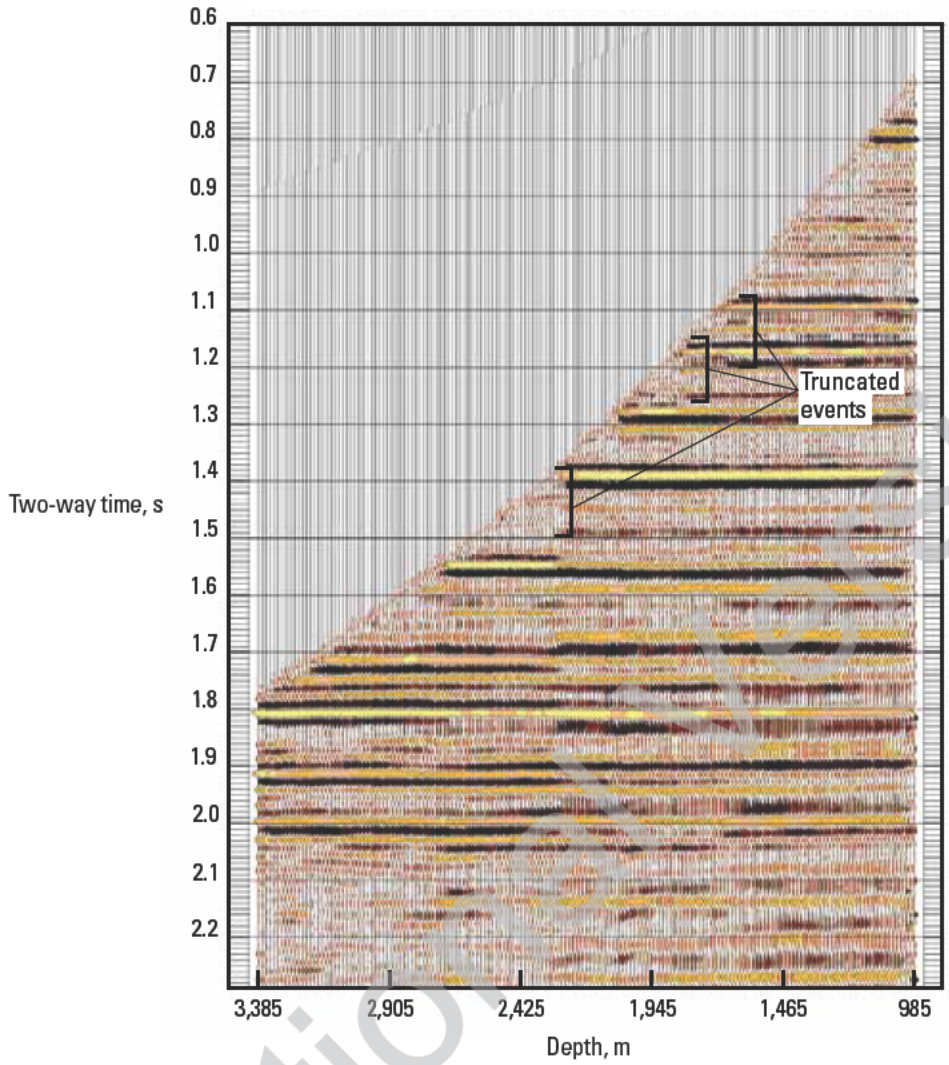

Figure 4-17. Upgoing wavefield in two-way tim The p t gain has been increased to make it easier to see truncating events (multiples) within th data. Multiples truncate at the trace with the same depth as the primary from which they are echoe . The multiple periods appear to correlate with the 100-ms-period multiple in the downgoing wavefield of g. 4-15.

consistent, and the geophone coupling is as reliable and quiet as can be exp cted. To support this, Fig. 4-18 shows the result after subtracting the median-filtered upgoing events of Fig 4-17 from the upgoing events in Fig. 4-16. There is little, if any, coherent noise in this residual, thus implying no trace-to-trace smoothing or mixing, either explicitly or implicitly.

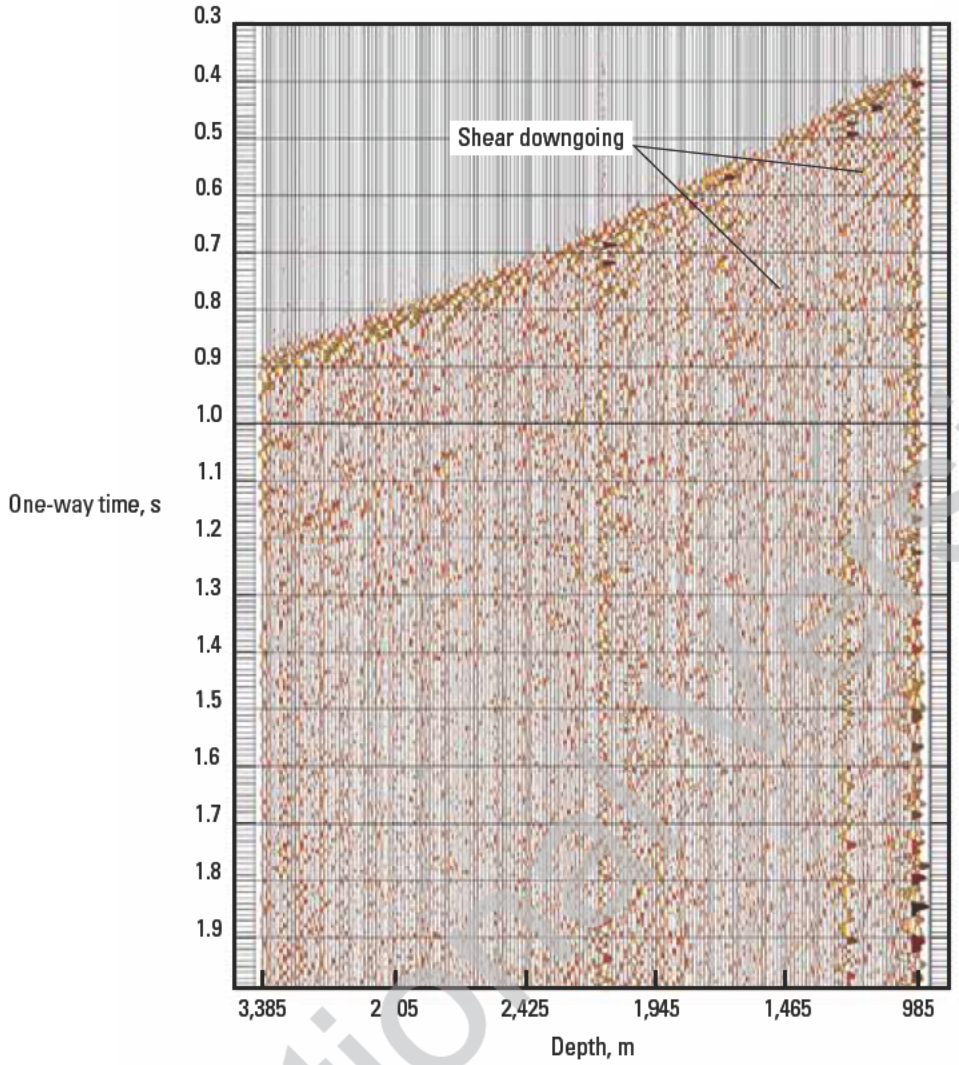

Figure 4-18. Residual wavefield after enhancing pgoing waves; plotted at a high gain (five-trace overlap). The wavefield is mainly random noise with me sh ar wave moveout events.

4.5.6 Waveshaping deconvolution

The downgoing wavefield whose extraction is described previously is the measured far-field signature recorded at each geophone position in the well. It includes the results of all the propagation effects that have occurred since the wavefield left the source. Any reflection from below a geophone contains the same pulse recorded at that geophone as the downgoing wavefield but scaled by the reflectivity. Therefore, the deconvolution problem for the VSP is to design an operator, or mathematical function, that will collapse the downgoing wavefield at each receiver to some desired output shape, usually a zero-phase wavelet, because that gives the best resolving power and leads to an unambiguous well tie. The operator is then applied to the same trace of the upgoing wavefield. The resulting output is an upgoing wavefield that is zero phase by definition (more correctly, where the reflection events are represented by a pulse with a precisely known shape) and of unambiguous polarity. Figure 4-19 shows the upgoing wavefield after deconvolution. The most obvious effect of the process, compared with Fig. 4-17, is that the data have been reduced to a set of discrete events with greater bandwidth. Multiples have been c llapsed back to their primaries, and the embedded wave et is now zero phase.

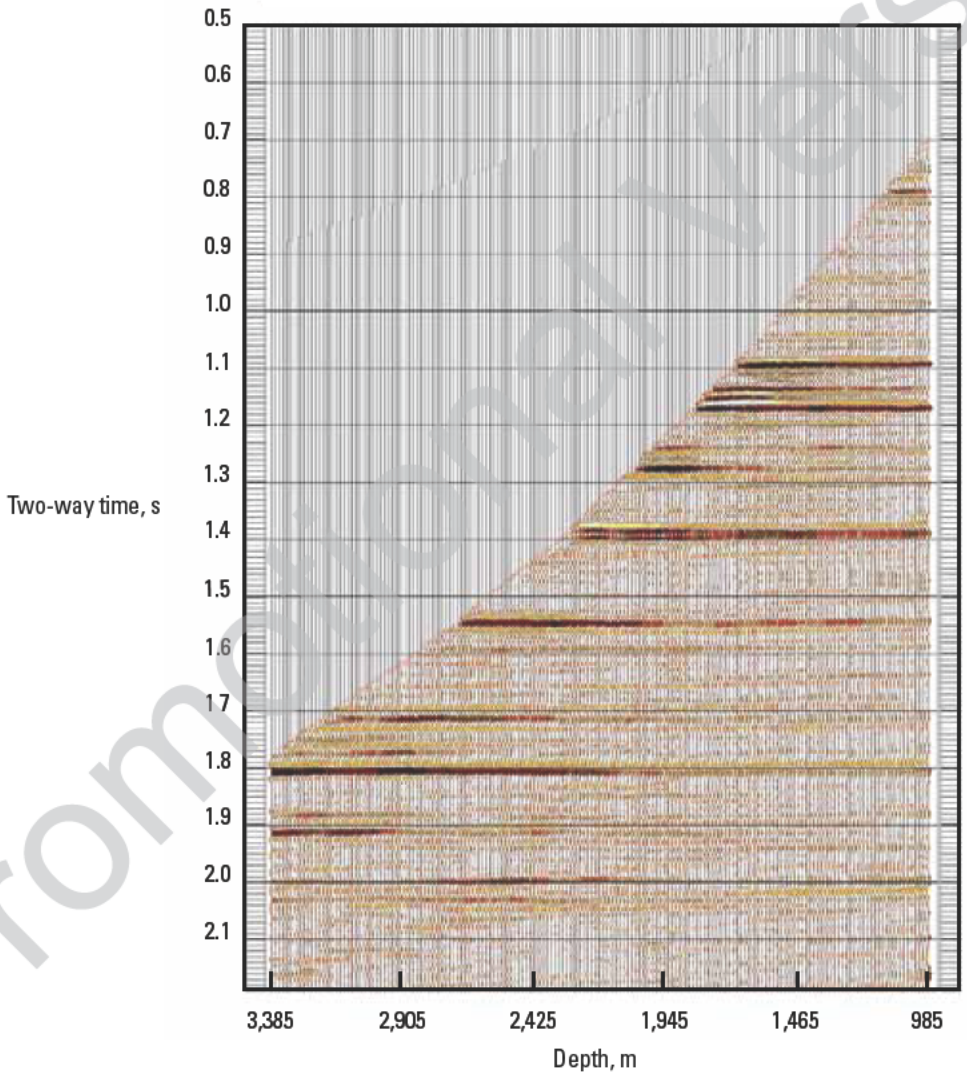

Figure 4-19. Upgoing wavefield after deconvolution. Note the improved character of the data—events stand out from the background. The events marked as multiples in Fig. 4-14 have been properly collapsed.

4.5.7 Corridor stack

The deconvolution result described previously is exact for reflections coming from interfaces near the geophone in question. These data arrive soon after the direct arrival at each geophone. Therefore, by looking at only a window of data, say 100 ms, after the direct arrival, a dataset can be extracted that conforms closely to the assumptions used in the processing. As noted earlier, upgoing multiples never extend to the direct-arrival curve; therefore, the window automatically excludes any multiples that might have been inadequately collapsed by deconvolution. Typically, this data window is then stacked to form a single trace, which is repeated for clarity (Fig. 4-20). This trace, known as a corridor stack, can be thought of as the measured, multiple-free, zero-phase, normal-incidence seismic response at the well. It is the best normal-incidence response that can be obtained at that point.

The corridor stack can be directly compared with either synthetic traces or seismic data (Fig. 4-21). For the synthetic data, it is a measured version of the inferred response from the logs. For surface seismic data, it is the actual normal-incidence trace without the assumptions that went into the surface seismic processing, and it can be precisely tied back to the geological events on the logs in depth. It is the bridge between the world of well logging (in depth) and the world of seismic cross sections (in time). Geological horizons in depth can be converted to time using the checkshot-corrected sonic data. The time scale of the VSP in two way time can be identical to that of the synthetic data so the horizons can be unambiguously carried across to the VSP corridor stack and then to the surface seismic data.

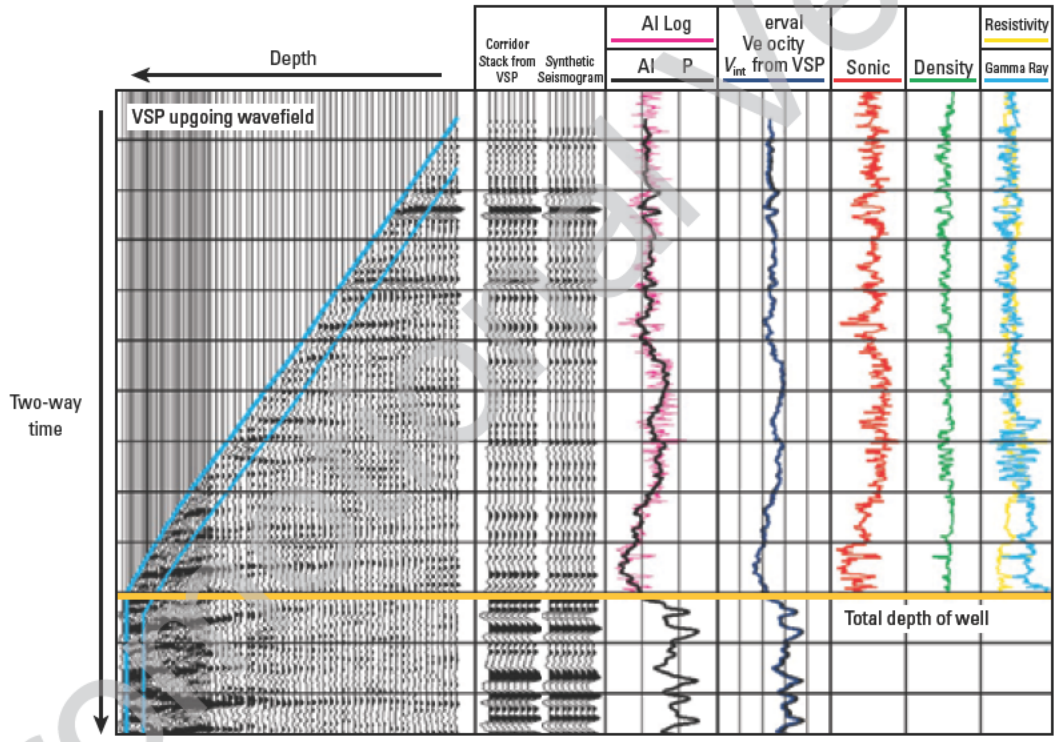

Figure 4-20. Corridor stack plotted adjacent to a synthetic seismic record obtained from the acoustic impedance (AI log, which is derived from the density and sonic logs. Gamma ray and resistivity curves are added for correlation. Because the logs have been corrected with the VSP arrival times, the time correlation between the seismic and synthetic data is unequivocal. Any apparent time differences remaining are part of the real seismic response. (From Campbell *et al.*, 2005.)

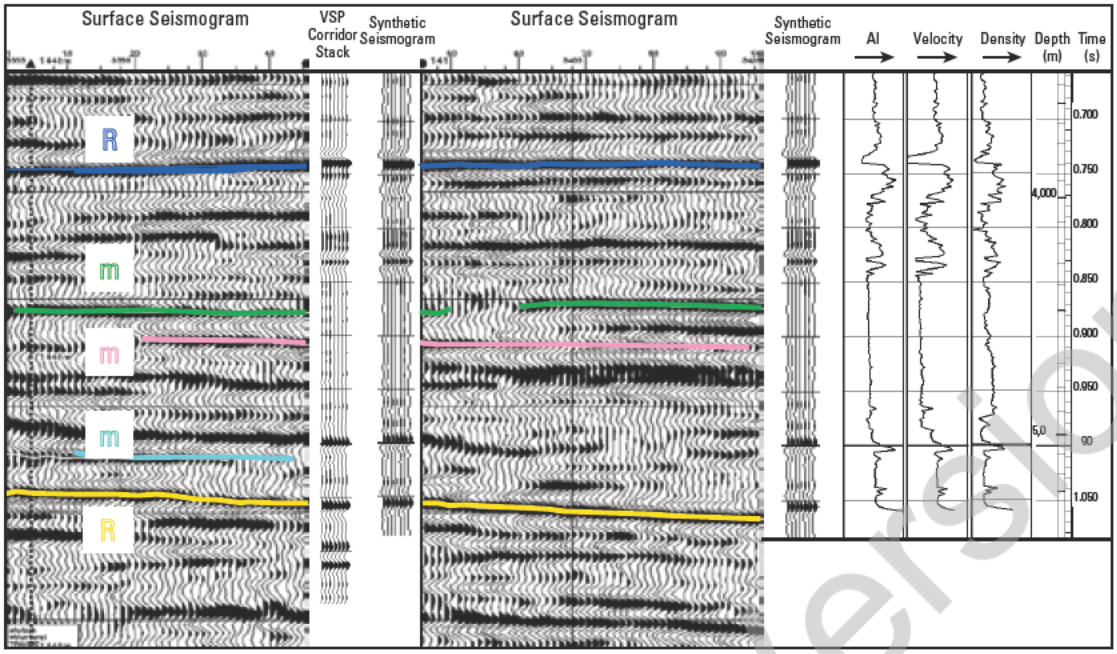

Figure 4-21. VSP corridor stack compared to surface seismic data and the synthe ic seismog am. Geological reflectors (R) and multiples (m) can be easily identified.

4.6 Identifying multiples

Identification and attenuation of multiple contamination is a major concern when interpreting seismic data. Multiples can be identified in surface seismic gathers by their periodicity or by their anomalous moveout. These properties of the multiples are used in mos atten a- tion processing schemes. A combination of st tistica ly derived deconvolution and residual moveou filtering is the usual tool. For most surface seismic datasets, it is difficult to identify the source of the multiples within a section; this decision is usually urely i terpretive. For shorter-period multiples, th moveout discrimination may be small.

The same multiple gene ating mechanisms affect a VSP dataset and a su face seismic trace. The relative amplitude and periodicity of all multiples in the section must be the s me, wi h the possible exception of the multiples that h ve the very near surface as a component b cause the reflectivity and velocity of this zone may be affected by weather conditions. Therefore, any multiples that can be identified and isolated in the VSP data are also present in the surface seismic data. In the simplest application, knowledge of the depth at which interbed multiples are generated allows the selection of deconvolution-design windows that contain, and do not straddle, the generators creating the contamination.

Most datasets are characterized by two classes of multiples. The largest-amplitude multiples generally are surface-generated multiples. In the land case, one of the bound ng interfaces is the surface or base of weathering; for marine data, one interface is the water surface and the other is the sea bottom. The other multiple class is that of interbed multiples, those in which both bounding interfaces are within the body of the data. Interbed multiples usually are lower amplitude because reflection coefficients within the body of the data are smaller. Surface-generated multiples trail every primary reflection in the sequence, whereas interbed multiples only exist in the section at times later than the reflection time of the top bounding interface of the multiple generator.

Although interbed multiples are generally of lower amplitude than those generated at surface, it is easy to devise reflector arrangements in which multiples have an amplitude relative to the reservoir reflector that is similar to the amplitude changes in that reflector that would be considered significant to the interpretation.

The zero-offset VSP geometry provides a tool to identify various multiple generators within the geological section and to measure their actual contaminating potential. Because VSP geophones are deployed as a vertical array, it is possible to see where multiples originate as a function of depth and to measure their amplitude relative to any primary they follow. Multiples may be observed on either upgoing or downgoing wavefields of the VSP, but for the downgoing wave, the SNR may easily be a factor of 10 higher than that in the reflection wavefield.

In Fig. 4-22, raypath colors correspond to beams indicating three downgoing events. The depth scales for the VSP traces correspond to the depths in the model. The synthetic data clearly shows how the downward-traveling multiples are present after the direct arrival for all geophone positions deeper than the top interface of the multiple-generating layer. In reality, there would be many other multiples in addition to those shown. Every pair of interfaces generates its own contribution to the total downgoing wavefield.

For a stack of layers with a wavefield propagating through them—the situation for the downgoing wavefield in the VSP—the number of first-order multiples can be rather large. In general, the number of downgoing multiples will be given by

$$N = \frac{n(n-1)}{2}, \qquad (4\text{-}14)$$

where N is the number of first-order multiples and n is the number of layers. Therefore, 10 interfaces can generate 45 possible first-order multiples, but for 50 interfaces, the number rises to 1,225. The large number of possible multiples can make them difficult to identify.

In the absence of any other propagation effects, the transfer function between any two geophone depth levels in the VSP will be the multiples newly introduced between those levels.

Figure 4-22 shows how the truncation of the multiple event occurs as the geophone rises above the generating layer. A surface seismic deconvolution operator designed in two-way time over a window corresponding to a depth window of 1,000 to 2,000 m will do a poor job of collapsing either multiple. Although not shown in this figure, the surface multiples being generated above the sh llowest geophone will be present on the trace for each geophone level in the well, and they will be paral el to the direct arrival (this scenario is shown in Fig. 4-24)

Once a multiple has been gene ted d ring the propagation of the wavelet, it can be thought of as part of the seismic signature from tha depth on It will be present after each primary upgoing event from every reflector deeper in the section. The rela ive amplitude of the multiple that crea es a y reflection event will be the same as the relative amplit de between the direct arrival and the sam downgo ng multiple. Figure 4-23 illustrates this for the same mode shown in Fig. 4-22.

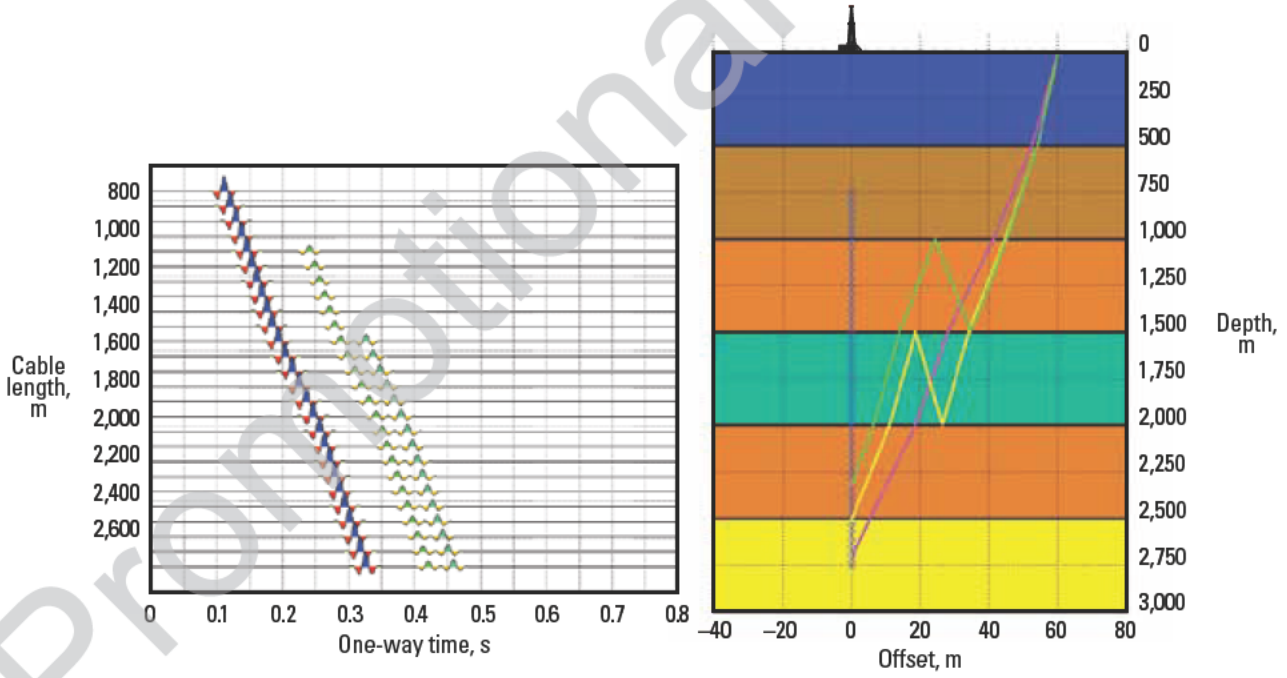

Figure 4-22. Model and corresponding synthetic VSP trace data for three downgoing events. Multiples in the downgoing wave appear only when the geophone is within or below the multiple generator.

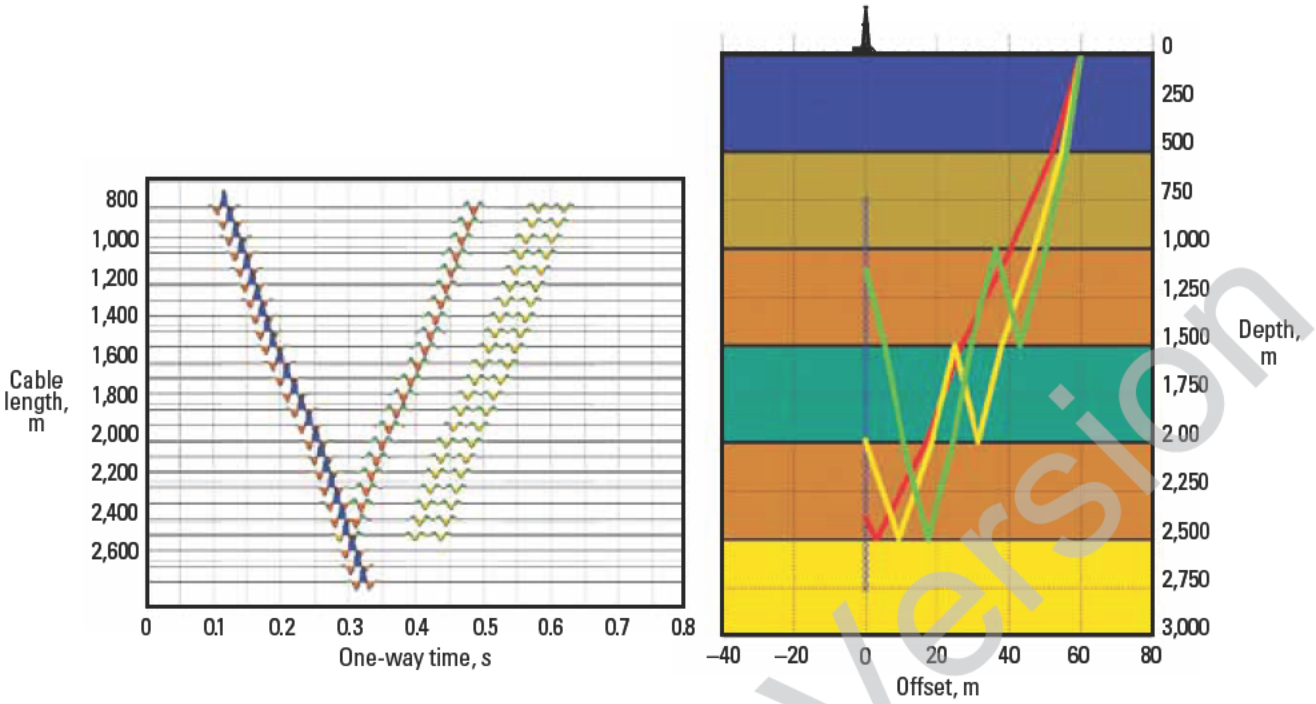

Figure 4-23. Same model as in Fig. 4-22. Multiples in the upgoing wave appear whenever the reflector is below the multiple generator but the geophone is above the primary reflector (at 2,500 m here).

The red beam indicates the single primary reflection. The multiples are generated as illustrated in Fig. 4-22 to form the other two indicated multiple events. The same-color arrows represent the same multiple generator and raypath on both figures. For clarity, the downgoing manifestations of these multiples have been omitted.

The upgoing multiples can exist only for geophones shallower than the reflection depth of the primary; so, identifying the depth of the truncation clearly indicates the primary event with which the multiple is associated. Also, any upgoing VSP event that intersects the direct arrival must be a primary reflection.

Note that once a multiple exists, it is present at all later times. In the downgoing wavefield of Fig. 4-22, the two multiples truncated at different depths and, hence, were identifiable. Once they exist in the upgoing wavefield (Fig. 4-23), they are distinguishable only by their period and in general, many multiples have similar periods and overlay or interfere with one another.

The kinematics for identification of multiples is straightforward, and in practice, to identify and measure surface-generated multiples is easy. Such events have high amplitude and strong continuity. However, interbed multiples are difficult to detect. Typically, they have 10% or less of the amplitude of surface multiples and appear in the downgoing wavefield at similar times. In Fig. 4-24, two multiples are included, a surface multiple and an interbed. The interbed is generated between two interfaces having reflection coefficients of approximately 0.1, and the surface multiple is between the surface with reflectivity of perhaps 0.5 and an interface with reflectivity of 0.3. The interbed multiple has a similar period to the surface multiple and is undetectable in the raw wavefield. In Fig. 4-24, the relative amplitude of the interbed has been increased to aid identification.

All multiples generated above the shallowest geophone in the VSP dataset are present to the same degree on all deeper traces. Therefore, a deconvolution operator designed on the shallowest trace collapses all multiples generated above that level for all the deeper traces. It effectively layer-strips the shallow multiples from the data; thus it leaves the interbed multiples behind for identification. Figure 4-24c shows the result after applying this procedure to the synthetic data in Fig. 4-24b. The interbed multiple is clearly visible after the deconvolution, and the depth at which it was generated can be interpreted.

The ability to recognize and classify multiples in the upgoing and downgoing wavefields offers some opportunities unavailable in surface-recorded data. At each geophone level in the well, the recorded downgoing wavefield is a directly measured far-field signature that includes all multiples generated in the Earth above

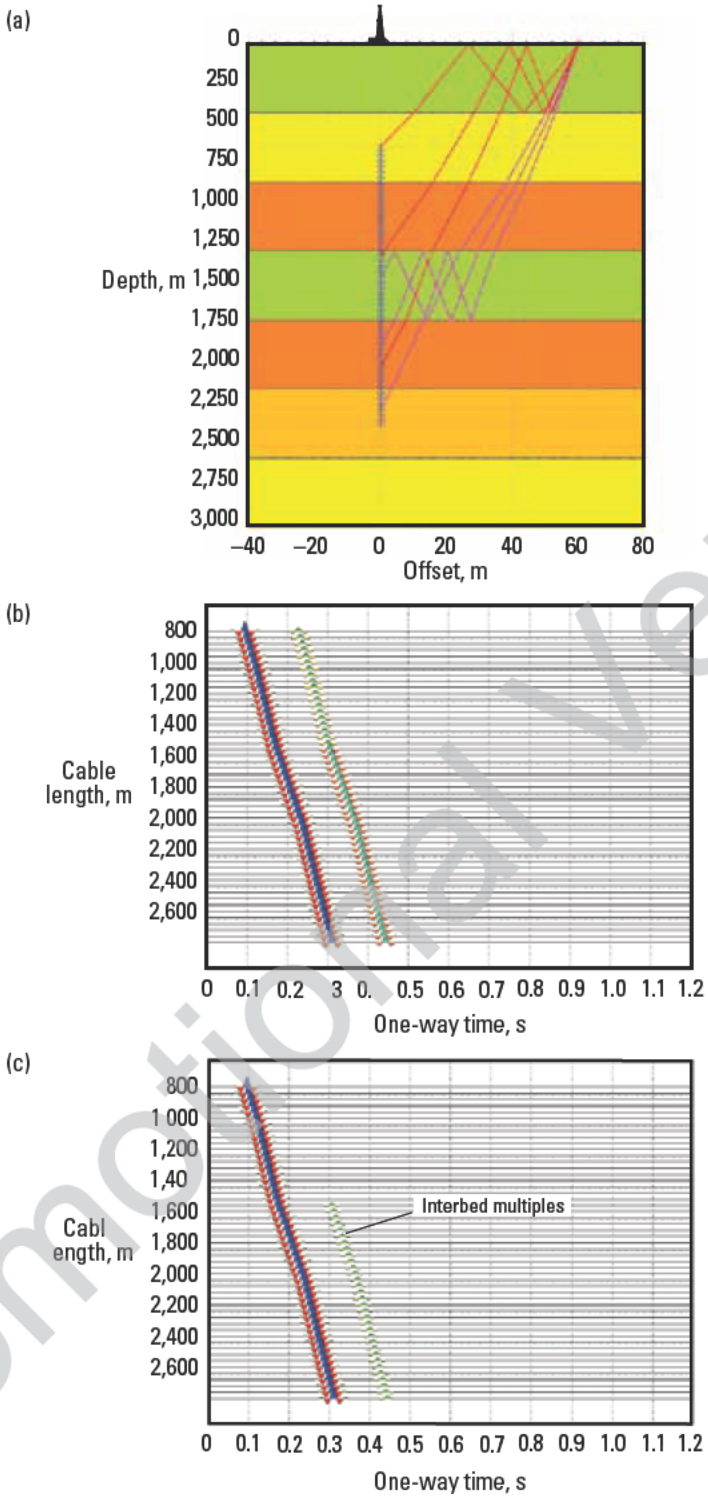

Figure 24. Modeled synthetic VSP data shows how interbed multiples can be difficult to identify as they become lost under high-amplitude surface multiples (b). Deconvolution designed on a shallow geophone trace can strip multiples generated above that depth (c).

that point. Thus, for each trace, a unique deterministic operator can be designed to collapse all the multiples that form the far-field signature. Figure 4-25 shows the effectiveness of this approach using synthetic data from the model in Fig. 4-24. The two multiples illustrated in Figs. 4-22 and 4-23 are considered here. The shorter-period multiple from the shallower reflector directly overlays and interferes with the primary reflection from the deeper reflector.

This process perfectly collapses the multiples for all geophones lying below the top of the multiple generator. As a reflection event is imaged by successively shallower geophones, it becomes progressively more contaminated by multiples from shallower multiple generators (e.g., the black arrows in Fig. 4-25). All surface-generated multiples are present for all geophone levels in the downgoing wavefield and, thus, are completely removed from all reflections. Only interbed multiples contribute to the contamination discussed here.

This trace-by-trace deconvolution scheme achieves precise results for reflection events observed shortly after the direct-arrival curve, so this scheme is generally used in the production of the corridor stack from the zero-offset VSP. The above discussion is also the justification for the claim that the corridor stack is zero-phase, multiple-free, Fresnel-zone averaged data. The synthetic from the sonic log is the inferred reflection response. The VSP is the most accurate measured response at the well, and the surface seismic data is the road map to the next well.

An alternative deconvolution or multiple removal scheme, particularly for offset VSP, is to design an operator from the downgoing wavefield recorded at a deep trace, possibly one immediately above the zone of interest. This trace will contain the response of all possible multiple generators above that point, and hence, the operator will collapse all multiples that contaminate the response on that reflector. Figure 4-26 is analogous to Fig. 4-25 but displays this "reference-trace" approach.

The left-hand side of Fig. 4-26 shows the result of designing an operator from a downgoing trace above Marker A that contains the downgoing multiple from A but not from B. As a result, Multiple A has been completely removed, but Multiple B remains visible. Notice that the removal of Multiple A interference from the deeper reflector event results in consistent amplitude for that event.

The right-hand side of Fig. 4-26 shows the result of designing the operator from a geophone below Zone B that contains both multiples. It is clear that the two primary reflectors have been completely demultipled over the entire geophone array. This type of result demonstrates successive "multiple stripping" to identify significant contributors to multiple contamination.

Given these results, it might appear that deconvolution design using the deepest possible geophone level would be the preferred approach. The foregoing discussion neglected the fact that the wavelet is also changing because of its propagation through the Earth. A single reference trace deconvolution operator could not compensate for this wavelet variation, even though it contains information about multiples. Thus, zero-phase and multiple-free results require additional steps, such as Q compensation, to correct for the inelasticity. The trace-by-trace approach, on the other hand, provides an exact result for all data close to the direct-arrival curve. Typically, the corridor stack consists of the first 100 ms or so of data; so, the only uncorrected propagation effects are those that would occur in 100 ms, which are assumed to be small.

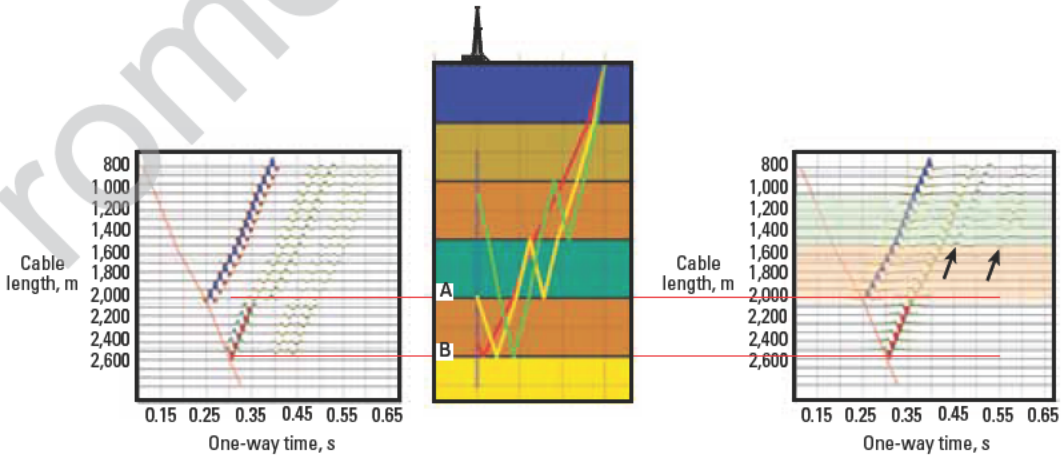

Figure 4-25. Model and synthetic data showing VSP deconvolution applied trace-by-trace.

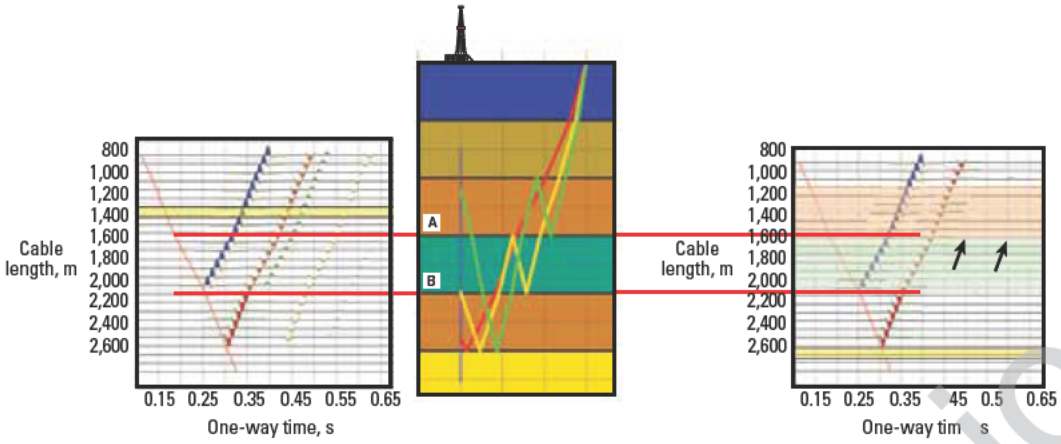

Figure 4-26. Model and synthetic data showing VSP deconvolution applied from specific traces (design traces highlighted in yellow). In the left example, the downgoing trace contained Multiple A but not B; in the right example, the downgoing trace contained both multiples.

VSP techniques improve an understanding of multiple patterns, particularly to distinguish surface-generated multiples from interbed multiples. Conventional seismic processing techniques can be effective for the former, but interbed multiples can pose a much more subtle problem.

4.7 Phase matching

It has been asserted throughout this chapter that the corridor stack from the zero-offset VSP is zero phase multiple free, and of known polarity. The corr dor st ck represents the way a normal-incidence seismic tra e should look if it were zero phase and m ltiple free. Unlike the synthetic trace, it continues elow he TD of the well, and does not truncate at the zone of interest.

The VSP measures the same geological sequence as the surface seismic trace. The comparison between the VSP corridor stack and the surf ce seismic trace at the well location allows determ ning the phase of the surface seismic signal and der ving a correction filter.

The convolution model of both the seismic trace for the VSP and fo the su face seismic data reveals that:

$$S_{\mathrm{VSP}}(t) = w_{\mathrm{VSP}}(t) \times R(t) \qquad (4\text{-}15)$$

$$S_{SS}(t) = w_{SS}(t) \times R(t), \qquad (4\text{-}16)$$

where $R(t)$ is the reflectivity, $w_{\mathrm{VSP}}(t)$ and $w_{SS}(t)$ are the wavelets in the VSP and surface seismic data, respectively, and $S_{\mathrm{VSP}}(t)$ and $S_{SS}(t)$ are the resulting traces. For each trace, the phase spectrum of the trace is the sum of the phase spectrum of the wavelet and the phase spectrum of the refl ctivity If the two traces are crosscorrelated, he phas spectrum of the correlation (φ_{CC}) is the difference of the phase spectra of the inputs, so that

$$\varphi_{CC} = \left(\varphi_{w_{SS}} + \varphi_R\right) - \left(\varphi_{w_{\mathrm{VSP}}} + \varphi_R\right) = \varphi_{w_{SS}} - \varphi_{w_{\mathrm{VSP}}}. \qquad (4\text{-}17)$$

Because the phase of the VSP wavelet is zero, the phase of the crosscorrelation function is the phase of the surface seismic wavelet. An extension of this idea is used in the partial coherence matching technique of White (1980), in which the underlying reflectivity match may be assessed and a match filter derived to either convert the VSP wavelet to that of the surface seismic or to convert the surface seismic wavelet to zero phase.

4.7.1 Matching VSP to surface seismic data

In general, the phase of the operator is frequency dependent. There is no fixed-phase rotation that can achieve the same effect as that of applying the operator. Despite this, there is often a desire to determine the closest fixed-phase rotation. One practical way to extract this is to make use of the fact that, for a wavelet, the peak of the instantaneous amplitude function is at the zero time of the zero-phase wavelet that has the same amplitude spectrum. Therefore, phase rotation of the crosscorrelation until the central peak of the correlation coincides in time with the peak of its amplitude envelope measures the best fixed-phase rotation needed for surface seismic data (Fig. 4-27).

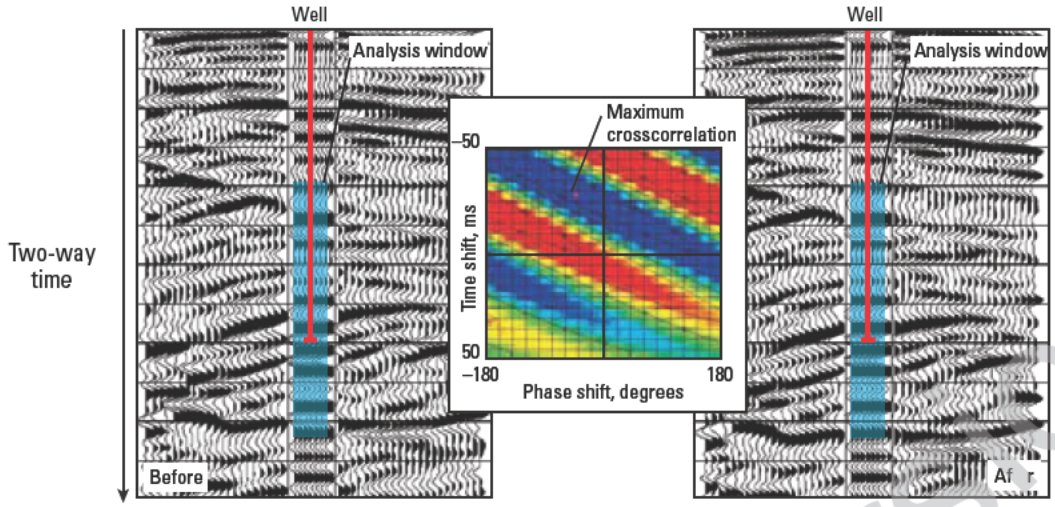

Figure 4-27. Left: Corridor stack compared with surface seismic data before analysis. Right: Comparison after phase correction. The right image shows a much improved well-seismic tie. The blue-shaded area shows the time window used in the analysis. The central panel shows a map of the crosscorrelation amplitudes from which the time and phase difference between the VSP and the seismic data were determined. (From Campbell *et al.*, 2005.)

If the surface seismic wavelet is, indeed, a simple phase rotation away from zero phase, the crosscorrelation function under the optimal phase rotation becomes a symmetrical autocorrelation. Therefore, from a qualitative point of view, the degree of asymmetry in the crosscorrelation under the "best" rotation is an indication of the amount of frequency dependence of the wavelet phase.

Figure 4-28 shows a match using the more advanced method of White. The surface seismic traces at the well have been matched with the VSP corridor stack trace. The raw match is shown in (a); although the match does not look very convincing, the statistics show a good underlying reflectivity match. By applying the operator shown in (b), which is clearly not zero phase, to the VSP corridor stack, a much better match to the surface seismic data may be obtained, as shown in (c).

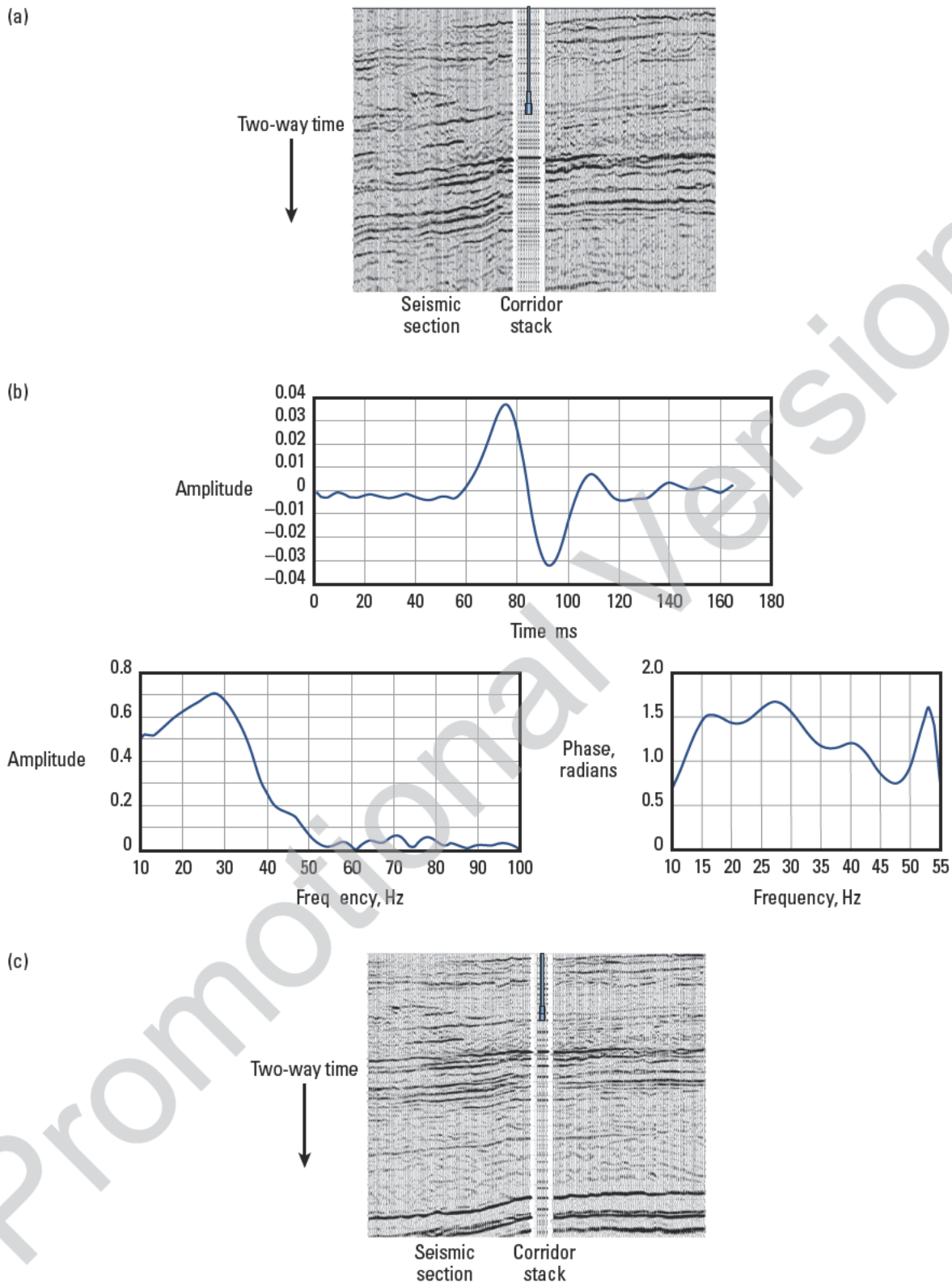

Figure 4-28. VSP raw match to surface seismic data (a). By applying operator shown in (b) to the VSP corridor stack, a much better match to the surface seismic data is obtained (c). (Graphic in (c) from Armstrong *et al.*, 2004.)

4.7.2 Converting surface seismic data to zero phase

The wavelet embedded in a corridor stack from a VSP is not only of known phase; its amplitude spectrum is also precisely known and normally is designed to have favorable spectral characteristics. The procedure of match filtering adjusts the wavelet in the surface seismic data to that in the VSP so that the filtered seismic data contains the same embedded wavelet.

Equation 4-16 indicates that a filter designed to shape the surface seismic trace at the well to the corridor stack trace will provide the necessary correction to the wavelet. The design of the filter can be done either by spectral division or by conventional least-squares Wiener filtering. The filter application can include the whole filter or can use a whitened version of the filter to shape only the phase spectrum of the surface seismic data. Provided that the basic assumptions are honored in the data, a good match between the filtered trace and the desired output should be achievable with a short filter length, possibly on the order of the length of the wavelet. If a longer operator is necessary, then the differences between the traces represent more than just the embedded wavelet. For this discussion, short-period multiples may be considered to be part of the wavelet.

Figure 4-29 shows an example of the effectiveness of match filtering. A seismic dataset from a 3D surface seismic volume is shown on the left. Well 2 penetrated 33 m of reservoir sand; Well 3 encountered only 3 m. The synthetic seismic data are shown for both wells. A VSP existed within the survey volume, and this was used to derive a matching filter that was then applied to all traces of the 3D volume. The result is shown on the right. The sidetrack from Well 3 encountered 7.5 m of sand, visible in the match-filtered seismic section. The match-filtered section clearly shows an event dying out between Wells 2 and 3, thus suggesting that the thicker unit extends to approximately common depth point (CDP) 150.

In deeper wells or wells where the lithology changes significantly with depth, different filters may be designed for each zone. This procedure should be applied with care, however, because if the wavelet is considered to be the main variable between the datasets, the only thing that will affect its shape during propagation will be dispersion. More variability than this would stem from errors in processing, static problems, inaccurate normal moveout (NMO) correction, or migration artifacts. It is

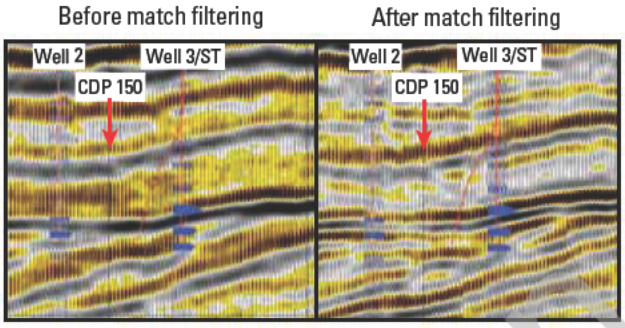

Figure 4-29. A matching filter was applied to the seismic data on the left. The match-filtered data on the right ties both wells much better, and the improved resolution shows the objective of the sidetrack at Well 3.

unreasonable to expect the match filter, itself a simple one-dimensional process, to solve these problems.

The results from match filtering in areas where the assumptions are honored can be exceptional—previously invisible lateral detail can be revealed by this procedure. No new two-dimensional detail is introduced by the filtering—it all must have been there in the original data.

4.8 Q-factor

Wavelets broaden as they propagate. Often we are unable to quantify the dispersion and simply assume that wavelets do not change much over the deconvolution design window. Figure 4-30 shows why this is an optimistic assumption. These VSP downgoing wavelets span a time window of only 600 ms in one-way time (1.2 s two-way time), and yet, the high-frequency loss and change in wavelet phase are impressive. The wavelet is not constant over this window. The width of the direct-arrival trough aligned at 0.0 s has increased by nearly 50%, and the high frequencies in the following peak have been damped from a triplet at a depth of 350 m to a broad, loopy, single peak at 2,700 m.

The VSP geometry provides an ideal opportunity to measure Q directly and then to observe the effects of its compensation because the downward-propagating pulse can be isolated at each depth in the well. The downgoing wavefield at each geophone depth is like a snapshot of the wavefield past that point. Not only can the loss of high frequencies be measured but also the changes in wavelet shape that result.

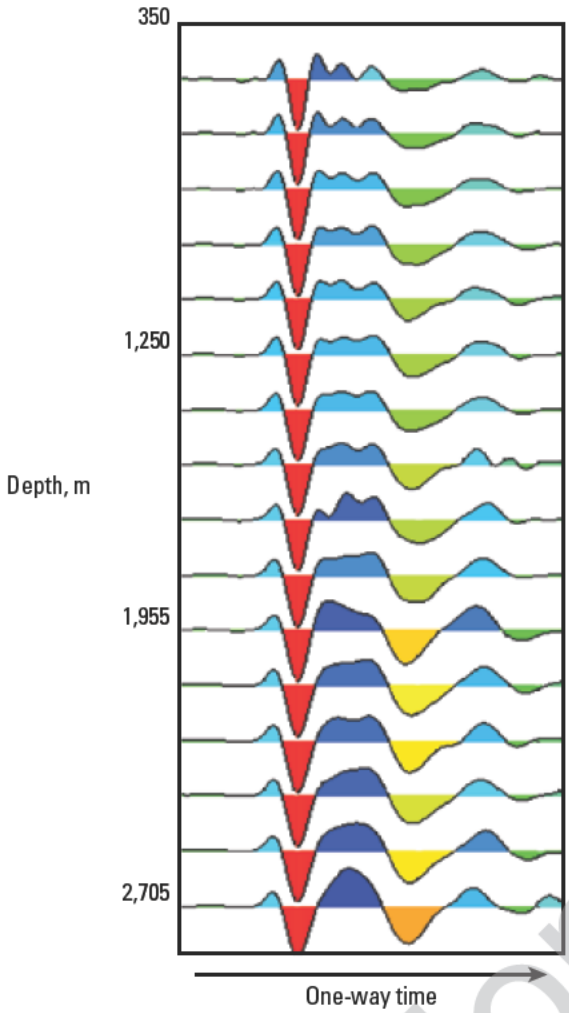

Figure 4-30. VSP data from a zero-offset VSP. No the decay of the high frequencies in the shape of the direc arrival wavelet as it propagates from shallow to deep geophones. Thi is shown by the broadening of the main direct-arrival trough and by t shape of the blue peak following it.

4.8.1 Measuring *Q*

A method for measuring *Q* was presented in Section 4.3 in the discussion of drift with respect to sonic and seismic traveltimes. Equation 4-3 can be used to estimate *Q* from the gradient of the sonic drift as a function of depth. Two other methods are discussed here.

4.8.1.1 Measuring Q from zero-offset VSP spectral ratios

If it is accepted that a change in the wavelet is caused by dispersion, then *Q* can be measured directly as he rate of decay of higher frequencies relative to lowe frequencies with depth and distance prop gated

Figure 4-31 shows how the spectrum from the downgoing wavefield from the VSP data et in F g 4-30 changes over 2,400 m from near surface to the t rget horizon. The deeper geophone (red) shows lower overall amplitude, as expected, but more imp rtantly, the roll-off slope at higher frequencies up to a out 85 Hz (where noise begins to dominate) is steeper for the deep geophone than for the shallow one. It is the relatively greater loss in amplitude at the high r freque cies that needs to be measured.

Figure 4-32 quantifies the roll off by showing the ratio b tween the two spectra as a function of frequency. Abo e 80 Hz, the decay trend abruptly reverses because there is no longer any source energy at these frequencies nd the comparison is just between ambient noise recorded at two levels in the borehole. The straight line on the plot represents the best-fit line over the frequency range from 10 to 80 Hz and represents a value for *Q* of 65—a stronger effect and lower value than might be expected for rocks buried this deep.

Having derived a value of *Q* from the changes in the amplitude spectrum, the next step is to derive a filter to compensate for this effect on the wavelet. Simple spectral whitening is not adequate because this would imply a noncausal Earth filter. The necessary condition is that this filter is minimum phase, and this allows the construction of a Q-compensation filter.

Figure 4-33 shows the result after application of such a filter to the data in Fig. 4-30. The consistency of the wavelet as a function of receiver depth is obvious. The width of the main (red) trough is consistent, and the triplet character of the following (blue) lobe is seen throughout the depth range. In both plots, the amplitudes have been normalized, by trace, to the amplitude of the red trough. The assumptions inherent in deriving the compensation filter have been met—the compensating filter has produced the desired results. As expected, the Q-filter has also shifted the time of the wavelet peak earlier by about 6 ms. This is part of a much larger time shift between slownesses measured at sonic versus seismic frequencies.

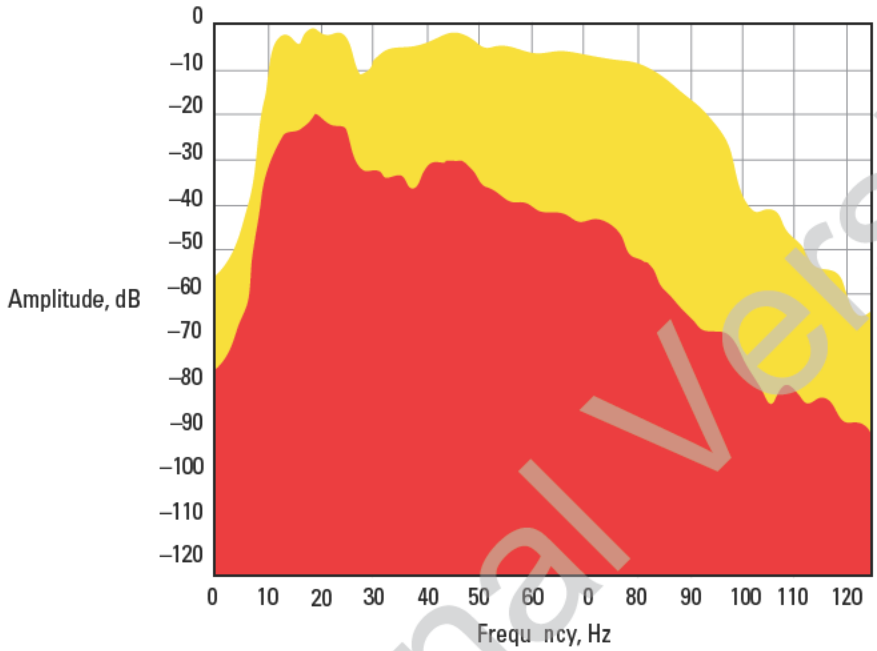

Figure 4-31. Amplitude spectra from a deep (red) and shallow (yellow) level in a zero-offset VSP. Note the greater decay of the high frequencies (up to about 90 Hz) for th deepe geophone position.

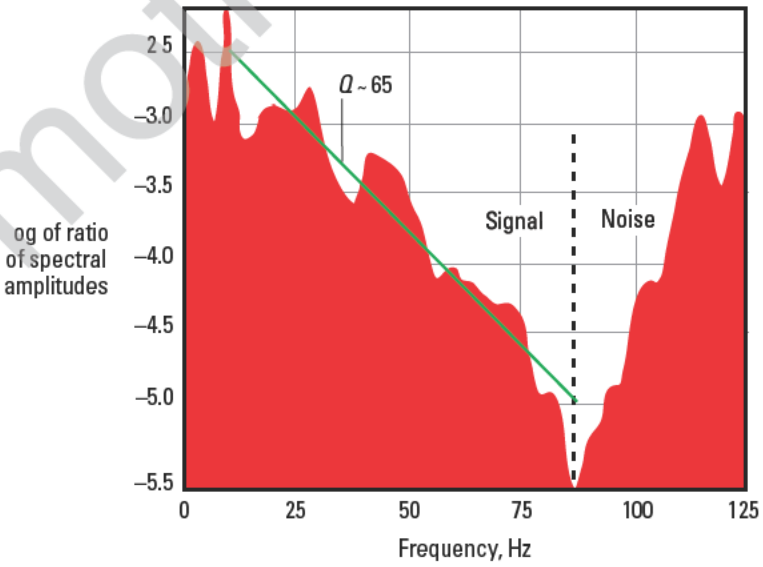

Figure 4-32. Logarithms of spectral ratios between the spectra of Fig. 4-31. The green line represents a best fit to the decay curve over the frequency range containing useful data. The apparent increase in the ratio at high frequencies merely reflects the ratio of noise between the two geophone depths, which ideally is unity.

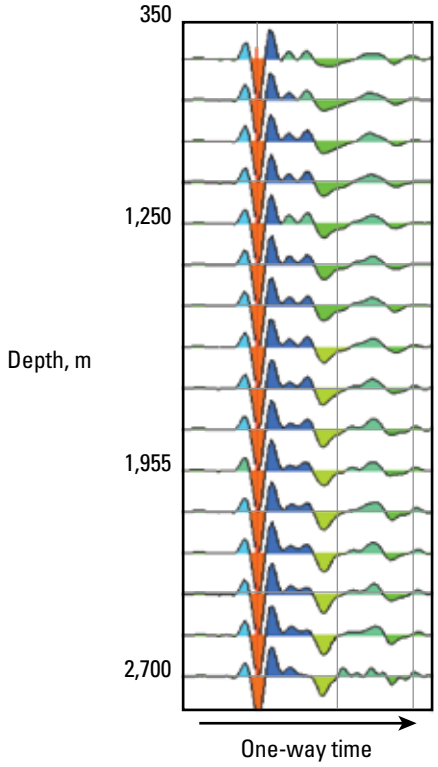

Figure 4-33. VSP data after Q-compensation using the value estimated from the spectral ratios. Note the recovered triplet character after the first trough and its consistency for all traces.

4.8.1.2 Measuring Q using coherency inversion

Measuring spectral ratios directly works well when the geophone array provides sufficient change in the length of the propagation path and the overall decay in the high-frequency spectral components between the top and bottom of a chosen depth interval can be measured. An alternative method, called coherency Q inversion, is particularly suitable for walkaway VSP geometries in which the receiver array usually spans only a small depth interval.

This method makes use of the change in p opagation distance through the Earth as the source position changes. An accurate Q-extrapola ion operator is applied to the data for a large number of ial Q values, and for each value, the semblance across the direct-arrival wavelets is calculated and pl tted against the Q values. The actual Q value is where the semblance is a maximum. Figure 4-34 shows the direct arrivals from a walkaway VSP as this pro ess is applied. The raw direct arrivals after long-gap p edictive deconvolution are shown at the top; the same arrivals after all frequency-independent amplitude corrections have been applied are shown in the middle; and the data after applying the correct Q-compensation are shown on the bottom.

Figure 4-35 shows the variation of semblance with Q, and the peak semblance at a Q value of 82 is ea ily chosen.

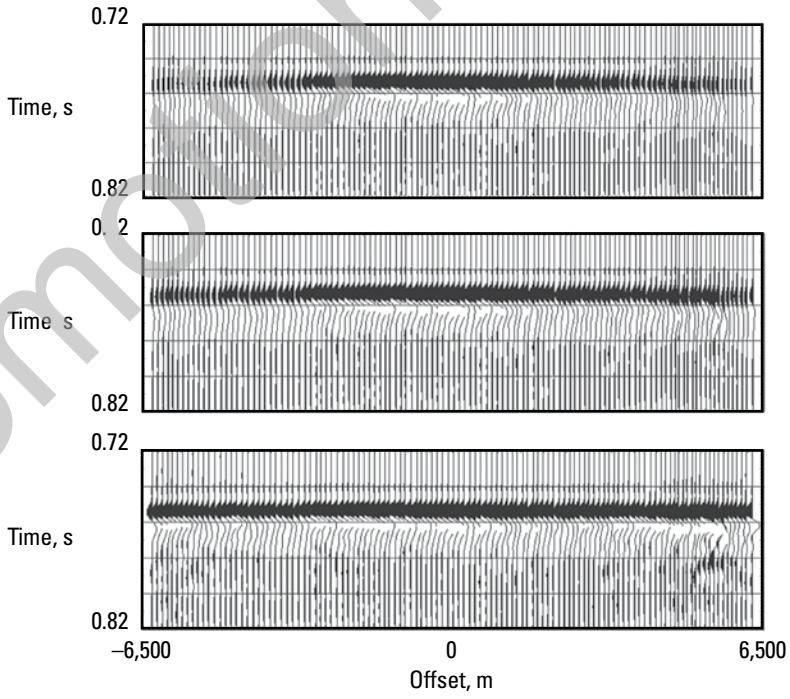

Figure 4-34. Walkaway VSP data under Q-analysis. Top traces show the data without any amplitude corrections; center traces show data after geometric spreading correction (a data-derived spreading correction would overestimate the exponent); and the bottom traces show data after Q-compensation. (From Leaney, 1999.)

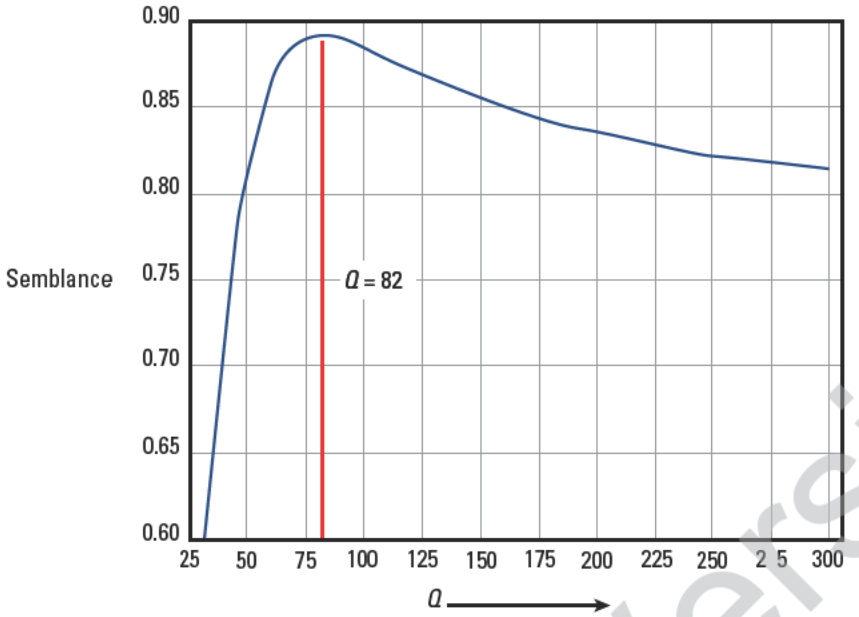

Figure 4-35. Average semblance plotted as a function of *Q*. (From Leaney, 1999.)

4.8.2 *Q* and geometrical spreading

Amplitude decay caused by attenuation is part of the loss compensated for with a t^n-type spreading correction. Compare amplitude decay as a function of depth for the VSP data in Fig. 4-10 with that measured after Q-compensation. If the ratio between them is plotted (Fig. 4-3), Q accounts for approximately $t^{0.7}$ of the total observed amplitude decay.

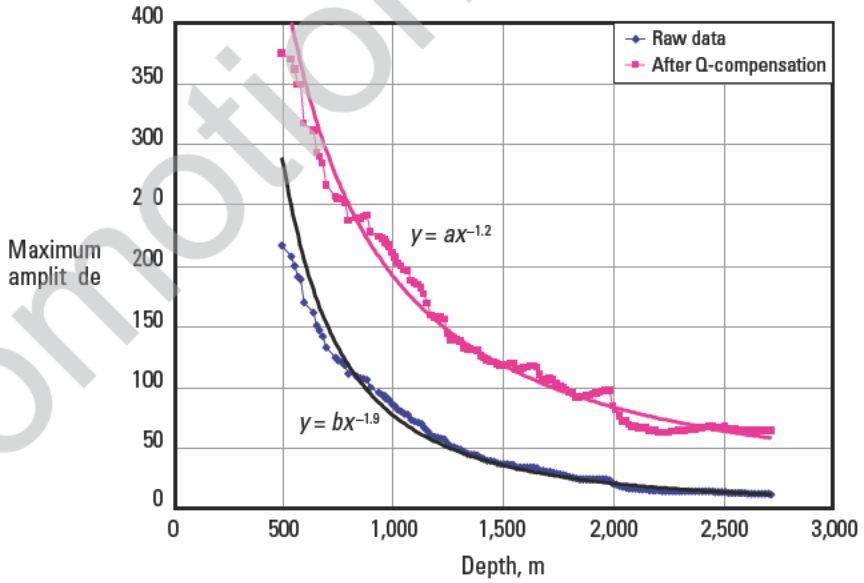

Figure 4-36. The direct-arrival amplitude for raw data and data after Q-compensation. The best-fit spreading exponent has changed dramatically.

4.8.3 *Q* and deconvolution

In the example shown here, the *Q* value has been measured over a time interval of approximately 0.6 s. This is an interval similar to what might be used for a deconvolution design window for surface seismic data. Clearly, the wavelet is not stationary over this window, and to extract a single wavelet-correction operator without Q-compensation results in a different response for shallow and deep reflectors, even over this relatively short window. Therefore, any deconvolution operator applied over this window would not be correct for all the events within the window.

The importance of *Q* on propagation should not be ignored, as illustrated in Fig. 4-37. Here a section of a surface seismic line is shown with and without Q-compensation. The Q-filtered version is clearly higher frequency, but perhaps more interestingly, lateral variations and truncations are much sharper and more interpretable. Further, it is interesting that this result was obtained with a relatively high value for *Q* of 100.

4.8.4 Importance of *Q* in processing

The parameter *Q* has a large and significant effect on the propagating wavelet. It affects

- phase of the wavelet as a function of time
- amplitude spectrum of the wavelet as a function of time
- timing of events
- overall amplitude decay of the data with time

All these effects need to be compensated correctly; if left uncompensated, they will lead to incorrect parameter selection in other processes to compensate for the effect of *Q*.

To directly measure *Q* is possible and simple with a VSP dataset, and to compensate for it is a relatively straightforward task. Note also that the transfer function between a shallow VSP geophone level and a deep one is a convolution of the Q-filter with interbed multiples and could be used in a compensation or deconvolution schem

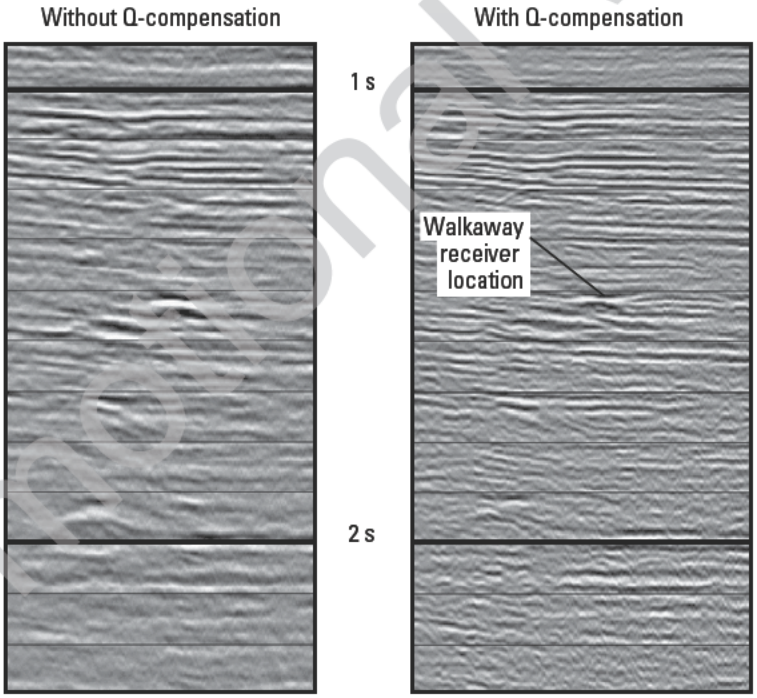

Figure 4-37. Surface seismic stack section with and without Q-compensation filtering.

4.9 References

Armstrong, P., Durrand, C., Barany, I., and Butaud, T.: "Seismic Measurements While Drilling Reduce Uncertainty in the Deepwater Gulf of Mexico," *Expanded Abstracts*, 74th SEG Annual International Meeting and Exposition, Denver, Colorado, USA (October 10–15, 2004) 23, 2470–2473.

Campbell, A., Fryer, A., and Wakeman, S.: "Vertical Seismic Profiles—More Than Just a Corridor Stack," *The Leading Edge* (July 2005) 24, No. 7, 694–697.

Grech, M., Jones, M., and Schmitt, D.R.: "Proper Amplitude Recovery in VSPs," *Expanded Abstracts*, 68th SEG Annual International Meeting and Exposition, New Orleans, Louisiana, USA (September 13–18, 1998), 385–388.

Leaney, W.S.: "Walkaway Q Inversion," *Expanded Abstracts*, 69th SEG Annual International Meeting and Exposition, Houston, Texas, USA (October 31–November 5, 1999), 1311–1314.

Nyquist, H.: "Certain Topics in Telegraph Transmission Theory," *Transactions of the American Institute of Electrical Engineers* (April 1928) 47, 617–644. Reprinted in: *Proceedings of the IEEE* (February 2002) 90, No. 2, 280–305.

O'Doherty, R., and Anstey, N.: "Reflections on Amplitudes," *Geophysical Prospecting* (1971) 19, No. 3, 430–458.

Stewart, R.R., Huddleston, P.D., and Kan, T.K.: "Seismic Versus Sonic Velocities—A Vertical-Seismic-Profiling Study," *Geophysics* (1984) 49, No. 8, 1153–1168.

Ursin, B.: "Offset-Dependent Geometrical Spreading in a Layered Medium," *Geophysics* (1990) 55, 492–496

White, R.E.: "Partial Coherence Matching of Syntheti Seismograms with Seismic Traces," *Geophysical Prospecting* (1980) 28, 333–358.

Ziolkowski, A., and Fokkema, J.: "Th Pr gressive Attenuation of High-Frequency Energy in Seismic Reflection Data," *Geophysica Pro p cting* (1986) 34, No. 7, 981–1001.

Anisotropy and AVO Measurements from VSPs

Steve Horne, Scott Leaney, Lisa Stewart, and Michael Jones

5.1 Introduction

Anisotropy can be defined as the variation of a material's property with respect to the direction in which it is measured. Anisotropy may exist at many scales. For example, a mineral crystal and a sedimentary basin may each exhibit directional variations in physical properties. Anisotropy occurs when there is a spatial ordering of components—be it atoms, crystals, grains, cracks, bedding planes, or fractures—on a scale smaller than the length scale of the measurement. Rock formations can be anisotropic in terms of a variety of measurements, including resistivity, permeability, and elastic properties. Because seismic wave propagation is controlled by the elastic properties of a material, materials with elastic anisotropy exhibit directional variations in the speed of waves traveling through the material.

For years, the existence of elastic anisotropy was largely ignored by exploration and production geophysicists. In many cases, the effect of anisotropy is small and, therefore, can be justifiably neglected. Early data-acquisition geometries were not designed to expose elastic anisotropy, and processing techniques that assumed an isotropic Earth delivered adequate results. However, with new acquisition techniques such as long-offset, wide-azimuth, and full-wavefield recording, the effects of anisotropy are readily observed and cannot be reconciled using isotropic assumptions. Furthermore, with today's enhanced computing power, even subtle anisotropic effects can be gleaned from large, complex datasets.

The effects of elastic anisotropy convey information about the nature of rock formations, but because the wavelength of the measurement is much greater than the size of the aligned features, the measurement is unable to resolve individual features. Nonetheless, indications of the alignments that cause anisotropy can still help improve our understanding of the subsurface. Borehole seismic surveys are now designed to characterize elastic anisotropy so that the results may be used not only to create better borehole seismic images but also to select infill well locations or drilling directions for naturally fractured reservoirs, design perforating jobs and hydraulic fracture stimulation treatments in tight formations, identify fluid types from amplitude variation with offset (AVO) analysis, and improve surface seismic imaging results in anisotropic conditions.

Because the main forces acting on Earth materials are generally vertical and horizontal, the main types of alignment are also vertical and horizontal. Gravity causes sediments to be deposited horizontally, which creates the most commonly detected type of elastic anisotropy. Typical stress regimes at depth tend to cause near-vertical fractures to be open, which leads to a second common cause of anisotropy, fracture-induced anisotropy. This chapter explains how these two types of anisotropy affect seismic waves, how the effects are measured, and what the results reveal about subsurface properties and structure.

5.2 Vertical transverse isotropy or polar anisotropy

One of the most common causes of elastic anisotropy is layering-induced anisotropy. The horizontal layers may have isotropic elastic properties that differ between layers, or they may be anisotropic themselves. When this stack of layers is probed with seismic waves of wavelength larger than the individual layers, the result is an averaged, or effective, response that depends on direction. Such a medium is said to have vertical transverse isotropy (VTI) (Fig. 5-1). Alternatively, this form of anisotropy is referred to as polar anisotropy because properties only vary with the propagation direction measured from the vertical pole. In this case, the effective vertical compressional velocity is less than the compressional velocity in the horizontal direction.

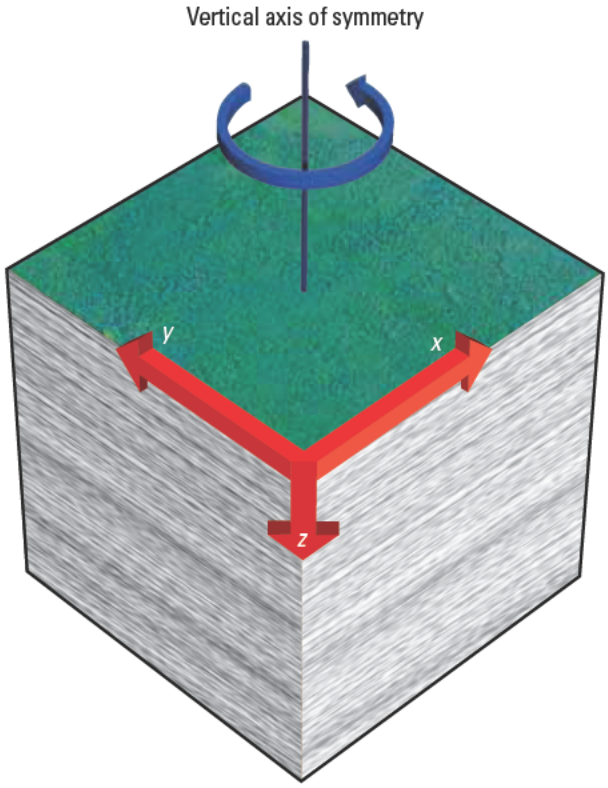

Figure 5-1. A medium with vertical transverse isotropy (VTI) has polar anisotropy. The curved arrow indicates the rotational symmetry axis about which the properties are invariant. Velocities are proportional to the length of the red arrows. (Adapted from Armstrong *et al.*, 1994.; this graphic is copyright Schlumberger td. Used with permission.)

5.2.1 Measuring polar anisotropy

Direct measurements of shale properties in the laboratory and in the field have documented anisotropy in excess of 20% (e.g., Wang, 2002; Leaney *et al.*, 2001). Such large anisotropies can have a significant impact on seismic imaging. Neglect of the effect of anisotropy causes mispositioning and degraded focusing of reflections and also affects AVO analysis. Theoretical, computational, and software developments now allow migration velocity models to incorporate a sotropy Anisotropic moveout equations are available to orrect prestack gathers (Alkhalifah and Tsvank n, 1995).

Polar anisotropy may be measured in different ways depending on the problem to be so ved. For seismic imaging, average properties between the source, image point, and receiver are needed, wherea AVO interpretation requires local elastic properties on either side of a reflector. Both effective and ocal types of measurement can be obtained with walkaway VSPs.

As discussed in Chapter 2, the walkaway VSP comprises a static array of downhole receivers and a series of shots at progressively greater offsets (walking away) from the receiver rray (Fig. 5-2). This configuration is ideal for measuring layering-induced anisotropy because it samples a wide-angle angular aperture from the vertical to horizontal directions. Direct and reflected arrivals at the full array of receivers can be used to estimate local anisotropic properties, whereas traveltimes between

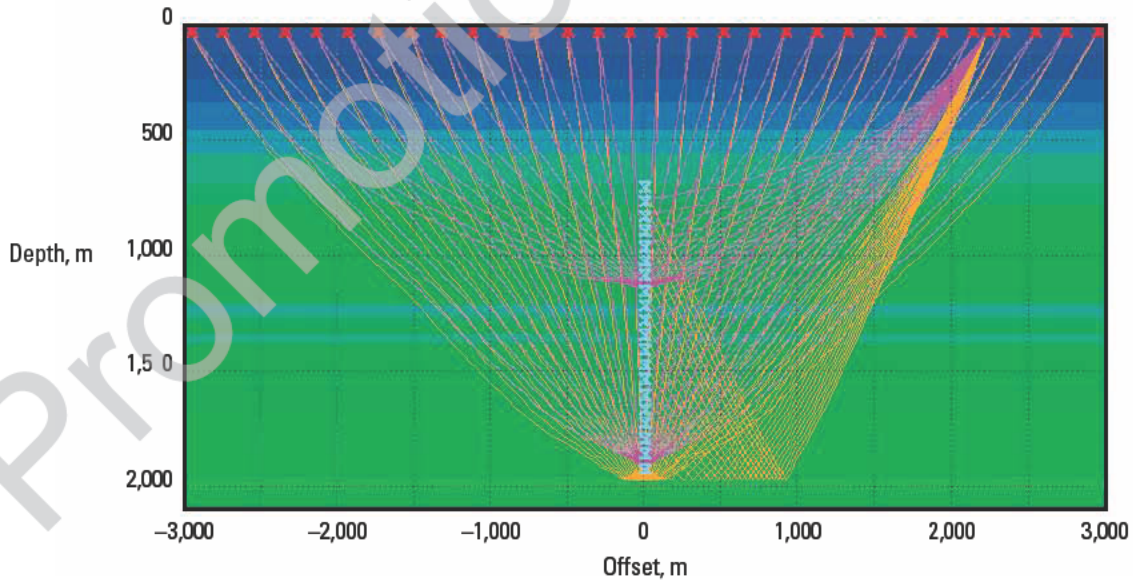

Figure 5-2. A walkaway VSP survey schematic showing direct arrivals (magenta) and reflections (orange) into the bottom receiver (for AVO measurements) and from one shot into all receivers (for imaging). A walkaway survey shot into a large array of receivers allows depth-dependent polar anisotropy to be measured. (From Leaney, 2008.)

source-receiver pairs can be used to calculate average anisotropic effects. Several methods have been developed for extracting anisotropy information in each case.

5.2.1.1 Describing anisotropy

There are a number of different ways to simplify the mathematical description for VTI anisotropy, but the one method that has gained most popularity is that of Thomsen (1986). There are three Thomsen parameters that are used to describe VTI anisotropy: epsilon (ε), delta (δ), and gamma (γ). The Thomsen epsilon and gamma parameters are the most easily understood of the three parameters. Epsilon is a measure of the difference between the horizontal and vertical propagation velocities for compressional waves. Similarly, the Thomsen γ parameter is a measure of the difference in the horizontal and vertical propagation velocities for horizontally polarized shear waves (SH-waves). The Thomsen parameter δ is not easily described either mathematically or qualitatively. Nonetheless, its determination is important for the processing of reflection seismic data.

For the special case in which $\varepsilon = \delta$, the velocity curves for the P-waves are exactly elliptical, whereas the SV-curve remains circular, or isotropic. Deviation from this condition is referred to as anellipticity, and it is usually positive with $\varepsilon > \delta$. There are several formulations called anellipticity, which are forms of $\varepsilon - \delta$. When the Thomsen parameters are equal to zero ($\varepsilon = \delta = \gamma = 0$), the material is isotropic.

Another often-used parameter to quantify anellipticity is called eta (η) (Alkhalifah and Tsvankin, 1995), where $\eta = (\varepsilon - \delta)/(1 + 2\delta)$. Parameter η is commonly used for nonhyperbolic velocity analysis, which will be discussed later.

Another common combination of Thomsen's parameters that is referred to in the literature is sigma (σ). Sigma is a combination of epsilon and delta and is used to describe the anisotropy of vertically polarized shear waves (SV-waves).

$$\sigma = (\varepsilon - \delta) \times (V_P / V_S)^2. \qquad (5\text{-}1)$$

An example showing velocities for a material with anisotropy values similar to those observed in a walkaway VSP is shown in Fig. 5-3. This figure shows phase slowness and group velocities for the P-, SV-, and SH-waves. In terms of the group velocity, the vertical P-wave velocity (red line) is about 2.25 km/s, whereas the horizontal P-wave velocities are about

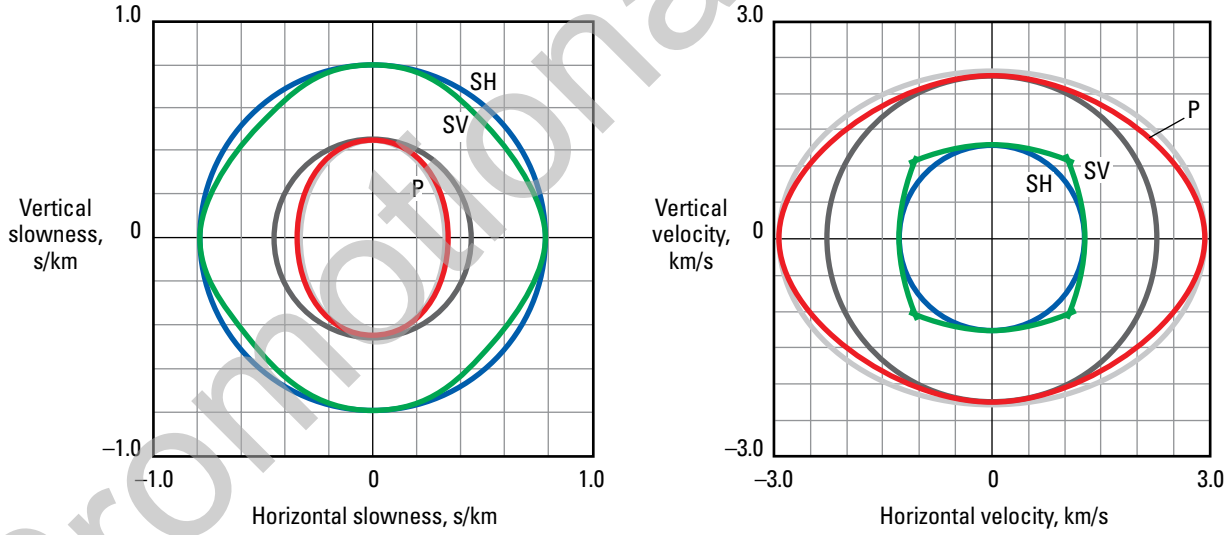

Figure 5-3. Modeled phase slowness (left) and the corresponding group velocities (right) for a VTI shale with $\varepsilon = 0.327$, $\delta = 0.029$, and $\gamma = 0.00$. It can be seen that the curves are not circular, which would be the case if the material were isotropic, and that the velocity in the horizontal direction is larger than the velocity in the vertical direction. The gray lines indicate circular and elliptical velocity variations for reference.

16% faster (~2.9 km/s). This variation is quantified by the Thomsen epsilon parameter, which for this example is 0.327. Note that the SH-wave group velocity (blue line) is circular, which indicates that the velocity is invariant with propagation direction. This is consistent with the Thomsen $\gamma = 0.0$. In the case of the SV-wave (green line), there are triplications, also known as cusps, in the group velocity at a propagation angle of approximately 45° from vertical. Also shown for reference are isotropic and elliptical velocity variations. Note that the P-wave is not elliptical, and this is quantified by the difference between the Thomsen epsilon (ε) and delta (δ) parameters.

An important comment regarding conventional walkaway VSP measurements is that they generally measure P- and SV-wave effects. Therefore, they do not characterize the Thomsen parameter γ, which controls SH-wave propagation. However, γ is important in interpreting microseismic data (see Chapter 8).

5.2.2 Effective anisotropy

Because polar anisotropy can have a significant effect on surface seismic imaging, it is important to develop anisotropic velocity models that can be input to seismic migration. Time migration and depth migration have different requirements. Time migration requires effective parameters that describe reflection moveout trajectories in common-midpoint (CMP) gathers. Depth migration requires calibration of an Earth model populated by velocities achieved by raytrace traveltime inversion. Examples of each method are shown.

5.2.2.1 Nonhyperbolic moveout

Assuming that the Earth is composed of flat, homogeneous isotropic layers, the moveout curves for reflection events obey the hyperbolic moveout equation. Anisotropic media can lead to nonhyperbolic moveout behavior; so, to develop the associated velocity models requires extensions to the standard hyperbolic moveout equation. The industry standard for the nonhyperbolic moveout equation is the eta (η) equation of Alkhalifah and Tsvankin (1995). The free parameters in the eta equation are the moveout velocity (V_{nmo}) and a nonhyperbolic, or anellipticity, parameter η. Eta connects V_{nmo} to the horizontal velocity (V_H). Knowing receiver depth and average vertical velocity (V_v) from a walkaway VSP, we can invert the walkaway direct-arrival times for the Thomsen parameters.

A field example from onshore shows how large the nonhyperbolic effect can be (Fig. 5-4). In this case, a 154-receiver synthetic aperture walkaway VSP was acquired by repeating vibrator source points along the source line 22 times, each time moving a seven-level VSI tool to a new depth (Leaney *et al.*, 2003). The picked P-wave first-arrival times fit with a hyperbolic moveout curve produced large errors. The data fit better with a nonhyperbolic moveout curve, which produced a set of anisotropy parameters—delta, eta, and epsilon—for that depth. The process, repeated for the remaining 153 receivers, produced plots of anisotropy parameters varying with depth (Fig. 5-5).

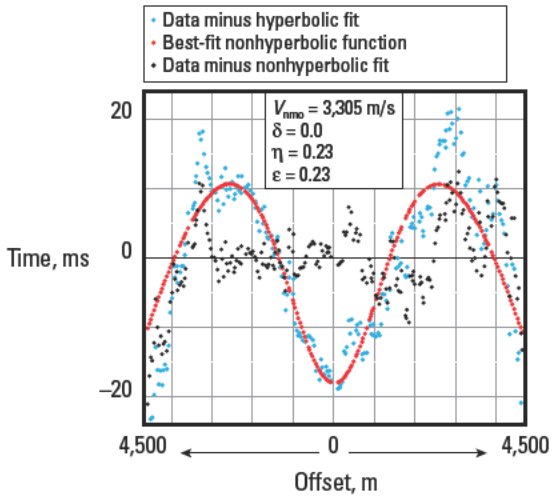

Figure 5-4. Results of nonhyperbolic moveout curve fitting for an onshore example that show data at a single receiver in a 154-receiver walkaway VSP. The fit of the picked P-wave first-arrival data with a hyperbolic moveou curve produces large errors. The differences between the arrival times and the best-fitting hyperbola are sho n in lue. The best-fit nonhyperbolic function is shown in red. Differences between arrival times and the non ype boli fit are shown in black. The anisotropic parameters extracted from this process appear in the inset. The pr ess, repeated for the other 153 receivers, yields the depth-dependent property curves in Fig. 5-5. (From Lean y et al., 2003.)

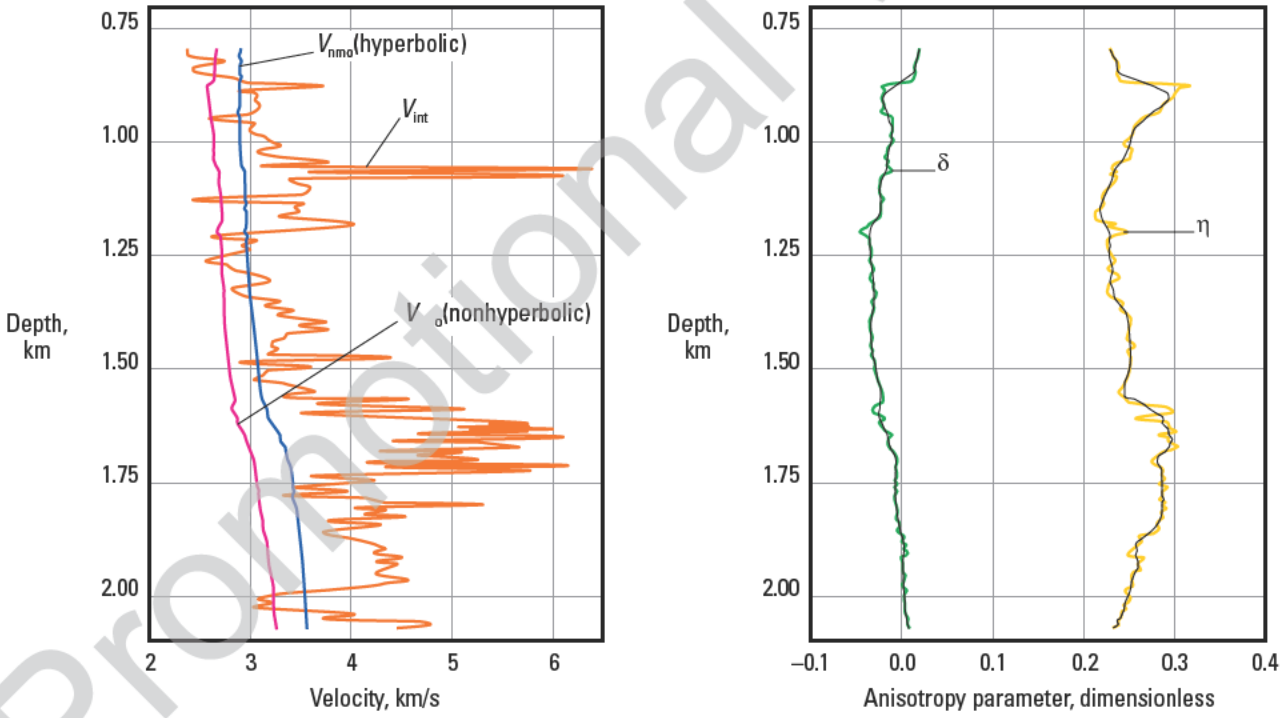

Figu e 5-5. Effective anisotropic parameters versus depth for a 154-receiver synthetic-aperture walkaway VSP. Interva velocities (V_{int}) from the 154 stations (orange) are plotted with hyperbolic (blue) and nonhyperbolic (magenta) NMO velocities on the left. On the right are plotted the Thomsen delta parameter (green) and the eta parameter (yellow) extracted from the walkaway data. (From Leaney, 2008.)

5.2.2.2 Raytrace traveltime inversion

Depth migration requires a different description of anisotropy parameters. The idea here is to calibrate an existing velocity model by using ray tracing to match walkaway VSP arrival times. Starting with an initial velocity model, direct walkaway VSP traveltimes are iteratively fit picked by perturbing interval anisotropy parameters. Constraints should be consistent with geologic knowledge, such as compaction trends or formation age.

In one example from deepwater offshore Nigeria, a 72-receiver synthetic-aperture walkaway VSP dataset spanned a depth interval of 1,065 m. Residuals between observed traveltimes and an isotropic model were large and increased with depth, whereas residuals based on an anisotropic model were small (Fig. 5-6). Anisotropic velocities and parameters shown in this figure were used to model an AVO response (Fig. 5-7). The overall impact of anisotropy on the AVO response is small because the

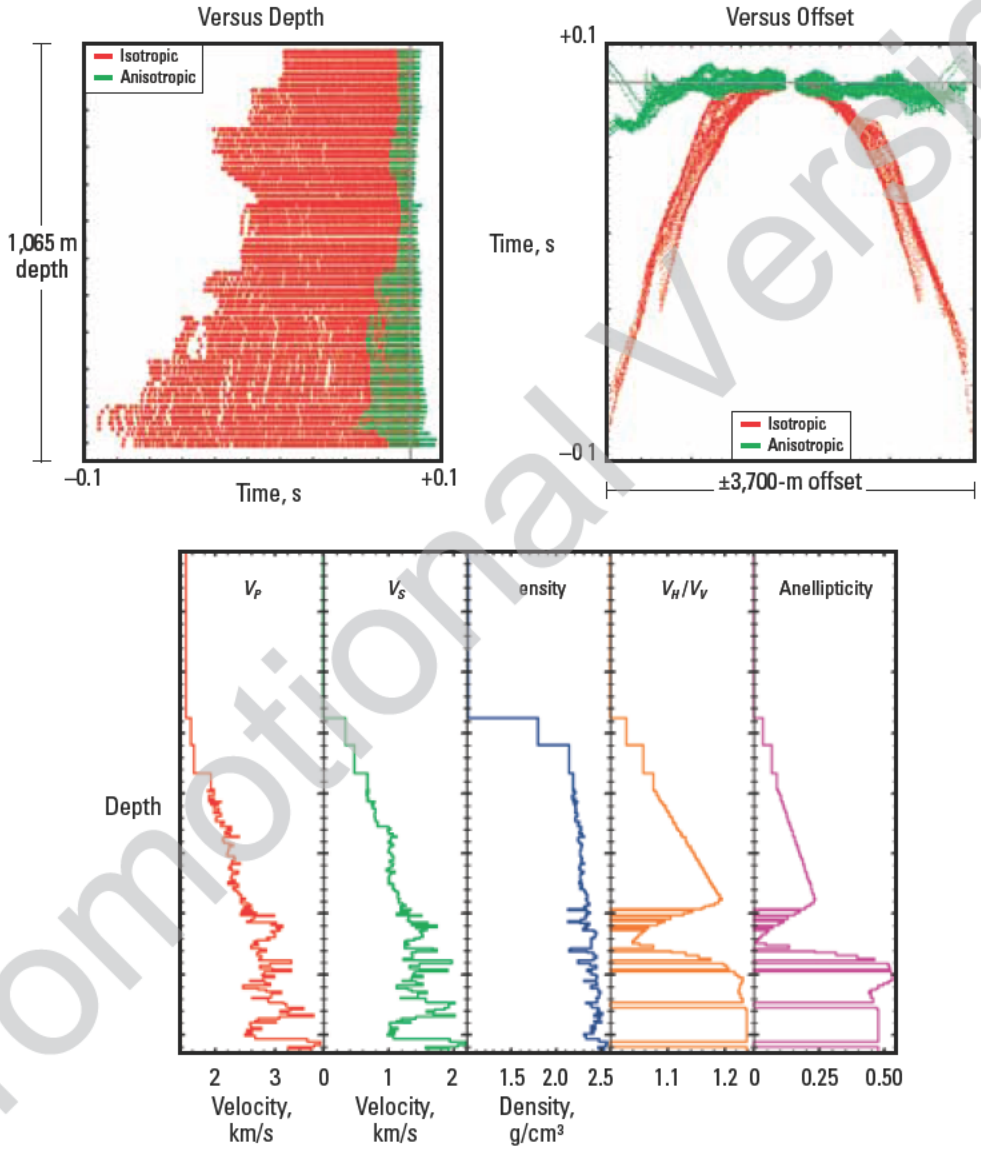

Figure 5-6. Direct-arrival traveltime residuals for a deepwater offshore Nigerian well (top). Residuals for all offsets versus depth (left) and for all receivers versus offset (right) show that the anisotropic model (green residuals) fits the data much better than an isotropic model (red residuals). The resulting laterally invariant VTI model (bottom) was used to model the anisotropic AVO response that is shown in Fig. 5-7. Layers with V_P/V_S values below a threshold (reservoir sands) were made isotropic. These are indicated as layers with anellipticity values of zero. (From Leaney, 2008.)

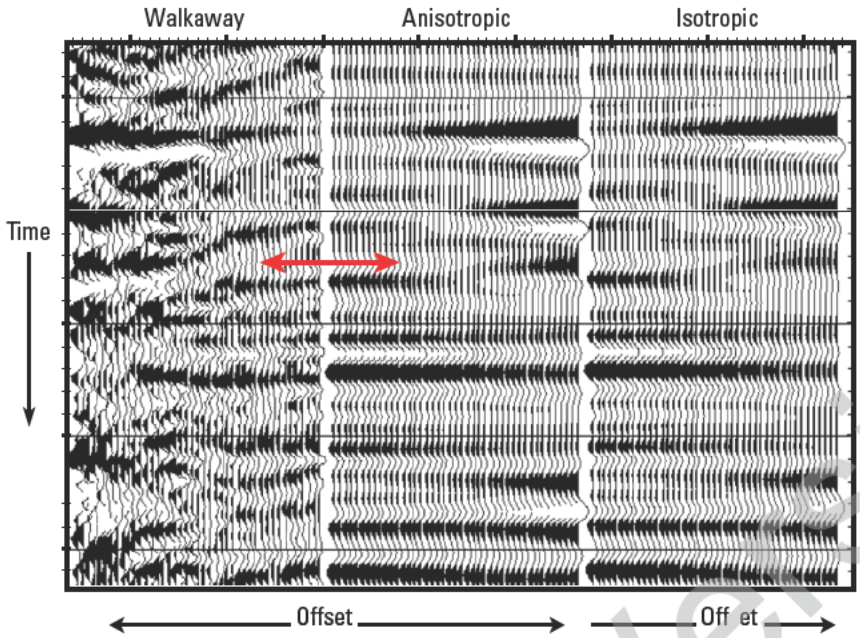

Figure 5-7. An NMO-corrected walkaway receiver gather processed for true amplitude (left) ompar d with anisotropic (center) and isotropic (right) AVO simulations using the calibrated odel of Fi 5-6. At the event indicated by red arrows, the AVO response in the walkaway data is better matched by the anisotropic model than by the isotropic model. (From Leaney *et al.*, 2002; Leaney, 2008.)

results of the anisotropic model are similar to those of the isotropic model, but there are levels at which the anisotropic model agrees better with the walkaway gather. The level indicated by red arrows is a zone in which the larger change in AVO response is better matched by the anisotropic model.

5.2.2.3 Impact on imaging

Anisotropy has a significant effec on imaging. In anisotropic media, to migrate wi h an anisotropic velocity model that has been calibrat d using direct-arrival times can have a marked imp ct on the accuracy of reflection positioning and dip. This can be seen in the migration results of a spiral 3D VSP. A line extracted from such a VSP acquired over a salt body shows a large variation of traveltim residual with offset when an isotr pic model is used (Fig. 5-8). However, a VTI velocity model more accurately predicts the traveltimes and results in much lower residuals.

Isotropic and anisotropic velocity models used in the migration of the 3D VSP data produce markedly different results (Fig. 5-9). Migration using the anisotropic model delineates faults more clearly and decreases the depth of some deeper reflections by up to 270 m relative to the image produced with an isotropic velocity model.

Another example that shows the impact of anisotropy on imaging comes from the western Canadian foothills (Fig. 5-10). Anisotropic shales above the imaging target are tilted at 45°, thus causing a significant lateral mispositioning error. Fault truncations in the zone of interest have been laterally misplaced by approximately 100 m in the prestack depth migration data using an isotropic velocity model.

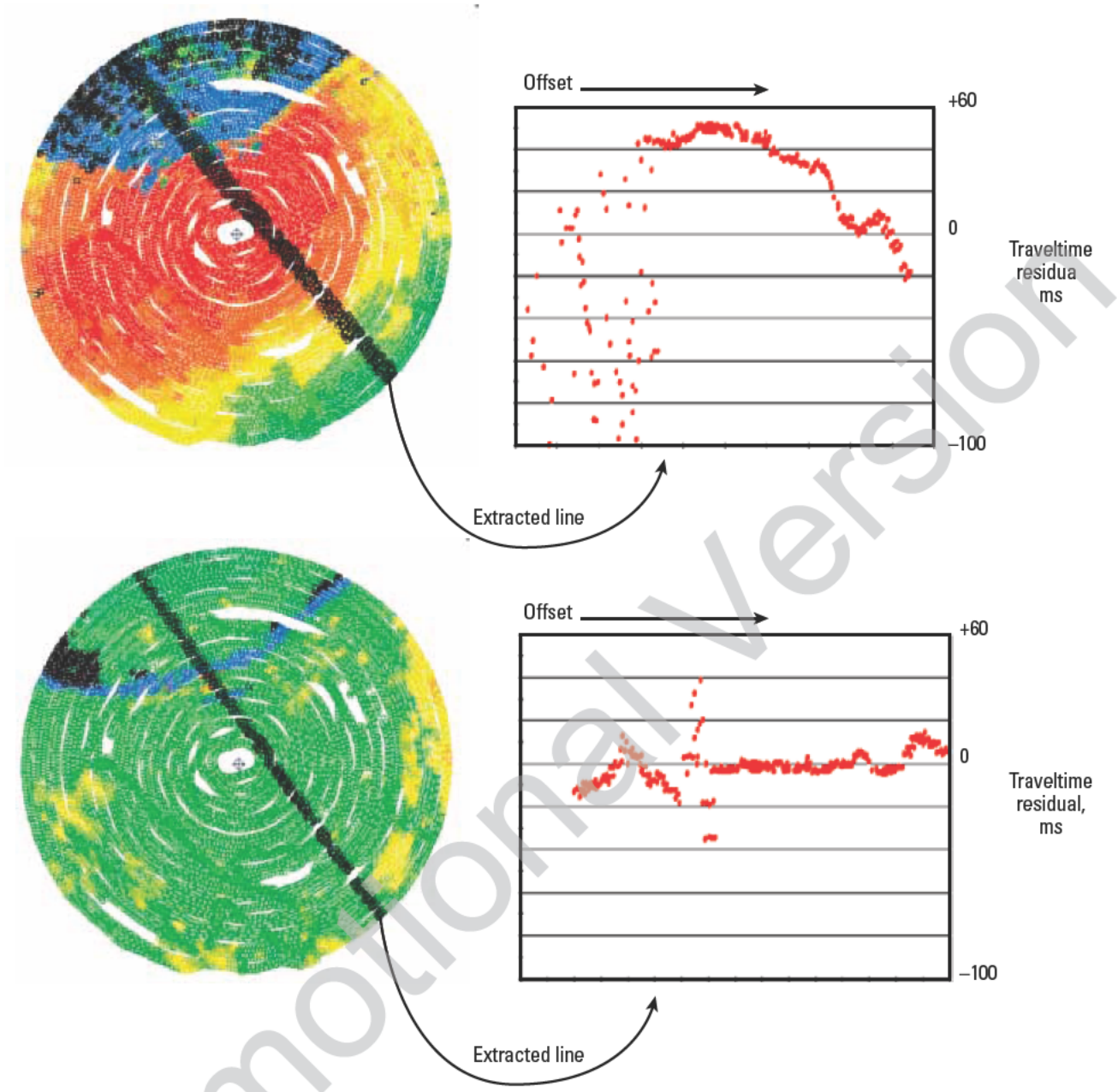

Figure 5-8. Using isotropi top) an anisotropic (bottom) velocity models on a 3D VSP. Shotpoints (left) are color-coded by traveltime re idual: high residuals are red, low residuals are green and blue. Black points along the extracted line a e sho points of the extracted line whose residuals are plotted on the right. Black points off the line re ray-t acing failures. Rays from sources at those positions were refracted by salt and did not manage to a ive at borehole receivers. Application of a velocity model with polar anisotropy (bottom) produ s low r residuals. (From Leaney, 2008.)

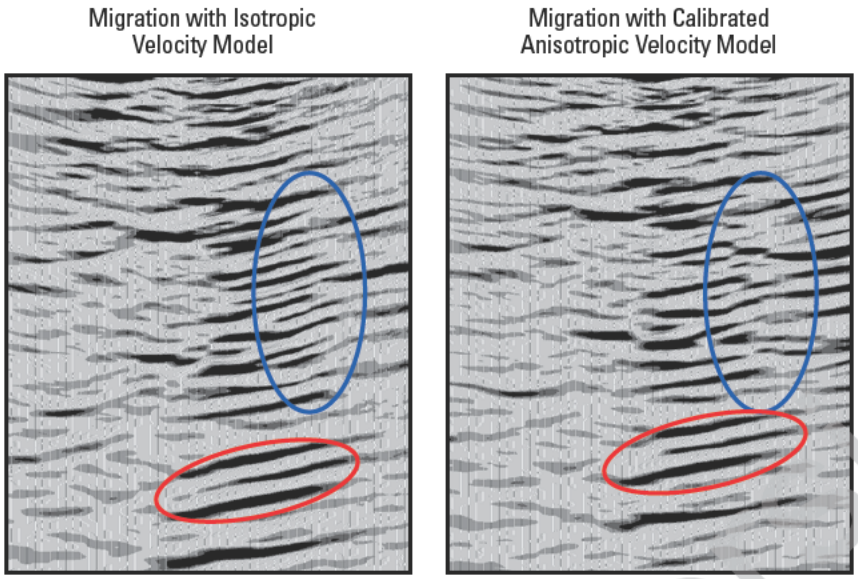

Figure 5-9. Results of 3D VSP migration using isotropic (left) and calibrated VTI anisotropic (right) vel city models. The calibrated anisotropic model resulted in a significant depth shift and improved fault focu ng c mpared with the isotropic results as highlighted by the red ellipses and data inside the blue ovals. (From Leaney, 08)

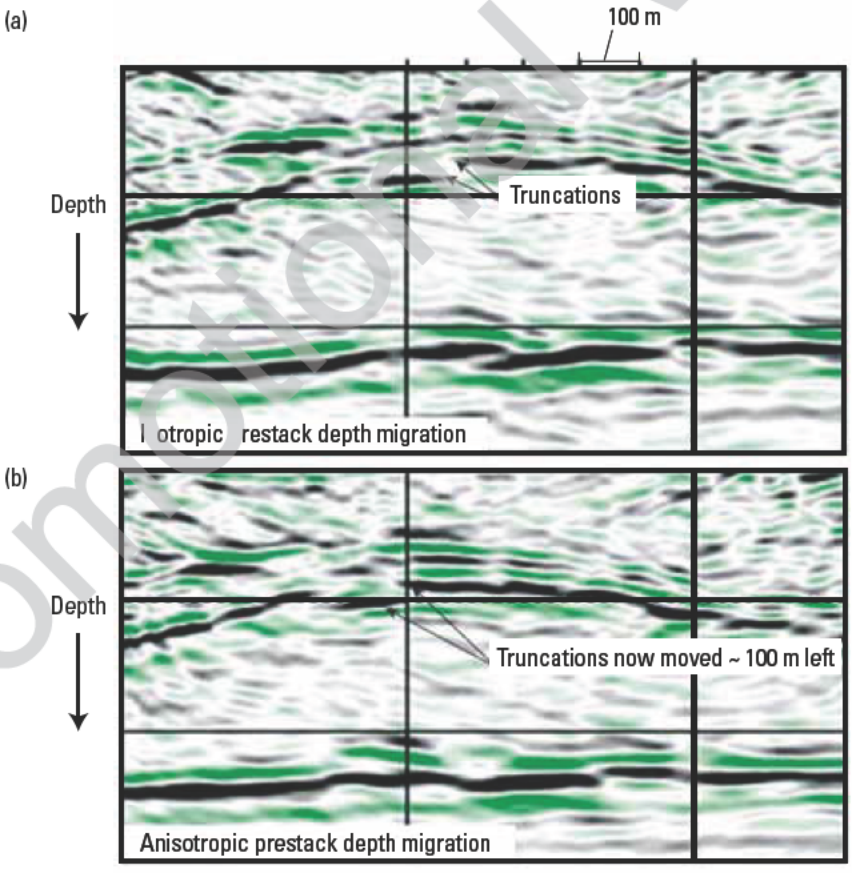

Figure 5-10. Migration using (a) isotropic and (b) anisotropic velocity models. The imaged zone is beneath a massive tilted shale showing approximately 15% difference between vertical and horizontal slownesses. Drilling targeted at the truncations shown in (a) would miss the target by 100 m. Solid lines are a reference grid.

5.2.3 AVO and local anisotropy

The interpretation of AVO responses from surface seismic common depth point (CDP) gathers is recognized as a potential hydrocarbon discriminator (Ostrander, 1984). Figures 5-11 and 5-12 illustrate the principle. The crossplot of V_P versus V_P/V_S (Brie *et al.*, 1995, 1998) in Fig. 5-11 shows that the V_P/V_S ratio for a porous rock can change significantly depending on the fluid that fills the pore spaces. Figure 5-12b shows how the P-wave reflection coefficient varies with angle of incidence at a shale/sand interface depending on the nature of the pore fluid in the porous sand. The principle states that if the amplitude of reflection seismic data from a horizon can be recovered for shot and receiver positions that give different angles of incidence for the reflection, the V_P/V_S ratio contrast of the interface can be estimated.

Despite all the advances in logging technology, rock physics, and surface seismic data acquisition and processing, some steps in the workflow are still incomplete. Discrepancies between reflection response amplitudes from modeling and those extracted from the seismic data are the rule rather than the exception. The modeling process encounters difficulties with upscaling from log scales to seismic scales and with the need to include anisotropy in the model when measured parameters are normally unavailable. The surface seismic experiment falls short of the ideal in several areas in both acquisition and processing. Perhaps the most unsatisfactory feature of these shortcomings is that, in practice, the errors that they introduce are unquantifiable. Some of these deficiencies include the following:

- *Source directivity*. Seismic sources, such as dynamite, vibrators, or airgun arrays do not radia e energy equally in all directions. There will be a directional bias in the amplitude of the da as the source takeoff angles change.
- *Receiver array directivity*. The general use of receiver arrays introduc s directivity from the array response. Furthermo e th general use of vertical-component geophones in land acquisitions introduces an in insic overweighting of amplitudes from shorter offsets

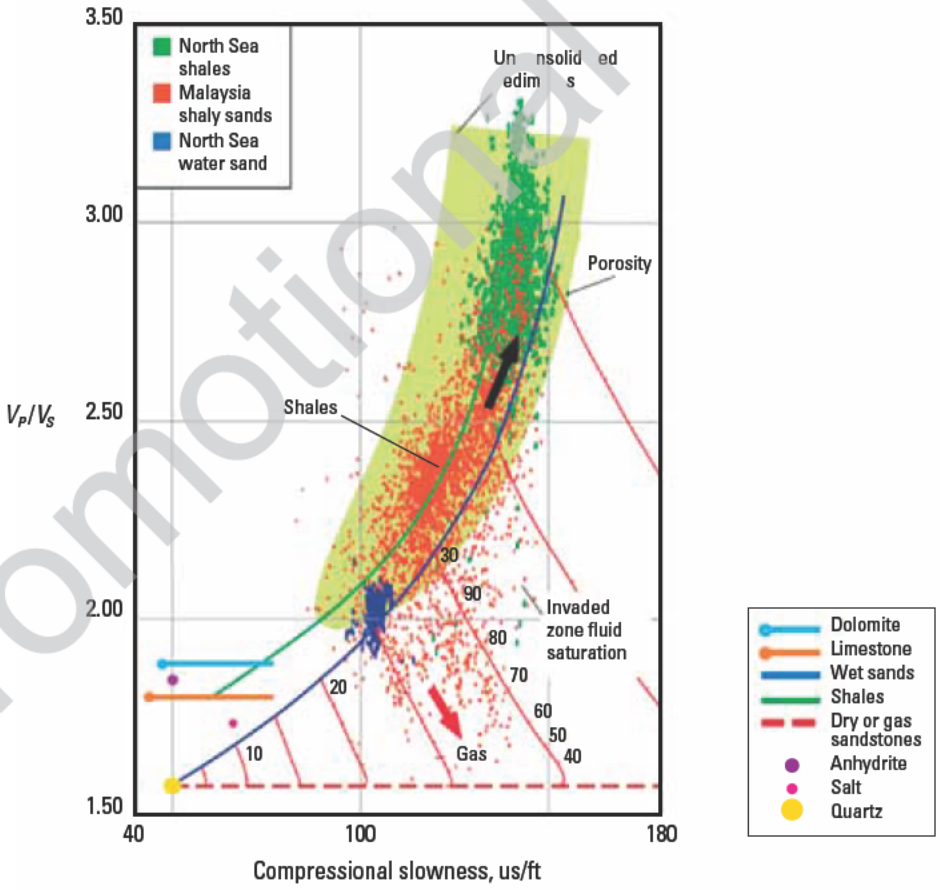

Figure 5-11. Sonic crossplot showing the velocity response to both pore-fill and lithology. Wet formations, such as the wet sand trend (blue curve), show an increase in their V_P/V_S velocity ratio because of decreasing shear velocity caused by fluid-rock coupling. Shales (green curve) show an even greater effect. (From Brie *et al.*, 1995, 1998.)

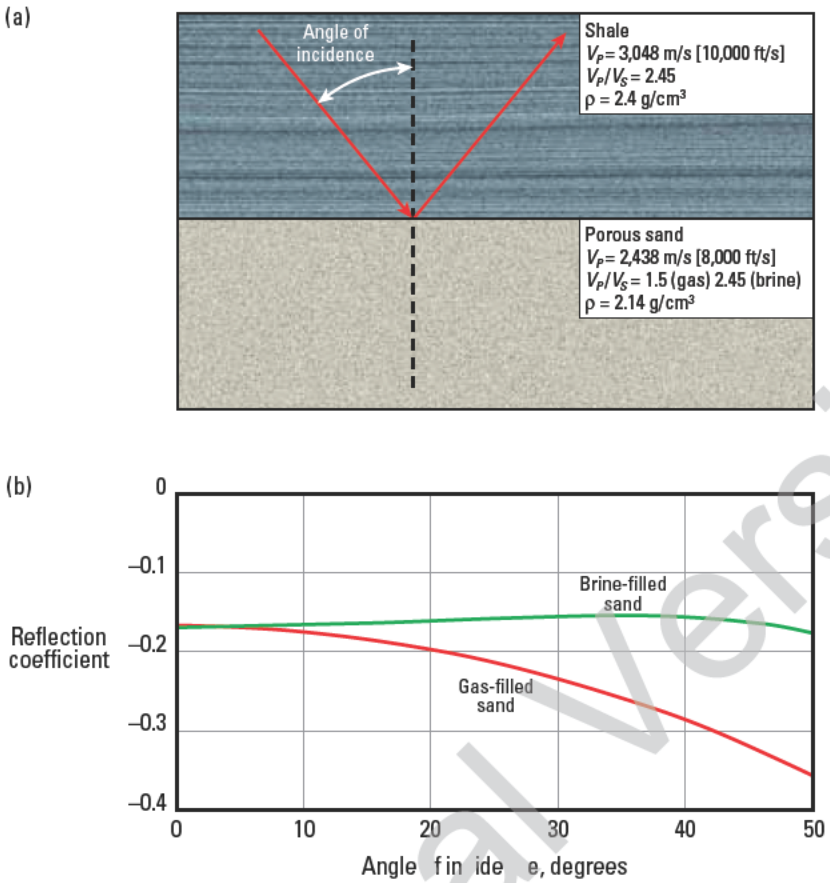

Figure 5-12. (a) Rock properties used to calculate reflectivity (after Ostrander, 1984). (b) Amplitude versus offset response of a gas-filled sand compared with a brine-filled sand.

- *Reflection-point scatter*. Over a source-to receiver raypath that may be 6 or 7 km long, reflection points at the zone of interest that will be geometrically binned into the same CMP gather will actually be scattered over much more than that nominal CMP spacing. This could allow lateral variations in reflectivity to masquerade as offset-dependent effect.
- *Propagation effects*. Geometrical spreading, refraction, dispersion, transmission losses, tuning, and anisotropy are all offset-dependent processes that will affect the AVO response at the target.
- *Relative amplitude*. It is impossible to reduce the seismic data to absolute reflection coefficient values. Therefore, only relative amplitudes are available for interpretation. If only relative amplitudes are available, any apparent AVO response can only be identified relative to other reflectors. This implies an assumption that the average reflectivity exhibits no reflectivity change with offset or at least that some particular reflector in the section has a known AVO response against which others can be measured.

To calibrate the AVO process by forward modeling of the response from well logs also implies assumptions. For measured log data, there are uncertainties that come from the initial data and borehole effects through the modeling process. Although the problem usually encountered in geophysical exploration is that of reconstructing the high frequencies in the seismic data, the reverse problem of upscaling the well log data can be significant as well.

The walkaway VSP can provide a direct measured AVO response at the well free from many of the assumptions introduced for the surface seismic analysis and independent of logging conditions and modeling assumptions.

The basic geometry is shown in Fig. 5-13. Rays from the source are recorded at an array of geophones immediately above the zone of interest. This positioning of the receivers prevents most of the problems encountered in the surface seismic geometry:

- Reflection points are constrained to be very close to the borehole.
- The recorded downgoing wavefield contains all the propagation effects that will be present in the reflected waves because the two rays travel the identical raypath. In fact, the upgoing reflection from the target divided by the downgoing wavefield is the band-limited reflectivity.
- Source and receiver directivity are the same for both upgoing and downgoing wavefields, so they are automatically compensated for.
- Three-component (3C) data are recorded so that a complete wavefield analysis can be made. Not only P-P reflectivity, but also P-SV amplitudes can be measured. In fact, even if only the vertical component geophones are used, the upgoing and downgoing emergence angles are the same, hence the directional effects cancel out.

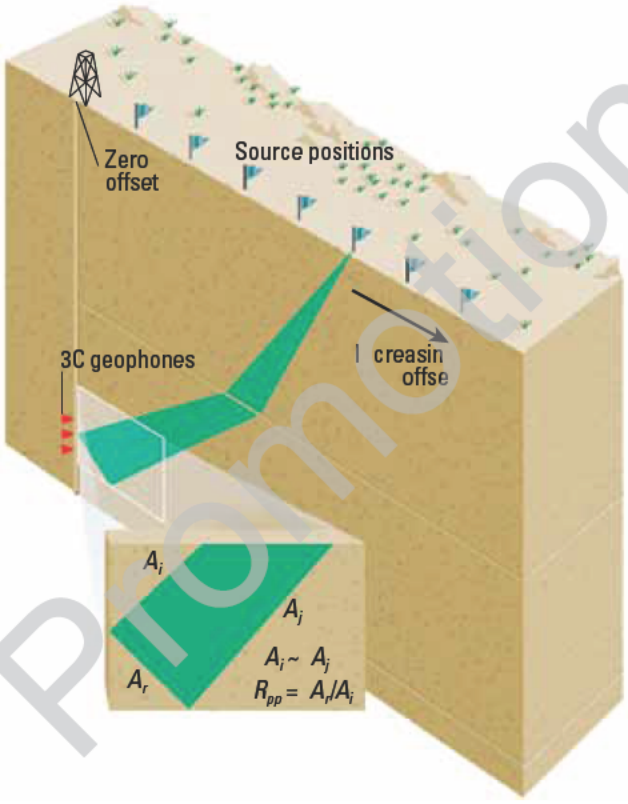

Figure 5-13. Walkaway VSP geometry designed for AVO analysis showing source and receiver locations. A_i and A_j are downgoing wave amplitudes, A_r is the reflected wave amplitude, and R_{pp} is the P-wave reflection coefficient for the measured interface.

The source-receiver geometry in Fig. 5-13 was designed for AVO analysis of an onshore example. The target is approximately 1,400 m deep, with the farthest offset source at approximately 850 m. Ray tracing predicts the incident angle at the target to be 35° for the largest offset. An extract of the data is shown in Fig. 5-14. The target reflector is the event labeled "Lithic." As can be seen, the amplitude of the trough increases with offset and can be classified as a Type III AVO anomaly. The AVO response measured in the AVO walkaway VSP was used as a calibration point to correct the amplitudes in the 3D surface seismic data over the reservoir interval.

The correct AVO response can be used to confirm other aspects of the interpretation. Walkaway VSP data were acquired in the Forties field in the North Sea (Armstrong *et al.*, 1995) and are shown in Fig. 5-15. The reservoir top at 2.105 s is represented by a black peak. Its amplitude varies as the source offset increases.

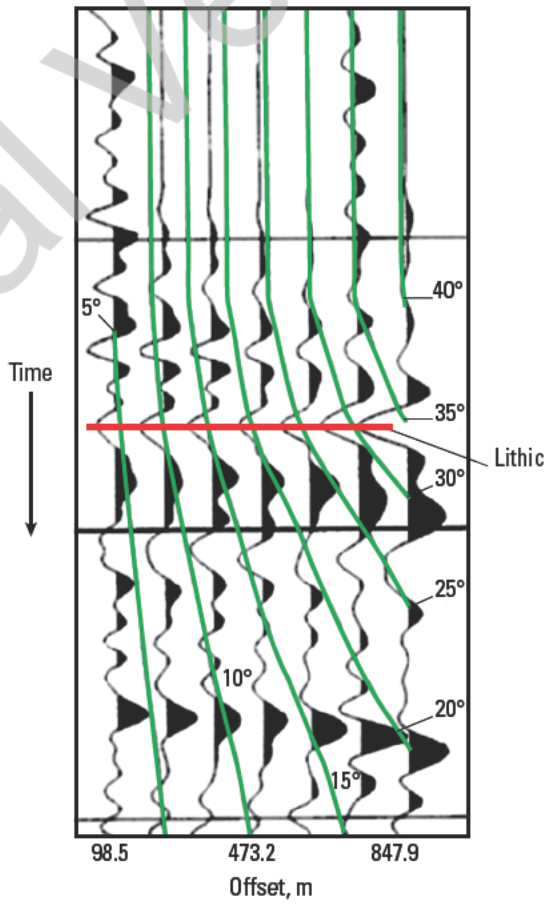

Figure 5-14. Walkaway VSP results: the trough amplitude (Lithic) increases with offset. Offsets are (left to right) 98.5 m, 222.9 m, 347.7 m, 473.2 m, 597.7 m, 723 m, and 847.9 m. Ray-traced incidence-angle contours are shown from 5° to 40° (green). (From Chen *et al.*, 1998.)

A modeling study was performed to better understand this amplitude response. A velocity model was built using compressional and shear logs, and two synthetic walkaway datasets were calculated (Fig. 5-16). The left-hand dataset has isotropic velocities in the layers, and the right-hand dataset has an anisotropic shale layer immediately above the reservoir. Anisotropic elastic parameters were calculated from the walkaway

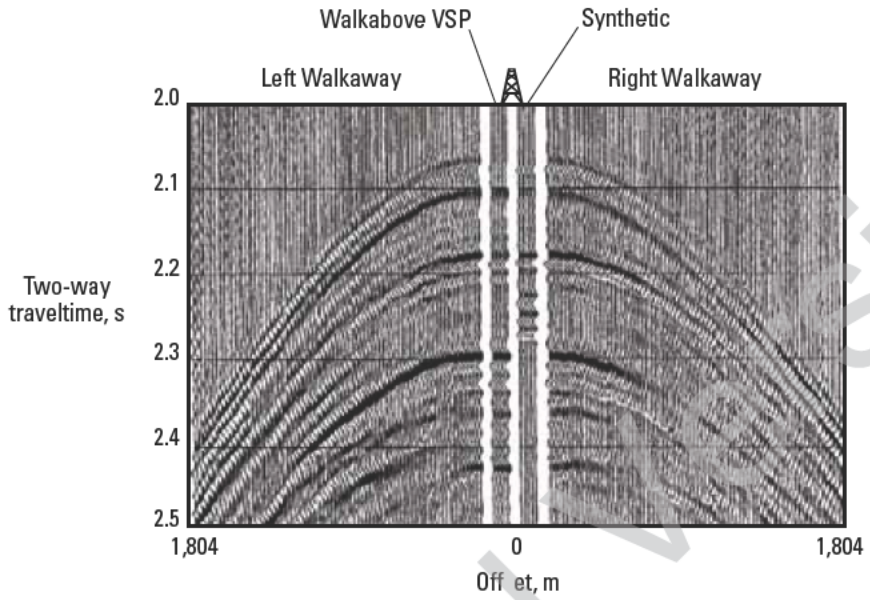

Figure 5-15. A comparison of walkaway, walkabove, and synthetic data. (From Armstrong *et al.*, 1995.)

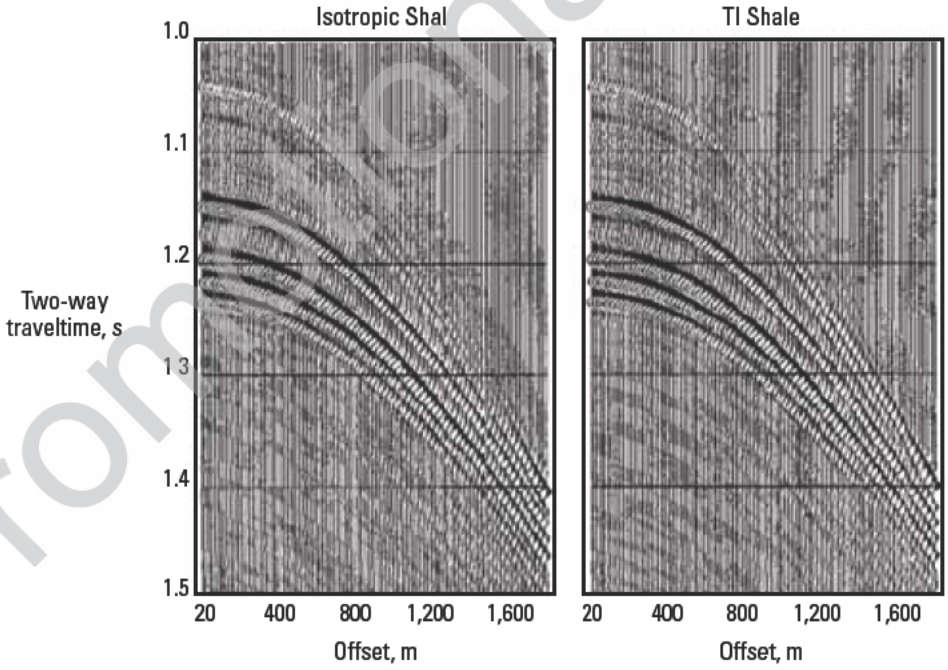

Figure 5-16. Isotropic and transverse isotropic (TI) models. In the first model, the shale overlying the reservoir sand is assumed to be isotropic (left). For the second model, key anisotropy factors calculated from the walkaway traveltime surface were used to make the shale TI (right). Differences in AVO behavior are visible in the reflection at 1.07 s, zero-offset time. The TI model shows an earlier increase in amplitude than the isotropic model. (From Armstrong *et al.*, 1995.)

traveltimes (see Section 5.2.3.1). Figure 5-17 shows the comparison between the modeled and measured amplitudes for the top- and base-of-reservoir events. The match is very good at the base of the reservoir. At the shale/sand interface (top of the reservoir), the agreement is also excellent; although, at longer offsets and larger angles of incidence, the synthetic data from the model with anisotropic overlying shale is a much better match than data from the isotropic case.

Further details and examples may be found in Coulombe *et al.* (1996) and Leaney *et al.* (1999).

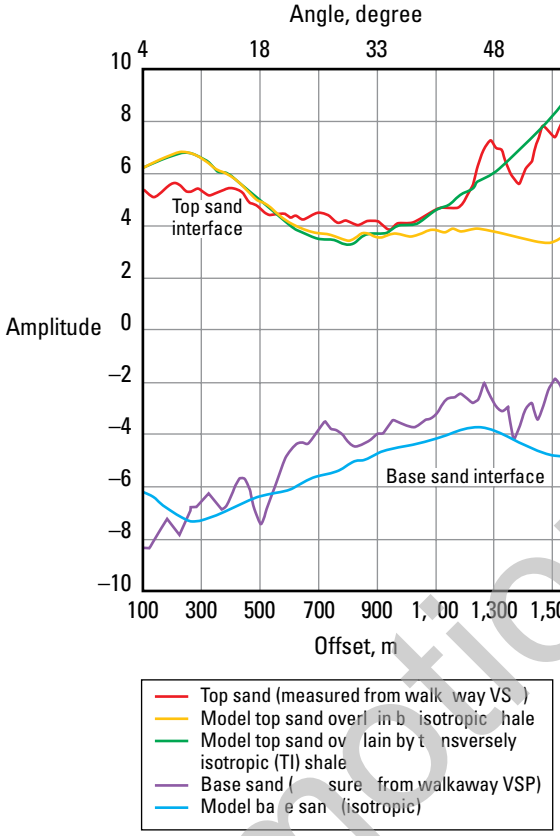

Figure 5-17. AVO calibration. Measured walkaway AVO response at the caprock/oil sand interface is shown as a red line (top), and the response at the base of the sand as a purple line (bottom). The equivalent modeled response using an isotropic caprock shale is shown in orange and provides a poor fit to the measured response at long offsets. Including anisotropy (VTI) in the caprock shale (green) gives a better match with the observed data. However, the shale below the base of the sand can be adequately modeled as isotropic. The sand is modeled as isotropic in all cases. (From Armstrong *et al.*, 1995.)

5.2.3.1 Polar anisotropy estimation

Polar anisotropy (VTI) local to the receiver array can be estimated using two methods. Techniques that fit direct-arrival times or differentiated direct-arrival times, called phase slowness methods, work best offshore—or when statics are not relevant—and in areas in which the velocity profile exhibits no velocity inversions. These methods assume a laterally invariant medium with horizontal slowness constant everywhere along the ray that connects source and receiver. Horizontal slowness is calculated by differentiation across offset (feasible only when static corrections are not significant) and is best measured by recording turning rays, which is possible only in the absence of velocity inversions. When these conditions cannot be met, the second method, which uses apparent slowness across the receiver array and wavefield polarizations, can be used.

Phase slowness method

In the case in which the overburden is approximately horizontally layered from the surface to the bottom of the receiver array, it is possible to reconstruct the velocity curves as a function of angle around the receiver array. Strictly speaking, the measurements obtained are slownesses rather than velocities. Nonetheless, the two can be easily converted from one to another.

To estimate the elastic parameters for an anisotropic medium, the horizontal and vertical phase slownesses can be measured for wavefronts propagating through the medium at various angles. Given these slowness components, which define the phase slowness surface, inversion for the elastic parameters can then be performed. In the case of VTI anisotropy, inversion for some of the elastic parameters (i.e., c_{11}, c_{33}, c_{55}, c_{13}) can be obtained using the procedure described in Miller and Spencer (1994).

The vertical array of geophones in a VSP provides the vertical phase slowness, which is the inverse of the moveout of the direct arrival across the array of geophones. If the depth increment between receivers is Δz, and the difference in traveltime from the source to two receivers is Δt, the vertical phase slowness is

$$\frac{\Delta t}{\Delta z}. \qquad (5\text{-}2)$$

In the special case in which there are no lateral velocity variations, the horizontal phase slowness can be obtained from walkaway VSP data (Fig. 5-18). The obvious, but impractical, direct measurement would be

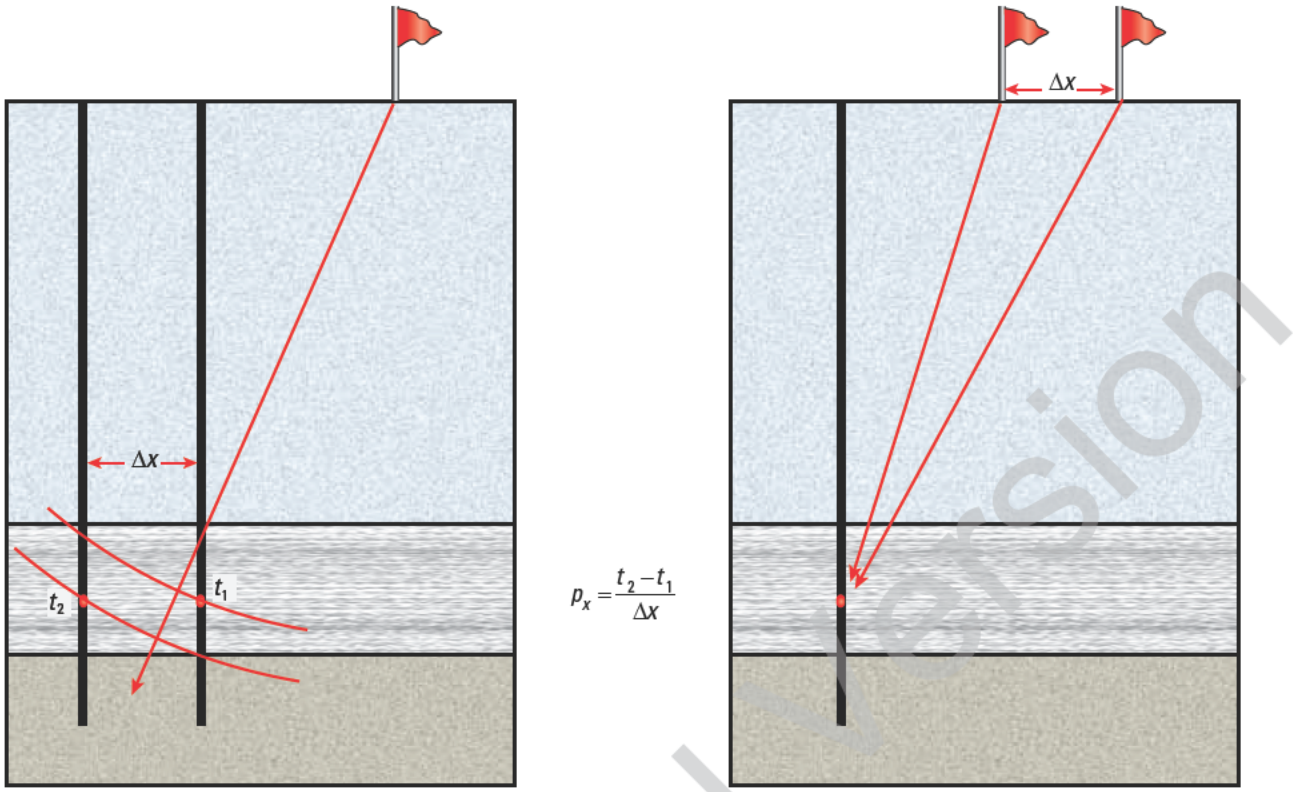

Figure 5-18. Measuring the horizontal phase slowness in a laterally homogen us Ea th. The two geometries in this figure are equivalent in the case in which the Earth is horizontally ayer d

to have two geophones within the medium at the same depth and separated by a short horizontal distan e. If velocities are laterally constant, the source-recei er pair can be moved horizontally without affe ting the traveltime, so that a horizontal movem nt of the source is equivalent to a horizontal movement f the receiver by the same amount. Therefore the horizontal phase slowness is

$$\frac{\Delta t}{\Delta x}, \tag{5-3}$$

where Δx is the horizontal separation between the two source points. From t e above argument, it should also be noticed tha the ho izontal slowness being measured is that of t e medium in which the seismic receiver is placed. The time difference is independent of the overburden velocity as long as it is laterally homogeneous.

To illustrate the phase slowness method, data from a marine walkaway VSP experiment is used (Fig. 5-19) (Miller *et al.*, 1994). In this figure, representative data are shown in the form of a common shot gather and a common receiver gather. Red lines indicate the apparent velocities of the direct arrivals. The reciprocals of these apparent velocities are equal to the slowness components. By combining the computed horizontal and vertical slowness components from the common-shot and common-receiver domains, it is possible to reconstruct the slowness curve for the local anisotropy around the receiver array (Fig. 5-20). This slowness curve can then be inverted to yield estimates of the elastic anisotropy. In this case, the Thomsen anisotropy parameters are estimated to be $\varepsilon = 0.13$ and $\delta = -0.17$.

The phase slowness method can work well but, because of its restrictive assumptions, has a limited range of application. A more general technique to obtain local anisotropic parameters is the slowness and polarization method.

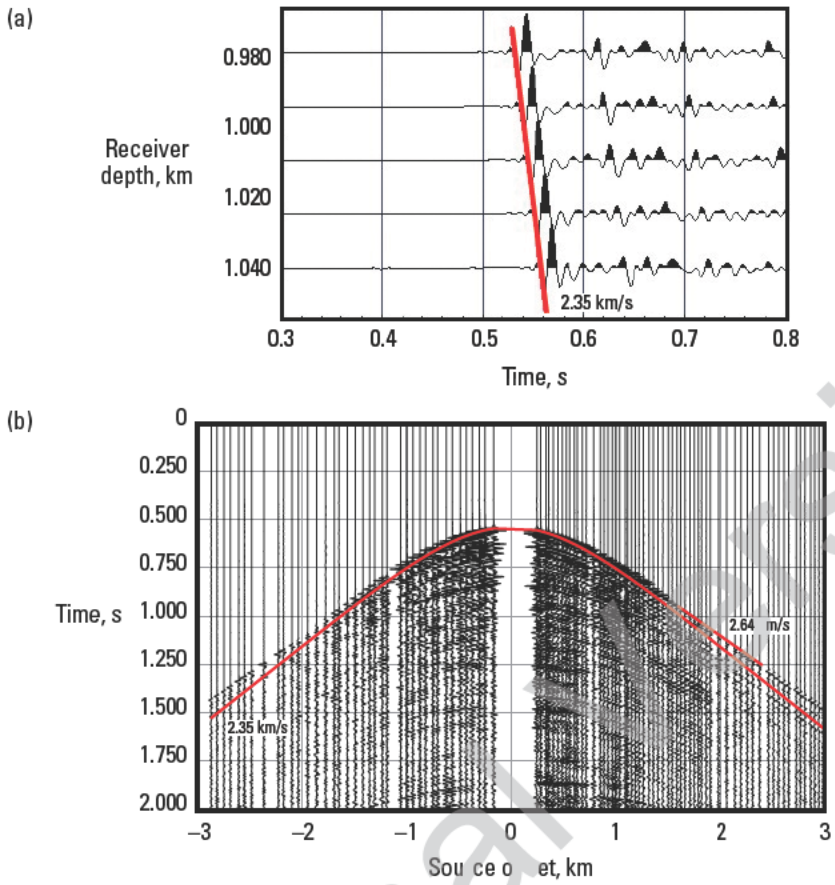

Figure 5-19. Radial common shot gather (a) and common receive gath r (b) from a marine VSP walkaway survey. The apparent velocity of the direct arrival is indicated by he red lin s. The reciprocal of this apparent velocity across the vertical receiver array is equal to the verti al slowness component. Similarly, the reciprocal of the apparent velocity measured in the c mmon eceiver gather is equal to the horizontal slowness component. (From Miller *et al.*, 1994.)

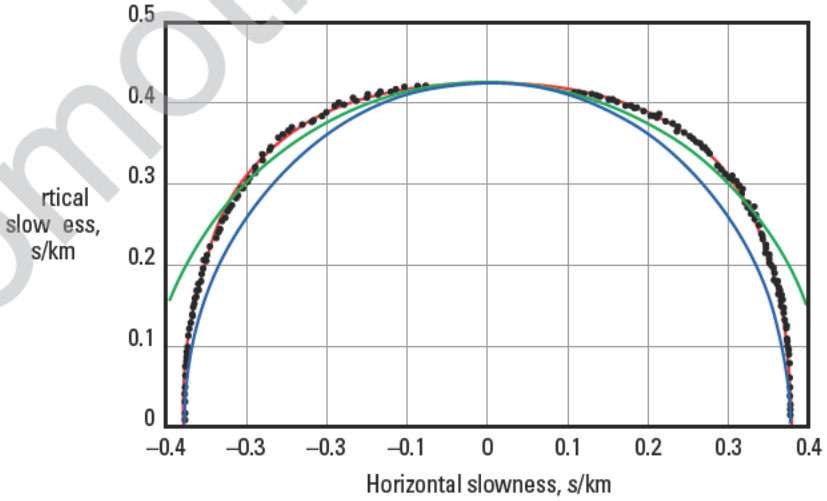

Figure 5-20. Slowness data (black dots) derived from the walkaway VSP data shown in Fig. 5-19. The best-fitting anisotropic slowness curve (red line) has Thomsen anisotropy parameters of $\varepsilon = 0.13$ and $\delta = -0.17$ (from Miller *et al.*, 1994). Also shown for reference are an isotropic slowness curve (green line) and an elliptical slowness curve (blue).

Slowness and polarization method

In isotropic media, the wave motion displacements (polarizations) associated with the propagating waves can be polarized either parallel to the direction of wave propagation, as in the case of compressional waves, or perpendicular to the direction of propagation, as in the case of shear waves. This constraint no longer holds true for waves propagating in anisotropic media (Fig. 5-21). In the isotropic case, the slowness curves are circular, which indicates that the velocity is invariant with propagation direction. The inner slowness curve corresponds to the compressional wave, for which the direction of particle displacement—its polarization (shown by short green lines)—is parallel to the direction of wave propagation (shown by red arrows). The outer curve corresponds to a shear wave whose direction of wave displacement lies in a direction perpendicular to the direction of wave propagation. In the isotropic material, it is quite clear that the polarization directions are either parallel to (for the compressional w ves) or perpendicular to (for the shear waves) the directi n of wave propagation.

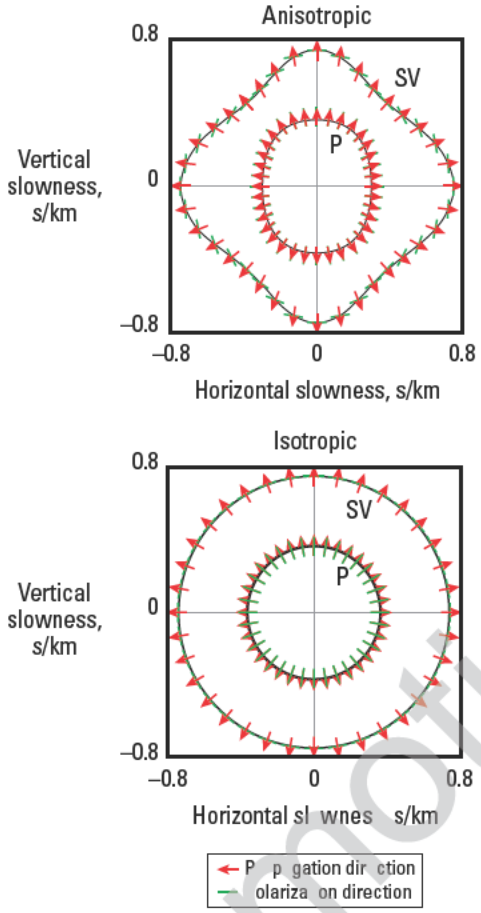

Figure 5-21. Slown ss surfac s and polarization directions for P- and SV-waves in anisotro c and isotropic media. In the isotropic case, the slownes curves are circular, indicating that the velocity is invariant th prop gation direction. The inner slowness curve co responds t the compressional wave, for which the direction of partic e displa ement, or polarization (green bars), is paral- l l to t e direction of wave propagation (red arrows). The outer cur corresponds to a shear wave whose direction of particle displa ment lies in a direction perpendicular to the direction of wave propagation. In the anisotropic case, it is clear that the polarization direction of the SV-wave (green) is not aligned with the slowness surface. This anisotropy is based on elastic models from Jones and Wang (1981).

However, in the anisotropic case this property no longer holds true. Note that th re is a small angle between the polarization dir ctions and propagation directions, as indicated b the small green and red sticks, respectively. The cle rest difference can be seen in the behavior of the SV-wave where it can be seen that the polarizati ns a e generally not tangential to the slowness surfac

Thes differen es between the polarization and slowness vectors can be more readily seen by plotting the polarization angles against the vertical slowness component (Fig. 5-22). Such information can be used to estimate the local anisotropy in the vicinity of the receiver array.

The slowness-polarization method was proposed in the 1990s but seldom applied because of the difficulty in obtaining slownesses and polarizations of sufficient accuracy to allow inversion. However, improvements in downhole instrumentation and methods for wavefield separation now allow sufficiently accurate measurements.

The example comes from Algeria (Fig. 5-23). Apparent slownesses for up- and downgoing P- and SV-waves are cross plotted against polarization, with 90° subtracted from the SV polarization so that the points will plot in the same area of the graph as the P-waves. The shape of the SV data is a signature of polar anisotropy, but the tilt results from the combination of a 34° well deviation and a 6° tilt of the axis of symmetry, as determined by the best-fitting transversely isotropic (TI) model. The anisotropy is very large, with $\varepsilon = 0.58$ and $\delta = -0.05$.

The inversion of slowness and polarization data does not rely on structural simplicity in the overburden, as is the case for the phase slowness method. This technique is more robust if SV data are included; therefore, the method works best when strong mode-converting reflectors are present just above or below the receivers.

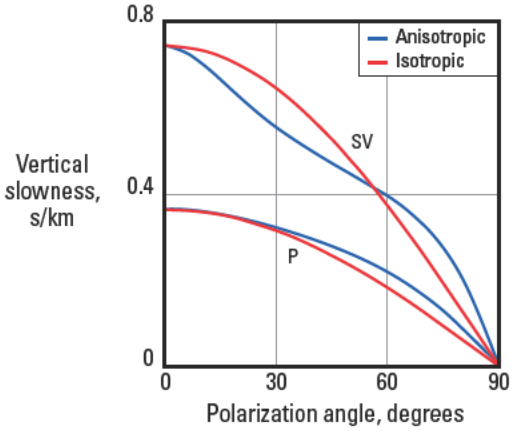

Figure 5-22. Polarization-slowness plot for isotropic (red) and anisotropic (blue) media. For display purposes, 90° was subtracted from the SV polarizations. Plotted in this way, the differences between anisotropic and isotropic behavior are more apparent.

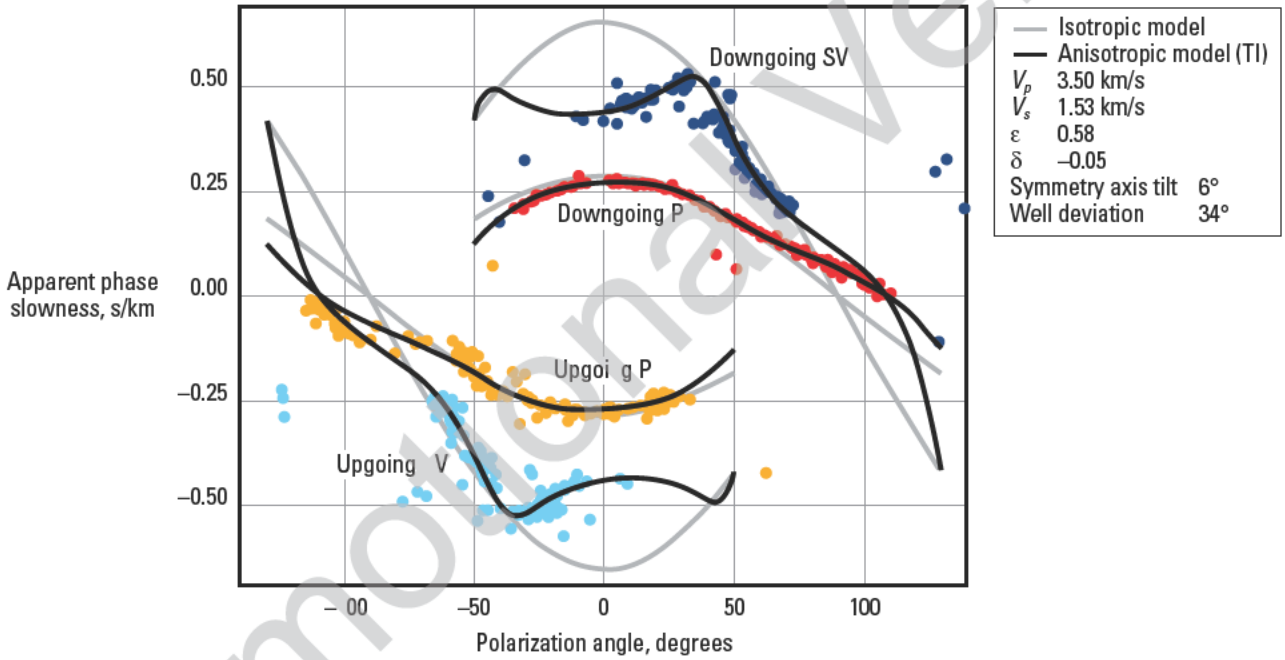

Figure 5-23. A slowness-pol rization plot for a 240-shot walkaway VSP in Algeria, with slownesses measured across a five-receiver su array. For display purposes, 90° has been subtracted from the SV polarizations. The shape of the SV d ta is a r sult of polar anisotropy where the asymmetry results from the combination of a 34° well deviation and 6° tilt f the axis of symmetry. The best-fit tilted transversely isotropic model (black) fits the data ch be er than the isotropic model (gray) and allows determination of a 6° tilt in the symmetry axis. (Graphic r produc d with permission from the In Amenas consortium [BP, Statoil, and Sonatrach]; from Leaney, 2008.)

5.3 Horizontal transverse isotropy

The second common cause of seismic anisotropy is related to aligned fracture systems. Fractures are usually near-vertical because of the typical stress regimes at depth, which tend to close near-horizontal fractures. When an aligned system of fractures is sampled with seismic waves with wavelengths much longer than the individual fractures, the net result can be directionally dependent—i.e., anisotropic. In some situations, the alignment of the vertical fractures can lead to a response that is approximately invariant, with rotation about the fracture normal direction, which lies in the horizontal plane. In these cases, the

anisotropy is termed horizontal transverse isotropy (HTI), and as illustrated schematically in Fig. 5-24. In the scenario shown, waves traveling in the plane of the fractures (e.g., in the y- or z-directions), will have greater velocities than those traveling in the direction perpendicular to the fractures (i.e., in the x-direction).

HTI can also be described by the Thomsen parameters, but the angles must now be referenced relative to the horizontal fracture normal direction. As a result, variations also occur with respect to both the azimuthal and incidence angles. Thus, HTI describes one form of azimuthal anisotropy.

More complex forms of anisotropy can be constructed, for example, with multiple fracture sets or by embedding aligned vertical fracture systems in a VTI medium. In such cases, the resulting anisotropy becomes more complicated, with more elastic constants required to define the elasticity.

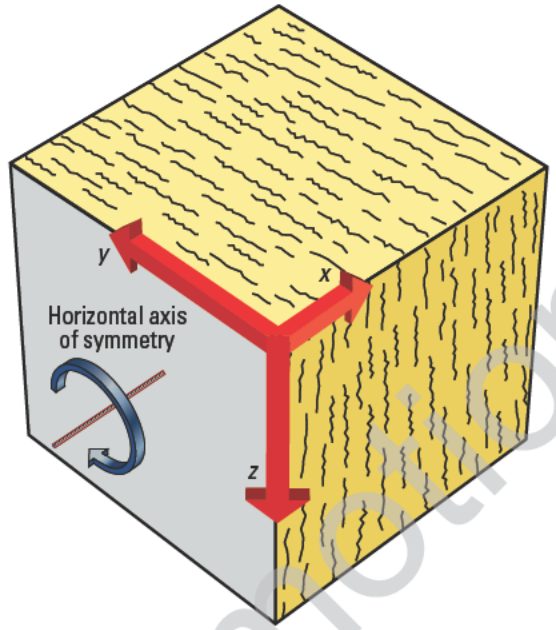

Figure 5-24. Schematic representation of fracture-induced anisotropy where the fractures are vertical and aligned in the *yz* plane. Such an arrangement can lead to horizontal transverse isotropy (HTI) with the symmetry axis oriented in the fracture normal direction. Seismic waves traveling in the plane of the fractures will have greater velocities than those traveling in the direction perpendicular to the fractures. (Graphic adapted from Armstrong *et al.*, 1994.; this graphic is copyright Schlumberger, Ltd. Used with permission.)

Oriented fractures can have a profound effect on reservoir productivity and fluid movement. For this reason, geologists, geophysicists, and reservoir engineers can use measurements of azimuthal anisotropy for well planning and to build better reservoir models.

To measure azimuthal anisotropy, measurements can be made along several different azimuths. Acquisition scenarios that fulfill this requirement include multiazimuth walkaway VSPs and walkaround VSPs, both of which can be considered subsets of a 3D VSP.

5.3.1 Multiazimuth walkaway

Walkaway VSPs may be used to measure the reflectivity response of an interface as a function of offset; this is known as amplitude variation with offset (AVO). In the case in which the interface separates materials with azimuthal anisotropy, perhaps because of aligned vertical fractures, the reflection response from the interface not only changes with offset but can also change with azimuth. Such variations are sometimes referred to as amplitude variation with offset and azimuth (AVOAZ). Such variations can be measured if walkaway VSPs are acquired along different azimuths.

In the example (Fig. 5-25), walkaway VSPs were acquired along eight different azimuths, and the reflectivity of the upgoing wavefield was analyzed by examining the AVOAZ (Leaney *et al.*, 1999). The observed AVO is plotted as a function of incidence angle and azimuthal angle (Fig. 5-26). A modeled response from a best-fitting model clearly shows the systematic azimuthal variation. The maximum AVO gradient is observed in a direction that is coincident with later arrivals (slower velocity), and the critical angle is reduced in the direction associated with earlier arrivals (faster velocity).

In a second example, multiazimuthal walkaway VSPs were acquired along three lines in an area with suspected fracture-induced anisotropy in the reservoir interval (Horne *et al.*, 1998). Slowness and polarization data derived from the VSP data were then inverted for azimuthal anisotropy parameters, including strike and dip angles of the fracture system (Fig. 5-27). The better-fitting solutions correspond to near-vertical fractures (less than 6° of dip) striking ESE or WNW, which are consistent with core data and suggest the presence of near-vertical open fractures in these directions.

It is also possible to derive slowness curves from each walkaway VSP and to then invert the azimuthal slowness curve variations to yield anisotropy estimates (Miller and Spencer, 1994).

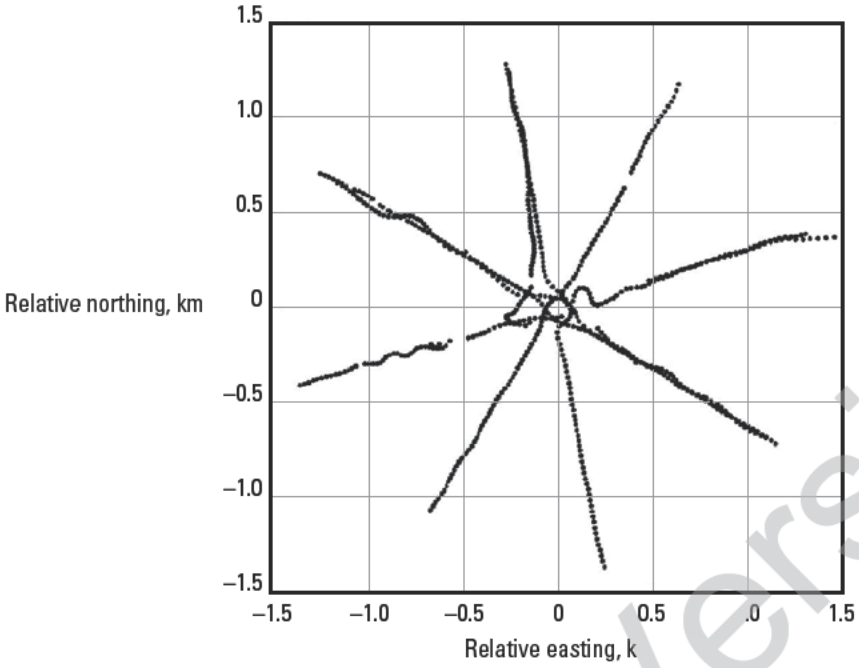

Figure 5-25. Plan view of shotpoints recorded in a multiazimuthal walkaway VSP for me suring zimuthal anisotropy. The borehole containing the receivers is in the center, and walkaway lines eman te n eight directions away from it. (From Leaney *et al.*, 1999.)

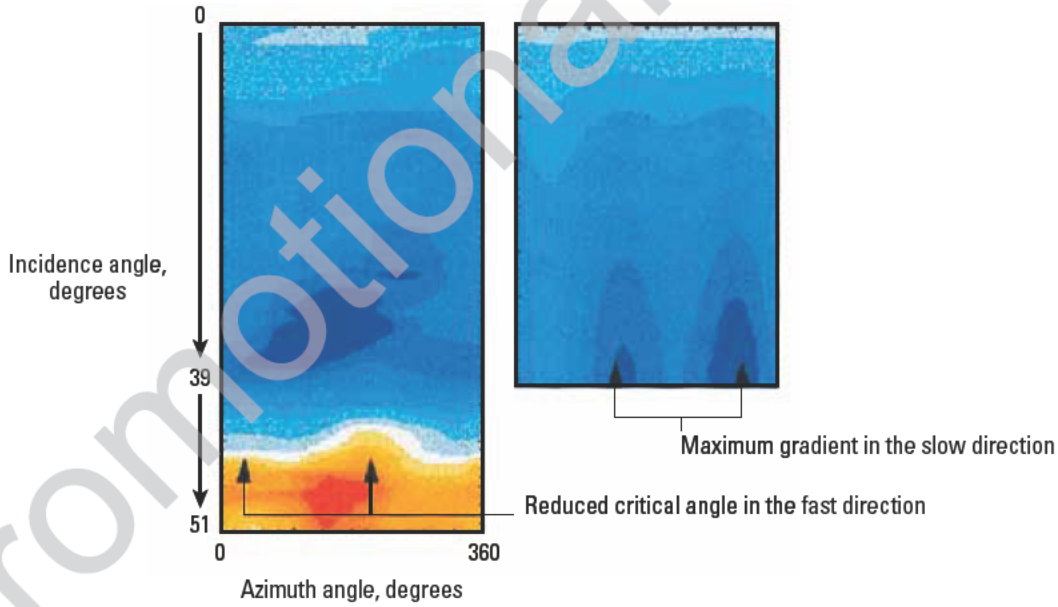

F gure -26. Amplitude variations with incidence angle (vertical axis) and azimuth (horizontal axis) from a mul azimuth walkaway VSP. Blue corresponds to positive reflection amplitudes and orange to negative amplit des. The angle at which polarity changes varies with azimuth and is at minima for the medium's fast direction. The plot on the right shows synthetic data for a least-squares-fitting model applied to the precritical data. (From Leaney *et al.*, 1999.)

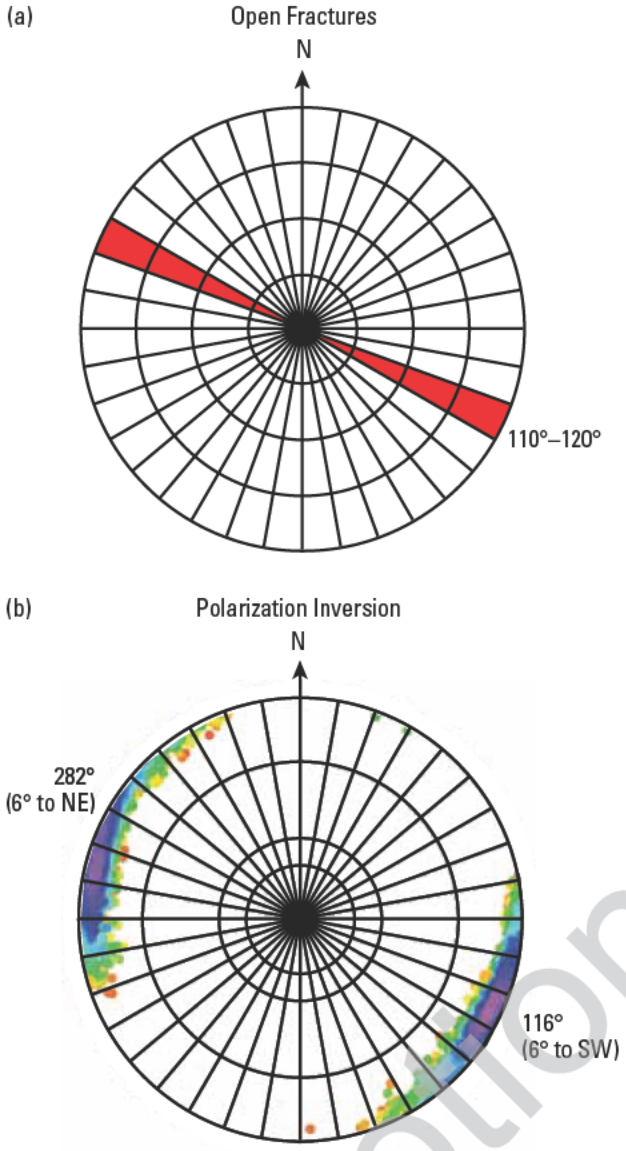

Figure 5-27. Fracture strike and dip results from core data (a) compared with results from a nonlinear version of multiazimuth walkaway data (b). In the polarization inversion results, each colored point corresponds to a different fracture orientation and is colored according to the quality of the data fit such that the purple colors indicate a good fit to the data and the yellow colors indicate a poorer fit to the data. The best-fitting models correspond to near-vertical (6° dip) fractures striking at an azimuth of 116° (ESE) or 282° (WNW), which is consistent with the core data (From Horne *et al.*, 1998).

5.3.2 Converted-wave VSP—Walkaround VSP

Shear waves are also sensitive to anisotropy and in a more complicated way than P-waves because of a phenomenon known as shear-wave splitting or shear-wave birefringence. Shear-wave splitting can occur when a shear wave propagates in an anisotropic medium (Fig. 5-28). As the shear wave, or converted shear wave, enters the anisotropic region, it can split into two waves—a fast shear wave and a slow shear wave. As these two waves travel through the anisotropic medium they separate because of the difference in their velocities so that, on emerging from the anisotropic medium, there is a time delay between the arrival of the fast and slow shear waves.

Such shear-wave splitting can be observed in converted waves from offset VSPs. A shear-wave VSP in which a shear-wave source is used to directly excite shear waves. Walkaround VSPs can measure converted-wave behavior as a function of azimuth from which azimuthal anisotropy attributes can be estimated.

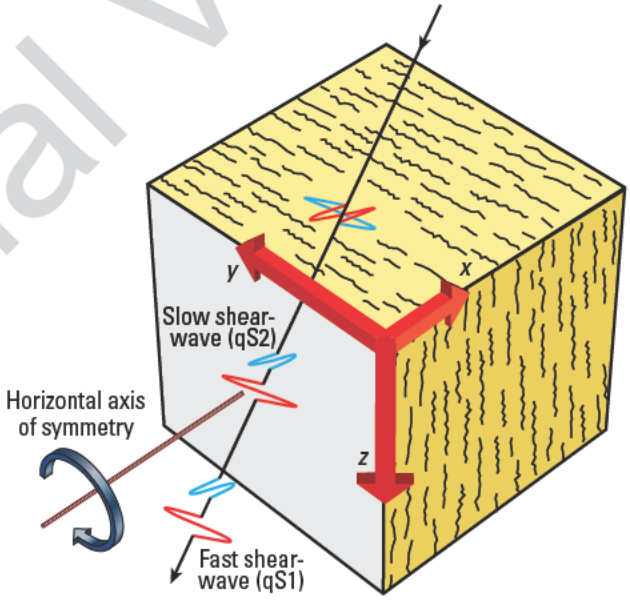

Figure 5-28. Shear-wave splitting. In some circumstances, an S- or P-wave that is incident on a medium with azimuthal anisotropy can excite two shear waves. The shear wave with particle motion polarized in the direction parallel to fractures or aligned features will have a faster velocity and is known as the fast shear wave (red; quasi S-wave [qS1]). The shear wave with particle motion polarized in the direction perpendicular to the fractures is known as the slow shear wave (blue; quasi S-wave [qS2]).

The walkaround VSP comprises multiple sources azimuthally distributed around a fixed multicomponent receiver (Fig. 5-29). Such a configuration allows the robust measurement of fracture-induced anisotropy by the analysis of certain seismic attributes with respect to azimuth. One set of useful attributes is associated with downgoing P-to-S conversions. As explained earlier, when azimuthal anisotropy is present, the downgoing S-wave can split into two shear waves. These two shear waves will then continue to propagate downward with different velocities and different polarizations, leading to nonlinear hodograms and energy on the transverse component. However, in certain directions, only one of the shear waves will be excited, and shear-wave splitting will not be observed. In the case in which anisotropy is caused by aligned vertical fracture systems, these directions will coincide with the fracture strike and fracture normal. If a suitable metric related to the shear-wave splitting is then calculated as a function of azimuth, then these directions can be identified and interpreted in terms of the fracture orientation. Attributes that have proven to be useful include the ratio of the root-mean-square (rms) energy on the transverse component to the rms energy on the radial component.

In this example, the survey comprised 16 shotpoints arranged in a semicircular pattern at a nominal offset of 1,370 m. The source was a vibroseis truck, and the receiver array spanned a depth range from 1,800 m to 1,890 m. After processing, a time window containing a downgoing P-to-S conversion was selected and two seismic attributes were computed as a function of azimuth. The first attribute measures the ratio of the rms energy on the transverse component to the rms energy on the radial component. The second attribute es entially measures the nonlinearity of the hodograms. For both of these attributes, one could expect to see a minimum value when the source-receiver azimuth s parall l to the fracture strike or fracture normal (Fig 5-30) To resolve which azimuth corresponds to the fracture strike, the data are rotated into one of hese directions and the component with the earlie arrivals is identified as the fast shear direction. At some azimuths, close to WSW and NNW, the attributes appro ch zero. At intermediate azimuths, the ttrib te approach maxima. Such behavior is consisten with vertical fracture system striking WSW. This interpretation agrees with other geological data from the field and with a crossed-dipole sonic log that was acquired in the same well (Walsh *et al.*, 2002).

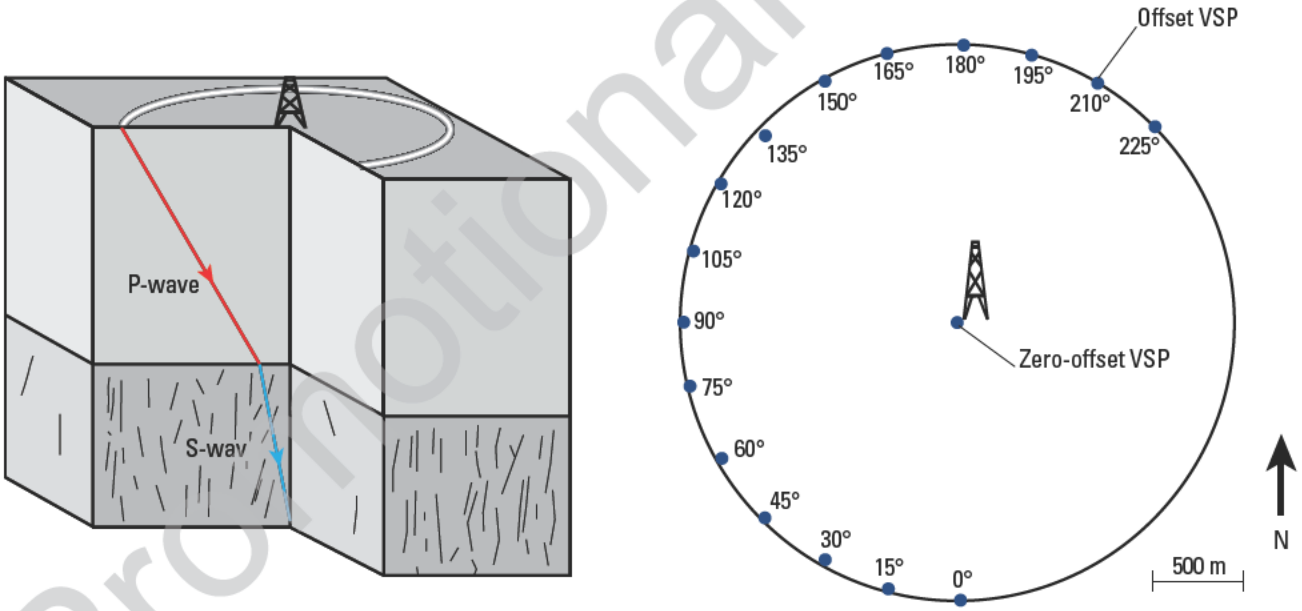

Figure 5-29. A walkaround VSP, using P-to-S converted waves generated by sources deployed at a range of azimu hs to investigate azimuthal anisotropy. The survey comprised 16 shotpoints arranged in a semicircular pattern at a nominal offset of 1,370 m. The source was a vibroseis truck, and the receiver array was deployed at a depth range from 1,800 m to 1,890 m. (From Horne *et al.*, 2002.)

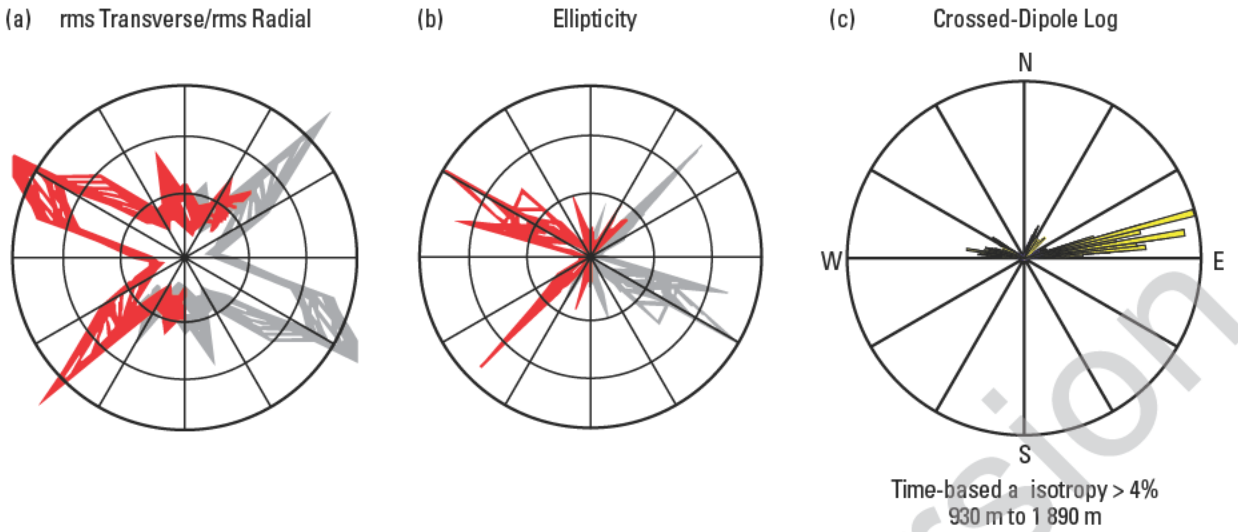

Figure 5-30. Rose plots of anisotropy attributes from a walkaround VSP and a dipole sonic log (far right). The first attribute (a) measures the ratio of the rms energy on the transverse component to the rms energy on the dial mponent. The second attribute (b) measures hodogram ellipticity. For both of these attributes, the minimum occu s when the azimuth between the source and receiver is parallel to the fracture strike or fracture normal. The r d lines a e the actual data points, and the grey lines are simply mirrored through the origin to simulate a reciproca sourc re eiver azimuth. The rms attribute approaches zero close to the WSW and NNW azimuthal directio At interm diate azimuths, the attributes approach maxima. Such behavior is consistent with a vertical fracture system st iking WSW. This interpretation agrees with other geological data from the field and crossed-dipole sonic log data (c) that w acquired in the same well. (From Horne *et al.*, 2002; Walsh *et al.*, 2002.)

5.3.3 Shear-wave VSP

In the examples above, it was shown how compressional waves can excite shear waves, which can then be us d to measure the shear-wave splitting associated with azimuthal anisotropy (e.g., slowness polarization nversion, walkaround VSP, and hodogram analysis) However, it is also possible to directly excite shea waves One such shear-wave source is the shear-wave vibrator discussed in Chapter 3. The shear-wave vibrator uses a base plate that is pushed into the ground nd is hen shaken in a horizontal direction, rather than in the more typical vertical direction, ther by generating a shear wave. By orientating the base plate in different directions, it is possible to excite vertically propagating shear waves that are polarized in a given direction. By recording data from two or more different shear-wave source polarizations, it is possi e to robustly estimate shear-wave splitting u ing a echnique such as Alford rotation (Alford, 1986).

In this example, a shear-wave VSP was used to measure shear-wave splitting (birefringence) as a function of depth (Fig. 5-31). In several of the zones, the degree of shear-wave splitting correlated with sandstone intervals that were interpreted to be fractured (Horne *et al.*, 1997). The fast shear-wave direction derived from the survey was consistent with other geological information from the area.

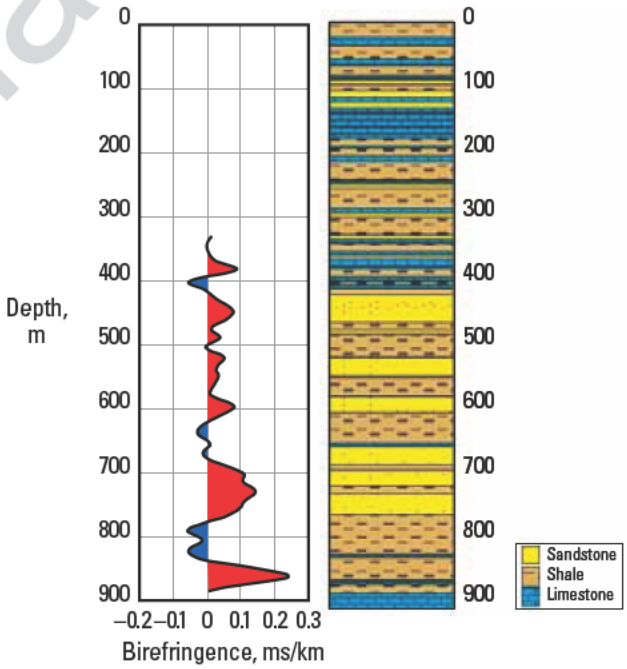

Figure 5-31. Shear-wave splitting, or birefringence, measured in a shear-wave VSP. The rate of birefringence plotted versus depth (left) correlates with various sandstone intervals, which are interpreted to be fractured. (Data from Horne *et al.*, 1997; figure from MacBeth and Li, 1999.)

5.3.4 Integration with other measurements

Azimuthal anisotropy caused by oriented fractures and tectonic stresses can be detected in other types of measurements, such as borehole sonic logs, and fractures themselves can be seen in borehole images and core. By combining results from measurements at different scales, interpreters gain confidence in their assessments of anisotropy and can construct more reliable Earth models.

The walkaround VSP example previously described from Rangely, Colorado (Figs. 5-29 and 5-30), combined information from a zero-offset VSP, an offset VSP, a walkaround VSP, and a crossed-dipole sonic log, all in a cased well (Thompson *et al.*, 2002; Horne *et al.*, 2002; Walsh *et al.*, 2002). These data were integrated with prior information from surface seismic, core analysis, borehole breakouts, minifrac tests, and well-to-well communication to evaluate fracture-detection methods. The VSPs and sonic logs were able to quantify fracture direction and anisotropy magnitude over large intervals as well as in thin layers.

In a more recent example from the Cuitláhuac field in Mexico (Fig. 5-32), shear-wave VSPs and crossed-dipole sonic measurements were acquired to determine stress directions for planning oriented perforating operations in tight gas sands (Saldungaray *et al.*, 2006; Barr entos *et al.*, 2006). The field is composed of 20 sand packages that must be stimulated to produce commercial qu ntit es of gas. Understanding of the stress direct on is crucial to planning hydraulic fractures and plac ng infill wells.

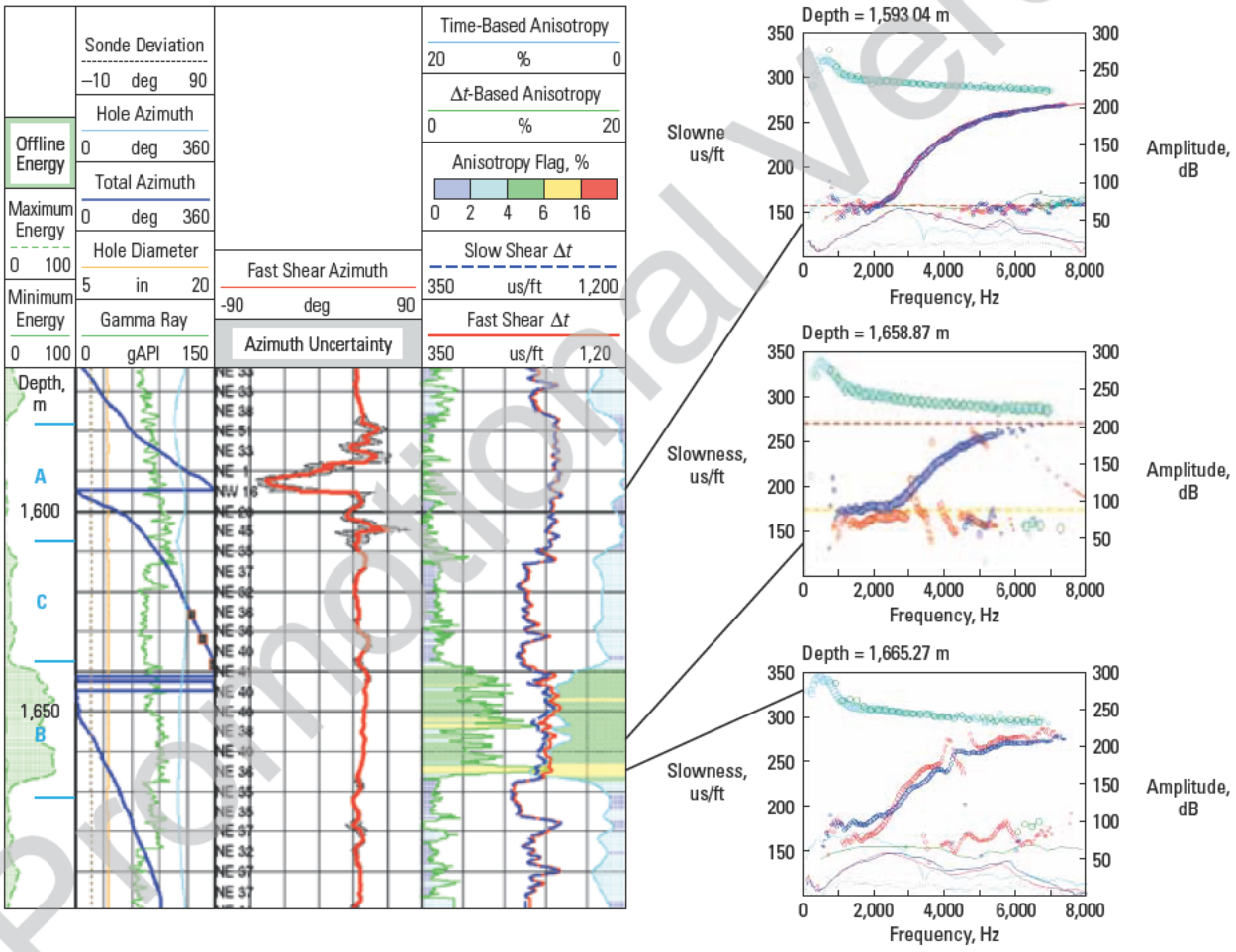

Figure 5-32. Crossed-dipole log from the Cuitláhuac field showing zones with isotropy (A) and zones with differing amounts of anisotropy (B and C). Zone A has low offline energy (Track 1) and a characteristic dispersion curve (top right). Anisotropic zones B and C have larger offline energy. At the bottom of Zone B, the dispersion curves cross each other (lower right), indicating stress-induced anisotropy. Shallower in Zone B, the dispersion curves appear as though they could cross (middle right), but the high frequencies of the fast shear waves (red dots) are lost. Open, induced fractures were visible in oil-base mud borehole image logs at this depth. (From Franco *et al.*, 2006, modified from Wielemaker *et al.*, 2005; this graphic is copyright Schlumberger, Ltd. Used with permission.)

The data from the sonic tool clearly showed isotropic and anisotropic zones, the latter identified by maxima in crossline energy, which indicates a directional preference in the data (Fig. 5-32). The anisotropic layers range in thickness from 5 to 80 m, with anisotropy magnitudes from 1% to 8%. The behavior of sonic slowness-frequency–dispersion curves reveals that different causes of anisotropy are at work in these layers. Stress-induced anisotropy is responsible for the shear-wave splitting in Zone B, whereas the presence of fractures causes anisotropy in other intervals.

Comparison of the fast-shear azimuth obtained from sonic logging with that interpreted in borehole image logs shows a good correlation between the two (Fig. 5-33). In the first case (Fig. 5-33a), the fast shear-wave direction, indicative of the maximum stress direction, matches the azimuth of tensile fractures seen in borehole images within that zone. In a second example (Fig. 5-33b), the fast shear azimuth correlates with the strike of bedding interpreted from image logs.

The shear-wave VSP was acquired by exciting two orthogonally polarized shear waves at the surface and measuring their propagation using multicomponent geophones in the borehole. Horizontal vibrators located near the well generated shear waves polarized in the E-W and N-S directions. Two vertically polarized vibrators, one near the shear vibrators and one about 1,600 m to the north, generated compressional waves.

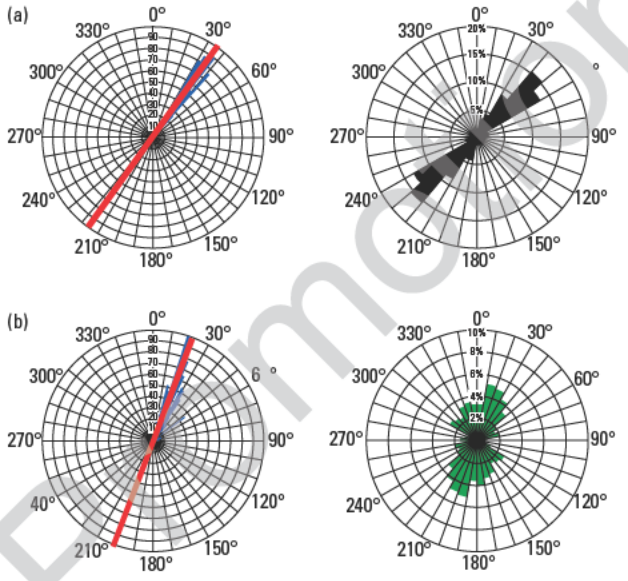

Figure 5-33. Rose plots showing the comparison of the fast-shear azimuth obtained from sonic logging (left) and the azimuth data derived from borehole image logs (right). (a) The fast shear-wave direction, indicative of the maximum stress direction, matches the azimuth of borehole-induced fractures seen in borehole images. (b) The fast-shear azimuth correlates with the strike of bedding interpreted from image logs. (From Barrientos *et al.*, 2006.)

Traveltime differences in the rotated data components of the shear wave were plotted against depth and showed an almost linear increase with depth, which indicated a consistent anisotropy of about 1.7 us/ft over the depth interval from 1,600 to 3,000 m. The shear-wave VSP results confirmed the general trends in anisotropy azimuth and magnitude that were observed in the cross-dipole sonic measurements. The shear-wave VSP delivers average fracture properties over a larger scale than those derived from cross-dipole sonic measurements. Both scales are useful for different app ications (i.e., calibration to surface seismic comes from he VSP data, prediction of borehole breakout comes from onic logs). In this particular example, both measu ements confirmed the general trends in aniso ropy azimuth and magnitude.

5.4 References

Alford R.M.: "Shear Data in the Presence of Azimuthal Anisotropy," *Expand d A stracts*, 56th SEG Annual International Meeting, Dilley, Texas, USA (1986) 5, 476–479.

Alkhalifah, T., and Tsvankin, I.: "Velocity Analysis for Transversely Isotropic Media," *Geophysics* (1995) 60, No 5, 1550–1566.

Arms ong, P., Ireson, D., Chmela, B., Dodds, K., Esmersoy, C., Miller, D., Hornby, B., *et al.*: "The Promise of Elastic Anisotropy," *Oilfield Review* (October 1994) 6, No. 4, 36–47.

Armstrong, P.N., Chmela, W., and Leaney, W.S.: "AVO Calibration Using Borehole Data," *First Break* (1995) 13 No. 8, 319–328.

Barrientos, C., Wielemaker, E., Plona, T., Haldorsen, J., and Saldungaray, P.: "Emerging Technology for Quantifying Minimal Anisotropy," *First Break* (2006) 24, No. 9, 87–91.

Brie, A., Endo, T., Hoyle, D., Codazzi, D., Esmersoy, C., Hsu, K., Denoo, S., *et al.*: "New Directions in Sonic Logging," *Oilfield Review* (Spring 1998) 10, No. 1, 40–55.

Brie, A., Pampuri, F., Marsala, A.F., and Meazza, O.: "Shear Sonic Interpretation in Gas-Bearing Sands," paper SPE 30595, *Proceedings*, SPE Annual Technical Conference and Exhibition, Dallas, Texas, USA (October 22–25, 1995), 701–710.

Chen, T., Goodway, B., Zhang, W., Potocki, D., Uswak, G., Calow, B., and Gray, D.: "Integrating Geophysics, Geology and Petrophysics: A 3D Seismic AVO and Borehole/Logging Case Study," *Expanded Abstracts*, 68th SEG Annual International Meeting and Exposition, New Orleans, Louisiana, USA (September 13–18, 1998) 17, No. 1, 615–618.

Coulombe, C.A., Stewart, R.R., and Jones, M.J.: "AVO Processing and Interpretation of VSP Data," *Canadian Journal of Exploration Geophysics* (1996) 32, No. 1, 41–62.

Franco, J.L.A., Ortiz, M.A.M., De, G.S., Renlie, L., and Williams, S.: "Sonic Investigations In and Around the Borehole," *Oilfield Review* (Spring 2006) 18, No. 1, 14–33.

Horne, S., MacBeth, C., Queen, J., and Rizer, W.: "Fracture Characterization from Near-Offset VSP," *Geophysical Prospecting* (1997) 45, 141–164.

Horne, S., Thompson, C., Moran, R., Walsh, J., Hyde, J., and Liu, E.: "Planning, Acquiring and Processing a Walkaround VSP for Fracture-Induced Anisotropy," paper Z-99 presented at the 64th EAGE Annual Conference and Exhibition, Florence, Italy (May 27–30, 2002).

Horne, S.A., McGarrity, J.P., Sayers, C.M., Smith, R.L., and Wijnands, F.: "Fractured Reservoir Characterization Using Multi-Azimuthal Walkaway VSPs," *Expanded Abstracts*, 68th SEG Annual International Meeting and Exposition, New Orleans, Louisiana, USA (September 13–18, 1998), 1640–1643.

Jones, L.E.A., and Wang, H.F., "Ultrasonic Velocities in Cretaceous Shales from the Williston Basin," *Geophysics* (1981) 46, No. 3, 288–297.

Leaney, W.S.: "Polar Anisotropy from Walkaway VSPs," *The Leading Edge* (2008) 27, No. 10, 1242–1250.

Leaney, W.S., Bale R., Wheeler M., and Tcherkashnev, S.: "Borehole-Integrated Anisotropic Processing of Converted Modes," *The Leading Edge* (2001) 20, No. 9, 996–1007.

Leaney, W.S., Hope, R.R., Tcherkashnev, S., and Wheeler, M.T.: "Long Offset AVO and Anisotropy Calibration Deep Offshore Nigeria," *EAGE 2002 Extended Abstracts,* 64th EAGE Annual Conference and Exhibition, Florence, Italy (May 27–30, 2002) 476–479.

Leaney, W.S., Sayers, C.M., and Miller, D.E.: "Analysis of Multiazimuthal VSP Data for Anisotropy and AVO," *Geophysic* (1999) 64, No. 4, 1172–1180.

Leaney W.S., Tcherkashnev, S., Wheeler, M., Idrees, M., Hastings, A., Touami, M., Mekmouche, S., and Kasmi, R.: "In-Line Walkaway Processing and Integration," *Expanded Abstracts*, 73rd SEG Annual International Meeting and Exposition, Dallas, Texas, USA (October 26–31, 2003), 2203–2206.

MacBeth, C., and Li, X-Y.: "AVD—An Emerging New Marine Technology for Reservoir Characterization: Acquisition and Application," *Geophysics* (1999) 64, No. 4, 1153–1159.

Miller, D.E., Leaney, S., and Borland, W.H.: "An In Situ Estimation of Anisotropic Elastic Moduli for a Submarine Shale," *Journal of Geophysical Research* (1994) 99 (B11), 21659–21665.

Miller, D.E., and Spencer, C.: "An Exact Inversion for Anisotropic Moduli from Phase Slowness Data," *Journal of Geophysical Research* (1994) 99 (B11), 21651–21657.

Ostrander, W.J.: "Plane-Wave Reflection Coefficients for Gas Sands at Nonnormal Angles of Incidence," *Geophysics* (1984) 49, No. 10, 1637–1648.

Saldungaray, P., Barriento , C., Wielemaker, E., Plona, T., Haldorsen, J.B.U., and Arroyo, J.L.: "Anisotropy Evaluation in the Cuitlahuac Field, Mexico, from Cross-Dipole Sonics and Borehole Seismics Generated by Two Orthogonal Shear Vibrators," *Transactions of the SPWLA 47th Annual Logging Symposium*, Veracruz, Mexico (June 4–7, 2006), paper UU.

Thompson, C., Moran, R., Horne, S., Walsh, J., and Fairbairn, J.: "Seismic Fracture Characterization of Sandstone Reservoir—Rangely Field, Colorado, *Expanded Abstracts*, 72nd SEG Annual International Meeting and Exposition, Salt Lake City, Utah, USA (October 6–11, 2002), 1049–1052.

Thomsen, L.: "Weak elastic anisotropy," *Geophysics* (1986) 51, No. 10, 1954–1966.

Walsh, J., Urdea, J., Hyde, J., Simon, H., Horne, S., Thompson, C., De, G., and Moran, R.: "Determining Fracture or Stress Direction through Casing: A Case Study," *Transactions of the SPWLA 43rd Annual Logging Symposium*, Oiso, Japan (June 2–5, 2002), paper D.

Wang, Z.: "Seismic Anisotropy in Sedimentary Rocks, Part 2: Laboratory Data," *Geophysics* (2002) 67, No. 5, 1423–1440.

Wielemaker, E., Saldungaray, P., Sanguinetti, M., Plona, T., Yamamoto, H., Arroyo, J.L., and Mercado Ortiz, M.A.: "Shear-Wave Anisotropy Evaluation in Mexico's Cuitlahuac Field Using a New Modular Sonic Tool," *Transactions of the SPWLA 46th Annual Logging Symposium,* New Orleans, Louisiana, USA (June 26–29, 2005), paper V.

6 Imaging VSP

Michael Jones and Alejandro Martinez Pereira

6.1 Introduction

All exploration techniques aim to generate either a map of some property or a vertical cross section through the Earth. The latter is by far the more compelling visualization. This visualization is the objective of geological cross sections, multiwell petrophysical analysis and, of course, the seismic method.

Surface seismic methods generate huge volumes of 2D and 3D data from which vertical cross sections may be extracted over potential exploration prospects and confirmed reservoirs. Borehole seismic methods provide an alternative way to achieve a vertical cross section over a restricted lateral extent away from a borehole. Some of the reasons why this might be advantageous are listed below.

- *Tie into the seismic grid.* Exploration wells are often drilled on 2D data and the well location is frequently far from the surface seismic line, either because of surface access limitations or because of well-spacing restrictions. Borehole seismic images allow the w ll to be "tied back" to the surface grid.
- *Delineate the reservoir.* If a successful wel has be n drilled, borehole seismic provid s an oppo tunity to delineate the extent of the hydr carbon pool in an extremely short time frame. To plan, permit, acquire, and process a surface seismic survey may take months, whereas borehole seismic results may be available for interpretation less than a week after the well has been drilled
- *Steer the well for mall targets.* Borehole seismic images acquired when the well is at an intermediate depth can p ovide the data to steer the well trajectory into the target The additional cost is normally much less than the cost of a sidetrack to a missed target.
- *Find a mis ed target.* If the well encounters the target horizon on the downthrown side of the fault, th VSP can image the distance that will be necessary to whipstock in order to hit the upthrown side. If the target is a reef and the well encounters off-reef or reef-flank facies, the offset VSP can determine if the target reef is present or determine the distance to the crest.

6.2 Walkabove VSP

In deviated and horizontal wells, walkabove VSP (vertical-incidence VSP) is the most common type o a borehole seismic survey. In VSP terms, a horizontal well is an extreme version of a deviated well Simil r to other VSPs, deviated well surveys may be used t locate the well in the 3D surface seismic volume and to assess the quality of surface seismic surveys. Also, the technique may be employed to measure lateral velocity variations and image faults a d structures below the wellbore.

The following example is a walkabove VSP carried out in late 1994 in a North Sea well with a 1.2-km horizontal section (Christ e *et al*., 1995). There were two main objectives: first, to measure a suspected lateral velocity anomaly that may have been creating artifacts in the surface se smic data (Fig. 6-1) and second, to obtain a high-resolution seismic image below the deviated portion of the well. An additional objective was to obtain a seismic image in the horizontal part of the well (Ediriweera *et al*., 1995).

As with any survey, the desired seismic image is produced using the reflected, or upgoing, wavefield. So, the first processing task is to separate downgoing waveforms from upgoing waveforms. For walkabove surveys in horizontal wells, this is not straightforward because, unlike vertical and deviated wells, there is no apparent time difference across the array between the downgoing and the reflected upgoing waves (Fig. 6-1). It is therefore impossible to use conventional techniques to distinguish between reflected and downgoing waves. To improve the image, a number of special techniques are used, including

- multichannel filtering to attenuate noise and sharpen the desired signal (Haldorsen *et al*., 1994)
- downgoing wavefield subtraction using a long filter length to estimate the downgoing wavefield
- median filtering techniques to estimate and subtract the energy scattered by faults
- enhancement of the desired upgoing signal
- equalization of the reflected wavefield amplitudes from the horizontal and the build-up sections.

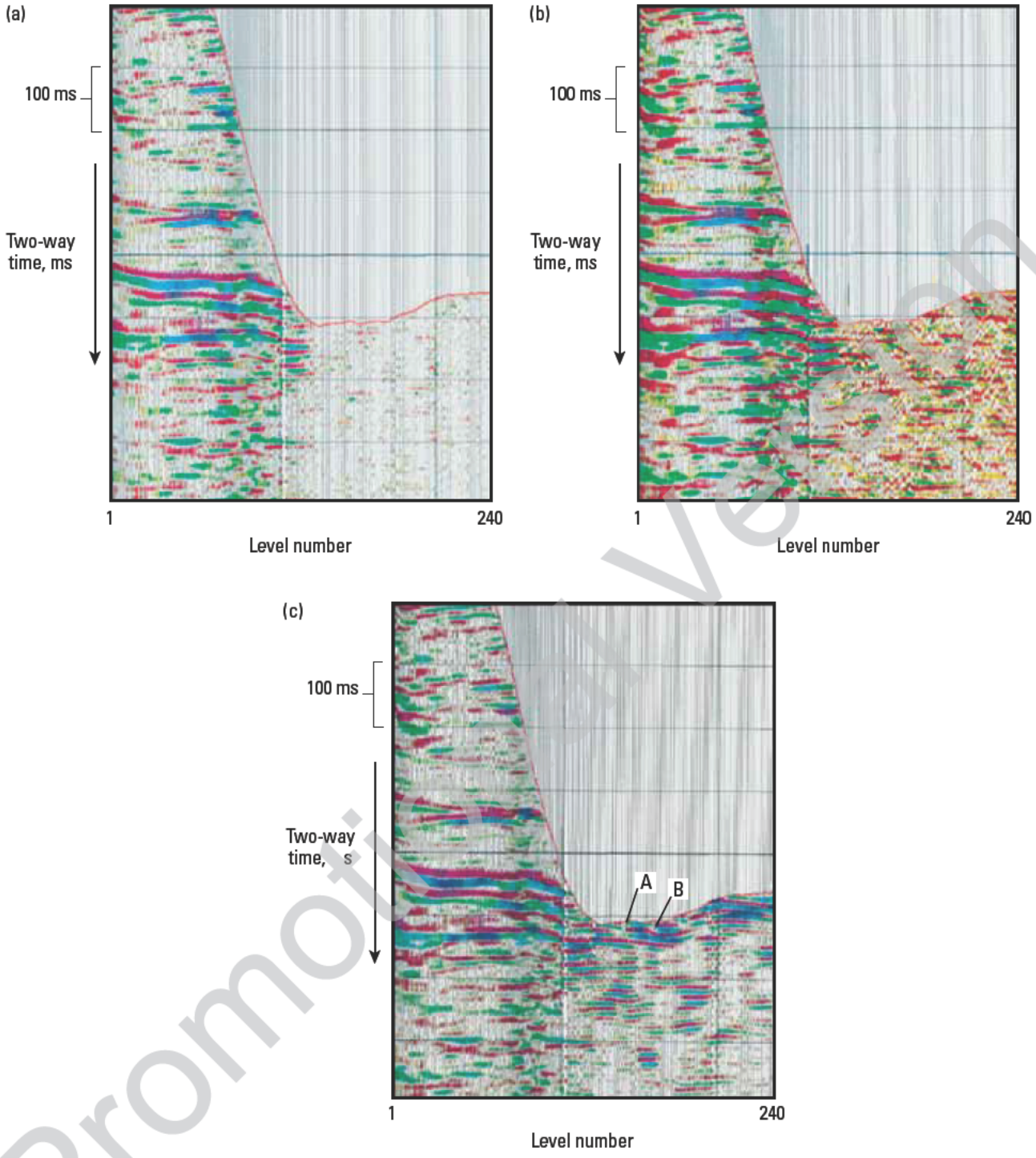

Figure 6 1. Walkabove VSP in a North Sea horizontal well. The first-arriving seismic signals are tracked with a red line, which also delineates the borehole trajectory in two-way time. The conventional processed VSP data (a) and the same processed data with boosted gain (b) show poor continuity of reflected events, and the fault-scattered energy further complic tes the image. In conventional methods of VSP processing, the lack of apparent velocity difference between downgoing and upgoing wavefields leaves little or no reflected upgoing energy after wavefield separation. Boosting the gain in the horizontal section is of little value. Horizontal VSP data after improved processing (c) show three important features: two faults marked A and B, which appear as anticipated in the reflected image, and evidence of dipping strata. The formation apparent dips appear parallel to the borehole until very near total depth. This was entirely consistent with the computed dips from Formation MicroScanner* data. (From Christie *et al.*, 1995; this graphic is copyright Schlumberger, Ltd. Used with permission.)

The final image showed three important features: two faults marked A and B, which appear where suspected in the reflected image, and dipping strata below the well (Fig. 6-1). The comparison of the VSP data with Formation Microscanner* data acquired during openhole logging confirmed the fault locations (seen as chevrons in the VSP) and the apparent dips.

The two datasets were then interpreted and refined together to provide a more complete description of near-well geology than was otherwise available. The results met the main objectives of the survey and delivered an image below the horizontal section.

An alternative strategy to acquire and process horizontal VSP data exploits the different responses of geophones and hydrophones to differentiate downgoing energy from upgoing energy in horizontal wells. Geophones are clamped to the formation and sense its motion. In contrast, hydrophones are suspended in the borehole fluid and are sensitive to fluid pressure changes as a seismic wave passes in any direction. Whereas the two sensor types show the same signal polarity for a downgoing wave, they show different polarities for the upgoing wave. For a signal consisting of a direct pulse followed by a reflected pulse, by taking the difference between signals received at the two types of sensors, the direct wave is canceled and the reflection is enhanced (Fig. 6-2).

Complications arise from differences in the coupling and impulse responses between geophones and hydrophones. Although this approach has been applied in the field to enable the extraction of reflected wavefields in a horizontal well and the imaging of reflectors below the receivers, data processing becomes challenging and in most cases impractical.

Geoscientists working on field-development projects are responsible for identifying promising targets within reach of existing wells. In many cases, the obvious traps have already been drilled. Any remaining reserves are contained in smaller, subtler features that can elude conventional surface seismic imaging. Images from borehole seismic surveys bring small structures and indistinct stratigraphic changes into focus and help asset teams place deviated drainholes with confidence.

In one North Sea example, a deviated development well was planned to penetrate a target that was identifiable on existing surface seismic data (Fig. 6-3). Before drilling, well planners needed to confirm the position and dip of the target horizon and of neighboring structural features. Initial time-depth conversion of the surface seismic image relied on information from a nearby vertical well. However, lateral velocity variations acutely limit surface seismic depth conversion accuracy. Depending on geological complexity, a time-depth conversion that is accurate at the control well may be tens of meters in error where the deviated development well penetrates the target. A VSP image was expected to reduce uncertainty by giving a clear picture of the region beneath the borehole.

A 210-level walkabove borehole seismic survey, acquired in 11.5 hours, provided data to refine the structural interpretation in the vicinity of the borehole. The high-resolution borehole seismic image illuminates the volume of subsurface below the well path and clearly reveals faults not discernable in the surface seismic image (Fig. 6-3). The dip, continuity, and extent of the target horizon as seen in the VSP image are significantly different from their representation in the surface seismic data.

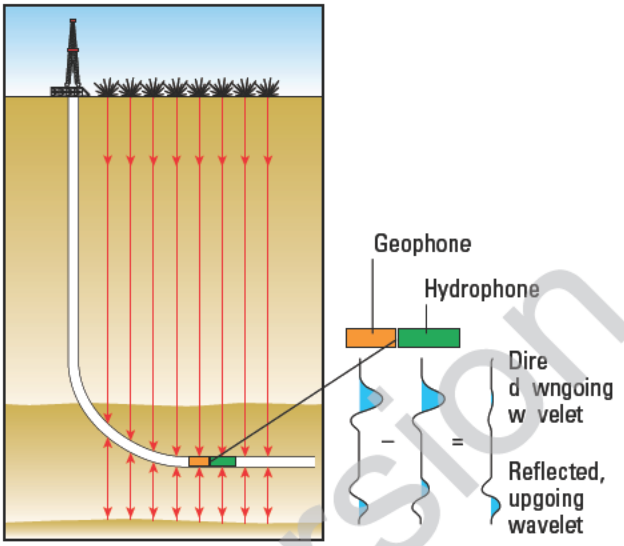

Figure 6-2. Separation of downgoing and upgoing waves in horizontal VSPs using geophone and hydrophone seismic signals. A wave arriving from above pushes the sensor in the geophone down, which records a positive motion (trace swing to the right). The same wave, having reflected below the geophone without changing polarity, pushes the sensor upward as it arrives from below (swing to the left). The resulting seismic trace consists of a positive downgoing pulse followed by a negative upgoing pulse. A hydrophone, by comparison, produces a seismic trace with two wavelets of the same polarity. Therefore, the reflected event as seen by a geophone is of opposite polarity to that seen by the hydrophone. Subtraction of one seismogram from another, after appropriate scaling, eliminates the downgoing wavelet and leaves the reflected signal. (From Christie *et al.*, 1995; this graphic is copyright Schlumberger, Ltd. Used with permission.)

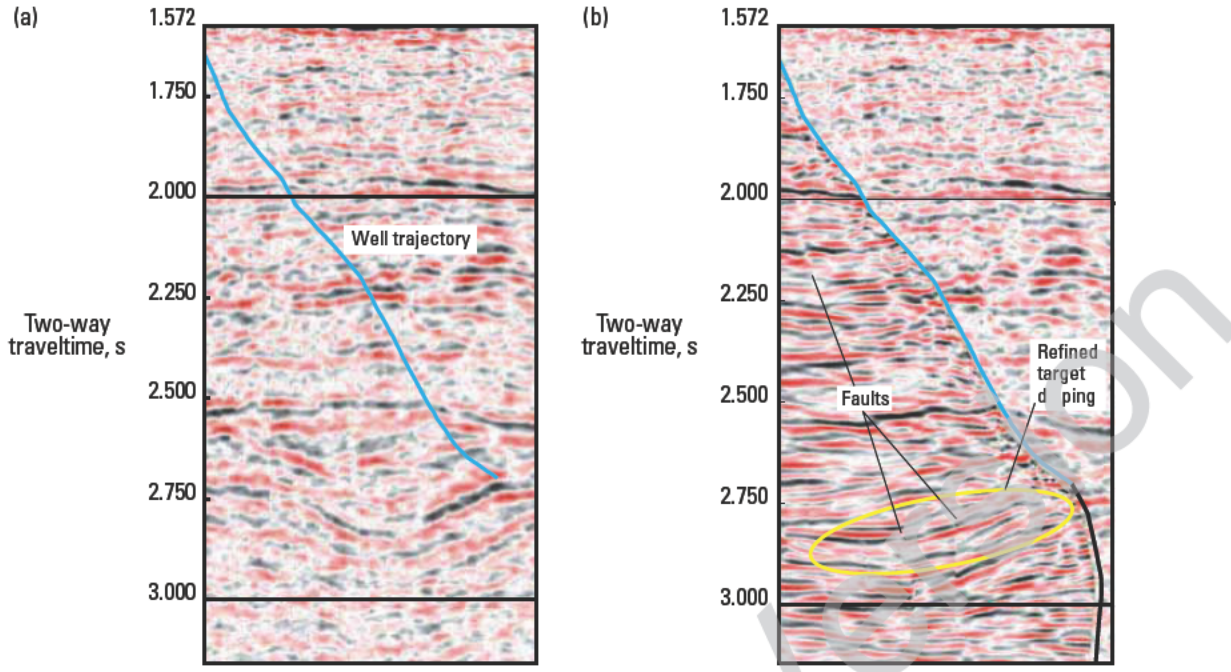

Figure 6-3. Surface seimic image (a) showing trajectory of a North Sea high-angle direc nal dev lopment well (blue line) intended to penetrate a dipping target identified on surface seismic data. High-resolution walkabove borehole seis ic mage (b) illuminates a target below the well path and reveals faults not clearly imaged in the surface seismic image. In th VSP image, the target horizon appears less continuous and with a different dip and crestal position than in the surface seismic section. (From Arroyo *et al.*, 2003; this graphic is copyright Schlumberger, Ltd. Used with permission.)

6.3 Offset VSP

In a borehole seismic experiment, whenever the position of the source(s) and receivers result in reflect on poi ts that exhibit lateral distribution, the potential exists to generate an image of the subsurface. Whenev r the geometry departs from the simple case of a ve tical ell (and hence, vertical receiver array), horizontal reflectors, and a source at the wellhead, imagi g will e a possibility. Figure 6-4 illustrates the thre obvious cases.

Whenever the source and rec iver are separated horizontally or the reflectors dip reflections will occur away from the borehole. Ob iously, any other combination of the cases in Fig 6-4 lso generates an image.

6.3 1 Presurvey considerations

The firs geophysical question that must be asked when planning an offset VSP survey with an imaging objective is: Can the zone of interest be imaged from the borehole to a great enough distance such that the image will be useful? Put more simply: How far can the VSP see? In offset VSPs, the image is built up as the geophone is raised inside the borehole. In this case, the shallower the geophone, the farther away it "sees." Alternatively, for a fixed geophone depth in the well, the greater the source offset, the farther away the reflection point will be.

For flat-layer geometries and straight raypaths, this can be answered analytically, and that analytical answer can be used as a first approximation for a more complicated reflector structure. Clearly, in the limiting case of the shallowest receiver at the surface, or of the reflector at infinite depth, the maximum reflection offset is one-half the distance to the source. Figure 6-5 shows the formula for finding the offset distance of the reflection point and a graphical set of curves for more practical application. This set of curves can be used to answer the two connected questions: How far away does the source need to be, and how shallow does the shallowest receiver location need to be?

As soon as the geometry becomes more complex, some form of modeling is required. As in surface seismic gathers, reflection points migrate up dip. It is easy to construct cases in which the illuminated zone lies on the side of the well opposite from the source. Deviated well trajectories further complicate the picture. Ray-trace modeling will show the extent of this effect by showing where the reflection points will be for a given source-receiver pair.

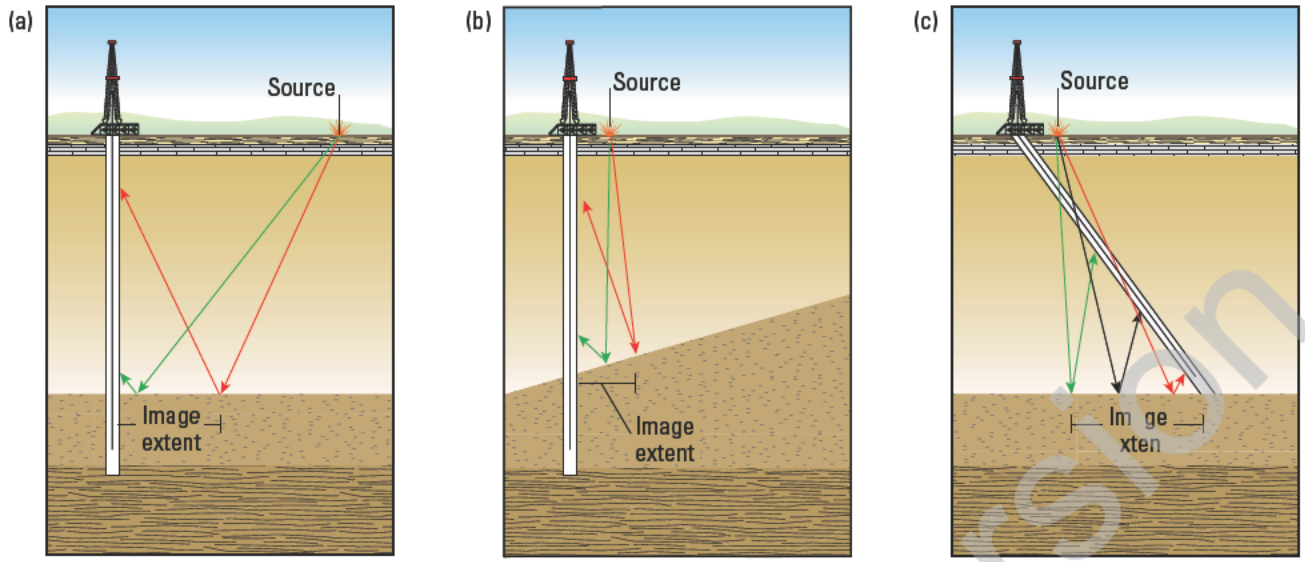

Figure 6-4. Different ways of generating lateral images from offset VSP: a) vertical well, flat reflectors, offset source; b) vertical well, dipping reflectors, zero-offset source; c) deviated well, flat reflectors, zero-offset source.

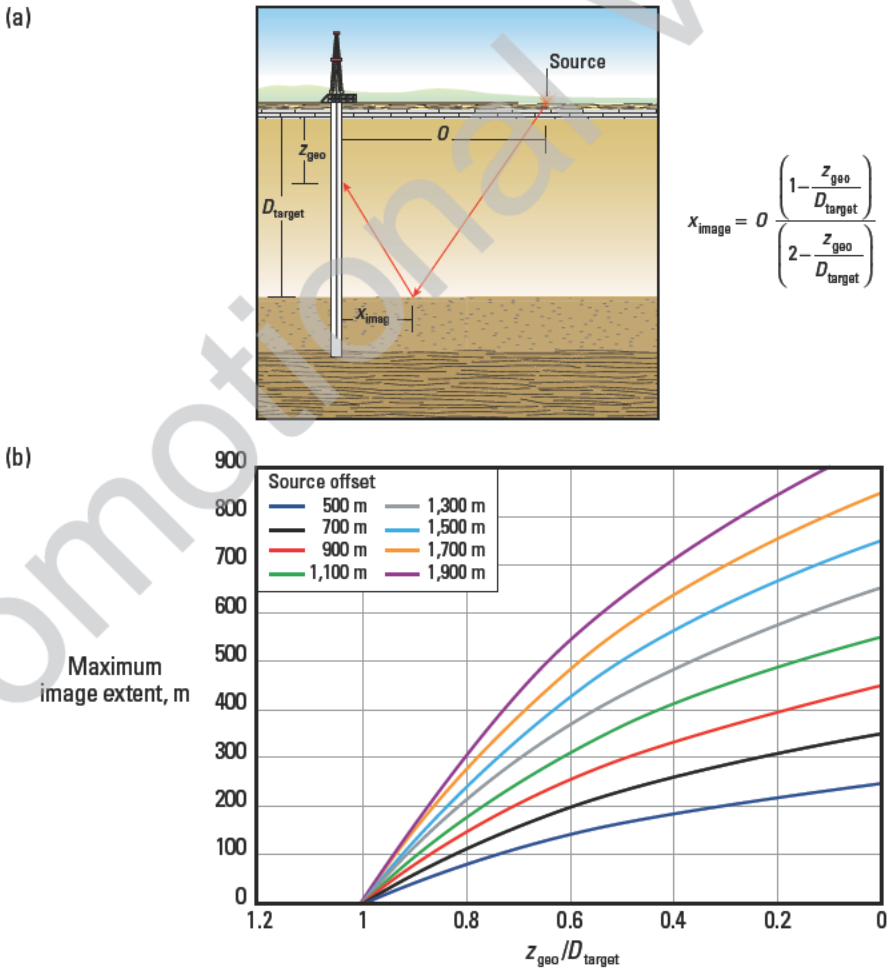

Figure 6-5. (a) Definition sketch for offset coverage from offset VSP: D_{target} = target depth, O = source offset, x_{image} = image extent, z_{geo} = geophone depth. (b) An image-extent graph for offset VSP is useful for practical applications.

The maximum source offset that can reasonably be used is another frequently asked question. To date, there is no absolute answer to this, and the guidelines vary according to the environment. The source-receiver offset distance in the VSP is equivalent to twice the source-receiver distance for surface seismic; i.e., the direct arrival on the VSP has the same angle of incidence as the reflection from the same depth in the surface seismic. Any offset distance that is more than one-half the maximum usable source-receiver offset from surface seismic gathers must be suspect, although the barrier is not absolute. Again, modeling is the way to gain understanding. An approximate rule of thumb might be that the maximum source offset should be about two-thirds of the well depth, although many good datasets have been acquired at longer offsets than this.

If offsets are large, the energy partitioning at the layers through which the ray traverses starts to favor shear waves over compressional waves. In some cases, P-S-P conversions may become significant, as in a case described by Layzell *et al*. (1987). This type of contamination is particularly damaging because the doubly converted wave is effectively a multiple source and cannot be properly compensated for.

Modeling provides the only way to analyze the more complicated cases. Ray tracing can locate reflection points, and then synthetic data can be produced to check the imaging from the migration algorithm and the sensitivity of the resulting image to uncertainties in the velocity field in two or three dimensions.

When structures are expected to be more c plex, the answers given by simple ray-tracing m dels may be inadequate. Ray-trace modeling, although fast and accurate, is normally based on the least time travel path through the model between source and re eiver. In complex geology, the recorded waveforms may c ntain multiple arrivals from the same inte face at different times. If the horizons exhibit con a e cu vature, this behavior is possible. Finite-difference modeling will be required to generate realistic synthe ic traces for such a case.

6.3.2 Acquisit on

Practical considerations may also impact the survey de ign On and, surface access to the required source location may b difficult. Equipment is large and heavy, and ground conditions, time of year, land and road own rship considerations, or environmental concerns may m ke access impossible. Oil exploration is often conducted in wild and sparsely populated areas where roads are few and expensive to build. Figure 6-6 shows an example in the Canadian Rocky Mountain foothills, in which the only practical sites for source locations are existing roads and drilling leases.

Offshore, the move away from the rig or platform adds the requirements for a boat, navigation control, remote firing systems, and mobile compressed-gas sources.

Figure 6-6. Aerial photograph in rugged terrain. Surface access is possible only along existing roads and at existing drilling sites.

6.3.3 Data processing

Figure 6-7 shows an example of data recorded from an offset VSP. Here only x- and y-components are shown. Because the source is horizontally displaced from the receivers, there is energy on the two horizontal channels of the recording, but it appears incoherent. There is also energy exhibiting two different moveouts for both upgoing and downgoing waves. This is shear wave energy converted from the compressional wave at every transmission and reflection.

The data processing elements discussed in this section may be extended to walkaway and 3D VSP processing, discussed later in this chapter.

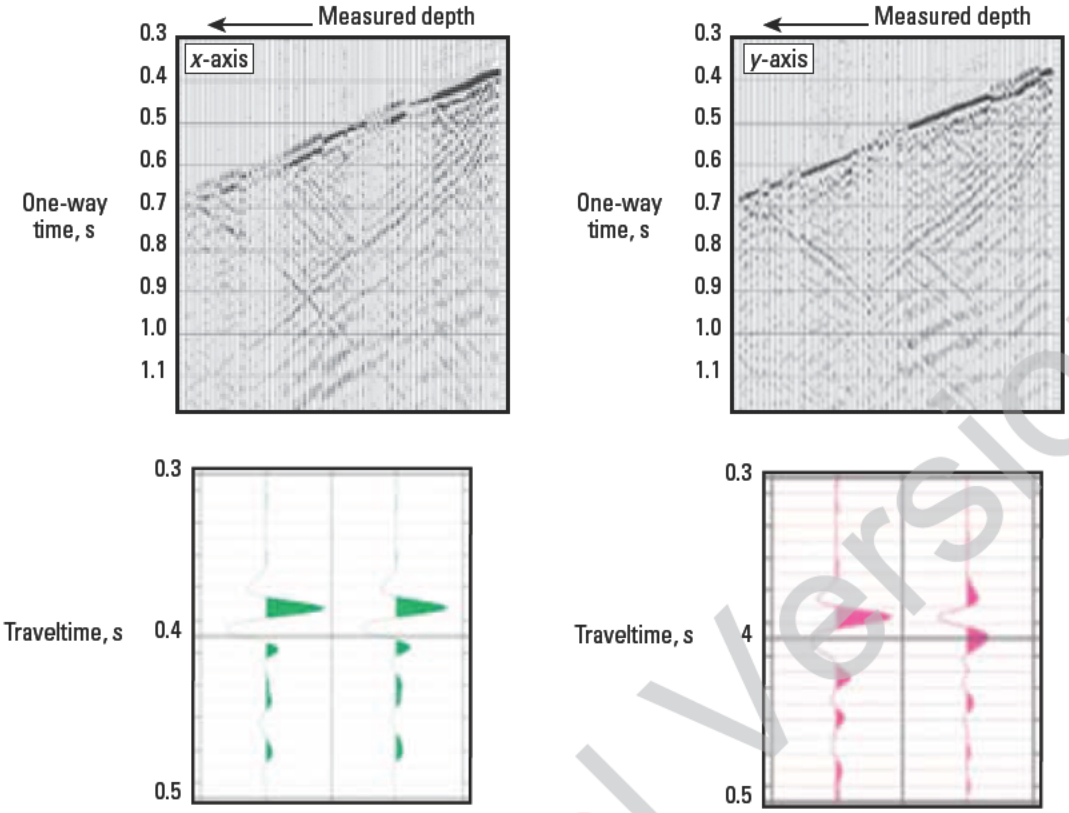

Figure 6-7. Wavefields and traces from horizontal-component data as re orded n the borehole for an offset-source VSP survey. Note the polarity flips in the direct arrivals as the tool ientation changes with depth. Green is the x-axis data; red is the y-axis data.

6.3.3.1 Data preprocessing and wave-component otation

An initial step of data preprocessing incl des loading and verification of the navigation or geographi al survey data for each offset location and the display of the data for each receiver level and for each of the three components for quality control p rposes

The orientation of the horizontal geophones in the wellbore is normally unk own and will generally vary between tool position as the tool rotates on the end of the wireline cable

The compr ssional wave direct arrival, however, has particl m tion parallel to its direction of propagation an will be the first energy to arrive at the geopho e. T erefore, if the data traces from the horizontal geophones are plotted against each other, sample-by-sample, over a short window around the time of the compressional direct arrivals, the resulting hodograms (Fig. 6-8) yield the tool orientation relative to the azimuth of the source. These data can then be transformed by an axis rotation to how they would have looked had they been recorded with a set of geophones oriented toward and perpendicular to the source azimuth (Fig. 6-9). The accuracy of this approach has been validated through testing. Several source positions were laid out at known azimuths in a semicircle around a well that had a geophone tool in it. Estimates of the azimuths were calculated from the data and compared with the actual azimuths. The results are shown in Fig. 6-10.

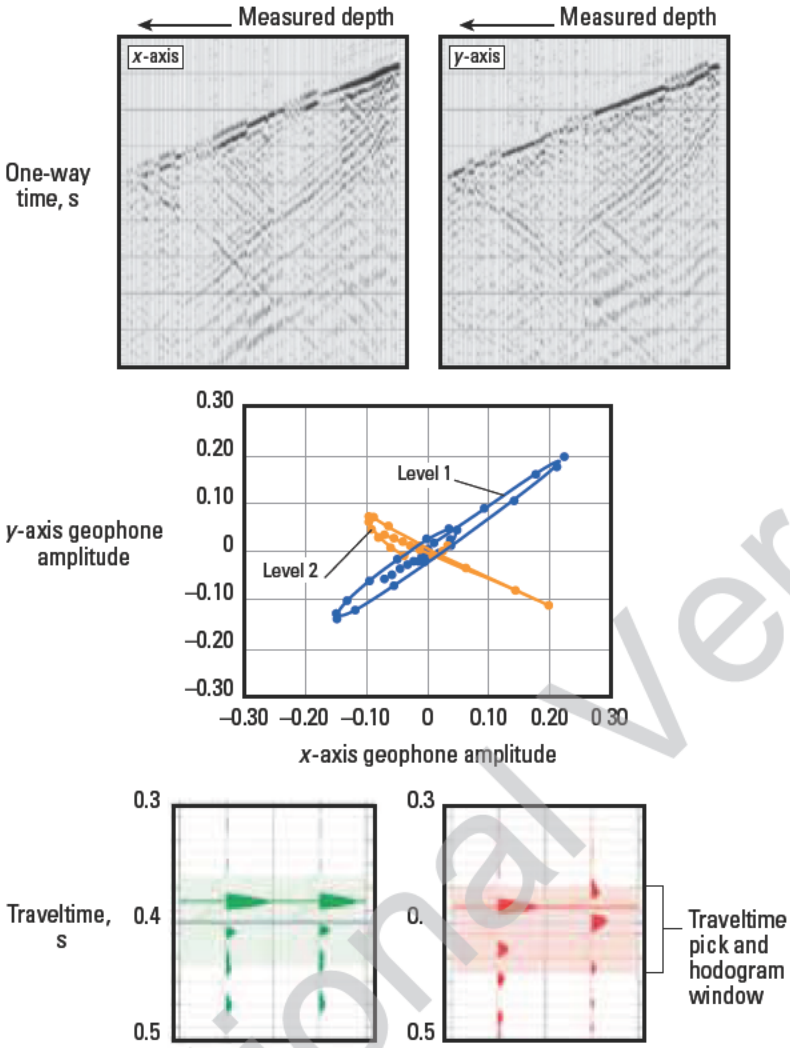

Figure 6-8. Wavefields, hodograms, and *x*- and axis t ces (green and red, respectively) for two geophone levels in a vertical well for the same of set source.

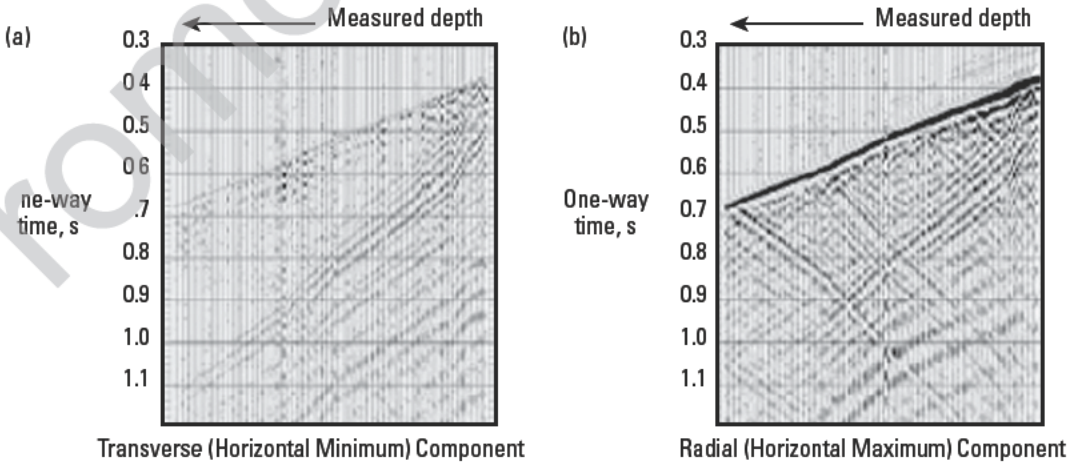

Figure 6-9. Wavefields for transverse (horizontal minimum) component data (a) and radial (horizontal maximum) component data (b) after rotation normal and parallel to the plane containing the particle motion of the direct-arrival compressional wave. The two wavefields are plotted at the same relative amplitude.

In isotropic media and in the absence of an out-of-plane structure, the process reduces the particle motion of the propagating wavefield at the borehole to a 2D motion in the vertical plane containing source and receiver. In this model, there is no coupling between particle motion in that vertical plane (P and SV) and motion perpendicular to it (SH). The horizontal component of the data oriented perpendicular to the plane after rotation should contain no energy, neither compressional nor shear, if the assumptions have been honored.

The vertical component and in-plane horizontal data show various types of wavefields passing across the receiver array. They are labeled in Fig. 6-11.

For moderate offsets, the compressional wavefield is much stronger on the vertical-axis geophone than on the horizontal one, and often the decision is made to process the vertical-axis data alone using a processing scheme similar to that used for zero-offset VSP data. However, the modern trend is to process the data from both components (i.e., the entire recorded wavefield). The VSI tool encourages this because the quality of data recorded by horizontal geophones is much better than it was only a decade ago. Horizontal geophones are more difficult to clamp tightly and uniformly in the borehole and are more affected by borehole irregularities or c sing form tion coupling. The VSI tool design, dire ted a remov ng reso-nances and improving tool-borehole con act geometry, allows the horizontal data to be us d qua titatively.

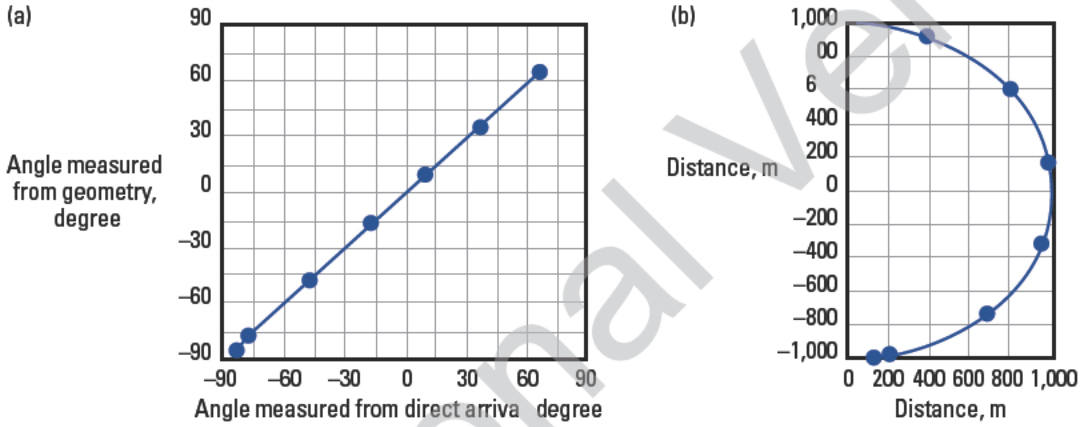

Figure 6-10. Graphs used to determine the sour e azim th from d rect-arrival polarization. (a) Source azimuth data versus geometry: points represent the a ual azi uth plotted against the measured azimuth. (b) Source positions in plan view. Th t ol d pth is 00 m, and the bedding is horizontal.

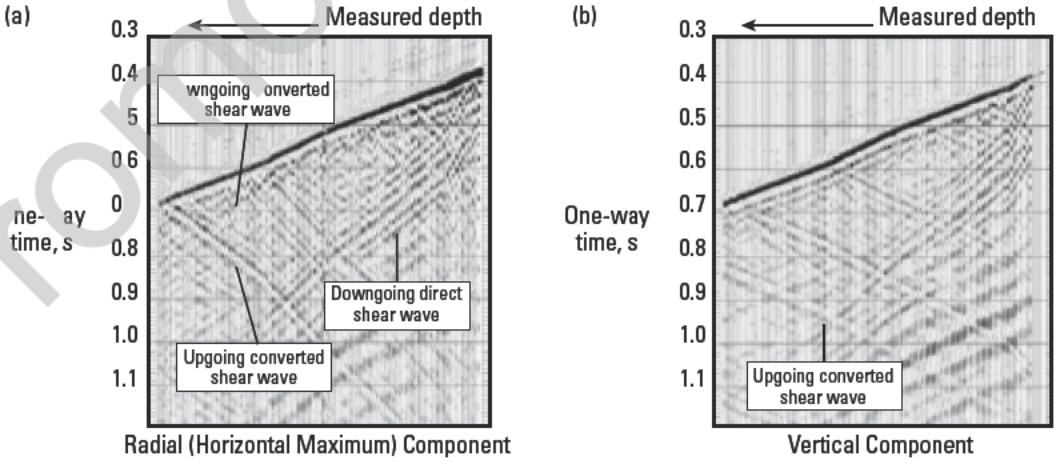

Figure 6-11. Wavefields for radial (horizontal maximum) component data (a) and vertical component data (b) after rotation. This well is vertical and situated in horizontally bedded strata.

6.3.3.2 Wavefield separation and deconvolution

Several techniques exist for separating the different wave types recorded by the array; they use the moveout differences, the particle motion polarization, or both. The data of Fig. 6-11 are shown in Fig. 6-12 after wavefield separation by parametric decomposition (Esmersoy, 1990; Leaney and Esmersoy, 1989). The assumption is made that the wavefield recorded across a subarray of the geophones can be described in terms of moveouts and polarizations from four propagating wave types: upgoing and downgoing compressional and shear waves. After each successful inversion, the subarray is moved up by one receiver position. This technique can be used either to invert for the material properties at the array or to use those properties to model the data and separate the components.

As in the case of the zero-offset VSP, deconvolution of the upgoing wavefield with an operator designed from the downgoing wavefield results in a zero-phase reflection section devoid of only the short-period multiples. Figure 6-13 shows the compressional data from Fig. 6-12 after deconvolution. The traces are still ordered by depth and do not yet represent an image of the subsurface. Special deconvolution methods have been developed for multioffset data (Haldorsen *et al.*, 1994)

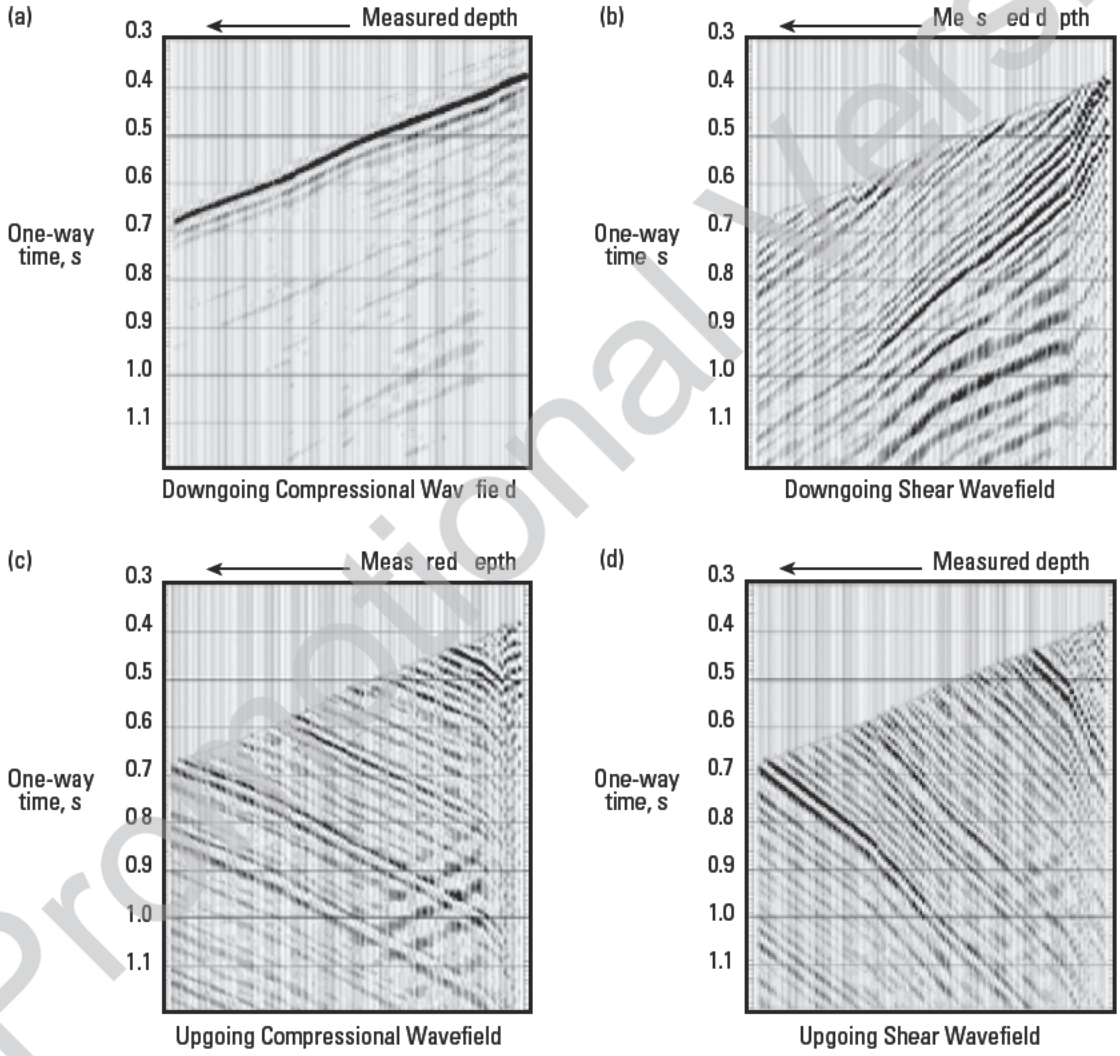

Figure 6-12. Downgoing compressional (a) and shear (b) wavefields from parametric decomposition. Most of the downgoing shear waves are mode conversions from the direct-arriving P-wave. The shear wavefield is plotted at 4 times the gain of the compressional wavefield. Upgoing (c) compressional and (d) shear wavefields from parametric decomposition. Most of the upgoing shear waves are mode conversions from the direct-arriving P-wave.

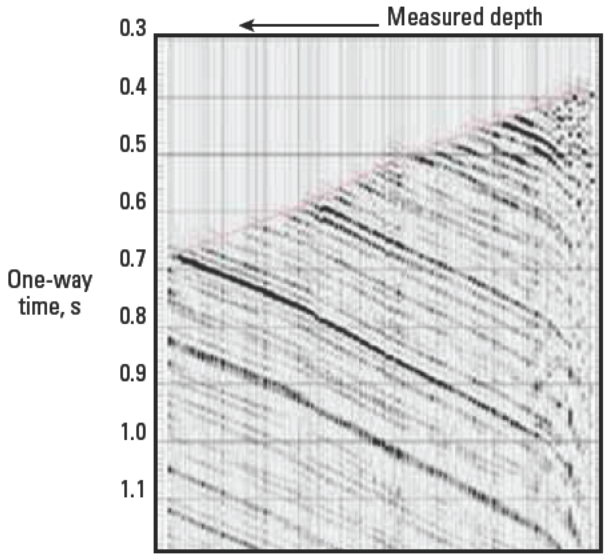

Figure 6-13. Offset VSP upgoing wavefield after waveshaping deconvolution (compressional data).

6.3.3.3 Data migration

To interpret the offset VSP data in the form of a vertical cross section requires transformation of the reflection data from the depth, one-way time domain to the depth (or offset), two-way time domain. This can be accomplished by either VSP common-depth-point (VSP CDP) mapping or migration.

An initial velocity model is the starting point for bo h of these processes. This can be generated from the s nic log, the VSP arrival times, traveltime in ersio , geolo i-cal models, seismic sections, or any other vail ble and relevant data.

Also discussed in this section is bor hole seismic interferometry, an emerging imaging technology aimed at transforming signals previously considered noise into valuable information.

VSP CDP mapping

For each source-receiver pair, ray tracing of reflection events to each nterfac is performed through the model. Each ray w ll hav a traveltime associated with it as well as a ref ection point in depth and offset. By interpolation, each time sample on each trace can be associated with a point in the model. Therefore, the image can be built by mapping the seismic amplitudes from the receiver traces (in time) to their spatial location in the model. This amplitude mapping builds an image in depth. The depth image can be converted, by using the velocity model, to CDP-style traces in two-way time.

The process above associates each time sample on a trace with a point in offset and depth in the model. If the depth term is converted to two-way time, the data can be mapped into two-way time as receiver traces—a model-based NMO correction. This intermediat step is particularly useful to interpret offset VSP data. I can be plotted with the offset values as a ontour display in an overlay. The overlay display all ws the user to see from where in the VSP domain a partic lar image point originated. Figure 6-14 shows such a display for the data of Fig. 6-13. In Fig. 6-14, th traces represent increasing offset from the well and two way time. They form a mini-seismic section that an e in rpreted in the same way as the surface eism c secti n.

Where a model of the shear velocity structure can also be derived, the imaging operation can be performed for converted shear-wave reflections as well as for the c mpressional wavefield. Because the underlying mapping is to a depth model, the shear and compressional images can be derived on a common depth scale with an abso ute match between the compressional and shear responses. Once mapped in depth, the images can be c nverted to two-way compressional time, two-way shear time, or converted-wave time to surface.

The procedure is a data-independent mapping—a direct mapping of sample amplitude value through a ray-traced lookup table—not a migration, which is a more rigorous and correct approach to the problem of imaging. Nevertheless, the products perform a useful interpretational service on structurally straightforward data, as it is very easy to identify receiver-dependent effects in the image. It is also easy to gain a visual impression of the density of reflection-point coverage as a function of image-point offset (reflection-point coverage is denser away from the wellbore and sparser near the well). In addition, because it is a simple mapping tool, it should not change reflection amplitudes because of any weighting factor. Thus, its results can be used to perform true-amplitude analysis in the model domain if the data are rigorously processed.

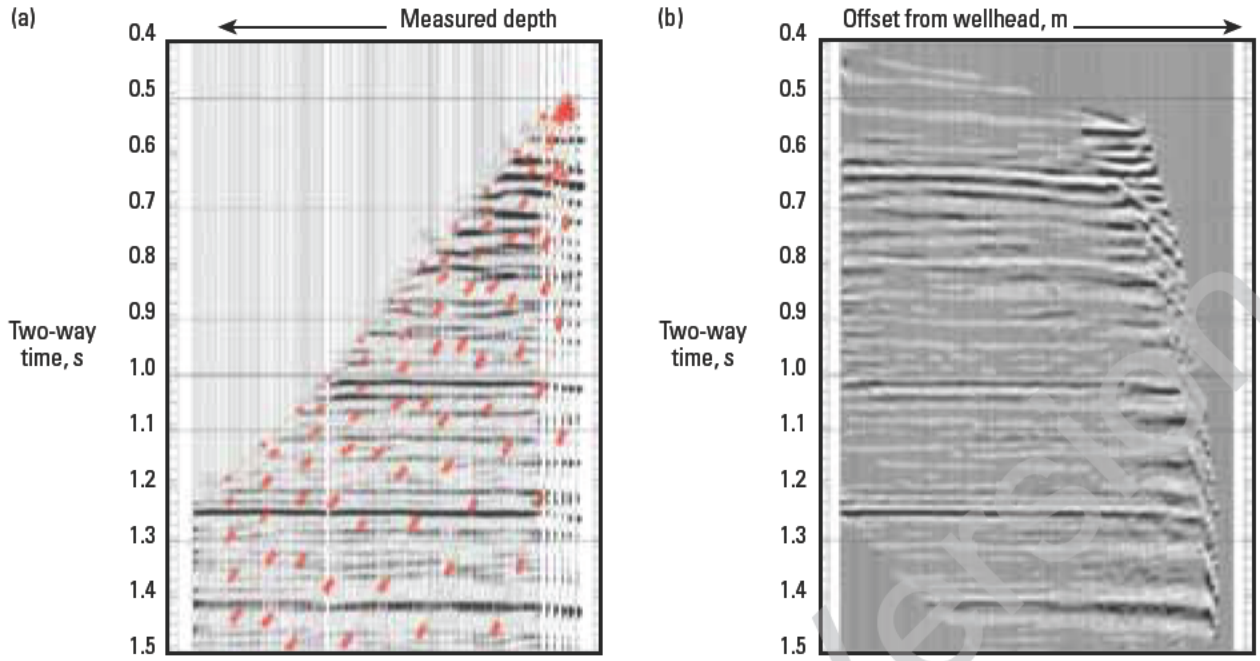

Figure 6-14. Offset VSP upgoing wavefield after NMO (a) and CDP (b) mapping. Note th contour of equal reflection-point offset on the NMO panel.

Migration

Although VSP CDP mapping is robust and effective, it is a model-based mapping process. It is based on the assumption that the structure in the velocity model is correct and that the geophone responses result only from specular reflection at the interfaces; there is no account for scattering. Migration, on the other hand, reconstructs an image of the subsurface by collapsing the diffraction response of each point ba k to its source (i.e., reflector or diffractor) using the velocity model to construct the shapes o the di fraction curves (Hagedoorn, 1954). Comput mig ation of seismic data emerged in the late 1960s as natural outgrowth of manual migration techniqu s based on wavefront charts and diffraction curves, and i has been developed by application of wave theory since the 1970s. Integral-equation techn ques (Schneider, 1978) and difference-equation techniques (Claerbout and Doherty, 1972) ha e b en developed. The basic idea of the integral-equation techniques is that each point in the Earth can b imaged by integrating the scattered signals from that point with weights over observations. The actual computation f the integral-equation technique appears as a weighted diffraction stack. Because the Green's function used to compute the weights is derived by ray tracing, the method is often referred to as ray-based migration. Kirchhoff and generalized Radon transform (GRT) mi ation methods are examples of integral-equation techn ques: Kirchhoff migration evolved from the clas- s cal diffraction stack first suggested in the Kirchhoff formula (French, 1974, 1975; Schneider, 1978). The GRT migration method formalizes the classical diffraction stack by relating it to linearized seismic inversion of velocity and the generalized Radon transform (Miller *et al.*, 1987). The formula used in GRT migration resembles standard Kirchhoff migration.

The difference-equation technique is generally referred to as wave-equation migration (WEM), and it tracks recorded signals downward to the reflectors using the finite-difference method. The use of difference-equation techniques was traditionally difficult for a complex survey geometry and velocity model because it required a huge computational effort. As a result, the integral-equation techniques have been predominantly used in borehole seismic data migration. However, with the recent development of new algorithms to solve the equations and the increase of computational power, the use of difference-equation techniques is rapidly increasing. Wave-equation migration and reverse time migration (RTM) are methods that use the difference-equation techniques: wave-equation migration is also called wave-extrapolation migration. The recorded waveforms are downward extrapolated using a one-way wave equation. This computation is done in the frequency-wavenumber domain in the horizontal

direction (Gazdag and Sguazzero, 1984). The image is extracted by image conditioning and by combining the impulse response from the source. RTM propagates the recorded waveforms backward in time (Baysal *et al.*, 1983).

Migration methods based on the difference-equation algorithm require much longer computation time than those based on the integral-equation technique. Theoretically, the wave-equation migration provides better images than the integral-equation technique because the former includes the frequency dependency, multipathing, and complex scattering; and it is free from ray-tracing failure, which causes noise artifacts and blanks in the image. Note that the quality and reliability of the migrated image is largely dependent upon the quality and accuracy of the velocity model.

The migration has two conceptual parts. The first is the determination of the traveltimes (within the model) from the source to each point in the subsurface and from any point in the subsurface to each receiver (Fig. 6-15). This set of traveltimes defines the set of moveout hyperbolae within the data from which scattered energy could contribute to the measured response at the receiver. The set of traveltimes is often referred to as a traveltime lookup table because it can be calculated once for any model and then used to look up the traveltim s fo any subsurface point and shot-receiver pair Fig. 6-16).

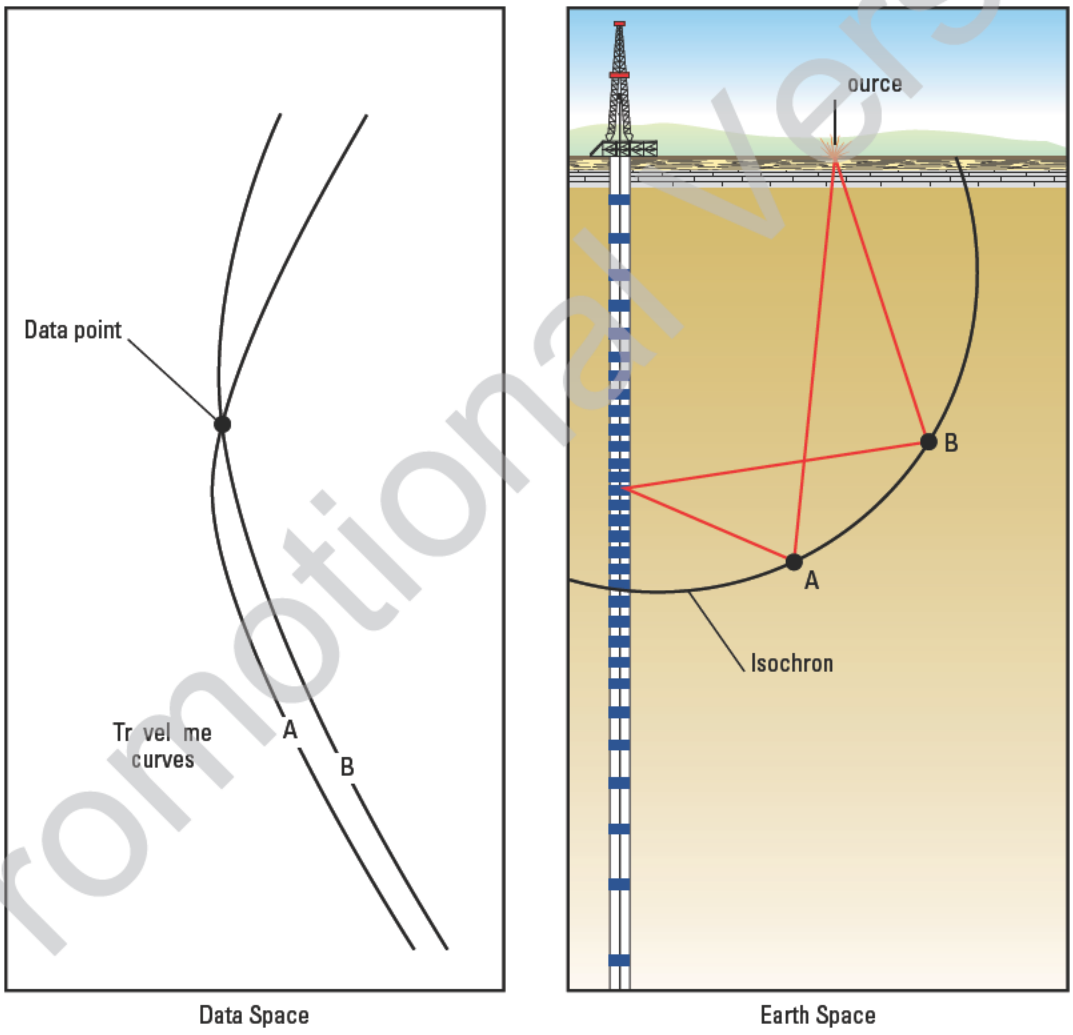

Figure 6-15. Each Earth-point scatterer contributes to any data point lying on its traveltime curve. Conversely, a data point represents the sum of wavefields scattered by all Earth points on its isochron, an ellipse drawn in Earth space with the source and geophones as foci. (From Beylkin *et al.*, 1987; this graphic is copyright Schlumberger, Ltd. Used with permission.)

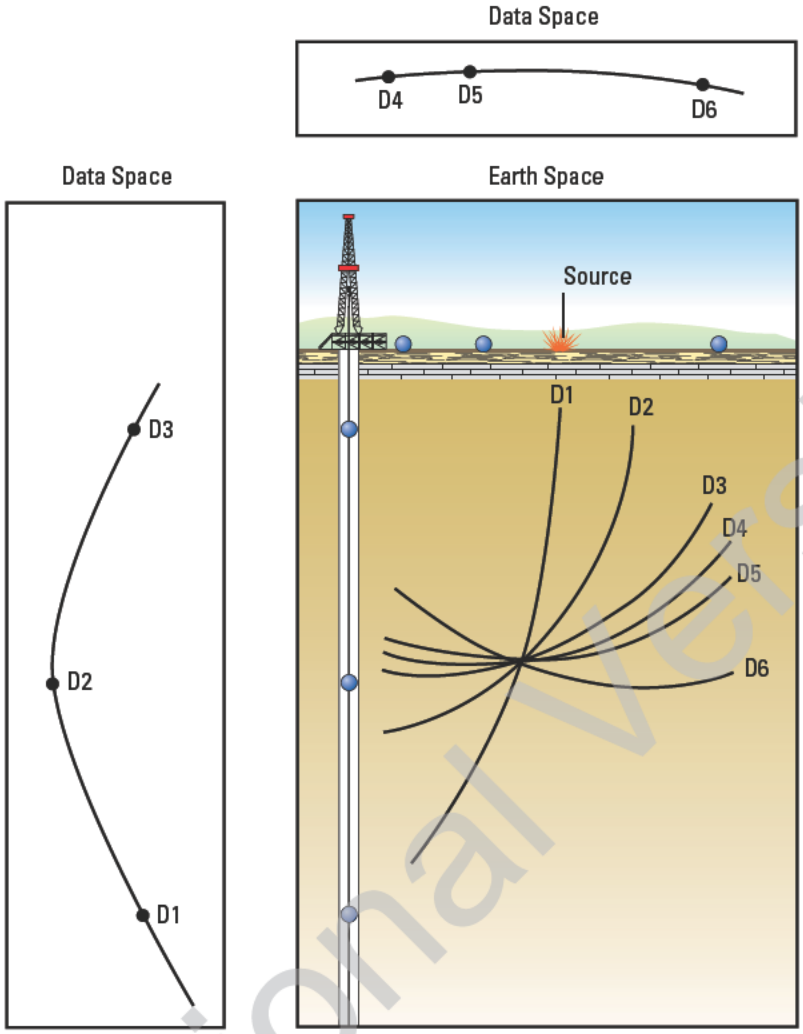

Figure 6-16. Radon's inverse transform applied to mig ting seismic data. Each point in the seismic image is reconstructed by calculating the Radon weigh d aver ge of data points whose isochrons pass through the point. (From Beylkin *et al.*, 1987; this gr phic is c pyright Schlumberger, Ltd. Used with permission.)

Traditional approache to uilding the traveltime lookup tables through the model have used ray tracing (i.e., Kirchhoff migra on). The following two problems are associated with this approach:

- In complex elocity models and in three dimensions, it may be very difficult (and time-consuming) to find som of the rays.
- Normally, some approaches will determine only the hortest traveltime in complex velocity fields in which multiple raypaths may exist, and most of the energy may not take the shortest timepath.

The traveltimes calculated through the model define the samples in the data that can contribute to the image of a point. The more complex part of this problem is the definition of weightings to apply to each data point in image reconstruction. This is particularly complex in the case of VSP data compared with surface seismic data because the range of incidence angles in VSP data is often much larger than that for a surface shot or CDP gather.

A synthetic dataset shown in Fig. 6-17 simulates a vertical-incidence VSP sampled with 80 geophone levels in a well deviated more than 60°. The velocity model includes dipping layers, a fault discontinuity, and a point anomaly. The migration method is a powerful method that can yield accurate mapping in such conditions. A comparison of the results from conventional imaging and GRT imaging methods is shown in Fig. 6-18 on a real seismic dataset. A CDP-based mapping technique does not render a clear stratigraphic picture, whereas the image obtained through the GRT imaging method clearly reveals the reservoir pinchout between the two wells. This explains why the well was dry.

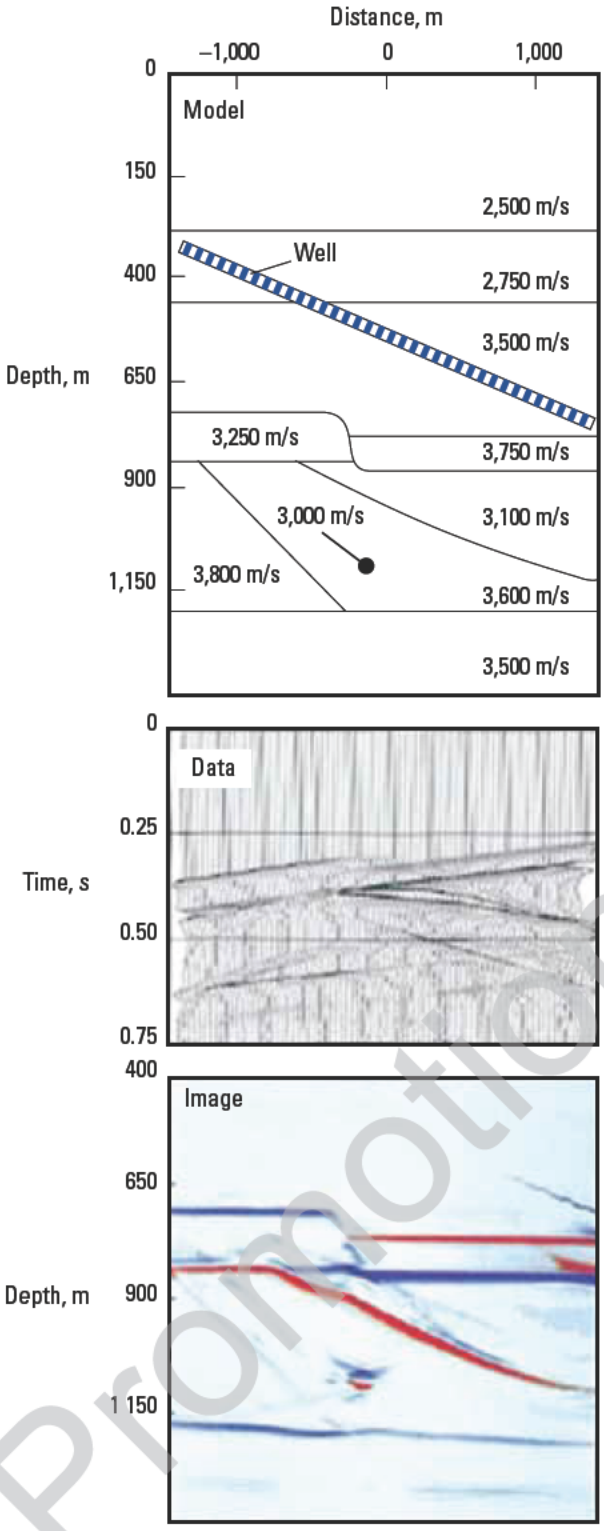

Figure 6-17. Computer simulation of GRT migration applied to a deviated-well offset seismic profile. Example is based on an 80-geophone dataset. (From Beylkin *et al.*, 1987; this graphic is copyright Schlumberger, Ltd. Used with permission.)

Extension of the GRT migration method uses compressional and shear waves in what is referred to as multiparameter migration or inversion (Beylkin and Burridge, 1987). This allows more realistic Earth models that consider that seismic energy is not scattered equally in all directions, which is the major limitation of previous migration techniques. This technique permits better lithologic and petrophysical interpretation of seismic images.

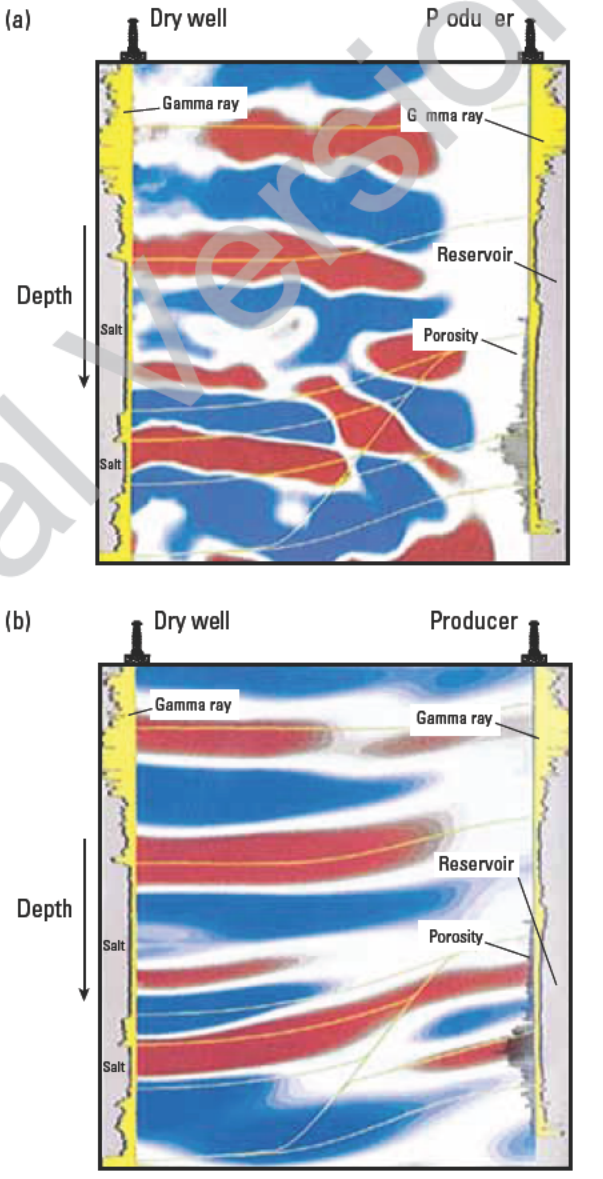

Figure 6-18. Images obtained when migrating same borehole seismic data differently. Image obtained with conventional reflection-point mapping (a) fails to illuminate stratigraphy properly. Image obtained with GRT migration (b) shows how the reservoir top, as interpreted from logs at the producer, pinches out before reaching the dry well. (From Beylkin et al., 1987; this graphic is copyright Schlumberger, Ltd. Used with permission.)

Interferometry

One promising processing technique is interferometry, which is the interference of two or more waves to produce an output wave that is different from the input waves. This technique is used to condition the seismic data prior to migrating it with any of the methods described previously. Researchers are investigating ways to use interferometry to transform signals previously considered as noise into valuable information. For instance, in typical VSP data-imaging workflows, only primary reflections are migrated. Free-surface multiple reflections are usually regarded as noise and thus eliminated before migrating the recorded data. Although benefiting from reduced attenuation and improved velocity control with respect to migrated surface seismic data, the resulting migrated VSP images are restricted to a relatively narrow zone of illumination lying below the borehole receivers. However, free-surface-related multiples contain valuable information about shallower subsurface structures, and if properly migrated, they can provide wider illumination and better vertical resolution of the subsurface properties than when imaging with primaries alone (Fig. 6-19). More detail on interferometry techniques can be found in Djikpesse *et al.* (2009).

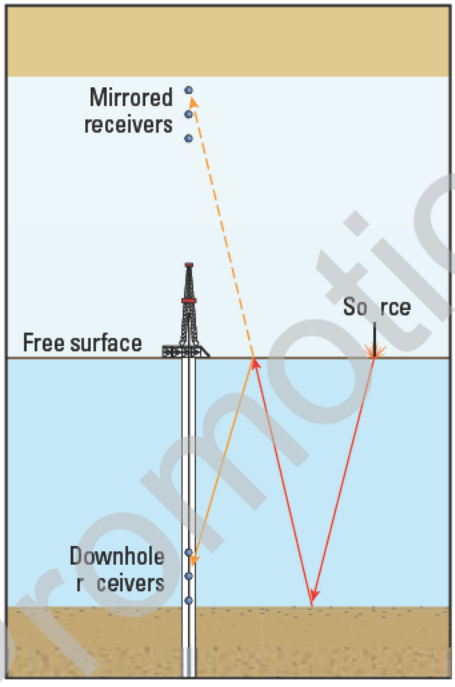

Figure 6-19. Mirror imaging is an example of interferometry. The free surface and the area above it are replaced by a mirror image of a medium with the same elastic properties as the medium containing the borehole and receivers. Receivers in the new material are the mirror image of the original receivers. Whereas the original borehole seismic experiment had a zone of illumination restricted to below the receivers, the mirrored experiment has a zone of illumination that extends to the former free surface. (From Blackburn *et al.*, 2007; this graphic is copyright Schlumberger, Ltd. Used with permission.)

6.3.4 Converted shear-wave imaging

Shear waves are an extremely useful tool with which to interrogate the Earth's geology. Their potential has been recognized for years in the surface seismic industry, but practical results have fallen short of expectations.

6.3.4.1 Benefits of shear waves

S-waves have slow velocity; therefore, they offer potentially greater resolution. For a given frequency content, the wavelength of the shear wave will be less than that of the equivalent compressional wave. Because resolving power is proportional to wavelength, the shorter wavelength of the shear wave gives it greater ability to resolve small events or thin beds.

S-waves convey different response and information compared with classic P-wave seismic data. Compressional waves respond to the acoustic impedance (density multiplied by velocity). They are not affected independently by the stiffness of the rock—they cannot distinguish between cork and rubber. Shear waves are sensitive to the shear modulus, and therefore, events with low compressional wave reflectivity may be strong converters of downgoing compressional waves to reflected or transmitted shear waves.

6.3.4.2 Limitations of shear waves

In the surface seismic experiment, shear waves often failed to live up to expectations, and as a result, their use was not widespread. However, there is a current resurgence of interest with the increasing use of ocean-bottom cable (OBC) acquisition of marine data with four-component sensors.

The main problem has been that the shear wave has to spend part of its traveltime in the unconsolidated near-surface section, either on the way up to the geophone in the case of a converted wave or on the way both down and up in the case of a surface shear source. The near surface stratal interval is one part of the Earth that cannot support shear stress, and as a result, the shear waves that are recorded tend to be noisy and of low frequency.

A second limitation is the availability of sources. There are not many surface sources that can generate direct shear waves (shear vibrator discussed in Chapter 3; and the less-common impulsive shear sources such as the inclined accelerated weight drop and inclined airguns). These sources are sparsely distributed geographically, so mobilization costs to acquire such data tend to be high.

6.3.4.3 Converted shear-wave VSP

One way to avoid most of the limitations is to restrict consideration to converted shear waves and the offset VSP (or the walkaway) geometry. Here there is no need for a specialized shear-wave source, and the shear wave spends no part of its travel path in the unconsolidated near-surface section. The receivers are well coupled to the Earth in the borehole, with a positive anchoring force significantly greater than their own weight, and are in a much quieter environment than they would be if on the surface.

The starting point for this illustration is the 3C data shown in Fig. 6-11 after decomposition into the four basic scalar wavefields (Fig. 6-12). The upgoing shear wavefield shows many distinct, upgoing shear events. The depths at which the mode conversions occurred that created them are clearly identifiable (the depth at which the upgoing shear event intersects the downgoing, compressional direct-arrival curve). Figure 6-20 is an enlargement of the relevant portion of Fig. 6-11. If one tracks the event indicated as its travel path as a shear wave lengthens, it is clear that the frequency content does not change very quickly. This indicates that, in the surface seismic case, it is indeed the near-surface unconsolidated material that attenuates the high frequencies.

At the point of conversion from compressional to shear, the frequency content of the two waves must be identical (extra peaks and troughs cannot be created or destroyed), and the only net effect of the conversion is a change in amplitude, analogous to the reflectivity for a P-to-P reflection. Therefore, the waveshaping deconvolution operator derived from the downgoing P wavefield is directly applicable to the upgoing shear wavefield; it collapses those multiples that were generated in the P-wave portion of its travel path and transforms them to zero phase (assuming the desired output from the waveshaping was zero phase). The result of the deconvolution operator applied to the upgoing shear waves from Fig. 6-20 is shown in Fig. 6-21.

The deconvolved shear waves can be VSP CDP-mapped or migrated to form an image in the same way as that of the compressional reflected wavefield. The NMO-corrected traces with overlaying offset contours are shown in Fig. 6-21, and the image in offset and compressional two-way time is shown in Fig. 6-22. The shear-wave velocities must be known for the model, derived either from shear sonic logs (from the parametric inversion) or by traveltime inversion if the shape of the geological interfaces is known.

Because the VSP migration process is a depth migration (as is VSP CDP mapping), the resulting images for both compressional and shear data will be in depth and can be displayed adjacent to each other on the same scale and at the same scale as the corrected sonic and synthetic data. Thus, an absolute correlation can be made between the compressional and shear responses to a given geological interface. Figure 6-22 shows a composite display of these in P wave time. The absolute correspondence of event

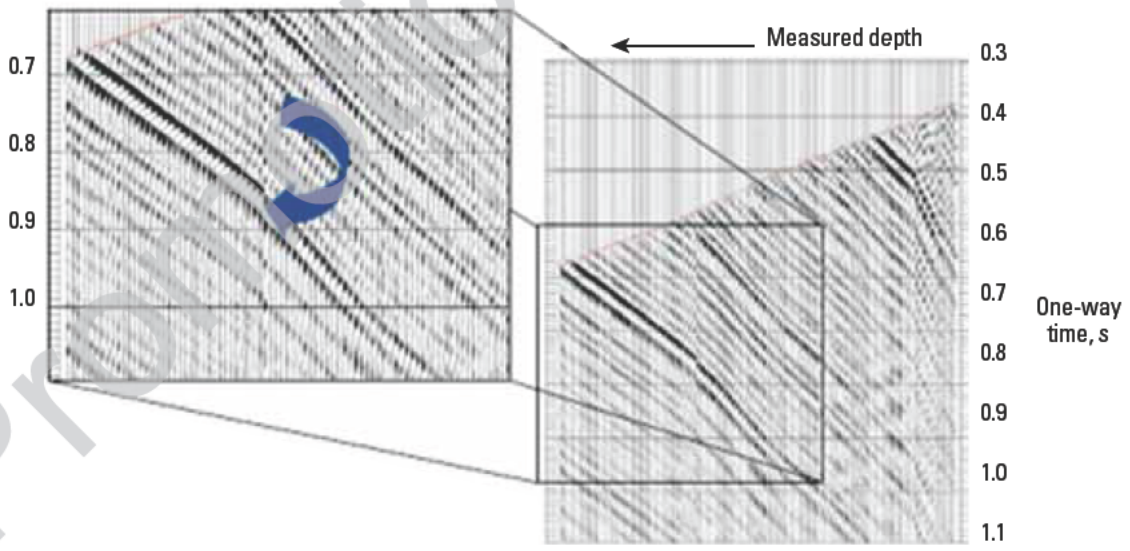

Figure 6-20. P-S mode-converted upgoing shear event reflected from an interface near the bottom of the well in Fig. 6-11. Note the consistency of the event as the distance from the reflector to the geophone increases (deep to shallow: left to right).

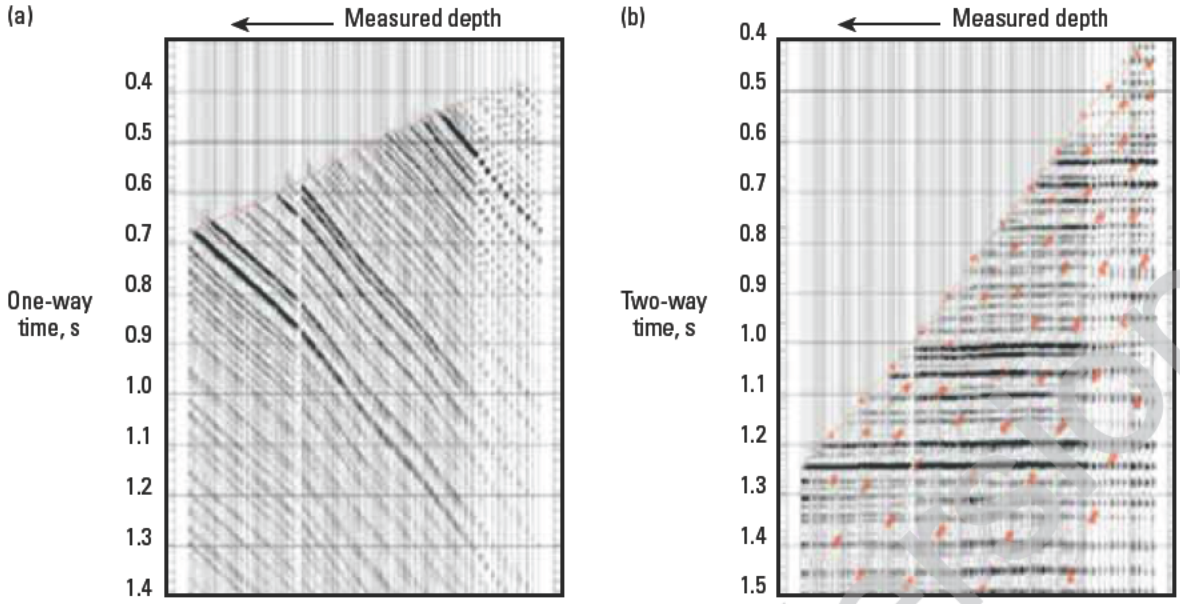

Figure 6-21. Converted shear-wave data from Fig. 6-20 after deconvolution (a) and after subsequent NMO recovery (b).

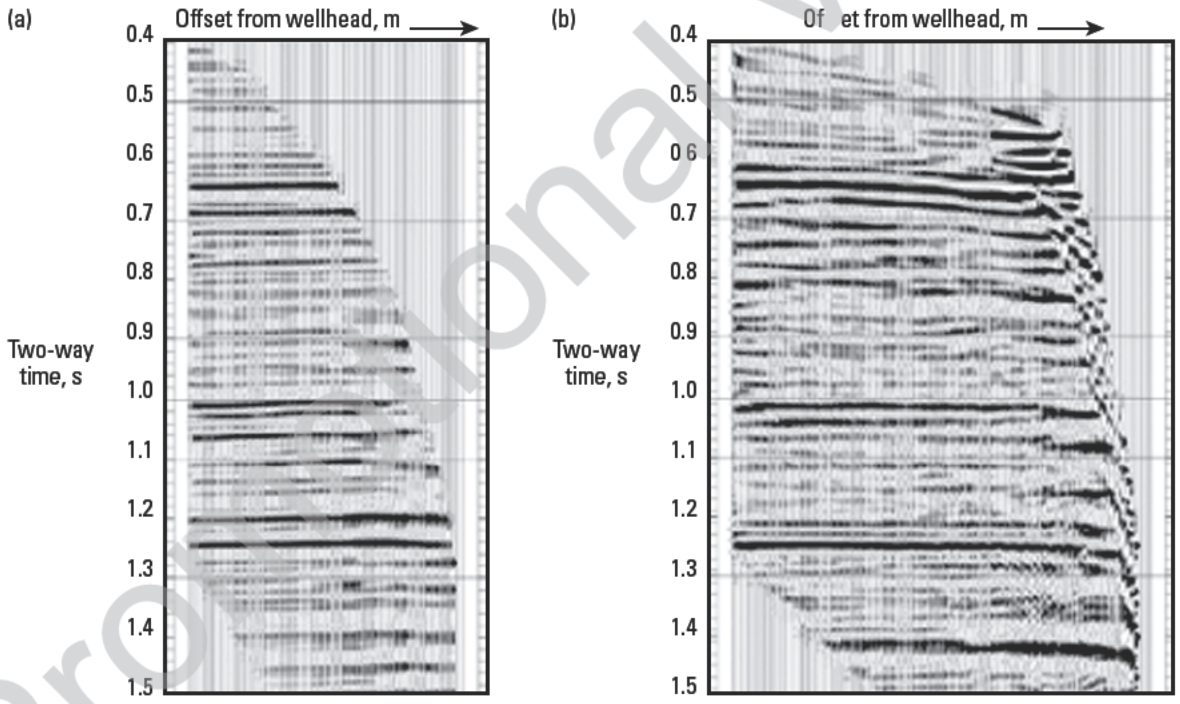

Figure 6-22. VSP CDP maps of shear-wave image (a) and compressional-wave image (b) displayed in two-way P-P time (data from Figs. 6-20 and 6-21).

times between the compressional and shear images and the further absolute correspondence to well logs that have been converted from time to depth using the same velocity function are crucial and unique benefits of the VSP in the interpretation of converted-shear seismic. There is no other way to unambiguously correlate reflection events between their compressional and shear manifestations and to tie them directly to events in depth in the borehole logs.

The shear-wave image provides resolution at least as good as the compressional image and emphasizes different events because it discriminates only stiffness and is unaffected by compressibility.

6.3.4.4 Case study—Shear waves from VSP

The Cuitláhuac field, located in the Burgos basin of northern Mexico, became a candidate for reactivation (Arroyo *et al.*, 2003). The 200-km² field has been producing since 1951. This field is composed of about 20 sand packages that have experienced NW-SE trending normal faulting. Each fault block acts as a separate production area and has different pressures and seismic velocity variations.

The field engineers sought new technologies to help identify undrained areas and found success with the results obtained by the VSI borehole seismic acquisition system. Using P- and S-wave velocities and impedance values derived from zero-offset and offset VSPs, interpreters hoped to track lithology and hydrocarbon-bearing sands to assist future well placement. The VSI tool recorded 3C wave motion with high fidelity, which yielded accurate P and S wavefields even when the source type and acquisition geometry was not favorable (Armstrong *et al.*, 2001). An example (Fig. 6-23) from the Cuitláhuac field shows strong shear signals from a vibrating source, designed to emit only P-waves, in a zero-offset source geometry with nearly flat-layer geology. The panels of shear data show the expected downgoing P-wave and P-waves converted to both downgoing and upgoing S-waves. In addition, there is an S-wave propagating directly from the source along with S-wave reflections.

These zero-offset VSP data, processed for P-to-P reflections and S-to-S reflections, yield two corridor stacks that may be compared with synthetic seismograms computed from compressional and dipole shear sonic logs calibrated with the VSP velocities (Fig 6-24).

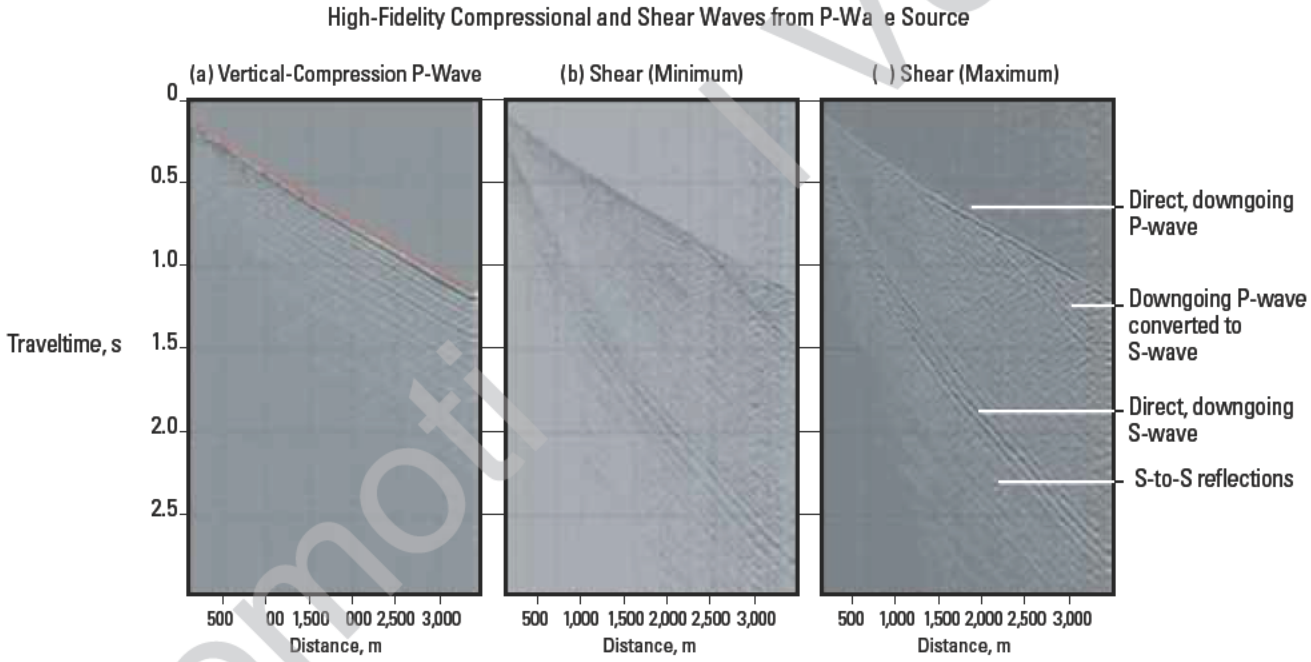

Figure 6-23. Multicomponent data from zero-offset, vertical-well VSP, processed to yield P and S wavefields. The acquisition configuration, with the source near the rig and the receivers in a vertical well, is not ideal for recording shear-wave energy. However, the VSI tool acquires excellent multicomponent data. The vertical component data shown in (a) contains P-wave arrivals. The tool's two horizontal components have been mathematically rotated to produce one component aligned with the direction of minimum S wave energy (b) and one component aligned with the direction of maximum S-wave energy (c). (From Arroyo *et al.*, 2003; this graphic is copyright Schlumberger, Ltd. Used with permission.)

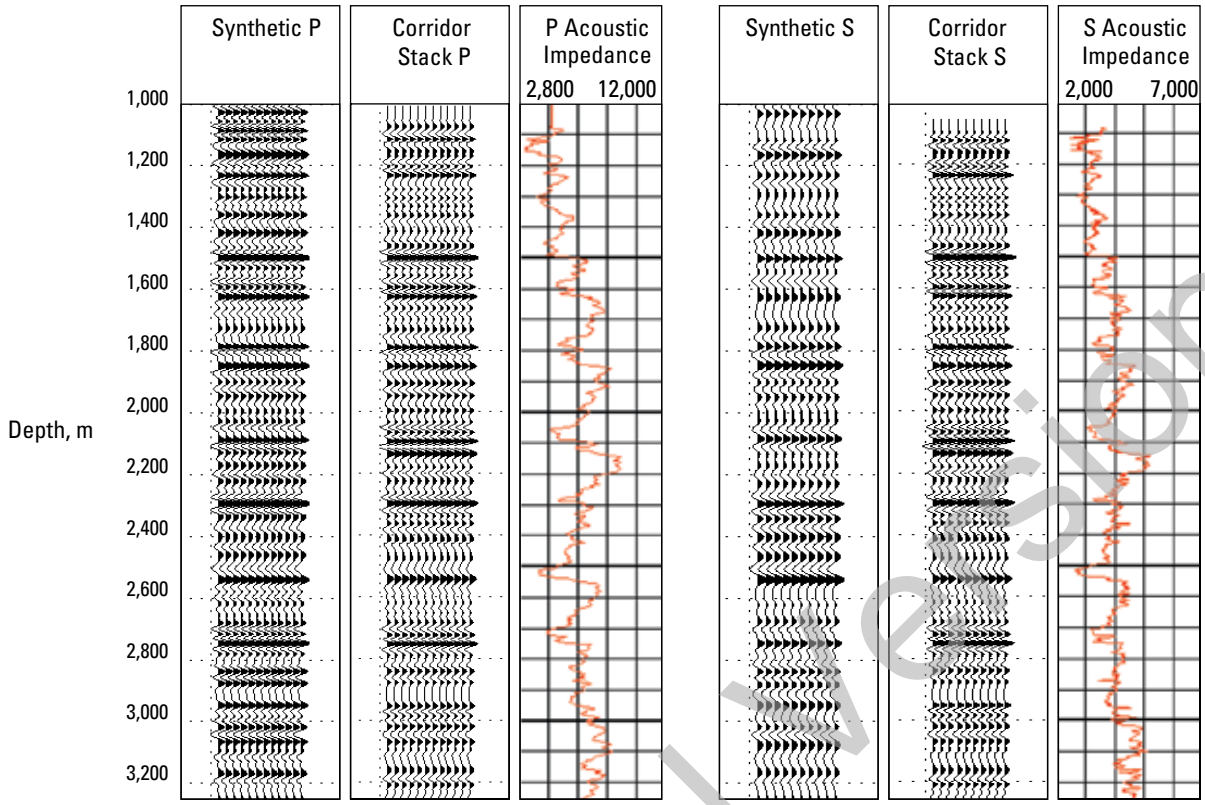

Figure 6-24. Comparison of VSP corridor stacks, synthetics, and acousti imp dance models for P and S wavefields. The high-quality match between corridor-stack data and syn etics shows that the acoustic-impedance model is a good representation of subsurface e astic properties. (From Arroyo *et al.*, 2003; this graphic is copyright Schlumberger, Ltd. Used w th pe ission.)

The excellent match shows that the acous ic-imped-ance model fits the properties of the layers in the vi in-ity of the borehole, and that normal-incidence seismic amplitudes may be used to infer reservoir properties in this field.

The offset VSP data were processed to produce images of the subsurface (Fig. 6-25). One image shows the standard P-to-P reflec ons, whereas the other shows P-to-S reflections. Both disp ay a good match with the surface seismic section t the well location.

The P-wave and S-wave velocity and impedance information derived from these and other zero-offset and offset VSPs are being used to constrain lithology and fluid-contact interpretations from existing surface seismic data as well as from additional multicomponent surveys acquired. Velocity and attenuation information from the VSPs is expected to help in the processing of the multicomponent surface surveys and to define a clearer picture of bypassed hydrocarbons in the Cuitláhuac field.

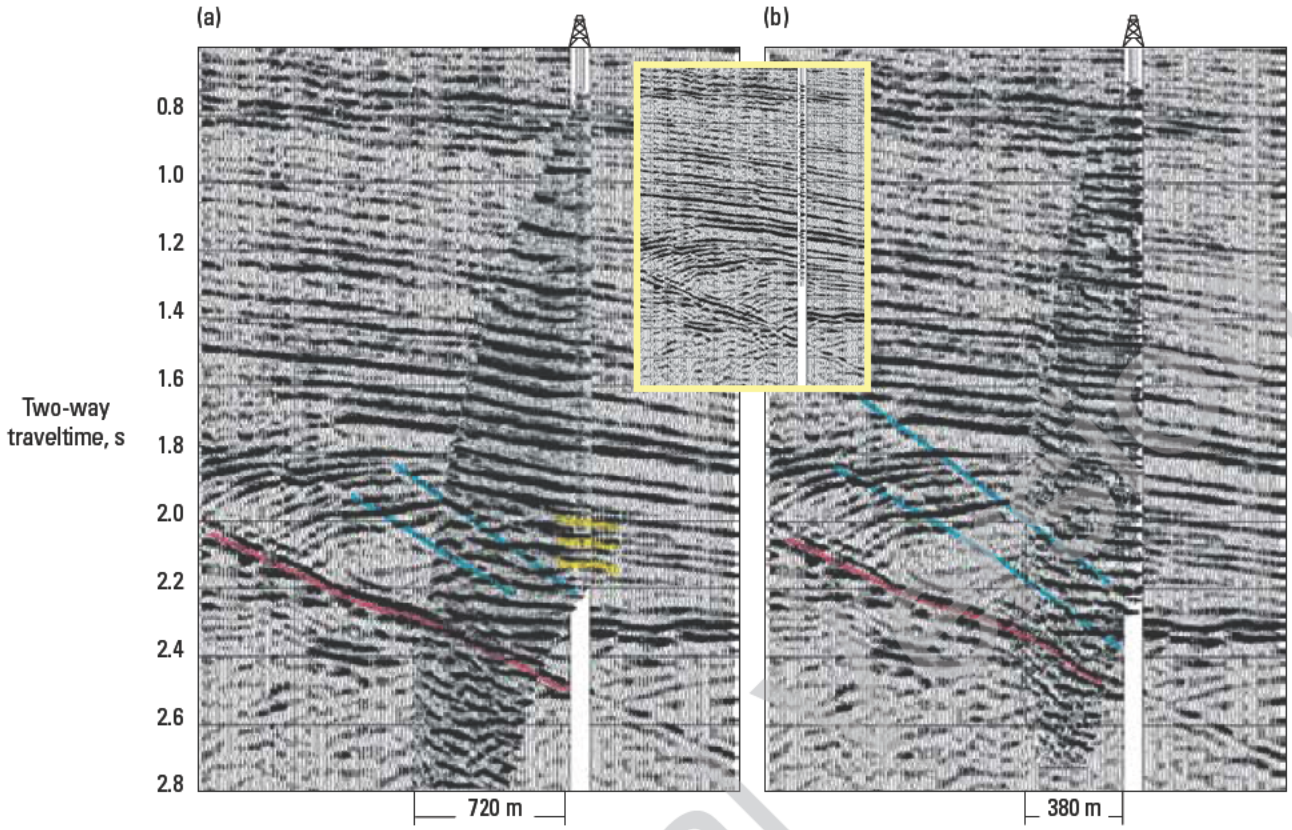

Figure 6-25. Comparison of surface seismic section with offset-VSP images from P-to-P reflections (a) and from P-to-S reflections (b). Productive sands are shown in yellow whe e the intersect the borehole. A regional fault is interpreted in red. The VSP images give clear indic tions of maller-scale faults (blue) and broken reflections that are only implied in the surface seismic sectio (insert). The image derived from S-wave reflections (b) has higher vertical resolution and therefo e images finer-scale features than the P-wave reflection image (a). (From Arroyo *et al.*, 2003; this graphic copyright Schlumberger, Ltd. Used with permission.)

6.4 Imaging walkaway VSP

Walkaway VSP imaging encompasses the survey geometries in which the sour e position moves from shot to shot. As in walkabove VSP (Section 6.2), the image extent is built up by e change in the position of both the receiver in the bore ole and the seismic source at surface. For th walkaway VSP, the number of geophone stations is u ual y limited and remains constant, whereas the numbe of source points on the surface is large and closely paced Both walkaway and walkabove survey ypes an be considered the special cases of an ideal ima ing VSP with receiver sampling over the entire borehole f r a set of closely spaced shotpoints on the surface.

Reduction in the number of source points, as in the offset VSP, or reduction in the number of borehole receiver stations, as in the walkaway VSP, compromises the quality of the image that could have been formed had the full-aperture dataset been available. A discussion of the effects of limited aperture is presented in Miller *et al.* (1987). A modeling study published by Payne *et al.* (1994) showed the results after the migration of various subsets of a synthetic dataset consisting of 166 sources at 6.1-m spacing received by 290 borehole receivers at 3-m spacing. They concluded that reduction of the lateral coverage had serious detrimental consequences on the image resolution. The authors further concluded that reduction of the number of sources has a more deleterious effect than

reduction of the number of receivers in the borehole, provided that the reflectors are more horizontal than vertical. Surprisingly, they also suggested that imaging salt flanks from the borehole would be best accomplished using a survey in which both source and receiver were in the borehole.

The moving-source approach to building image coverage has the greatest operational advantages in the offshore environment, especially with the VSI tool, which can record several geophone positions in the borehole for the same surface shot. In the marine environment, the boat deploying the source can steam along a line, firing the source as fast as the acquisition system can handle the data.

To move sources in the onshore environment is more difficult. Either vibrator trucks must move from shotpoint to shotpoint along the acquisition line (or grid), or dynamite shotholes must have been predrilled before the survey. Access to all desired surface locations may not be possible, and access to others often involves time-consuming detours. Most onshore VSPs for imaging are acquired with a small number of source locations and with lateral coverage built up from the length of the receiver array in the borehole.

Figure 6-26 shows the three possible geometries considered in this section:

- vertical well with moving source
- deviated well with source line at 90° to deviation
- deviated well with source line parallel to deviation and possibly with the receiver array moving to remain vertical beneath the source.

It should also be understood that these geom tries are special cases of the more general concept of 3D VSP in which, rather than a discrete line, the source points would constitute an areal array from which any s t of source points could be selected to form an arbitrary line. Such a dataset might be acquired as stand-alone project, but an alternative approach is to et the receiver tool in the borehole and reco d the shots of a surface seismic 3D survey (Section 3.9). This simultaneous approach can offer significant advantages in the field. It makes dynamite an e onomically viable source for onshore survey sig ificant y speeds up acquisition, and makes any such ffort ffectively free (no cost).

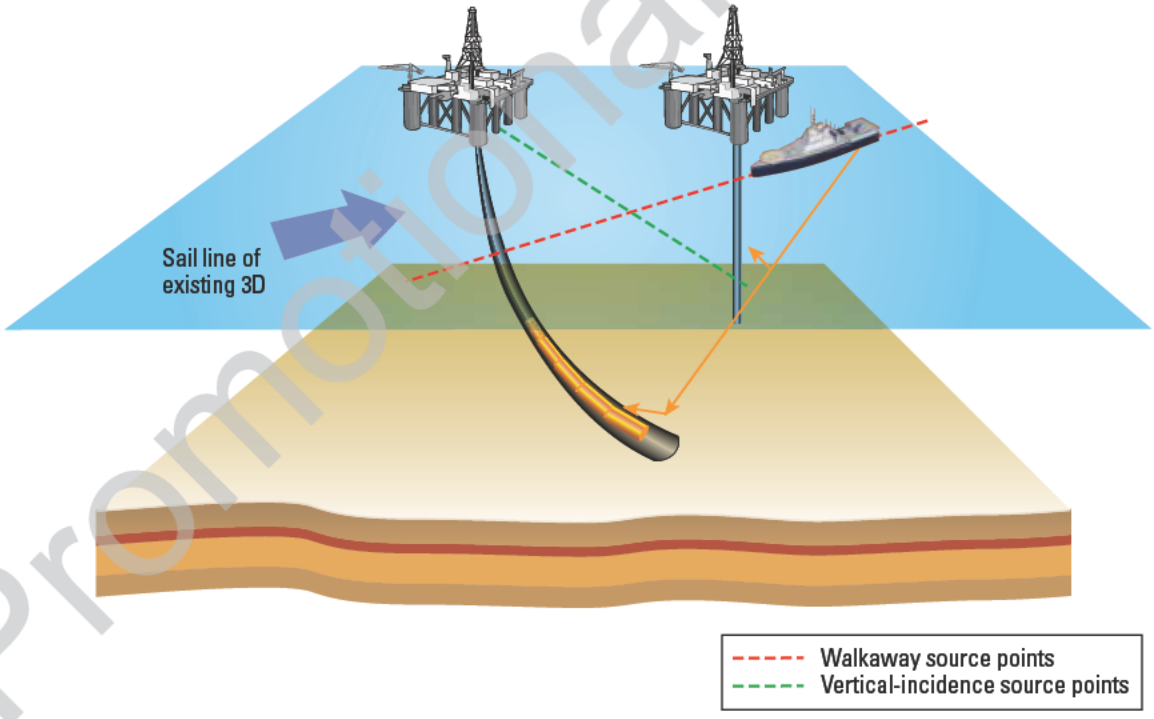

Figure 6-26. Three possible walkaway geometries: right well, moving source (rig on the right); deviated well, source line at 90° to deviation (left rig and red sail line); deviated well, source parallel to deviation (left rig and green sail line).

6.4.1 Presurvey considerations

The same survey planning and modeling concerns that were discussed with respect to offset VSP surveys (Section 6.3.1) are also relevant for walkaway surveys. Here, however, the question "How far away should the source be placed?" is replaced with "At what depth should the geophones be placed in the well to optimize the image?"

The maximum coverage for a given offset will occur when the receivers are very shallow. Conversely, the shallower the receivers, the advantage gained from the VSP geometry is less because the receivers are further from the objective and there is a longer, uncompensated propagation path. In practice, receiver array deployment is often at about one-half the depth of the target horizon. Modeling is the essential tool for answering this type of question.

6.4.2 Acquisition

One of the main operational concerns for conducting walkaway VSP surveys is the navigation. It is vital that each shot recorded can be matched with the location at which it was fired and that the shots are fired along the required line. This imposes a requirement for real-time navigation control that can display the boat's position as a function of time and the desired shot locations (see Chapter 3 and Fig. 3-16).

Airguns need air supply on the boat, which is supplied by either a compressor or a stack of compressed gas bottles. Liquid nitrogen is another alternative if a large number of shots is planned or deck space on the boat is limited.

Estimation of the minimum required compressor capacity, storage capacity, leveling-out time, and the cyclic air consumption is paramount in survey planning. Table 6-1 illustrates the air-flow requirements for different survey types when using a 750-in^3 [21.2-L] gun cluster using 2,000 psi [137.9 bars].

If a compressor is to be used, it is important to consider how quickly the compressor can charge the gun array between shots. For example, for a boat speed of 4 knots [approximately 7 km/h] and a desired shotpoint spacing of 25 m along the line:

$$\text{boat speed} = \frac{4 \times 1{,}852 \text{ m/h}}{3{,}600 \text{ s/h}} = 2.06 \text{ m/s} \left[7 \text{ km h} \right],$$

$$\text{time between shots} = \frac{25 \text{ m}}{2.06 \text{ m/s}} = 12 \text{ s}. \qquad (6\text{-}1)$$

Therefore, the gun array will have to fully recharge in 12 s from the air supply available, and the acquisition system must be able to accept the next shot in the same time span.

If 6 s of data are to be recorded for each record, then the minimum time possible between shots would be 6 s, which represents a maximum possible boat speed of 8 knots [15 km/h], even with instantaneous gun recharging and data acquisition. Note that a towing speed of 8 knots [15 km/h] is not practical for VSP sources because of huge tensions in the towing cable and turbulence affecting the near-field hydrophones. In practice, 5 knots [9 km/h] is the maximum water speed allowed when towing sources or streamers. (Water speed corresponds to the algebraic summation of boat and current speed.)

The seismic array will remain clamped at the same depth for the duration of the boat pass along the desired sail line. Therefore, it is essential that the array is located with the best possible coupling of the receiver to the formation. The internal shakers in the tool can help the engineer to position the tool so that the clamping will be optimal before the acquisition begins.

Table 6-1. Air-Flow Considerations for Different Survey Types

Survey	No. Shots per per Level	Shot Cycle Time, s	Hold Time Between Levels or Lines, s	Air Compressor Rate, L/min
Checkshot	3	8	240	1,200
Zero-offset VSP	5	8	180	2,600
Walkaway VSP			1,200	11,450†
seismic Vision while tripping	10	10	120	7,400
seismicVison one stand	10	10	3,600	1,150

Assumptions: 750-in^3 [21.2-L] gun cluster, minimum firing pressure = 2,000 psi [137.9 bar], air-storage capacity = 10% compressor capacity, and number of levels or stations = 50 for all surveys.

† Boat speed should be < 6 knots [< 3.086 m/s], and 15 min minimum between sail lines.

6.4.3 Data processing

The data processing schemes currently employed for walkaway VSP follow the same basic principles as the processing of a large number of discrete offset VSP datasets. For each shotpoint, there will be data traces from the array of geophones. These traces make up a mini-VSP for each source point; and most of the processing, tool orientation, wavefield separation, and deconvolution are implemented in that domain. In general, this imposes the restriction on the minimum length for the geophone array. The array must have at least five geophones to adequately separate upgoing and downgoing P and S wavefields.

It is only the walkaway migration that is performed strictly in the common-receiver domain, although the mechanics of the algorithm are the same as for the offset VSP imaging case.

If the geophone array is long enough and the number of shots is large, it may be possible to "bin" deconvolved data in a pseudosurface-seismic manner to calculate residual statics, nonhyperbolic moveout parameters, and AVO attributes.

6.4.4 Case study

In a deepwater field offshore West Africa, a nearly vertical exploration well encountered the first of what was hoped to be multiple reservoir sands (Dingwall *et al* 2003). To assess reservoir quality away from the well, the geophysicists wanted to measure and calibrate the AVO response of the top reservoir sand. When modeled as isotropic, the sand exhibited a flat AVO response, but a significant brightening of amplitude with offset was evident on the acquired CMP gathers. They also wanted to measure anisotropy in the overburden and intervening shales and to obtain a high-resolution image of the deepwater reservoir targets.

Two perpendicular walkaway VSPs were acquired using an eight-level VSI tool positioned in a shale zone above the target reservoirs. Survey planning showed that, for the velocities and structure expected, walkaway line lengths of 4.5 km would produce a suitable range of direct and reflection angles to characterize the AVO behavior of the target horizon at about 3,900 m depth. The two survey lines intersected the well position. The SWINGS navigation system assured source-position accuracy.

Overall data quality was excellent. To measure anisotropy and identify AVO anomalies requires comparison between the walkaway data and synthetics from an isotropic elastic model. The elastic model, built from dipole sonic and density logs, was extended up to the seabed with the help of estimates of velocities and densities from compaction and lithology trends (Fig. 6-27). The extension of this model to include anisotropy was achieved by VTI gradient traveltime inversion using the walkaway arrival-time information and the calibrated elastic model. Anisotropy in the sand rich layers of the model could be switched off by following a V_P/V_S threshold criterion.

Anisotropy was found to be significant, with horizontal velocities surpassing vertical velocities by 20% in the shales. An AVO processed CMP gather from the walkaway data shows good correlation with a synthetic gather generated from the calibrated VTI model (Fig. 6-28). The excellent tie validates the model used for AVO simulations. Anisotropy has a marked effect on AVO response and must be taken into account when analyzing AVO behavior at the target levels (Fig. 6-29). The Target 1 sand, which before walkaway calibration exhibited ambiguous AVO properties, shows a clear brightening, or increase in amplitude with offset, when anisotropy is included in the model.

The amount of anisotropy was greater than expected in the survey plan and was found to dramatically modify raypaths to the point at which even the longest offsets did not reflect at large angles at the deepest target. Future survey planning needs to consider extremely long offsets if AVO information is needed at reflection angles greater than 40° in similarly anisotropic formations.

The anisotropic model was used to migrate the walkaway data to produce high-resolution images of reservoir targets below the well (Fig. 6-30). The inline walkaway image shows an excellent tie with a relevant line extracted from the 3D marine seismic volume and illuminates targets with greater resolution than does data existing in the surface seismic survey.

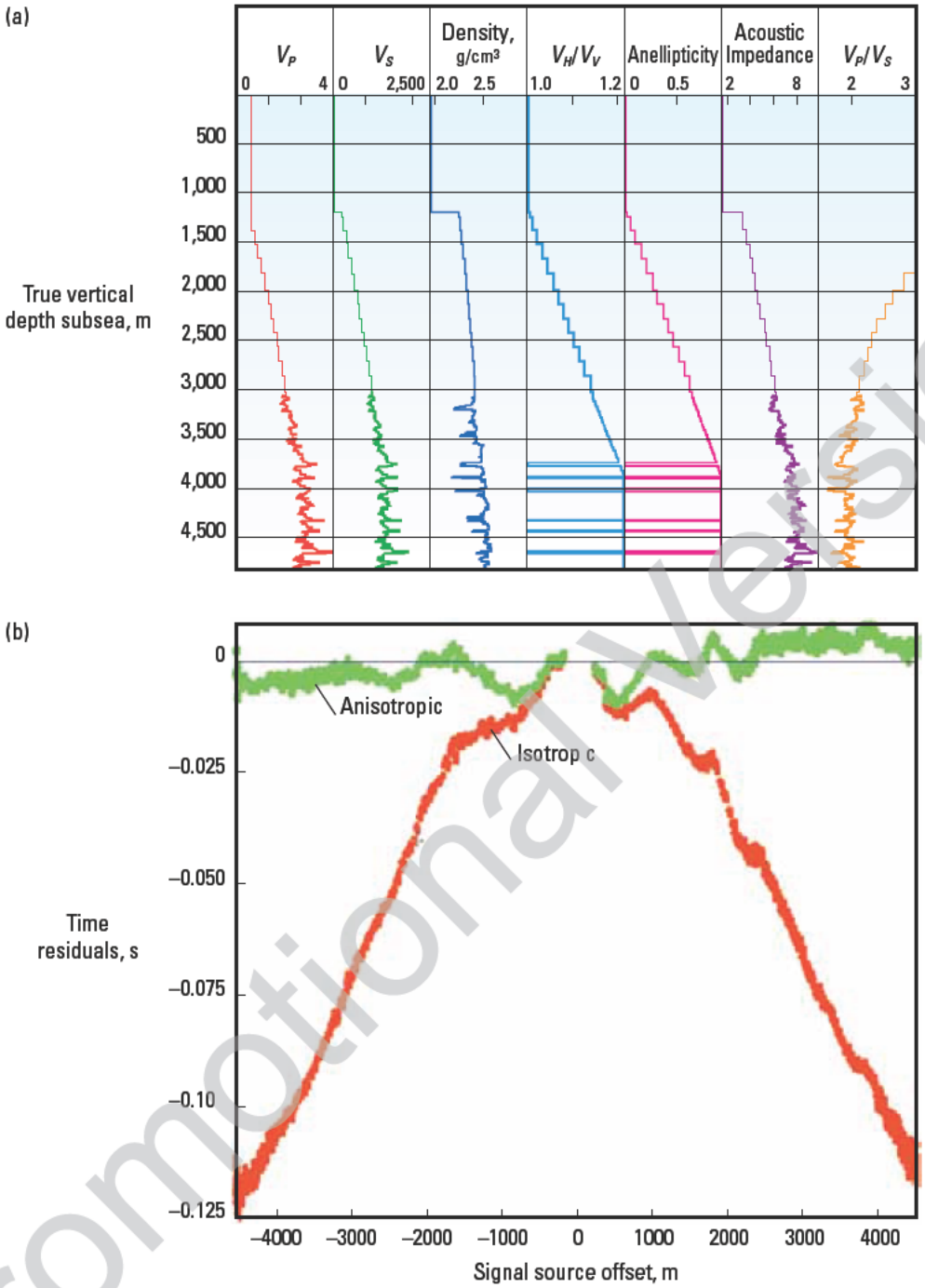

Figu e 6 27. E stic model (a) for an offshore West Africa field built initially from sonic and density l gs and djusted to include anisotropy in the shale layers. Shale layers are identified by a V_P/V_S atio >1 85. The residual plot (b) shows the difference between observed traveltimes and those from iso ropic (red) and anisotropic (green) models. (From Arroyo *et al.*, 2003; this graphic is copyright Schlumberger, Ltd. Used with permission.)

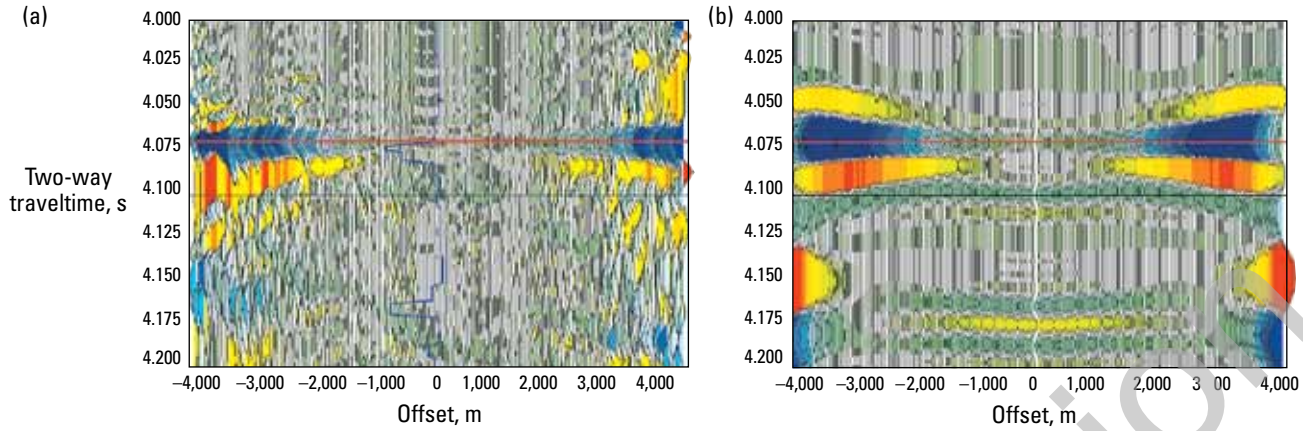

Figure 6-28. Comparison between the observed walkaway AVO response for P-to-P reflection data (a) and the modeled response (b) for an anisotropic formation at a deepwater target (red horizontal line). Amplitudes vary from negligible at zero offset to highly negative at long offsets. A density log (blue curve) in the center of the measured AVO response (a) swings to the left at reservoir targets. (From Arroyo *et al.*, 2003; this graphic is copyright Schlumberger, Ltd. Used with permission.)

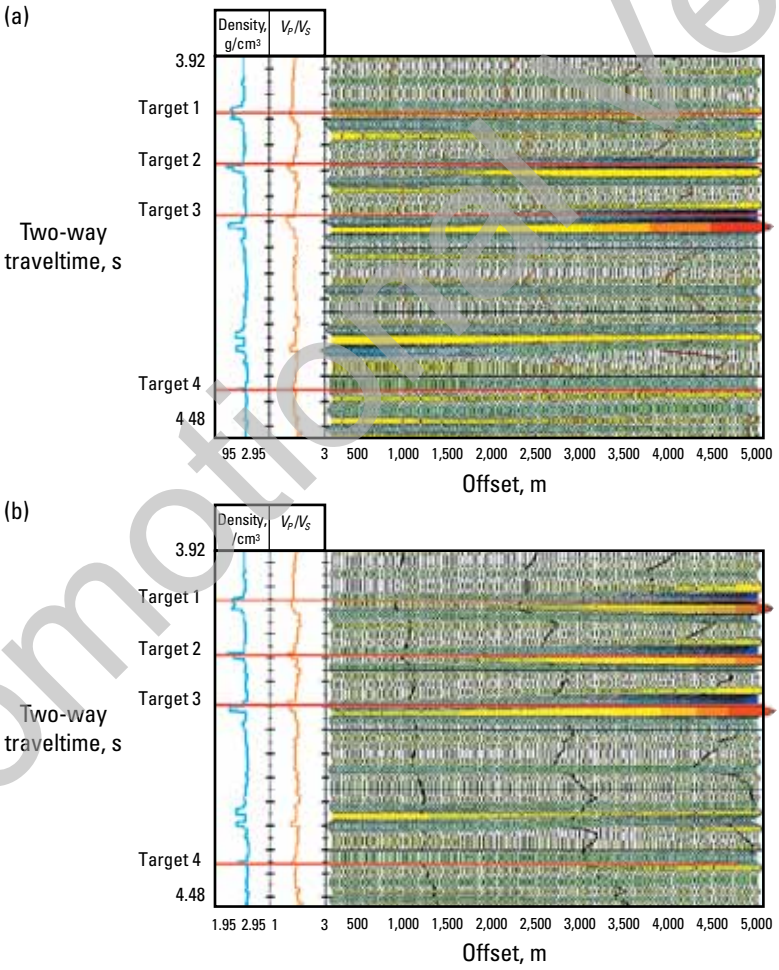

Figure 6-29. Isotropic model (a) compared with anisotropic model (b) of surface seismic AVO response at four targets. The uppermost target, Target 1, is the level shown in the measured AVO walkaway data in Fig. 6-28. The isotropic model yields no perceptible amplitude variation with offset at this reflector, whereas the anisotropic model produces a clear brightening from dim, negative amplitudes at zero offset to bright, highly negative amplitudes at long offset. The phase-angle curves plotted behind each set of modeled traces represent angles of 10°, 25°, and 40°, from left to right. (From Arroyo *et al.*, 2003; this graphic is copyright Schlumberger, Ltd. Used with permission.)

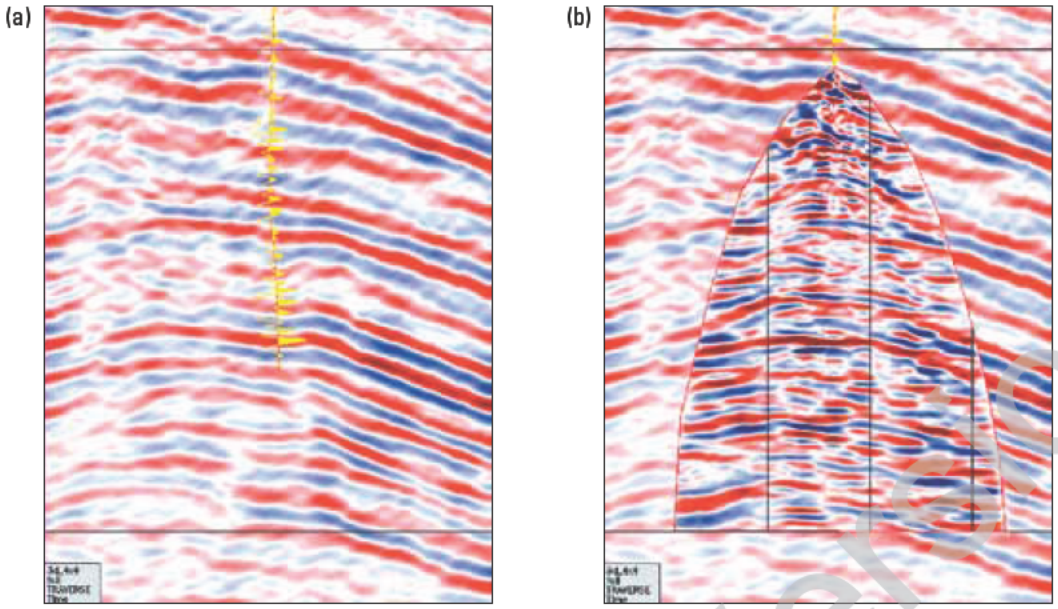

Figure 6-30. Surface seismic section (a) from an offshore West Africa 3D seismic volume and a high resol tion walkaway image (b) along the corresponding line. A corridor-stack trace (yellow) marks the borehole trajectory in the surface seismic image. The walk-away data, migrated using an anisotropic velocity model, appear to illuminate faults d other yer discontinuities that are not seen in the surface seismic section. (From Arroyo *et al.*, 2003; this graphic is copyright Schlumberger, td. Used with permission.)

6.5 Three-dimensional VSP

The widespread use of 3D surface seismic imaging has demonstrated the value of including a third dimension in the acquisition and processing of seismic data In fac many subsurface imaging problems cannot be solved without a 3D survey. When the problem also requires the survey to be performed in a bor hole, he s lution is the 3D VSP.

6.5.1 Acquisition

Figure 6-31 shows a sketch of a marine 3D VSP acquisition. The boat in the sketch is steaming in a series of parallel lines over a grid. This acquisition geometry is common when borehole seismic data is acquired in conjunction with surface seismic data. However, in the case of a stand-alone 3D VSP survey, spiral patterns are the preferred sailing geometry, which has the advantage

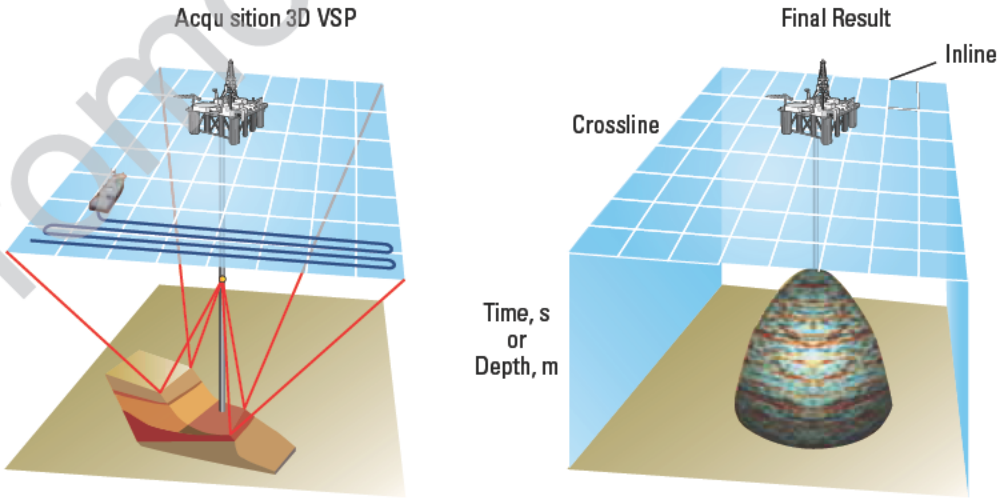

Figure 6-31. Sketch showing a marine 3D VSP acquisition. (From Barzaghi *et al.*, 2000.)

that the source can shoot continuously. There is no acquisition downtime while the boat turns around at the line ends. On land, a pseudorandom source arrangement on the surface may be preferred.

Normally, a walkaway VSP is acquired first and analyzed onboard to confirm the validity of the survey parameters planned for the 3D survey.

To minimize rig time and maximize 3D coverage, long toolstrings are used downhole; typically this is a VSI tool with 20 to 40 shuttles. Operating-efficiency concerns about tool deployment speeds with such long arrays are dispelled when operating crews achieve rig-up times of 1½ hours in the case of a 20-shuttle VSI tool and less than 4 hours for the 40-level tool. The toolstring remains in the same position for the walkaway and the 3D VSP survey, and it is not rare to have the tool continuously in the borehole for more than 10 days.

Presurvey acquisition parameters planned for a 3D survey include shotpoint separation, distance between spiral arcs, and maximum spiral radius. These parameters are typically selected by oil company experts to assure adequate imaging quality.

After the walkaway acquisition, the shooting vessel navigates into position at the center of the spiral and acquires the 3D survey. Acquisition typically uses a flip-flop source configuration in which airguns fire from the left side, then from the right side, of the vessel in an alternating pattern. By starting at the center of the spiral, the most important data could be acquired first, in case unforeseen weather changes force cancellation of the survey. It is critical that the actual acquisition geometry follows the plan to a high degree of accuracy (Fig. 6-32).

In a 3D VSP survey, the acquisition system not only has to store large amounts of data but also has to be in a ready state to record the next shot. In the deepwater project shown in Fig. 6-32, Schlumberger engineers aimed to acquire the data with a 13-s cycle time using 2-ms sampling; they actually achieved a 12-s cycle time. Total nonproductive time was only 6% in 58 hours of operating time.

One of the main concerns for a 3D VSP survey is the cost of rig downtime. Surveys can last for more than 10 days at more than USD 500,000 in deepwater offshore rig costs. Long arrays, efficient acquisition techniques, and equipment reliability are a must. Significant cost reduction is achieved by deploying downhole tools in "rigless" or offline VSP acquisition mode in a single derrick-drilling rig (Hornby *et al.*, 2007). The technique requires a remote-operated vehicle (ROV), which directs and stabs the seismic tool into the submarine wellhead. Figure 6-33 shows geophones entering the wellhead at 1,350 m water depth. The winchman and logging engineers coordinate tool deployment with the ROV operator by video. The first successful use of this technique occurred during the Thunder Horse 3D VSP survey that Schlumberger conducted for the operator in the Gulf of Mexico (Ray *et al.*, 2003) and is discussed in the following section.

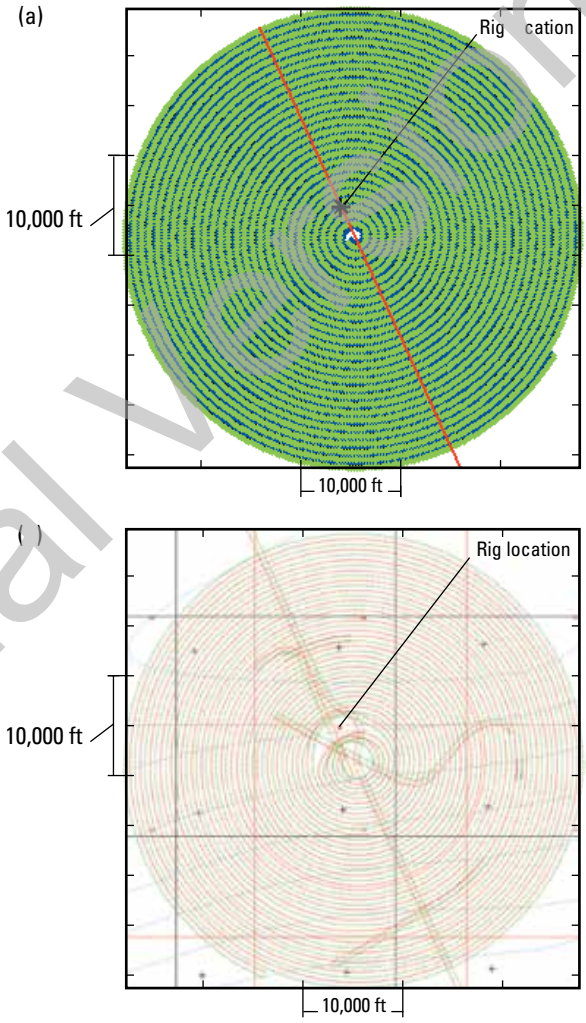

Figure 6-32. Planned acquisition geometry (a) compared with actual acquisition geometry (b) for spiral 3D VSP and walkaway surveys. A 20-shuttle VSI tool with 30-m shuttle spacing acquired both datasets. Results from the 16-km walkaway VSP (red line in (a)) helped geophysicists validate acquisition parameters for the 3D survey. The center of the spiral was offset from the rig. The actual 3D survey geometry closely matched the planned spiral. In the actual survey, red denotes the port source, green denotes the starboard source. (From Arroyo *et al.*, 2003; this graphic is copyright Schlumberger, Ltd. Used with permission.)

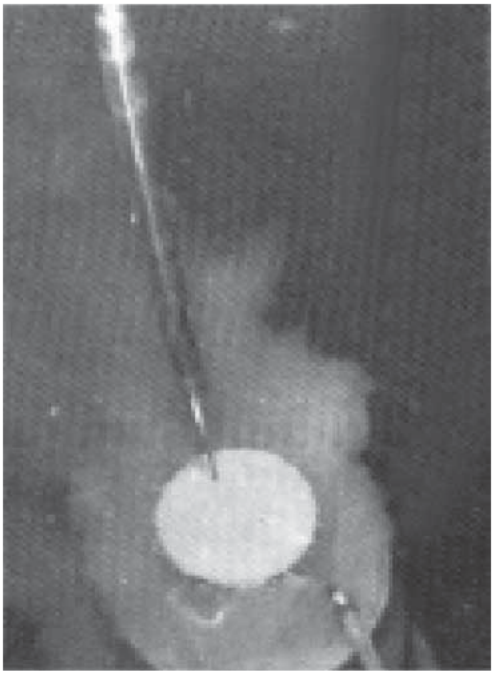

Figure 6-33. View of rigless-deployed geophones entering the wellhead at water depth of 1,350 m. (Modified from Hornby *et al.*, 2007.)

6.5.2 Case studies

The survey shown in Figs. 6-34 and 6-35 was acquired as a series of parallel lines—58 lines forming a 4-km × 4-km square, with 160 shotpoints for each line. A five-level tool was in the well over a 60-m interval. Data acquisition took 65 hours (Barzaghi *et al.*, 2000).

An example of the vertical-component data is shown in Fig. 6-34, displayed as a common-receiver gather. Most of the energy on this display is downgoing compressional wave energy. This large-amplitude wavefield masks the reflected energy until the wavefields have been separated, using all three components of the recorded wavefield, into upgoing compressional and s ear waves and downgoing compressional and shear aves An upgoing compressional wavefield is shown in Fig 6-35. Again, it is displayed as a common-rec iver gather, and lateral variations along the source ine can be seen, particularly at a time of approximately 1 8 s.

Data are migrated in way similar to that described for the offset VSP. Tra eltimes are derived from a background velocity model nd are used to define the diffraction r sponse in the dataset from each point in the

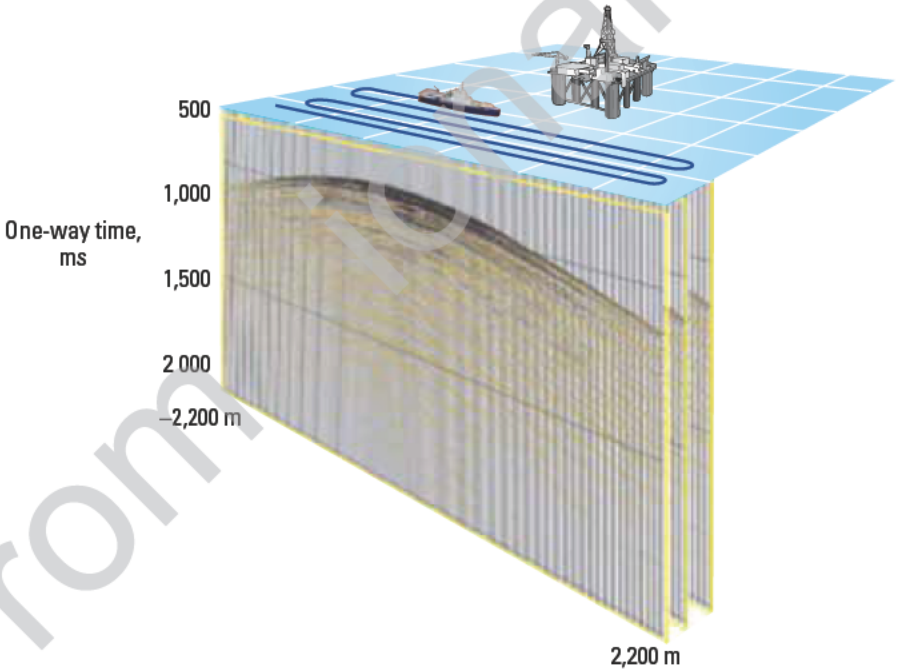

Figu e 6-34. The vertical component for one walkaway line (common-receiver gather) before data processing. This sc ematic shows a typical inline survey. Most of the energy contained in the wavefield is associated with downgoing waves that mask weaker, upgoing reflections. (From Barzaghi *et al.*, 2000.)

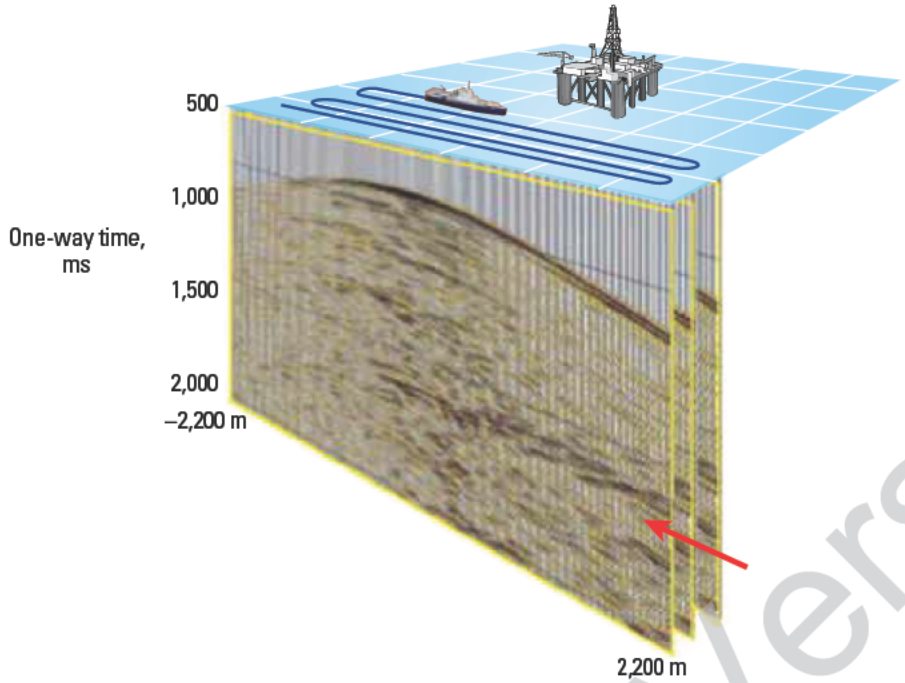

Figure 6-35. The upgoing wavefield after data processing. After wavefield separation, e upgo ng waves are extracted. The asymmetric distribution of events confirms the complexity of the subsurface lay The curved signal at 2,000 ms on the right-hand side, indicated by the arrow, is probably c used by an isolated faulted block. The spatial position of these events is not yet defined at this stage of processing (From Barzaghi *et al.*, 2000.)

subsurface. The data are summed along the diffraction curves to form the image. Figure 6-36 shows a cent al crossline and inline from the 3D VSP dataset. The zo e around the horizon at 2.8 s is shown at an expanded scale in Fig. 6-37. Time slices through the ataset at 2.79 s and 2.81 s show that this event crests abo t 500 m northeast of the well.

An alternative 3D visualization is presented in Fig. 6-38. This shows the fault rom F g. 6-35 and the interpreted event plotted with color scale based on amplitude. Again, the maximum amplitude of this upper horizon (red) occurs abou 500 m northeast of the well.

This exercise dem nstrates how a 3D VSP dataset can be acquired, processed, nd interpreted on an interpretation workstat on similar to the way we handle surface seismic data vo umes. he VSP data has better potential resolution and pha e control from the downgoing wavefield.

The high-resolution imaging power and target cover ge of 3D VSPs and today's other complex borehole seismic surveys rely on a series of recent developments. The carefully engineered multicomponent VSI tool and accompanying acquisition technology, advanced understanding of anisotropic wave propagation, and the ability to model 3D-survey-acquisition response to an Earth model all contribute to successful seismic surveys in the borehole. Improvements can still be made in certain areas Characterization of the seismic source is one topic on which work continues. Some borehole seismic experts consider that digital recording of the full source signature at each shot is necessary to ensure that subsequent borehole seismic processing fully preserves amplitudes. Monitoring source response at each shot permits the acquisition crew to correct for any source variation or failure. Source-signature consistency is particularly desirable for processing walkaways (3D VSPs) that will be used as a reference for AVO calibration. The time spent to properly design, acquire, and process a borehole seismic survey is paid back in the achievement of key objectives such as accurate time-depth conversion, high-resolution images, enhanced illumination of subtle features, reliable quantification of anisotropy, and more confident interpretation of fluids and lithology from AVO data.

In the Riacho de Barra field, a mature field in the Recôncavo basin of northeast Brazil, Petrobras sought to reduce risks in an infill drilling campaign (Blackburn *et al.*, 2007). Structural and stratigraphic traps were difficult to identify using conventional 3D surface seismic because of a high-velocity conglomerate formation in the overburden (Fig 6-39). This formation attenuates seismic signals and reduces bandwidth, which renders poor-resolution images and makes it difficult to define reservoir boundaries (Sanchez and Schinelli, 2007).

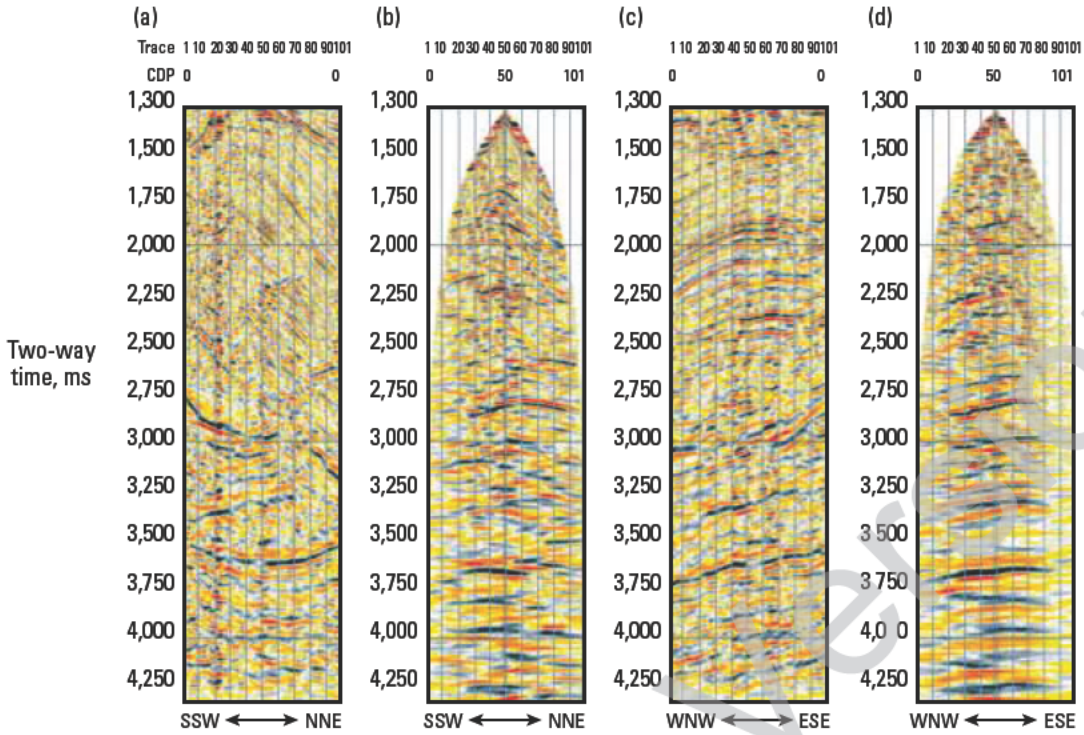

Figure 6-36. Migration results for an inline and crossline from surface seismic 3D data (a, c) and from 3D VSP data (b, d). The reflection event at 2,800 ms on the VSP dataset represents the target horizon. This event is not present on the surface seismic image. (From Barzaghi *et al.*, 2000.)

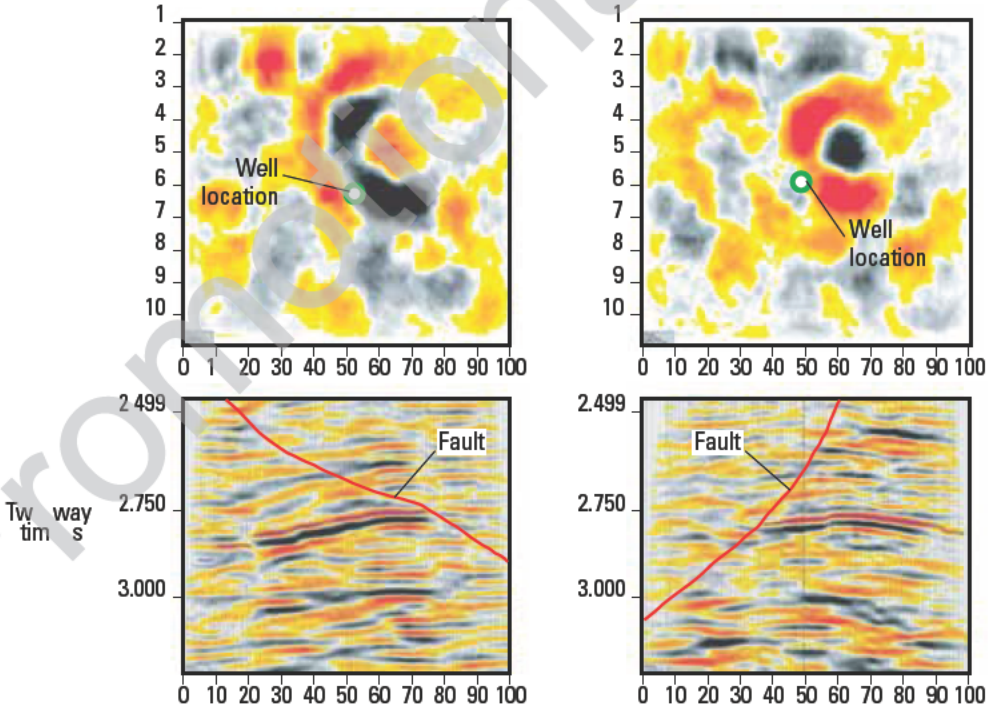

Figure 6-37. Seismic display of the reflection event at 2.8 s on the two 3D VSP lines from Fig. 6-36 displayed at an expanded scale (lower sections). Also, shown above the seismic sections are time slices of seismic amplitude at 2.79 s (left) and 2.81 s (right). The downward projection of the well is shown on the time slices. Both visualizations show the structure cresting approximately 500 m northeast of the well. (From Barzaghi *et al.*, 2000.)

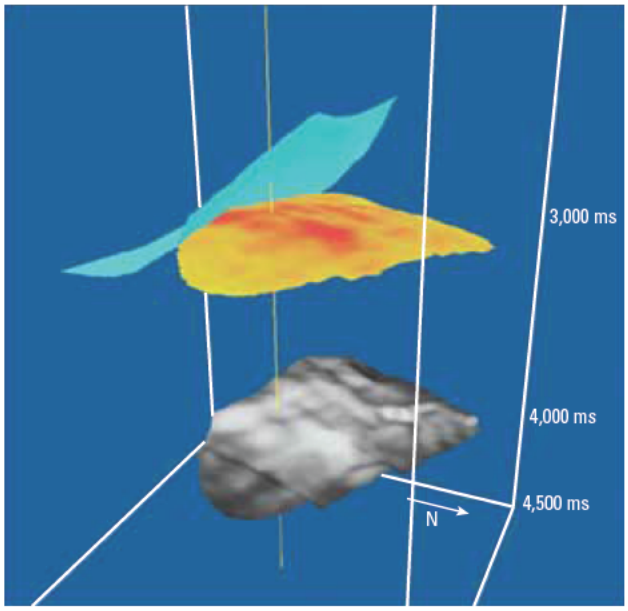

Figure 6-38. 3D visualization of the event at 2.8 s noted in Figs. 6-36 and 6-37. Fault is shown in cyan. The surface in time (ms) is color-coded by the amplitude of the seismic response at that point. (From Barzaghi *et al.*, 2000.)

A 3D VSP acquired in existing wells was recommended to improve the seismic image. The main goal of the survey was to resolve erosional truncations of the upper reservoir and delineate a deeper target that had been poorly defined by surface seismic imaging.

An initial velocity model was constructed from the 3D surface seismic data and calibrated by log data from more than 30 wells in the area. Ray tracing through the model was used to maximize coverage at the targeted interfaces by optimizing location of sources and receivers

The 3D VSP design comprised 2,700 shotpoin s over a 13-km^2 area to be recorded from two neighboring wells simultaneously, which was the best way to mprove downhole coverage (Fig. 6-40). The seismic crew performed essential survey operati ns s ch as locating shotpoints and drilling the 4-m sh t holes for deployment of the dynamite sources. Rugged topography and a forested landscape added difficulty to the acquisition campaign. VSI tools were depl yed in rigless operations in both wells.

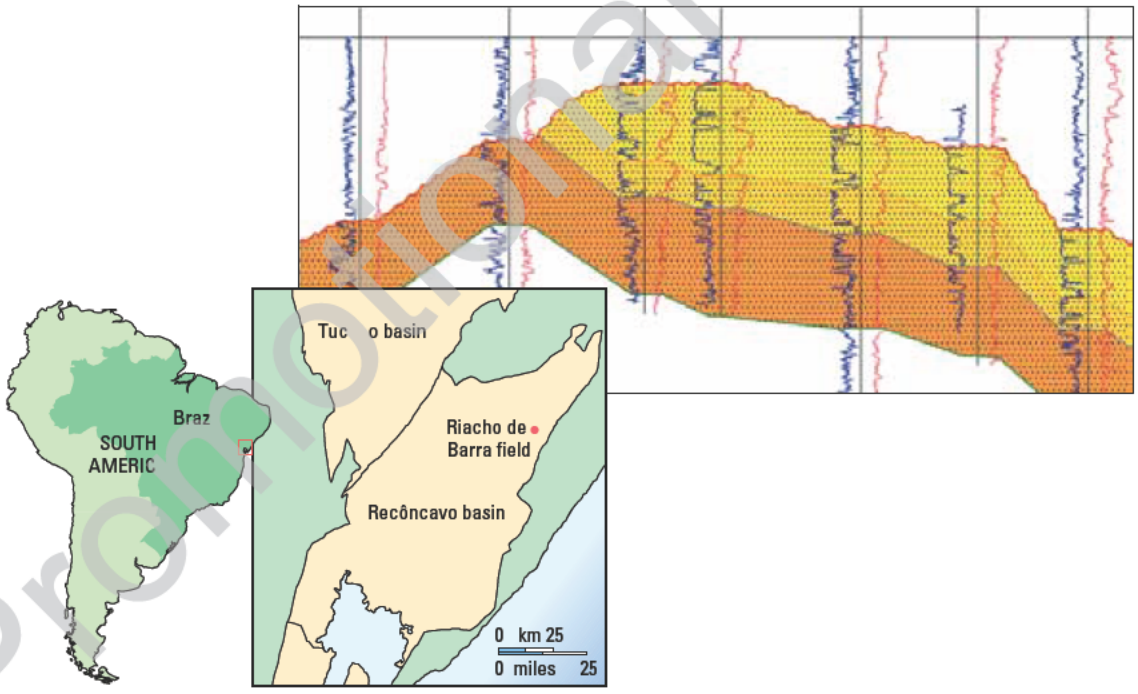

Figure 6-39. The Riacho de Barra field, onshore Brazil. A cross section interpreted from well logs shows the main reservoir (yellow) and the lower target (orange). Both are truncated at their upper surfaces by erosion and are overlain by a conglomerate that obscures seismic signals. After a 3D surface seismic survey failed to adequately image the erosional truncation, Petrobras acquired a 3D VSP to better delineate the limits of the reservoir. (Modified from Sanchez and Schinelli, 2007. From Blackburn *et al.*, 2007; this graphic is copyright Schlumberger, Ltd. Used with permission.)

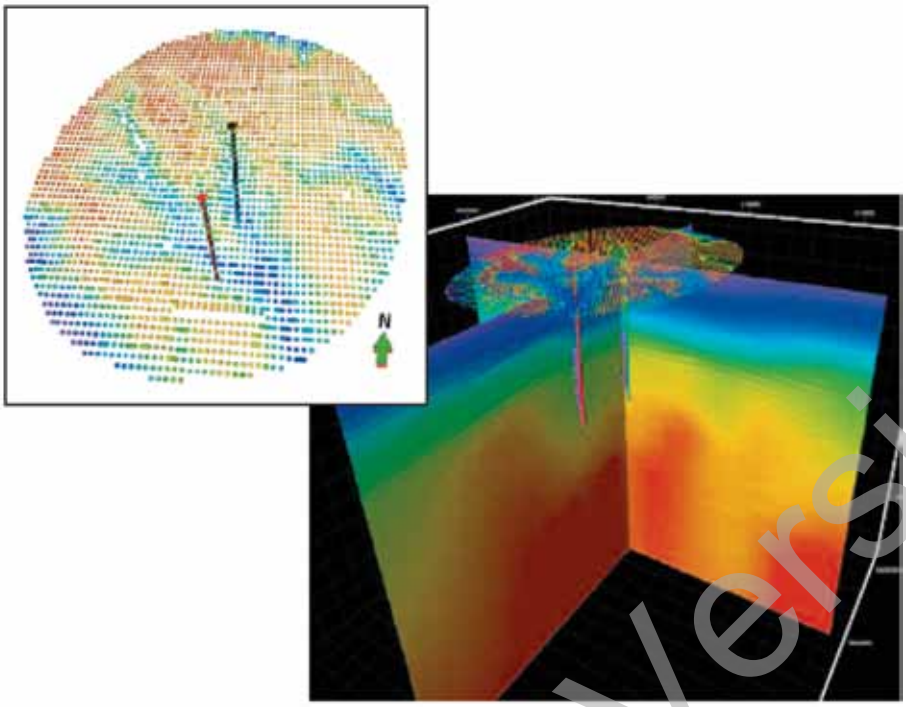

Figure 6-40. Double-well 3D VSP acquisition design. More than 2,700 shotpoints were planned in nes over a 13-km² area. The area covered joins two circles centered on two wells (eft). Shot locations are color coded from low elevation (blue) to high elevation (red). A velocity model from e isting 3D surface seismic data (right) was useful in planning the 3D VSP. In the velocity model, low velocities re blue and high velocities are red. (Modified from Sanchez and Schinelli, 2007. From Blackburn *et al.*, 07; thi graphic is copyright Schlumberger, Ltd. Used with permission.)

To ensure good seismic data quality, coupling between casing and formation was evaluated for cement-bond quality in the two wells. Cement-squeeze operations were required in both wells to guara tee g od cement bonding throughout.

Before acquisition of the 3D VSPs, a zero offset VSP was acquired in each well. The VSPs helped to optimize the final placement of the VSI arr ys for the 3D acquisition, and the velocity information from each well was used to facilitate processing of the 3D VSP.

The 3D VSP data p ocessing for each well was handled separately and hen merged prior to final migration. The imaging result from the 3D VSP shows an increase in resolution ov r that of the 3D surface seismic data (Fig. 6 41). Interpreters are currently working with the new 3D VSP data to define the limits of the reservoir.

Another marine VSP example comes from the Thunder Horse field in the southcentral Mississippi Canyon, Gulf of Mex co. The field is in water depth of approximately 1,920 m (Blackburn *et al.*, 2007).

Seismic imaging in the area is extremely complicated because of the abundance of overlying salt bodies. Surface seismic images fail to resolve structural complexity and stratigraphic detail because both water-bottom and salt-sediment multiples obscure major subsalt targets. Also, targeted areas are very deep and seismic energy is highly attenuated in its two-way time.

A 3D VSP was designed to reduce wave propagation through the salt (Fig. 6-42). In the 3D VSP configuration, the reflected energy travels a shorter path and passes only once through the salt body, thus reducing attenuation and improving resolution. The 3D geometry also produces data from a wide range of azimuths, a feature that improves illumination in surface seismic surveys (Camara Alfaro *et al.*, 2007).

In 2002, when the survey was acquired, only a 12-shuttle VSI configuration was available. The tool was positioned at three consecutive depths to produce an effective 36-level VSP. A spiral source pattern was selected for efficiency and was repeated for each receiver array depth. A total of approximately 30,000 shots were fired, generating more than one million traces. The VSP image was found to be much superior to the available surface seismic data as shown in Fig. 6-43.

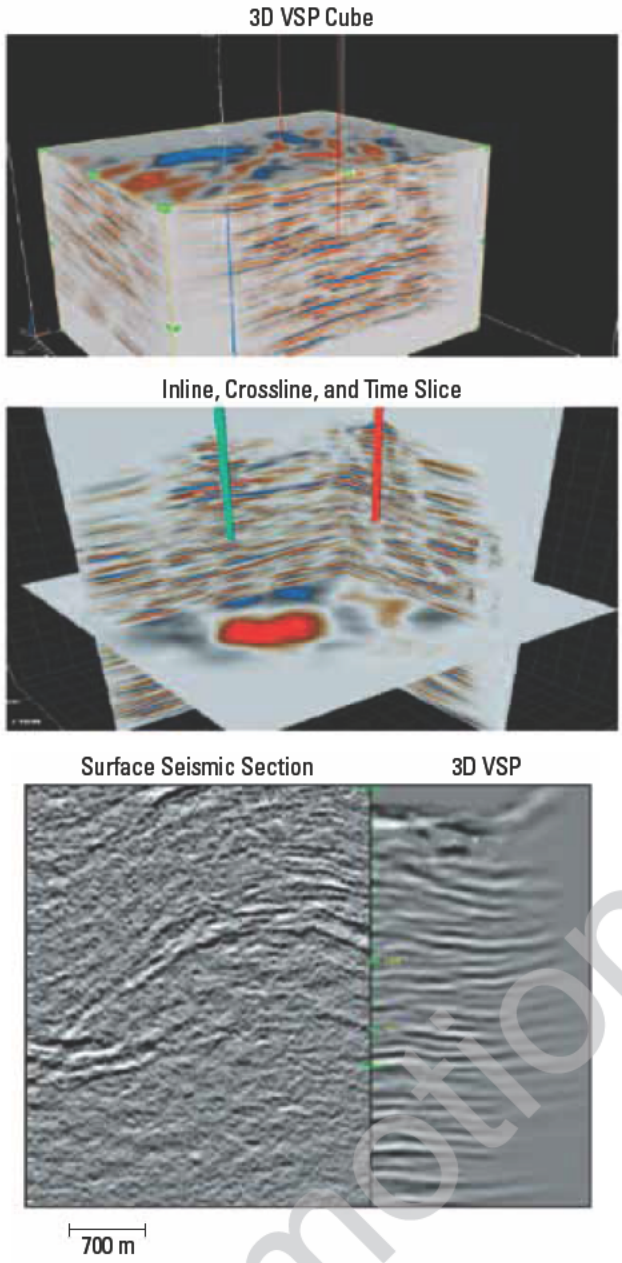

Figure 6-41. Results from th Petrob s 3D VSP survey in the Riacho de Barra field, onsho Brazil The borehole survey produced high-resolution results includi g cube displays and inline, crossline, and time-slice dis lays, w ch can be interpreted using software designed fo D surf e seismic data interpretation. The resolution of he 3D VSP ata was superior to that of the surface seismic data ver the ame a ea. (Modified from Sanchez and Schinelli, 2007. rom Blackburn *et al.*, 2007; this graphic is copyright Schlumberger, Ltd. Used with permission.)

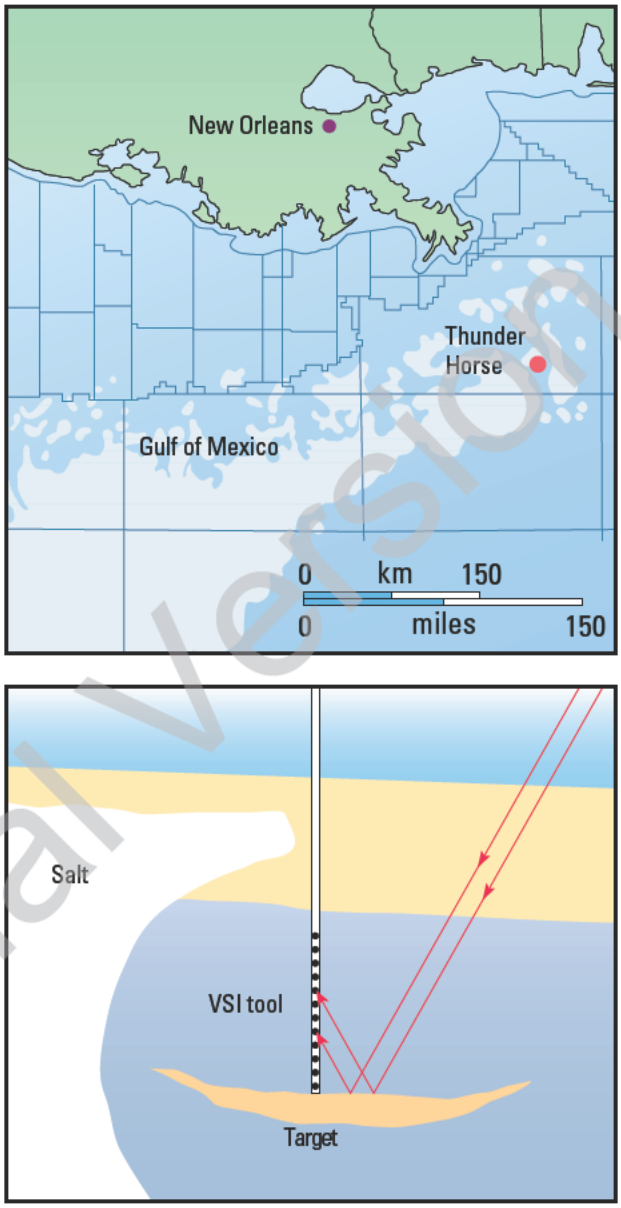

Figure 6-42. Location map of Thunder Horse field in the Mississippi Canyon, Gulf of Mexico (top). The operator ran several 3D VSPs in this area, which has numerous salt intrusions that reduce the effectiveness of surface seismic surveys. Three-dimensional VSPs can be designed so that many raypaths avoid propagation through the salt (bottom). (From Blackburn *et al.*, 2007; this graphic is copyright Schlumberger, Ltd. Used with permission.)

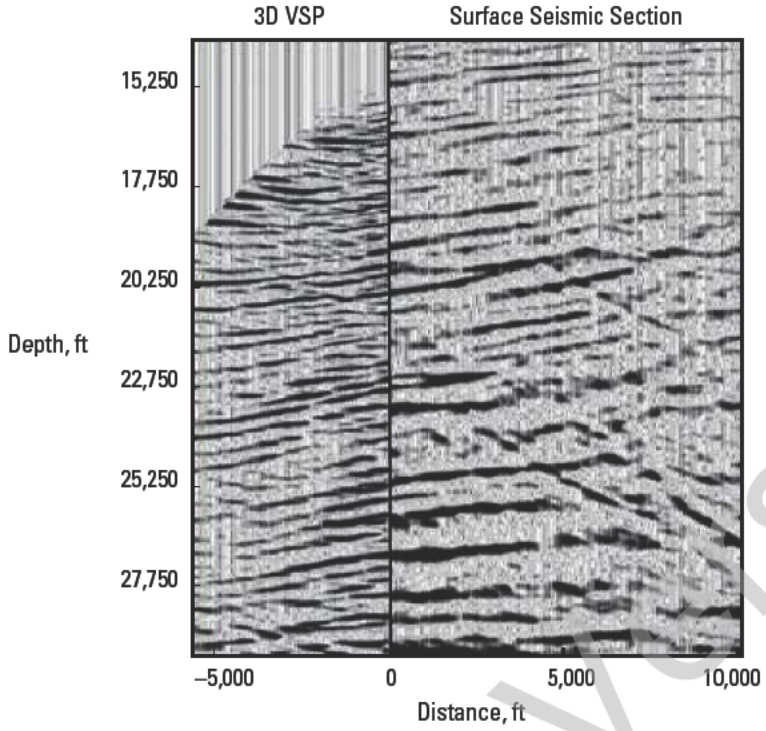

Figure 6-43. Comparison of 3D VSP results with a 3D surface seismic line, M ssissippi Canyon, Gulf of Mexico. The 3D VSP data (left) show higher resolution everywhere compared with surface seismic data (right). (Modified from Ray *et al.*, 2003. From Blackburn *et al.*, 2007; this graphic is copyrig t Schlumberger, Ltd. Used with permission.)

High-resolution images from 3D VSPs can also be used to guide placement of development wells An example of this particular use comes from the Mad Dog field in the Green Canyon area of the Gulf of Mexico. Again, complex salt bodies overhanging the targeted areas were shadowed in surface seismic data (Hornby *et al.*, 2007).

A 20-level VSI array with 30-m spacin between shuttles was run rigless into 1,370 m of open water and then placed into the wellhead by an ROV. The source vessel, WesternGeco *Snapper*, sh t two walkaway lines and then shot the spiral su vey ge metry, which rendered a 32,000-shot 3D VSP in six d ys. The operator achieved substantial savings by not sing rig time for the acquisition.

Results rom the Mad Dog 3D VSP helped produce an improved image (Fig. 6-44). A fault of approximately 500-m throw, not visible on the surface seismic image, was mapped; it caused a first well drilled in this zone to completely miss the pay interval. A second well barely interse ted the same reservoir. The operator determined that the cost of drilling two of the sidetracks could potentially have been saved if the 3D VSP had been acquired before drilling the first well.

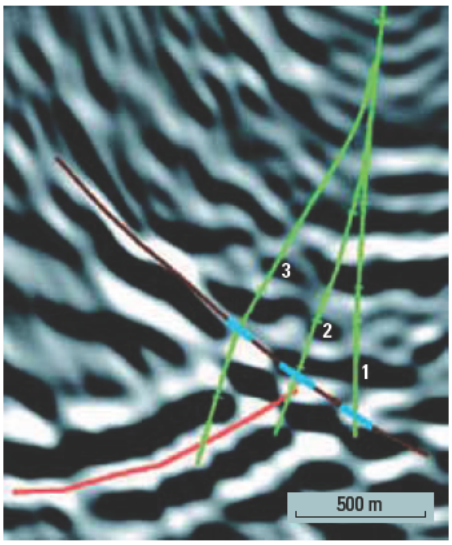

Figure 6-44. Image from the 3D VSP survey in Mad Dog field, Green Canyon area, Gulf of Mexico. A large-throw fault (purple) explains why some wells drilled into the structure did not hit the pay zone (red). Well 1 encountered the fault but failed to reach the reservoir. Well 2 intersected a small portion of the pay zone, and Well 3 hit the pay in the correct location. Fault location and dip information from dipmeter logs (blue) confirm the fault interpretation on the VSP image. (Modified from Hornby *et al.*, 2007. From Blackburn *et al.*, 2007; this graphic is copyright Schlumberger, Ltd. Used with permission.) Surface seismic section for this area (not shown) shows no evidence of faulting or reservoir delineation.

6.6 Salt proximity surveys

Borehole seismic techniques encourage the design of unconventional solutions to solve specific problems. One of the best examples of this is the quest to define the boundaries of large salt bodies.

Salt bodies may cause massive structural deformation of stratigraphic sequences. Huge pillars of salt push upward through the overlying strata, and as the pillar rises, it drags the edges of the strata upward, at the same time sealing the truncation. These deformations, and the salt that caused them, give rise to prolific hydrocarbon traps and simultaneously create imaging problems that make it difficult to locate those traps. The seismic imaging problems are caused by the steep or overhanging nature of the sides of the salt features against which the hydrocarbons are trapped and by the large velocity difference between the salt and the surrounding sediments. Unconventional methods have been derived to better detect the reservoir rock truncations against the salt flanks.

Salt proximity surveys have been used in the search for oil and gas since the 1930s. Several papers published at that time (McCollum and LaRue, 1931; Gardner, 1949) detail the earliest attempts at hand-calculating the necessary traveltime inversions.

Since those early days, the technique has grown from a simple traveltime calculation in a two-layer velocity model to a full three-component solution in three dimensions through an arbitrary velocity model. The acquisition hardware measures all three components of the wavefield and can monitor the azimuthal orientation of the sensors in the borehole. Processing accounts for the traveltimes from the source and the emergence angle at the sensor.

6.6.1 Geologic setting

There are several basins around the world in which the migration and trapping of hydrocarbons are at least partially controlled by salt tectonics, such as in the Gulf of Mexico (Fig. 6-45). During Jurassic time, the Gulf of Mexico was periodically isolated from ocean water. The limited water supply and arid paleoclimate led to extensive evaporation. As the basin water evaporated, it became increasingly saline, which led to precipitation of evaporite minerals such as halite (salt) and anhydrite. The massive salt sheet deposited about 170 million years ago is known as the Luann Salt. After salt deposition in the Late Jurassic, large sediment loads from continental shedding and periodic carbonate precipitation resulted in the development of a series of clastic and carbonate transgressive sequences. The heavy load on top of the salt caused (and continues to cause) plastic deformation of the relatively fluid salt body. Salt is buoyant because it is much less dense than the surrounding strata, and it rises when nearby salt is driven sideways by differential loading. Buoyancy caused by the difference in density becomes significant at depth. Thermal convection is an additional force that occurs when the geothermal gradient heats the base of a thick salt layer.

Salt diapirs are isolated, vertical domal structures that are most common on the upper continental slope. A salt diapir starts in the pillow stage as a salt mound with a fairly planar base and is concordant with the overlying bedding. In the diapir stage, the salt stock pierces the overlying strata. In the postdiapir stage, necking of the salt occurs (pinching out from the mother salt), and the dome overhangs other sediments. These overhangs are

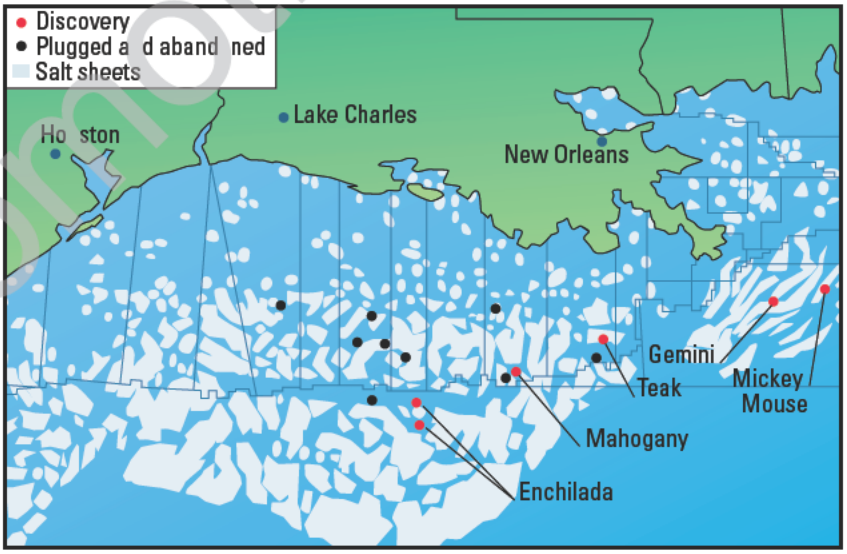

Figure 6-45. Map of salt bodies in the US Gulf of Mexico. (From Farmer *et al.*, 1996; this graphic is copyright Schlumberger, Ltd. Used with permission.)

potential hydrocarbon traps. Some examples of salt traps illustrated in Fig. 6-46 include salt-dome overhangs, anticlines formed as salt rises through overlying strata, and salt-reservoir contact traps.

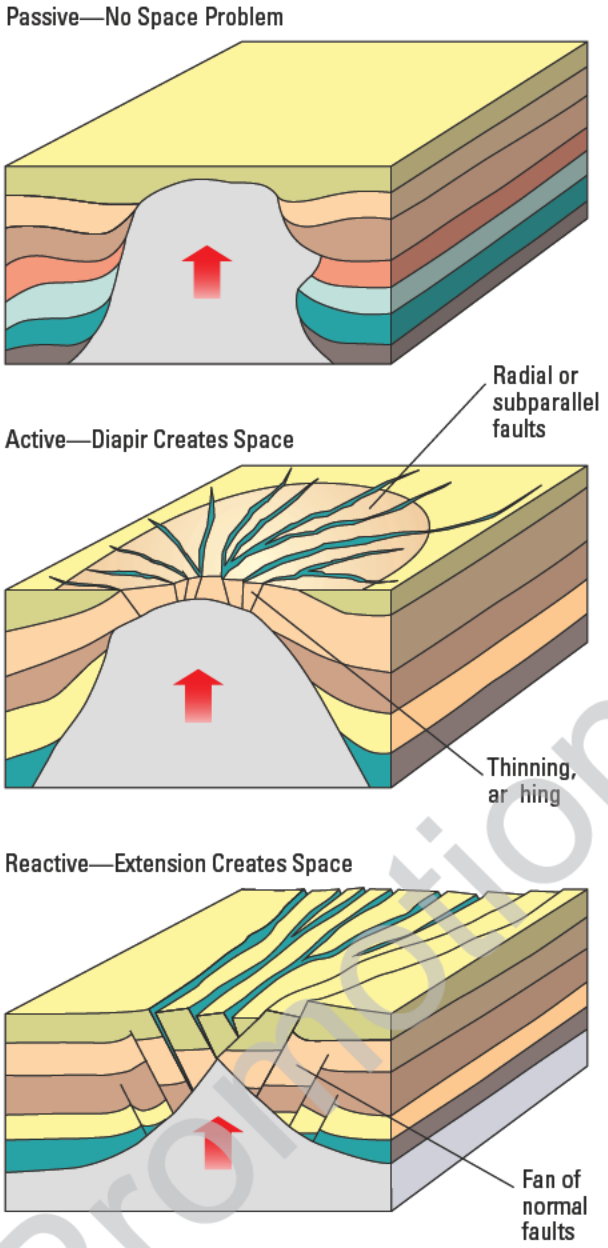

Figure 6 6. Examples of potential salt traps. (Modified from Jackson *et al* 994.)

6.6.2 Geophysics

Exploration, production, and service companies have expended much time and effort to delineate the flanks of salt domes. For decades, interpreters used the terminations of sedimentary reflectors as indicators of the salt-sediment interface. During the last 15 years, turning wave migration was developed to directly image the flanks of domes. Turning wave migration attempts to correctly position reflections from nearly vertical interf ces such as salt-dome flanks. Recently, complex seism c attributes, such as instantaneous phase and frequency, have been employed to identify salt-sed ment interface points. Unfortunately, none of these approaches yields precise terminations of the sediment ry reflectors, and the lateral uncertainty can ea ily be s veral hundred meters. The salt proximity tec nique tands out as one of the most reliable methods in the elusive search for accurate updip potential

As Fig. 6-47 from McCollum and LaRue (1931) illustrates, a seism c so r e is laced above the salt dome. Receivers are lowered i to a wellbore on the flank of the salt dome Discre e stationary traveltime measurements are made in the w ll from the source to each receiver. If he locations of the source are known and the seismic inter al velocities are known for each layer traversed by the seismic wave, the salt/sediment interface position can b calculated.

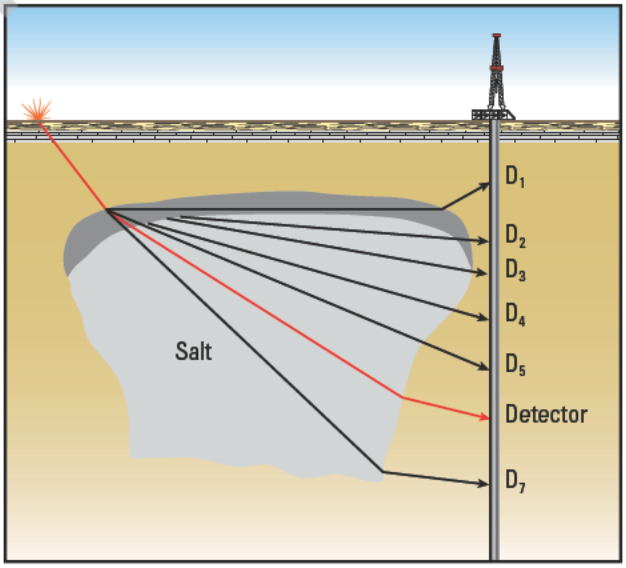

Figure 6-47. Schematic of raypaths through a salt dome with source located above the dome and receivers in a well along the flank of the dome. (From McCollum and LaRue, 1931; AAPG © 1931, reprinted by permission of the AAPG whose permission is required for further use.)

The conditions for successfully mapping the position of the salt flank are as follows:

- The salt velocity must be constant, known, and significantly higher than the surrounding sedimentary rocks. The smaller the velocity difference between the salt and the surrounding sediments, the lower the accuracy of the technique.
- The velocity field in the sedimentary rocks must be well known. To achieve this, the sonic log can be used as well as the traveltime differences between each pair of receivers in the wellbore.
- The top of the salt must be fairly shallow so that the rays from the source can all be assumed to enter the salt at the same point to yield an accurate 2D solution. For a 3D solution, this requirement is relaxed if the velocity structure down to the top of the salt is known.

During the first several decades of salt proximity processing, the traveltime inversion was two-dimensional. Downhole seismic tools contained only a geophone package oriented along the axis of the tool. This is what today would be called a vertical geophone. This geophone package was not gimballed, and there were no horizontal geophones.

The earliest method of traveltime inversion is illustrated in Fig. 6-48. Assume a two-layer isotropic velocity model. A seismic source is located on one edge of the model. Several seismic receivers are located on the other edge of the model. The traveltime of sound is measured from the source to one receiver. Given accura e knowledge of the source-to-receiver position and the two distinct velocities in the model, inversion will derive the traveltime. Figure 6-49 illustrates this inversion. There are an infinite number of paths that sound can travel from source to receiver and arrive at the ex ct measured transit time. Each of these paths results in slightly different refraction points at the layer velocit boundary. The curved (orange) line drawn through all these refraction points for each path is cal ed an aplanatic surface (surface of equal time). I is the locus of all possible locations of the salt boundary that would satisfy the observed traveltime between source and receiver. Note that the prerequisites for this solution are the exact positions of source nd receiver and the two interval velocities involved (Landgren and Deri, 1987).

Dur ng the 1980s, 3C geophone design technology bec me feasible and popular. These three-axis geophones were also gimballed, so the measurement could always be recorded in a gravity-oriented reference frame. With three gimballed, orthogonal geophones in the downhole tool (one always vertical and the other two always horizontal) and 3D modeling software, a 3D solution for the salt exit point became practical.

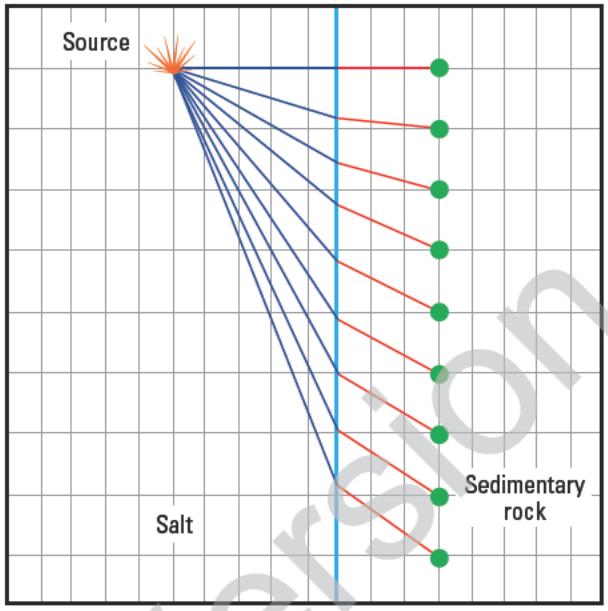

Figure 6-48. Illustration o two-l yer isotropic velocity model. Rays from the source pro agate th ough the fast salt (blue raypaths) and then refra into the s ower sedimentary rocks (red raypaths).

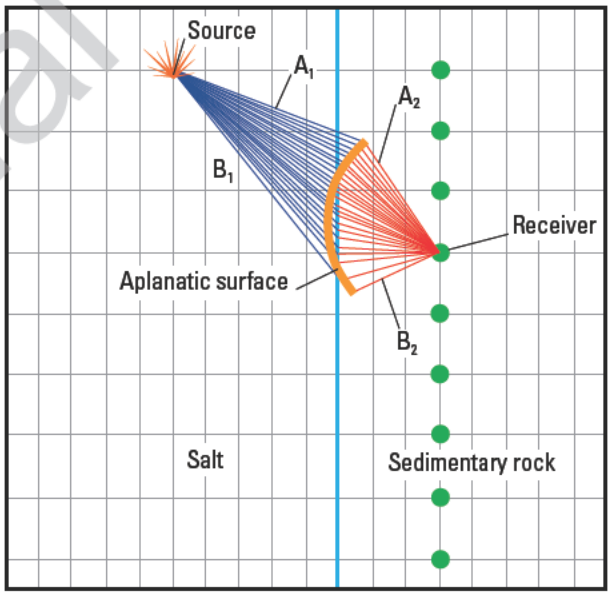

Figure 6-49. Construction of the aplanatic surface (orange line) for one source-receiver pair; see text for discussion.

In a preferred method today, VSI and gyro tools are combined to accurately orient the seismic sensors without the shortcoming of noise-prone gimballed geophones. A 3D calculation of the traveltime inversion involves finding the unique solution using both the traveltime and the arrival angle of the wave at the tool. The 3D version of the aplanatic curve, the aplanatic surface, can be found

kinematically by ray tracing from the source toward the receiver in the borehole. The actual point on this surface that represents the salt exit point is found by tracing a ray that starts out in the direction indicated by the 3C energy arrival vector at the geophone, which is back toward the origin of the direct energy arrival, and intersects with the aplanatic surface. If this analysis is performed for each source-receiver pair, the result will be a collection of points in three dimensions that will lie on the salt surface (Fig. 6-50). To interpret a surface from these points will involve other geometrical constraints or data from other source positions or boreholes.

6.6.3 Near-salt survey design

To improve imaging below or near salt bodies, Schlumberger uses an innovative 3D survey-design technique. A VSP source, positioned precisely for optimal subsurface coverage, improves imaging of reservoir reflectors, even with proximity to salt. The salt geometry derived from these VSPs can then be used to look ahead of the bit for deeper potential targets and to evaluate lateral changes in reservoirs.

The salt-proximity VSP combines borehole and surface seismic modeling, which encompasses three steps. The first step is to define the subsurface area to be imaged,

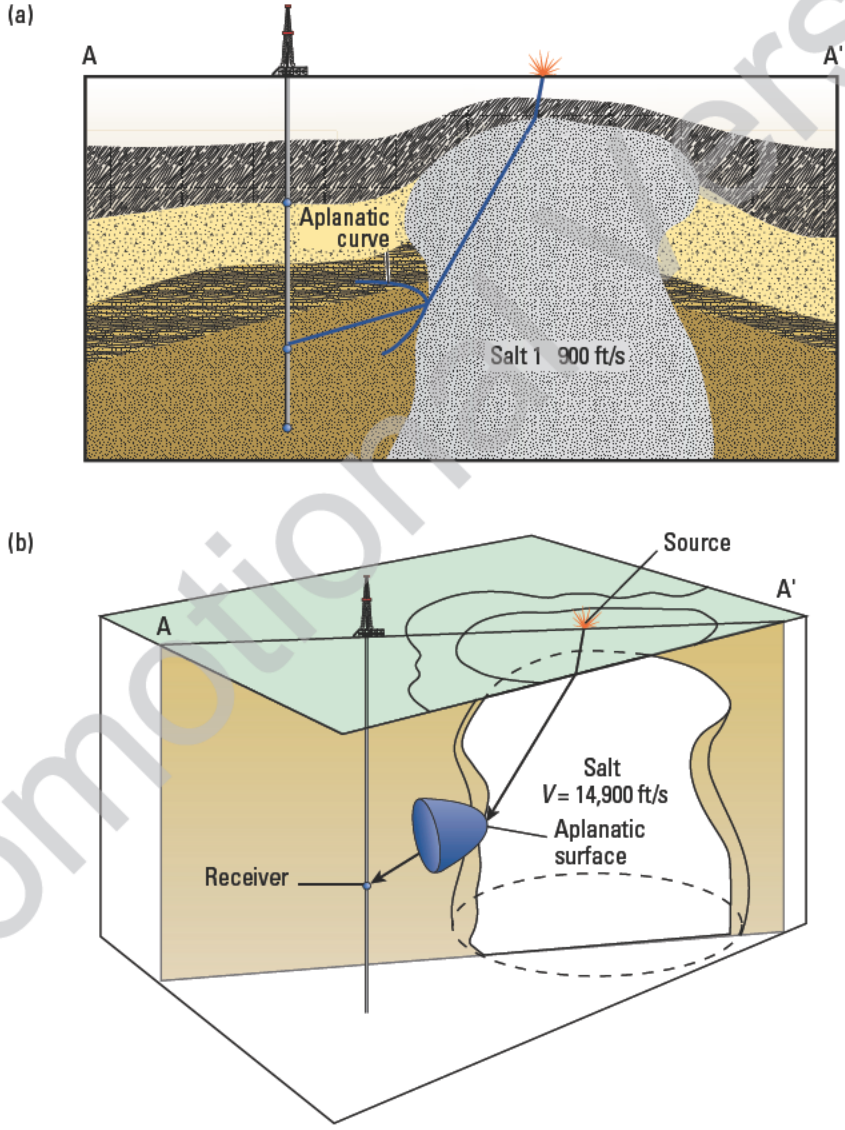

Figure 6-50. In the real world, the flank of the salt dome is tangent to the aplanatic surface where the minimum-time ray intersects it (a). In three dimensions (b), the aplanatic curve becomes a cone for each source-receiver pair. (From Gardner, 1949.)

which is done by aiming rays down the ray cones, as seen in Fig. 6-51. In the second step, rays are shot from the image area to the surface. An analysis of the rays arriving at the surface indicates the optimal source location (Fig. 6-52). The third step encompasses ray tracing from the optimal source location to the image area and then to the receivers (Fig. 6-53). This last step confirms that the desired target area will be optimally imaged.

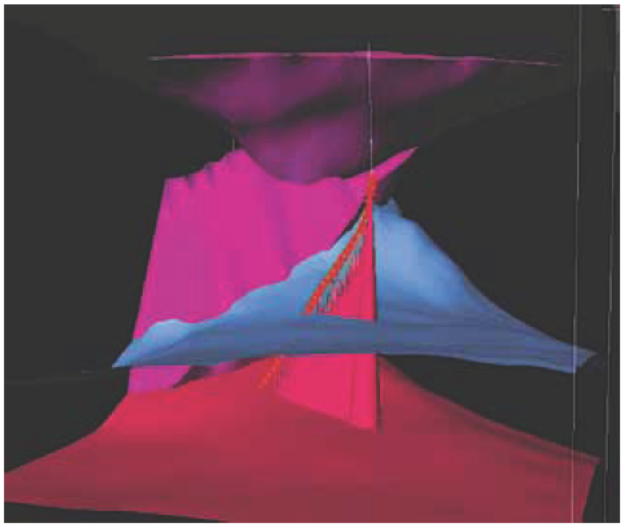

Figure 6-51. 3D presurvey modeling—shooting rays along ray cones to horizon of interest. (From Campbell *et al.*, 2006.)

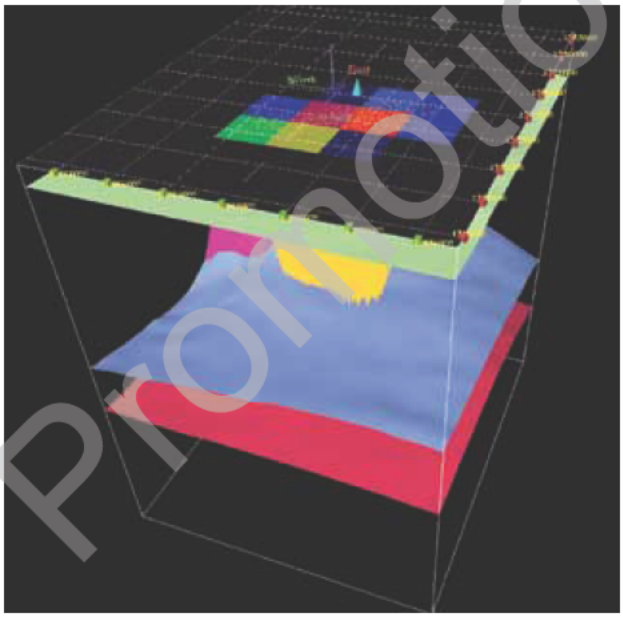

Figure 6-52. 3D presurvey modeling—histogram of rays intersecting top surface of model to define optimal source location. (From Campbell *et al.*, 2006.)

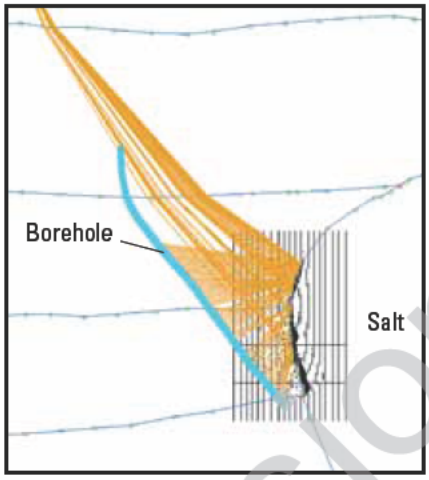

Figure 6-53. Ray-trace modeling that shows energy bouncing off a salt flank.

Presurvey modeling can include ray-trace and finite-difference simulation of the survey (Fig. 6-54). These techniques can determine the feasibility of the salt-flank imaging and help interpretation of the recorded wavefields. A ray-trace simulation provides a quick look at the expected travel paths of selected seismic wavefields.

Finite-difference wavefield snapshots aid in the interpretation of all the complex wavefields that can be recorded near salt. These snapshots can also confirm that the ideal source position defined in the 3D modeling will, in fact, provide a VSP free of harmful salt effects.

In the Gulf of Mexico, an operator was drilling near a salt body that was causing undesirable effects that limited the resolution of surface seismic data and, subsequently, the proper delineation of reservoirs (Fig. 6-55). Images from Well 1 presented a series of amplitude anomalies near the salt flank (Fig. 6-56). This well encountered a prolific pay zone in the sands indicated in the seismic section. Well 3, an updip development well, was drilled to evaluate reservoir continuity. This well found pay in a zone equivalent to that of Well 1, but a possible stratigraphic variation between wells was suspected. Understanding the continuity of the reservoir was crucial to develop the optimal depletion plan for the field (Campbell *et al.*, 2006). An offset VSP survey was devised primarily to confirm the lateral extent of a reservoir zone at TD. The VSP image was also used to look ahead of the bit for deeper potential targets and to evaluate lateral changes in the reservoir. Another goal of the survey was to determine the distance of the bit from the salt flank.

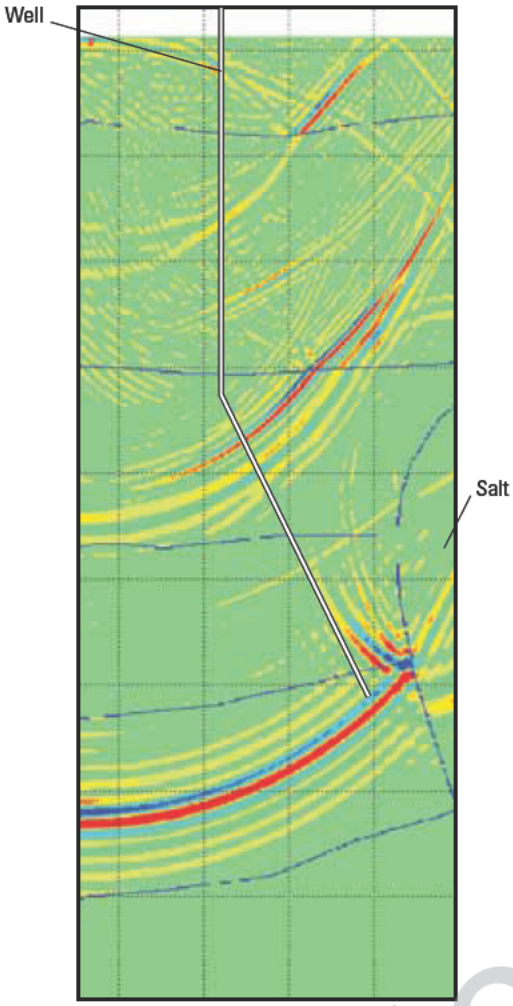

Figure 6-54. Snapshot from finite-difference modeling that shows energy bouncing off a salt flank.

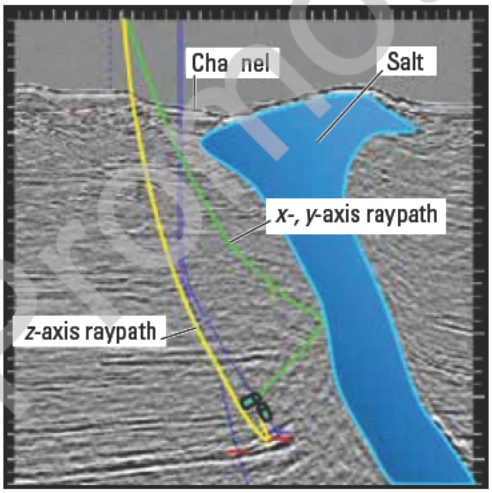

Figure 6-55. Acquisition setup for a VSP survey to image the reservoir and the salt flank. Well trajectories are indicated by the blue lines. (From Campbell *et al.*, 2006.)

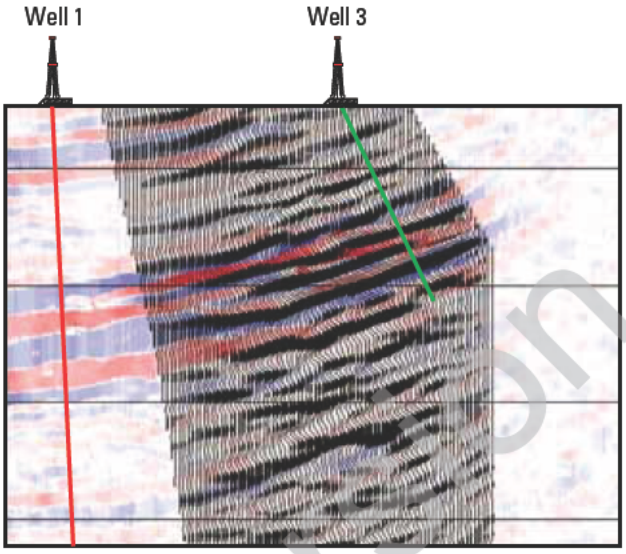

Figure 6-56. High-resolution VSP reservoir image overlying surface seismic image. (From Campbell *et al.*, 2006.)

The borehole seismic survey was modeled using the 3D survey technique to position a VSP source for optimal subsurface coverage. The VSP data were then quickly processed for reservoir evaluation, resolution of any deeper targets, and estimation of the distance to nearby salt flanks.

To process the VSP data for a high-resolution reservoir image, the data were taken through amplitude correction, wavefield separation, wave-shaping deconvolution, and migration using a GRT algorithm. The VSP image in Fig. 6-56 has a 40% to 50% wider bandwidth than the surface seismic image, which improves the estimate of reservoir continuity.

Salt reflections—typically horizontally polarized events recorded on the horizontal geophones—were isolated and migrated using GRT migration (Fig. 6-57) after the processing was completed for a reservoir image. The improved subsurface resolution of the VSP image allowed confident interpretation of stratigraphic relationships and provided a high-confidence interpretation of the updip reservoir boundary, which resulted in better understanding of reservoir reserves.

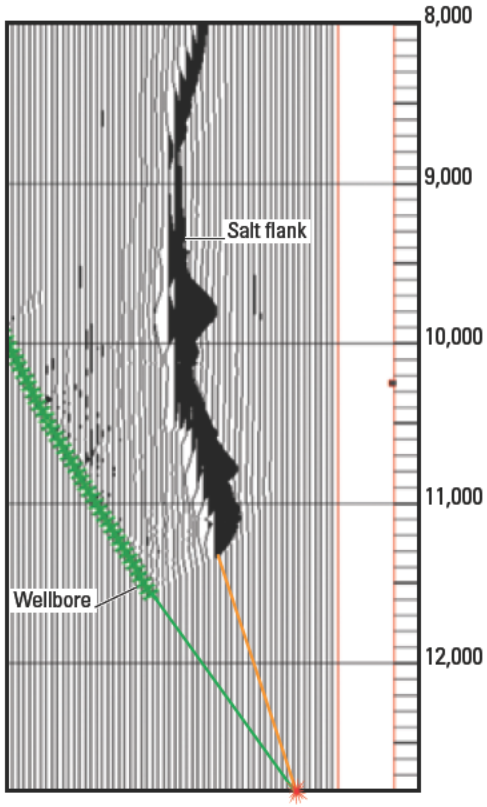

Figure 6-57. Migrated salt-flank image from VSP data with extrapolation of the wellbore (green) to the salt entry point. (From Campbell *et al.*, 2006.)

6.7 Crosswell seismic surveys

Unlike surface seismic surveys, which provide an image of reflector location and acoustic impedance, crosswell surveys directly map velocity between wells by measuring traveltimes. An example (Fig. 6-58) shows the velocity changes associated with movement of a steam front in the Athabasca tar sands of Alberta, Canada. A base survey was run between two wells before steam was injected into a third well located halfway between the two survey wells. The monitor survey, taken about thre months after steam injection began, shows a de rease in velocity caused by increased temperature near and above the perforated interval (Justice *et al.*, 199).

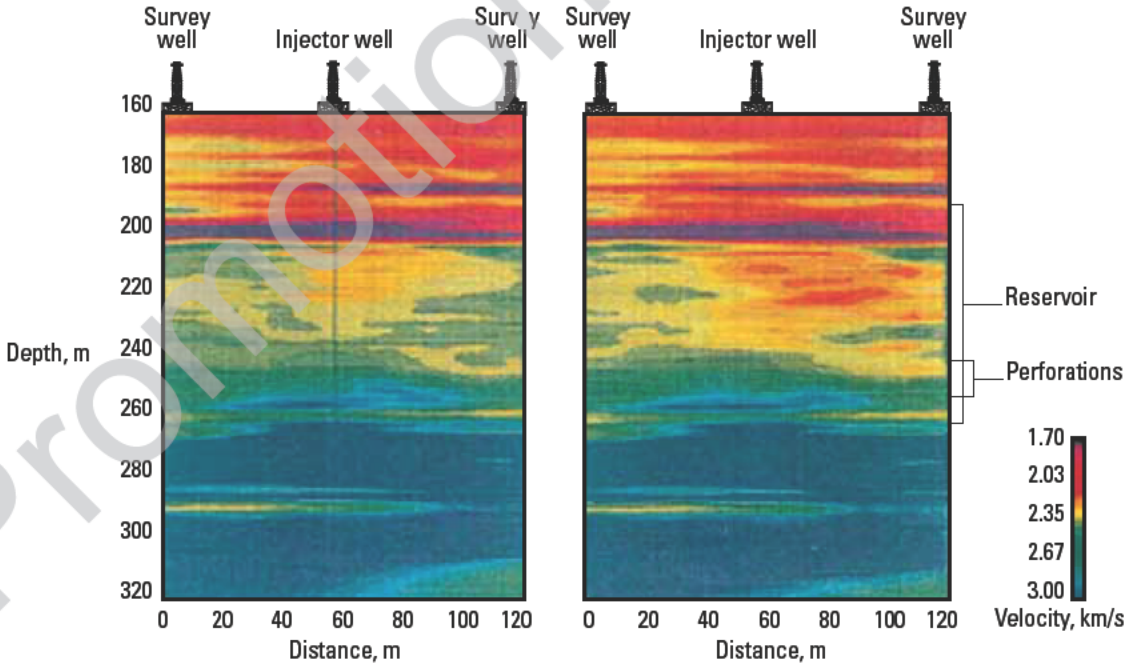

Figure 6-58. Crosswell images before and after steam injection in the Athabasca tar sands, Alberta, Canada. The base survey (left) was acquired before steam injection. The injection well is halfway between the survey wells. The monitor survey (right) was run three months after steam injection began. The reservoir interval is at 190 to 260 m depth, with a gas cap from 197 to 205 m. Perforation interval is at 240 to 250 m depth. As seen from the velocity decrease—more orange and red—the steam has risen and retreated to the right. (From Albright *et al.*, 1994; this graphic is copyright Schlumberger, Ltd. Used with permission. Courtesy of John Fairborn, Chevron Petroleum Technology Company, La Habra, California, USA.)

6.8 Time-lapse seismic surveys

A more quantitative way of using 4D seismic to monitor fluid movement is to include synthetic seismic sections and reservoir fluid-flow simulations in the calibration and interpretation. Norsk Hydro is using this technique to track a gas/oil contact (GOC) during gas injection (Johnstad and Ahmed, 1992; Johnstad *et al*., 1993). Two 3D surface seismic surveys were acquired 16 months apart in the Oseberg field, Norwegian North Sea. Special care was taken to preserve true amplitudes during processing. The base survey served several purposes. It provided structure for the initial reservoir model and input for further drilling and development decisions as well as acoustic properties of lithologies and fluids. Amplitudes of the base survey were used to derive acoustic impedances through inversion. Then, acoustic impedances were related to rock types and fluid saturations by using the reservoir fluid-flow model derived from production data.

The injection of gas into the Oseberg field pushed the GOC deeper and farther from the injection well. Dual-Burst* Thermal Decay Time measurements in a well bordering the monitored area show the displacement of the GOC with time (Fig. 6-59). This displacement agrees with that shown on the surface seismic image and with the simulated reservoir fluid flow for the period between the seismic surveys (Fig. 6-60). VSP images support the same interpretation. Time-lapse VSP data from the same well that has the Thermal Decay Time logs also sh w downward movement of the GOC (Fig. 6-61).

Another interesting example comes f om the Violet Grove pilot project, 100 km sou hwes of Edmonton, Alberta (Couëslan *et al*., 2006). Carb n dioxide is being injected into the Cardium Form tion n the Pembina field for enhanced recovery and c rbon sequestration purposes. The reservoir is being monitored using simultaneously acquired time-lapse multicomponent surface and borehole seismic su veys The baseline walkaway

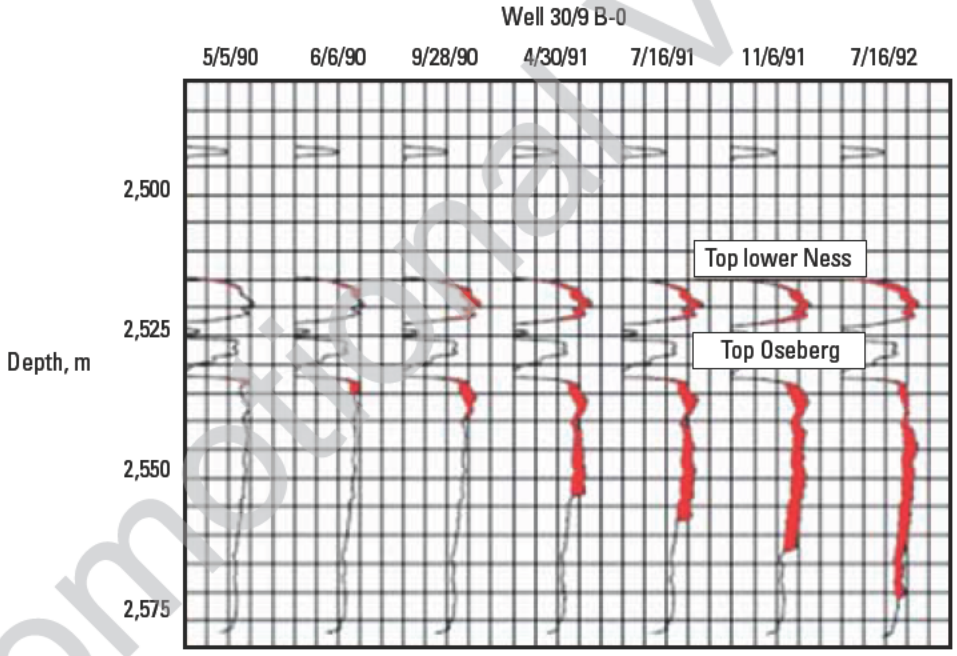

Figure 6-59. D al-Burst The mal Decay Time logs showing thickening of a gas cap with time. The well location is a he sout n edge of the monitored area. The Dual-Burst Thermal Decay Time tool emits pu ses o high- peed neutrons and measures the rate at which thermal neutrons are captured. Gas is dentified by an in rease in the count rate. (From Johnstad *et al.*, 1993.)

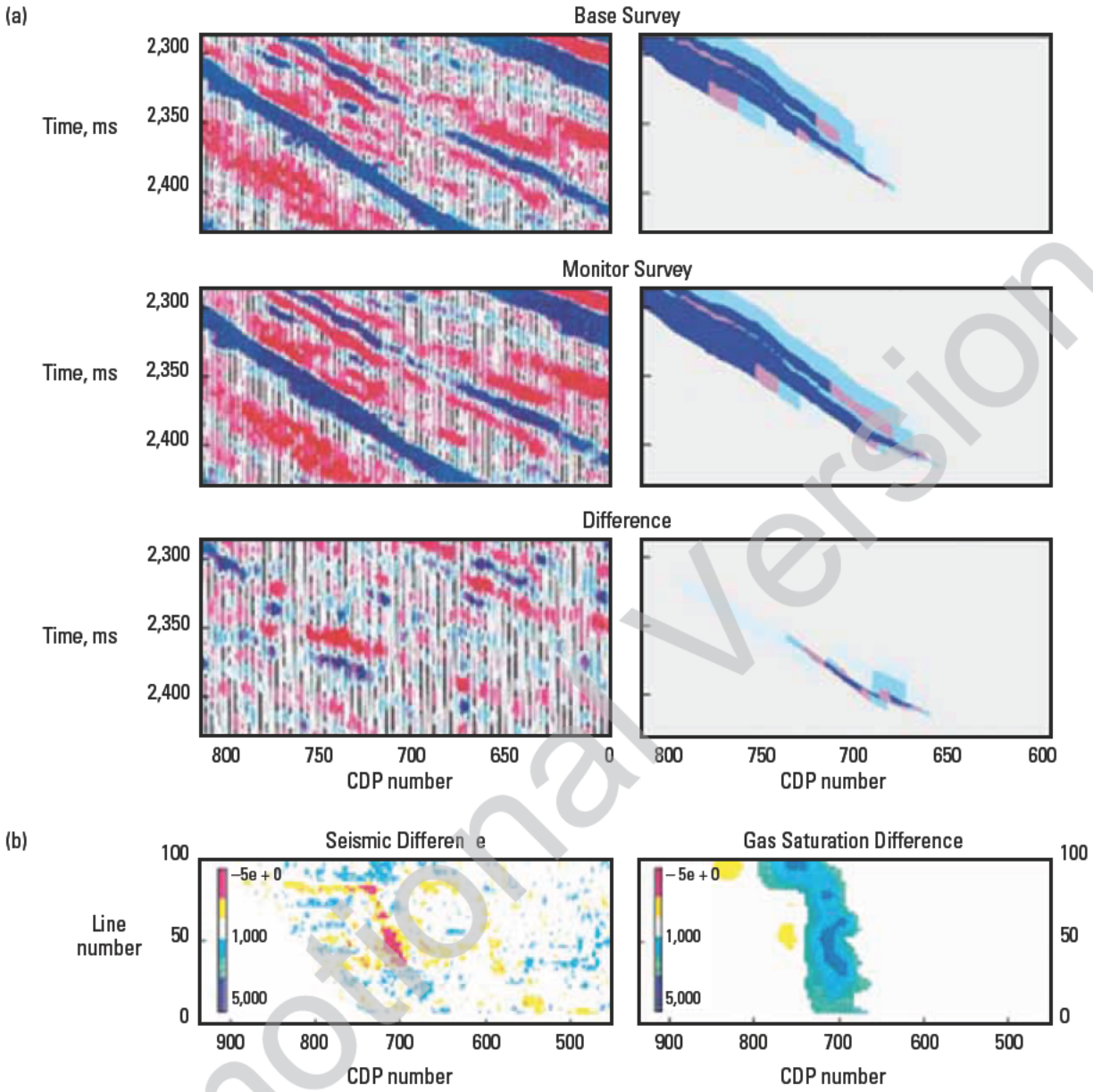

Figure 6-60. Oseberg seism c-d fference ections and simulated reservoir model sections. Vertical sections (a), from top to bottom, of ismic li e 60 from the base and monitor survey and their difference are shown on the left. Simulated gas satur ions at the time of the base and monitor surveys and their difference are shown on the right in (a). Horizon al se tion (b) made through the middle of the reservoir at a time slice at 2,356 ms in the seismic-differ nce volu e (left) shows the greatest difference around Line 50, CDP 700. The correspond-ing horizontal slice hrough the simulated gas-saturation-difference volume (right) predicts the same location for th great t difference in gas saturation. (From Johnstad *et al.*, 1993.)

sur y was acquired in March 2005, prior to CO_2 injection. T e first monitor survey was acquired in December 2005, after eight months of CO_2 injection. The geometry of the survey is shown in Fig. 6-62. The two datasets were processed identically, and each survey was migrated using the calculated anisotropic velocity model. Figure 6-63 compares the P-wave surface seismic data profile with the P- and SV-wave VSP data. The walkaway VSP image is in good agreement with the surface seismic data; it shows enhanced both vertical and lateral resolutions.

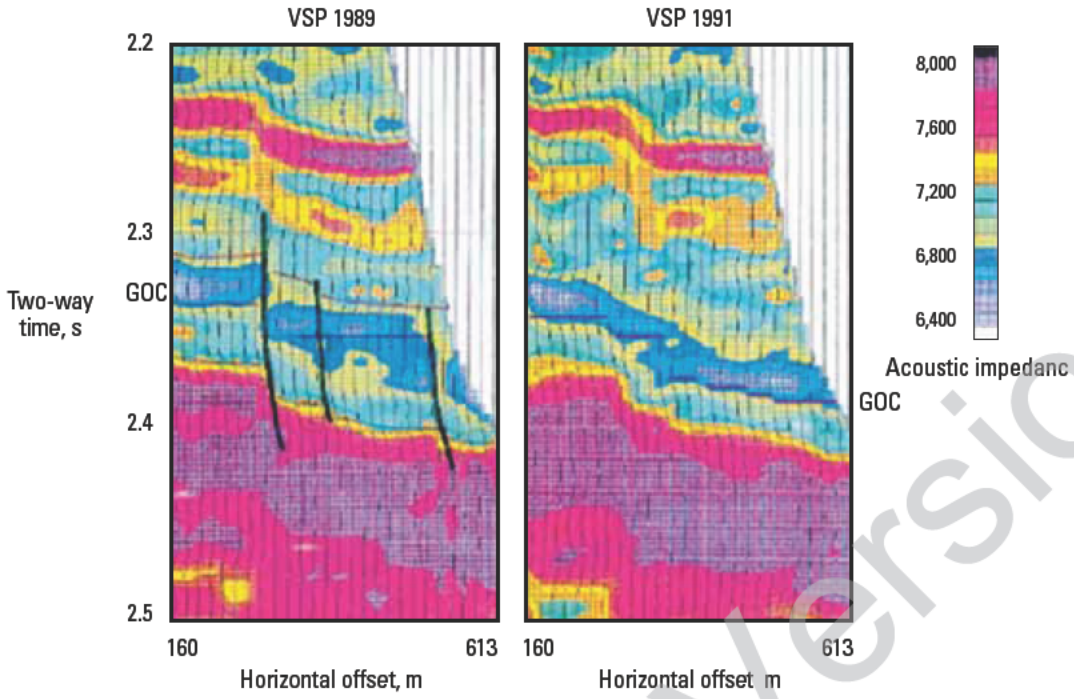

Figure 6-61. Repeated VSPs from 1989 and 1991. Overlay pattern is acoustic impedance v lues. VSPs shot 22 months apart show the downward progression of the GOC (blue line) from 2.354 s to 2.390 s. With the known seismic velocity for the interval, this traveltime difference translates to a 44-m d op in the GOC—in agreement with thermal decay time observations in the same well (Fig. 6-59). (From Albrigh *et al.*, 1994; this graphic is copyright Schlumberger, Ltd. Used with permission; Johnstad and Ahmed, 199)

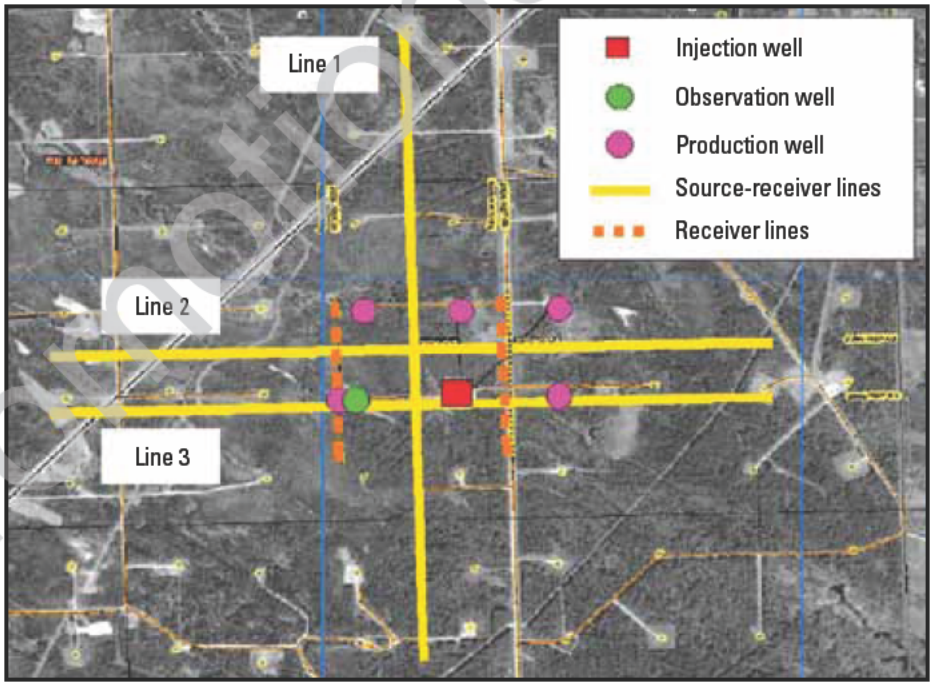

Figure 6-62. Aerial photograph of the Violet Grove CO_2 injection site. (From Couëslan *et al.*, 2006.)

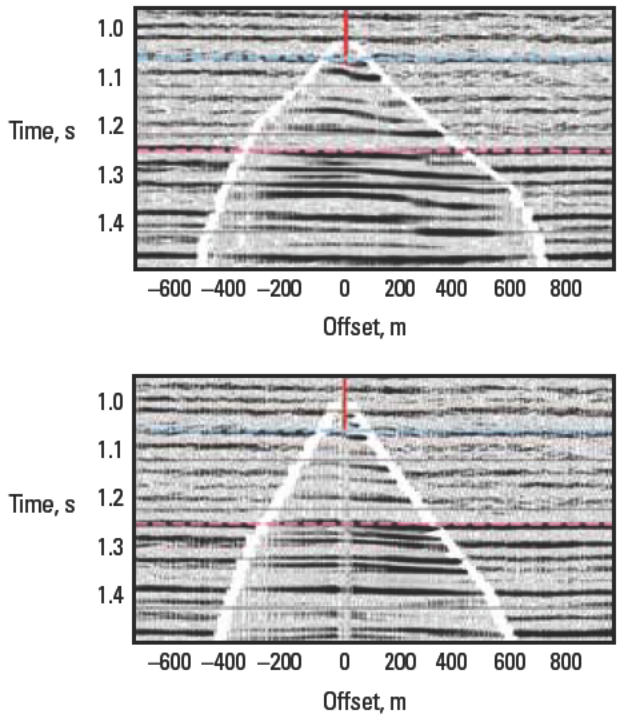

Figure 6-63. Seismic images showing tie between the P-wave VSP (top), SV-wave VSP (bottom), and surface seismic data for Line 3, Violet Grove pilot project (Fig. 6-62). The Cardium Formation is in blue, the Viking Formation is in pink. (From Couëslan *et al.*, 2006.)

Comparison of the baseline and monitor surveys reveals changes in amplitude at the Cardium Formation event; amplitudes have increased with time. A bulk time shift is also observable, especially in SV data, which may indicate fluid displacement. Figure 6-64 shows the differences obtained using the P- and SV-wave data from Line 2 in Fig. 6-62. There is no increase in amplitude for seismic events at later times. Aided with this information, geoscientists interpret that the CO_2 flood is moving southwest of the injector along a dominant fracture trend in the area.

6.9 Obtaining images in extreme conditions

In the North Sea, an operator was drilli g a well with TD greater than 4,600 m and t mpe atures in excess of 193 degC. The well trajectory wa deviated above a chalky formation and then was sidetracked out of the plane of deviation as depth increased. The slim analog seismic tool, as desc ibed in Chapter 3, was used to acquire a VSP in this borehole environment. To prepare for the high tension expected on the wireline, high-strength wireline able and dual-drum capstan were required (Fig. 6-65).

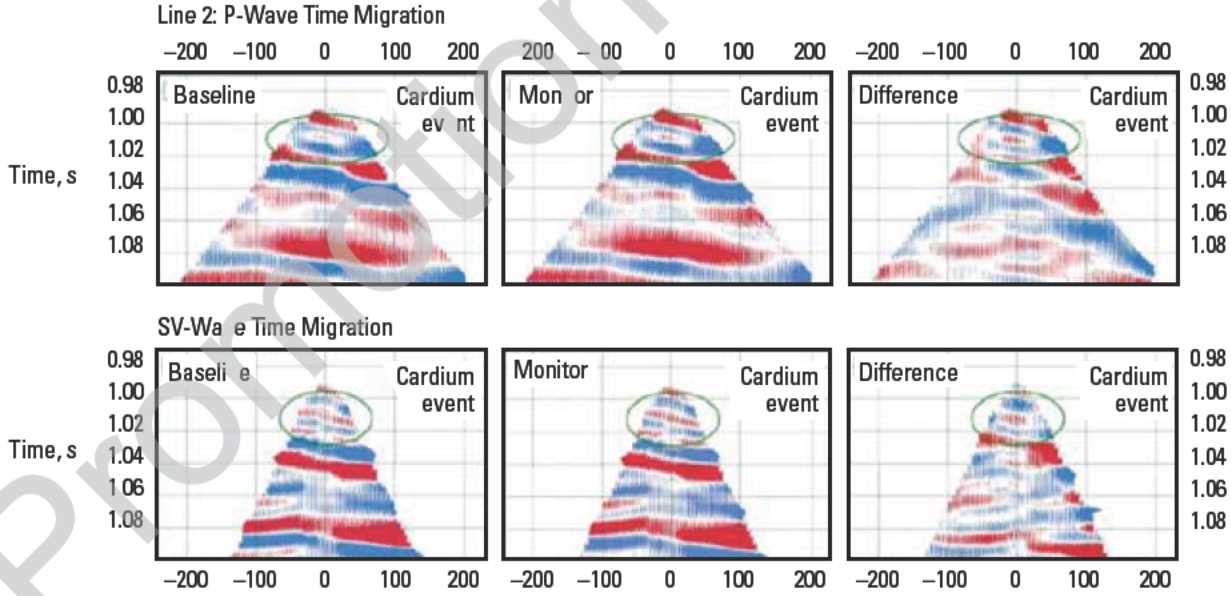

Figure 6 64. Baseline and monitor survey time migrations and difference displays for the P- and SV-wave data from Line 2, Violet Grove pilot project (Fig. 6-62). Amplitudes at the Cardium Formation have increased up to 50% on some traces. (From Couëslan *et al.*, 2006.)

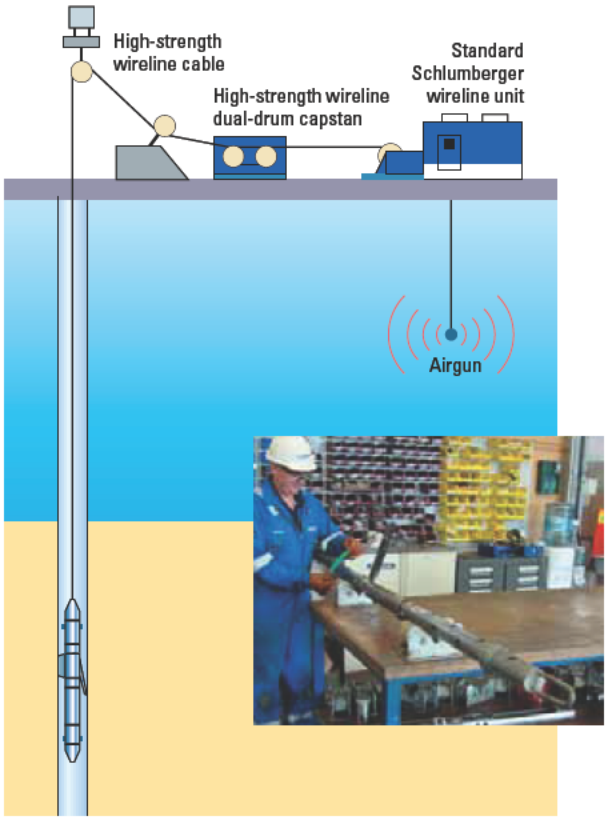

Figure 6-65. Borehole seismic acquisition tool for extreme conditions. The SlimXtreme* slimhole, high-pressure, high-temperature logging platform operates in conditions up to 30,000 psi and 260 degC. Operating companies have used the tool in condition up to 238 degC. (From Blackburn *et al.*, 2007; this graphic is copyrig t Schlumberger, Ltd. Used with permission.)

The operator had several reasons o run a VSP in this well:

- VSP would generate an accurate time-depth correlation between well data and the time based 3D marine seismic data over the targe . The reflection at the base of the chalk was clearl int rpretable in seismic sections, whereas the deeper eflectio at the top of the reservoir was not. This lea ly pr sented problems in confidently interpreting he shape and extent of the reservoir.
- VSP would provide an accurate depth-based image of the reservoir and layers below TD. Surface seismic data suffered with noise from multiples, which could be corrected with a VSP image that may contain fewer multiples (Chapter 4). This noise appears as horizontal reflections that interfere with the signals from the dipping reservoir layers. With the image extended below the well, the correlation with layers identifiable on surface seismic data becomes possible.
- VSP would provide better estimates of formation velocities to improve reprocessing of the 3D marine seismic data. Velocities of the chalk and u derlying formations were not reliable. Impro ed velo ities in this section would produce more a curate 3D images and potentially lead to reduced risk in future drilling in the area.

The survey was designe to acquire 73 stations every 15 m, spanning a depth interval from the reservoir up through the chalk and more widely spaced intervals higher in the s ction At TD, the temperature reached 193 degC. An airgun cluster with three 150-in^3 guns was used as the seismi source deployed at the rig in a zero-offset survey configuration.

Processing the 3C data to determine from where the reflec ions originated included standard steps as well as a s ecial correction for the 3D nature of the borehole trajec ory. This allowed the VSP data to be migrated using a 2D algorithm. Details of the processing can be found in Blackburn *et al.* (2007).

The VSP detected higher velocities in the chalk layer and lower velocities below the chalk than was seen in the surface seismic velocity model. These differences translated into misties observed between the VSP image and the surface seismic image below the chalk interval (Fig. 6-66). The depths of reflectors in the VSP image also matched those of a synthetic trace generated from sonic and density well logs, thus confirming the accurate depths of the VSP image in spite of the conflict between the 3D nature of the acquisition objective and the 2D approach to solve it (Fig. 6-67).

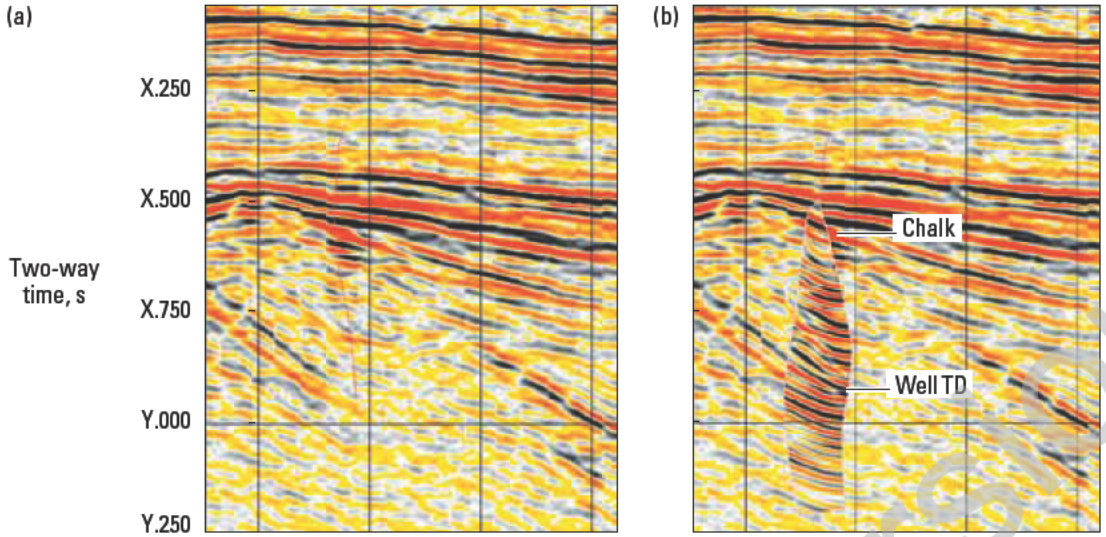

Figure 6-66. Comparison of surface seismic data (a) with VSP data (b). The surface seismic image produced using chalk velocities that are too low, fails to tie with the VSP. (The VSP shown in (b) is the small inserted region with higher amplitudes and higher resolution than the surrounding surface seismic image. The mismatch can be seen at several intervals. (From Blackburn *et al.*, 2007; this graphic is copyright Schlumberger, Ltd. Used with permission.)

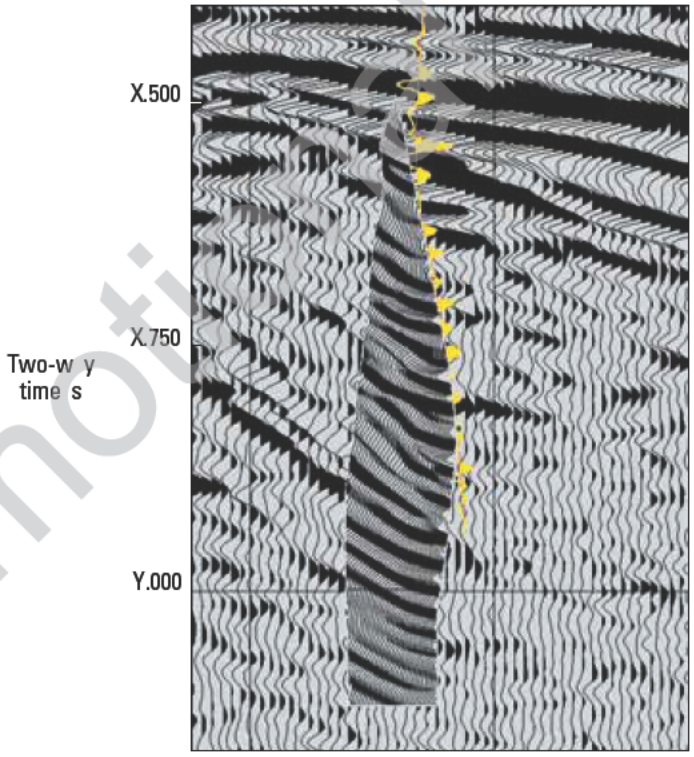

Figure 6-67. Matching reflector depths in a VSP image and a log-derived synthetic trace. One test for properly depth-correlated seismic data is to match data with a synthetic trace generated from sonic and density well logs. In this case, the synthetic trace is plotted in yellow for visibility, and only positive amplitudes are plotted so as not to obscure the seismic data. Throughout most of the well, the positive amplitudes in the synthetic trace correlate with those in the VSP, which lends confidence to the projection assumptions made during processing. The VSP image extends beyond the bottom of the well. (From Blackburn *et al.*, 2007; this graphic is copyright Schlumberger, Ltd. Used with permission.)

6.10 References

Albright, J., Cassell, B., Dangerfield, J., Deflandre, J-P., Johnstad, S., and Withers, R.: "Seismic Surveillance for Monitoring Reservoir Changes," *Oilfield Review* (January 1994) 6, No. 1, 4–14.

Armstrong, P., Verliac, M., Monroy, N., Ramirez, H.B., and Leite, A.O.: "Shear Wave Applications from Zero-Offset VSP Data," presented at the 63rd EAGE Annual Conference and Exhibition, Amsterdam, The Netherlands (June 11–15, 2001).

Arroyo, J.L., Breton, P., Dijkerman, H., Dingwall, S., Guerra, R., Hope, R., Hornby, B., *et al.*: "Superior Seismic Data from the Borehole," *Oilfield Review* (Spring 2003) 15, No. 1, 2–23.

Barzaghi, L., Continisio, R., Miranda, F., and Ogliani, F.: "A 3D VSP Case History from the Adriatic Sea," *Italy 2000—Value-Added Reservoir Characterization*, Milan, Italy, Schlumberger Italiana S.p.A. (2000), 94–103.

Baysal, E., Kosloff, D.D., and Sherwood, J.W.C.: "Reverse Time Migration," *Geophysics* (1983) 48, No. 11, 1514–1524.

Beylkin, G., and Burridge, R.: "Multiparameter Inversion for Acoustic and Elastic Media," *Expanded Abstracts*, 57th SEG Annual International Meeting and Exposition, New Orleans, Louisiana, USA (October 11–15, 1987), 741–749.

Beylkin, G., Miller, D., and Oristaglio, M.: "The Generalized Radon Transform: A Breakthrough in Seismic Migration," *The Technical Review* (1987) 35, No. 3, 20–27.

Blackburn, J., Daniels, J., Dingwall, S., Hampden-Smith, G., Leaney, S., Le Calvez, J., *et al.*: "Borehole Seismic Surveys: Beyond the Vertical Profile," *Oilfield Review* (Autumn 2007) 19, No. 3, 20–35.

Camara Alfaro, J., Corcoran, C., Davies, K., Gonzalez, P.F., Hill, D., Hampson, G., Howard, M., *et al.*: "Reducing Exploration Risk," *Oilfield Review* (Spring 2007) 19, No. 1, 26–43.

Campbell, A., Nutt, L., Smith, R., and Chang, H.: "Designing Borehole Seismic VSPs for Complex Subsalt or Near-Salt Reservoir Evaluation," *First Break* (2006) 24, No. 5, 69–74.

Christie, P., Dodds, K., Ireson, D., Johnston, L., Rutherford, J., Schaffner, J., and Smith, N.: "Borehole Seismic Data Sharpen the Reservoir Image," *Oilfield Review* (Winter 1995) 7, No. 4, 18–31.

Claerbout, J.F., and Doherty, S.M.: "Downward Continuation of Moveout-Corrected Seismograms," *Geophysics* (1972) 37, No. 11, 741–768.

Couëslan, M.L., Lawton, D.C., and Jones, M.: "Time-Lapse Monitoring of CO_2 EOR and Storage with Walkaway VSPs," *Expanded Abstracts*, 76th SEG Annual International Meeting and Exposition, New Orleans, Louisiana, USA (October 1–6, 2006), 3130–3134.

Dingwall, S., Puech, J.C., and Louden, F.: "Resolving an AVO Ambiguity with Borehole Acoustic Data—A Case Study," presented at the 65th EAGE Annual Conference and Exhibition, Stavanger, Norway (June 2–3, 2003).

Djikpesse, H., Dong, S., Haldorsen, J., and Miller, D.: "Comparing Interferometric Migration and Mirror Imaging of 3D VSP Free-Surface Multiples, *Noise and Diffuse Wavefields—Extended Abstract of the Neustadt Workshop*, C. Sens-Schönfelder, J. Ritter, U. Wegler, and C. Grosse (eds), Mitteilungen der Deutschen Geophysikalischen Gesellschaft Sonderband II (special volume 2) (2009), ISBN 978-3-00-027952-2, 79–85.

Ediriweera, K., Smith, N., and Prudden, M.: "Borehole Seismic Surveys in Horizontal Wells—A Case Study from the North Sea," paper B018 presented at the 57th EAEG Annual Conference and Exhibition, Glasgow, Scotland (May 29–June 2, 1995).

Esmersoy, C.: "Inversion of P and SV Waves from Multicomponent Offset Vertical Seismic Profiles," *Geophysics* (1990) 55, No. 1, 39–50.

Farmer, P., Miller, D., Pieprzak, A., Rutledge, J., and Woods, R.: "Exploring the Subsalt," *Oilfield Review* (Spring 1996) 8, No. 1, 50–64.

French, W.S.: "Two-Dimensional and Three-Dimensional Migration of Model-Experiment Reflection Profiles," *Geophysics* (1974) 39, 265–277.

————————: "Computer Migration of Oblique Seismic Profiles," *Geophysics* (1975) 40, 961–980.

Gardner, L.W.: "Seismograph Determination of Salt-Dome Boundary Using Well Detector Deep on Dome Flank," *Geophysics* (1949) 14, No. 1, 29–38.

Gazdag, J., and Sguazzero, P.: "Migration of Seismic Data by Phase Shift Plus Interpolation," *Geophysics* (1984) 49, 124–131.

Hagedoorn, J.G.: "A Process of Seismic Reflection Interpretation," *Geophysical Prospecting* (1954) 2, 85–127.

Haldorsen, J., Miller, D., and Walsh, J.: "Multichannel Wiener Deconvolution of Vertical Seismic Profiles," *Geophysics* (1994) 59, No. 10, 1500–1511.

Hornby, B.E., Sharp, J.A., Farrelly, J., Hall, S., and Sugiantro, H.: "3D VSP in the Deep Water Gulf of Mexico Fills in Subsalt 'Shadow Zone,'" *First Break* (2007) 25, No. 6, 83–88.

Jackson, B., Vendeville, C., and Schulz-Ela, D.D.: "Salt-Related Structures in the Gulf of Mexico: A Field Guide for Geophysicists," *The Leading Edge* (1994) 13, No. 8, 837–842.

Johnstad, S.E., and Ahmed, H.: "Reservoir Monitoring by Application of the VSP Technique in the Oseberg Field," presented at the 54th EAEG Annual Conference and Exhibition, Paris, France (June 1–5, 1992), 200–201.

Johnstad, S.E., Uden, R.C., and Dunlop, K.N.B.: "Seismic Reservoir Monitoring over the Oseberg Field," *First Break* (1993) 11, No. 5, 177–185.

Justice, J.H., Mathisen, M.E., Vassiliou, A.A., Shiao, I., Alameddine, B.R., and Guinzy, N.J.: "Crosswell Seismic Tomography in Improved Oil Recovery," *First Break* (1993) 11, No. 6, 229–239.

Landgren, K.M., and Deri, C.P.: "A Mechanized Process for Proximity Survey Interpretation," *First Break* (1987) 5, No. 2, 59–66.

Layzell, M.G.J., Whittaker, R.D., and Colton, P.B.: "Amplitude Partitioning and Elastic Wave Conversion in a Western Canada Offset VSP," *Expanded Abstracts*, 57th SEG Annual International Meeting and Exposition, New Orleans, Louisiana, USA (October 11–15, 1987), S13.7, 707–710.

Leaney, W.S., and Esmersoy, C.: "Parametric Decomposition of Offset VSP Wave Fields," *Expanded Abstracts*, 59th SEG Annual International Meeting and Exposition, Dallas, Texas, USA (1989) 8, 26–28

McCollum, B., and LaRue, W.W.: "Utilization of Existing Wells in Seismograph Work," *Bulletin of the American Association of Petroleum Geologists* (1931) 15, No. 12, 1409–1417.

Miller, D., Oristaglio, M., and Beylkin, G.: "A New Slant on Seismic Imaging: Migration and Integral Geometry," *Geophysics* (1987) 52, No. 7, 943–964.

Payne, M.A., Eriksen, E.A., and Rape, T.D.: "Considerations for High-Resolution VSP Imaging," *The Leading Edge* (1994) 13, No. 3, 173–180.

Ratcliff, D.W., Gray, S.H., and Whitmore N.D.: "Seismic Imaging of Salt Structures in the Gulf of Mexico," *The Leading Edge* (1992) 11, No. 4, 15–31.

Ray, A., Hornby, B., and Gestel, J.: "Largest 3D VSP in the Deep Water of the Gulf of Mexico to Provide Improved Imaging in the Thunder Horse South Field," *Expanded Abstracts*, 73rd SEG Annual International Meeting and Exposition, Dallas, Texas, USA (October 26–31, 2003), 422–425.

Sanchez, A. and Schinelli, M.: "Successful 3D-VSP on Land Using Two Wells Simultaneously," *Expanded Abstracts*, 77th SEG Annual International Meeting and Exposition, San Antonio, Texas USA (September 23–28, 2007), 3074–3078.

Schneider, W.A.: "Integral Formulation for Migration in Two and Three Dimensions," *Geophysics* (1978) 43, No. 1, 49–76.

Drilling Solutions

Michael Jones and Alejandro Martinez Pereira

7.1 Introduction

In the oil industry, projects at all stages of exploitation are driven by attempts to ascribe costs to uncertain risks. Unfortunately, the risk analysis applied is often invalid—risk is seldom a random process to which statistical methods can be applied with certainty. Data has a price, and the project management process involves balancing the amount (and selection) of data that is necessary to reduce the decision-making risk to meet some criterion. Decisions are normally made with inadequate data but with an acceptable amount of uncertainty.

The economic risk associated with drilling into overpressured zones is such a process. For most offshore wells and some remote onshore wells, the most expensive item is the rig costs, which can exceed USD 500,000 per day. Attempts to predict the presence of overpressure or the remaining distance from the drill bit to expected overpressured zones when using conventional VSP techniques can be expensive in rig time. In fact, it may be so expensive that the risk associated with the uncertainty is less expensive than the potential remedy. Any dataset that can be acquired without incurring these high rig-time costs offers a substantial benefit to the drilling process.

Seismic surveys in the borehole can help drillers identify horizons and targets in a region ahead of and around the current well trajectory. Called look-ahead VSPs, these surveys are acquired during interruptions in the drilling process. If they are acquired and processed quickly, look-ahead VSPs provide vital information about targets and hazards early enough to influence drilling decisions. Normal acquisition of a zero-offset VSP survey in a 4,000-m well might take 10 hours of rig time. If a special bit trip must be made for this acquisition, the downtime of the drilling process is substantially longer and more expensive.

One solution to this problem is to acquire the data without interrupting the drilling process—to acquire the data simultaneously with drilling. Two possibilities exist for this: VSP acquisition as part of the MWD process with a seismic tool incorporated into the drillstring and acquisition of reverse VSP data using the drill bit as the seismic source as it drills.

Having access to a real-time seismic velocity measurement and time-depth curve, and possibly to a real-time look-ahead VSP, opens several windows of opportunity to enhance both the efficiency and safety of the drilling process.

The practical-solution products for drillers are obtained through VSP inversion, which enables the use of existing seismic, density, and sonic velocity information (acquired data) to infer formation characteristics ahead of the drill bit that can be correlated to these quantities. The basics of this technique are described next.

7.2 VSP inversion

Inversion is so named because of its function as the inverse of forward modeling. Forward modeling takes an Earth model of layers with densities and velocities (i.e., acoustic impedance), combines it with a basic seismic pulse, and produces a realistic seismic trace. Inversion takes a real seismic trace, removes a basic seismic pulse, and delivers an Earth model of acoustic impedance. Seismic reflections are sensitive to acoustic impedance contrasts, not absolute impedance magnitude. Borehole seismic and sonic data provide interval traveltimes at known depths, thus constraining the velocities of individual layers.

After these velocities are combined with densities, acoustic impedances are known for one well location. A synthetic seismic trace is next computed using the known acoustic impedance and a basic seismic pulse. A filter is then derived that matches the surface seismic data at the well with the synthetic trace. The same filter is applied everywhere to the surface seismic section to extrapolate the well-based information away from the well using the surface seismic as a guide.

The simplest Earth models contain layers with densities and compressional velocities, but more elaborate inversions yield models with shear velocities as well. Ideally, inversions combine surface seismic, VSP data, and sonic and density log data.

The main use of inversion for reservoir management comes through log-property mapping. The seismically derived acoustic impedance values are tested for correlation with log data at the well location, using data such as porosity, lithology, water saturation, or any attribute that can be found to correlate.

Adequately processed seismic data are critical for inversion, but the optimal processing required to prepare data for inversion is the subject of much debate, as is the optimal inversion calculation itself. The trait that sets inversion apart from the standard processing chain for structural interpretation is the need for preservation of true relative amplitudes. Changes in trace amplitude from one location to another may reveal porosity or other formation-property variations, but these amplitude changes are subtle and may be obliterated by conventional processing.

Inversion can be performed before or after the seismic traces have been stacked (summed to create a single trace at a central location), but care must be taken to ensure that stacking does not alter amplitudes. In some cases, such as in regions where seismic reflection amplitudes vary with angle of incidence at the reflector, stacking does not preserve amplitudes and inversion must be performed prestack.

The simplest inversion scheme derives relative acoustic impedance changes for one seismic trace by computing a cumulative sum of the amplitudes in the trace. The gradual trend of increasing acoustic impedance with depth, which is invisible to seismic waves, is taken from density and cumulative sonic traveltime and added to the relative acoustic impedance results.

One of the most popular and important applications of VSPs is that of acoustic impedance inversion for overpressure prediction ahead of an intermediate TD. Because wireline VSPs generally have higher SNR than surface seismic data, they are the preferred data to use for acoustic impedance inversion. The known petrophysical correlation between increased shale porosity, or pore pressure, and decreased acoustic impedance is exploited to interpret zones of overpressure. The problem then is to transform the plot of acoustic impedance inversion versus two-way time to something meaningful to a driller (such as equivalent mud weight versus depth).

Overpressure can be interpreted as a zone of anomalous, low acoustic impedance. The output of VSP inversion is acoustic impedance in two-way time. To get inversion results in depth, a velocity profile for time-to-depth conversion must be used. This depth conversion below intermediate TD depth is based on Gardner's relation (Gardner *et al.*, 1974). Gardner expresses bulk density in terms of velocity raised to some power. It was originally derived from brine-saturated sediments composed predominantly of shale. It takes the form:

$$\rho = aV^b, \tag{7-1}$$

where a and b are coefficients, and V is velocity.

This formula indicates that the inverted acoustic impedance ($AI = \rho V$) is proportional to V^{1+b}; therefore, with a regionally determined estimate of the coefficients a and b, the inverted acoustic impedance can be transformed to velocity. From the interval velocity at each two-way-time sample below the intermediate TD, a time-versus-depth profile is then obtained.

Because velocity versus depth is estimated with the above technique, any method relating pore pressure gradient and velocity or slowness could be used (Hottman and Johnson, 1965; Eaton, 1975; Bowers, 1995). For example, the Hottman-Johnson approach is the empirical relation between reservoir fluid pressure gradient (or equivalent mud weight) and observed-minus-expected (or normal) slowness. A possible fit to the Hottman-Johnson approach may take the form:

$$\text{ppg} = 0.1052 + cD^d, \tag{7-2}$$

where ppg = pore pressure gradient in psi/ft and D = differential slowness (observed slowness minus normal slowness) in us/ft. The coefficients for the Hottman-Johnson relation are $c = 0.00393$ and $d = 0.523$.

The problem with VSP and any other surface seismic inversion is that it is a nonunique solution because of the missing low- and high-frequency information in the seismic trace itself. The more important of the two is the low-frequency information, because to determine overpressure and an accurate time-depth curve below TD requires knowledge of the the low-frequency, long-wavelength trend that ultimately governs the time-depth relationship (Borland *et al.*, 1997).

7.3 Wireline solutions

Downhole sensors may be conveyed by wireline and clamped into open hole, cased hole, or drillpipe; they also may be conveyed by drillpipe or deployed while drilling (see Figs. 2-4 and 2-16).

7.3.1 VSP through drillpipe

An operating company in the UK sector of the North Sea needed to acquire a VSP for velocity control and high-resolution imaging of target reflections below the well TD. The original deviated well had contacted only a thin, pinched-out reservoir section, so a sidetrack was planned to intersect the reservoir where it was presumed to be thicker (Fig. 7-1). However, in some places the existing well deviated by as much as 60°, and conventional wireline logging was not recommended. To run the VSI tool on drillpipe would have required removal of the drillstring.

Instead, the VSI array was pumped down the drillstring using Through-Drill Seismic borehole seismic through drillpipe service, and the sensors were coupled to the drillpipe (Fig. 7-2). Between station levels of VSP acquisition, pipe reciprocation and limited mud circulation helped prevent stuck pipe. With the VSI tool, a walkabove 160-level VSP was completed within 7 hours from rig-up to rig-down. The SWINGS seismic navigation system helped to ensure accurate source positioning. Data quality was high, even when acquired through drillpipe with 13⅜-in casing. Preprocessing was carried out at the wellsite, and compressed stacked waveforms were sent to the office by e-mail for refined processing.

The VSP provided updated velocity information to reposition the well trajectory on the surface seismic image (Fig. 7-3). Time-depth information from the VSP resulted in a modified trajectory and seismic tie to the well TD, with true TD at a deeper seismic reflection than originally supposed. The high-resolution seismic image obtained from the walkabove VSP revealed structural and stratigraphic details that are not evident in the original surface seismic image (Fig. 7-4). Faults and additional facies pinchouts were identified that could affect the success of the proposed sidetrack and subsequent production. Similar Through-Drill Seismic surveys have been acquired in boreholes with deviations ranging from 7° to 90°.

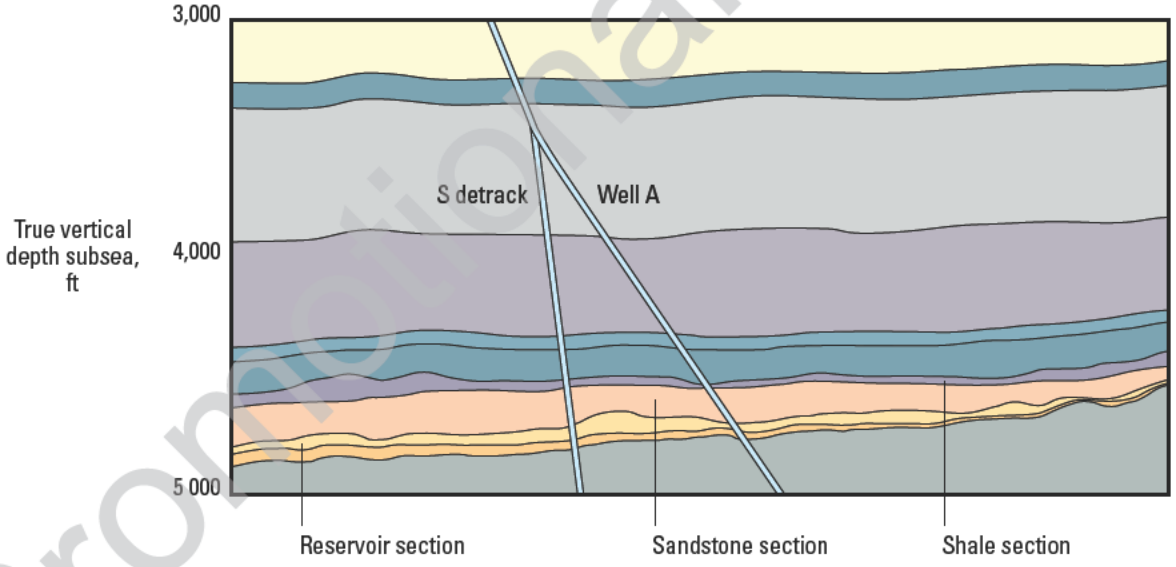

Figure 7- Cross section of layers, including a thin reservoir interval, intersected by high-angle directional Well A in the North Sea UK sector. A sidetrack was designed to penetrate what was interpreted to be a thicker part of the reservoir, but before the sidetrack was drilled, a walkabove VSP was commissioned to image the reservoir more clearly. (From Arroyo *et al.*, 2003; this graphic is copyright Schlumberger, Ltd. Used with permission.)

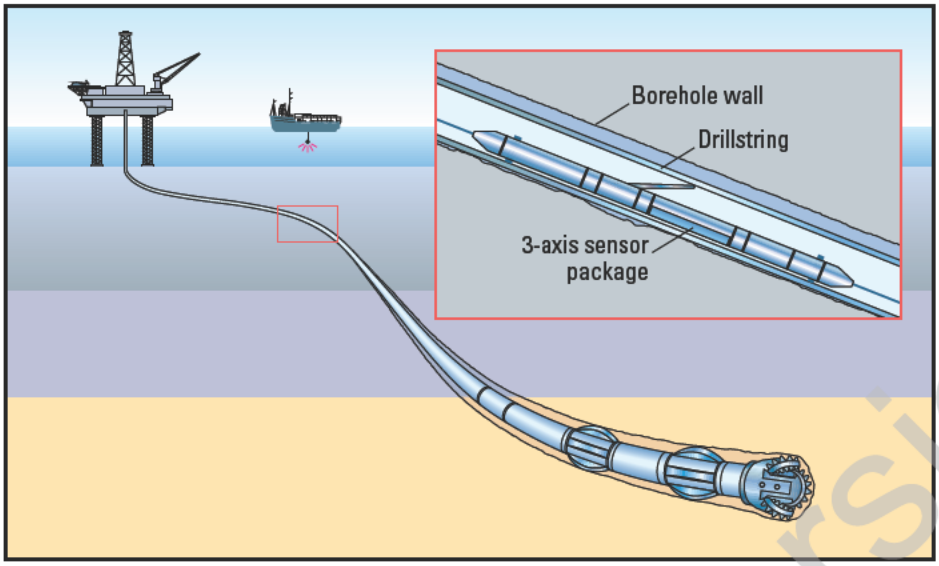

Figure 7-2. The VSI array, pumped down the drillstring and anchored inside the drillpipe to acqui e an intermediate walkabove VSP without pulling drillpipe. The VSI tool acquired high-quali data ev n through drillpipe plus 13⅜-in casing. (From Arroyo *et al.*, 2003; this graphic is copyright Schlum erge td. Used with permission.)

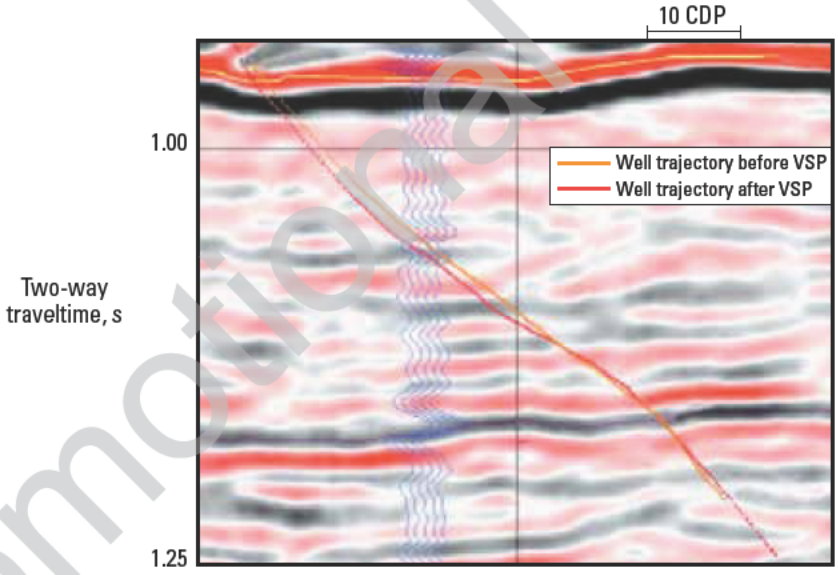

Figure 7-3. Ori ina (orange and updated (red) well trajectories plotted on the surface seismic image. Time-depth information fro the VSP tied the well TD to a later reflection in the seismic section than the original tim -depth conversion. The blue traces represent the corridor stack or the VSP reflections extracted along the orehole The ho zontal scale refers to common depth points (CDPs). (From Arroyo *et al.*, 2003; this graphic is opyright Schlumberger, Ltd. Used with permission.)

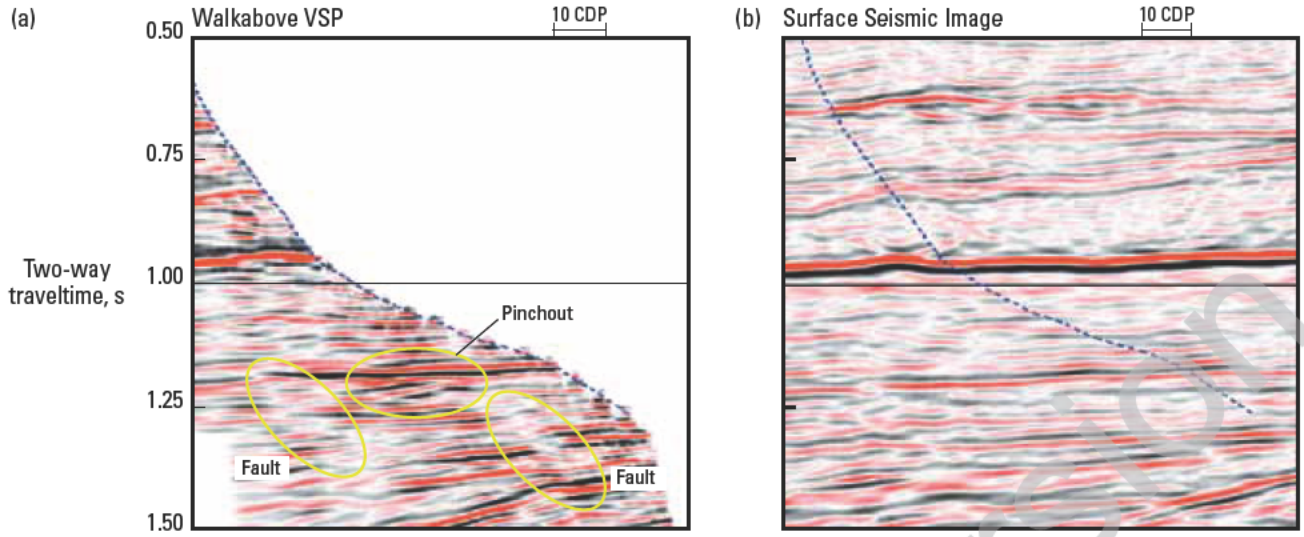

Figure 7-4. Seismic image obtained from the walkabove VSP (a) shows higher resolution below the deviated well than did the surface seismic section shown in (b). The VSP image highlights faults and stratigraphic pinchouts that are not seen in the original surface seismic image. (From Arroyo *et al.*, 003 this graphic is copyright Schlumberger, Ltd. Used with permission.)

7.3.2 Look-ahead zero-offset and walkaway VSPs

In one example, a North Sea operator faced drilling uncertainties in a vertical exploration well. After the well was drilled to within what was thought to be about 500 m of final TD, the distances to three target horizons were still unknown. To see ahead of the current borehole depth of 3,825 m, an intermediate VSP was run using a rig-bas d seismic source and a VSI tool. From rig-up to ig-d wn, it took 7 hours to acquire 123 levels of data. Data we e processed at the wellsite, and stacked wa eforms were sent to the nearby Schlumberger off e for processing and inversion. Within a few hours of acquisition, the final results were available (Fig. 7-5).

The VSI dataset showed thr e main events ahead of the current well depth, and the inversion accurately constrained the depths of hose targets and a prediction of the final target TD of 4,247 5 m. The VSI results were used in the decision to s t liner and drill the final section to reach those targets. Final TD was reached at 4,245.5 m, within 2 m of he dep h predicted by the intermediate VSP. A final VSP, pe formed after drilling ended, validated the inve sion results of the intermediate VSP (Fig. 7-6).

In another example, the operator was drilling onshore for deep, high-pressure gas. Success and safe drilling depended on tracking the position of the bit on a seismic section, on which the gas-filled formation was clearly visible. However, at the depths in question (> 4,500 m), time-depth conversion of surface seismic data has large uncertainties. Before drilling, uncertainty in the target depth was estimated at ±250 m. As an additional complic tion, much of the overburden was suspected of being anisotropic, with horizontal velocities faster than verti al velocities. If unaccounted for, anisotropy adds to the uncertainty in time-depth conversion and affects the q ality and accuracy of the seismic image.

Plans were developed for an intermediate look-ahead VSP that could deliver an updated velocity field to improve the time-depth conversion and fine-tune the target depth quickly to allow drilling to proceed safely. It was determined that, with urgent processing, the data could be acquired and processed in 24 hours. At a position about 1,500 m above the target, a 12-shuttle VSI tool acquired an intermediate look-ahead zero-offset VSP and a walkaway VSP with source positions that covered 12 km (Fig. 7-7). The walkaway survey helped to create an independent 2D image of the geological structure in the target area, and it also contained long-offset data with information about overburden anisotropy that would enhance the look-ahead prediction.

The first intermediate VSP, acquired at the same time as the walkaway survey and processed using stacking velocities and other information from the walkaway, reduced depth uncertainty to ±75 m. A second intermediate VSP, acquired 200 m above the target depth estimated by the walkaway, reduced uncertainty to ±10 m. LWD information, acquired during the last 200 m, provided gamma ray and resistivity correlation with a nearby well, further reducing uncertainty to ±5 m.

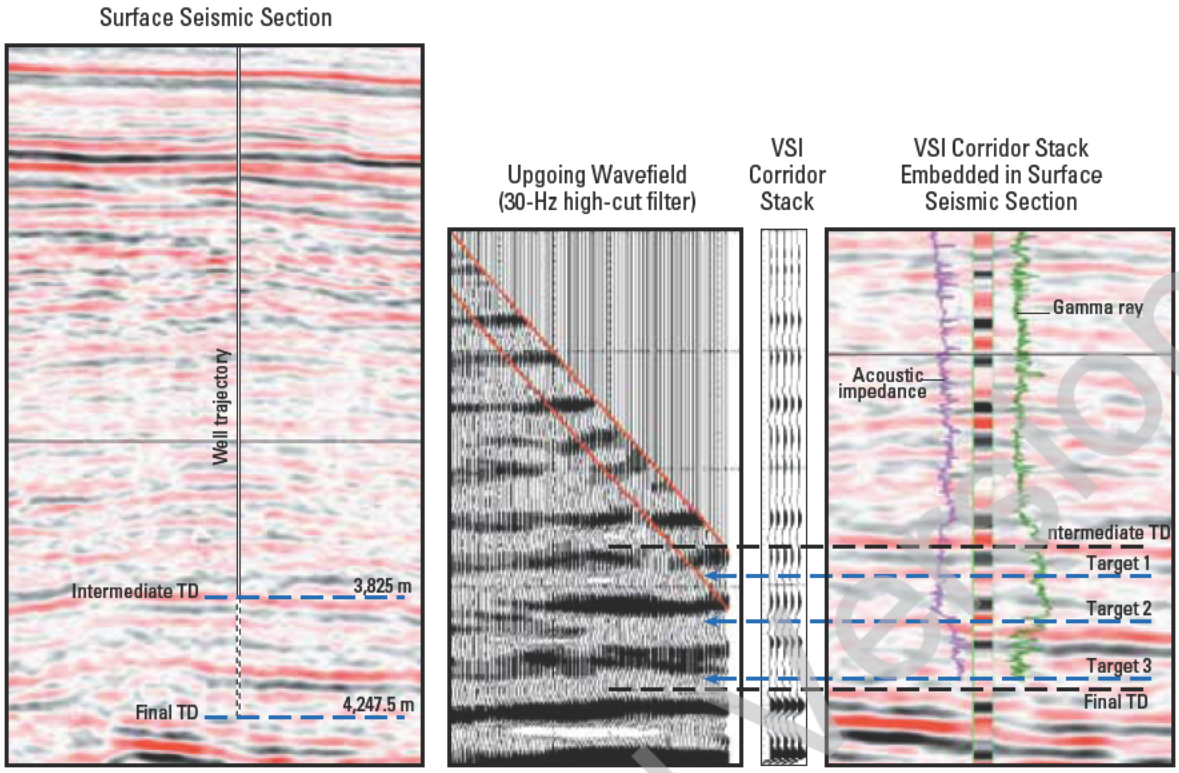

Figure 7-5. Improved surface seismic interpretation derived with an intermediate look-ahead VSP acquired with a VSI tool. The look-ahead VSP, acquired at an intermediate well depth (cen er), shows hree main events ahead of the bit and predicts final TD to be 4,247.5 m. Final TD was reached at 4,245.5 m, w thin 2 m of the depth predicted by the intermediate VSP. (From Arroyo *et al.*, 2003; this graphic is copyright Schlumberger, Ltd. Used with permission.)

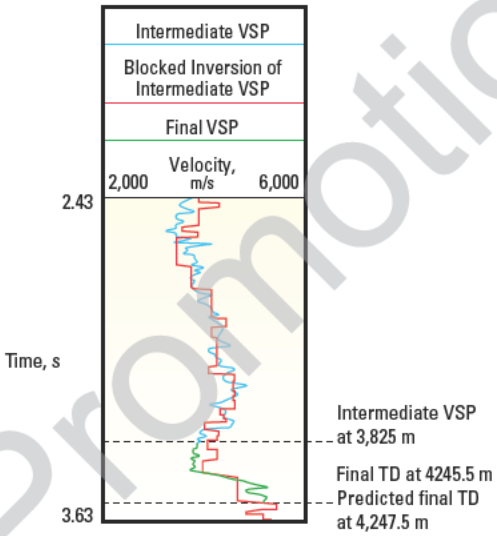

Figure 7-6. Comparison of velocity models obtained from VSPs run at intermediate and final TD. Velocities from the look-ahead VSP traveltimes (blue) and from the final VSP run at TD (green) overlay above the intermediate TD. Velocities inferred from acoustic-impedance inversion of the look-ahead VSP (red) are blocky, but yield a reasonable prediction of the velocity trend ahead of the intermediate depth to TD. (From Arroyo *et al.*, 2003; this graphic is copyright Schlumberger, Ltd. Used with permission.)

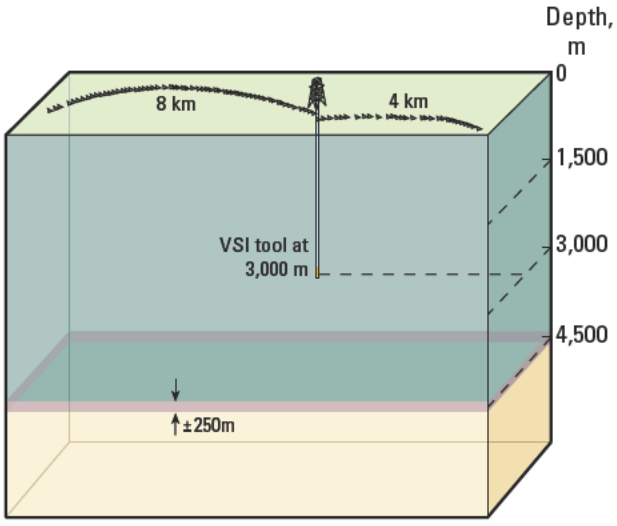

Figure 7-7. Configuration of a land-based look-ahead walkaway with source positions along a 12-km line, target at 4,500 m, and the VSI tool with 12 shuttles spaced 15.12 m apart, deployed 1,500 m above the target. Uncertainty in the target depth was ± 250 m before the look-ahead VSP was acquired. (From Arroyo *et al.*, 2003; this graphic is copyright Schlumberger, Ltd. Used with permission.)

The walkaway dataset contained more information about long-wavelength velocity variation and could be processed to predict the target depth with less uncertainty. A first pass at processing the walkaway data used a simplified, anisotropic velocity model with vertical transverse isotropy—each flat layer had vertical and horizontal velocities that, although different, remained constant within the volume investigated and could be described by two anisotropic parameters. Results from this processing step were delivered to the client via a secure Web site within the time period requested (Fig. 7-8). Once the total depth was reached, it was determined that this prediction, made from an intermediate well depth about 1,500 m above the target, was within 58 m of the target.

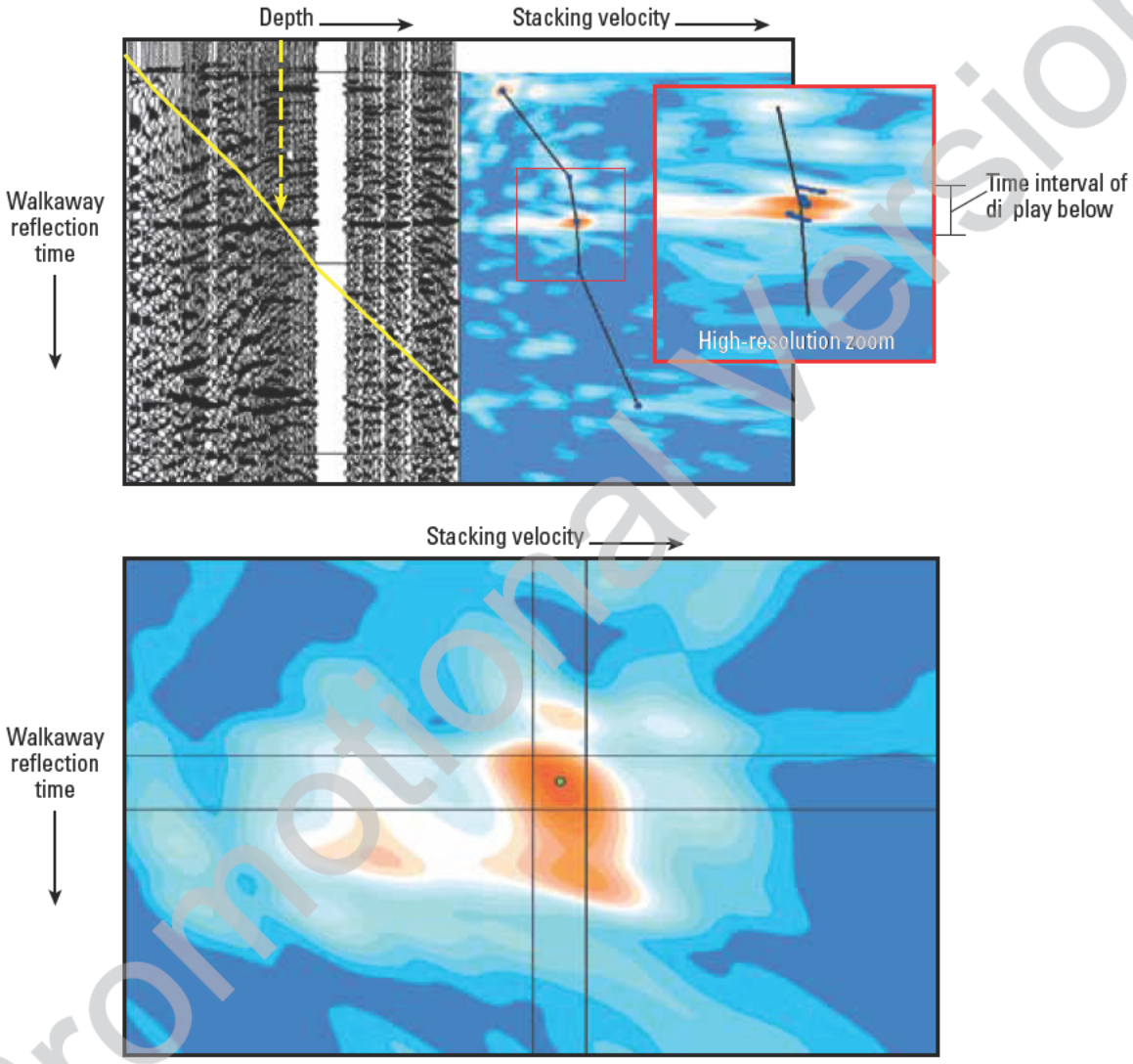

Figure 7- Target depth prediction from velocity analysis of a walkaway VSP acquired 1,500 m above the target (top). The additional information from the long offsets in the walkaway reduced uncertainty in the target-depth prediction to approximately ± 58 m as compared with the zero-offset VSP, which predicted the target depth to within 200 m. The target uncertainty of 58 m corresponds to the size of the darkest orange contour on the plot of stacking velocity versus time (inset at right). This result from early processing, delivered to the client within 24 hours, assumed an anisotropic model, but with time- or depth-invariant vertical transverse isotropy (VTI) below the receiver. Target-depth prediction from velocity analysis of walkaway data is improved by allowing for more complex anisotropic velocity (bottom). After total depth was reached, the walkaway processing scheme was revisited and optimized. By allowing time- or depth-variant anisotropy below the receiver, uncertainty in the target-depth prediction was reduced to ±5 m (orange contour). This new method now can be applied to other look-ahead walkaways for rapid predictions. (From Arroyo *et al.*, 2003; this graphic is copyright Schlumberger, Ltd. Used with permission.)

Since that time, improvements have been made to the processing software, and it is now possible to automatically scan the data for depth-dependent anisotropy. By reprocessing using the depth-dependent, anisotropic velocity model derived from the walkaway data, geophysicists now know that the walkaway data could have predicted TD within 5 m at a distance of 1,500 m above the target. Intermediate walkaway VSPs run in the future can be processed in the same way for improved look-ahead predictions and reduced drilling risk.

7.3.3 Finding reefs and geosteering

One application of offset VSP imaging is to proactively acquire the survey to revise surface seismic interpretation before committing the entire well investment. This allows the drilling engineer to steer the bit to the subsurface location with minimum risk.

Figure 7-9 shows an example of surface seismic images from the Cotton Valley reef play in Texas. The play consists of pinnacle reefs with quite limited lateral dimensions. Regional dip and the possibility of lateral velocity gradients exist, which make the migration imaging difficult and the exact lateral positioning of the reef questionable.

By running offset VSPs at an intermediate depth, the increased vertical and lateral resolution of the VSP was used to reduce the uncertainty in the image quality and positioning. The receivers are much closer to the target horizon, so the migration errors will be much smal er than for the surface seismic if we can combine the dat with a proper estimate of overburden velo ities. On the basis of the updated target information, the w ll trajectory is adjusted when drilling resumes The offset VSP image is shown overlaid on the surface s ismic in Fig. 7-10. Improved resolution in the illuminated area around the reef is clearly visibl . The well was subsequently retargeted using the VSP and the pinnacle was successfully drilled on the first attempt. For a full discussion, see Meyer nd Tittle (1998).

Consider the economic benefits of this strategy if the drilling history has been anything less than 100% successful on first attemp s. In the case of an unsuccessful first attempt, th following possible consequences arise:

- cost f logging a dry hole
- cost of sidetracking, with no guarantee of success for e second attempt because it is largely targeted with the same data as the initial attempt

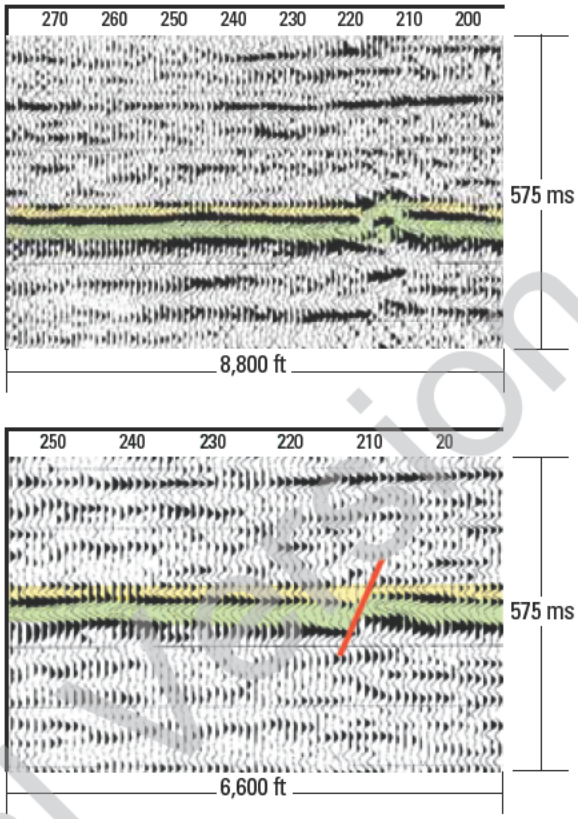

Figur 7-9. Reefs or something else? Reef-like structures on surface s smi images can be processing artifacts. What appears to be a ef before integrating VSP information (top) is exposed as a fault (red) after applying the correct velocities measured by the VSP (bottom). As a result of a look-ahead VSP survey, the drill bit could be steered away from the fault into the nearby reef to make a successful well on the first attempt. (From Hope *et al.*, 1998; this graphic is copyright Schlumberger, Ltd. Used with permission.)

- cost of running a VSP at TD to reduce risk for the sidetrack—the TD VSP will cost the same as, or more than, the proactive look-ahead VSP because the well will be deeper and the time pressure intense
- cost of continuing to drill sidetracks when the reef may not be there or abandoning the well after an unsuccessful sidetrack when there was a reef to be found.

Figure 7-11 shows a sketch of the source positions and well track for the survey from which Figs. 7-9 and 7-10 were extracted. Although not strictly 3D, it represents a series of single-plane images at variable azimuths around the apex of the reef.

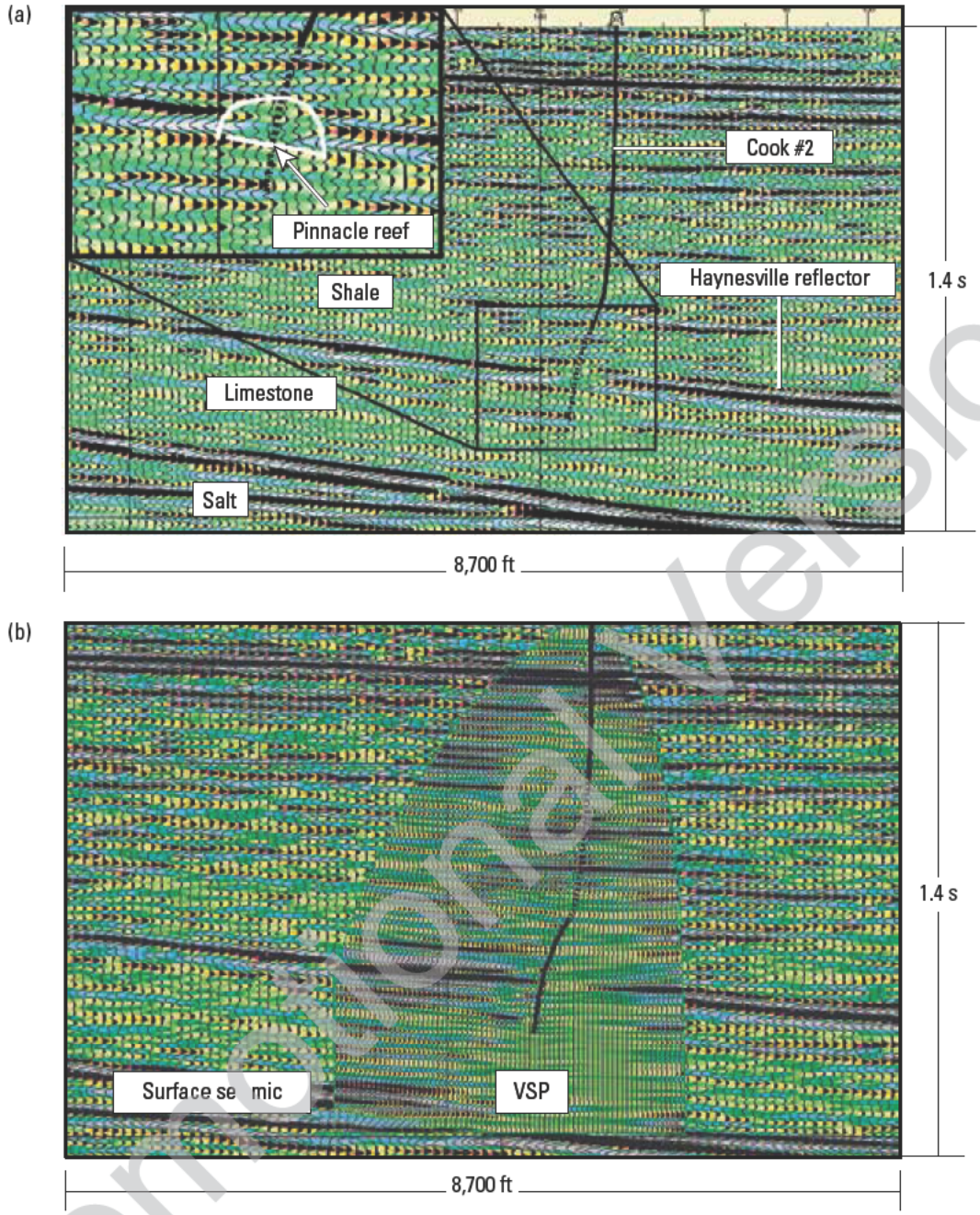

Figure 7-10. Surface seismic image before and after VSP integration to image a reef. The surface seismic image (a) shows a hint of a reef as a disruption of the regional limestone reflector. With the VSP image inserted (b), the disruption of the regional reflector is clearer, delineating the extent of the reef. The well trajectory is indicated by the vertical line. (From Hopper *et al.*, 1998; this graphic is copyright Schlumberger, Ltd. Used with permission.)

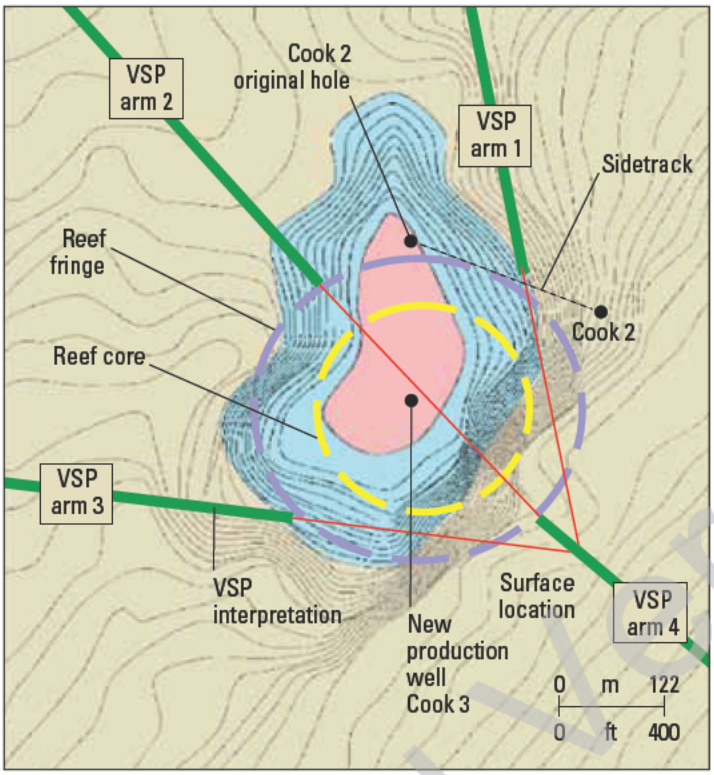

Figure 7-11. Multiple interpretations of the Cook field reef in the Cotton Valley Pinna le Reef play. The original well, Cook 2, was drilled to a nonpay zone on the fringe of the reef, then sidetra ked e st into a dry hole. Four VSPs (arms 1, 2, 3, 4) were shot to illuminate the reef by imaging the extent of the reg ona lim tone reflector that is disrupted by the presence of the reef. The segments of the limestone reflector imaged by the VSPs are shown as green lines. The absence of a green line indicates the presence of a reef (dashed purple circle), and the interpreted extent of the reef core is outlined with the dashed yellow circle. Following his interp etation, Well Cook 3 was drilled into the center of the reef and is now producing at a distance of only 400 ft om the abandoned Cook 2. The blue elongated feature with a pink core is the new interpretation of the eef sha e ba ed on surface seismic data remigrated with VSP velocities. (From Hope *et al.*, 1998; this graphic is c pyright Schlumberger, Ltd. Used with permission.)

7.3.4 Geosteering validation using high-resolution sonic imaging

Recent hardwar advances are incorporated in the latest Schlum erger dipole Sonic Scanner* acoustic scanning pla form, which has greatly improved the quality of soni images. It is beyond the scope of this book to d scuss onic logging methods; however, some particular applications of this technology lie withi the oundaries of borehole seismic applications (Fig. 7- 2).

Borehole sonic tools are typically used to measure various characteristics of critically refracted waves and borehole acoustic waves. However, if these traditional sonic arrivals (i.e., compressional and shear head waves and Stoneley waves) are removed from each waveform, it is possible to recover acoustic reflections. Similar to the processing of surface seismic data, waveforms are processed with depth-migration techniques, which position reflections in their correct spatial location using a velocity model.

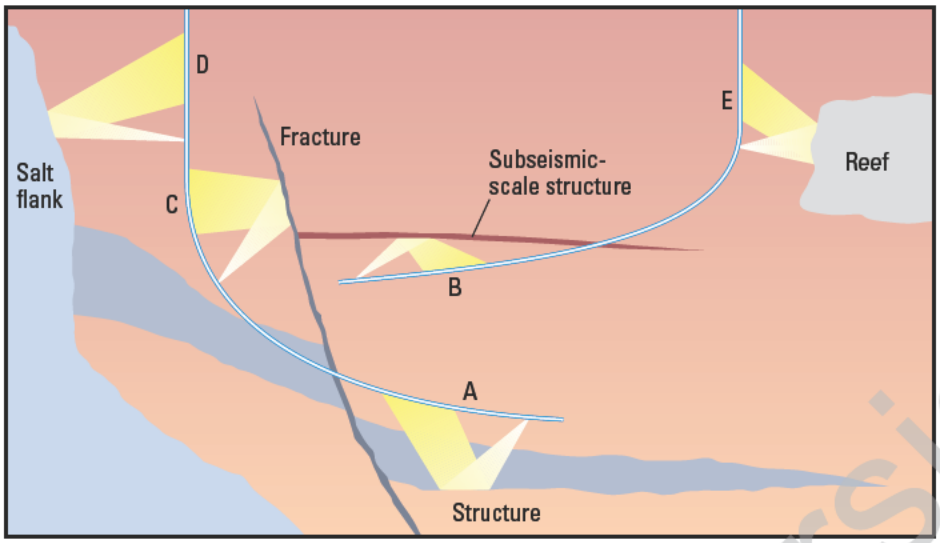

Figure 7-12. Applications for sonic imaging. The proven applications include: (A) imaging reservoir structu e for high-resolution verification of the wellbore trajectory relative to geological markers, (B) imaging s bseismic-sc le reservoir structure for understanding overall porosity and permeability characteristics, and C) de ecting fractures away from the wellbore to distinguish them from localized drilling-induced cracks. Other potentia appli ations, such as (D) imaging salt flanks and (E) reefs, generally require greater range. (From Chang *et al*, 1998; this graphic is copyright Schlumberger, Ltd. Used with permission.)

Depending on the duration of waveform recording and the choice of transmitter spacing, reflections may come from formations up to 10 m away from the borehole.

High sonic frequencies—8,000 Hz—provide a high resolution image tied back to the well trajectory. The long array of hydrophone-receivers also allows AV response of a particular reflector to be analyzed A relative-bearing measurement is used to dete mine the azimuth of the reflections, in particul r if th y are bove or below the borehole.

An operator in the Middle East i using this borehole acoustic reflection survey (BARS technique to characterize a low-relief carbonate r servoir with a thin oil column and a lar e aq ifer that is sealed with water-reactive shale (Borland *et al.*, 2007). The optimal horizontal well locatio is between 0.5 and 1.5 m below the shale cap and with no contact with the shale to avoid loss of oil pro uction and to delay the onset of water production from coning. Wells encountering shale need ma si int rvention, which is both time-consuming and expensive, and very often, they need to be plugged and aba doned. Conventional formation evaluation logs—nuclear and resistivity—poorly locate the reservoir cap i this environment because of saturation of the shallow-reading nuclear measurements and the low resistivity contrast between the reservoir and the shale cap.

In this particular field, the reservoir-to-shale acoustic contrast is enough to induce a discernable acoustic reflection. The acoustic image in this case was used to validate geosteering in the surveyed well and to improve the accuracy of geometric well plans for adjacent new wells. This is particularly useful when the placement of the wellbore near the reservoir top is critical, but it is difficult to establish from conventional LWD measurements when the markers within the reservoir cannot be used to infer the well location with respect to the reservoir cap. Figure 7-13 shows the image obtained from the BARS service, oriented along the wellbore trajectory. It clearly shows the location of the shale cap, which is further corroborated with the gamma ray reading at the shale cap exit.

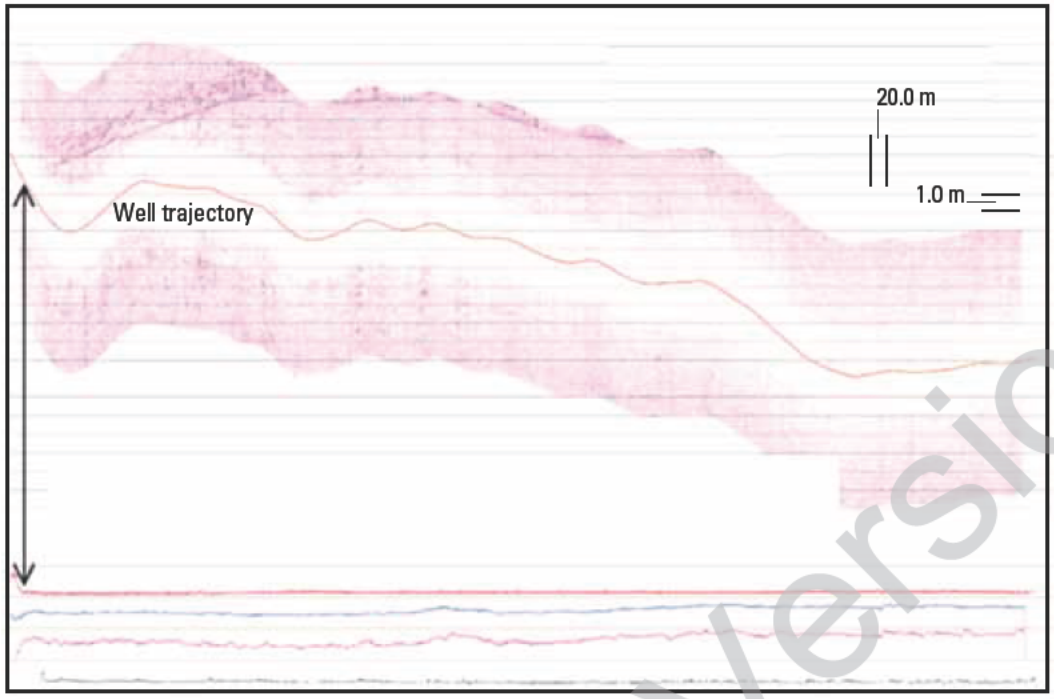

Figure 7-13. BARS image displayed along well trajectory. The reflector correlates with the gamma ray drop at shale cap exit; this is evidence that the reflector is the shale cap. Co relation logs, from top to bottom: gamma ray, compressional sonic, shear sonic, and caliper. (From Borland *et al.*, 2007.)

7.4 Seismic while drilling

The main goal of seismic while drilling is to make dri l-ing decisions (i.e., geosteer the drill bit, detect drilling risks ahead of the bit) in real time and with ncreas d drilling efficiency.

Drilling to a target location is often etermined from a surface seismic section, which is an nterpretation of subsurface reflectors presented in the time domain. Unfortunately, the depth of a refl ctor may not be established accurately, particularly for exploration wells. Conversion from traveltim to depth requires knowledge of the seismic velocity of all rocks from surface to the target (velocity model), ut velocities are often unknown or assumed from nearby basins. Nonetheless, drilling decisions must be made based on such data.

Often, casing points are selected to avoid drilling into a hazard with a long, openhole section above. Casing the well allows changing mud weight to accommodate the hazard ahead without endangering the overlying formations. Before drilling begins, there may be hundreds of meters of uncertainty in the required location of casing points, which introduces unacceptable risk. During drilling in development areas, uncertainty can be decreased by examining cuttings or LWD responses to compare with geological markers in nearby wells. In a new basin, recognized markers may not be established, so other means must be used to improve the velocity model and locate the drill bit on the seismic section.

Using real-time LWD sonic measurements alone to construct a velocity model is not usually possible because typically these logs are not available all the way to the surface, and integrated sonic can have large errors in predicting traveltimes as a result of sonic-seismic drift (change of effective velocity with frequency).

As discussed in Secton 7.3, intermediate wireline VSP measurements can help to build more accurate velocity models; however, the measurement interrupts the drilling process and costs are very high as a result of lost rig time. Therefore, it is not economical to make many repeat surveys during drilling. The solution is to make the key measurements, namely checkshot and look-ahead imaging, while drilling.

In addition to more accurate placement of drilling targets, an improved velocity model also helps to identify drilling hazards such as high pore pressure. Empirical relationships between formation velocity and pore pressure allow the seismic velocity measurements to be transformed to pore pressure. This parameter can help to continuously update estimates of minimum safe mud weights. Comparison between a predicted and expected trend will show divergence when the pressure begins to rise at the top of an overpressured section.

Conventional VSPs acquired at the time of a bit trip may be used to predict the distance to an overpressured zone. However, because the inversion is nonunique and the density used to convert predicted impedance into velocity is unknown, there is still uncertainty in the estimated distance. While-drilling traveltime data allows the distance to a seismic target to be continuously refined.

7.4.1 Drillbit seismic surveys

In the mid-1990s, drillbit seismic data surveys were the only option for while-drilling checkshot surveys. Energy radiated from the bit can be recorded after reflection from deeper interfaces to form a conventional reverse VSP image ahead of the bit. Data quality is not always sufficient to achieve this, but examples exist in which high-quality VSPs have been generated from the drilling-noise source (Haldorsen *et al.*, 1995).

This technology works well in some environments, but it is unreliable if formations are soft, and it cannot be used in highly deviated holes or, in general, with polycrystalline diamond compact (PDC) bits (Borland *et al.* 1997).

Figure 7-14 gives a pictorial overview of this concept. The acoustic energy generated in the drilling process follows two paths. Most of the acoustic energy is radiated into the surrounding formation and can be monitored by a surface geophone array. The remainder travels up the drillstring and can be recorded by accelerometers mounted on the swivel (Fig. 7-15).

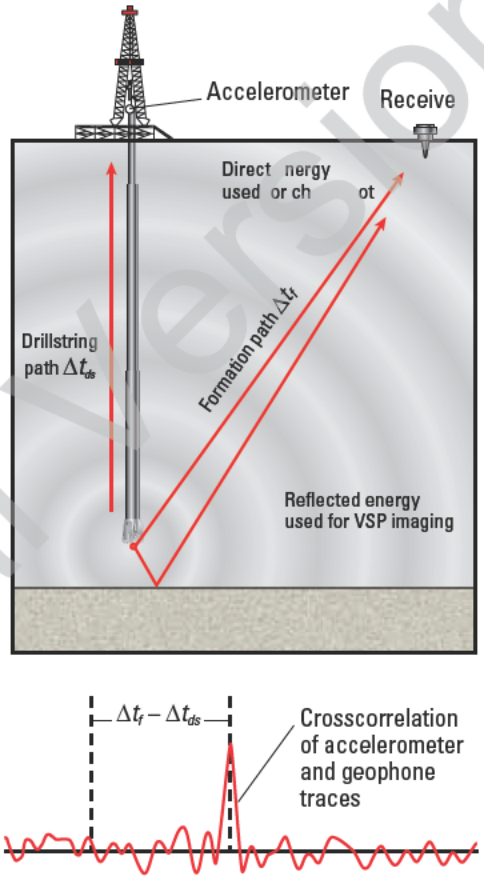

Figure 7-14. Conceptual configuration for a Drill-Bit Seismic VSP with drillbit source survey. Roller cone bits send out seismic energy that can be measured by receivers in a surface-array configuration. The drillstring signal from axial vibrations is measured by drillstring accelerometers and correlated with receiver data to determine seismic traveltimes and produce a checkshot survey. The checkshot traveltime is calculated using the traveltime through the formation (Δt_f) and the traveltime through the drillstring (Δt_{ds}). (From Breton *et al.*, 2002; this graphic is copyright Schlumberger, Ltd. Used with permission.)

Figure 7-15. Accelerometers mounted on the auxiliary entry port of the gooseneck on the topdrive unit of the rig at San Andreas Fault Observatory at Depth (SAFOD). This is the preferred mounting position: directly above the drillstring and as close as possible to the last pipe in the drillstring.

By correlating drilling-vibration events between the drillstring accelerometer and the geophone array signals, the seismic traveltime to surface from the drill bit is simply

$$\text{traveltime} = t_{\text{array}} - t_{\text{accelerometer}} - t_{\text{drillstring}}. \qquad (7\text{-}3)$$

So, measuring the seismic traveltime requires determining the time the signal takes to traverse the drillstring ($t_{\text{drillstring}}$) for any depth.

The drill bit radiates energy continuously. Unlike conventional active seismic experiments, there is no time break when the shot discharges—no signal generator to provide the pilot and reference for a vibrator unit. However, it is still possible to extract timing information from the recorded signals. The important thing is that the generated signal must vary continuously, not simply repeat for every drillbit revolution.

Two signal sets are recorded in the experiment: the surface geophone signals and the accelerometer signal that has traveled up the drillstring. Crosscorrelation of these two signals yields the relative traveltime between the drillstring path and the formation travel path. To find the absolute traveltime in the formation it is necessary to determine the traveltime along the drillstring.

In principle, if the characteristics of the drillstring were known, the traveltime of the sound waves along the drillpipe could be calculated. If the velocity of drillpipe and the length of pipe in the hole are known, then the drillstring traveltime is simply

$$t_{\text{drillstring}} = \frac{\text{depth}}{V_{\text{drillpipe}}}. \qquad (7\text{-}4)$$

In reality, this is an oversimplification. Different pieces of drillpipe have different velocities, and the various assemblies along the drillstring also affect the velocity.

In practice, it is more robust to extract the traveltime directly from the accelerometer data by using the technique of "drillstring imaging." If the drillstring is considered as a stack of layers of equal traveltime, the accelerometer signal can be deconvolved to yield a series of reflection coefficients that represent the various discontinuities in acoustic impedance along the drillstring. Identification of the reflection coefficient that represents the bit-formation discontinuity yields the traveltime of the drillstring. This technique also yields an operator that can be used to demultiple the accelerometer signal after the crosscorrelation.

If the drillstring image is plotted for different depths in the progress of the well, Fig. 7-16 is obtained. The image of the bit and bottomhole assembly is clearly visible and its moveout across the traces with increasing drillstring length can be seen. The drillstring velocity can be calculated from this moveout, as shown in Fig. 7-16.

Having determined the drillstring response, not only is the drillstring traveltime known, but also the impulse response of the drillstring (Booer and Meehan, 1992). This allows multiples in the drillstring signal to be deconvolved out of the response after crosscorrelation with the surface sensor signals.

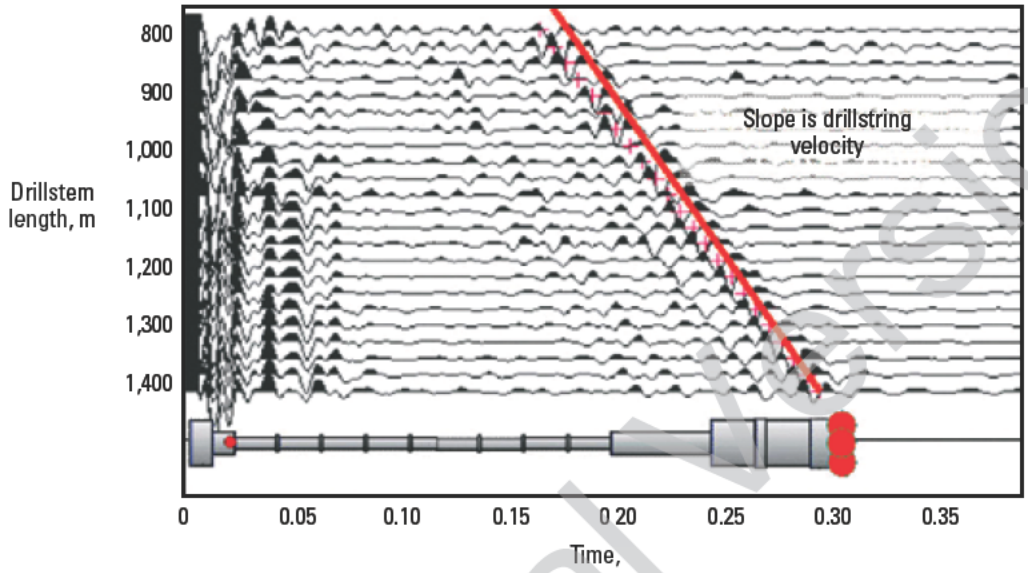

Figure 7-16. Drillstring image. The drillstring image is the reflectivity fu ction o he drillstring used to drill the well. Prominent reflections in the drillstring image correspond to the great st changes in mass of the drillstring. These changes occur at the bit, top of the BHA, top of the heavy weig t drillpipe, and top of the drillstring at the topdrive or swivel unit. The reflection coefficient series represen ng the BHA and bit moves out to the right as the drillstring becomes longer. The drillstring velocity and time shift of e Drill-Bit Seismic waveforms are calculated from the slope of the moveout. (Original data taken from Khaled et al., 1996.)

7.4.2 seismicVISION service while drilling

Until now, two options have been available to drillers for converting seismic traveltime to depth. The first, which interrupts drilling, is to acquire a VSP using a wireline-conveyed seismic tool. Although this provides a high-quality measurement, the logging run requires substantial rig time, which adds cost and additional risk. Even worse, the measurement may be scheduled too early or too late to be useful—before or after a casing point or hazard is reached.

An alternative means to acquire a checkshot while drilling is with the Drill-Bit Seismic system described in the previous section. This technology works well in many situations but is unreliable in soft formations, in highly deviated holes, and when PDC bits are used.

The introduction of a while-drilling seismic tool (Esmersoy *et al.*, 2001) in the drilling assembly provides a third solution. This new solution provides VSP surveys approaching wireline quality in relevant real time without additional rig time (Fig. 7-17). The seismicVISION tool has the seismic receiver in an LWD assembly and uses conventional surface seismic sources to generate the seismic waves. An MWD telemetry system transmits real-time data to surface. The seismicVISION measurement can be used in situations that the Drill-Bit Seismic service cannot, but it does require the tool on the BHA, and MWD telemetry must be in place if real-time measurements are required. On the other hand, a wireline seismic survey provides better quality data for reservoir characterization studies than either the seismi VISI N tool or the Drill-Bit Seismic measurement.

Both the seismicVISION technique and the hardware used for measurements are described in Chapte 3.

Checkshot times are automatically d tected downhole, and full waveform data m y be ent uphole via MWD telemetry for processing visu lization, and interpretation. The bit location can be converted to true vertical depth by using a re ord of measured depth and inclination along the well trajectory.

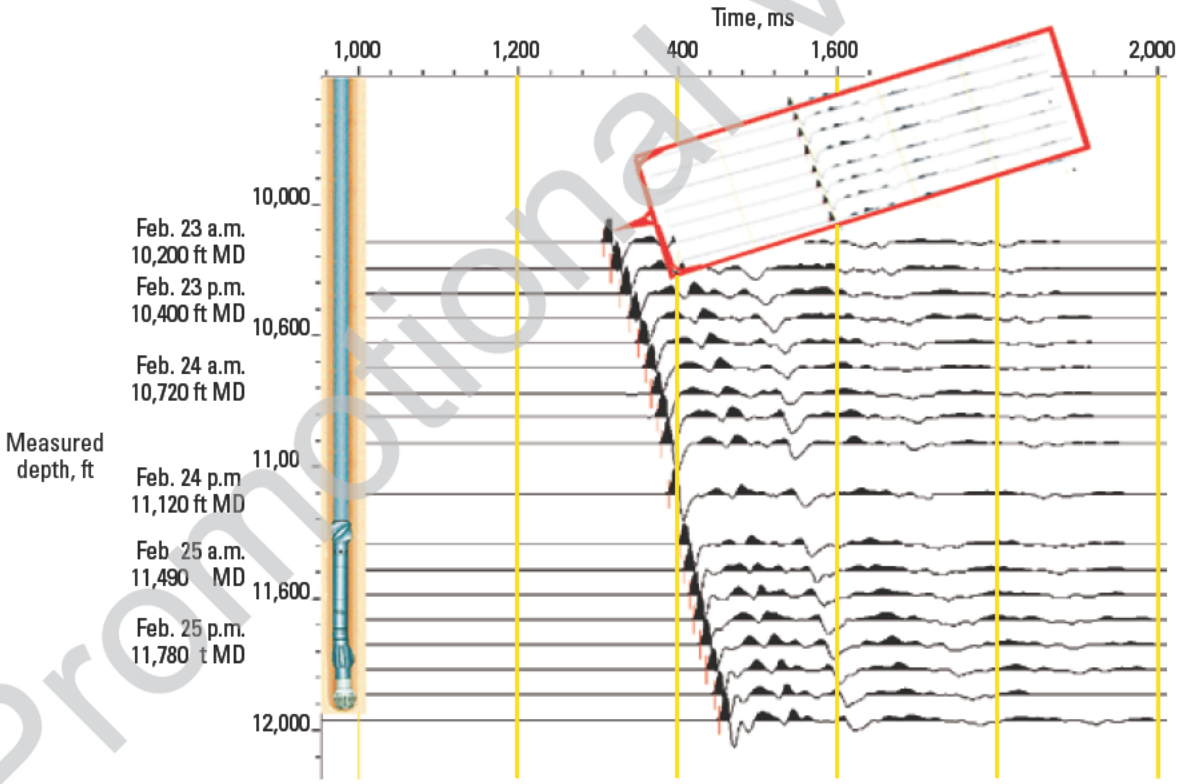

Figure 7-17. Raw real-time stacked waveforms as drilling progresses. Each waveform is obtained by stacking a number of consecutive shots, as shown in the red box. Time picks are sent to the surface in real time and provide an immediate time-depth relation. As drilling approaches a perceived target, waveforms sent to the surface via telemetry can be processed to obtain a look-ahead image. MD = measured depth.

With checkshot data obtained at each pipe connection or more frequently if deemed necessary, the location of a bit on a seismic section can be determined while drilling. It is usually not practical to reprocess the complete surface seismic section in real time, but it is quick, easy, and usually accurate enough simply to stretch or compress the depth-domain seismic section using real-time checkshot data (Fig. 7-18). The updated section can be used to predict the distance to the next drilling objective or hazard. Visual aids, based on this updated information, notify the rig crew of potential drilling hazards, thus decreasing the risk for drilling ahead. This provides a great advantage for drillers and also delivers updated information more quickly to geoscientists to refine interpretations.

As the wellbore approaches a casing point or target depth, updated information reduces uncertainty to an acceptable level (Fig. 7-19). Specialized software captures this information from MWD telemetry and, in real time, updates the seismic section, location of major markers, estimated target position, and depth uncertainties (Fig. 7-20). In some areas, there are no obvious markers to tie a seismic section to cuttings or other drilling parameters, and the only correlation is through a seismic while-drilling method. Improved knowledge of bit loca ion may result in the elimination of a casing point or, n some cases, the addition of one to mitigate risk

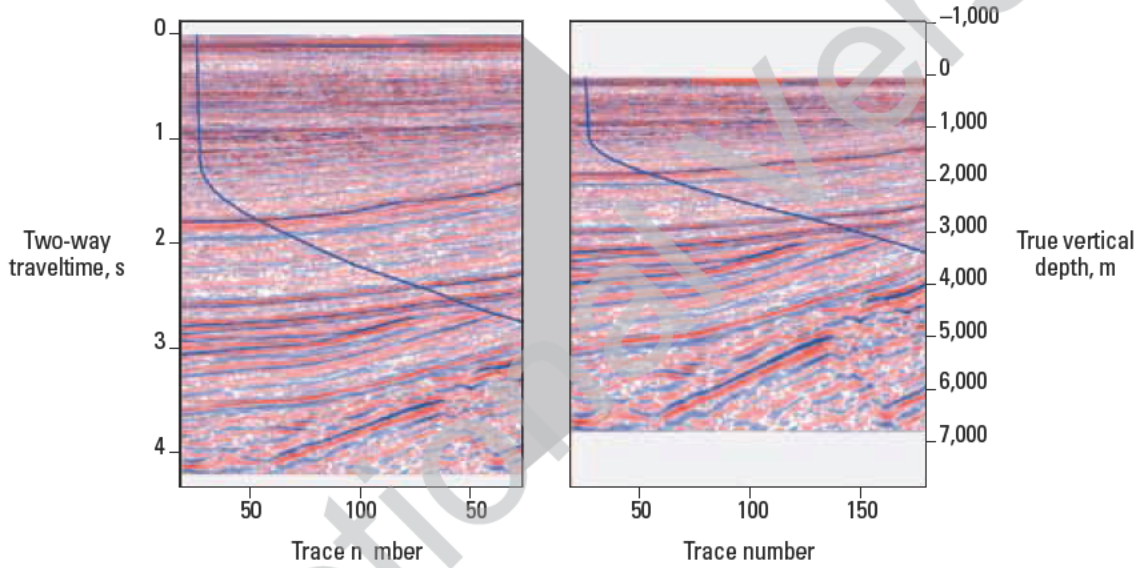

Figure 7-18. Stretched and compressed seismic sections. Normally, a seismic section in the time domain (left) is not reprocessed during drilling. he positi n of a bit is known from measured depth, inclination, and azimuth along the wellpath (blue) Ch cksh t measurements transmitted to surface while drilling locate the bit on the seismic section, thus allowin stretching or squeezing of the converted depth section to locate targets ahead (right). Each race s converted, but no lateral variation is applied. (From Bratton *et al.*, 2001; this graphic is copyright S hlumber er, Ltd. Used with permission.)

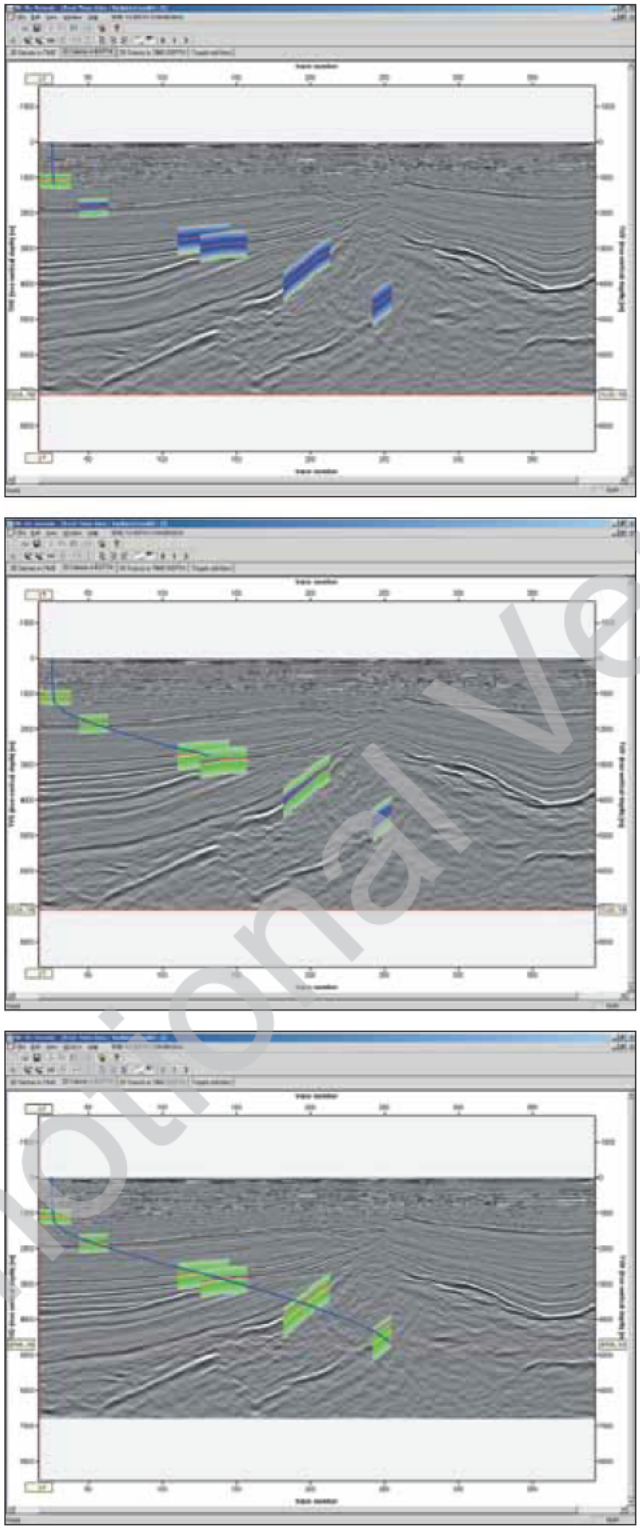

Figure 7-19. Decreasing uncertainty by increasing information. Three screens from Bit On Seismic* software illustrate how an advancing wellbore decreases uncertainty by increasing information. The well (thin blue line) begins in the upper left of this depth-converted seismic section. Marker locations are predicted at each step (red line), with uncertainty bands around them (blue band). One marker bed was intercepted before the trajectory began deviating to the right (top). Because that marker depth is known, its blue uncertainty band has disappeared. The software displays the predrill prediction of depth (yellow line) and uncertainty (green band) for comparison to measured depth (Fig. 7-20). Drilling through more markers provides additional information (bottom) and improves time-to-depth conversion along the trajectory. Predictions of depths of lower markers are updated, and their uncertainty decreases. No uncertainty remains after drilling into the last marker bed. (From Bratton *et al.*, 2001; this graphic is copyright Schlumberger, Ltd. Used with permission.)

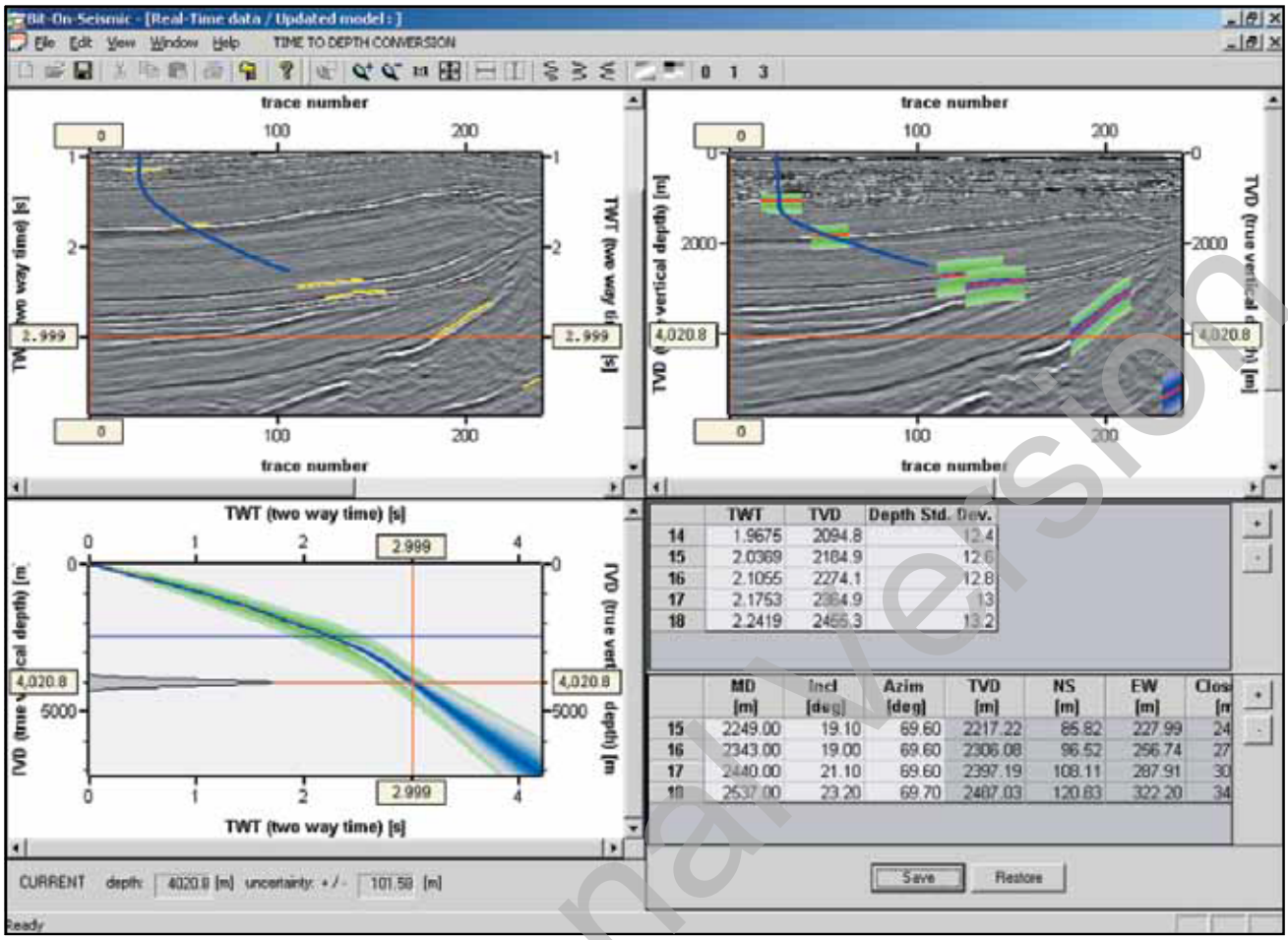

Figure 7-20. Bit On Seismic software display. A well tr ectory (lue) is shown on a time-domain seismic section with specific markers highlighted (yellow). As drilling continues, the well trajecto y extend on the display (upper left). The seismicVISION checkshot data are used to locate the bit in the depth-converted seismic section The s m markers, with color-coded uncertainty bands, are shown on this display (upper right). Depths ahead of the bit have increasing y wide u certainty bands, as shown by the uncertainty distribution for a specific marker (lower left). Depth, inclination, and azimuth information a e entered to convert the traveltime to depth (lower right). (From Bratton *et al.*, 2001; this graphic is copyright Schlumberger, Ltd Used with permission.)

The seismicVISION to l was us d on a directional well in an exploratory field in the Caspian Sea (Bratton *et al.*, 2001). An overpress re zone was to be avoided near the crest of th structure, and the reservoir target was difficult to locate beca se there was a series of faults in an overthrust are with beds dipping at 40°. Based on surface seismic interpretation, the well trajectory was 4,500 m long. However, uncertainty in the true vertical depth of the top of the reservoir was 700 m. This was a critic l problem because missing the target by 100 m could put the well on the wrong side of a fault. Because sediments in this area are soft, using bit noise as a seismic source while drilling was not feasible. The seismicVISION tool was used to obtain a vertical-incidence checkshot survey and to update the bit location while drilling.

Results indicated that the predrill surface seismic interpretation was accurate, but the survey provided additional confirmation as drilling progressed. After drilling, a fully processed walkabove survey compared very well with the while-drilling measurements (Fig. 7-21).

A full VSP was processed after the tool returned to surface—waveforms could not be transmitted in real time with this earliest version of the tool. The operator indicated that the measurement had no negative impact on drilling time, and it provided results comparable to conventional wireline VSP surveys. The cost of seismic source, boat, and personnel deployment was more than offset by drilling time saved when conventional surveys were not obtained.

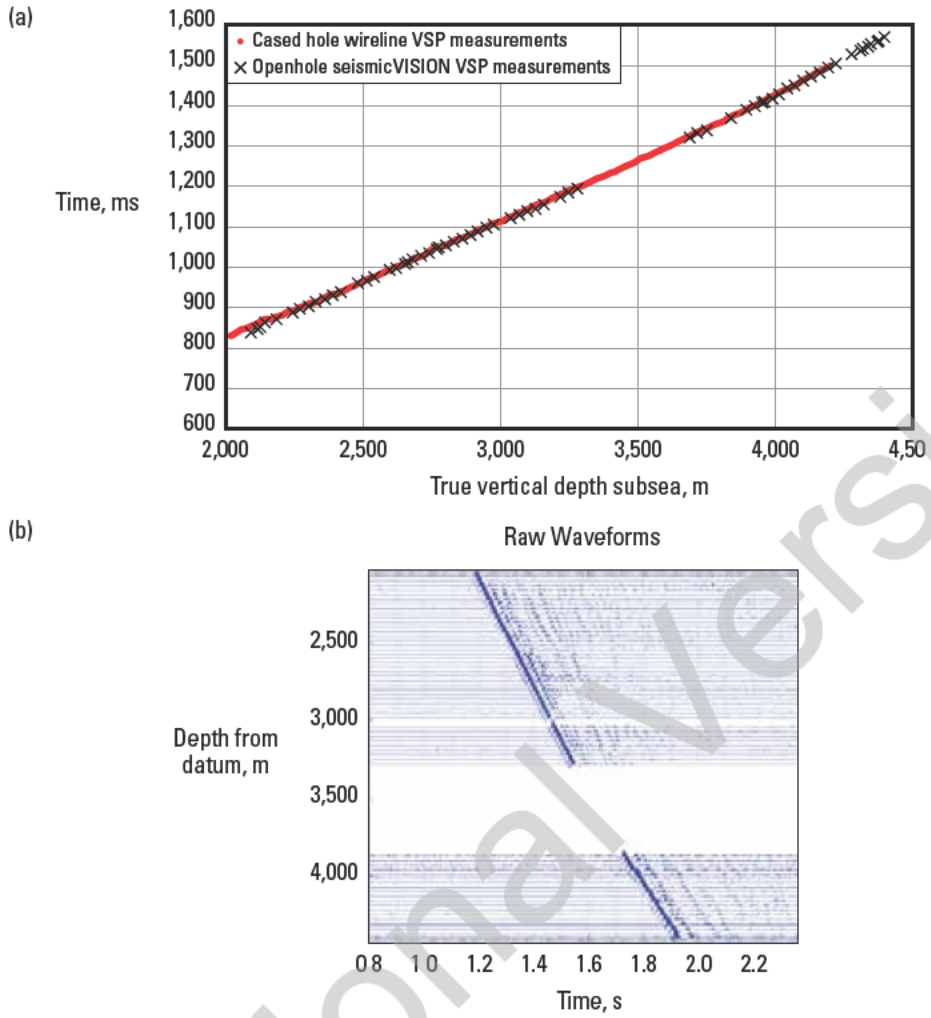

Figure 7-21. Comparison of VSP traveltimes. After t is Ca pian Sea well was drilled, a cased hole VSP (red) was run to determine a time-to-depth conv sion. The seismicVISION measurement (black) compares closely with wireline VSP data (a). Full-waveform seismi data were retrieved from the seismicVISION tool after tripping out. The resultant waveforms (b were of high quality and were used for VSP processing. The gap in the data was caused by a prob em with a crane supporting the seismic source on the boat. (From Bratton *et al.*, 2001; this graphic is copyr ght Sch umberger, Ltd. Used with permission.)

Another exploratio example comes from a remote area in deepwat offs ore Brazil. This exploration well had no near-well ontrol and there was significant uncertainty on he surface seismic velocity estimation. The ost ritical well-construction decision made on this we was the setting of the 13⅝-in casing string in loca ion between an anticipated fault and an upper targ t (Fig. 7-22). The problem was that the formation above nd below the fault was the same shale sequence, and the seismic uncertainty was such that the position in depth of the fault and the upper target overlapped. Conventional LWD tools must pass through a formation to give an appropriate response, but in this case, the casing string needed to be set above the upper target and below the fault. This was to seal the fault off from the upper target and to get appropriate logging tools into the target sand to correctly evaluate it. If the casing string were accidentally set above the fault, then another intermediate casing string would be needed to seal off the fault. Because anticipated pore-pressure issues deeper in the well would require multiple casing strings, to run an intermediate string here would mean that the well would not be able to reach the primary target toward the end of the well as a result of hole size limitations. The optimal positioning of casing strings in the deepwater exploration market as well as setting

casing strings above known problematic formations in development areas are key well-construction decisions that have a tremendous impact on the cost and success of a particular well. These decisions need to be made in real time and are one of the primary uses of seismic-while-drilling techniques. In this particular example, checkshot measurements were taken during the drilling of the 17½-in hole section. These constrained the uncertainty in depth of the fault and upper target such that the casing string could be placed below the fault and above the target. The casing shoe in this example was moved 80 m deeper (Fig. 7-23). If the original prediction from the surface seismic velocity estimation had been used, the casing shoe would have been placed above the fault, thereby necessitating an intermediate casing string, and the well could not have been drilled to the target reservoir.

In many cases involving a directional well, a near-vertical pilot hole is drilled to determine the location of markers or target depths. This pilot hole is then cemented back and sidetracked to land the well horizontally within the reservoir. Real-time seismic interpretation may eliminate the need to drill a pilot hole, thereby substantially reducing well-construction costs.

An operator was drilling an exploratory well in the Gulf of Mexico. The reservoir target was a series of oil and gas sands close to a fault. The operator needed to position the wellbore under the fault to intersect multiple targets. There was poor control of the updip geological features near the fault, including no time-depth conversion relations in an environment where high velocity uncertainty was expected. In this scenario, accurate real-time geosteering was sought to drill reservoirs at optimal locations, to minimize the impact of sidetracking, and to optimize the casing string along the wellbore. Because of prohibitive rig-time cost (USD 200,000 per day), a wireline-conveyed checkshot survey was undesirable. The solution was to conduct a VSP while drilling by using the seismicVISION tool.

An initial seismicVISION seismic-while drilling image acquired 305 m above the target indicated that the well would not reach the target as planned (Fig. 7-24). The well was sidetracked and additional seismicVISION data were used to guide the well to the intended TD.

This job was the industry's first successful real-time VSP imaging application. During acquisition, the client received three updates per day by using real-time data. When the seismicVISION job finished, the tool was retrieved to the surface, the memory data were recovered, and reprocessing confirmed the real-time results.

These examples have highlighted the real-time decision making that is possible using while-drilling seismic measurements, and as has been shown, these can have a tremendous impact on well-construction decisions and costs.

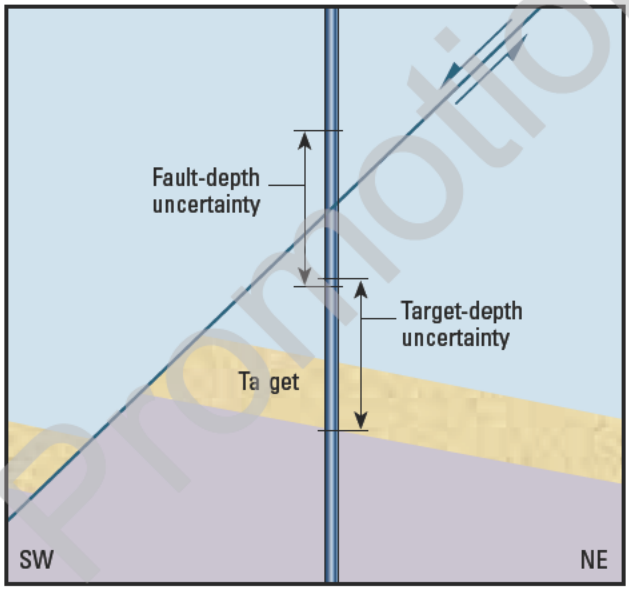

Figure 7-22. The predrill prediction was plagued by a ±10% uncertainty in the location of a fault and a 2.2-Ma target. The error bars for these events overlapped, which made it difficult to set the 13⅝-in casing shoe. (From Breton *et al.*, 2002; this graphic is copyright Schlumberger, Ltd. Used with permission.)

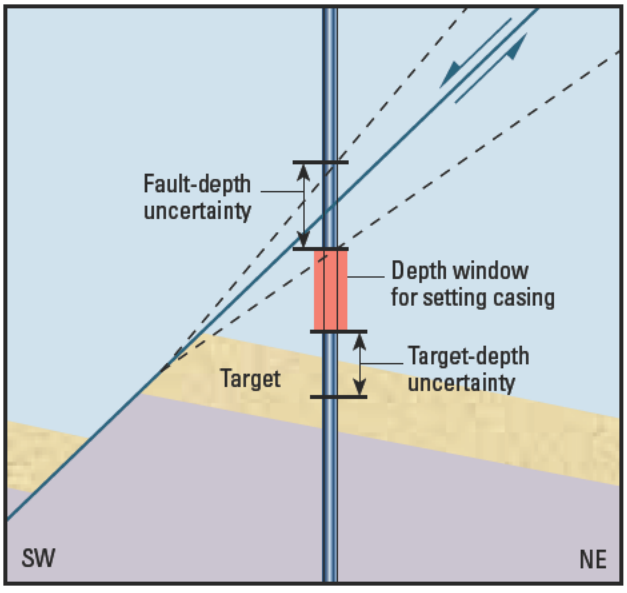

Figure 7-23. Real-time seismicVISION information reduced depth uncertainty to ±1%, which allowed the casing shoe to be comfortably placed between the deepest possible fault location and shallowest possible target location. (From Breton *et al.*, 2002; this graphic is copyright Schlumberger, Ltd. Used with permission.)

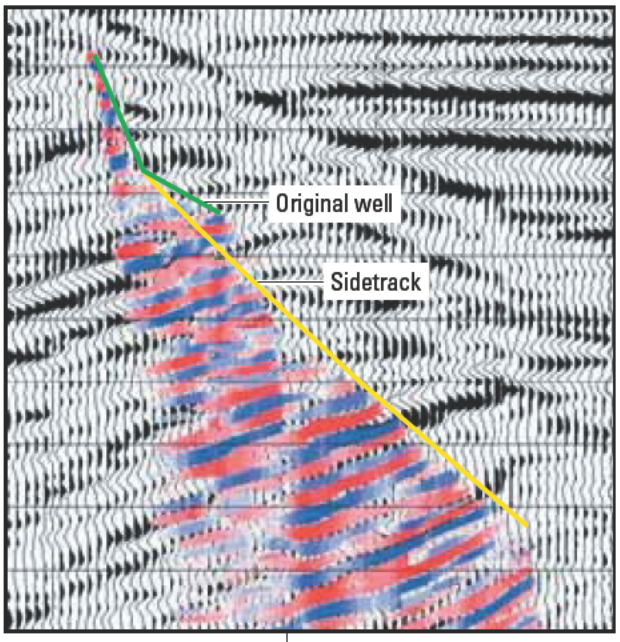

Figure 7-24. Two seismic images acquired while drilling (red and blue), superimposed on preexisting surface seismic data (black and white). The first seismic image (left of vertical black line), acquired in the original well (green), indicated to the interpreters that the well would not reach the target as planned.The well was sidetracked (yellow), and another seismic image acquired while drilling (right of vertical black line) indicated that the well would reach the target (From Blackburn *et al.*, 2007; this graphic is copyright Schlumberger, Ltd. Used with permission.)

However, there is another growing trend to use seismic-while-drilling techniques to gain velocity measurements when it is difficult, prohibitively expensive, or impossible to use conventional wireline techniques. These areas include highly deviated wells and wells in which hole conditions exclude the use of openhole wireline techniques. The fact that LWD tools are extremely robust and are part of the drilling assembly means that their data can be acquired while drilling a well thus eliminating rig costs associated with other acquisition methods. This enables some operators to acquir velocity data in wells in which wireline would not ave been considered as an option. In highly devia ed and horizontal wells, the tool can be placed downhole so hat, if a vertical-incidence survey is requir d, it can be shot after the well has reached TD and while the tools are being tripped out of the hole, thu minimizing the cost of boat sources by condensing to a pecific time period.

The other area that fall dire tly into the seismic-while-drilling regime is r serless drilling in deepwater. Here the application may not be for real-time measurements but only to acqui e any velocity measurements. Wireline operations in a riserless hole are costly and difficult, and often wireline has difficulty obtaining velocities in mul iple casing strings close to surface. As a result of the nature f surface seismic measurements, it is often in the tra eltime range of less than 1 second that significant velocity uncertainty occurs. Constraining these velocities in the overburden can have tremendous impact on pore pressure, casing, and mud-weight decisions far deeper within the well.

7.5 References

Arroyo, J.L., Breton, P., Dijkerman, H., Dingwall, S., Guerra, R., Hope, R., Hornby, B., *et al.*: "Superior Seismic Data from the Borehole," *Oilfield Review* (Spring 2003) 15, No. 1, 2–23.

Blackburn, J., Daniels, J., Dingwall, S., Hampden-Smith, G., Leaney, S., Le Calvez, J., Nutt, L., Menkiti, H., Sanchez, A., and Schinelli, M.: "Borehole Seismic Surveys: Beyond the Vertical Profile," *Oilfield Review* (Autumn 2007) 19, No. 3, 20–35.

Booer, A.K., and Meehan, R.J.: "Drillstring Imaging: An Interpretation of Surface Drilling Vibrations," paper SPE 23889 presented at the IADC/SPE Drilling Conference, New Orleans, Louisiana, USA (February 18–21, 1992).

Borland, W., Codazzi, D., Hsu, K., Rasmus, J., Eichcomb, C., Hashem, M., Hewett, V., Jackson, M., Meehan, R., and Tweedy, M.: "Real-Time Answers to Well Drilling and Design Questions," *Oilfield Review* (Summer 1997) 9, No. 2, 2–15.

Borland, W., Edwards, J., Kurniawan, H., Alexander, D., Goossens, P., and Zhu, F.: "Borehole Acoustic Reflection Survey for Geosteering Validation," 1st Annual SPWLA Middle East Regional Symposium (April 15–19, 2007).

Bowers, G.L.: "Pore Pressure Estimation from Velocity Data: Accounting for Pore-Pressure Mechanisms besides Undercompaction," *SPE Drilling and Completion* (1995) 10, No. 2, 89–95.

Bratton, T., Edwards, S., Fuller, J., Murphy, L., Goraya, S., Harrold, T., Holt, J., *et al.*: "Avoiding Drilling Problems," *Oilfield Review* (Summer 2001) 13, No. 2, 32–45.

Breton, P., Crepin, S., Perrin, J-C., Esmersoy, C., Hawthorn, A., Meehan, R., Underhill, W., *et al.*: "Well-Positioned Seismic Measurements," *Oilfield Review* (Spring 2002) 14, No. 1, 32–45.

Chang, C., Hoyle, D., Watanabe, S., Coates, R., Kane, M., Dodds, K., Esmersoy, C., and Foreman, J.: "Localized Maps of the Subsurface," *Oilfield Review* (Spring 1998) 10, No. 1, 56–67.

Eaton, B.A.: "The Equation for Geopressure Prediction from Well Logs," paper SPE 5544 presented at the SPE Annual Fall Meeting, Dallas, Texas, USA (September 28–October 1, 1975).

Esmersoy, C., Underhill, W., and Hawthorn, A.: "Seismic Measurement While Drilling: Conventional Borehole Seismics on LWD," *Transactions of the SPWLA 42nd Annual Logging Symposium*, Houston, Texas, USA (June 17–20, 2001), paper RR.

Gardner, G.H.F., Gardner, L.W., and Gregory, A.R.: "Formation Velocity and Density—The Diagnostic Basics for Stratigraphic Traps," *Geophysics* (1974) 39, 770–780.

Haldorsen, J.B.U., Miller, D.E., and Walsh, J.: "Walk-Away VSP Using the Drill Bit as a Seismic Source," *Geophysics* (1995) 60, 978–997.

Hope, R., Ireson, D., Leaney, S., Meyer, J., Tittle, W., and Willis, M.: "Seismic Integration to Reduce Risk," *Oilfield Review* (Autumn 1998) 10, No. 3, 2–15.

Hottman, C.E., and Johnson, R.K.: "Estimation of Formation Pressures from Log-Derived Shale Properties," *Journal of Petroleum Technology* (1965) 16, No. 6, 717–722.

Khaled, O.S., Al-Ateequi, A.M., James, A.R., and Meehan, R.J.: "Seismic-While-Drilling in Kuwait: Results and Applications," paper presented at the 2nd Middle East Geoscience Conference, Bahrain (April 15–17, 1996).

Meyer, J.H., and Tittle, W.: "Exploration Risk Reduction Using Borehole Seismic: East Texas Pinnacle Reef Applications," *Expanded Abstracts*, 68th SEG Annual International Meeting and Exposition, New Orleans, Louisiana, USA (September 1–18, 1998), paper BH 4.3, 369–372.

Passive Seismic Data

Joël Le Calvez, Gwenola Michaud, Craig Woerpel, and Alejandro Martinez Pereira

8.1 Introduction

Microseismic technology is becoming widely adopted by the oil and gas industry for application in hydraulic fracturing and microseismic reservoir monitoring as the science improves and the community increases its awareness of the potential of this rejuvenated technology. Following proper acquisition and processing, the analysis of microseismic data provides information on the location of stress changes (pore pressure changes) occurring within the reservoir and in the surrounding rock. Such information is critical not only to better monitor hydraulic fracturing but also to characterize the reservoir and to provide additional information for well placement, drilling, stimulation, and production decisions. This chapter details the benefits of microseismicity analysis and its mechanisms, describes data acquisition configurations for hydraulic fracture monitoring, and presents the processing workflow used by Schlumberger. The applications of microseismic technology are reviewed using examples from hydraulic fracturing and microseismic reservoir monitoring projects.

8.2 Definition and benefits

8.2.1 Microseismicity: Definition, mechanisms, and measurement

Microseismicity induced by changes in stress and pore pressure is generally associated with hydraulic fracturing, fluid injection or reservoir production. These microearthquakes result from localized failures along preexisting or new planes of weakness. The displacements generate acoustic energy that can be detected and recorded at seismic receivers. These recorded waveforms comprise microseismic data. Using detection and location algorithms to process the data yields the hypocentral loci of the microearthquakes. More advanced processing using power spectra provides source parameters associated with these localized failures (e.g., magnitude and moment).

There are three major models for microseismicity seismicity by failure on fracture planes, seismicity by volume change, and seismicity by thermal change.

- *Seismicity by failure along pre existing or new fracture planes*. Hydrocarbon reservoirs support different Earth stresses that, under normal conditions lock the naturally occurring fractures in the subsurface. As a result of the injection of fracturing fluids, effective-stress changes can trigger movement along these fractures (Rutledge *et al.*, 2003).
- *Seismicity by volume change.* Induced seismicity is created when any volume change occurs in the Earth (McGarr, 1976). The volume change may be associated with rock removal from a reservoir. Because vertical shear stress is expected to be at a maximum at the edge of an expanding reservoir, dip-slip events would also be expected at this edge. This geometry depends upon geomechanics and local geology. Local planes of weakness naturally fracture first, and large preexisting fractures are not required. Thus, mapping the induced events at the edge of the expanding reservoir may provide a time-lapse map of the reservoir extent, but if localized within the reservoir, microseismicity could track the progress of a reservoir flood.
- *Seismicity by thermal change.* Observed in geothermal wells, seismicity by thermal change can also occur in hydrocarbon reservoirs when the formation temperature and injection fluid temperature present large contrast. This mechanism requires specific temperature-contrast conditions (Niitsuma *et al.*, 1999).

If an array of triaxial seismic receivers is situated at depth near the hydraulic fracture, compressional (primary or P-) and shear (secondary or S-) waves can be detected (Fig. 8-1). If we know the Earth's shear wave and compressional wave profiles (i.e., velocity model), the location of any individual microseism is generally deduced from arrival times of the P- and S-waves and particle motion of the P-wave. The difference in the wave arrival times provides information on the distance,

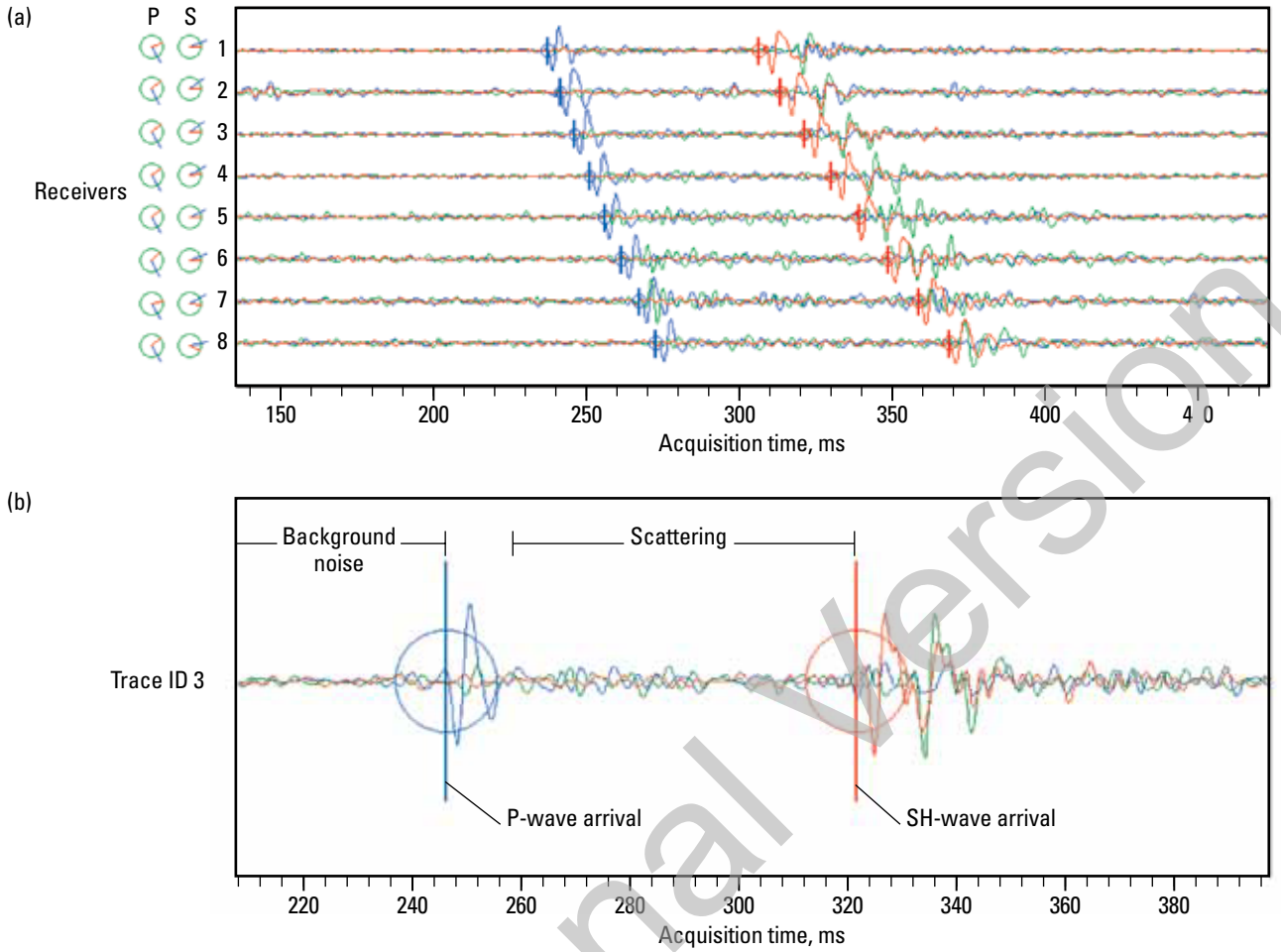

Figure 8-1. Typical eight-array, 3C accelerometer seism grap disp ay (a) of data recorded for an event located above the toolstring as indicated by the moveout. Blue red, a d green races represent P-, SH-, and SV-waves, respectively. Left of the traces, circles and tadpoles summariz the results rom the hodogram analysis: left circle is for P-wave arrivals, right circle is for S-wave arrivals. Bl e adp les po nt toward the azimuth of the source; red tadpoles indicate relative inclination. Note the consistent azimu h and clination evolution from bottom to top, thus confirming the moveout observation. Also note that the S wave b e tadpole is oriented 90° relative to the P-wave blue tadpole. View (b) shows the detail of a typical P-, SH and S waveform recorded on a single level with background noise, scattering, and the wave arrivals noted. The h pocent l location can be determined using these parameters (in association with a detailed velocity model) a ell as sour e parameters and, in some cases, focal mechanisms (when data from several appropriately located monitor ng wells are used).

whereas the p rticl motion derived from hodogram analysis provid s information related to the direction of the incoming energy.

From the polarity of the incoming energy, the microseismic focal mechanisms can be estimated. They are reported by using "beach-ball" diagrams, which indicate the f ult plane and auxiliary plane for each microseism (Fig. 8-2). For a double-couple source, the first motions define four quadrants—two compressional and two dilatational. The division between quadrants occurs along the fault plane and the auxiliary plane. As described by Oppenheimer (1996), fault-plane solutions describe the type of faulting taking place (Fig. 8-2).

If a fracturing model is assumed, from the fitting of the displacement spectrum defined around the wave arrivals, source parameters can be estimated to indicate the size (magnitude) of the event, its released energy or the stress drop, and many other parameters.

Limitations on the accuracy of source-parameter determination and microseismic locations are related to the accuracy of receiver position and orientation, the signal-to-noise ratio (SNR), the accuracy of phase-arrival picks and particle motion estimates, knowledge of the velocity structure in the reservoir, and the fracture model.

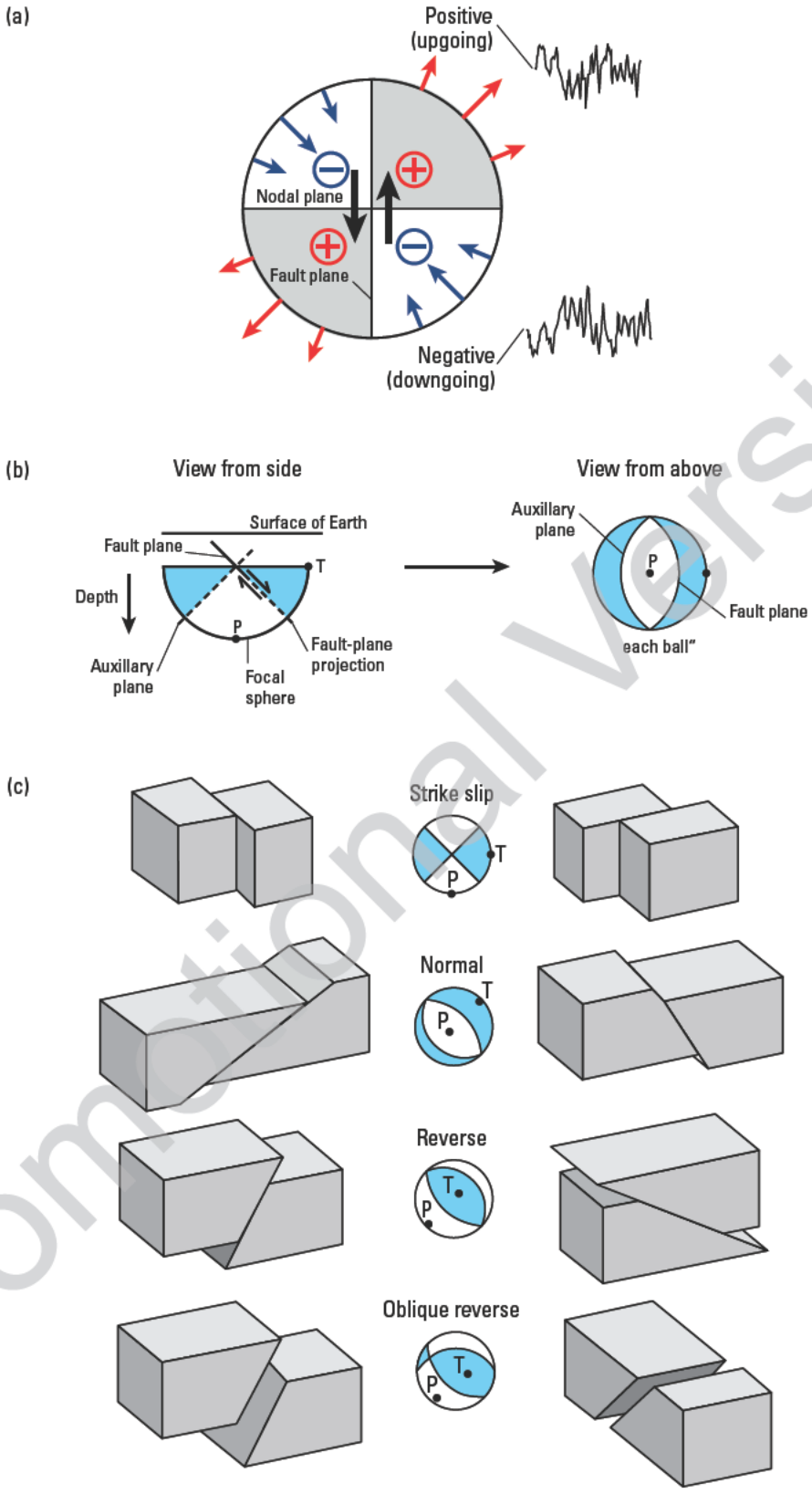

Figure 8-2. Seismic focal mechanisms. View (a) illustrates a fault-plane solution. Beach-ball diagrams (b) and 3D models of the relative slip direction on associated faults describe the four basic earthquake focal mechanisms (c). P = pressure axis; T = tension axis. (From Oppenheimer, 1996.)

Both the vector fidelity of the VSI tool and the quality of the coupling to the formation are critical to ensure proper SNR during data recording. If an optimal four-geophone-array configuration can be used (Jones and Asanuma, 2004) to ensure good vector fidelity, signal processing techniques such as filtering can improve the SNR and, therefore, the quality of the arrival time and polarization angle estimations. Improved knowledge of the velocity structure can be achieved by velocity model calibration (discussed in Section 8.3.4) or by acquisition of additional sonic or seismic data in the zones of expected seismic wave propagation, which generally are not limited to the zones to be stimulated. Analysis of the residuals in arrival times and polarization angles helps to distinguish between velocity model error and station position error. Such analysis is critical to improve the accuracy of source location and source parameters (Thurber and Rabinowitz, 2000).

8.2.2 Benefits

The monitoring of microseismic activity provides insights into the location of strain associated with stress changes within the reservoir and the surrounding formation, identifies reactivated faults, and identifies lithologic contrasts. Mapping microseismic activity at the reservoir scale over a period of time may highlight fluid-front movements, flow path anisotropy, compaction, fault delineation, and borehole instability. Whereas the monitoring period can vary from hours (e.g., hydraulic fracturing in coalbed methane formations or in the Barnett Shale Formation) to months (as in reservoir monitoring), the key information is the same—yielding the ability to dynamically map the microseismicity associated with fracture treatments or reservoir production. As such, the monitoring of induced microseismicity is a powerful tool to better understand the development (i.e., time domain) and geometry (i.e., spatial domain) of hydraulically induced fracture systems as well as of fluid injections and strain propagation through the formation of interest and the surrounding rocks.

In both hydraulic fracture monitoring and microseismic reservoir monitoring applications, the ability to integrate the characteristics of induced fracture systems such as fracture length, width, and height, with well stimulation parameters responsible for such characteristics and, later, with well performance data, can provide additional insight into the effectiveness of a stimulation treatment and help to improve reservoir management. Microseismic monitoring can also help to identify hydraulically conductive fault structures acting as flow channels for fluid breakthrough, which may affect pressure maintenance, as well as other things. On a field-wide basis, microseismic monitoring may be used to optimize well placement (Le Calvez *et al*., 2005) and improve the next well completion method (Le Calvez *et al*., 2006). Real-time microseismic monitoring, however, may be used to map microseismic activity within seconds of its occurrence (Le Calvez *et al*, 2007). This monitoring method allows a new perforation scheme to be implemented "on the fly" when using the plug and-perf approach, and it allows real-time decisions as to the treatment schedule (Daniels *et al*., 2007) or to optimize diversion techniques (Tinkham *et al*., 2009). In addition, along sealing faults, pore pressure can also increase, and faults can be reactivated due to stress change in the reservoir associated with production or injection activity. More specific to microseismic reservoir monitoring, compaction or reservoir subsidence as well as potential borehole instability during the reservoir life creates obvious major pressure changes.

Knowledge gained from these analyses can help to identify areas of the reservoir that are supported by pressure maintenance, represent a drilling risk, undergo compaction processes, or suffer caprock integrity issues. In addition, information about the dynamic state of the reservoir and the surrounding formations allows improved management of production and injection processes. It also may help target new production or injection wells. An understanding of the reservoir derived from microseismic data analysis may be enhanced by complementary data such as conventional borehole and surface seismic data.

8.3 Data acquisition configuration

Microseismic data acquisition uses multicomponent seismic sensors located in or near the reservoir unit under investigation to continuously record microseismic activity. Data acquired with a sampling rate typically of 0.25 ms to 1 ms are digitized downhole. Data are then transmitted to a surface acquisition unit. Data transmission from this surface unit to the processing site may take place by means of

- Ethernet or fiber-optic cable if the processing unit is near the acquisition unit
- radio if the processing unit is too far away from the acquisition unit for a proper physical connection while still in the line of sight
- air card, cell phone, or phone mast if wireless coverage exists
- secured satellite link if remote access is required.

The acquisition unit then provides the processing unit with either the acquired raw data or just the triggered events, (i.e., waveforms that satisfy some preset threshold criteria: SNR, repeatable occurrence, etc.).

8.3.1 Hydraulic fracture monitoring

The typical data acquisition network used for monitoring hydraulic fracturing consists of a multilevel (i.e., 8–20 levels), 3C, high-fidelity geophone array lowered in a monitoring wellbore close to the target depth (Fig. 8-3). Currently, more than 90% of hydraulic fracture monitoring surveys are performed using only one monitoring well, typically located within 750 m of the zone of interest in and around the treatment well. However, different attenuation values in the rock formations and seismic energy release may allow closer or wider spacing between the monitoring and the treatment wells.

Multiwell monitoring of a treatment is possible with geophone arrays located in distinct nearby wells. GPS time stamping of the recorded events is, in this case, particularly critical for data synchronization of the different receiver arrays. Typically in the context of real-time monitoring, each well is processed independently for faster turnaround. However, more sophisticated analysis is performed by using multiwell processing techniques.

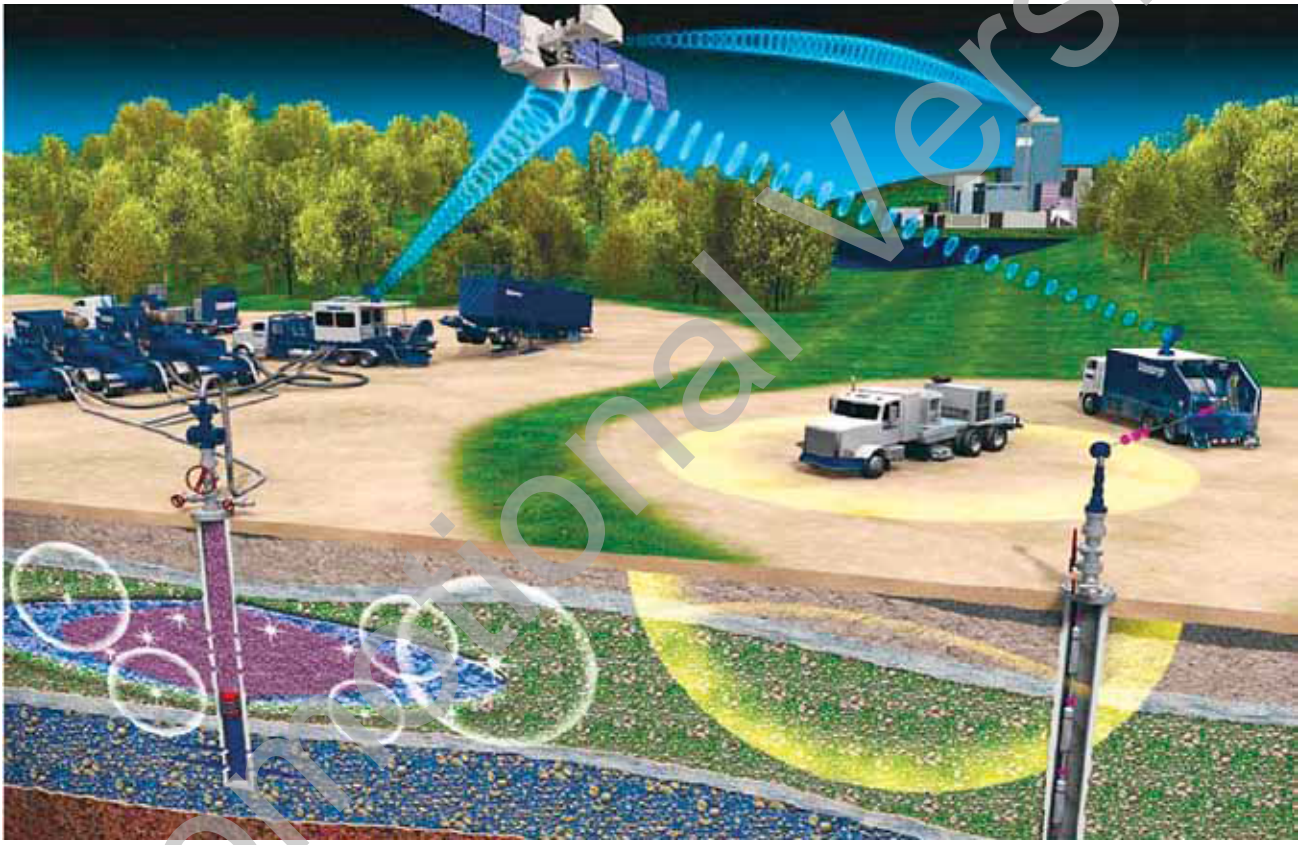

Figure 8-3. Illustration of different components involved in a typical hydraulic fracture monitoring campaign. In the lower left corner, the treatment well is connected at the surface to the pumping trucks, blenders, POD* programmable optimum density blender, and FracCAT* fracturing computer-aided treatment units. Underground, the stars represent the microseismic events taking place in the formation per se (green), at the edges of the fluid front (blue), or within the propped zone (purple). Acoustic waves (white circles) propagate from the source (hypocentral location) to the geophones located in the monitoring well. In the lower right corner, the 3C geophone array clamped against the casing of the monitoring wellbore is connected via wireline cable to the acquisition unit, where the processing is taking place. Additionally, a vibroseis truck is shown generating a sweep to interrogate the formation with a DSI* Dipole Shear Sonic Imager or a Sonic Scanner* acoustic scanning system to help improve the initial velocity model generally created using a traditional electric log. Both the monitoring and the treatment locations can be connected via Ethernet cable or satellite to exchange information if a decision is to be made on site. But, as illustrated, if the pads are in a remote location or decisions regarding the treatment are to be made off site, then both the monitoring and the treatment locations can be connected via satellite with the decision-making center from which the recommendations will be relayed back to the field.

In some cases, the seismic array may be positioned in the deviated part of a nearby monitoring wellbore or even be placed in the horizontal leg of a nearby lateral well. This monitoring configuration is intended to provide valuable information because the tool is logistically located close to the treatment zone while also providing good coverage of the stimulated area.

Another configuration often called "same well monitoring" or "treatment well monitoring" requires a seismic array to be placed in the stimulated well to be monitored. In this particular monitoring configuration there are two configurations that will provide effectiveness: one is to place a rathole below the lowest zone to be treated so that the monitoring array can reside there while the treatment takes place; the other would be to ensure effective acoustic isolation between the toolstring and the interval to be treated.

8.3.2 Microseismic reservoir monitoring

Reservoir monitoring of microseismic activity is achieved by continuously recording with multicomponent seismic sensors located in or near the reservoir unit under investigation for durations of weeks to years (Fig. 8-4). In addition to wireline-deployed tools commonly used for hydraulic fracture monitoring, different receiver configurations may be considered, such as permanent nonretrievable systems (e.g., cemented sensors in dedicated monitoring wells). A permanent or semipermanent retrievable system is composed of a tubing-clamped monitoring system and uses bow-springs or eccentralizers to allow geophones attached to the tubing to couple with the formation. Semipermanent microseismic monitoring devices such as the PS3-MW (Permanent Seismic Sensing System-monitoring well version) use the tubing to couple the sensor package to the formation. The use of eccentralized standoffs bends the tubing to achieve a suitable coupling force against the casing. Finally, a permanent or semipermanent retrievable system with acoustically isolated tubing-deployed geophones, such as the PS3 Ω-Lok system, offers a way to isolate the sensors from the tubing while clamping the sensor package to the casing (Jaques *et al.*, 200). For all these configurations, it is important to note that coupling to the formation requires a good cement bond between casing and formation.

8.4 Processing workflow for monitoring microseismicity

Microseismic monitoring campaigns commonly consist of velocity model building, survey design, receiver orientation, velocity model calibration for layering and anisotropy purposes, seismic data acquisition, and a processing phase that is completed with an interpretation phase. Microseismic processing, display, and interpretation are increasingly being used by operators to provide solutions in real time. The term real time derives from its use in early simulation procedures. Originally, real time

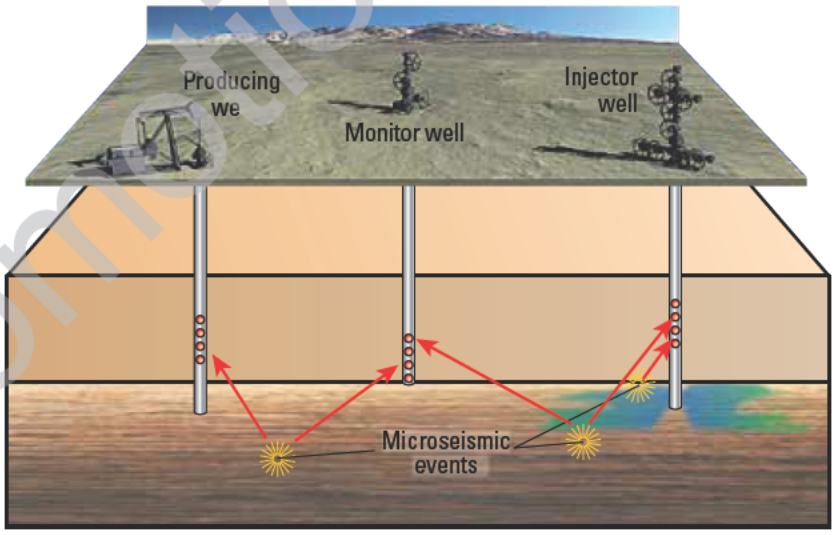

Figure 8-4. Three-dimensional view of an active oilfield showing microseismic events recorded by detectors located in producing, monitor, and injector wells.

referred to a simulation taking place at a rate matching that of the real process being simulated. Current usage implies that a computation that is "fast enough" is real-time computation. In the hydraulic fracture monitoring business as handled since 2007, a system is said to be a real-time system if the correctness of an operation depends not only upon the logical correctness of the operation but also upon the time at which it is performed and its relevance to the end user.

8.4.1 Velocity model building

Typically, a dipole sonic log, a cross-dipole sonic log, or a more sophisticated log from the Sonic Scanner* acoustic scanning platform is used to create an initial velocity model. Figure 8-5 shows the raw log data curves for compressional slowness (red), shear slowness (dark blue), and density (green), which are required to build a proper velocity model in association with the gamma ray data (cyan, column 4) for correlation pu p ses.

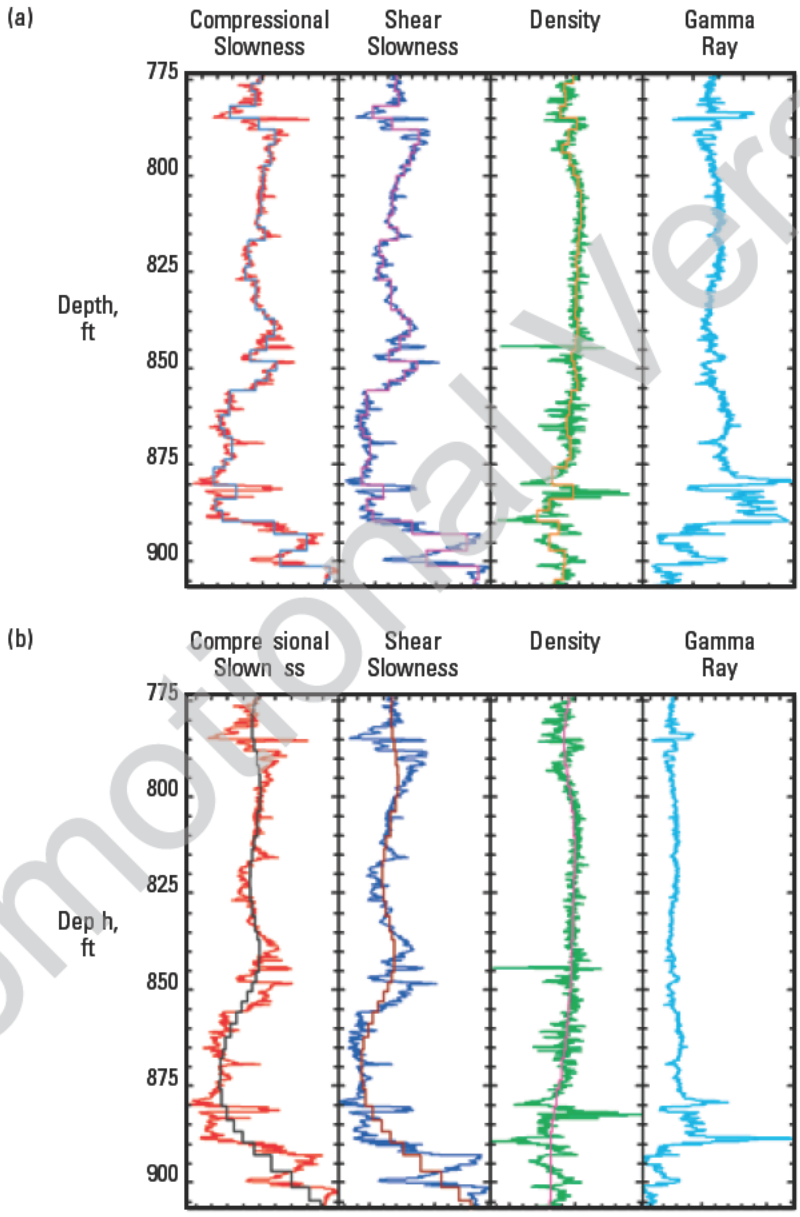

Figure 8-5. Example of a velocity model used to calculate microseismic hypocentral locations. Typically, a velocity model is constructed from wellbore sonic logs by first smoothing (up-scaling) the data using Backus averaging. Then the data are blocked to form a 1D, vertical transverse isotropic model. The anisotropic components for a 1D model are calibrated using recorded crosswell data such as string shots or perforation shots. A 20-ft blocked and smoothed velocity profile overlies the log data in columns 1–3 (a). The same log data are shown with an overlay blocked and smoothed to 200-ft intervals (b).

Interfaces are extracted and blocking is generated (20-ft blocking in this case) to minimize the number of layers while ensuring that enough layers are used to adequately represent the formations traversed by the propagating waveforms. Blocked curves are the sharp-edged curves (highlighted in blue, magenta, and orange) overlaid on the data curves in columns 1–3, respectively (Fig. 8-5a). After the blocked curves have been created, they are optimally smoothed to maximize ray-tracing stability used during the processing. The overlay in Fig. 8-5a has been smoothed to 20-ft intervals; the overlay in Fig. 8-5b was smoothed to 200-ft intervals. Note that the higher the smoothing value, the poorer the fit with the original curves. The logs used should be from the monitoring or treatment well or from a nearby well to ensure adequate knowledge of the local velocity structure. If available, several logs should be used to ensure consistency and allow for reciprocal checks. With the advance of sonic technology brought by the Sonic Scanner platform, it is now possible to improve velocity knowledge in terms of vertical resolution and to evaluate local anisotropy.

In addition, advanced borehole seismic surveys (i.e., crosswell tomography, walkaway) may be used to improve the knowledge of anisotropy and attenuation values in the far field.

8.4.2 Survey design

Once a velocity model is created, the geophysicist determines what receiver configuration will optimize the likelihood of successful data acquisition, while minimizing the uncertainty of microseismic event locations. Sometimes, survey design is constrained by practical restrictions such as plugs or any other limitations in the monitoring well below which the receiver cannot be deployed. Modeling tools are used to qualify and quantify the expected results and their uncertainties (Fig. 8-6). Besides the velocity model, a feasibility study requires knowing well spacing between injectors and producers and the monitoring wells, as well as the well geometry and trajectory (i.e., deviation surveys). In addition, the temperature profile and completion design

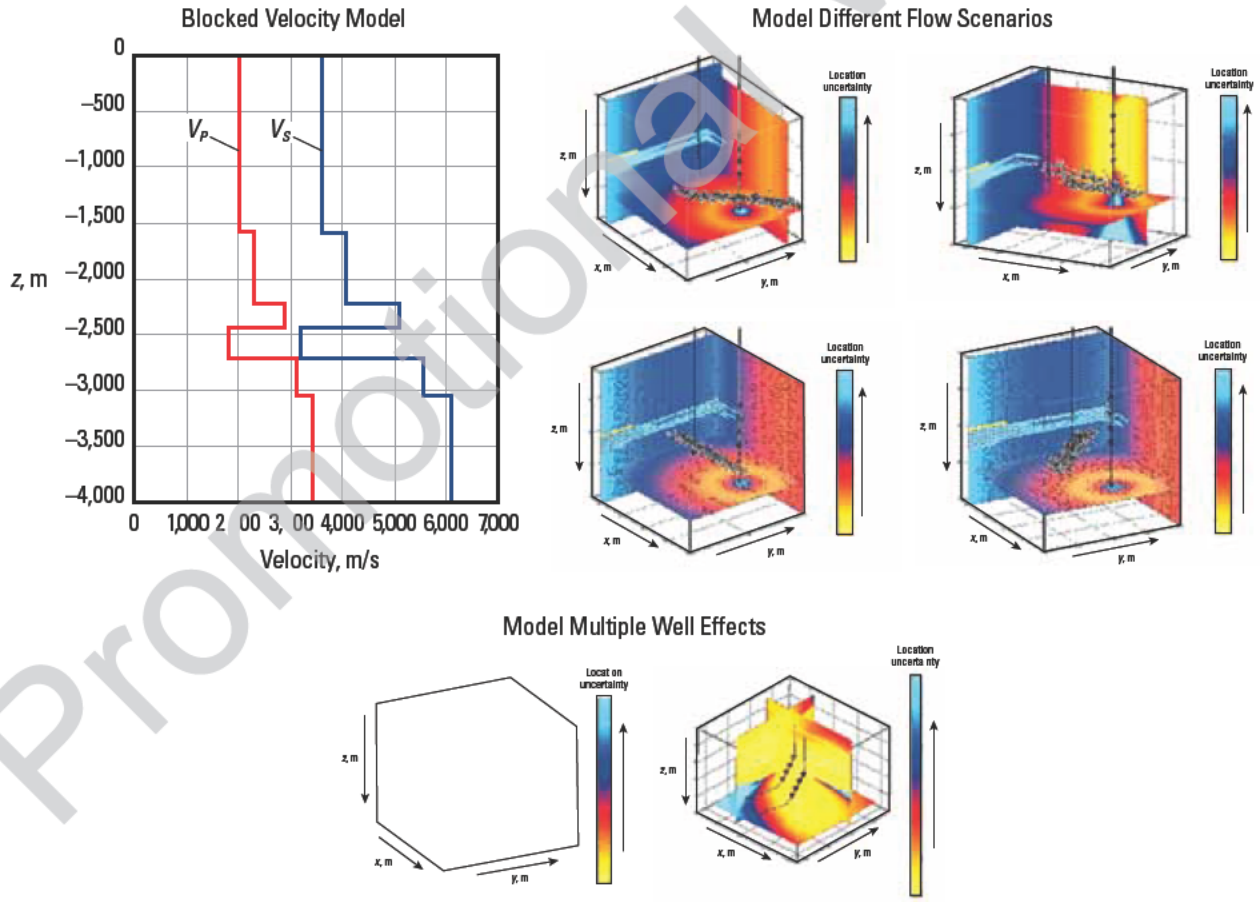

Figure 8-6. Survey-design examples. Top left illustrates a simplified blocked velocity model used in the modeling. Top right shows the different flow scenarios using a single monitoring well. Bottom highlights how different receiver array configurations affect overall monitoring.

(i.e., casing size, cementing information, tubing details, tubing hanger, tubing expansion, safety valve, wellhead, other control lines, and completion fluid) are mandatory to recognize any practical restriction in terms of tool deployment. Finally, information associated with the reservoir itself is useful to define the target area in which microseismicity is likely to occur. Reservoir parameters include pressure, formation tops, lithologic distribution, petrophysical information, fracture direction, stress direction, and the reservoir activity or injection plan. The best receiver configuration is then proposed as the monitoring geometry.

8.4.3 Receiver orientation

A critical and essential step of the data processing is the determination of the geophone sensor orientation in the monitoring wellbore. Typically, cable-spaced seismic stations within an array freely rotate as they are lowered into the borehole. String shots, perforation shots, or surface seismic sources are recorded prior to monitoring to resolve this issue (Fig. 8-7). The receiver orientation is achieved by computing the relative bearing angle of each 3C receiver by taking into account the hole azimuth and inclination, the measured polarization estimated from the hodogram analysis around the P-wave arrival, and the vector from the source location at each receiver.

8.4.4 Velocity model calibration

By comparing the locations of the observed calibratio shots with the known (sometimes estimated) ocations, it is possible to calibrate the velocity model to minimi e the difference between actual and observed po itions. This velocity model calibration can be done interactively by modifying the velocity model parameters, such as P- and S-wave velocity and anisotropy coefficients, and visually observing the fit of the new modeled P- and S-wave arrival times on the waveforms.

Another approach is based on the inversion, considering the minimization of the times and angles to find the best velocity model parameters. This approach takes into account all the receiver orientation obtained from all sources at once.

If the perforation shot timing is measured, thi timing is used in the calibration of the initial velocity model (Warpinski *et al.*, 2003). When the perforation shot timing is known, the number of un nown pa ameters is then reduced to only the sp tial coordinates, the inversion of the location is improved, nd therefore, the velocity model can be bette calibrated.

8.4.5 Event detection

During data acquisi on, background noise and microseismic events a e continuously recorded by the monitoring array and transmitted to the acquisition unit. Microseismic events can be separated from the backgro nd noise at the acquisition unit level using a simple event detector based on SNR estimates. For each component, the ratio of average amplitudes calculated in short-term and long-term windows represents the SNR If this ratio exceeds a predefined threshold on a certain number of traces, then a microseismic event is determined as detected. Detected microseismic events are then transmitted for processing and analysis to a processing unit, which could be either on site in the field or in a remote location such as an office.

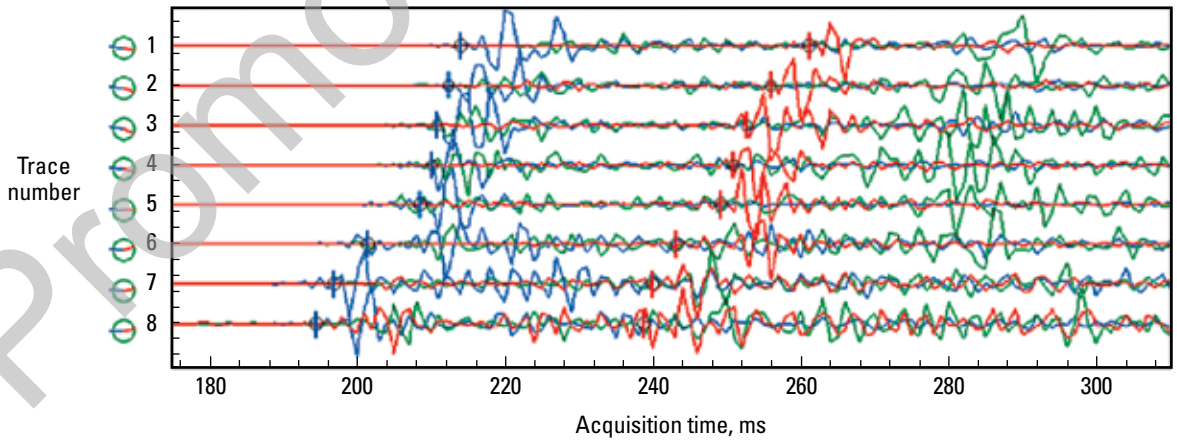

Figure 8-7. Example of traces acquired during a string shot. The *x*-, *y*- and *z*-components are plotted in blue, red, and green. Note on the left side on the graph the polarizations of the P-waves presented by the tadpoles (azimuth angle in blue and inclination angle in red). The polarization angles result from the hodogram analysis determined at the estimated P-wave arrival times represented by the blue ticks located in this figure between 193 ms and 214 ms.

Of course, raw data can be continuously analyzed as well in real time at the onsite processing-unit level. After the data acquisition phase, recorded data can be fully analyzed in the office for full validation of the real-time solution.

8.4.6 Event location

The main processing phase of the acquired data estimates microseismic event locations. Manual or automatic time-picking of wave arrivals (P and S) takes place to calculate the distance of the microseismic event to the geophone using the properly calibrated velocity model. A polarization analysis using hodogram analysis estimates both inclination and azimuth angles, which fully describes the microseismic event location (Fig. 8-8).

Once the times and angles are estimated, a location algorithm estimates the source location by comparing modeled and estimated times and angles. The location algorithm searches a full model space for a position presenting the maximum likelihood of location (Tarantola and Valette, 1982). Another location algorithm finds a minimum, starting from an initial guess and iteratively searching for the position leading to a minimum residual. This method, called Geiger algorithm (Geiger, 1912), is based on the fact that a perturbation of the source location and the resulting perturbations of the wave arrival times are linearly related. The problem is solved by iterations and generalized least-squares inversion. This method uses both arrival times and polarization angles as input data (Lee and Stewart, 1981).

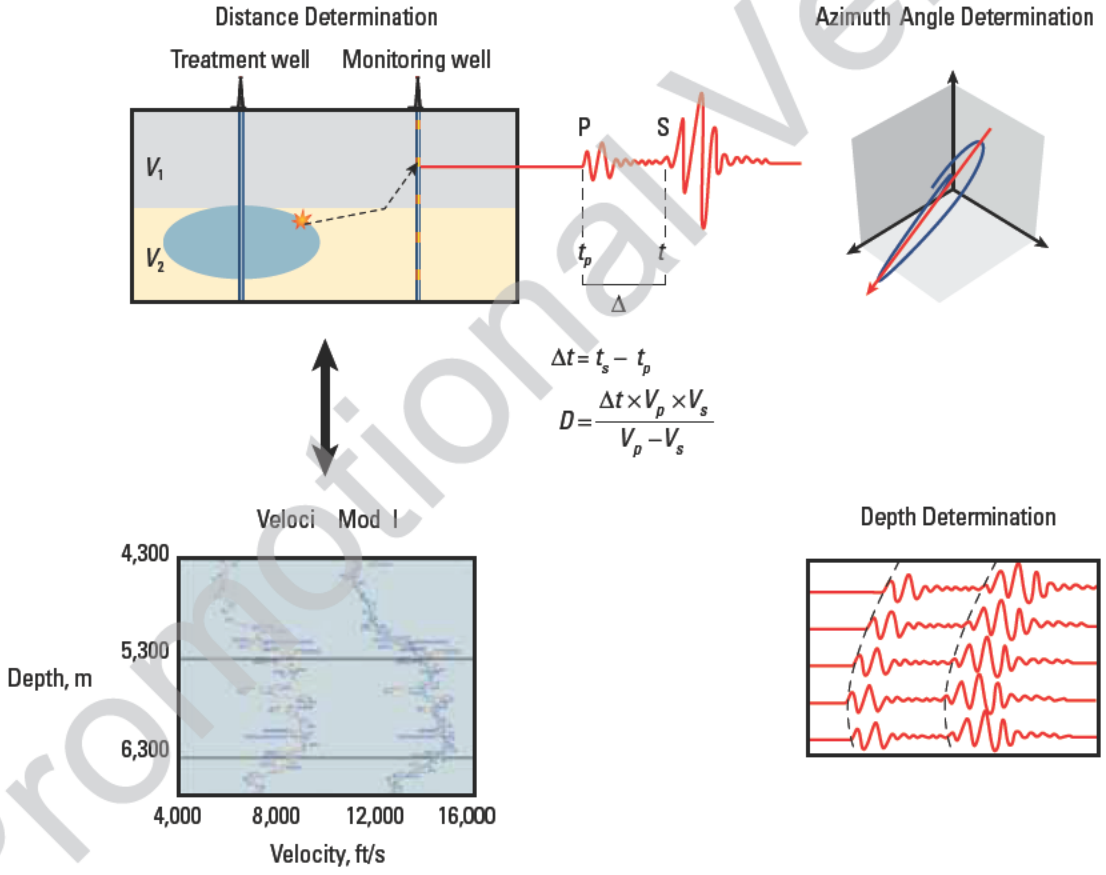

Figure 8-8. Microseismic generation, propagation, and measurement. In an over-simplified Earth model (top left), the distance (D) between the event and a monitoring triaxial geophone can be constrained by measuring the difference (Δt) between the arrival times of the P-waves and the S-waves (i.e., t_P and t_S, respectively). The value D is heavily dependent on the velocity model (bottom), which is usually described by the P- and S-wave velocities (V_P and V_S, respectively) of each layer in the model. The second coordinate, the azimuth to the microseismic event, is determined by examining the particle motion of the P-waves using hodograms (top right). The depth of the microseismic event, the third coordinate, is constrained by examining the P- and S-wave arrival delays between receivers (or the moveout) at the monitoring well. (From Bennett *et al.*, 2005/2006; this graphic is copyright Schlumberger, Inc. Used with permission.)

Typically, hydraulic fracture treatment generates a significant amount of microseismic events. Manual picking is a cumbersome and lengthy process that may lead to improper event location determination. This naturally leads to an incorrect interpretation of the hydraulically induced fracture system development.

Methods requiring manual time-picking are robust and have proved to be quite efficient when processing time is not an issue or when the SNR is fair to excellent. However, currently, processing should be completed within minutes (or seconds) of the acquisition of a detected microseismic activity. Therefore, hydraulic fracture monitoring requires an automated microseismic event detection and location capability using continuous spatial mapping to enable a true real-time processing (Drew *et al.*, 2004, 2005) (Fig. 8-9). This method detects and locates microseismic events without requiring the identification and picking of discrete arrival times at each sensor. This method is based on continuous updating of a spatial map in which each grid position corresponds to modeled traveltimes for P- and S-waves from this grid position to each receiver position. At each grid position, all SNRs corresponding to the waveforms at the modeled traveltimes of P- and S-waves for the entire receiver array are mapped for the entire receiver array. This method not only enhances the detectability of microseismic events but is both robust and fully automated.

8.4.7 Source parameters

Once the event location has been determined, source parameters can be estimated. The waveforms are rotated toward the source positions and are corrected for the instrument response and converted from acceleration to displacement values. Signal losses account for both geometrical spreading and attenuation. The displacement spectrum of the S-wave arrival is fitted to find three spectrum parameters: low-frequency level corner frequency, and high-frequency slope. From these three parameters of the displacement spectrum the source radius, seismic moment, stress drop, moment magnitude, and radiated energy are estimated nd sha ed with the 3D visualization tool for further in erpr tation.

The source radius may be omputed as a function of the ratio of the S-wave velocity at the source location estimate and the corner frequency of the S-wave displacement spectrum (Madariaga, 1976). In general, source radius paramete s are determined based on earthquake se smo ogy equations. Given the scaling issues existing b tween rthquakes studied from global network rrays and microseismic events studied from borehole-center d rrays, the validity of these equations and their appropriateness for microseismic fracture mechanics is currently under investigation.

The eismic moment is a function of the source-re ei er distance, formation density, S-wave velocity, low-frequency level, and the average value for the S-wave radiation pattern (Brune, 1970).

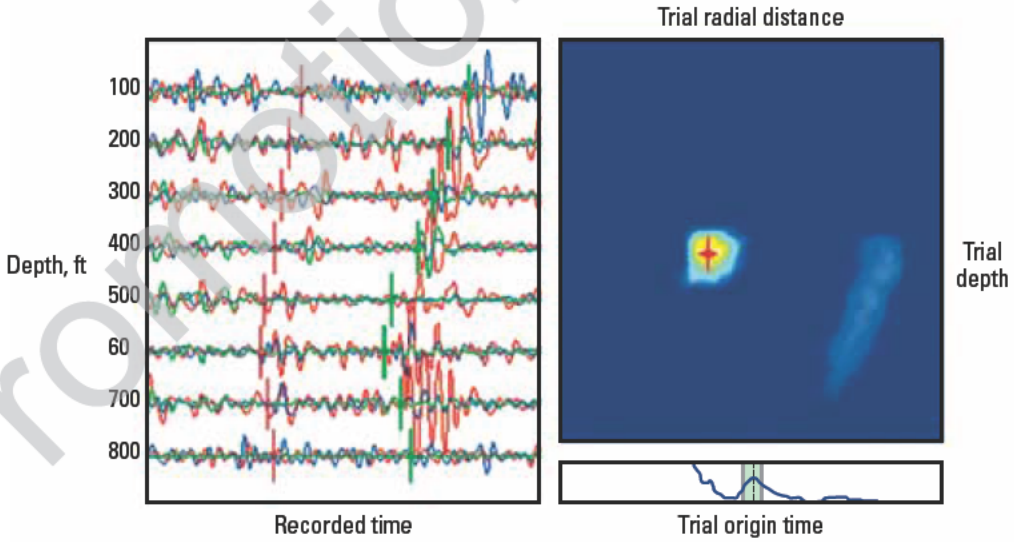

Figure 8-9. Coalescence mapping migration. This figure illustrates a dynamic process using a still picture. In this method, potential modeled time picks (vertical ticks along the trace) exist and are fitted to the data (waveform). If the moveout and timing are sensible, then it is considered that the modeled time picks are adequate and an event location is extracted from the lookup table. The strength of this method relies on its ability to not fall within local minima as well as to detect minute events.

The stress drop is derived from the moment and the source radius. The moment magnitude can then be estimated as a function of the moment (Hanks and Kanamori, 1979).

Magnitude attribute can be plotted as a function of the source-receiver distance for different stages of a hydraulic fracture monitoring dataset (Fig. 8-10). Small-magnitude events close to the receivers are detectable. Events farther from the tool must have higher magnitude to be detected. This is part of a monitoring bias and requires additional monitoring positions properly located to maximize coverage of small-magnitude events.

8.4.8 Multiplet identification

A group of microseismic events with high waveform correlation despite differences in the origin time can be found by observation of the various seismograms recorded. Such a group of events is referred to as a "multiplet." In this case, the events may be considered to be related to identical failure mechanisms (i.e., focal mechanisms).

The hypocenter distribution within a multiplet cluster often highlights planar structures, which might potentially indicate reactivation of fracture systems (Eisner *et al.*, 2006). Early detection of cross-stage fracturing may help the stimulation engineers to adjust, in real time, the pumping parameters associated with a hydraulic fracturing treatment.

8.4.9 Collapsing method

Once the event locations have been estimated, the interpretation of the "cloud" of events should consider the uncertainties of the locations. Uncertainty in location is typically represented as an error ellipse that contains the possible microseismic location with an assigned level of probability. An inspection of the many uncertainty ellipsoids would be tedious, difficult, and impractical. The idea of the collapsing method prop sed by Jones and Stewart (1997) is to consider th location uncertainties as a guide in the refinement of th locations. The locations are moved inside their un ertainty ellipsoids toward a center of gravity of a group of events to reach a refined picture of the spat al ev nt distribution. This has been proved to be useful to ighlight linear structures and identify faults

8.4.10 Interpretation phase

When record d microse smic events have their locations determined, the final analysis of the microseismic events yields an estimate of the induced fracture system geometry Traditional 2D displays are useful. H wever, to help fully assess the 3D geometry of the indu ed fracture system as well as its evolution through time, a visualization package is needed (Fig. 8-11). Integration of fracture geometry (length, width, height, and asymmetry), well logs, and geological information leads to an improved understanding of the reservoir haracteristics. When the characteristics are merged

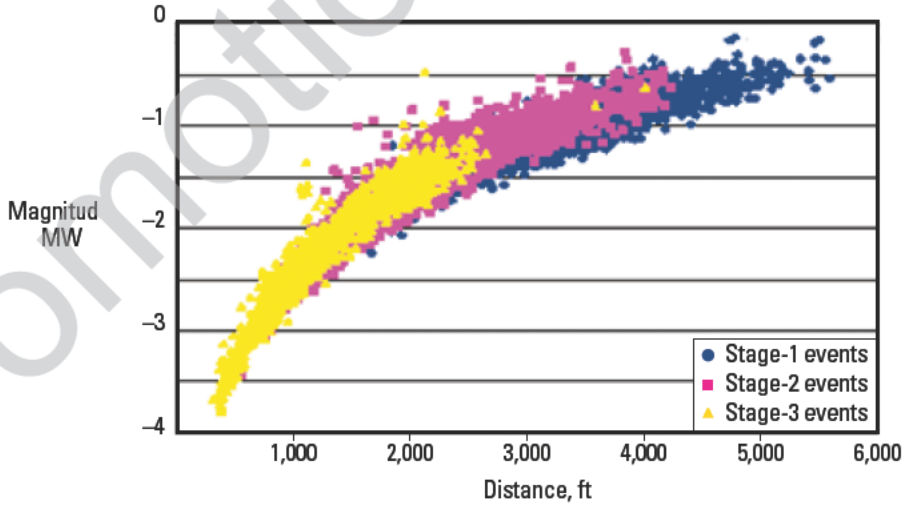

Figure 8-10. Magnitude of induced microseismic events plotted versus distance to the center of the monitoring array for three treatment stages. Such a plot can be useful to determine the maximum distance at which a microseismic event could be monitored (i.e., about 5,500 ft in this case).

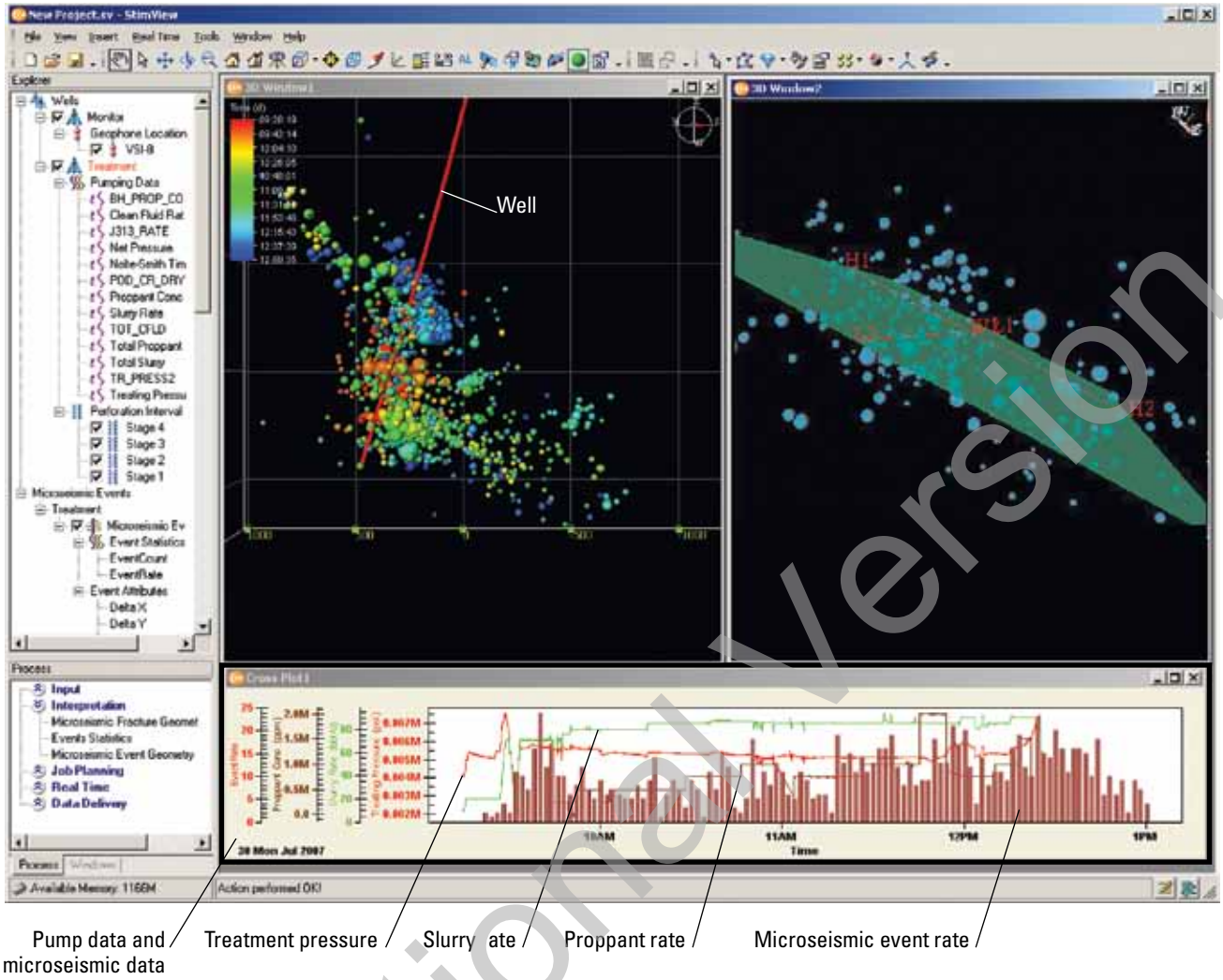

Figure 8-11. A display taken from the StimM * hyd aulic fracture stimulation diagnostic data system. Various types of data (microseismic event locations versus time nd tre tment parameters) can be displayed simultaneously and in real time to visualize and interpret the hydraulica y indu ed fracture system in relation to the well geometry and location. The left window is a map view of the overa mapped microseismic activity (colored spheres) as it relates to the well trajectory. Events are color-coded by time and siz d by m ment magnitude. Early events are red; most recent events are dark blue. The higher the moment magnitude, t e larg he sphere. The right window is a 3D view of a subset of microseismic events through which a plane is fitted o simula e a potential fracture plane.

with fracture-pumping information, the hydraulic fracture treatment is bet er monitored (Le Calvez *et al.*, 2007) Acc rate, real-time treating pressures, fluid and proppa t rat s, chemical additive rates, and various ther treatment data have increased the success and eff tiveness of stimulation treatments. To extract maximum value from the real-time processed, accurate microseismic event locations, it is critical to visualize in real time those locations in relation to the treatment geometry (e.g., well locations and trajectories, perforation locations, local lithology) and to the actual pumping parameters (Peterman *et al.*, 2005; Le Calvez *et al.*, 2006).

8.5 Examples—Microseismic applications

8.5.1 Enhance reservoir development

Low production and a low recovery factor are expected in formations presenting low permeabilities in the microdarcy to millidarcy range. Such formations are characterized as tight gas reservoirs.

Microseismically determined fracture system half-lengths tend to be approximately 50% shorter than the originally designed ones and display greater vertical development than the anticipated ones. Quite often, observed fracture systems exhibit strong asymmetry that appears not to be related to the monitoring geometry. In the case study discussed below, despite that six independent stages were performed, microseismic mapping illustrates that several stages are overlapping. An initial plot of the microseismic events against the gamma ray log (Fig. 8-12) highlights which zones are effective barriers that hinder fracture development perpendicular to the layering and which zone does not prevent fracture height development.

To analyze the commingled production, a production log is used to quantify the contribution from each stimulated interval (Table 8-1). These data indicate that the second stage does not contribute to the total production, whereas the contribution from the shallower third stage is minimal. On the other hand, the fourth and fifth stimulated intervals appear to contribute to two-thirds of the total production. Combining the production log results and the flowing wellhead pressure creates or each stimulated interval an allocated producti rate and its corresponding flowing pressure curve (Fig. 8-1). This allows each individual zone to be analyzed separately using numerical or analytical tools. Table 8-2 summarizes the production-matching results obtained using analytical simulation.

Table 8-1. Production Allocation from Production Log

Interval	Percent of Total Flow, %
Stage 6	8.2
Stage 5	23.0
Stage 4	41.4
Stage 3	4.0
Stage 2	0.0
Stage 1	23.4

Table 8-2. Summary of Results from Product on Matching

	Observed Fracture Half-Length, ft	Fracture Cond tivity, mD-ft	Formation Permeability, mD
Stage 6	205	16	0.0055
Stage 5	220	88	0.0047
Stage 4	40	12	0.0014
Sta e 3	411	24	0.0012
St ge 2	254	na	na
St ge	221	68	0.0039

a = not applicable.

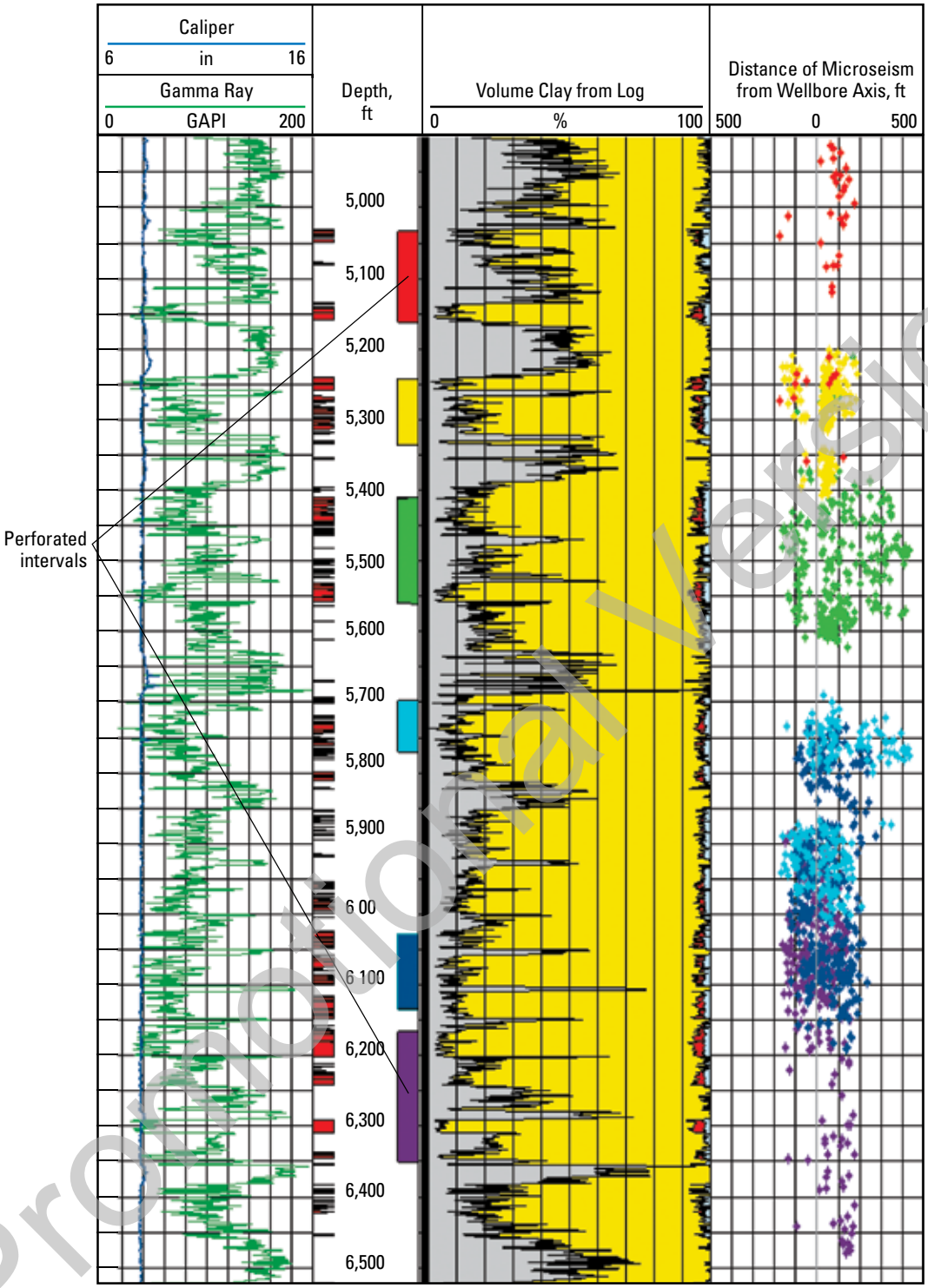

Figure 8-12. Two-dimensional display of all mapped fracturing stages in relation to conventional electric logs. Microseismic events are shown as dots, color-coded for each stage. Events are projected along a plane going through the perforation sets and aligned with the acoustically determined fracture system azimuth. Even though such an illustration gives a valuable snapshot of the fracture system geometry, only a 3D time-lapsed animation can reveal the true complexity of the geometrical characteristics of such mapped fracture systems. (From Peterman *et al.*, 2005 Copyright © 2005 SPE, reproduced with permission.)

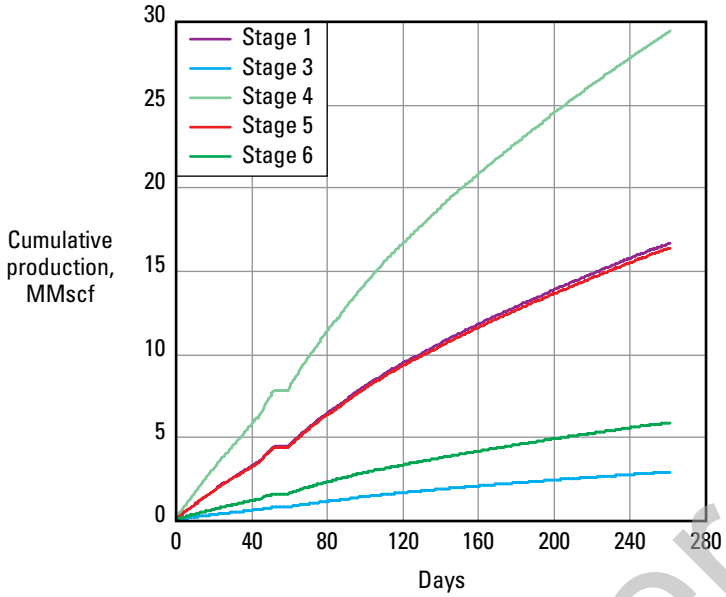

Figure 8-13. Cumulative allocated production for each stimulated interval shown in Fig. 8-12. (From Peterman *et al.*, 2010. Copyright © 2005 SPE, reproduced with permission.)

Typically, commingled production associated with varying fracture half-lengths and fracture asymmetries leads to a complex simulation scenario. One way to analyze the impact of such fracture geometries is to use a multilayered finite-difference reservoir simulator. Such a tool provides enough flexibility to model the production response from the observed fracture geometries. In this particular case, microseismic-based observed fracture lengths are noticeably shorter than the initially modeled and anticipated ones. Additionally, microseismic-based observed fracture systems are asymmetric, whereas the initial model anticipates them to be symmetric with a given orientation relative to north. To study the impact of shorter-than-expected fracture half-lengths and asymmetric geometries on production rates and recoverable reserves in very low-permeability formations, the previous one well analysis was extended to an existing area to help quantify the recovery after 10 years of production. The first model (Fig. 8-14 left) initially assumed production properties and assumed symmetric fracture half-lengths (approximately 500 ft) oriented parallel to a northeast-southwest direction. The second model (Fig. 8-14 right) uses the production properties derived from the afore-mentioned workflow as well as the fracture geometries observed from the microseismic mapping. Figure 8-14 (right) represents a map view of the modeled pressure distributions after ten years of production.

In low- and extremely low-permeability reservoirs presenting either commingled production or not, it is critical to effectively understand the hydraulically induced fracture system geometries and azimuths to optimally exploit the reserves. By combining various tools, such as microseismic mapping, production analysis, reservoir modeling, and simulation, an optimal drilling pattern can be determined to develop the reservoir to its full potential.

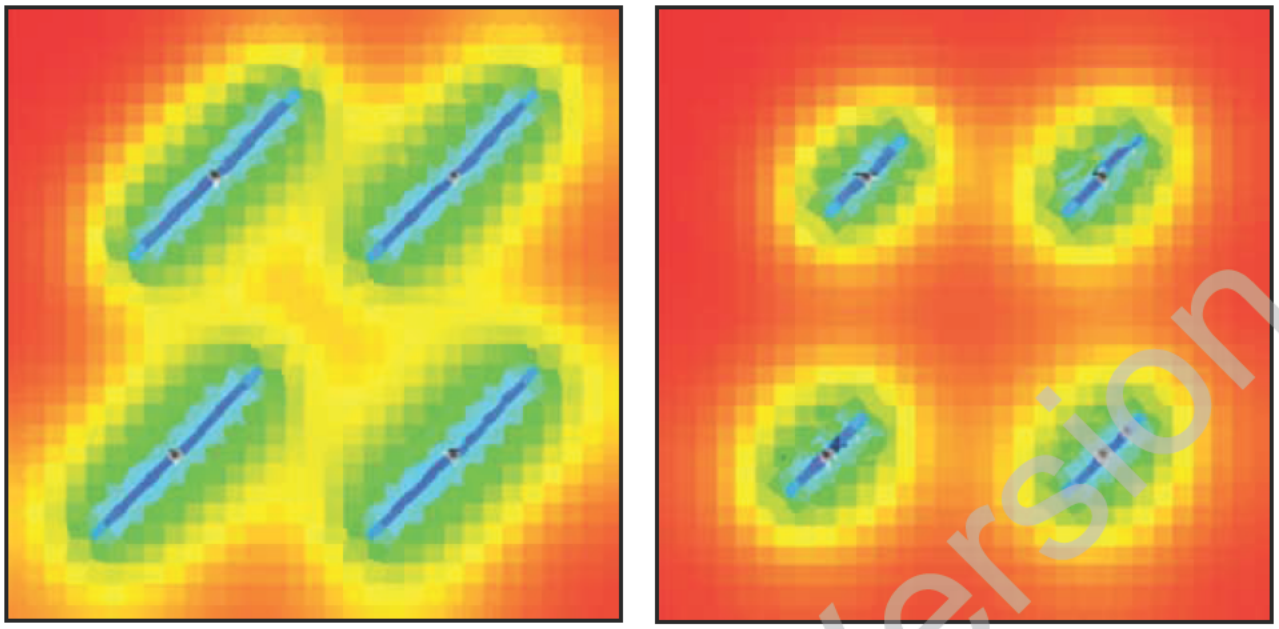

Figure 8-14. Map view of modeled pressure distribution assuming designed fracture properties (left) and observed (microseismic mapping) fracture properties (right). Blue represents rea deple d of gas; red represents area with abundant gas. (From Peterman *et al.*, 2005. Copyright © 2005 PE, reproduced with permission.)

8.5.2 Optimize completion strategy

The organic-rich shale gas fields underlying the Appalachian, Illinois, and Michigan basins are potentially the most productive source of natural gas in th United States. As in the Barnett Shale in Texas or he Fayetteville Shale in Arkansas, huge volum s of gas are being currently produced from thes Devonian shale reservoirs. Overall, these formations ar 100 to 500 ft thick, promising substantial reserv s However, two main geologic factors govern the production from these gas-bearing formations: ult a low matrix porosity (ranging from 2% to 6%) and permeability (ranging from 0.00005 to 0.0005 mD) and fracture-induced permeability. These formations must b effectively hydraulically fracture stimulated to yield economic production.

To avoid making t o many assumptions as to the induced fractur system geometry and to better understand the c eated fracture geometry for various completion des gns, monitoring of the induced fracture system geometry may be used.

In the following case study (Daniels *et al.*, 2007), real-time fracture monitoring using induced microseismic activity provided the stimulation engineer with information pertaining to geometry (3D) and development (4D) of the hydraulically induced fracture network. Many parameters can be monitored in real time to optimize the completion. The most important contributions are the generation of the estimated stimulated volume and microseismic event graphs that enable the engineer to make treatment-in-progress decisions about the stimulation and to make changes to the treatment in an effort to contact more of the reservoir. In this example, a mixture of fibers and other particulates was used to control the fracture geometry while pumping. This mixture was able to divert fluid flow in a fracture, build net pressure, and induce the creation of additional fractures in situ and at the wellbore, as desired. There are several challenges to creating diversion in this nonhomogeneous medium. First and foremost, although blocking of the fracture pathways is critical for creating diversion events, the pathways themselves must contribute significantly to production. Therefore, the diversion must be temporary as well as nondamaging to the fracture network. As reservoir conditions change, the degradable nature of the material must be controllable from field to field, well to well, and perhaps even stage to stage. Laboratory testing has been performed to ensure proper bridging for safe diversion and postjob cleanup.

In the Barnett Shale, both natural and induced fractures are nonhomogeneous. This situation creates a challenge to block many different fracture geometries simultaneously and temporarily. To address this problem, a multicomponent blend of materials was used. The particle size and percentages of each of these blends were engineered on the basis of the expected range of fracture geometries in the given wellbore. The fracture geometry was estimated from image logs and validated by real-time microseismic monitoring. Once the fracture network was effectively diverted, a pressure differential sufficient to generate the net pressure required to initiate a fracture elsewhere was maintained within the initial fracture. This pressure differential was in the range of hundreds of psi, making successful diversion difficult to determine by fracturing pressures alone. The example well was drilled parallel to the direction of minimum horizontal stress to create several transverse hydraulic fractures. This infill well has five offset wells crossing the heel section of the lateral. By projecting the lateral trajectory onto a resistivity log from a vertical offset well (Fig. 8-15), the toe of the lateral was positioned so that the first-stage perforation clusters encountered both the highest and lowest resistivities found in the reservoir. Effectively contacting all this section of the res rvoir in this environment would be difficult because of the itho-logic and stress variations from one perforation cluster to another.

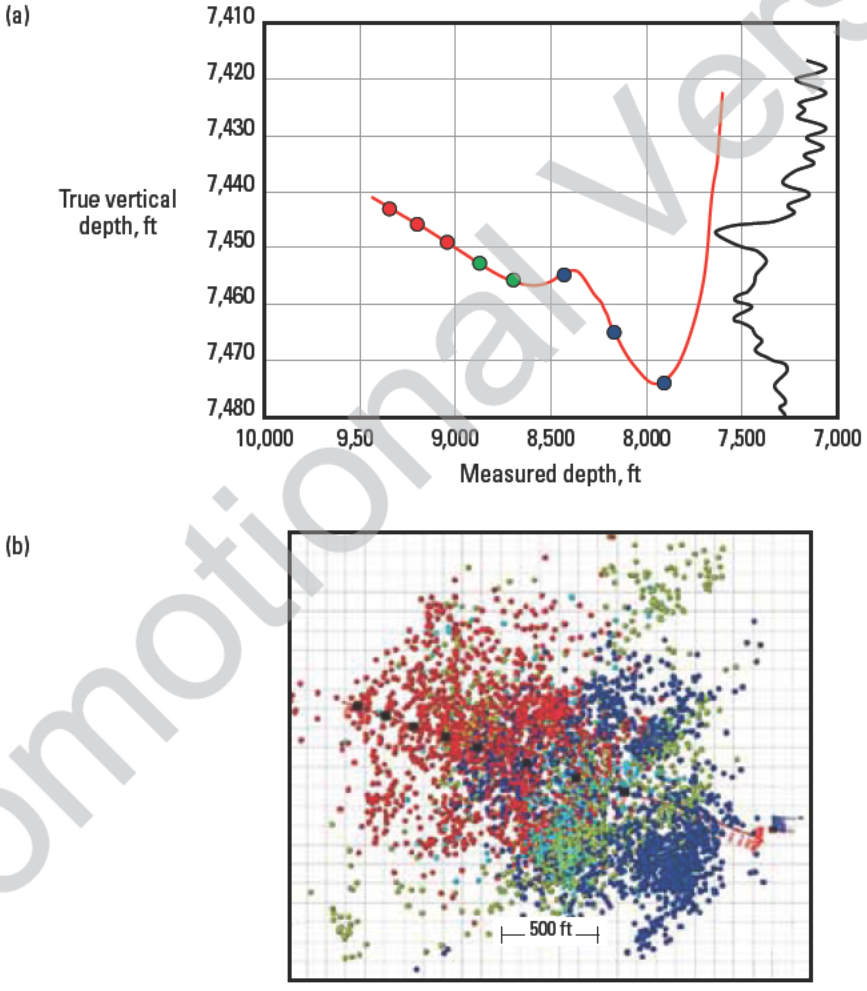

Figure 15. In the plot (a) of the wellbore trajectory overlying a resistivity log, the perforations are represented by dots. The five perforation clusters at the toe, shown in red and green, are the entry points for the Stage-1 treatments. However, the two green clusters were the only ones active for Stage 1a and Stage 1b. During Stage 1c, the red toe clusters and fractured rock in this section of the reservoir were activated. The overhead view (b) shows the location of the mapped microseismic events for all of the stages. Stage 1a is light blue, Stage 1b is green, Stage 1c is red, and Stage 2 is dark blue. (From Daniels *et al.*, 2007. Copyright © 2007 SPE, reproduced with permission.)

8.5.3 Better understand fracture system development

In several cases, a horizontal wellbore was treated in several stages from toe to heel using a given set of perforation clusters. Prefracture instantaneous shut-in pressures measured for each stage showed decreasing pressures from toe to heel, thus clearly illustrating stress variability along the horizontal leg of the wellbore. Microseismic monitoring confirmed these observations by highlighting variability in fracture system development. For example, in a high horizontal stress, anisotropic environment confirmed by image log as well as by new sonic log technology (e.g., Sonic Scanner log), the fracture system tends to develop along a clearly delimited narrow zone with its long axis oriented parallel to the maximum stress azimuth and its small axis oriented perpendicular to it (Fig. 8-16). Usually in such an environment, the lateral is aligned along the direction of minimum stress. On the other hand, in low horizontal stress, anisotropic environments, most of the microseismic monitoring campaigns show that the hydraulically induced fracture system is not properly defined along a given azimuth but has a large footprint (Fig. 8-16).

8.5.4 Improve perforation cluster strategy

Proper cluster spacing generally prevents competition between individual fractures; thus it minimizes fracture linking and maximizes the creation of multiple, independent, parallel fracture system sets. Initial microseismic studies illustrated this concept, now known in the industry as stress shadowing, with its positive and negative effects. For example, with perforation clusters too close to one another, stress shadowing leads to restricted development of the fracture systems located in the middle of the lateral. On the other hand, at both the toe and the heel of the lateral, the fracture systems tend to develop in a disproportionate manner.

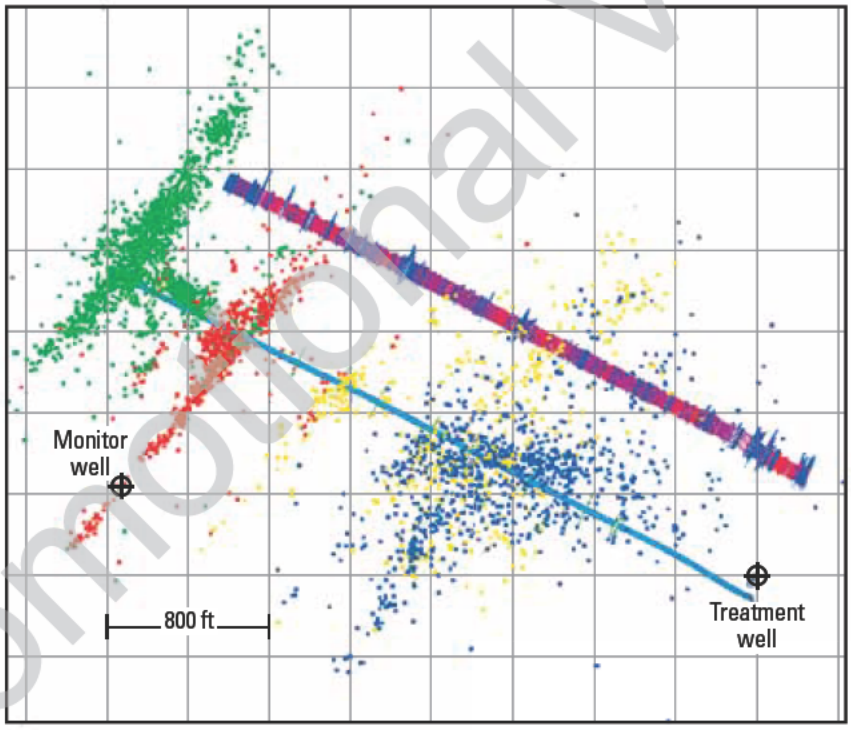

Figure 8-16. Overhead view of mapped microseismic events during a four-stage fracturing treatment. The first two stages (Stage 1 = green events, Stage 2 = red events) are well constrained laterally (i.e., planar fracture system with dense microseismic activity). The data from the last two stages (Stage 3 = yellow, Stage 4 = blue) show they are less constrained laterally, as also observed in the image log. Sonic Scanner data plotted above the well trajectory indicate the last two stages are in a generally less stressed environment (red). (Modified from Daniels *et al.*, 2007. Copyright © 2007 SPE, reproduced with permission.)

This pattern can have a negative effect if, for example, unexpected vertical development of the fracture systems leads to connecting the wellbore to a water-bearing zone (Fig. 8-17). If perforation clusters are properly spaced along the lateral, induced fracture systems have a tendency to simultaneously develop, and the fracture system development is enhanced along a direction perpendicular to that of the lateral. Additionally, microseismic monitoring mapping also highlights the need to separate perforation clusters with a distance of approximately 1.5 times the expected height of the fracture systems as well as to maintain a perforation cluster length of not more than 4 times the wellbore diameter to allow noncompeting induced fracture system sets to develop.

8.5.5 Manage unwanted fracture placement

In an uncemented lateral, fluid is pumped under pressure within the borehole until the rock breaks in some specific zone. Pumping pressure then suddenly decreases until it builds up again. From the surface, there is no way to know where the fluid and proppant are being placed because none of the zones is mechanically separated using some type of plugging device. In some cases, microseismic mapping shows that the fluid indeed is not reaching the expected zones but is breaking only the heel of the wellbore, for example, which greatly diminishes the value of the hydraulic treatment.

When surface seismic data are not available, well placement can be decided using microseismic analysis to highlight fluid paths and sealing or reactivated faults. In this case, microseismic data brings additional value not only to the stimulation engineers who stopped the wasteful pumping of expensive fluids and propp nt into the ground, but also to the geologists and geophys cists who improved their knowledge of he ar a of in erest.

In some cases, as in the Barnet Shale Formation, the interval of interest lies abov a wa r-bearing zone (e.g., Ellenburger Formation) Mi r seismic monitoring can help to detect early that the injected fluids are not remaining in the zone and, therefore, that pumping should be halted. Performed i real time, this monitoring technique can elp to void creation of a wet well (Le Calvez *et al* 200)

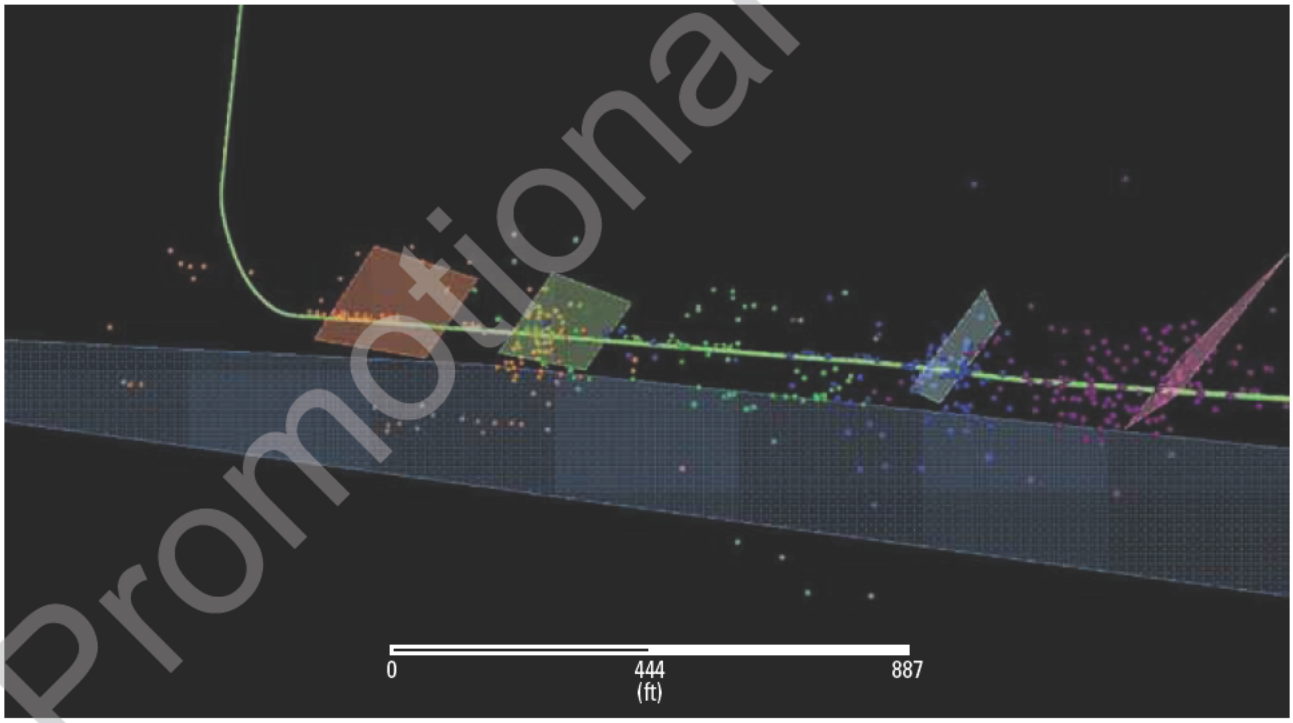

Figure 8-17. Mapped microseismic events along a well trajectory showing potential penetration of the hydraulically induced fracture system into the underlying water-bearing formation. Top of the water-bearing formation is in blue. Colored panels along the well trajectory are potential fault planes derived from either seismic or log information. (From Le Calvez *et al.*, 2007. Copyright © 2007 SPE, reproduced with permission.)

8.5.6 Monitor fluid-front movement and bypassed productive zones

In 2002, a microseismic reservoir monitoring project was carried out in the Yibal field, Oman, to monitor movements of fluids and stress changes in the reservoir as a result of pressure fluctuations. From the analysis of a high level of microseismicity over a monitoring area of 10 km^2, the microseismic events are distributed along structures of various intensity and size. These events are associated with active or reactivated faults (Fig. 8-18). From interpretation of the microseismic event distribution and parameters, a compartment has been identified within the gas reservoir as well as a high-permeability fracture corridor that acts as a water pathway. This trial has successfully demonstrated the potential of microseismic analysis to contribute to the reservoir management decision-making process.

8.5.7 Conclusions

From these examples, it is clear that the goal of today's effort to monitor hydraulic fracture treatments is to assess fracture system geometry (i.e., azimuth, height, length) and complexities associated with the interference between natural fracture systems. Other typical objectives are to identify local stress orientation and to evaluate hydraulically induced fracture containment. Being able to visualize hydraulic fracture system characteristics allows stimulation, production, and completion engineers to qualify the impact of the treatment and to potentially improve the next design. For example, the engineer can alter the placement and spacing of the perforation clusters. The engineer can also change the initial pumping schedule or even modify the nature of the proppant-carrier fluid. In some cases, diversion techniques can also be used if required.

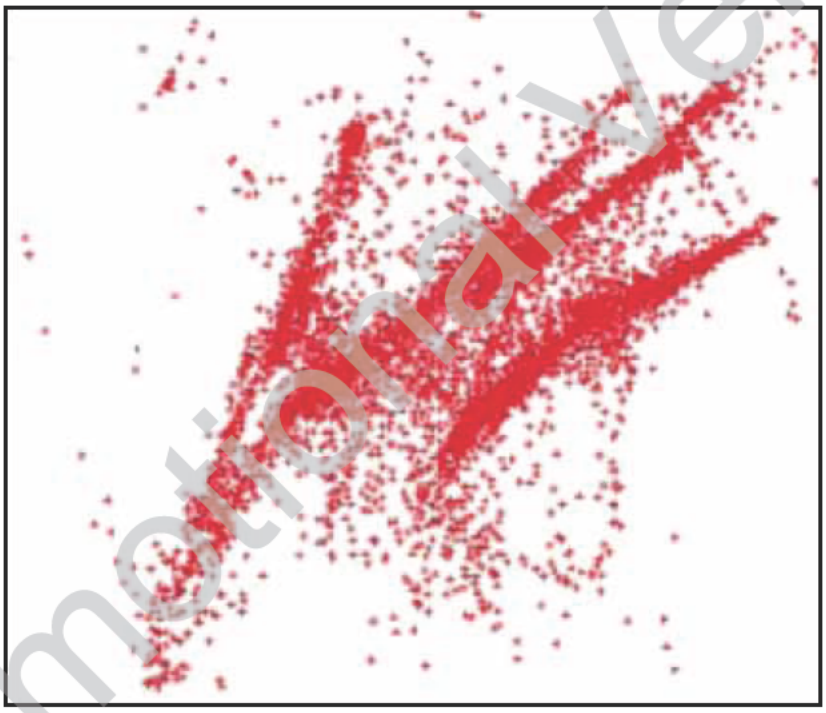

Figure 8-18. Map view of fault structures delineated by microseismicity.

Hydraulic fracture monitoring of induced microseismic events is a useful observation tool to understand the behavior of the hydraulically induced fracture system in a given environment under a given set of treatment parameters. Based on these observations, conclusions can be drawn and hypotheses can be tested, hopefully leading to better well placement, well design, well completion, and overall improved productivity and economics, while reducing the environmental footprint.

8.6 References

Bennett, L., Le Calvez, J., Sarver, D.R., Tanner, K., Birk, W.S., Waters, G., Drew, J., *et al.*: "The Source for Hydraulic Fracture Characterization," *Oilfield Review* (Winter 2005/2006) 17, No. 4, 42–57.

Brune, J.N.: "Tectonic Stress and the Spectra of Shear Waves from Earthquakes," *Journal of Geophysical Research* (1970) 75, 4997–5009.

Daniels, J., DeLay, K., Waters, G., Le Calvez, J., Lassek, J., and Bentley, D.: "Contacting More of the Barnett Shale through an Integration of Real-Time Microseismic Monitoring, Petrophysics, and Hydraulic Fracture Design," paper SPE 110562 presented at the SPE Hydraulic Fracturing Technology Conference, College Station, Texas, USA (January 28–31, 2007).

Drew, J., Bennett, L., Le Calvez, J., and Neilson, K.: "Challenges in Acoustic Emission Detection and Analy is for Hydraulic Fracture Monitoring," *Proceeding f the 17th International Acoustic Emission Symposium,* Tokyo, Japan (November 9–12, 2004), 15–22.

Drew, J., Leslie, D., Armstrong, P., and Michaud, G.: "Automated Microseismic Event Detection and Location by Continuous Spatial Mapping," paper SPE 95513 presented at the SPE Annual Technical onference and Exhibition, Dallas, Texas, USA (October 9–12, 2005).

Eisner, L., Fischer, T and Le Calvez, J.H.: "Detection of Repeated Hydraulic Fr cturing (Out-of-Zone Growth) by Microseismic Monito ing, *The Leading Edge* (2006) 25, No. 5, 548–554

Geig r L.: "Probability Method for the Determination of Earthquak Epicenters from the Arrival Time Only," *Bulletin of St. Louis University* (1912) 8, 60–71.

Hanks, T.C., and Kanamori, H.: "A Moment Magnitude Scale," *Journal of Geophysical Research* (1979) 84, B5, 2348–2350.

Jaques, P., Ong, H., Jupe, A., Brown, I., and Jansenns, M.: "Permanent Downhole Seismic Sensors in Flowing Wells," *SEG Expanded Abstracts,* 1st EAGE North Africa/Mediterranean Petroleum and Geosciences Conference and Exhibition, Tunis, Tunisia (October 6–9, 2003), T016, 2282–2284.

Jones, R.H., and Asanuma, H.: "Optimal Four Geophone Configuration, Vector Fidelity and Long-Term Monitoring," *Expanded Abstracts*, 66th EAGE Annual Conference and Exhibition, Paris, France (2004 , P294

Jones, R.H., and Stewart, R.: "A Method f r Determ ning Significant Structures in a Cloud of Earthquakes," *Journal of Geophysical Research* (1997) 102, 8245–8254.

Jones, R.H., Raymer, D.G., Mueller, G , Rynja, H., and Maron K.: "Microseismic Monitoring of the Yibal Oilfield," *Expanded Abstracts* 66th EAGE Annual Conference and Exhibition Paris, Fr nce (2004), A007.

Jupe, A.J., Jones, R.H Wilson, S.A., and Cowles, J.F.: "Micros ismic M nitoring of Geomechanical Reservoir Processes a d Fracture-Dominated Fluid Flow," *Geological Society of London Special Publications* (2003) 209, 77–86.

Le Calvez J.H., Bennett, L., Tanner, K., Grant, W.D. Jr , N tt, L., Jochen, V., Underhill, W., and Drew, J.: "Monitoring Microseismic Fracture Development to Optimize Stimulation and Production in Aging Fields," *The Leading Edge* (2005) 24, No. 1, 72–75.

Le Calvez, J.H., Klem, R.C., Bennett, L., Erwemi, A., Craven, M., and Palacio, J.C.: "Real-Time Microseismic Monitoring of Hydraulic Fracture Treatment: A Tool to Improve Completion and Reservoir Management," paper SPE 106159 presented at the SPE Hydraulic Fracturing Technology Conference, College Station, Texas, USA (January 28–31, 2007).

Le Calvez, J.H., Tanner, K.V., Glenn, S., Kaufman, P., Sarver, D.S., Bennett, L., Panse, R., and Palacio, J.C.: "Using Induced Microseismicity to Monitor Hydraulic Fracture Treatment: A Tool to Improve Completion Techniques and Reservoir Management," paper SPE 104570 presented at the SPE Eastern Regional Meeting, Canton, Ohio, USA (October 11–13, 2006).

Lee, W.H.K., and Stewart, S.W.: *Principles and Applications of Microearthquake Networks*, New York, Academic Press (1981).

McGarr, A.: "Seismic Moments and Volume Changes," *Journal of Geophysical Research* (1976) 81, No. 8, 1487–1494.

Madariaga, P.: "Dynamics of an Expanding Circular Fault," *Bulletin of the Seismological Society of America* (1976) 66, 639–666.

Niitsuma, H., Fehler, M., Jones, R., Wilson, S., Albright, J., Green, A., Baria, R., *et al*.: "Current Status of Seismic and Borehole Measurements for HDR/HWR Development," *Geothermics* (1999) 28, 475–490.

Oppenheimer, D.: "Focal Mechanisms," *USGS Earthquake Hazards Program* (1996), http://earthquake.usgs.gov/learn/topics/beachball.php (accessed May 5, 2010).

Peterman, F., McCarley, D.L., Tanner, K., Le Calvez, J.H., Grant, D., Hals, C.F., Bennett, L., and Palacio, J.C.: "Hydraulic Fracture Monitoring as a Tool to Improve Reservoir Management," paper SPE 94048 presented at the SPE Production Operations Symposium, Oklahoma City, Oklahoma, USA (April 16–19, 2005).

Tarantola, A., and Valette, B.: "Inverse Problems = Quest for Information," *Journal of Geophysics* (1982) 50, 159–170.

Thurber, C.H., and Rabinowitz, N. (eds.): *Advances in Seismic Event Location*, New York, Springer-Verlag New York LLC, Modern Approaches in Geophysics Series, Vol. 18 (2000).

Tinkham, S.K., Lecerf, B., Samuelson, M., Potapenko, D., Gillard, M.R., Birk, S.B., and Le Calvez, J.: Barn tt Shale Re-Fracture Stimulations Using a Novel D version Technique," paper SPE 119636 presented a the SPE Hydraulic Fracturing Technology Conference, The Woodlands, Texas, USA (January 19- 1, 2009)

Warpinski, N.R., Sullivan, R.B., Uhl, J E., Waltman, C.K., and Machovoe, S.R.: "Improved Micro eismic Fracture Mapping Using Perforati n-Timing Measurements for Velocity Calibration," paper SPE 84488 presented at the SPE Annual Te hni al Conference and Exhibition, Denver, Colorado, USA (October 5–8, 2003).

9 Survey Design and Modeling

Michael Jones

9.1 Introduction

Seismic modeling, or numerical prediction of experimental results, has several objectives:

- to understand and visualize theoretical concepts
- to analyze feasibility
- to optimize source and receiver geometries to achieve a desired result as input in survey design before any real data have been acquired
- to image or invert recorded data to arrive at a spatial distribution of material properties
- to test hypotheses in the interpretation phase.

Often it is necessary to check whether an inferred solution would indeed generate the observed data.

All borehole seismic surveys that deliver a multitrace, spatially variant result require modeling in their design and interpretation. This even applies to "simple" checkshot surveys in deviated wells or in the presence of strong horizontal velocity gradients or lateral velocity changes related to structure. Even if modeling is not explicitly conducted before acquiring the data, it is implicit in the data processing and migration.

The general problem of determining the spatial distribution of the elastic properties of a heterogeneous Earth volume from data recorded at a few discrete points around its periphery (i.e., in wells and on the surface) has a nonunique solution. These answers are provided by simulated synthetic measurements close to those that are actually observed around that periphery. The goal is to minimize the differences between observed and modeled data. This inversion process produces a model with calibrated material properties that represents our understanding of the subsurface, thus implying a necessity to conduct forward modeling through the inferred result.

This chapter discusses general concepts of survey design and modeling. More specific concepts are already discussed briefly in previous sections of this book. For example, Chapter 5 includes concepts on fluid discrimination and AVO modeling, whereas Chapter 6 presents considerations on time-lapse modeling and time-lapse AVO to identify changes in the reservoir caused by production or injection. Chapter 5 makes reference to modeling of anisotropic effects, both VTI and HTI, to understand their effect on AVO responses, effect on salt-proximity results, and effect on imaging—both in focusing and event positioning. Salt-proximity modeling, which constitutes one of the main uses of 3D ray-trace modeling today, was discussed in Chapter 6. Modeling related to hydraulic fracture monitoring and survey design aspects (i.e., effect of anisotropy on hydraulic fracture monitoring event locations, optimization of receiver locations, and modeling of microseismic events, including source radiation pattern) is discussed in Chapter 8.

9.2 Understanding the essentials

The underlying mechanical principles behind the science of seismology (elasticity, Huygens' and Fermat's principles) are well understood, at least for homogeneous media. Predicting the results when applying those principles can be very complex, considering the heterogeneity of the Earth at all scales. Modeling can help us gain insights into how those principles operate in a given situation and can help us to develop a framework for understanding the observed results.

In Chapter 2, Fig. 2-2 showed an example of this approach applied to the underlying relationship between a VSP dataset and the surface seismic CDP or shot gather that might be acquired at the same place. The figure shows how reflections, direct arrivals, multiple events, and mode conversions are recorded by the receiver array. It demonstrates how the VSP and CDP gather share a common trace, the one with the receiver at the surface at the well location. At this receiver location, the events (or at least those that propagate to the surface) must show continuity between the two datasets.

During feasibility analysis, modeling may confirm that a predicted effect can indeed be observed. This is not the end of the modeling process, because some form of sensitivity analysis is also needed. It is necessary to determine whether, if the modeled conditions had been slightly different, the observed result would have been *measurably* different. If the subsurface differences that are desired to be understood generate results that are too similar to distinguish, the actual survey will have little value. In more concrete terms, the interpretation

of a fault location requires not only that the fault appear in the data, but also that its position can be determined to the desired accuracy under the uncertainties of the velocity model and the actual geometry of the fault.

Often models are used to generate synthetic data for two possible scenarios, and the objective is to determine whether there are observable differences between the two synthetic datasets. Usually the modeling will show observable differences between the cases, but it is important to remember that when the real data are acquired, the problem is whether we can determine, from one of the datasets, which case it represents. One reason why this may be difficult is that the model implies a simplification of the geology, not only for the zone that may be under investigation but for all the other layers that contribute to the seismic response. We seldom have the luxury of interpreting a single event in isolation from its reflectivity environment.

9.3 Survey design questions

Unlike surface seismic presurvey planning, which seldom extends beyond normal-incidence synthetic modeling (i.e., considering only rays perpendicular to the interfaces), most offset and walkaway VSPs are modeled extensively in advance, including non-normal-incidence modeling, to predict full waveform response and true amplitudes. Another objective is to estimate the illumination of target horizons for the tested geometry. Modeling is required for all borehole seismic acquisition geometries when sources or receivers are offset from the well or when there is significant well deviation or structural dip.

The procedure to achieve a successful borehole seismic survey begins with a clear specification of the objectives of the survey. What are the questions to which it is hoped the survey will provide complete or partial answers? Often these questions hinge around imaging issues: Can the survey geometry provide subsurface illumination in the target area, or can the data from such a survey provide an unambiguous image to interpret?

After the survey objectives are defined, the design process continues with the practical and theoretical concerns of whether a survey can be designed that would meet those objectives (Table 9.1).

Modeling can provide answers to questions about amplitude, resolution, propagation, traveltime, image extent, mode conversion, anisotropy, AVO, and the ability to process the resulting data. In today's multidisciplinary industry, the model can be the common language among the various specialists.

Table 9-1. Practical and Theoretical Concerns of Survey Design

Concern	Detailed Question
Can objectives be met?	1. What frequencies are necessary to resolve the target?
	2. Can we expect a signal as a result of impedance change, AVO, or anisotropy?
	3. Do the possible reflection points cover the target area?
	4. For 4D, do the changes in the reservoir cause enough change in elastic parameters to be observable?
	5. For 4D, if the changes are observable, can they be inverted to define the reservoir changes that caused them?
Technical (practical) feasibility	1. Can the source generate the necessary frequencies in this environment?
Economic feasibility	1. How much will the technically feasible survey cost?
	2. What third-party costs will be incurred (navigation, rig time, boat time)?
	3. Are the preferred source points accessible and permitable with seismic equipment?
	4. What is the minimum survey configuration that will meet the objectives?

9.4 Types of modeling

There are three classes of modeling for seismic surveys:

- Simple convolution of the reflectivity log with a chosen wavelet generates a normal-incidence synthetic (Fig. 9-1). The reflection coefficients are derived from the acoustic impedance (Eq. 9-1), assuming normal incidence.

$$R = \frac{Z_2 - Z_1}{Z_2 + Z_1}, \qquad (9\text{-}1)$$

  where R is the reflection coefficient, and Z_1 and Z_2 are the acoustic impedance values of the layers above and below the interface, respectively. A wavelet is selected, specified by its bandwidth and phase, and each reflection coefficient is replaced by a copy of this wavelet, scaled by the value of the reflectivity. When the wavelets from more than one reflection coefficient overlap, their values are summed. This modeling does not account for propagation effects or multiples.

- Ray-trace modeling explicitly propagates energy through the model, from source to receiver, using ray propagation theory (Fig. 9-2). Refraction at interfaces or through velocity gradients follows Snell's law, and reflection is specular. Snell's law states that

$$\frac{\sin i}{\sin r} = \frac{V_1}{V_2}, \qquad (9\text{-}2)$$

  where i is the angle of the incident wave, V_1 is the velocity of the incident medium, r is the angle of refraction, and V_2 is the velocity of the second medium. In reflection from an interface, the angle of incidence equals the angle of reflection (Fig. 9-2). The path of a ray from the source to the receiver for reflection at a given interface can be calculated by using the properties of reflection and refraction. Because the velocity in the model is known, the traveltime of the ray can be calculated. A reflection coefficient can be inserted into the receiver trace at this time. The process can be repeated for each interface in the model. The resulting reflection coefficient series can be convolved with a desired wavelet to produce a synthetic trace for each source-receiver pair. In practice, many more physical effects can be modeled in a ray-tracing scheme: attenuation, nonzero-incidence reflectivity, implied multiples, and complex structures. Ray tracing can be performed in one, two, or three dimensions through quite arbitrary velocity models, and anisotropy may be incorporated into the layers, if desired. Although ray tracing is often thought of in relation to traveltime determination, it also allows very accurate modeling of amplitudes. Ray-trace modeling has the huge benefit that the modeled response can be confined to selected events or regions of the subsurface that represent a subset of the full wavefield response.

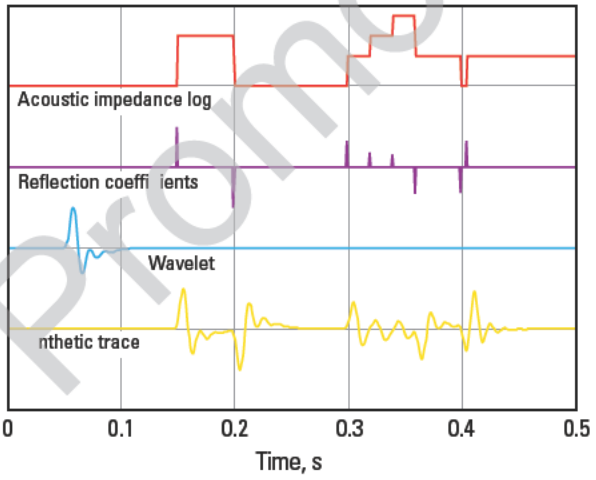

Figure 9-1. Simple convolutional synthetic seismic trace. The reflection coefficients are derived from the acoustic impedance, if we assume normal incidence.

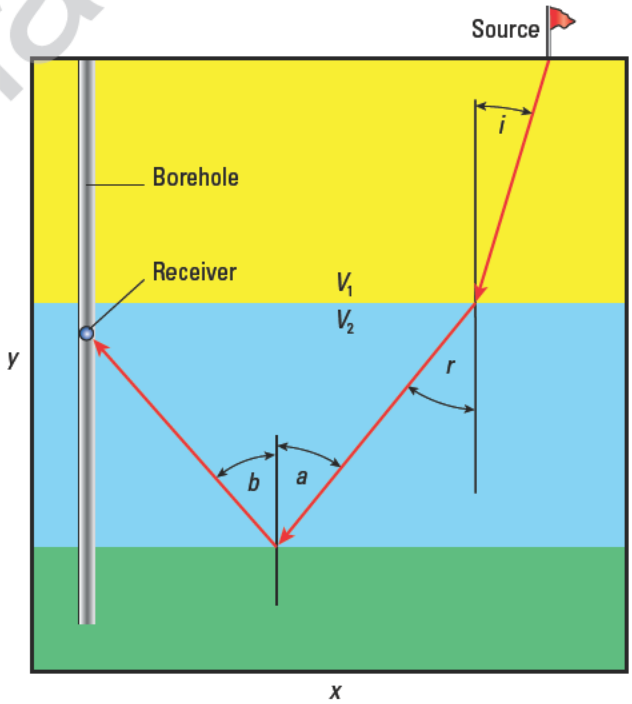

Figure 9-2. Schematic of ray-trace modeling principle and Snell's law. In reflection from an interface, the angle of incidence (*a*) equals the angle of reflection (*b*). Symbols: i = angle of the incident wave, V_1 = velocity of the incident medium, r = angle of refraction, V_2 = velocity of the second medium.

- Finite-difference modeling provides a more general solution to the problem of generating the modeled Earth response (Fig. 9-3). Finite-difference modeling will provide a very complete synthetic seismic response, including all the multiple reverberations. It has the advantage that the generated response includes all possible travel paths from source to receiver, whereas the ray-trace technique will normally find only the shortest-time travel path for a particular mode. In complex geological structures, this may be significant because the multipathing may be rampant. Finite-difference modeling can be performed in one, two, or three dimensions, though in three dimensions, it is computationally intensive and demanding on both processor cycles and core memory. Finite-difference approaches are usually thought of in terms of modeling full-wavefield responses at relatively high computational cost, but they are also the basis for eikonal equation solvers that can determine point-to-point shortest traveltimes extremely fast.

The preceding classification is neither perfect nor complete. There are also hybrid modeling schemes that use different modeling techniques in different regions to exploit the respective strengths of either technique. Hybrid models separate the modeled volumes into a simple, or even constant, model outside the zone of interest and a changing model within the zone. There are also techniques that model two-dimensional responses from one-dimensional models by using "propagator-matrix" methods.

The following sections will consider some of these questions, ordered according to increasing complexity.

9.4.1 One-dimensional modeling and vertical resolution

The simple 1D question of temporal (o depth) resolution is often answered by modeling In the simplest case, a synthetic seismogram derived f om an acoustic impedance log is a modeling re ult Simple extensions to this would be to model pin houts or channel responses by deforming the log used for the adjacent successive synthetic traces.

Synthetic s ismograms re widely used to tie the seismic reflection da a wi h the geology derived from the log data. The synthetics are generated by convolving the normal-in idence reflectivity sequence with a desired wavelet, usually zero phase. Every reflection coefficient in the sequence "sees" the same wavelet, and changes in the wavelet shape caused by its propagation

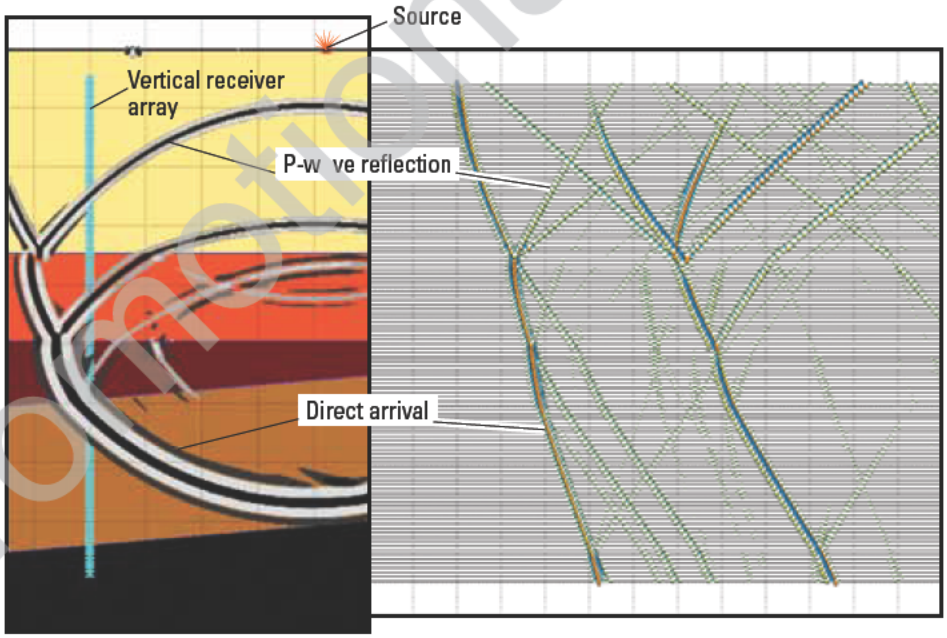

Figure 9-3. Representation of finite-difference modeling. The velocity model (left) is represented as a fine grid. The initial disturbance (the source function) is then propagated through the grid, cell by cell, time-step by time-step, to arrive at a full synthetic seismogram (right) for the receiver locations specified.

through the Earth are ignored (or, phrased another way, the assumption is made that those propagation effects present in the real data can be adequately compensated for in the processing of the seismic data). The synthetic terminates at the depth of the deepest formation in the well for which logs are available.

In an actual dataset, the resolution is further limited by the loss of high frequencies during the wavelet's propagation through the Earth. Absorption of energy from the wavefield, usually expressed in terms of the quality factor Q, is discussed in Chapter 4. This is the loss of high-frequency energy to friction in the rock. It is often a concern for surface seismic surveys, but as the frequency requirements for adequate resolution become higher, the importance of absorption also increases. For cross-well studies, attenuation is the crucial limiting factor for image resolution and maximum possible well-to-well range.

A second mechanism that reduces high frequencies and that is usually neglected is the elastic effect of repeat layers. A stack of thin layers, such as coals, will generate a series of notches in the spectrum of the propagating wavelet as the wavelet reverberates within the layers and interferes with its undelayed version. For examples, analysis, and discussion of this phenomenon, see Coulombe and Bird (1996), O'Doherty and Anstey (1971), or Ziokowski and Fokkema (1986). In practice, the first notch will usually define the maximum usable frequency in the zone of interest.

Figures 9-4 and 9-5 show synthetic seismograms illustrating these effects. The same impedance log and input wavelet are used for each version. Figure 9-4 shows a "primaries-only" synthetic and one that includes multiples. The time of the deepest, isolated reflec ion was chosen to be later than the multiples generated etween the repetitive layers and the shallow reflect r so that the response of this reflector is no affected by he first-order multiples following after the repe itive layers at 0.4 s. The two spectra shown in the fig re are for windows of the trace taken abou the shallower reflector (no multiple distortion) and the deeper one (including the transmission filtering). Figure 9-5 shows the case in which a Q of 80 is included i the primaries-only synthetic. In both case there s an amplitude effect and a phase effect on he w velet.

It is asy to see that even the apparently straightforward procedu e of generating a 1D synthetic is subject to interpretation and carries potential pitfalls.

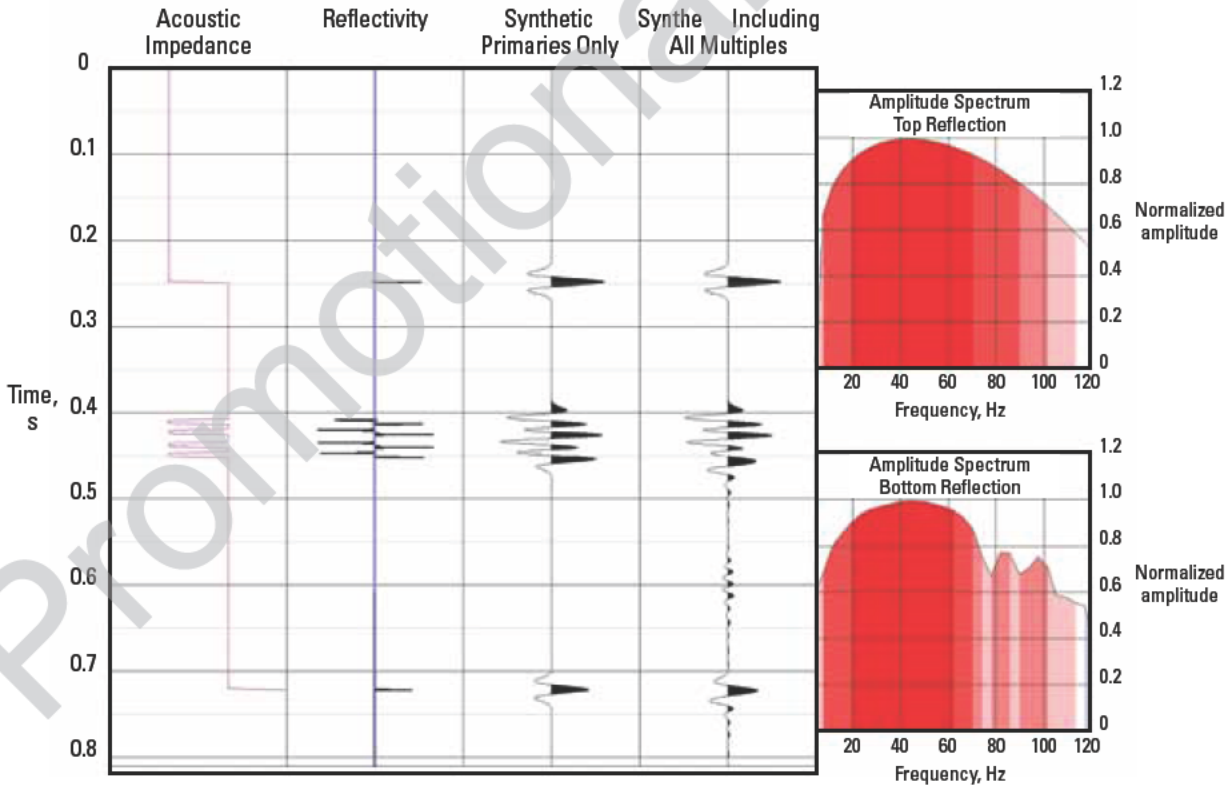

Figure 9-4. 1D synthetic seismic trace showing the effect of transmission filtering by thin layers (e.g., coals) on the amplitude and phase of deeper reflections.

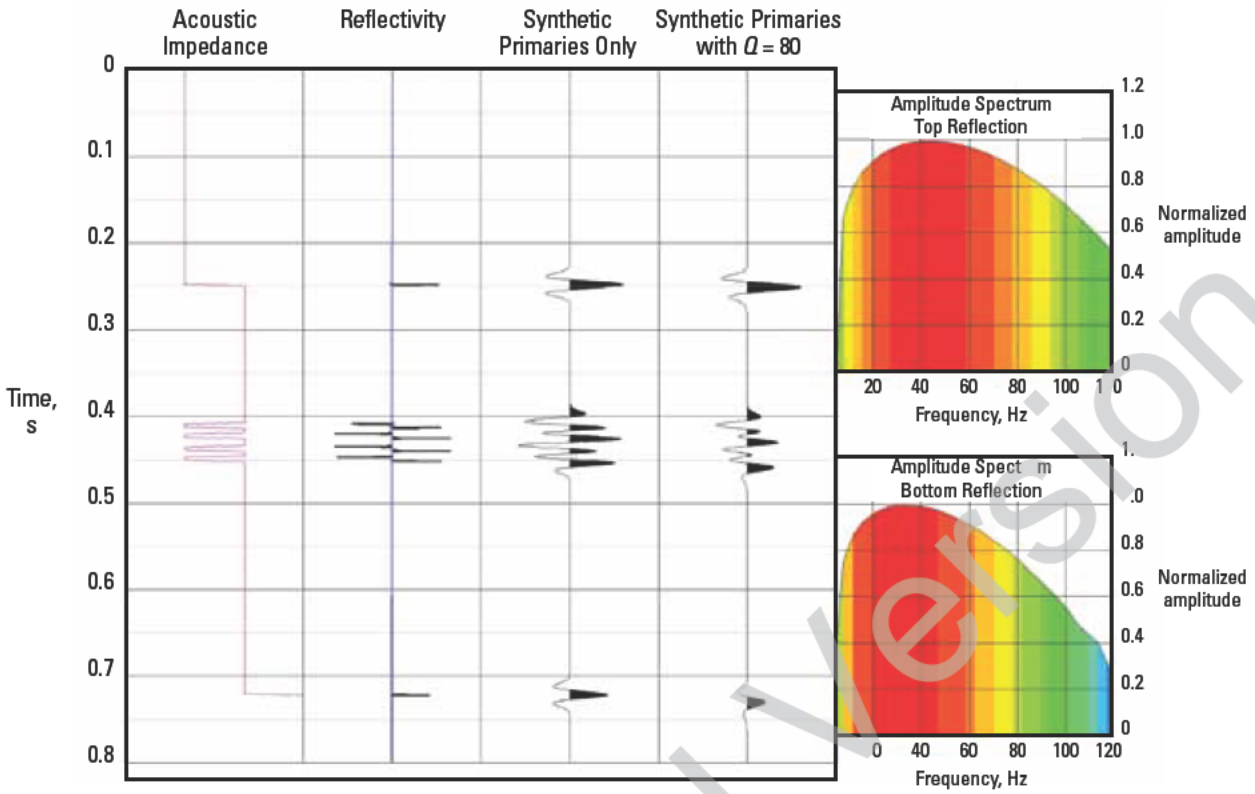

Figure 9-5. 1D synthetic seismic trace showing the effect of anelastic atten a ion (Q 80) on the amplitude and phase of deeper reflections.

9.4.2 Two-dimensional modeling and lateral resolution

Interesting questions arise in the more ge era topic of imaging lateral variations in geology. ateral variations can range from major structural feature having large relief to lateral changes in porosity with no vertical relief at all. Between these extremes a e the imaging of faults in relatively flat backgrounds and the imaging of low-relief reefs. At the extrem end of the structural branch, salt-flank imaging is perform d in which the target to be imaged may be vertical or overhanging.

Figure 9-6 shows a simple model of a fault adjacent to a well. For implici y, the layers in this model have been chosen wi h no internal vertical or horizontal velocity gradients, and the rocks are assumed to be sotrop c. No other physical property has any effect on th seismic response, either in the model or in the physical world. Porosity, permeability, and lithology can be observed only if their variation causes variation in the elastic parameters.

Figure 9-6 also shows the raypaths of the compressional P-waves for reflections from the top of the faulted horizon. Figures 9-7a, 9-7b, and 9-7c show the results of imaging synthetic data from this model using a VSP CDP transform.

The imaging step assumes that the velocity model is completely known before the image is interpreted. The real question, however, is whether the correct interpretation can be recovered if the velocity model is only imperfectly known. Figure 9-7a shows the data mapped through the same velocity model from which the synthetic was created, whereas Fig. 9-7b shows the data mapped through a 1D (flat) velocity model containing no fault but matching the velocity structure at the wellbore. Figure 9-7c is the image resulting from mapping the synthetic data through a model that includes a fault but in the wrong lateral position. This image is clearly distorted by the error in the structure in the velocity model. Obviously, less information is better than erroneous information.

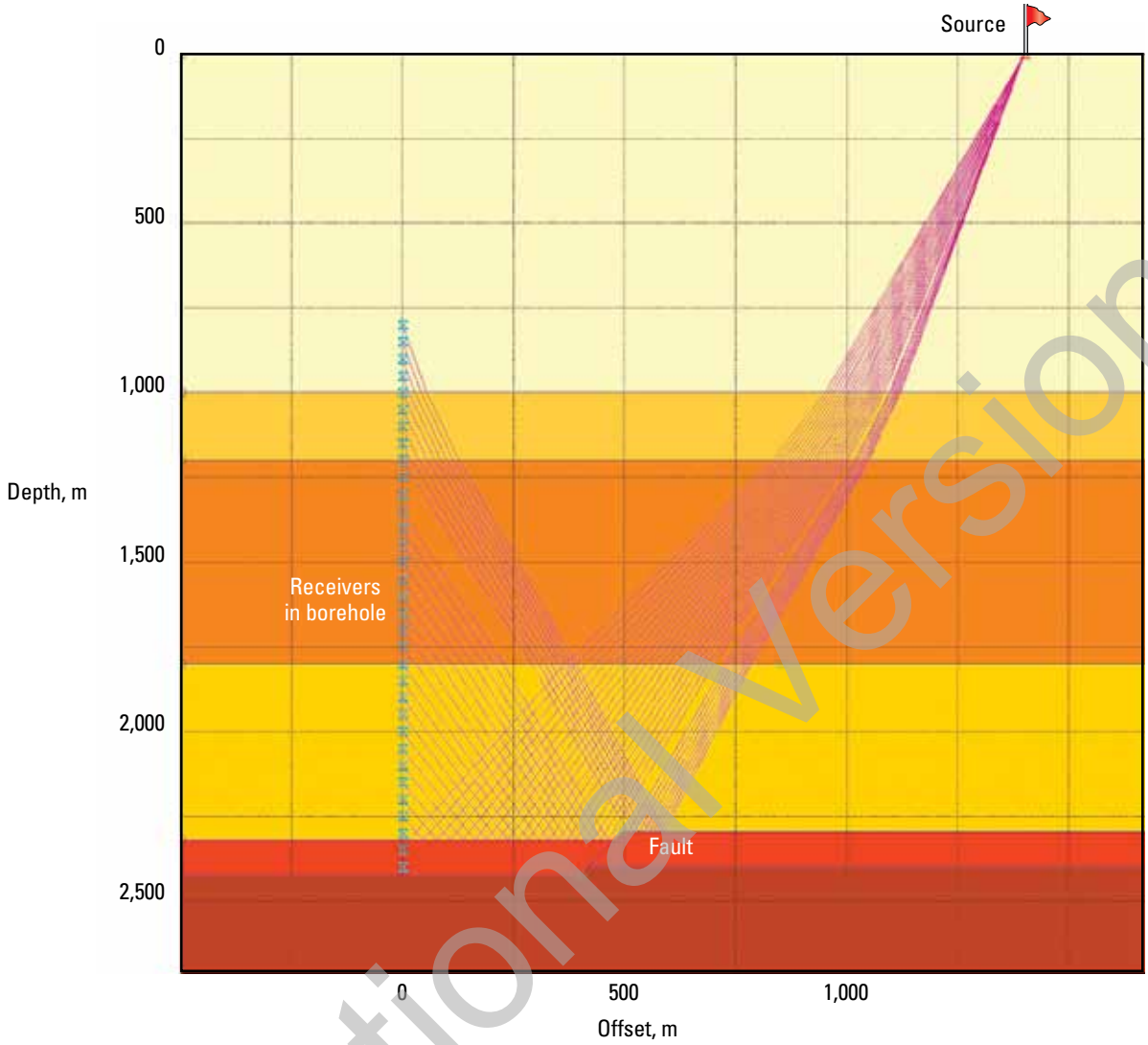

Figure 9-6. 2D fault model showing modeled r ys for th top of the faulted layer.

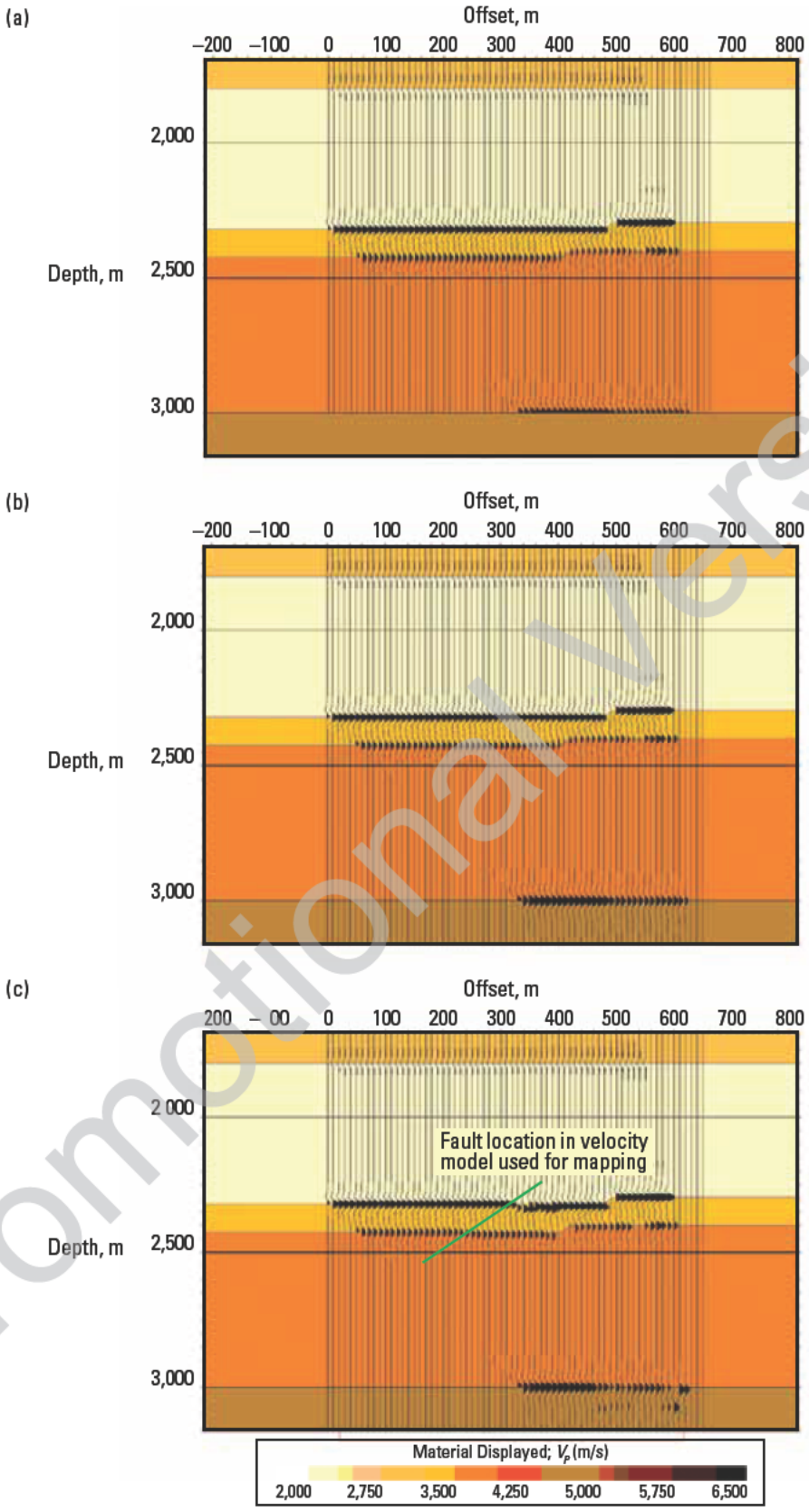

Figure 9-7. Comparison of offset images of a fault through VSP CDP mapping when using the exact velocity model (a), when using a flat velocity model from velocities at the well (b), or when using a velocity model with the fault 150 m closer to the borehole than it actually is (c).

9.4.3 Three-dimensional modeling

The computational and conceptual advantages of 2D visualization mean that many, possibly most, exploration problems are resolved into dip and strike direction components that are then considered as separate problems, each in two dimensions. Lack of absolute rigor is balanced by the conceptual simplicity and interpretation insights that result.

This may be too much of a simplification in many cases, as it is only in the dip direction in a pure 2½-dimensional case that 2D modeling is a correct approximation. Even in the strike direction, the reflection points do not lie vertically beneath the sources or receivers.

Some cases must be modeled with 3D tools, such as when dips have different azimuths at different horizons, when source and receiver are oblique to strike, or when the surface of interest is contorted in three dimensions. A few examples are illustrated in the subsequent sections (Figs. 9-8 to 9-18).

9.5 Zero-offset VSP

Even the simplest source and receiver geometries, such as the zero-offset VSP in a vertical well, may require 3D modeling to truly determine from where the reflections are coming. Figures 9-8 to 9-10 show 3D ray tracing results for a simplified model in which a reflector occurs below an irregular salt body. The array of receivers in the borehole is within the salt body, and the source is on the surface adjacent to the wellhead. It is the classic zero-offset VSP geometry. The ray tracing in Fig. 9-9 shows how the reflection points at the base of the salt and the dipping reflectors lie along completely different azimuthal directions from the well, separated by approximately 120°. Even though the vertical distance between reflectors is quite small, the reflection points are spatially well separated. Any 2D modeling would be unable to account for this in any quantitative manner. The third figure in the sequence, Fig. 9-10, shows some different representations and visualizations

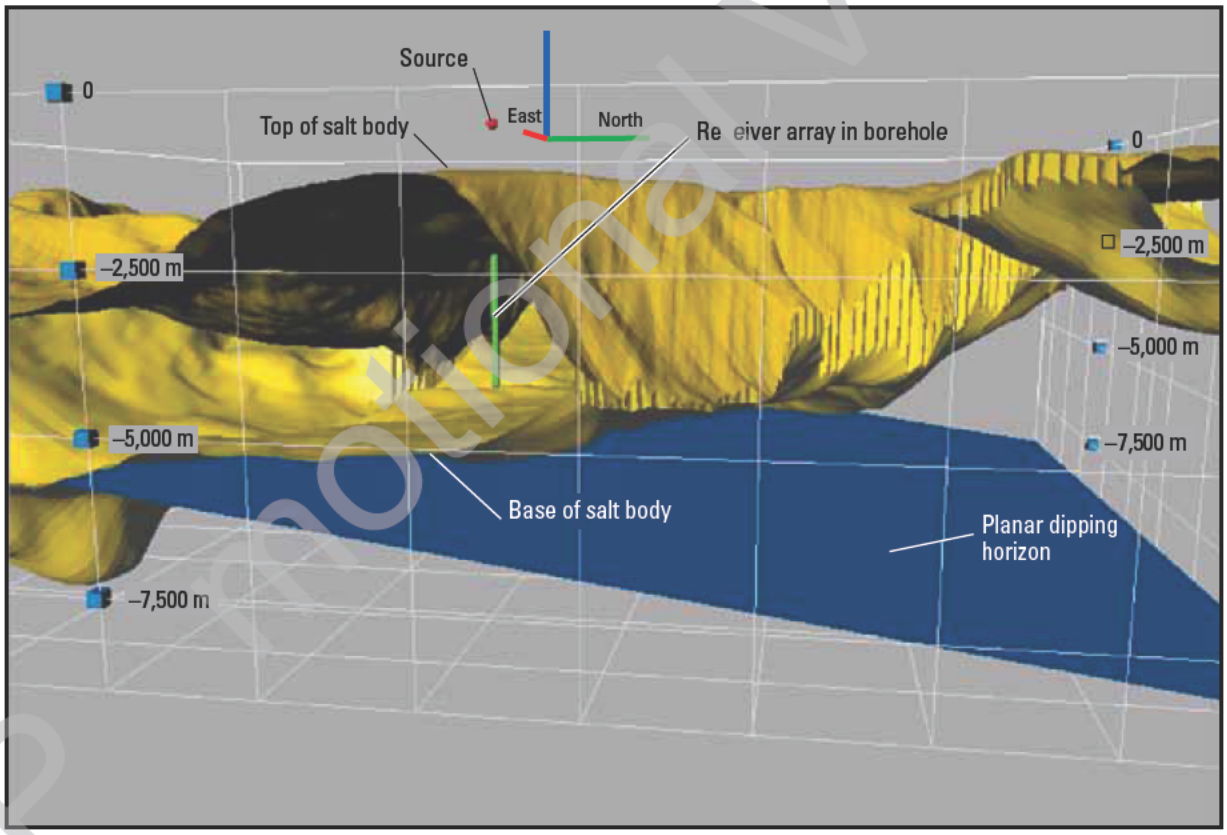

Figure 9-8. A 3D model of top and bottom of a salt body with an underlying planar dipping horizon. A vertical array of receivers is shown in green within the salt body. Same model is depicted in Figs. 9-9 through 9-16.

that follow the ray tracing. Figure 9-10a shows the reflection points at each interface, color-coded by the angle of incidence at the horizons, which vary from 0° to about 6°.

An alternative viewpoint through the model is shown in Fig. 9-10b to enhance the visualization of the reflection-point azimuths at the different horizons.

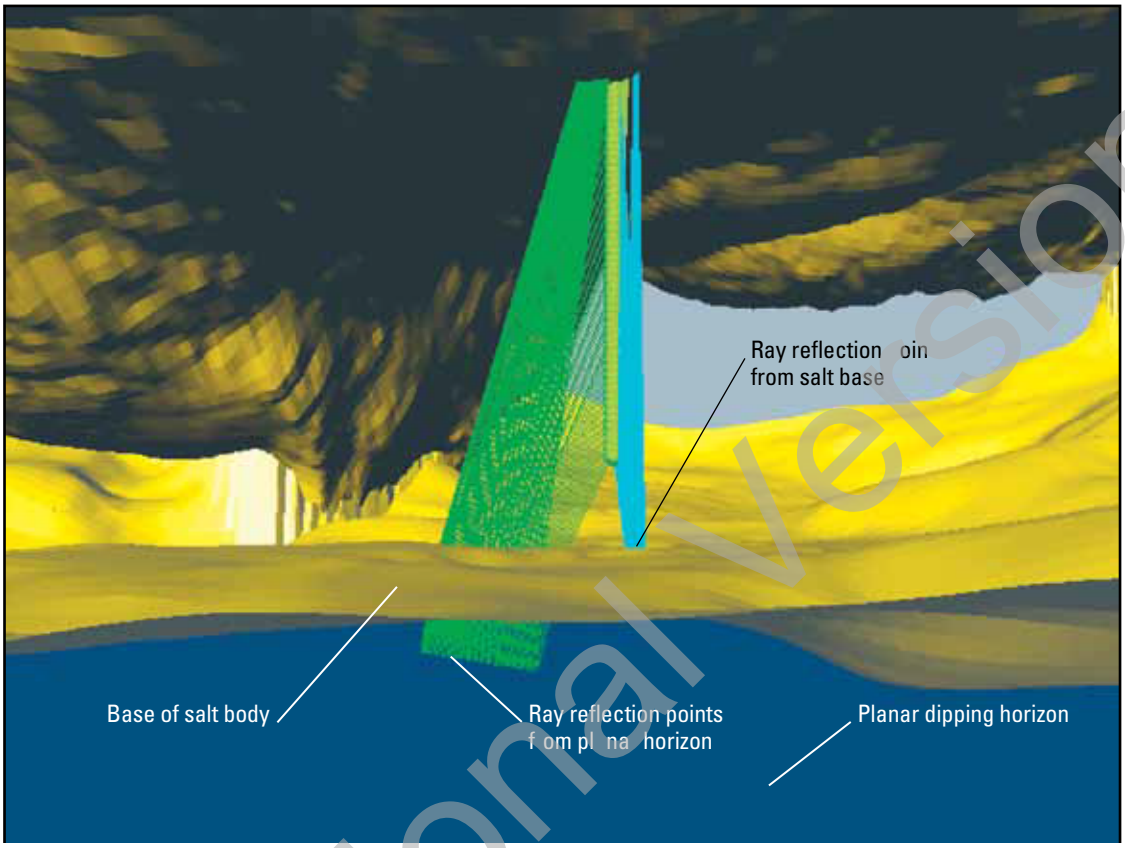

Figure 9-9. The 3D model of Fig. 9-8 showing rays, raced from a source on the surface adjacent to the wellhead, reflected into the array from differe horizo s at different azimuths and reflection-point offsets.

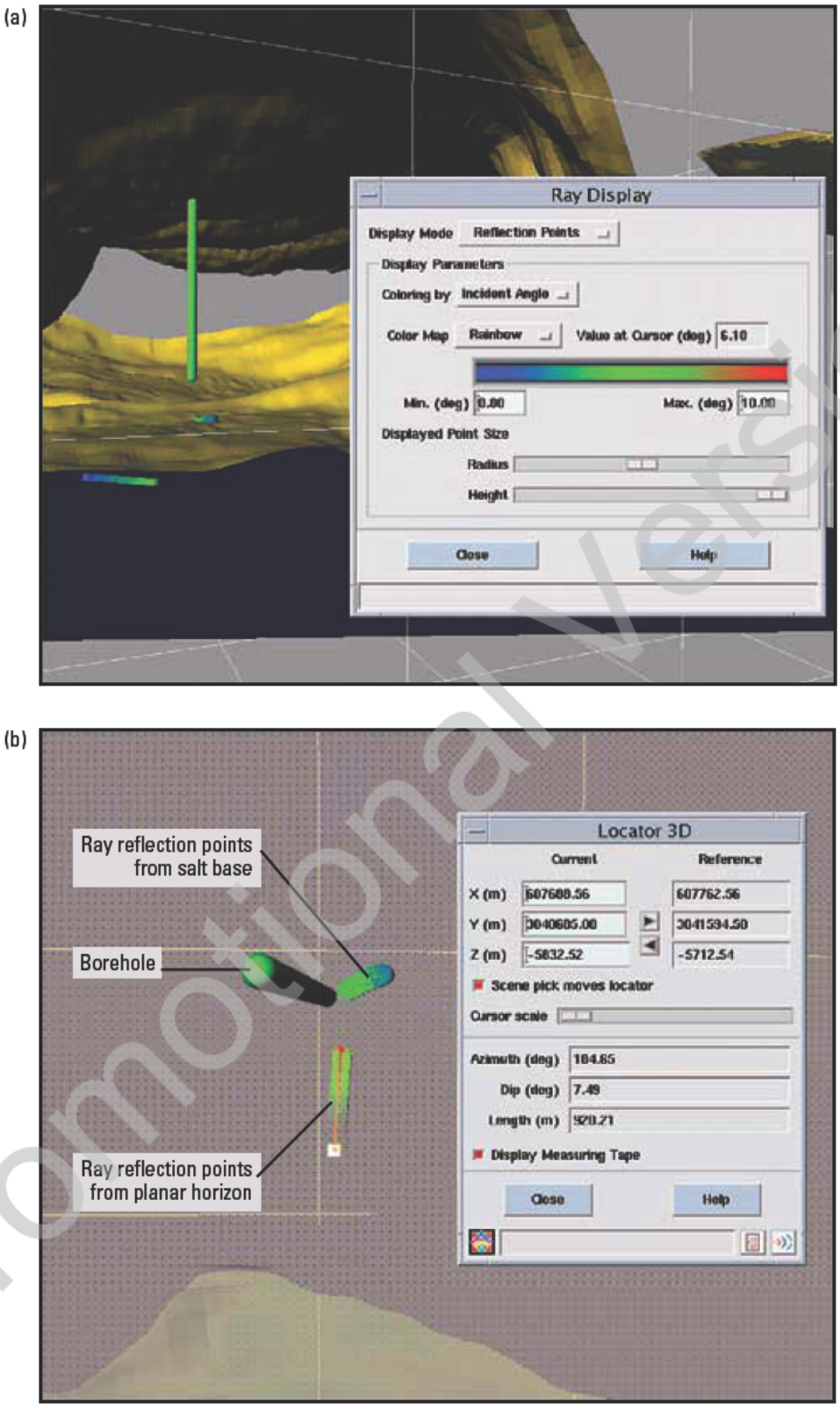

Figure 9-10. Alternative visualizations in 3D ray-trace modeling. In view (a), the 3D model in Fig. 9-8 is shown with reflection points displayed and coded by angle of incidence. A 3D perspective view from surface (b) shows the difference in the directions of coverage for the two horizons.

9.6 Tomographic velocity inversion survey design

The image of the subsurface derived from recorded seismic data is only as good as the knowledge of the velocity structure of the Earth. Borehole seismic data provides an excellent mechanism to calibrate subsurface velocities by inverting the traveltimes from source to receiver to give the velocity structure in the illuminated region. Unfortunately, the method contains an implicit concern—the very velocity field that one seeks to derive affects the paths the rays take between source and receiver through that field. If that velocity structure causes the raypaths to "miss" the rock volume under investigation, the desired velocity cannot be derived. The survey design presupposes some knowledge of the structure and stratigraphy under investigation. Multiple scenarios, usually no more than two or three, can illustrate the sensitivity of the survey objectives to the uncertainty of velocity knowledge.

3D modeling offers an opportunity to predict some of the effects of the velocity structure on the raypaths to optimize the source locations used for the experiment with respect to the anticipated velocity field. Rather than a trial-and-error approach to locate the sources, the reciprocity principle can be used by defining the target area and propagating rays from the receivers to that zone and then propagating them onto the surface containing the sources. Figure 9-11 shows the same model used in Fig. 9-10, but the problem in this case is to determine the surface source locations for obtaining useful coverage through the Earth to the receivers. The figure shows a 45° cone, with its apex at the receiver array a d a cone of rays shot within that 45° from the eceiver array to the surface. The emergence points of he rays at the surface do not coincide with circl drawn around the wellhead. A pattern of source points distributed over the emergence cone area would give co erage from 0 to 45° at the receivers.

Alternatively, the rays cou d be traced from surface locations to the receiver array (Fig. 9-12) and the emergence angles at the receiver can be determined.

Figure 9-11. 3D ray-trace model showing a 45° cone (maroon) from the receiver array to the surface and the actual raypaths (blue) with take-off angles within the cone. The emergence points at the surface are displaced from the straight-ray construction.

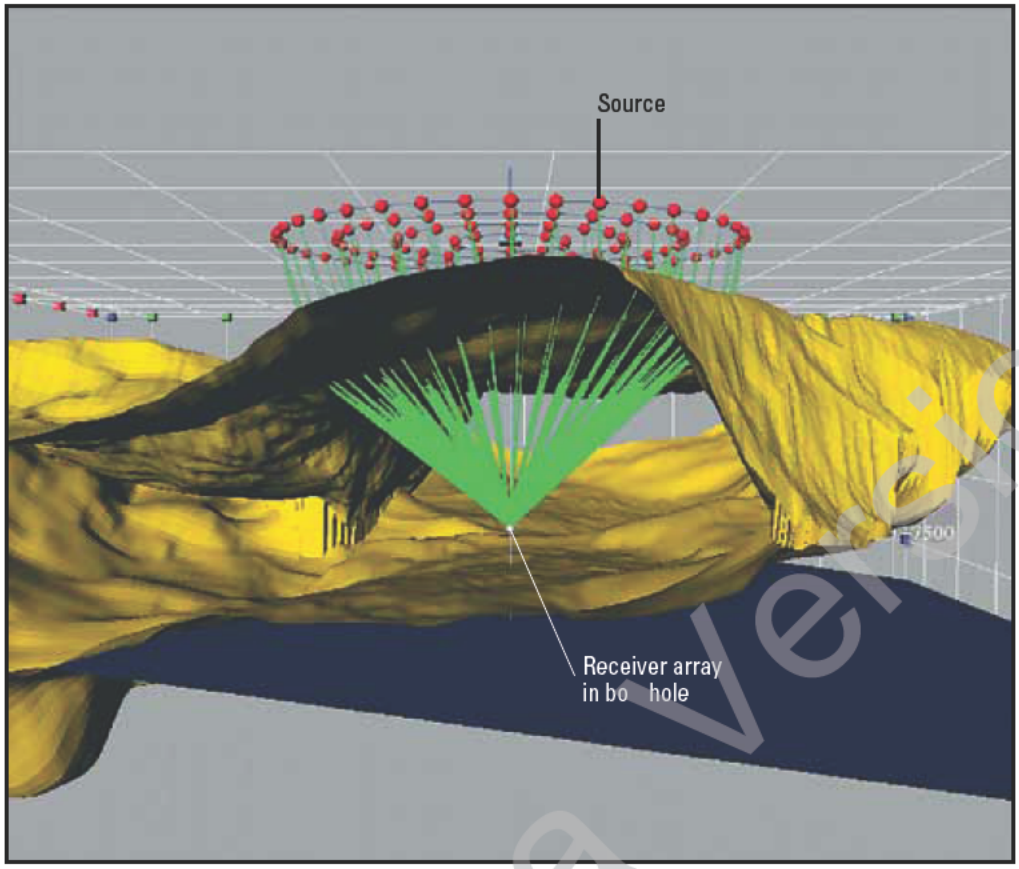

Figure 9-12. Alternative 3D ray-trace model showing rays shot from s rface sour e locations to the receiver array using point-to-point ray tracing.

9.7 Optimizing offset-VSP source locations

A similar approach to that described previous y can be taken to determine a suitable source location for an offset VSP designed for imaging reflec ors in the subsurface. From the receiver array, a cone of rays can be directed downward in the direction of the desired image, reflected at that reflector, and continued until they reach the surface of the Earth. The d nsity of emergent rays can be plotted on the surface. Figure 9-13 shows the cone of rays shot from the receiv r array The cone width can be adjusted in either horizonta direc ion. The density of rays emerging from the surface is shown in Fig. 9-14, and the source position can be planned to coincide at the position of highest density. This will be the source location that will give the greatest number of rays that will image the desired area in the subsurface. Figure 9-15 is the final ray tracing from the source to the receivers via the image points at the base salt and deeper planar reflector.

Figure 9-16 shows the modeling associated with a walkaway survey having two orthogonal source lines intersecting at the wellhead. The figure shows the rays traced to the target horizon and the reflection point locations at that level.

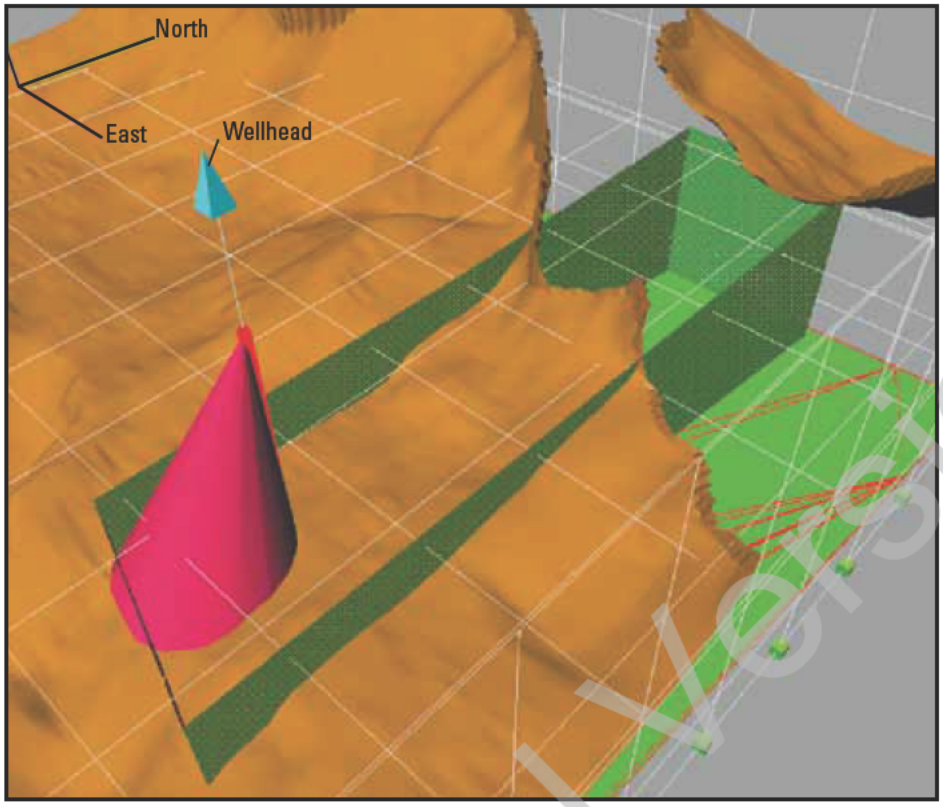

Figure 9-13. 3D ray-trace model with cone of reflected rays traced from he re eivers back to their reflection point in the desired imaging area beneath the salt. This technique may b used to optimize offset VSP source locations for imaging beneath salt.

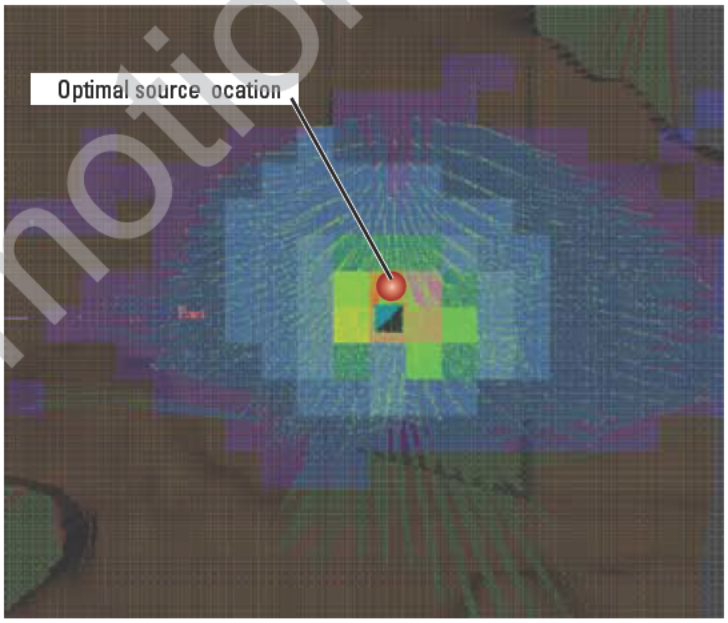

Figure 9-14. Map of the density of 3D-modeled rays traced from each receiver to points in the desired image area and then reflected and traced to the surface. The point of greatest density of emerging rays (marked by the red dot) is the source point that would generate the most rays illuminating the desired image area.

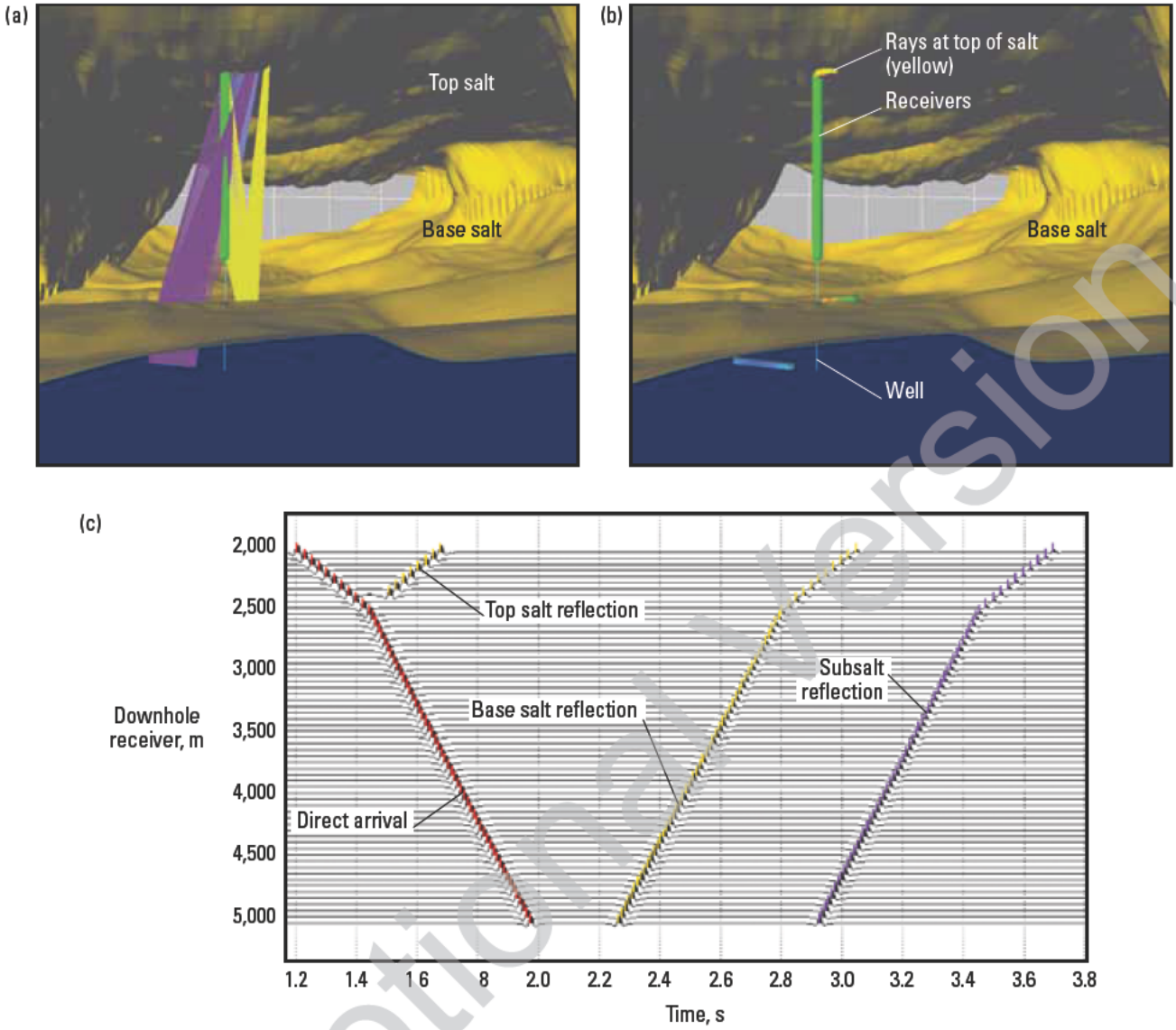

Figure 9-15. Modeling from source to receiver. The 3D final raypaths are traced from the chosen source location, to the reflectors, and the receivers (a). Notice that the coverage at the deepest reflector is on the opposite side of the well from the source location. The reflection points are displayed by their angle of incidence, low angle to high angle, respectively, and the range of colors: blue, green, red, and yellow. The rays traced are recorded on the synthetic seismic record (c).

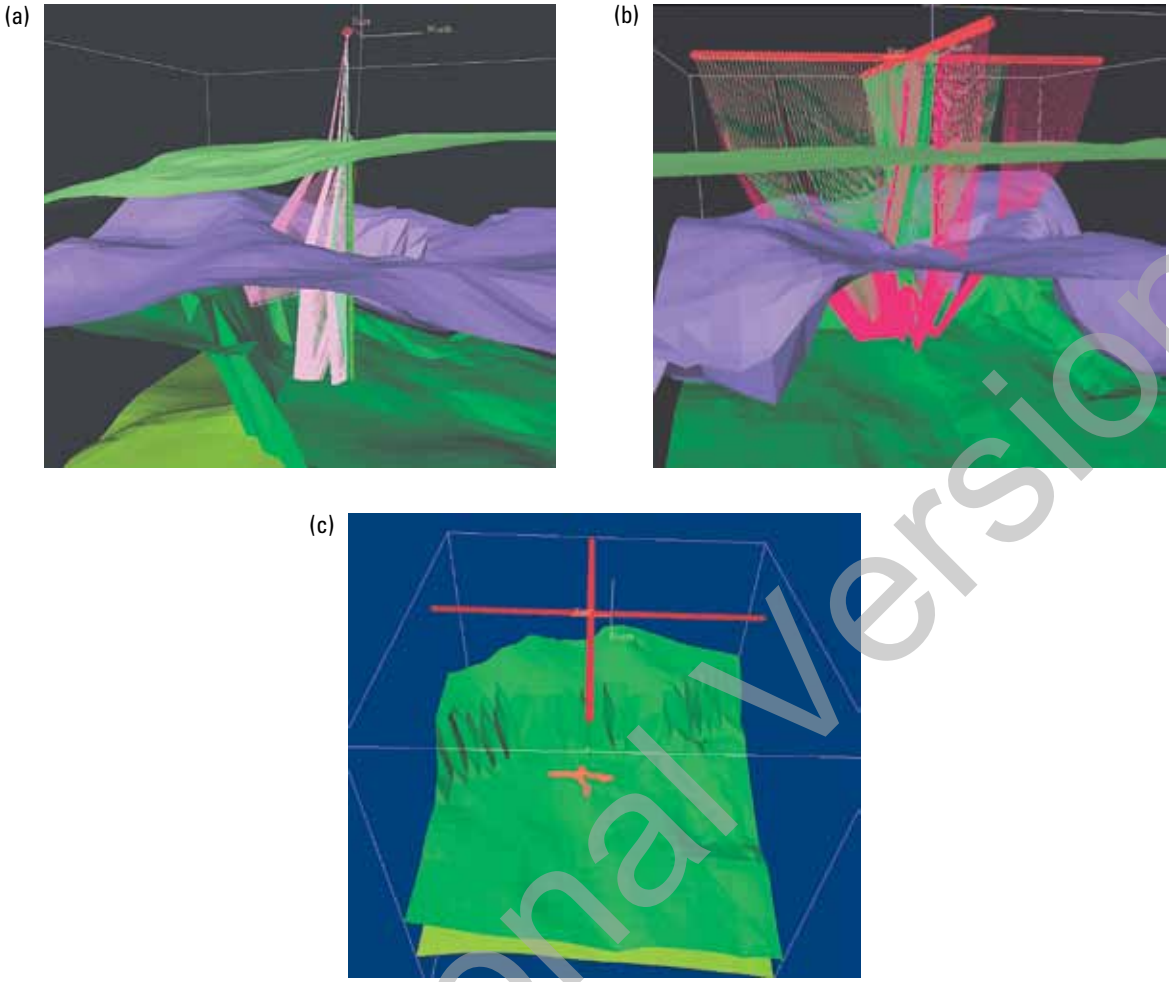

Figure 9-16. 3D ray-trace models of a walkaway survey: (a) ray tracing through a complex structural model from a near-wellhead source location, (b) simulation of two orthogonal walkaway lines to image at the deeper green horizon, and (c) reflection points from (b) observed from a slightly rotated viewpoint.

Another example is shown in Figure 9-17. Here the same deviated well is used to model three different survey types. The first is a walkabove VSP; the second, an AVO walkaway for either AVO calibration or anisotropy inversion; and the third is the coverage from an imaging walkaway. It is interesting to note in this scenario that the walkabove survey would probably provide more coverage under the wellbore than the walkaway survey geometry (although those reflected rays have not been traced in the figure).

Figure 9-18 shows an example of modeling a 3D VSP with source lines perpendicular to the receiver array in the deviated borehole.

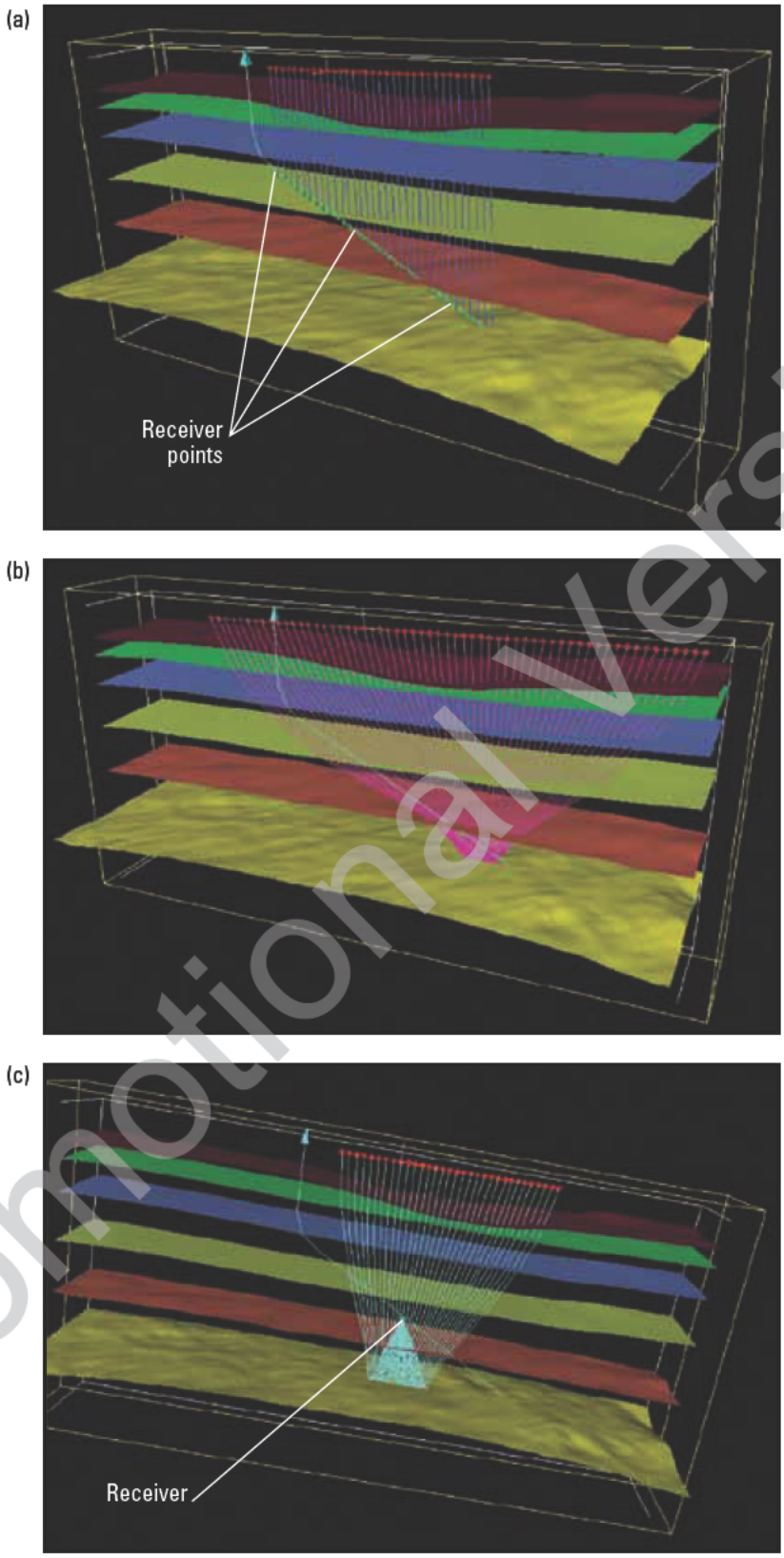

Figure 9-17. 3D ray-trace models of three types of surveys displayed for the same wellbore: (a) walkabove, (b) AVO walkaway, and (c) imaging walkaway.

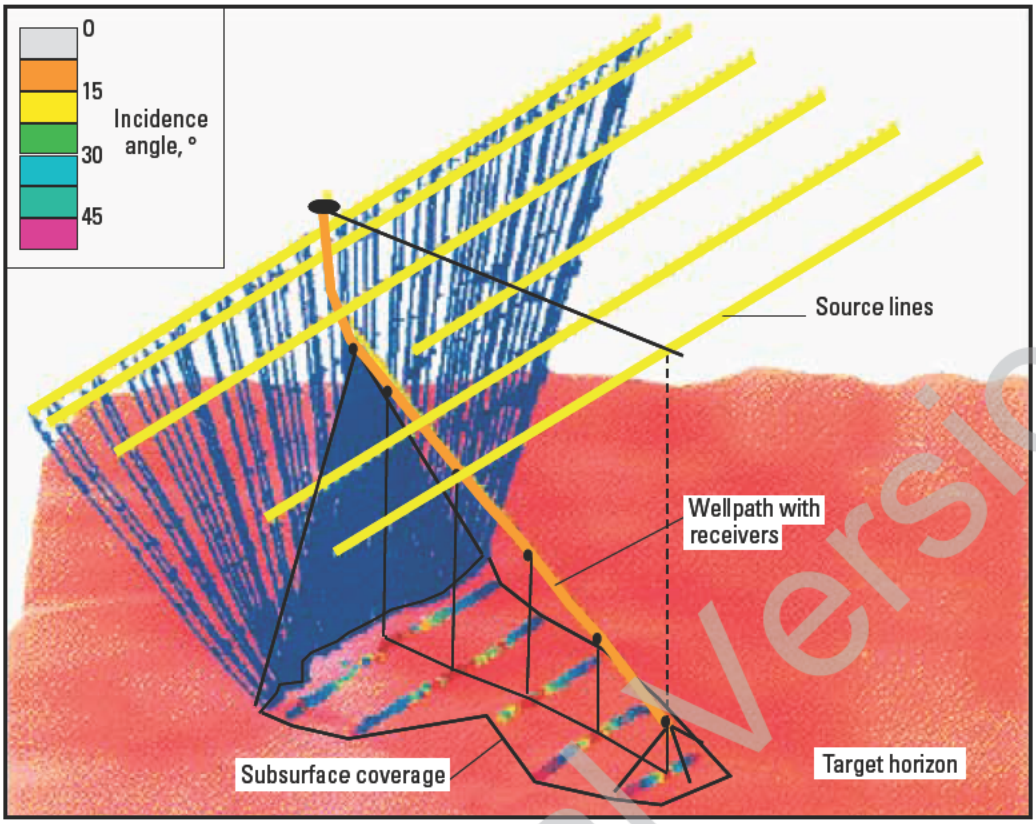

Figure 9-18. Ray-trace model of reflection points for a walkaway 3D VSP su vey with source lines perpendicular to the borehole trajectory.

9.8 Conclusions

Modern modeling techniques coupled with the speed of modern computers make it possible to simula e the full elastic response of quite heterogeneous Earth models. Full-waveform modeling can incorporate anisotropy, dispersion, and complex structure in simu ations that can be run within a manageable time frame. Given the availability of these tools, ther is litt e justification for not engaging in presurvey modeli g of borehole seismic surveys. A small expenditur before the survey can establish a fit-for-purpose desig which is critical to increase the success and hence value of the actual survey. Another benefit of modeling study is that negative modeling results an p event the wasting of valuable acquisition dollars on a program whose failure could have been pre icted. Taken one step further, the synthetic wavefields from the modeling can be used to prescribe proper processing flows, especially in complex environments in which standard workflows and rules of thumb collapse.

It does not automatically follow that the appropriate approach to a modeling problem is to always use the most sophisticated software, the largest sledgehammer. Modeling should be aimed at answering specific questions and, by doing so, gaining insight into the processes connecting impulse and response. The secret to effective modeling is to use enough complexity to answer the questions but no more than is required by the problem.

9.9 References

Coulombe, C., and Bird, D.: "Transmission Filtering by High-Amplitude Reflection Coefficients: Theory, Practice, and Processing Considerations," *The Leading Edge* (1996) 15, No. 9, 1037–1042.

O'Doherty, R.F., and Anstey, N.A.: "Reflections on Amplitudes," *Geophysical Prospecting* (1971) 19, No. 3, 430–458.

Ziolkowski, A., and Fokkema, J.T.: "Tutorial on the Progressive Attenuation of High-Frequency Energy in Seismic Reflection Data," *Geophysical Prospecting* (1986) 34, No. 7, 981–1001.

Symbols

Roman symbols

a	angle of incidence
A	amplitude
A_i	amplitude of downgoing wave
A_r	amplitude of reflected wave
A_0	initial amplitude
A_1	amplitude at point 1
A_2	amplitude at point 2
b	angle of reflection
b	coefficient
b	velocity gradient
c	Hottman-Johnson coefficient
$c(f)$	phase velocity at a frequency f
c_{11}, c_{13}, c_{33}, c_{55},	elastic stiffness parameters
d	Hottman-Johnson coefficient
D	differential slowness (observed – normal slowness)
D	distance; depth
D_{target}	depth of target
E	energy in a wave
E_1	Energy at point 1
E_2	Energy at point 2
f	frequency
$f_{\max}$	maximum frequency
$f_{\min}$	minimum frequency
f_1	first frequency value
f_2	second frequency value
F_{notch}	frequency of signature with n notches caused by ghost interference
G	proportionality factor in drift correction
i	angle of incident wave
n	a number (quantity; 0, 1, 2, 3, …)
N	number of first-order multiples
O	offset of source
p	slowness
p_x	horizontal slowness
P	primary or compressional wave
P_P	downgoing P wave reflected as upgoing P-wave
P_S	downgoing P-wave reflected as upgoing S-wave
Q	quality factor
Q	P-wave quality factor
Q_S	S-wave quality factor
r	angle of refraction
r	distance
r_1	distance at point 1
r_2	distance at point 2
R	reflection coefficient
$R(t)$	reflectivity
R_{PP}	P-wave reflection coefficient
S	secondary or shear wave
$S_{SS}(t)$	seismic trace in surface seismic
$S_{\text{VSP}}(t)$	seismic trace in VSP data
t	traveltime
$t_{\text{accelerometer}}$	seismic traveltime to the accelerometer
t_{array}	seismic traveltime to the array
$t_{\text{drillstring}}$	seismic traveltime along the drillstring
t_{ghost}	traveltime of reflected pulse (ghost)
t_P	arrival time for P-wave
t_S	arrival time for S-wave

t_1	traveltime at point 1
t_2	traveltime at point 2
t_{2-1}	arrival time difference between geophones 2 and 1
V	velocity
$V_{\text{drillpipe}}$	velocity along the drillpipe
V_H	horizontal velocity
V_{int}	interval velocity
V_{nmo}	normal moveout velocity
V_P	P-wave velocity
V_S	S-wave velocity
V_{slip}	slip velocity
V_V	vertical velocity
V_{water}	velocity in water
V_0	initial velocity
V_1	velocity of first medium encountered
V_2	velocity of second medium encountered
$w_{SS}(t)$	wavelet in surface seismic data
$w_{\text{VSP}}(t)$	wavelet in VSP data
x_{image}	image extent
z	depth
z_{geo}	depth of geophone
z_1	depth at point 1
z_2	depth at point 2
Z	acoustic impedance
Z_1	acoustic impedance of layer above interface
Z_2	acoustic impedance of layer below interface

Greek symbols

γ	Thomsen parameter: difference in the horizontal and vertical propagation velocities for SH-waves
δ	Thomsen anisotropy parameter for SV-waves
ΔP	change in pressure
Δt	difference in traveltime
Δt_{corr}	adjusted change in traveltime
Δt_{corr1}	adjusted change in traveltime at point 1
Δt_{corr2}	adjusted change in traveltime at point 2
Δt_{ds}	traveltime through the drillstring
Δt_f	traveltime through the formation
Δt_{min}	minimum threshold slowness value
$\Delta t_{\text{seismic}}$	change in traveltime derived from seismic data
Δt_{sonic}	change in traveltime derived from sonic log data
Δt_1	traveltime at point 1
Δt_2	traveltime at point 2
Δx	change in horizontal separation between two points
Δz	change in depth
ε	Thomsen parameter: difference between the horizontal and vertical propagation velocities for P-waves
η	nonhyperbolic or anellipticity parameter
ρ	density
σ	anisotropy of SV-waves
ϕ	phase
φ_{CC}	phase spectrum of crosscorrelated trace
φ_R	phase spectrum of the reflectivity
$\varphi_{w_{SS}}$	phase spectrum of surface seismic wavelet
$\varphi_{w_{\text{VSP}}}$	phase spectrum of VSP wavelet

Latin symbols

$Ø_{ds}$	drillstring path distance (drillbit VSP survey)
$Ø_f$	formation path distance (drillbit VSP survey)

Nomenclature

1D	one-dimensional
2D	two-dimensional
3C	three-component
3D	three-dimensional
4D	four-dimensional
AI	acoustic impedance
ALARP	as low as reasonably practical
AVA	amplitude variation with angle of incidence
AVO	amplitude vaariation with offset
AVOAZ	amplitude variation with offset and azimuth
BARS	borehole acoustic reflection survey
BHA	bottomhole assembly
CCL	casing collar locator
CDP	common depth point
CMP	common midpoint
E&P	exploration and production
GAC	geophone accelerometer
GOC	gas/oil contact
GPS	global positioning system
GR	gamma ray
GRT	generaliz d Radon transform
HFVS	High Fid lity Vibratory Seismic
HSE	hea th, saf ty, and environment
HTI	orizontal transverse isotropy
WD	logging-while-drilling
MD	measured depth
MEM	microelectromechanical
MWD	measurement-while-drilling
NMO	normal moveout
OBC	ocean-bottom cable
OD	outside diameter
PBR	primary-to-bubble ratio
PDC	polycrystalline di m nd compact
ppg	pore pressure gradient
PSDM	presta k depth mighration
P-wave	pr mary wave (compressional wave)
QC	qual ty control
QHSE	quality, health, safety, and environment
QMS	Quality Management System
rm	root-mean-square
ROV	remote-operated vehicle
RTM	reverse time migration
SAF	San Andreas fault
SH-wave	horizontal shear wave
SNR	signal-to-noise ratio
SV-wave	vertical shear wave
S-wave	shear wave
TD	total depth
TDT	thermal decay time
TI	transversely isotropic, transverse isotropy
TSS	transmitting seismic source
USD	United States dollars
VSP	vertical seismic profile
VTI	vertical transverse isotropy
WEM	wave-equation migration

SI Metric Conversion Factors

atm	×	1.013 250†	E+05 = Pa
bar	×	1.0†	E+05 = Pa
bbl	×	1.589 873	E–01 = m^3
ft	×	3.048†	E–01 = m
degF		(degF – 32)/1.8	= degC
gal	×	3.785 412	E–03 = m^3
in	×	2.54†	E+00 = cm
in^3	×	1.638 706	E–05 = m^3
L	×	1	E–03 = m^3
lbf	×	4.448 222	E+00 = N
lbm	×	4.535 924	E–01 = kg
lbm/ft^3	×	1.601 846	E–02 = g/cm^3
lbm/bbl	×	2.853	E+00 = kg/m^3
lbm/galUS	×	1.198	E+02 = kg/m^3
lbm/galUS	×	1.198	E–01 = kg/L
mile	×	1.609 344†	E+00 = km
psi	×	6.894 757	E+03 = Pa
sq mile	×	2.589 988	E+00 = km^2

† Conversion factor is exact.

Index

Note: Page numbers in *italic type* refer to illustrations.
Page numbers followed by a "t" refer to tables in the text.

C

D

E

F

G

H

I

K

L

M

N

O

P

Q

R

S

T

U

V

W

Y

Z

09-FE-0001

ISBN-13: 978-097885307-5
ISBN-10: 097885307-5

90000
9 780978 853075

Schlumberger